SYNTHESIS AND BIOLOGICAL INTERACTIONS OF RUTHENIUM SUPRAMOLECULAR ASSEMBLIES

Kate L. Flint

A thesis presented to The School of Physical Sciences at the University of Adelaide in fulfilment of the requirements for the degree of Doctor of Philosophy

November, 2021

Department of Chemistry
The University of Adelaide
North Terrace Campus
Adelaide, South Australia 5005

Supervisors:

Em. Prof. F. Richard Keene

Prof. Christopher J. Sumby

Contents

Abstract

The use of ruthenium-containing compounds in biological settings has been widely explored, showing efficacy for a broad range of applications. The geometry of Ru(II) and Ru(III) is octahedral, and through judicious ligand design a variety of supramolecular architectures can be accessed. These topologies can give rise to highly selective binding to biological targets, particularly sequence-specific interactions with DNA. Ruthenium helicates are a largely unexplored class of compounds. Whilst exhibiting anti-cancer, or anti-bacterial activity, the manner of their interaction with DNA is less well understood.

This thesis describes the synthesis of a series of ruthenium(II) compounds, with a primary focus on dinuclear double- and triple-stranded helicates. For many compounds, concurrent formation of the rare mesocate isomer was also observed. Separation of these isomers, and chiral resolution of the helicates allowed study of potential stereoselective interactions with DNA.

Chapter 1 introduces the great structural variety of metallohelicates, illustrating the importance of chirality which can be influenced synthetically, or in cases where the achiral mesocate is formed, avoided all together. The stereoselectivity of metallosupramolecular assemblies can result in crucial differences in the strength and nature of biological interactions. Hence, there is potential for the optimisation of DNA binding through the design of chiral compounds.

Chapter 2 presents the synthesis of a double-stranded helicate and mesocate pair, incorporating a di(terpyridine) ligand. Herein, the product distribution was probed, and interestingly, the two compounds showed significant differences in structural flexibility and photophysical properties. Finally, partial resolution of the helicate enantiomers was achieved chromatographically.

Chapter 3 explores biological interactions of the double-stranded compounds synthesised and resolved in Chapter 2. DNA binding was screened by dialysis and linear dichroism experiments, and while all compounds were found to interact with DNA, no clear enantiomeric preference was observed. Binding selectivity with three oligonucleotide sequences was studied by NMR experiments, identifying that all double-stranded compounds bound weakly in the minor groove. Some precipitation was observed in all cases upon mixing the compounds with DNA, which limited further studies.

Chapter 4 presents the synthesis of triple-stranded diruthenium(II) compounds, probing the product distribution upon modification of a ligand containing a flexible spacer. By using a relatively inert metal centre mesocate/helicate pairs were accessed, breaking the odd/even rules of dinuclear compound formation that are observed for more labile metals. The resolution and isomeric separation of some of these compounds is reported, as well as interesting photoisomerisation for compounds containing an *n*-propyl spacer ligand. Biological studies were also undertaken for many of the triple-stranded species, with weak, non-selective interactions found with DNA.

Finally, in **Chapter 5**, the synthesis of larger architectures containing Ru(II) metal centres was attempted. $[RuL_3]^{2+}$ building blocks and $[Ru_8L_{12}]^{16+}$ cubes were designed, incorporating ligands with variable steric bulk. Product distribution varied greatly depending on reaction conditions. For some ligands, $[RuL_3]^{2+}$ building blocks were formed, whilst sterically-hindered ligands potentially favoured larger assemblies. Preliminary studies suggested that ligand design may influence product distribution, but synthetic conditions are also a key factor, paving the way for further investigation.

Declaration

I certify that this work contains no material which has been accepted for the award of any other degree or diploma in my name, in any university or other tertiary institution and, to the best of my knowledge and belief, contains no material previously published or written by another person, except where due reference has been made in the text. In addition, I certify that no part of this work will, in the future, be used in a submission in my name, for any other degree or diploma in any university or other tertiary institution without the prior approval of the University of Adelaide and where applicable, any partner institution responsible for the joint-award of this degree.

I give permission for the digital version of the thesis to be made available on the web, via the University's digital research repository, the Library Search and also through web search engines, unless permission has been granted by the University to restrict access for a period of time.

I acknowledge the support I have received for my research through the provision of an Australian Government Research Training Program Scholarship.

Kate Flint

November 2021

Acknowledgements

I would like to express my sincere appreciation to my supervisors Em. Prof. Richard Keene and Prof. Christopher Sumby for their patience and perseverance. Thank you for the many opportunities you have given me throughout my PhD, and the countless hours put into preparing this thesis. The guidance and knowledge that you have shared during the course of my candidature has been of immeasurable valuable and I will be forever grateful.

It is my pleasure to acknowledge the many other researchers who have contributed to this project.

A huge thank you must go to Prof. Grant Collins whose expertise and enthusiasm was instrumental in tackling many of the NMR studies in this thesis. Even though I only made it to Canberra once, you have been an amazing unofficial supervisor via emails and Zoom, and I am grateful to you and Julie for looking after me so well during my visit.

I would like to extend thanks to Prof. Trevor Smith and Dr. Siobhan Bradley for their willingness to assist with the emission spectroscopy experiments throughout the course of this project. Many thanks are also due to A/Prof. David Huang, who had the courage to let me have a go at computational chemistry, and provided much useful advice and assistance. I am also grateful to Prof. Janice Aldrich-Wright and Dr. Dale Ang for their expertise and providing me with the opportunity to visit WSU for LD studies. In addition, I extend a warm thank you to A/Prof Tara Pukala and Dr. Blagojce Jovcevski for their assistance with mass spectrometry. Finally, I wish to thank Dr. Marie Squire for her contribution to the mass spectrometry measurements in the early stages of my project.

Many thanks are due to Matthew Bull for single-handedly resurrecting the CD spectrophotometer, without which my project would have been much more challenging. In addition, I am grateful for all of the technical support, fixing of instruments, and great advice he has provided me over the course of my PhD. I would also like to thank Phil Clements whose assistance with NMR studies has been invaluable.

I would like to extend my gratitude to the past and present members of the Sumby-Doonan Group, as well as the wider Chemistry department. In particular, thanks must go to Dr. Alexandre Burgun who was enormously helpful during the early stages of my project. To all the chemists on Level 1 of the Badger Building, I am incredibly grateful for all

the chats, snacks, and impromptu gardening that helped me get through my candidature. Thanks must especially go to the occupants of Lab 4 and Prof. Hugh Harris for allowing me to use all of your fume cupboards.

A big thank you to all my of friends (both inside and outside chemistry) for their support over the years. Special thanks to Andrew, who has always been there with excellent advice even from the other side of the world. To Natasha and Oliver, I will forever be grateful for the friendship and support that you have shown me, there's no-one else I would rather have shared this journey with.

Last of all, but not least, I would like to express a very special thank you to my family for all of their love and support. In particular, I would like to thank my parents and sister, Claire, who have always been filled with enthusiasm for whatever I was doing. Finally, to my partner Angelo, without your patience and kindness I would not have made it to the end and I can't wait to see what the future holds.

I wish to acknowledge and pay respect to Aboriginal people past and present as the traditional owners of the land on which I conducted this research, namely the Kaurna people of the Adelaide Plains, whose ancestral lands the University of Adelaide is built upon.

Abbreviations

A adenine

bpm 2,2′-bipyrimidine

bpy 2,2′-bipyridine

C cytosine

CD circular dichroism

cisplatin *cis*-diamminedichloroplatinum

CLSR chiral lanthanide shift reagents

ct-DNA calf thymus DNA

DCM dichloromethane

DFT density functional theory

DMF dimethylformamide

DNA deoxyribonucleic acid

DOSY diffusion-ordered spectroscopy

EDTA ethylenediaminetetraacetic acid

EDX energy-dispersive X-ray spectroscopy

EtOAc ethyl acetate

EtOH ethanol

Eu(tfc)$_3$ europium tris[3-(trifluoromethylhydroxymethylene)-(+)-camphorate]

FID free induction decay

G guanine

HR ESI-MS high resolution electrospray ionisation mass spectrometry

HSQC heteronuclear single quantum correlation

$\boldsymbol{k_n}$ non radiative rate constant

$\boldsymbol{k_p}$ radiative rate constant

LD linear dichroism

LDA lithium diisopropylamide

MeOH methanol

MLCT metal ligand charge transfer

MOC metal-organic cage

MOF metal-organic framework

NMR nuclear magnetic resonance

NOE nuclear overhauser effect

NOESY nuclear overhauser effect spectroscopy

$\boldsymbol{\tau_p}$ phosphorescence lifetime

phen 1,10-phenanthroline

qpy quinquepyridine

RNA ribonucleic acid

ROESY rotating-frame overhauser effect spectroscopy

SCXRD single crystal X-ray diffraction

SEM scanning electron microscopy

T thymine

THF tetrahydrofuran

TLC thin layer chromatography

TMS-acetylene trimethylsilyl-acetylene

tpy 2:2′,6′:6″-terpyridine

TRISPHAT Δ-tris(tetrachloro-1,2-benzenediolato)phosphate(V)

UV ultraviolet

UV-Vis ultraviolet-visible

CHAPTER 1

Introduction

1.1 Supramolecular Chemistry

Supramolecular chemistry involves the self-assembly of smaller molecular subunits into larger chemical species via weak intermolecular forces. Early work by Pedersen,[1] Lehn,[2] and Cram,[3] led to the discovery of crown ethers, cryptands, and spherands, for which they were awarded the Nobel Prize in Chemistry in 1987. In this previous work the ability for small complementary molecules to interact by hydrogen bonding, ion-ion/ion-dipole/dipole-dipole, donor-acceptor, π-π, van der Waals, and other noncovalent interactions was demonstrated. Examples of these interactions appear widely in nature, being evident in the structures of complex biological macromolecules, such as deoxyribonucleic acid (DNA), proteins, and micelles.

Within this broad heading lies the field of metallosupramolecular chemistry, where the intermolecular forces assembling structures are characterised by metal-to-ligand coordination interactions. Metal-ligand interactions are highly directional allowing a designable approach to the synthesis of unique assemblies where structural, chemical, and physical properties can be controlled. Assemblies of this type can range from extended polymers to discrete structural units. Of particular interest are discrete assemblies such as metallocycles,[4–7] metallohelicates,[8–11] and metal-organic cages, which can come in many forms, such as tetrahedra,[12–17] cubes,[18,19] or other polyhedra.[20–25] Interest in coordination cages has extended beyond novel structural design, and functionality for catalysis,[26–28] drug-release,[29–31] molecular separation,[32–34] and sensing[35–37] have been widely explored. Supramolecular structures can also have dynamic properties, as in the case of rotaxanes and catenanes, which led to the development of molecular machines, for which Stoddart, Sauvage, and Feringa were awarded the Nobel Prize in Chemistry in 2016.[38–41] Finally, metal-ligand interactions can result in the formation of polymeric structures called coordination polymers. A subset of these materials, metal-organic frameworks (MOFs), are two- or three-dimensional structures which extend infinitely and often have large pore volumes and high surface areas, making them attractive materials for use in catalysis,[42] gas sorption,[43] and molecular separations.[44]

As demonstrated by the wide variety of metallosupramolecular species described above, careful selection and design of components can influence the metal-ligand interactions present, and thus lead to a plethora of possible chemical products, some examples are illustrated below in Figure 1.1.

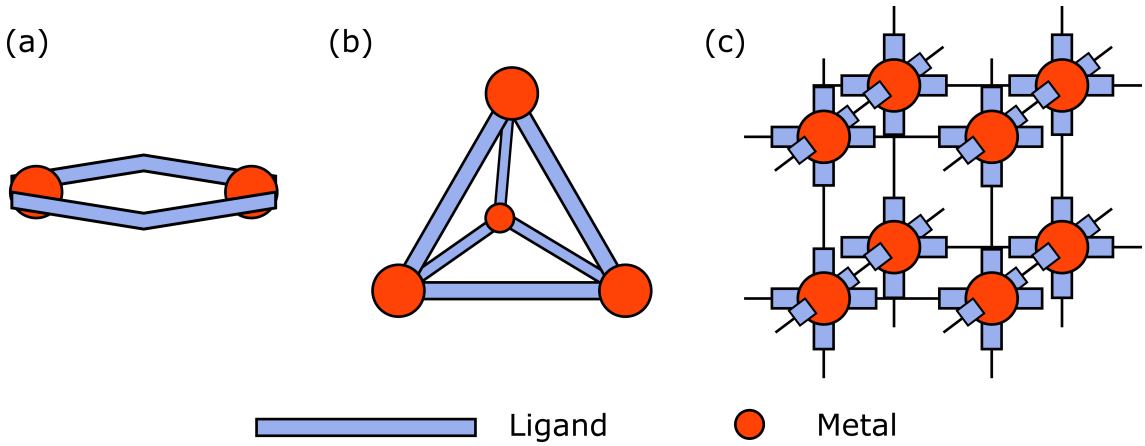

Figure 1.1: Schematic representations of various possible structures resulting from metal-ligand interactions, including an (a) M_2L_2 metallohelicate, (b) M_4L_6 tetrahedron, (c) MOF.

The key advantage of utilising metal-ligand interactions in the synthesis of metallosupramolecular assemblies is the ability to control the design and topology of the final product, through judicious choice of metal and ligand combination. The use of metal ions allows a wide range of geometries to be accessed, with metal centres having coordination numbers from two to eight, or higher. Geometry of the metal centre will vary based on the number and type of ligands involved, as well as the coordination preference of the metal ion. By exploiting this coordination preference different metallosupramolecular species can be accessed. For example, Pd(II) and Pt(II) prefer a square planar geometry, while four-coordinate d^{10} ions (Cu^+ and Zn^{2+}) favour tetrahedral geometries. Many other transition metals are six-coordinate, forming assemblies based on an octahedral motif. It should be noted that these general rules are often able to be broken, and more unusual metal geometries accessed.

Ligand design also plays a key role in the formation of supramolecular assemblies. The complexity of the final structure can be greatly influenced by changing the number and identity of donor groups, which often include nitrogen-containing heterocycles and carboxylates. Additionally, the distance and angle of separation of these donor groups and overall flexibility of the ligand are crucial considerations.

In concert, the choice of metal ion and ligand greatly influence the nature of the metallosupramolecular structure formed, and specifically whether a polymeric or discrete assembly is favoured. Convergent components, such as silver(I) and copper(I), tend to form polymeric structures, while divergent components, such as palladium(II) and ruthenium(II), favour the formation of discrete metal-containing compounds. Ruthenium(II), which has octahedral geometry, was used extensively in the synthesis of discrete metallosupramolecular assemblies throughout this project, as will be further discussed in this thesis. Of particular

interest are discrete assemblies utilising multiple octahedral metal centres to form dimetallic or larger species, with functionality being added through the inherent chirality of such molecules.

1.2 Metallohelicates

The expression 'helicate' was first introduced by Lehn *et. al.* in 1987 to describe a metal-containing species, comprised of copper ions linked by oligo(bpy) ligands (bpy = 2,2′-bipyridine), where the twisting of the ligands around the metal centres showed a helical motif.[45] However, this is not the earliest report of a structure of this type in the literature, with helical iron and nickel compounds being reported by Stratton and Busch in 1958.[46] Metallohelicates, composed of flexible ligands coiled around metal ions to form helical structures, have since been widely explored in the literature, employing transition metals and more recently lanthanides as the metal centres.[47–50]

The structure of metallohelicates is greatly dependent on the geometry of the metal centre, as well as the denticity of the ligand. Lutzen *et. al.* synthesised metallohelicates using a di(bpy) ligand, and found that by altering the metal ion a range of helical structures could be generated.[51] Using silver(I) and copper(I) with four-coordinate geometry, double-stranded metallohelicates were formed, whereas by employing iron(II) and zinc(II) as six-coordinate building blocks, triple-stranded structures could be generated.

Metallohelicate structure can be defined in terms of the number and type of ligand strands, and the metal node. In the case of Lutzen *et. al.*, double- and triple-stranded species were formed depending on the geometry of the metal centre. For these molecules the di(bpy) ligand has bidentate coordination sites, so product formation was directed by the metal ion. The design of the ligand can be tuned to suit a particular coordination environment. For example, ligands containing tridentate coordination sites have been used for the synthesis of double-stranded helicates when combined with octahedral metal centres, including Cu(II), Co(II), Fe(II), and Zn(II).[52–54] Additionally, Chen *et. al.* have reported the synthesis of quadruple-stranded tetranuclear helicates with lanthanides, with each ligand being tetradentate.[55] A schematic representation of possible metallohelicate structures is shown in Figure 1.2; it should be noted that in all cases the nature of the ligand and metal centre can be modified to access a wide range of species.

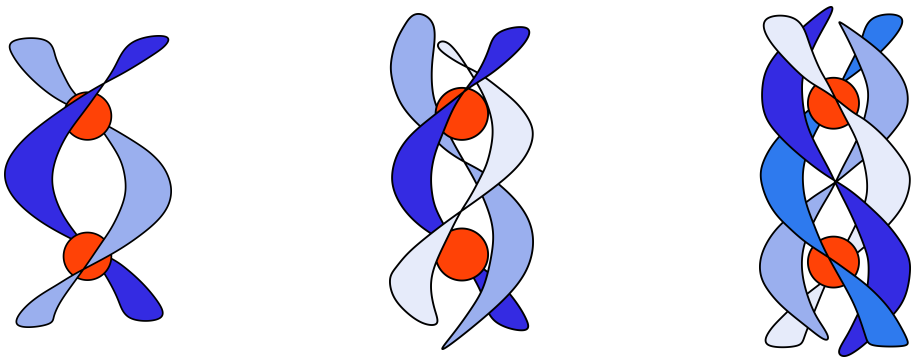

Figure 1.2: Variety in metallohelicate structure, showing possible double-, triple-, and quadruple-stranded species.

While dinuclear helicates are the most widely found in the literature there are reports of extended helical structures. A tetranuclear copper helicate was reported by Furusho *et. al.* in 2011, where Cu(I) metal centres were coordinated to bpy-based ligands containing four bidentate coordination sites to form a double helix.[56] Circular helicates are also possible, where the bridging ligand wraps around metal ions that are arranged in a cyclic pattern.[57–59] Furthermore, metallohelicates can be constructed from multiple different ligands to form hetero-stranded structures. This was demonstrated by Hasenknopf *et. al.*, where a trinuclear hetero-double-stranded copper helicate containing pentacoordinated copper ions was formed from a mixture of bpy and tpy (tpy = 2:2′,6′:6″-terpyridine) containing ligands.[60]

1.2.1 Chirality

Helicates are fundamentally chiral – either being right-handed (plus, P) or left-handed (minus, M) and the ability to separate these chiral forms from a racemic mixture is crucial (see Figure 1.3). The use of achiral ligands generally leads to the formation of racemic mixtures, although Scott and co-workers have shown that stereochemically-pure compounds can be generated by linking enantiomerically-pure monometallic precursors which retain their initial stereochemistries, allowing for a modular synthesis.[61] Inclusion of chiral ligands can also influence the overall stereochemistry, as was shown by Constable *et. al.* where use of a chiral quarterpyridine ligand resulted in production of one helicate enantiomer when coordinated to copper(I).[62]

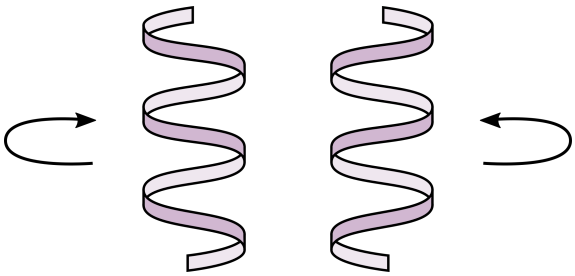

Figure 1.3: Schematic representations showing the chirality of helices indicating left-handed (minus, *M*) (left) and right-handed (plus, *P*) (right) twists.

In biology helical structures often exist with unequal abundance of the left- and right-handed forms. One example is DNA where the right-handed form (B-type) can be found in naturally higher abundance. Based on this observation it is proposed that *P* and *M* metallohelicates are likely to show differences in biological activity. Aside from the examples of ligand pre-organisation described above (which can be somewhat limiting in overall synthetic design), resolution of metallohelicates can be achieved in a variety of ways. Post-synthetic resolution of helicates has been shown using stereoselective crystallisation and, pertinently to this thesis, chromatographic methods.[63,64]

The first chromatographic resolution of a helicate was shown by Rapenne *et. al.* for an Fe(II) double-stranded species.[65] The use of an eluent containing a chiral anion ((-)-*O,O′*dibenzoyl-(L)-tartrate) on an SP-Sephadex C-25 ion exchange support, allowed separation of the two helicate enantiomers. The same approach was later employed by Glasson *et. al.* for the resolution of a triple-stranded ruthenium helicate.[66] Alternatively, a cellulose solid-phase support in conjunction with a mobile-phase containing achiral anions has been widely employed Hannon and co-workers for the resolution of a number of metallohelicates.[67,68] The ability to separate enantiomers of metallohelicate species is crucial to allow investigation of binding, both in biological and host-guest contexts, where enantiospecific interactions may be observed.

When forming metallohelicates there is a third stereoisomer option which has only recently begun to be explored – the achiral mesocate. These molecules are less commonly found than helicates in the literature, with the first X-ray structure of a mesocate only reported in 1995 by Albrect and Kotila.[69] Since that time, several helicate/mesocate mixtures have been observed in solution, with Zhang and Dolphin reporting the first separation of a pair of helicate/mesocate diastereomers in 2009.[70] A schematic representation showing the chiral helicate in comparison to the achiral mesocate for a triple-stranded species is shown below (Figure 1.4). As illustrated, in helicate structures the ligands coil around the metal centres, leading to identical stereochemical configuration at each metal

centre. For mesocates, ligands align on the same side of the compound, leading to opposing configurations at each metal centre. A helicate and mesocate pair are diastereomers, and while the helicate can have two possible enantiomers, the mesocate exists as a single achiral molecule overall.

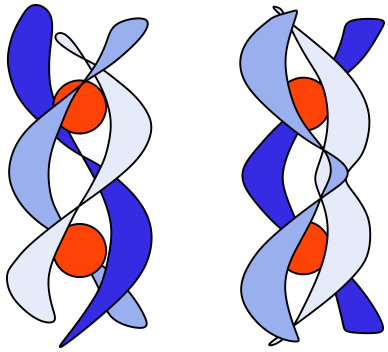

Figure 1.4: Schematic representations showing the chiral helicate (left) and achiral mesocate (right) for a triple-stranded compound.

1.2.2 Design of metallohelicates and mesocates

A range of metal ions have been used for the synthesis of metallohelicates to date. Of particular interest to this thesis are those containing either iron or ruthenium metal centres. Iron(II) and ruthenium(II) have octahedral geometry making them excellent candidates for the formation of either double- or triple-stranded compounds when used in conjunction with ligands containing tridentate or bidentate chelation sites, respectively. Iron, as a relatively labile metal ion, has been widely explored in metallohelicate synthesis previously. Notably, Hannon and co-workers have employed a multitude of metal centres in the synthesis of triple-stranded metallohelicates using a di(pyridylimine) ligand, including iron(II) and ruthenium(II) alternatives, for which biological activity has also been explored.[71–73] As mentioned previously Rapenne *et. al.* utilised a highly robust di(tpy) ligand to synthesise a double-stranded Fe(II) helicate; however, despite the racemic mixture being resolved, no biological studies were carried out.[65]

While reports of iron helicates are abundant in the literature, far less research has been focussed towards their ruthenium equivalents. There are only a handful of examples outlining the synthesis and characterisation of such structures, compared to those synthesised using other transition metals. The allure of using ruthenium as the metal node stems from a range of advantageous properties. Ru(II) compounds have been developed for anti-cancer and anti-bacterial purposes, illustrating the relatively high biocompatibility and potential as therapeutics. In addition, when complexed to polypyridyl and related N-aromatic ligands ruthenium has the added benefit of being luminescent, which makes

it an extremely useful tool for probing DNA binding and monitoring action within cells. Finally, the use of a relatively inert metal ion such as Ru(II) could allow synthesis of highly stable compounds.

The inert nature of ruthenium is certainly a beneficial property in terms of forming stable supramolecular structures; however, it also presents synthetic challenges. While iron helicates can be formed under relatively mild reaction conditions within minutes or hours, the syntheses of analogous ruthenium compounds employ extreme temperatures over a time-scale of days. The synthesis is additionally complicated by the formation of kinetically-favoured products, including polymers and oligomers which may hinder isolation of the desired helicate for the Ru centre, compared to the more labile Fe centre where rearrangement to the thermodynamic product is more likely.

The difficulty in incorporating inert ruthenium metal ions has been addressed by designing heterobimetallic systems. This was demonstrated by Torelli *et. al.* in a triple-stranded helicate where ruthenium occupied one metal node, and a lanthanide was employed as the other binding partner.[74] Fletcher *et. el.* explored the same heterobimetallic concept through selective stepwise metallation and ligand modification to form an Fe(II)/Ru(II) helicate.[75] Fe(II)/Ru(II) helicates have also been reported by Elliott and co-workers, prepared via a stepwise metallation pathway.[76]

The first report of a homonuclear ruthenium helicate was by Pascu *et. al.*, synthesising a triple-stranded species in 1% yield after extensive purification.[73] The ability of the Ru(II) compound to bind and coil DNA was demonstrated, as well as anti-cancer and anti-viral activity.[77–79] Subsequently, Glasson *et. al.* employed a quaterpyridine ligand to synthesise a triple-stranded ruthenium helicate.[66] In this approach a significantly higher yield of 36% was attained, and the chromatographic resolution and DNA binding of the different enantiomers studied. More recently, Kumar *et. al.* have synthesised a triple-stranded ruthenium helicate and explored the anti-bacterial properties, describing activity against both Gram positive and Gram negative bacteria as "extremely modest".[80]

There are even fewer reports of double-stranded diruthenium(II) helicates. The earliest of these was described by Crane and Sauvage, utilising a di(tpy)-based ligand in 1992.[81] While full structural determination was not possible, this compound is one of only two existing saturated double-stranded ruthenium helicates in the literature. Similarities in the ligand structure can be seen in the iron(II) helicate reported by Rapenne *et. al.* which has been discussed previously, using a similar di(tpy) ligand framework.[65] The first Ru(II) helicate/mesocate pair was recently reported by Allison *et. al.* for which the diastereomers were chromatographically separated and anti-cancer activity of these compounds assessed,

showing promising selectivity and cytotoxicity.[82] The only other example of a diruthenium helicate in the literature was reported by Ho *et. al.* incorporating a quinquepyridine (qpy) ligand.[83] In this case, while the structure is helical in nature, the ligand itself does not occupy all of the coordination sites on the ruthenium ion, with two sites being occupied by monodentate solvent or anion ligands.

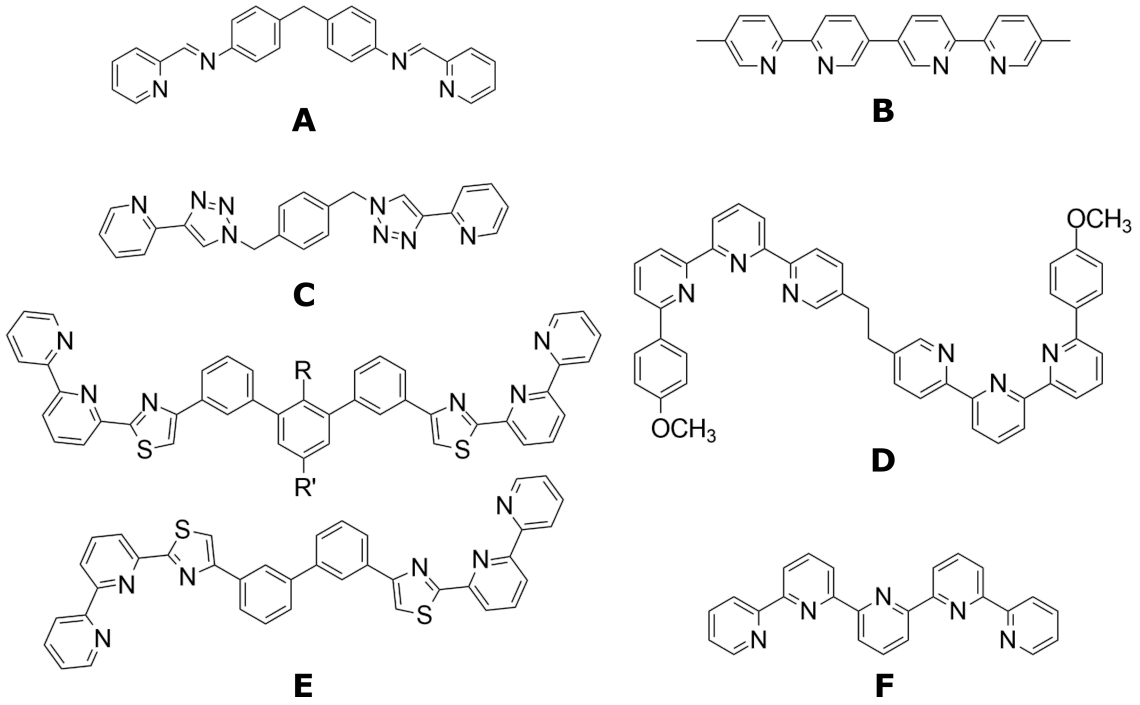

Figure 1.5: Ligands utilised for the synthesis of Ru(II) helicates and mesocates by **(A)** Pascu *et al.*,[73] **(B)** Glasson *et al.*,[66] **(C)** Kumar *et al.*,[80] **(D)** Crane and Sauvage,[81] **(E)** Allison *et al.*,[82] and **(F)** Ho *et al.*[83]

To date there are few studies of Ru(II) helicates, and even fewer of mesocates, illustrating the scope for further investigation into the synthesis of these compounds and the basis for much of this thesis.

1.3 Beyond dinuclear assemblies

In the self-assembly process the balance between enthalpic and entropic demands can be seen in the formation of larger supramolecular assemblies which contain the same metal-to-ligand ratio as dinuclear species. In studies of Cu(I) compounds Lehn and co-workers observed the formation of M_2L_2, M_3L_3, and M_4L_4 compounds, corresponding to a copper helicate, triangle, and square, respectively.[84]

Lehn and co-workers subsequently showed that reaction time, and thus thermodynamic effects could be used to control the distribution of higher-order products. Using a tri-bidentate hexapyridine ligand in conjuction with Ni(II) or Fe(II), it was found that a

trinuclear triple-stranded helicate ($[M_3L_3]^{6+}$) could be generated under short reaction times (as the kinetic product), while a pentanuclear circular helicate with a Cl^- guest ($[M_5L_5 \cdot Cl]^{9+}$) was the thermodynamic product, and was isolated after longer reaction times.[85] A schematic of these two possible structures is shown in Figure 1.6.

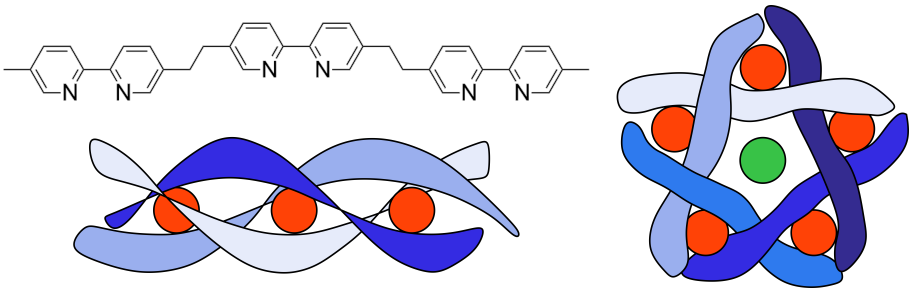

Figure 1.6: Schematic representations showing the assemblies synthesised by Lehn and co-workers using a tri-bidentate hexapyridine ligand (top left), forming a triple-stranded helicate (bottom left) and pentanuclear circular helicate containing a Cl^- guest (right).

1.3.1 Use of octahedral metal centres

As discussed above, appropriate selection of a metal ion and ligand is crucial in governing the products generated via supramolecular assembly.[6] Octahedral metal centres can be used in conjunction with di(bidentate) ligands in a 1 : 1 ratio to form compounds with the general formula $[M_nL_n]$. These include $[M_2L_2]$ helicates and mesocates, as described above, triangles ($[M_3L_3]$),[86] and squares ($[M_4L_4]$).[87] Alternatively, combining octahedral metal centres with tri(bidentate) ligands in a 2 : 3 ratio will yield compounds with the formula $[M_{2n}L_{3n}]$.[88] In this case triple-stranded helicates and mesocates ($[M_2L_3]$) can be produced,[66,70,71,80] as well as larger metal-organic cages such as tetrahedra ($[M_4L_6]$),[89–91] and cubes ($[M_8L_{12}]$).[92,93]

While dinuclear helicates and mesocates may be of great interest in biological contexts, by increasing the size of assemblies other useful properties can be explored. Notably host-guest chemistry can be performed within the cavities of metal-organic cages, which has given rise to a range of new applications being explored for compounds of this type.[94–96] While vast numbers of cages incorporating transition metal ions have been reported, there are very few examples of those containing Ru(II) as a structural component. One such cage has been described by Newcombe and co-workers,[97] who reported a tpy-based spherical cage of the type $[Ru_6L_4]^{12+}$. This Ru(II) cage is a key example of a structure where ruthenium is saturatively incorporated without additional capping or bridging ligands present.

Mixed-metal cages incorporating Ru(II) are more common in the literature; where

ruthenium can be present either within a metalloligand or a node. Of particular interest are the hybrid Ru(II)/Cd(II),[98] Ru(II)/Co(II),[99] and Ru(II)/Ag(I) cages,[100,101] reported by the Ward research group containing di(pyridyl-pyridine) ligands. These cages were generated via a stepwise synthetic approach where monoruthenium species were reacted with a more labile transition metal centre to build the supramolecular assembly. This process is similar to that taken for the synthesis of mixed-metal helicates by Torelli,[74] Fletcher,[75] Elliot,[76] and co-workers, described above.

As for the dinuclear species discussed previously, Ru(II) is relatively inert and incorporation of this metal ion can lead to highly stable supramolecular assemblies. Furthermore, metal-organic cages can also be chiral, a property that may be exploited in host-guest chemistry.[102] As noted, ruthenium helicates and mesocates are rare, but ruthenium cages are rarer still. The dearth of cage structures reported in the literature is likely due to challenges in controlling the product distribution for metal centres of this type, where thermodynamics are not necessarily the sole driver.

1.4 Interactions with biomacromolecules

Helical structures and chirality can be found in abundance both in the natural world and in artificial systems. A fundamental example of one such structure is DNA, in which base-pairing forces a coupling of the sugar-phosphate backbone to form the iconic double helix. The helical motif can also be seen in the secondary structure of proteins, specifically in the formation of α-helices, mainly due to hydrogen bonding in polypeptide chains.

It is the prevalence of helices in these biological systems which makes recreating helical structures artificially so enticing. Protein-DNA and protein-protein binding are both extremely important processes in cellular function. In protein-DNA interactions, proteins often bind to specific sites on DNA to fulfil regulation of gene expression or maintenance tasks. Protein binding occurs predominantly in the major groove of DNA, although minor-groove binding has been demonstrated, with interactions via hydrogen bonding with specific bases or deformation of the helix. Protein-protein interactions involve intentional physical contact between protein domains (some of which are helical in nature) to carry out specific cellular functions. Understanding these interactions is of great interest to assist in characterising the function and behaviour of a protein, and action of binding.

Interest in designing helical mimics is not restricted to metallosupramolecular structures, with small molecules containing helical features being synthesised by Campbell *et. al.* to inhibit the p53-*h*DM2 helix mediated protein-protein interaction.[103] Furthermore,

small molecules have been used to target nucleic acid binding in DNA or single-stranded ribonucleic acid (RNA), and show great potential as anti-cancer targets. Small molecules – including those containing transition metals – have been shown to bind DNA through various mechanisms including covalent attachment, major- and minor-groove binding, and intercalation between base pairs. A notable example is *cis*-diamminedichloroplatinum (cisplatin) which has been used alone and in conjunction with other drugs for the treatment of a range of solid tumours.[104–106] The primary target of cisplatin is believed to be DNA, and upon crossing the cell membrane the Pd(II) compound is aquated, allowing it to covalently bind to the purine bases of DNA, thus distorting the helical structure.[107–110] Distortion of the DNA structure allows recognition by cellular proteins which block repair, eventually leading to cell apoptosis.[111] The therapeutic applications of cisplatin and analogues are constrained by a vast array of side effects, stemming from the lack of specificity and resistance of tumour cells.[112–114] As a result there is considerable interest in the development of anti-cancer drugs based on alternative transition metals, including ruthenium.[115–117]

Ruthenium is uniquely positioned as a desirable alternative to platinum in this context. As mentioned previously, the inertness and biocompatability of Ru(II) compounds have led to the numerous investigations into their anti-cancer properties.[118,119] Fundamental to the use of these compounds as therapeutics is an understanding of their interactions with DNA. Unlike cisplatin, which covalently binds to DNA, many ruthenium species interact associatively, either through groove binding or intercalation, and the strength and manner of these interactions can vary based on the sequence of bases. This suggests the possibility of targeted therapeutics, offering selective binding to specific DNA sequences.

1.5 Project Origins and Proposed Work

Interest in metallohelicates and mesocates has grown since the first identification of these structures in 1987; however, the incorporation of ruthenium in compounds of this type has not been widely explored. In this research the synthesis of double- and triple-stranded ruthenium compounds was attempted, utilising existing and novel methodologies. Fundamental to this project – given the chirality of biological helices – was an investigation into whether racemic mixtures of ruthenium helicates could be resolved by chromatographic methods. Discrimination of enantiomers and the characterisation of the specific mode of biological interactions of these species – in particular the ability to bind DNA – could allow their development as mimics of biological helices (such as nucleic acids) and use as

therapeutic agents. Further to this, knowledge gained in the synthesis of dinuclear species was applied to synthesise larger ruthenium supramolecular assemblies, to investigate the factors driving product distribution when using a relatively inert metal centre.

More detailed introductions associated with the specific areas of study are included in each Chapter.

Chapter 2 presents the synthesis and study of a double-stranded diruthenium(II) helicate and mesocate pair, utilising a di(terpyridine) ligand. The product distribution was probed by variation of the reaction conditions, and the two diastereomers were separated chromatographically. The photophysical properties of the two compounds were studied using steady-state and time-resolved emission spectroscopy, and the helicate was partially resolved by chromatographic means. This resolution allowed study of the DNA binding of the two enantiomers, as well as the achiral mesocate, in later chapters. Some of the results presented in **Chapter 2** have been published in a peer-reviewed journal.[120]

Chapter 3 examines the biological interactions of the double-stranded compounds synthesised and resolved in **Chapter 2**, with initial screening studies conducted using dialysis and linear dichroism (LD) spectroscopy with calf thymus DNA (ct-DNA). Interaction with DNA by groove-binding was observed, and the compounds were further studied with three oligonucleotide sequences by nuclear magnetic resonance (NMR) methods to determine the mode of interaction.

Chapter 4 examines the formation of triple-stranded diruthenium(II) compounds from a family of ligands sharing identical triazole-pyridine chelation sites. The diastereomer product distribution was probed by modifying ligand flexibility, which, in conjunction with the relatively inert metal centre, allowed formation of previously unexplored assemblies. The structures of these were probed by X-ray crystallography, while relative energy modelling of the synthesised compounds and their theoretical helicate/mesocate counterparts, was also conducted. Preliminary biological studies were performed for a number of compounds, where the interactions with DNA were probed by dialysis and LD techniques.

In **Chapter 5** an approach to the synthesis of larger supramolecular assemblies containing Ru(II) nodes is presented. Ligands with variable steric bulk were selected, and stepwise and one-pot synthetic pathways followed to construct $[RuL_3]^{2+}$ building blocks and $[Ru_8L_{12}]^{16+}$ cubes. These preliminary investigations into the impact of ligand design and reaction conditions on product distribution provide a good basis for the development of future synthetic strategies to form Ru(II) cages.

CHAPTER 2

Synthesis and Resolution of Double-Stranded Metallosupramolecular Assemblies

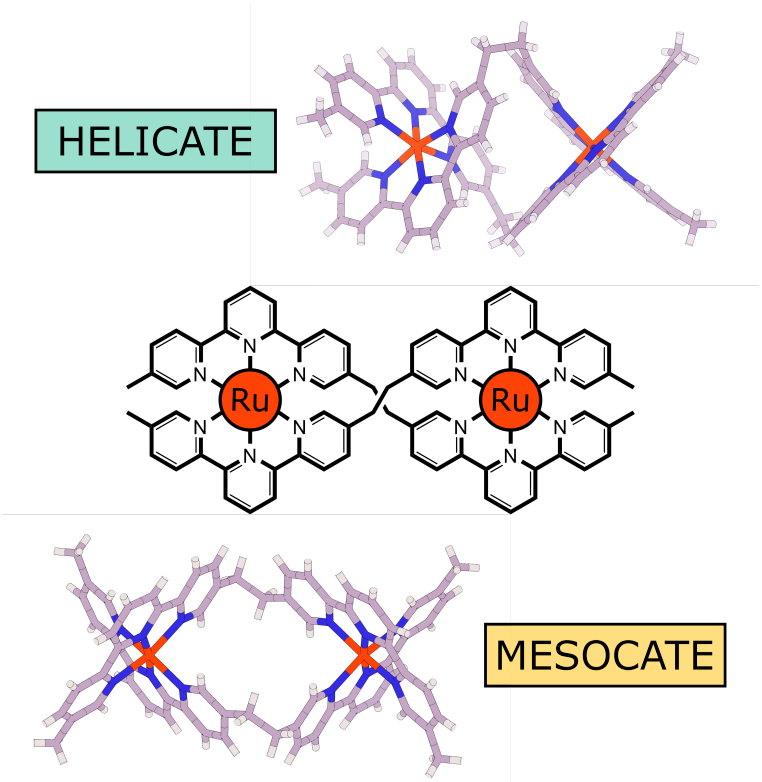

2.1 Introduction

Double-stranded metallohelicates are formed by two linkers wrapping around two or more metal centres. One of the first examples of inorganic double-stranded helices was reported by Lehn and co-workers, utilising oligopyridine ligands and copper(I) cations.[45] In this case a di(bidentate) ligand was used in conjunction with a tetrahedral metal centre to produce the desired double helix; however, in order for octahedral metal centres to be used di(tridentate) ligands must be employed. The first example of a double-stranded helicate incorporating fully ligand bound octahedral metal centres was reported by Constable and Ward forming a $[Cd_2L_2]^{4+}$ compound with a sexipyridine ligand.[121]

2.1.1 Ligand design strategies for metallohelicate synthesis

Ligand design in the formation of metallohelicates is extremely important. A significant number of ligands used for this purpose incorporate heterocyclic nitrogen donors, notably pyridine, as in aromatic or unsaturated systems the nitrogen atom is sp^2-hybridised, making it an excellent donor for metal ions. Over the last 30 years ruthenium polypyridyl compounds have been an extremely popular area of study, with thousands of new compounds synthesised and their properties analysed.[122] The discovery of $[Ru(bpy)_3]^{2+}$ by Paris and Brandt in 1959 generated great interest in the field, with later discoveries showing that ruthenium polypyridyl species were useful as catalytically active compounds for water oxidation.[123] Additionally, ruthenium(II) polypyridyl compounds have been shown to display interactions with nucleic acids and other biomolecules.[124] Ru(II) compounds are also diamagnetic, allowing formation and biological interactions to be probed using nuclear magnetic resonance (NMR) spectroscopy. However, forming discrete polypyridylruthenium species is not without challenges; ruthenium(II) is very inert, and as a result the desired products can instead be trapped as polymeric species, with the structure unable to rearrange.

Aside from the donor atoms, the nature of the spacer, located between the binding domains of the ligand, is important in allowing the ligands to complex with multiple metal centres. When designing the spacer it is important that it is flexible enough to wrap around the metal but not so flexible as to allow two binding units of the same ligand to coordinate to one metal centre. The simplest example of this is the use of methylene or ethylene spacers. These are commonly used in ligand design for metallohelicate synthesis as they allow rotation of the spacer unit, while still being restrictive enough in length

to prevent the formation of mononuclear species. The use of an ethylene spacer was demonstrated in the earliest report of a double-stranded ruthenium(II) helicate by Crane and Sauvage, where it was used in a di(terpyridine) ligand, shown in Figure 2.1, with the authors especially noting the lack of significant amounts of mononuclear species formed.[81]

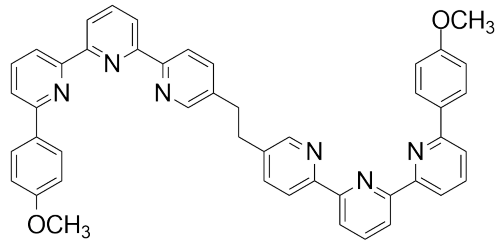

Figure 2.1: The di(terpyridine) ligand used by Crane and Sauvage.[81]

Alternatively, Rice and co-workers have shown that the formation of double-stranded ruthenium compounds can be controlled by the steric interactions between ligand strands.[82] In the synthesis of ruthenium(II) helicates and mesocates the authors employed ligands containing bulky spacers, comprised of substituted aromatic rings, to link the thiazole-bipyridine moieties. The structure of these ligands is shown in Figure 2.2. In this work it was found that the flexibility of the spacer and the steric interference caused by the methyl substituents played a key role in governing the isomeric ratio of products.

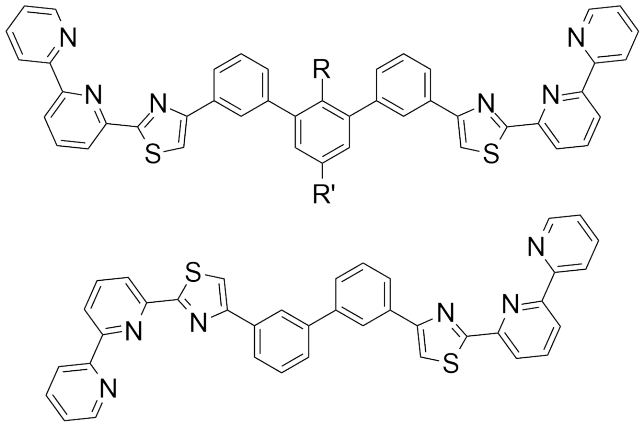

Figure 2.2: The di(thiazole-bipyridine) ligands used by Rice and co-workers.[82] Top: **L**^{1} (R=R′=H), **L**^{2} (R=Me R′=H), and **L**^{3} (R=OMe R′=Me). Bottom: **L**^{4}.

It is also possible to form ruthenium(II) helicates using a ligand which lacks a spacer. Ho *et al.* employed a quinquepyridine (qpy) ligand to produce a double-stranded helicate, where the vacant sites on one octahedral metal centre were occupied by monodentate ligands.[83] Later, this idea was adapted by Glasson *et al.* in a triple-stranded helicate, using a quaterpyridine ligand to form a $[Ru_2L_3]^{4+}$ species, where again there is no spacer between the two binding moieties.[66] The structures of these two ligands are shown in Figure 2.3.

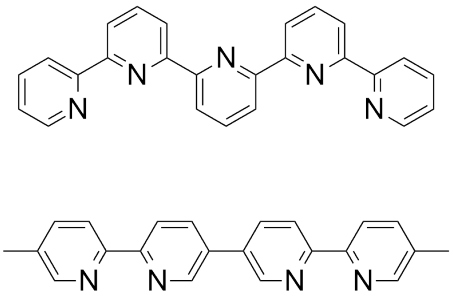

Figure 2.3: Top: the quinquepyridine ligand used by Ho *et al.*[83] Bottom: the quaterpyridine ligand used by Glasson *et al.*[66]

When the research outlined in this thesis commenced there were few examples in the literature of double-stranded ruthenium helicates, the exceptions being those outlined above. The motivation for pursuing the synthesis of a double-stranded species stems from an interest in biological activity. The formation of M_2L_2 compounds of a helical nature bear similarity to the shape of biological structures such as an α-helix, fuelling interest in potential biological applications.[125–127] Additionally, tridentate ligands confer greater stability than their bidentate counterparts due to the chelate effect, and as a result have a greater likelihood of forming the desired stable architectures, as well as being entropically more favourable.

2.1.2 Inspiration from Fe(II) analogues

One class of ligand incorporating a tridentate motif in its design are tpy derivatives (tpy = 2:2′,6′:6″-terpyridine). Ligands containing a tpy donor have previously been explored by Baum *et al.*, Crane and Sauvage (as described above), and Rapenne *et al.* in the synthesis of silver, ruthenium, and iron compounds, respectively.[81,128,129]

The particular choice of ligand in this work was inspired by that of Rapenne *et al.*, the structure of which is shown in Figure 2.4.[129] Originally the authors reported the synthesis of a dinuclear double helix constructed around two iron(II) di(tpy) centres as a precursor to a di-iron(II) molecular knot. The resolution of the helicate was subsequently reported, utilising column chromatographic techniques.[65] In the original work, the authors made particular comment on the ligand design. The $(CH_2)_2$ spacer was selected with the intention of avoiding the formation of a face-to-face dinuclear compound, which had previously been observed in the helicate precursors of copper knots made from similar ligands.[130,131] These face-to-face compounds could now be described in retrospect as mesocates.

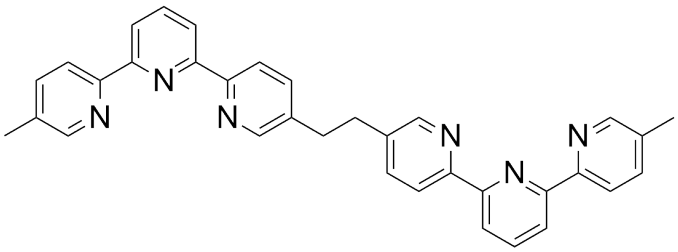

Figure 2.4: The di(terpyridine) ligand used by Rapenne *et al.*[129]

2.2 Synthesis of Ligands

As previously mentioned, the synthesis of a ruthenium helicate based on the iron(II) derivative described by Rapenne *et al.* was the focus for initial ligand and helicate synthesis. The robust nature and intrinsic elegance of the ligand design suggested that it would remain intact under the harsh reaction conditions that had been reported in existing ruthenium helicate synthesis. In addition, the iron(II) helicate was the first metallohelicate to be chromatographically resolved, a method which was hoped to be employed in this work.

The *precursors* – 5-methyl-2-(tributylstannyl)pyridine and 5,5″-dimethyl-2,2′:6′,2″-terpyridine (**1**) – were prepared according to the literature procedures.[132,133] The *ligand* 1,2-bis{5-5′-methyl-2,2′:6′,2″-terpyridinyl)}ethane (**2**) was prepared via the reaction of the dimethylterpyridine (**1**), with 1 equivalent of lithium diisopropylamide (LDA) in tetrahydrofuran (THF) at -78 °C, following the method outlined by Rapenne *et al.*[129] The benzylic anion formed was then reacted with 1,2-dibromoethane and the product purified by column chromatography. The crude ligand was further purified by reprecipitation from dichloromethane (DCM) using diethyl ether to give **2** in 26% yield. The reaction scheme is shown in Scheme 2.1.

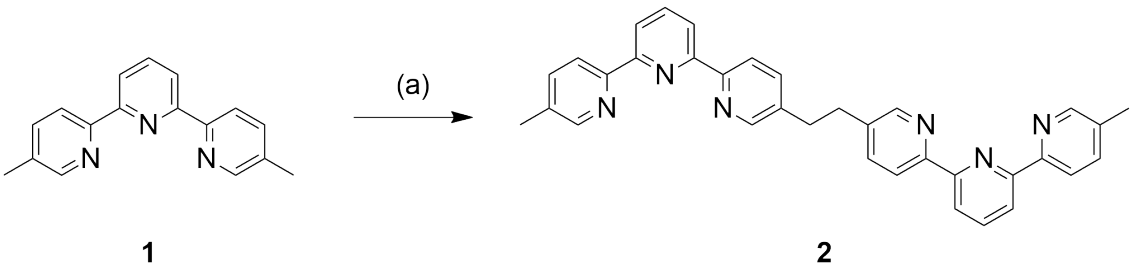

Scheme 2.1: (a) i) LDA, THF, -78 °C; ii) 1,2-dibromoethane, 26%.

2.3 Synthesis of Metallohelicates

Initial attempts to synthesise the diruthenium(II) double-stranded compound involving the ligand (**2**) were undertaken using a variety of ruthenium precursors – $RuCl_3 \cdot 3\,H_2O$, $[Ru(DMSO)_4Cl_2]$ and $[Ru(H_2O)_6](tos)_2$ – heated with the ligand in a range of organic solvents (including isopropyl alcohol, 2-methoxyethanol, and ethylene glycol) for various reaction times and conditions (e.g. reflux, microwave, and in sealed glass tubes in the oven).[134,135] All reactions yielded promising dark orange-red solutions but the majority were found to contain predominantly polymeric material. In these cases the desired product could not be separated, and was generally not readily identified by NMR spectroscopy. However, the product from the reaction of $RuCl_3 \cdot 3\,H_2O$ and **2** in ethylene glycol in a sealed tube in an oven at 200 °C for four days resulted in a more promising product mixture, with broad peaks visible in the aromatic region of the ^{1}H NMR spectrum corresponding closely to the coordinated ligand, shown in Figure 2.5.

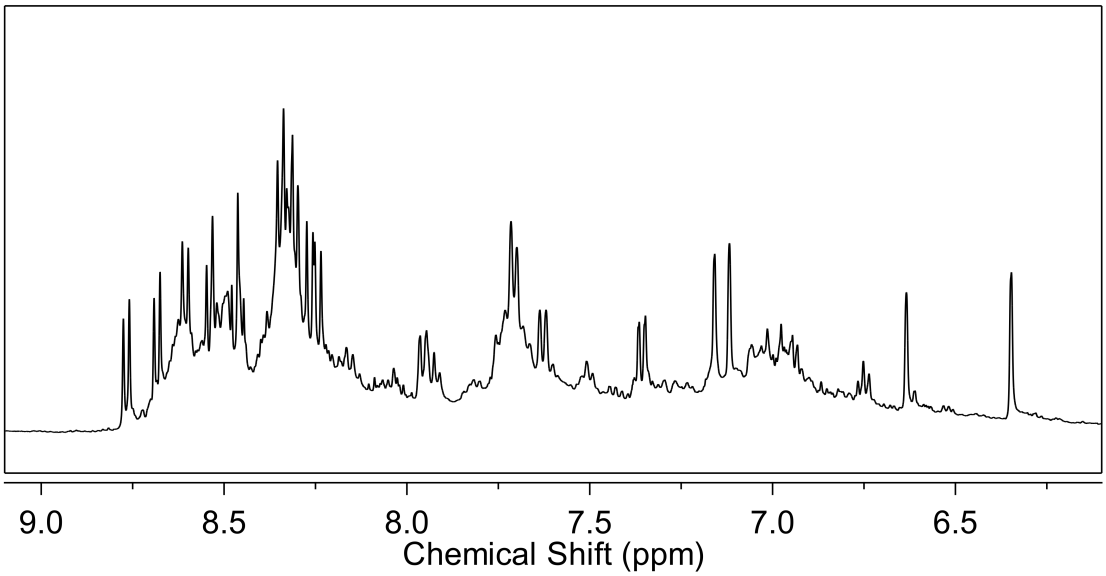

Figure 2.5: Partial ^{1}H NMR spectrum (500 MHz, CD_3CN, 298 K) showing the aromatic region of the crude reaction mixture from initial oven heating experiments at 200 °C. Two products are observable, as well as broad peaks corresponding to polymeric material.

The separation of the double-stranded compound from polymeric material was initially achieved by preparative thin layer chromatography (TLC) (silica) with a solvent mixture of 0.2 M NH_4Cl in dimethylformamide (DMF)/ H_2O (4 : 1). Upon isolation of the product, the ^{1}H NMR spectrum revealed that two species were present. These species had similar NMR signatures with both sets of signals being similar to those of the ligand.

2.3.1 Identification of twin products

Separation of these species was achieved initially by crystallisation, with the desired helicate (**3**) preferentially crystallising from the mixture using vapour diffusion of diethyl ether into an acetonitrile solution of the product and producing X-ray quality crystals. The secondary product, ultimately identified as the mesocate (**4**), was crystallised from the mixture using vapour diffusion of diisopropyl ether into an acetonitrile solution of the product. However, X-ray quality crystals could not be obtained in this manner from the initial mixture. HR ESI-MS revealed the two species to have ions of identical formula masses – m/z 767.1061 (**3**) and 767.1052 (**4**); corresponding to dinuclear $[Ru_2(\mathbf{2})_2 \cdot 2\,PF_6]^{2+}$) – indicating that the secondary product was likely the mesocate. The mass spectra of these sample can be seen in Figures B.10 and B.11 for the helicate (**3**) and mesocate (**4**) in Section B.4 of Appendix B, respectively.

Subsequent syntheses were performed under reflux conditions, heating for a 3-day time period, with separation of the diruthenium compounds from the polymeric mixture achieved by vacuum liquid chromatography, utilising TLC grade silica.[136] The yields of the two isolated compounds ($\sim$ 7 - 9% of each) were relatively low as expected because of the concomitant formation of the polymeric material and consistent with other studies of similar helical compounds.[73,82,137] It is interesting to note that in these syntheses while both the helicate and mesocate forms were produced, the helicate/mesocate ratio increased with time. It would therefore appear that the helical form was the more thermodynamically favoured - although in the synthesis of inert ruthenium(II) compounds involving polypyridyl ligands the observation of such thermodynamic equilibrium is not common. It has however been reported in the isomerisation of the $[Ru(Me_4phen)(bb_7)]^{2+}$ compound.[138]

Recent work by Rice and co-workers, involving ligands with two thiazole-bipyridine tridentate coordinating moieties, reported the first separation and characterisation of double-stranded diruthenium helicates and mesocates and a modification of those methods allowed separation of the two species in this work using vacuum liquid chromatography on TLC grade silica with the solvent mixture CH_3CN/H_2O/sat. aq. KNO_3 (7 : 1 : 0.5 by volume).[82] Two sets of signals corresponding to the different chemical environments present in the dinuclear species can be observed in the ^{1}H NMR spectra in the aromatic region for the mixture compared to the purified helicate (**3**) and mesocate (**4**) (see Figure 2.6). As noted crystallisation of the first fraction (containing the putative mesocate) by vapour diffusion of diisopropyl ether into an acetonitrile solution of the compound produced X-ray quality crystals from which the single crystal structure could be obtained,

which confirmed the identity of the mesocate.

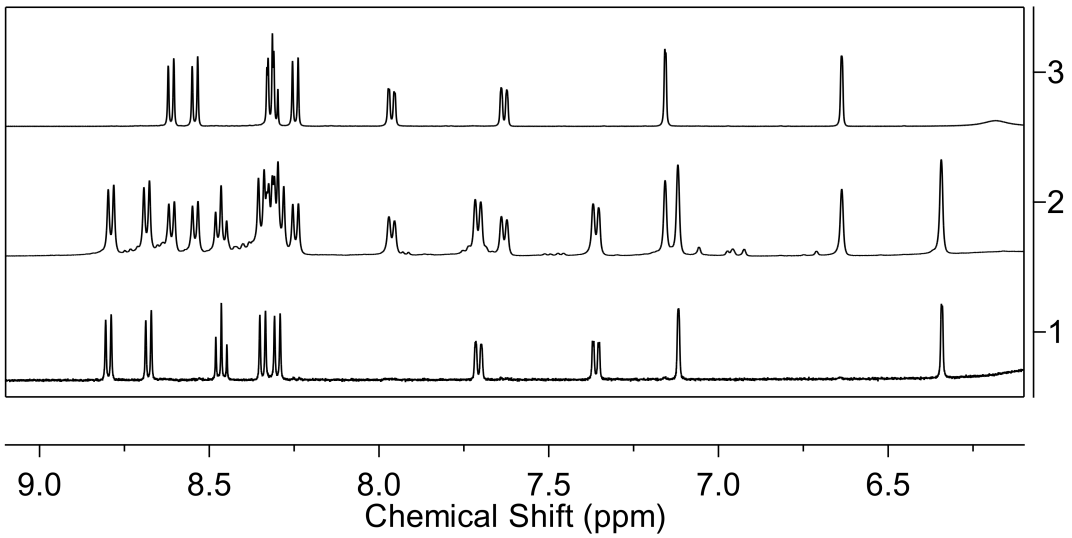

Figure 2.6: Partial ^{1}H NMR spectra (500 MHz, CD_3CN, 298) showing the aromatic regions of (1) the helicate (**3**), (2) the product mixture, and (3) the mesocate (**4**).

2.3.1.1 X-ray crystallography

The structures of the ruthenium(II) mesocate (**4**), and helicate (**3**) were solved and detailed below.

For the mesocate (**4**), crystals suitable for X-ray diffraction were grown by vapour diffusion of diisopropyl ether into an acetonitrile solution of the compound (**4**) and the resulting structure confirmed the formation of the mesocate of the type $[Ru_2\mathbf{2}_2]^{4+}$, shown in Figure 2.7. The structure crystallises in the space group *I*2/*a*. Present in the asymmetric unit are half of a ruthenium(II) mesocate cation and two PF_6^- anions. The two octahedral ruthenium(II) centres are separated by 9.305(2) Å and bridged by two ligands such that the stereochemistry of the metal centres of each discrete unit is $\Lambda\Delta$. Inclusion of a van der Waals surface shows a central cavity in the structure due to the spatial orientation of the $-CH_2CH_2-$ backbones, shown in Figure 2.8.

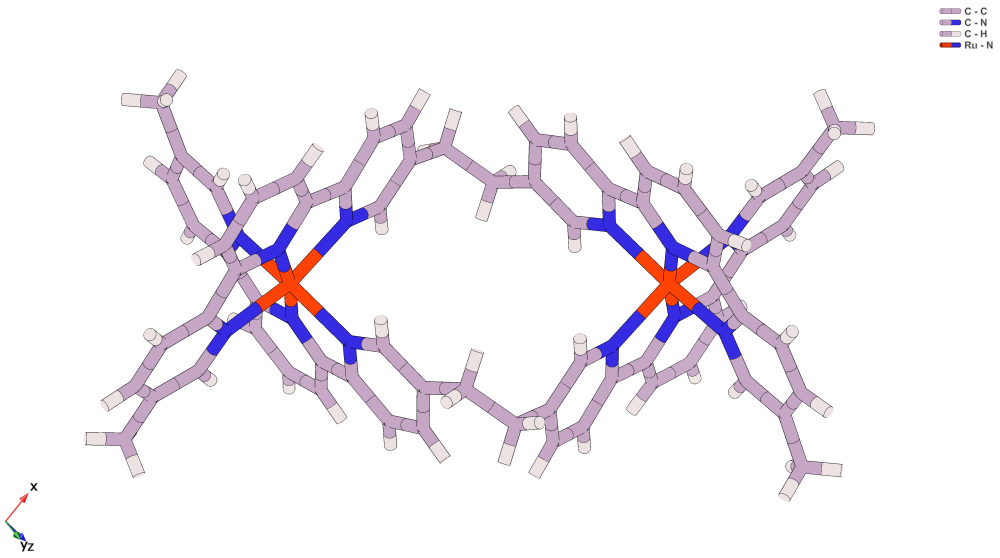

Figure 2.7: Crystallographic model showing the molecular structure of the ruthenium mesocate (**4**). Solvent molecules and counter ions have been omitted for clarity.

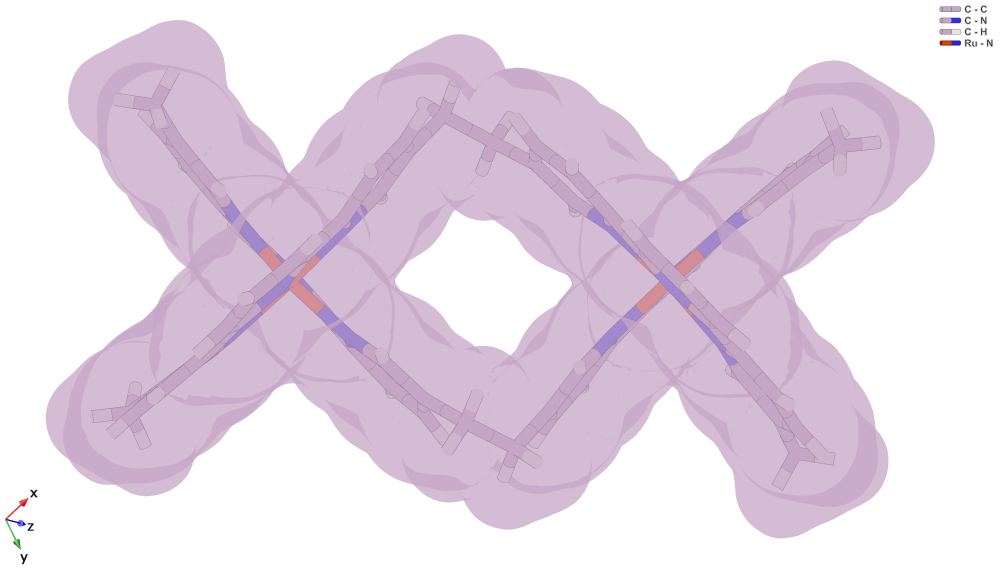

Figure 2.8: Crystal structure of the diruthenium mesocate (**4**), including van der Waals surface, illustrating the accessible central cavity.

For the helicate (**3**), crystals suitable for X-ray diffraction were grown by vapour diffusion of diethyl ether into an acetonitrile solution of the compound (**3**) and the resulting structure confirmed the formation of the helicate of the type $[Ru_2\mathbf{2}_2]^{4+}$, shown in Figure 2.9. The structure crystallises in the space group $P2_1/n$. Present in the asymmetric unit are one ruthenium(II) helicate cation and four PF_6^- anions. The two octahedral ruthenium(II) centres are separated by 7.6605(14) Å and bridged by two ligands such that the stereochemistry of the metal centres of each discrete unit is either $\Delta\Delta$ or $\Lambda\Lambda$. Inclusion of a van der Waals surface shows a significantly smaller central cavity than the mesocate, following the helical twist of the structure, as shown in Figure 2.10. The closer

interactions of the ligand backbone may contribute to the greater thermodynamic stability of the helicate compared to the mesocate.

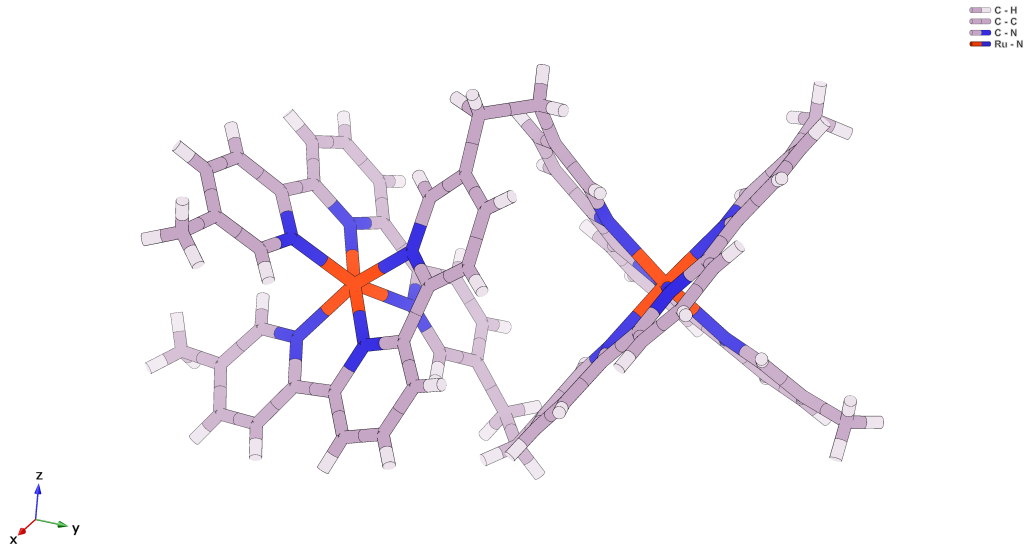

Figure 2.9: Crystallographic model showing the molecular structure of one of the two enantiomers of the ruthenium helicate (**3**). Solvent molecules and counter ions have been omitted for clarity.

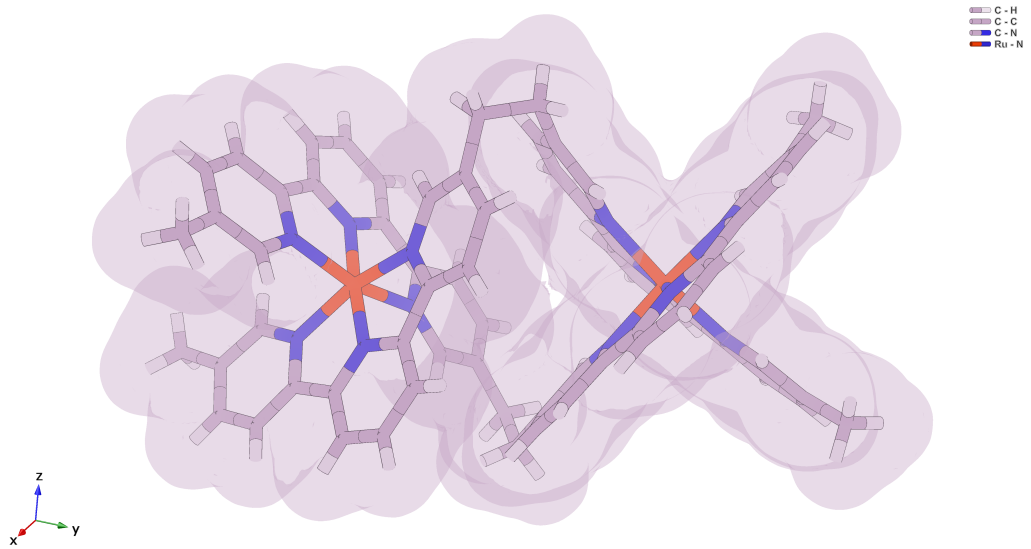

Figure 2.10: Crystal structure of the diruthenium helicate (**3**), including van der Waals surface, illustrating the inaccessible central cavity.

It is noted that for a di(2,2′:6′,2″-terpyridine) metal centre, $[M(tpy)_2]^{n+}$, the molecule possesses $\mathbf{C_{2V}}$ point group symmetry and is therefore achiral. While the dinuclear structures described this study possess such a di(tridentate) immediate coordination environment, it is noted that the tpy groups are unsymmetrically substituted with a methyl group in the 5″-position of the 'outer' pyridine ring and the ethyl bridge to the other tridentate unit in the 5-position of the 'inner' pyridine ring. This substitution

pattern means the di(tridentate) coordination moieties are asymmetric and therefore each metal centre will have a chirality. The chirality can be defined by the "di(bipyridine)" configuration using the two 'outer' pyridine rings of the tpy moieties - in which case the helicate will have a $\Delta\Delta$ or $\Lambda\Lambda$ configuration, and the mesocate will have a $\Lambda\Delta$ configuration. In Figure 2.9 the helicate is shown in the $\Delta\Delta$ configuration, while in Figure 2.7 the mesocate is shown with the Λ configuration at the top.

Comparison of the crystal packing of the helicate and mesocate structures revealed notably different densities - 1.319 and 1.708 g cm^{-3}, respectively. The lower density of the helicate is in the main due to the use of the SQUEEZE routine of *Platon* and exclusion of the solvent (which could not be identified) from the formula, artificially decreasing the density.[139] This is supported by the packing when viewed down the *a*-axis, which shows small voids, likely to contain disordered solvent and residual anions; while along the *c*-axis the packing is arranged with alternating cation and anion layers. In the *ab* plane the helicate molecules pack in a 'loose' herringbone pattern, also incorporating anions, in order to maximise π-stacking and edge-to-face π-stacking interactions (see Figures B.12 and B.13 in Section B.5 of Appendix B).

The packing of the mesocate shows layers comprised of integrated cation-anion entities, as shown in Figure B.14 (see Section B.5 of Appendix B). Examination of the (101) plane shows the mesocate molecules form columns by interdigitation, due to the formation of edge-to-face π-stacking interactions and methyl C - H $\cdots$ π-contacts (see Figure B.15 in Section B.5 of Appendix B).

2.3.1.2 NMR Studies

The observed ^{1}H and ^{13}C NMR resonances are consistent with the X-ray structures, with rotating-frame overhauser effect spectroscopy (ROESY) experiments assisting in the assignment of all signals. The assignment of ^{1}H NMR signals is summarised in Table 2.1 below. Interestingly the signal corresponding to the bridge ($-CH_2CH_2-$) in the helicate appears as a singlet whereas in the mesocate this signal is split. This is illustrated in Figure 2.11. This was supported by ROESY experiments, showing through-space correlations between the hydrogens on the bridge and aromatic signals (see Figures 2.12 and 2.13).

Table 2.1: Assigned ^{1}H NMR peaks for the mesocate (**4**), and helicate (**3**) (ND = not defined). *Note the structure below shows a 3D representation of helicate.*

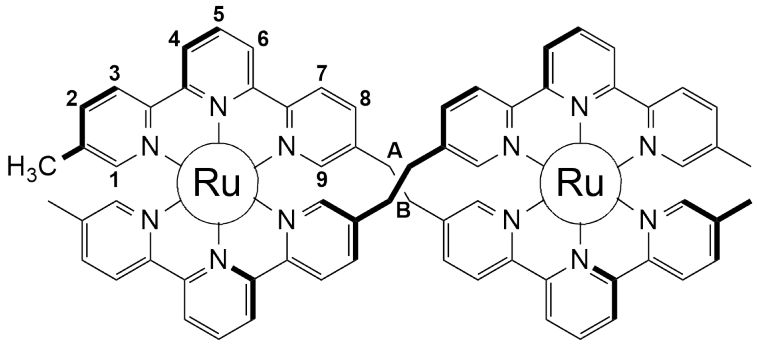

^{1}H NMR – Mesocate (4)

Assigned	Shift (ppm)	#H	Multiplicity	J (Hz)
H_6	8.65	4	d	8.14
H_4	8.58	4	d	8.11
H_5/H_7	8.35	8	m	ND
H_3	8.28	4	d	8.25
H_8	8.00	4	dd	1.50, 8.40
H_2	7.67	4	dd	0.64, 8.24
H_9	7.19	4	d	1.46
H_1	6.67	4	d	0.65
H_B	2.90	4	m	ND
H_A	2.50	4	m	ND
H_{methyl}	2.00	12	s	-

^{1}H NMR – Helicate (3)

Assigned	Shift (ppm)	#H	Multiplicity	J (Hz)
H_6	8.83	4	d	8.08
H_4	8.71	4	d	8.11
H_5	8.50	4	t	8.13, 8.13
H_3	8.38	4	d	8.29
H_7	8.34	4	d	8.24
H_2	7.74	4	d	7.30
H_8	7.40	4	d	10.36
H_1	7.15	4	s	-
H_9	6.38	4	s	-
H_A/H_B	2.63	8	s	-
H_{methyl}	2.03	12	s	-

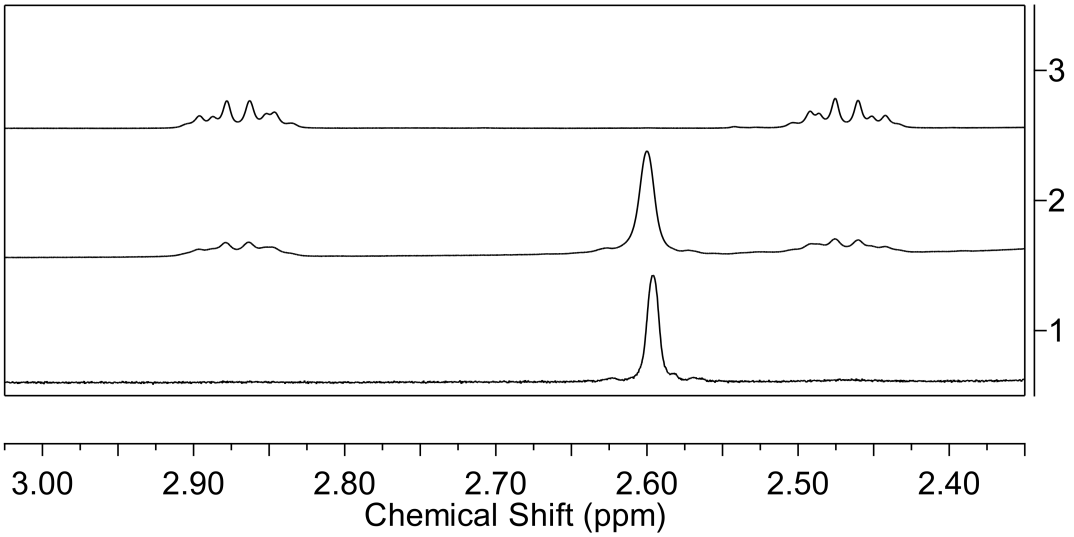

Figure 2.11: Partial ^{1}H NMR spectrum (500 MHz, CD_3CN, 298 K) showing signals in the aliphatic region corresponding to the $-CH_2CH_2-$ bridge of (1) the helicate (**3**), (2) the product mixture, and (3) the mesocate, (**4**).

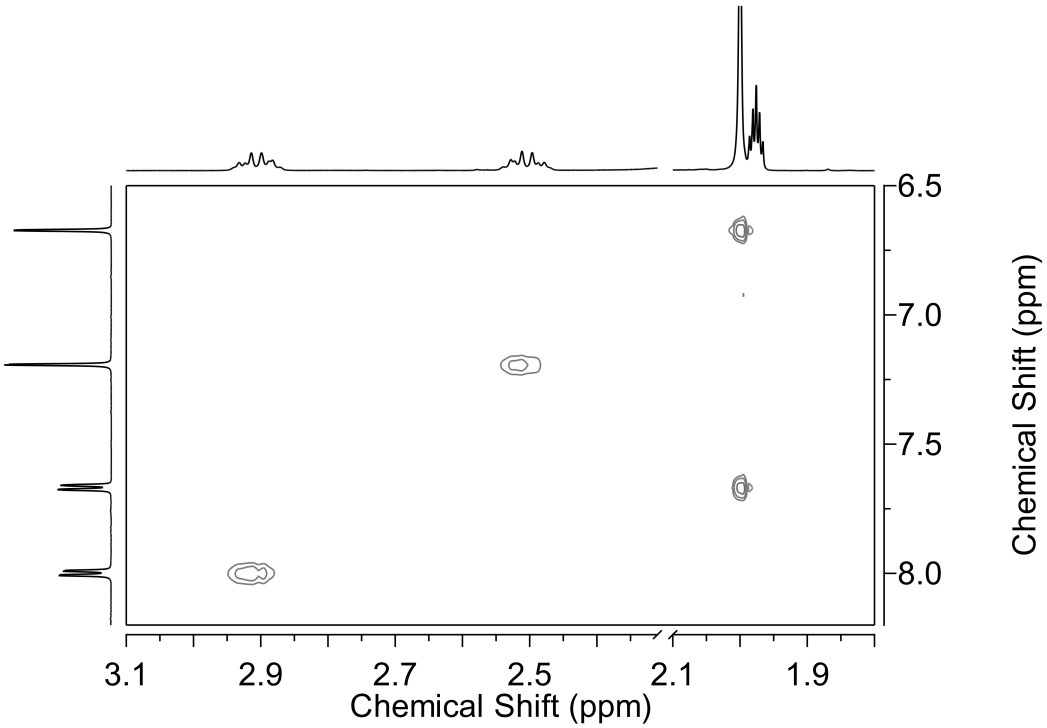

Figure 2.12: Partial ^{1}H-^{1}H ROESY NMR spectrum (500 MHz, CD_3CN, 298 K) showing signals in the aliphatic region corresponding to the $-CH_2CH_2-$ bridge of the mesocate (**4**) coupled to aromatic signals.

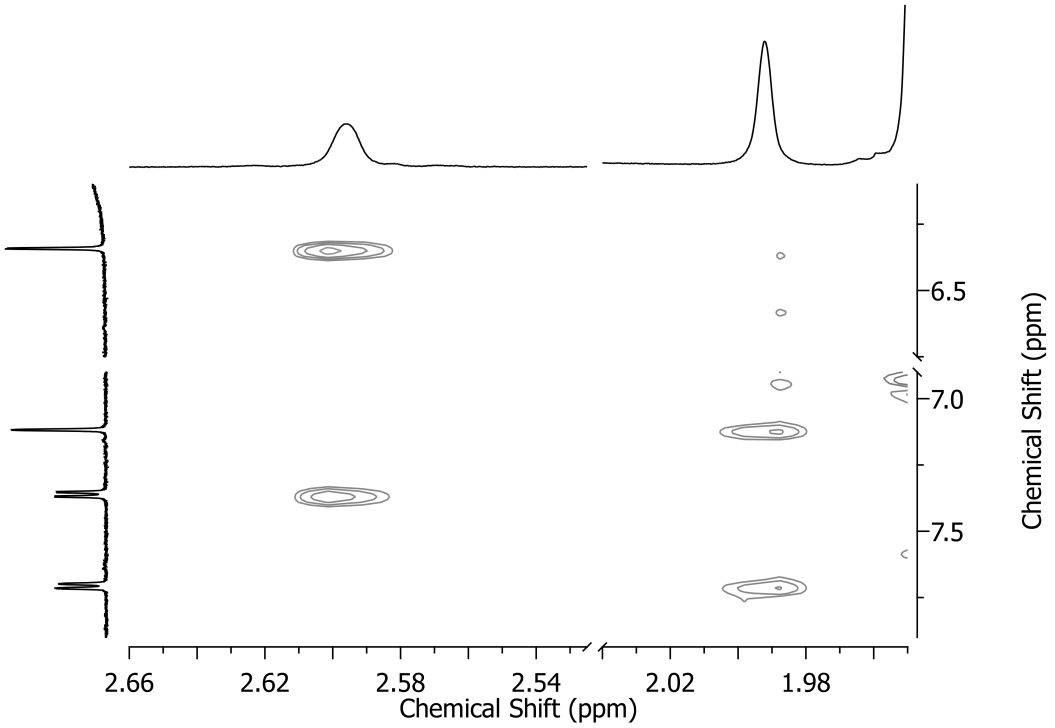

Figure 2.13: Partial ^{1}H-^{1}H ROESY NMR spectrum (500 MHz, CD_3CN, 298 K) showing signals in the aliphatic region corresponding to the $-CH_2CH_2-$ bridge of the helicate (**3**) coupled to aromatic signals.

Analysis of the through-space correlations of the bridge $-CH_2CH_2-$ hydrogen signals to aromatic hydrogens on the coordinated pyridine rings by ROESY NMR experiments coupled with the spatial distances elucidated from the crystal structure allowed assignment of the multiplet signals at 2.90 and 2.50 ppm for the mesocate. Using the annotation from the crystal structure, the multiplet at 2.90 ppm can be assigned as H1A/B and the multiplet at 2.50 ppm assigned as H2A/B in Figure 2.14. Based on the interatomic distances, H1A/B displays strong correlations with H44 and H14 while H2A/B has stronger correlations with H42 and H12. The elucidated interatomic distances and corresponding chemical shifts are recorded in Table 2.2.

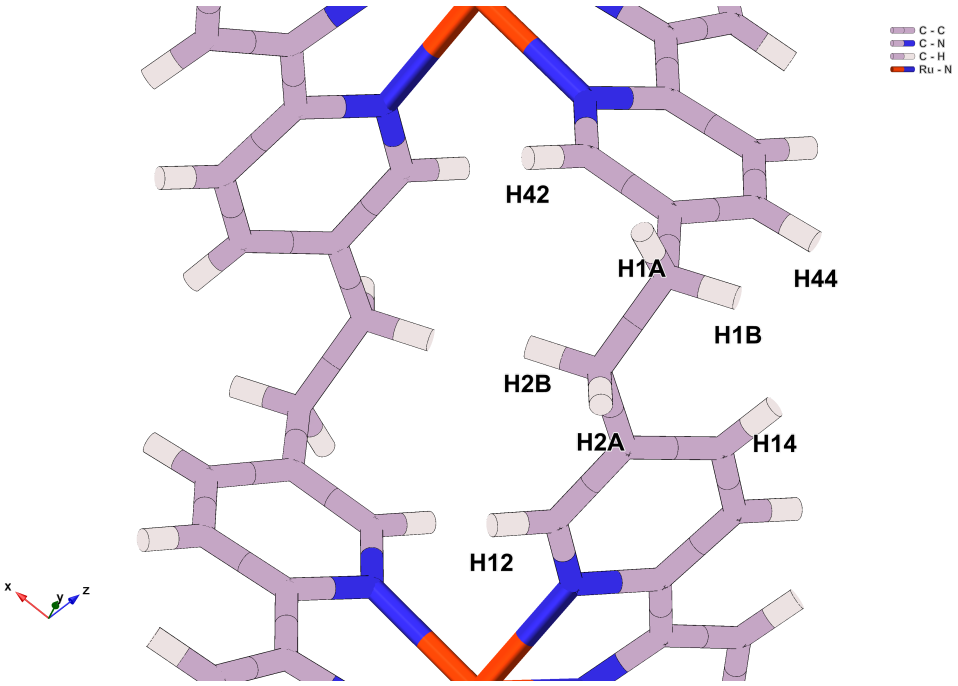

Figure 2.14: Assignment of -CH_2CH_2- bridge hydrogens of the mesocate (**4**) using interatomic distances from crystal structure.

Table 2.2: Interatomic distances for the $-CH_2CH_2-$ bridge hydrogens of the mesocate (**4**), and chemical shift details.

	Distance between atoms (Å)					Chemical Shift (ppm)
	H42	**H44**	**H12**	**H14**		
H1A	2.557	3.391	4.674	3.577	**H1A/B**	2.93
H1B	3.543	2.354	4.561	2.260	**H2A/B**	2.50
H2A	3.853	4.359	2.858	3.165	**H42/12**	7.19
H2B	2.614	4.297	2.537	3.524	**H44/14**	8.00

Significantly weaker correlations are also observed between H1A - H42 (2.90 - 7.19 ppm) and H2A-H14 (2.50 - 8.00 ppm), which is consistent with the interatomic distances and spatial arrangement of the mesocate. The splitting of signals, appearing as two multiplets rather than as a singlet (as in the case of the helicate), is due to the two CH_2 groups becoming chemical-shift inequivalent, combined with each pair of geminal hydrogens being magnetically inequivalent. As a consequence the AA′XX′ system appears as a complicated non-first order pair of multiplets. An heteronuclear single quantum correlation (HSQC) experiment was conducted to assist in assigning these multiplet signals to specific positions on the $-CH_2CH_2-$ bridge, based on the ^{1}H-^{13}C couplings. However, these showed the bridge carbons to be equivalent, with both multiplets correlated with a single carbon peak as $\sim$ 30 ppm, preventing confirmation by this method (see Figure 2.15).

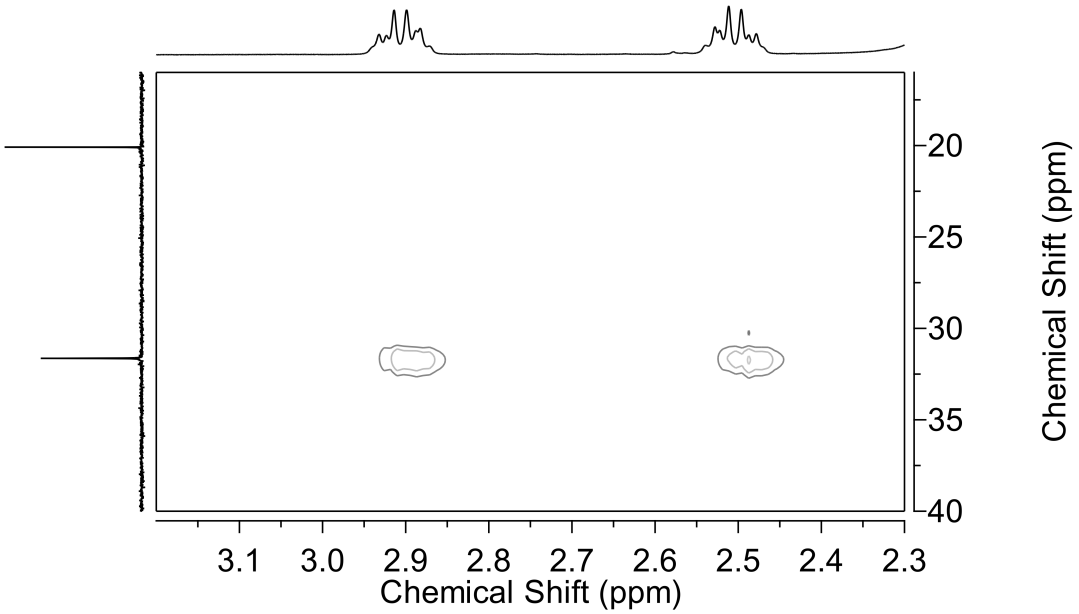

Figure 2.15: Partial ^{1}H-^{13}C HSQC NMR spectrum (CD_3CN, 298 K) showing signals in the aliphatic region corresponding to the $-CH_2CH_2-$ bridge of the mesocate (**3**) coupled to a single ethylene carbon signal

The splitting of the ^{1}H NMR signals corresponding to the ethylene bridge is not without precedent. Zhang and Dolphin reported similar observations for a Co(III) mesocate and helicate, containing a methylene bridge.[70] In the case of the helicate the CH_2 hydrogens appeared as a singlet while in the mesocate the authors describe the signals as two sets of doublets, although this could also be described as a non-first order multiplet.

To assess stability the Ru(II) helicate and mesocate products were heated at 200 °C over a period of 7 days as the PF_6^- salts in CD_3CN. Under these conditions no changes were evident in the ^{1}H NMR spectra, suggesting that both products were stable and not able to isomerise under reaction conditions.

2.3.2 Comparison to iron(II) analogue

Comparison of the Ru(II) dinuclear species described above to the Fe(II) helicate studied by Rapenne *et al.* reveal significant structural differences. Interestingly, the distance between ruthenium metal centres in the ruthenium helicate and mesocate varies significantly from the iron counterpart.[65] In the iron(II) helicate the Fe-Fe distance is reported to be 8.31 Å for the ΔΔ double helix (and 7.93 Å for the racemic mixture). For the racemate of the ruthenium(II) helicate reported in this thesis the Ru-Ru distance is 7.66 Å and for the mesocate the Ru-Ru distance is 9.31 Å. The shortening of interatomic distance going

from mesocate to helicate is not unexpected, with the same trend observed by Zhang and Dolphin for Co(III) compounds described previously.[70]

2.3.3 Computational modelling

Under the reflux conditions described above the diruthenium compounds **3** and **4** were formed in similar amounts, varying slightly from reaction to reaction. This product distribution contrasted significantly with the initial sealed tube reactions where the helicate was shown to be the dominant product. It is worth noting that the reaction time for the oven reactions was slightly longer than for reactions under reflux conditions.

Calculation of the relative stability of the helicate and mesocate forms of the diruthenium species was conducted using density functional theory (DFT). The calculations were performed both *in vacuo* and in a dielectric medium, with the dielectric constant of acetonitrile. Acetonitrile, the solvent used for NMR, has a similar dielectric constant to ethylene glycol, the reaction solvent, so roughly the same energies would be expected for ethylene glycol.

Table 2.3 shows the relative energy (ΔE) and relative Gibbs free energy (ΔG) *in vacuo* and in acetonitrile of the helicate with respect to the mesocate.

Table 2.3: Relative stability of the helicate (**3**) with respect to the mesocate (**4**).

	ΔE (kJ/mol)	ΔG (kJ/mol)
Vacuum	-11.0	-6.3
Acetonitrile	-55.4	-50.7

From these results it can be seen that the helicate is a more stable isomer than the mesocate both *in vacuo* and in a dielectric medium. This is consistent with experimental observations. The large increase in the stability of the helicate in relation to the mesocate in a dielectric medium (ΔE = -55.4 kJ/mol, ΔG = -50.7 kJ/mol) could potentially be related to the significant dipole moment present in the helicate, where the mesocate has no dipole moment. Full details of the methods and results of DFT calculations and modelled structures are presented in Section B.6.1 of Appendix B.

The results of these calculations support the notion that the helicate is the thermodynamic product whereas the mesocate is the higher energy kinetic product. However, due to the kinetically inert nature of Ru(II), both products are able to be observed experimentally. The discrepancy in the experimental product distribution when comparing the oven-heated

reactions to those under reflux conditions could be influenced by the variability in temperature when comparing reflux and pre-heated oven conditions. The oven is better able to regulate and so maintain a more constant temperature throughout the duration of the reaction, which may be enough to drive the equilibrium towards formation of the thermodynamic product. The inertness of the metal centre, when compared to more labile assemblies containing iron, plays a key role in this formation as the M – L bonds formed are unable to readily rearrange to form the desired thermodynamic product. Additionally, the slightly longer reaction time of the oven reaction, combined with the pressurised setup used plus the reaction mixture being sealed in glass, may have contributed to the difference in product distribution observed.

As mentioned previously, Rapenne *et al.* only reported the presence of a single isomer from the synthesis of the iron helicate. This suggests that the helicate, as in the case of ruthenium, must also be the most stable of the possible isomer products. To confirm this further DFT calculations were performed to ascertain the relative stability of the Fe(II) helicate and a theoretical mesocate form. The results of these calculations can be found in Table 2.4.

Table 2.4: Relative stability of the Fe(II) helicate with respect to the theoretical mesocate.

	ΔE (kJ/mol)	ΔG (kJ/mol)
Vacuum	-15.6	-9.4
Acetonitrile	-57.4	-51.2

As observed for the ruthenium compounds, the helicate is again the more stable product with a large difference in stability observed between the helicate and mesocate forms containing the Fe(II) metal centre (ΔE = -57.4 kJ/mol, ΔG = -51.2 kJ/mol, where the helicate is the lower energy isomer). The difference in energy was slightly larger than seen for the diruthenium(II) analogues. In the case of the more labile Fe(II) compounds, it is assumed that rearrangement is possible in the reaction process driving formation of the thermodynamic product, the helicate. This is supported by the report of Rapenne *et al.*,[65] where the helicate isomer is the sole product observed experimentally. Interestingly in this case, computational modelling indicates that a dipole moment is present for both the helicate and mesocate forms of the Fe(II) compound. Given that the same pattern in stability was seen as for the Ru(II) compounds (where the helicate is significantly more stable than the mesocate in a dielectric medium), it appears that other factors, aside from the dipole moment, must also influence compound stability in solution. The full results of

the DFT calculations and modelled structures are presented in Section B.6.2 of Appendix B.

2.4 Photophysics

Ruthenium(II) polypyridyl compounds have a rich photophysical and photochemical literature, particularly in the case of tri(bidentate) species based on 2,2'-bpy and 1,10-phen (phen = phenanthroline) and their derivatives. Such mononuclear species are highly emissive, even at room temperature, with the triplet metal ligand charge transfer (MLCT) excited state having a high quantum yield and a significant lifetime. In the case of $[Ru(bpy)_3]^{2+}$, emission occurs in aqueous solutions at room temperature at $\sim$ 625 nm with a lifetime of $\sim$ 600 ns and a quantum yield of $\sim$ 0.04.[140] Interestingly, the closely related di(tridentate) compound $[Ru(tpy)_2]^{2+}$ is not emissive at room temperature, attributed to non-radiative deactivation of the excited triplet state through coupling with a higher-energy metal-centred state. However, this compound shows significant emission (at $\sim$ 610 nm) at 77 K in an *n*-butyronitrile or ethanol (EtOH)/methanol (MeOH) glass.[141]

Investigations into the photophysical behaviour of the diruthenium helicate compounds was of great interest, particularly in the case where the Ru^{II} coordination environment involved the $[Ru(tpy)_2]^{2+}$ moiety, and to establish any variation between the helicate and mesocate forms. There are limited cases of photophysical studies of such species. In their studies of the double-stranded compound $[Ru_2(qpy)_2(C_2O_4)]^{2+}$, where one metal centre is coordinatively di(tridentate) and the other tri(bidentate), Ho *et al.* reported an emission centred at 715 nm at 77 K in an EtOH/MeOH glass, attributed to the ^{3}MLCT state.[83] For two cases of triple-stranded diruthenium helicates involving tri(bidentate) coordination, Pascu *et al.* and Glasson *et al.* reported emission at 705 and 604 nm respectively, at room temperature.[66,73] In the only analogous examples to the compounds presented in this chapter, Rice and co-workers reported diruthenium double-stranded helicate and mesocate forms which have been described above. While the two forms were apparently non-emissive at room temperature the authors noted that the helicate showed emission ($\sim$ 610 nm) at 77 K in an EtOH/MeOH glass, no comment was made regarding the mesocate form.[82]

2.4.1 Initial emission studies

Photophysical studies of the helicate and mesocate revealed that both forms showed no emission at $\sim$ 610 nm at room temperature. At 77 K in *n*-butyronitrile excitation at λ_{ex}

472 nm revealed that both isomers showed emission at $\sim$ 610 nm, as expected for the '$[Ru(tpy)_2]^{2+}$' moiety. However, the temporal emission characteristics were very different. Time-resolved studies showed the emission of the helicate species at 610 nm decayed with a dominant emission lifetime of $\sim$ 10 µs, which is analogous to the emissive properties of free $[Ru(tpy)_2]^{2+}$ under the same conditions.[141] For the mesocate, the emission lifetime was at least three orders of magnitude lower ($\sim$ 4 ns). The emission spectra and emission decay curves for the two isomers are shown in Figures 2.16 and 2.17, respectively. The reason for the large difference in emission timescales of the two compounds is not entirely understood at present. It is speculated that the short emission decay time of the mesocate relative to the helicate could be accounted for by a larger value of radiative rate constant (k_p) in the former compound compared to the latter. Since the emission intensities of the two compounds at 610 nm are reasonably similar ($\Phi k_{p(mesocate)} \sim \Phi_{p(helicate)}$), and given that $\Phi_p = k_p \tau_p$, and $\tau_p = 1/(k_p + k_n)$ (where k_n is the non-radiative rate constant and τ_p is the phosphorescence lifetime) an increase in the k_p, along with little difference in k_n, could lead to comparable emission intensities but different emission decay times. The difference in the radiative rate constant is presumably linked to the electronic interactions between the metal and ligand. These are in turn dependent on the structural differences of the respective compounds, and the associated strain/metal-ligand distance and angle.

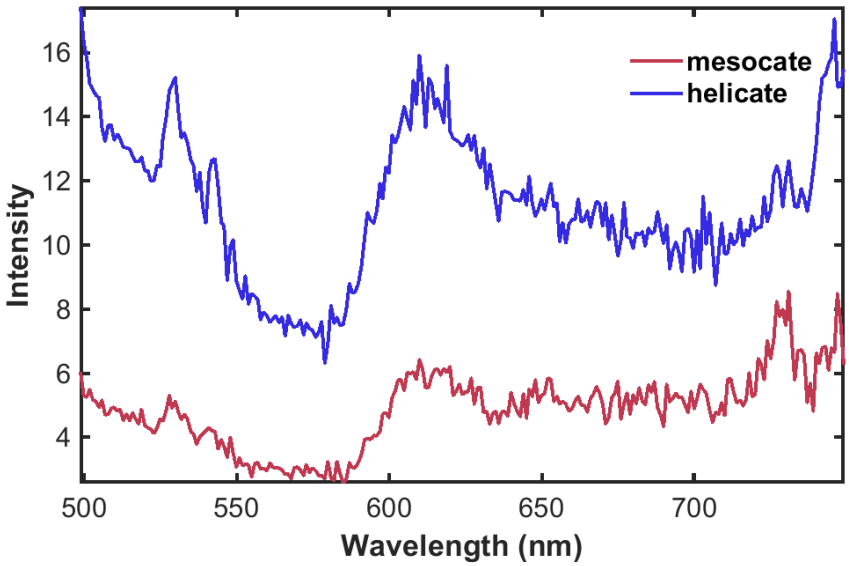

Figure 2.16: Steady-state emission spectra of the diruthenium(II) mesocate (**4**) and helicate (**3**) recorded at 77 K in an *n*-butyronitrile glass (λ_{ex} = 472 nm)

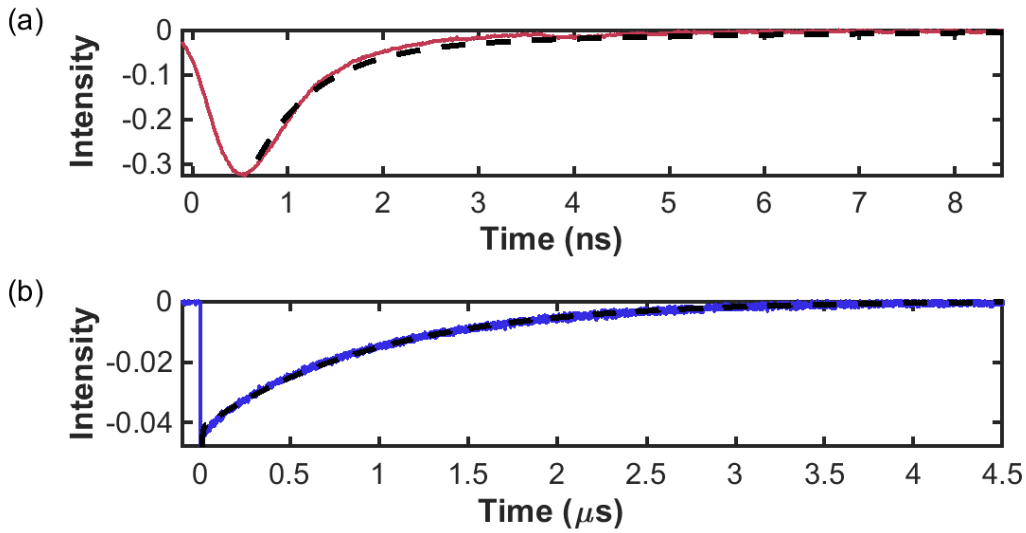

Figure 2.17: Emission decay profiles of (a) the mesocate (**4**) and (b) the helicate (**3**) recorded at 77 K, λ_{ex} 472 nm, λ_{em} 610 nm in an *n*-butyronitrile glass. The dashed line indicates a simple fit to the data. *Note the difference in timescales*.

Further studies using excitation at λ_{ex} 315 nm revealed significant additional emission at $\sim$ 400 nm in both isomers (at both 77 K and room temperature). By analogy with studies undertaken by Lakshmanan *et al.* on mononuclear compounds of a series of 4′-aryl-substituted tpy ligands which showed similar emission, these could be assigned to charge transfer between the ligand-centred (LC) transitions of the tpy ligand.[142] Time-resolved studies with UV excitation (λ_{ex} 315 nm) showed some of this emission decays on timescales of tens of nanoseconds at 77 K; however, this behaviour will not be explored further in this thesis.

2.5 Resolution of the Metallohelicate

As mentioned in the Introduction to this Chapter, the resolution of metallohelicates by chromatographic methods was first demonstrated by Rapenne *et al.* for an Fe(II) double-stranded helicate, analogous to the Ru(II) compound described in this Chapter.[65] Chiral anions have been extensively utilised for the resolution of enantiomers, whether in a chromatographic eluent or simply in solution. Where enantiomers of cationic metal compounds exist a single enantiomer of a chiral anion can be added and two possible diastereoisomeric salts formed. These two salts can vary in solubility, allowing separation of the two enantiomeric forms by fractional crystallisation. This technique has been widely used in the resolution of polypyridylruthenium compounds, employing (+/-)-*O,O′*-dibenzoyl-D/L-tartrate,[63,143,144] arsenyl-(+/-)-tartrate,[145,146] D-tartrate,[147] and antimonyl-D-tartrate,[148,149] among others.

The effectiveness of fractional crystallisation has been extended to chromatography, taking advantage of the preferential affinity of enantiomers in solution towards chiral groups. To this end chiral groups have been immobilised on solid-phase supports for resolution of enantiomers, such as HPLC incorporating a DNA-based solid-phase,[150] capillary electrophoresis,[151,152] DNA-embedded paper,[67] and TLC utilising chiral anions.[153] The use of DNA as a chiral group has been impressively harnessed by Smith and Keene, immobilising oligonucleotide sequences on a stationary phase to efficiently separate stereoisomers of dinuclear polypyridylruthenium(II) compounds by DNA-affinity chromatography.[154] Alternatively, cation-exchange chromatographic techniques can be applied, where excellent separation efficiency of enantiomers has been achieved by use of a chiral stationary phase coupled with an eluent containing a chiral anion.[155–157] This has been widely applied to resolve a broad range of polypyridylruthenium compounds,[64,158,159] and pertinently to this thesis was employed for the resolution of the Fe(II) helicate of Rapenne *et al.*,[65] and the Ru(II) helicate of Glasson *et al.*.[66] In these examples an SP-Sephadex C-25 solid-phase support (where SP-Sephadex C-25 is a cation-exchange support based on a chiral dextran), and eluent containing (-)-di-*O,O′*-4-toluoyl-L-tartrate, or (-)-*O,O′*-dibenzoyl-L-tartrate, respectively.

Inspired by the success of Rapenne *et al.* and Glasson *et al.*, resolution of the double-stranded diruthenium(II) helicate (**3**) was initially attempted using similar conditions. Elution with 0.075 M sodium (-)-*O,O′*-dibenzoyl-L-tartrate on an SP-Sephadex C-25 column was undertaken, however the ruthenium compound was observed to immediately precipitate at the top of the column upon addition of the chiral eluent. Subsequently, the vibrant orange band at the top of the solid support was unable to be fully removed by elution with any other salt solution trialled.

Persevering with cation-exchange chromatography, several other eluents containing a chiral anion were tested with the double-stranded helicate on SP-Sephadex C-25 to see whether resolution could be achieved using this stationary phase. The majority of eluents trialled caused precipitation of a bright orange solid on the top of the column, as had been observed with the 0.075 M solution of sodium (-)-*O,O′*-dibenzoyl-L-tartrate. Some helicate material could be recovered from these columns by washing with 2 M NaCl or 0.5 M sodium 4-toluenesufonate. However, no clear separation was observed. Given the limited success using eluents containing a chiral anion, attention turned to long chain fatty acids and other achiral eluents. To this end sodium hexanoate and sodium octanoate solutions as well as sodium 4-toluenesufonate solutions were prepared. It is possible to achieve resolution with achiral eluents due to the inherent chirality of the SP-Sephadex

C-25 stationary phase, which is comprised of propane-sulfonate-functionalised cross-linked α-D-glucopyranoside with five chiral centres in each unit.[155] There are a number of reports of sodium 4-toluenesufonate being used to separate diasteromeric mixtures,[160–167] as well as for the resolution of diruthenium polypyridyl species,[168] while simple long chain aliphatic anions have also been shown to effectively separate diastereomers.[169] Separation of diastereomers is thought to be due to a difference in affinity of the anion for one diastereomer, effectively lowering the apparent charge of the compound and assisting in separation.[64,168,169] A number of solutions containing achiral anions were trialled to probe the strength of interactions with the cationic double-stranded ruthenium helicate; however, in all cases clear separation was not detected. While the use of eluents containing chiral anions caused precipitation of the ruthenium compound at the top of the SP-Sephadex C-25 column, this was not the case for eluents containing achiral anions. In these cases elution was observed as a single band or the compound did not elute. A full set of SP-Sephadex C-25 column conditions and outcomes are shown in Table B.4 (Section B.7.3 of Appendix B).

Despite a wide range of eluents being tested it appeared that this choice of stationary phase, with eluents containing either chiral or achiral anions, would not be suitable for resolution of the double-stranded helicate (**3**). The resolution of this compound was of great importance to this project, as the intent was to study the interactions with DNA where, based on the literature for other Ru(II) compounds and helicates, enantiospecific binding was anticipated. To achieve resolution alternative stationary phase supports were investigated. Hannon and co-workers had previously shown that an alternative chiral stationary phase, cellulose, could be used to good effect to separate the enantiomers of a number of metallohelicates.[67,68,170] Initially, this was in the form of simple paper chromatography,[67] and subsequently scaled up using cellulose powder for column chromatography.[171] Taking advantage of the chiral solid-phase support the authors employed a range of aqueous eluents containing an achiral anion (NaCl), although subsequently a variety mixed aqueous NaCl/organic solvent mixtures were applied.[68] Of particular interest to this thesis was the resolution of a triple-stranded diruthenium helicate, described by the Hannon group, via this method.[172]

To probe the potential of cellulose chromatography for the resolution of the double-stranded helicate described in this Chapter, a number of eluents containing increasing concentrations of NaCl were trialled (20 mM, 200 mM, 2 M). Promisingly, unlike for the helicate on SP-Sephadex C-25, movement of the orange compound was observed. As the strength of eluent was increased, the orange compound band became more diffuse;

however, any fractions remained partially merged or a portion of the loaded compound remained smeared along the length of the column. For the fractions that could be isolated no meaningful circular dichroism (CD) activity was observed.

Given that movement of the ruthenium helicate had been observed on cellulose, in contrast to the SP-Sephadex C-25 where much of the compound precipitated upon addition of a chiral eluent, cellulose was selected as the preferred stationary phase moving forward. An added experimental advantage of cellulose was the potential for more efficient separation of the enantiomers. Comparing the column lengths required for the resolution of related species suggested cellulose to be a more practical choice. Rapenne *et al.* reported an effective column length of $\sim$ 6 m (recycled using a perstaltic pump) for resolution of the iron(II) helicate using SP-Sephadex C-25,[65] whereas Hannon *et al.* used a column length of only $\sim$ 200 mm for their triple-stranded ruthenium(II) helicate on cellulose.[172]

With this in mind a variety of eluents were screened for potential resolution of the helicate (**3**) using cellulose as a stationary phase. Interestingly, separation was seen using eluents containing a chiral anion. In the case of aqueous sodium (-)-*O,O′*-dibenzoyl-L-tartrate, at sufficiently high concentrations a distinct band eluted from the column while the remainder of the loaded compound remained precipitated at the top. The precipitated compound could generally be removed by application of 0.5 M sodium 4-toluenesufonate. Most promisingly, samples collected using 0.075 M sodium (-)-*O,O′*-dibenzoyl-L-tartrate followed by 0.5 M sodium 4-toluenesufonate displayed CD activity. The two obtained fractions were further examined using NMR and ultraviolet-visible (UV-Vis) spectroscopy which revealed that both contained identical species, although the two fractions did not contain equal portions of compound (by UV-Vis spectroscopy). As shown in Figure 2.18, the CD response for the first eluting fraction (F1) is significantly larger in magnitude compared to the second eluting (F2), when normalised for concentration. This result suggested that while some resolution of the helicate was achieved, both fractions contained some unresolved compound and were enantiomerically impure.

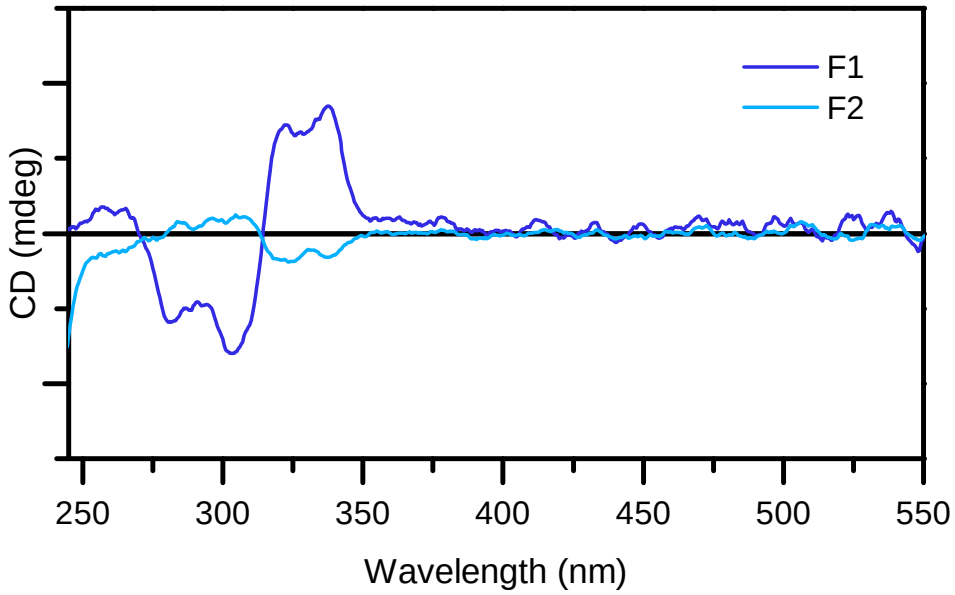

Figure 2.18: CD spectra of F1 and F2 of the diruthenium(II) double-stranded helicate (**3**) resolved on cellulose with 0.075 M sodium (-)-*O,O′*-dibenzoyl-L-tartrate (as PF_6^- salt, in CH_3CN. Spectra are normalised for concentration.

To improve the enantiopurity of the two fractions the concentration of sodium (-)-O,O′-dibenzoyl-L-tartrate solution was decreased. Given that F2 (the initial column precipitate) had shown a lower CD response, indicating lower enantiopurity, it was thought that lowering the concentration of chiral eluent might allow more helicate to remain in solution and undergo resolution. When the eluent concentration was lowered (0.0375 M), less precipitation of the compound on the column was observed but if the concentration fell too low (0.025, 0.018 M) no separation occurred, with the entire sample eluting as a single band. Alternative eluents containing other chiral anions were also trialled for resolution on cellulose, particularly those that had been used for the resolution of other Ru(II) compounds. Disappointingly, none of these showed meaningful separation, with the helicate eluting either as a single band or a portion remaining smeared on the column. Table B.5 in Section B.7.3 details the full library of eluents screened for resolution on cellulose (see Appendix B).

The most promising separation had been seen for the initial sodium (-)-*O,O′*-dibenzoyl-L-tartrate eluent where CD activity had been observed for both F1 (the first eluting fraction), and F2 (the precipitate, subsequently eluted with sodium 4-toluenesulfonate). However upon repetition of these conditions, it was found that the resolution was quite inconsistent with the enantiopurity varying greatly between samples. This was attributed to precipitation playing a key role, with recycling of sample back onto the column failing to improve the enantiopurity of either fraction.

Attention was next given to a chiral hexacoordinated phosphate ion, Δ-tris(tetrachloro-1,2-benzenediolato)phosphate(V) (TRISPHAT), the structure of which is shown below in Figure 2.19. TRISPHAT has been widely used as a chiral recognition agent for cationic molecules and is especially useful in this role due to its existence as an anion, meaning it can act as a counterion for cationic species and distinguish between isomers by chiral ion pairing.[173] This has led to its use as a chiral resolving agent for metal-containing compounds as well as being an indicator of optical purity in resolved species, being employed as a chiral NMR shift reagent.[153,174–176] The compound exists as two isomers both of which are conformationally stable in solution.

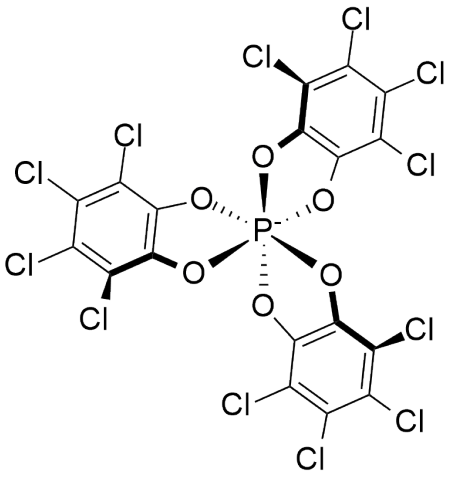

Figure 2.19: The structure of Δ-TRISPHAT

The interactions of TRISPHAT with a number of cationic metal species, including helicates, have previously been probed and evidence of enantiodifferentiation of the isomers by the anion has been demonstrated. Initially the versatility of TRISPHAT as a tool in probing the stereochemistry of organometallic compounds was demonstrated to great effect by Lacour and co-workers where it was used in chromatographic resolution as an asymmetric inducer for labile species and as an efficient NMR chiral shift reagent.[153,173,176]

To begin with the use of TRISPHAT for chromatographic separation on silica was the focus of investigation. The enantiopurity of the two fractions of helicate from cellulose chromatography (using 0.0375 M sodium (-)-*O,O′*-dibenzoyl-L-tartrate solution as the eluent) was first investigated by simple silica TLC, based on methods employed by Lacour and co-workers.[153] Four equivalents of TRISPHAT in acetone were added to a racemic mixture of the helicate as the PF_6^- salt (**3**-$(PF_6)_4$) as well as F1 and F2 and the resulting solutions adsorbed onto silica TLC plates. DCM was used as the developing solvent, as was used in the work by Lacour *et al.*, however no movement was observed for the adsorbed compounds. Development by elution with 9:1 DCM/MeOH showed some migration of

bands; however, definitive separation of the racemate could not be observed and F1 and F2 had similar Rf values. Addition of excess TRISPHAT to the solutions resulted in precipitation, suggesting that the [**3**]-[TRISPHAT]$_4$ had lower solubility in acetone than the original PF_6^- salts.

2.5.1 Identification of resolution by NMR shift reagents

Given the difficulty in achieving full resolution via the methods described above, alternative methods were trialled to quantify the extent of resolution of the helicate. In this case NMR experiments using chiral lanthanide shift reagents (CLSR) were undertaken. There are a number of reports in the literature of the determination of the enantiomeric purity of polypyridylruthenium compounds by ^{1}H NMR methods involving addition of the ruthenium compound to CLSR.[158,161,177] In this process the two enantiomeric forms of the compound will have different chemical shifts due to the interaction with the shift reagent.

CLSR were successfully used by Rutherford *et al.* to show the resolution of ruthenium compounds of polypyridyl ligands incorporating dicarbonyl species, a method which was adapted in the studies detailed in this Chapter.[158,161] Eu(tfc)$_3$ was selected for experiments in d_3-acetonitrile using the PF_6^- salts of separated fractions (from resolution on cellulose with 0.0375 M sodium (-)-*O,O′*-dibenzoyl-L-tartrate eluent). Despite multiple experiments using increasing amounts of lanthanide shift reagent, no spectral changes were observed for the [Ru$_2$**2**$_2$](PF$_6$)$_4$ compounds. After further investigation, this outcome seemed consistent with reports by Barton *et al.*, who saw similar trends in the use of europium tris[3-(trifluoromethylhydroxymethylene)-(+)-camphorate] (Eu(tfc)$_3$) with perchlorate salts of [Ru(phen)$_3$]$^{2+}$.[177] In this case only small changes in chemical shift (less than 0.15 ppm) were recorded and the authors attributed this to a combination of anion and solvent effects. Shifts of cations are lanthanide-induced by the anion coordinating to the lanthanide shift reagent, with the cation forming an outer-sphere complex with the coordinated anion. Barton *et al.* inferred that small, highly charged anions favour coordination as this allows the cation and shift reagent to locate more closely, resulting in greater observed shifts. The authors also noted that the use non-polar or slightly polar solvents can help maximise the concentration of ion pair-shift reagent complex, also yielding greater shifts. With this in mind NMR studies using the Cl^- salts of the helicate were undertaken with the same shift reagent. In this case changes in the chemical shifts were observed for the racemic mixture as well as the two collected fractions. These are summarised in the table below (see Table 2.5) for the racemate and the two partially resolved hands of the helicate (from

resolution on cellulose with 0.0375 M sodium (-)-*O,O′*-dibenzoyl-L-tartrate eluent).

Table 2.5: The effect of of [Eu(tfc)$_3$] on the ^{1}H NMR spectrum of the diruthenium helicate (as the Cl^- salt in D_2O).

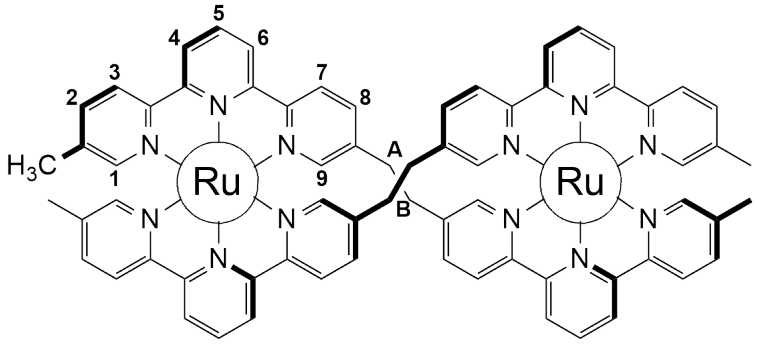

		Hydrogen Environments								
		H_1	H_2	H_3	H_4	H_5	H_6	H_7	H_8	H_9
No CLSR										
δppm	*rac*	7.23	7.73	8.51	9.76	8.77	9.95	8.44	7.31	6.18
CLSR										
δppm	F1	7.23	7.73	8.53	9.73	8.76	9.96	8.43	7.38	6.24
	F2	7.2	7.73	8.55	9.6	8.76	9.94	8.43	7.48	6.33
Δδ(ppm)	F1	0	0	0.02	-0.03	-0.01	0.01	-0.01	0.07	0.06
	F2	-0.03	0	0.04	-0.16	-0.01	-0.01	-0.01	0.17	0.15
ΔΔδ(ppm)		0.03	0	-0.02	**0.13**	0	0.02	0	**-0.1**	**-0.09**

In the results above it was seen that the most pronounced changes in chemical shift in the aromatic region were observed for H_4, H_8, and H_9 on the di(terpyridine) ligand. However, it should be noted that in all cases the observed change in chemical shift was extremely small and well below the magnitude of the smaller induced shifts reported by Barton *et al.* which were between 0.2 - 0.5 ppm. The small changes in chemical shift could be due to the use of a more polar solvent, in this case D_2O, which can coordinate to the shift reagent and compete with the Cl^- anion, or solvate the ions and shift reagent. While the use of D_2O was not ideal, limitations in solubility of the Ru(II) compound as the PF_6^- salt and then as the Cl^- salt, made it challenging to find a suitable anion/solvent combination. As NMR experiments to determine the enantiomeric purity of the ruthenium helicate using [Eu(tfc)$_3$] as a shift reagent were inconclusive, attention turned to alternative shift reagents to ascertain whether resolution had been achieved.

Given that the use of TRISPHAT for resolution of the helicate had not been as straightforward as hoped, attention turned to its potential as an NMR chiral shift reagent. Four equivalents of [*n*−Bu_4N][Δ-TRISPHAT] were added to a solution of the racemic helicate (**3**) in CD_3CN and the ^{1}H NMR spectrum recorded. At this ratio, as for the

TLC samples, significant precipitation was observed and the quality of the spectra was severely impacted. To improve the solubility of the racemic (**3**)-TRISPHAT$_4$ sample further experiments were conducted in d_6-DMSO. When the polarity of the solvent was increased the solubility of the compound significantly improved; however, very little splitting, separation in signals, or changes in chemical shift were evident in the NMR spectrum. As for the CLSR experiments detailed above this was attributed to the high polarity of the solvent, and to overcome this issue a mixed solvent system was trialled. The solvent mixture selected was based on work by Jodry and Lacour, previously used to show resolution of an iron helicate.[178] Promisingly, it was found that a solvent system composed of 20% d_6-DMSO in CD_3CN allowed good solubility of all compounds as the TRISPHAT salts. Comparison of the ^{1}H NMR spectra of *rac*-[**3**.$(PF_6)_4$] before and after addition of four equivalents of TRISPHAT revealed significant splitting in the aromatic region (see Figure 2.20). In addition, changes in the chemical shifts for helicate hydrogens were clearly seen in this region of the spectrum.

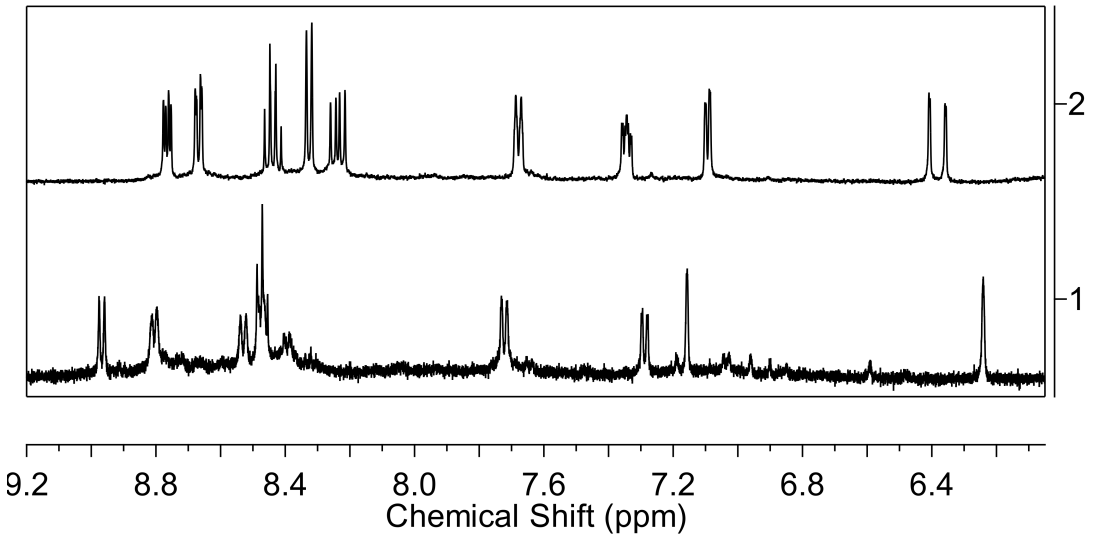

Figure 2.20: Partial ^{1}H NMR spectra (500 MHz, 20% d_6-DMSO/80% CD_3CN, 298 K) showing the aromatic region for (1) *rac*-[**3**]$(PF_6)_4$, and (2) *rac*-[**3**] upon addition of Δ-TRISPHAT.

Comparison of the ^{1}H NMR spectra for the helicate racemate as the PF_6^- and then Δ-TRISPHAT salt suggests that the two enantiomers present interact differently with the chiral anion, resulting in non-identical ligand environments and differences in the hydrogen resonances. This is concurs with the work of Jodry and Lacour, where TRISPHAT has been shown the interact dissimilarly with enantiomers of triple-stranded helicates.[178]

The optical purity of the two partially-resolved helicate fractions (from resolution on cellulose using 0.0375 M sodium (-)-*O,O′*-dibenzoyl-L-tartrate solution as the eluent) was

assessed by identical experiments to those performed on the racemic mixture. In this case the ^{1}H NMR spectra for both fractions upon addition of TRISPHAT were almost identical in the aromatic region. Some similarities in peak positions and multiplicities were also observed when compared to the spectrum of the racemate as the TRISPHAT salt. Comparison of these spectra in the aromatic region is presented in Figure 2.21 below.

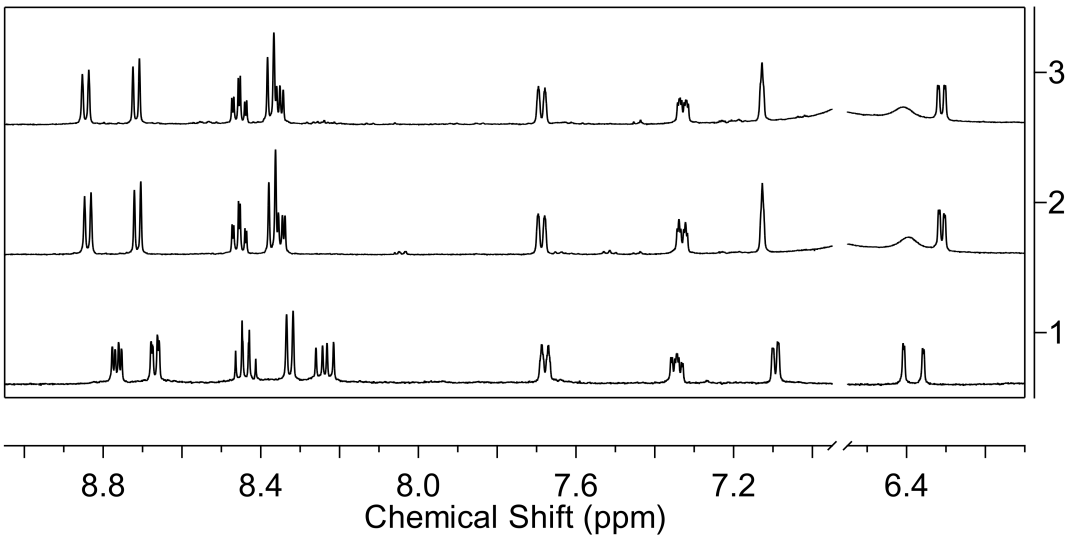

Figure 2.21: Partial ^{1}H NMR spectra (500 MHz, 20% d_6-DMSO/80% CD_3CN, 298 K) showing shifting and splitting of signals in the aromatic region for (1) *rac*, (2) F1, and (3) F2 of the helicate (**3**) upon addition of Δ-TRISPHAT.

Overall, while the racemate of the helicate had shown promising differentiation upon addition of TRISPHAT, NMR studies of the fractions from resolution with 0.0375 M sodium (-)-*O,O′*-dibenzoyl-L-tartrate solution on cellulose did not clearly demonstrate enantiomeric purity. Alongside the comparatively weak and unequal CD traces obtained, it was concluded that partial resolution of the helicate (**3**) may have been achieved through the use of 0.0375 M sodium (-)-*O,O′*-dibenzoyl-L-tartrate on a cellulose stationary phase; however, the collected fractions (F1 and F2) were not enantiomerically pure. Given that the intent was to fully resolve these compounds so that the interactions of the enantiomers biological molecules could be investigated, alternative resolution conditions were investigated.

2.5.2 A return to achiral eluents

Given that previous resolution attempts on SP-Sephadex C-25 using eluents containing a chiral anion had widely resulted in precipitation, efforts were renewed using cellulose as a solid-phase support. Reports by Hannon and co-workers indicated that increasing the

concentration of NaCl from 20 mM to 0.2 M and introducing medium pressure on top of the column led to clearer separations for both iron and ruthenium triple-helicates.[172] Inspired by this approach similar conditions were utilised, with negative pressure introduced via a peristaltic pump.

Most excitingly, by this method separation of the loaded orange compound into two bands was observed. Complete separation was not possible with the two bands partially overlapping, and efforts to improve this separation by varying column length or concentration of NaCl solution were not successful. However, by carefully collecting samples from the first-eluting and last-eluting portions and analysing these by CD spectroscopy it was evident that partial resolution of the helicate had occurred. The extent of resolution could be estimated by comparison of the CD response for each fraction. When normalised for concentration the CD response of the first eluting fraction (F1) was larger in magnitude than the final eluting fraction (F2) (see Figure 2.22).

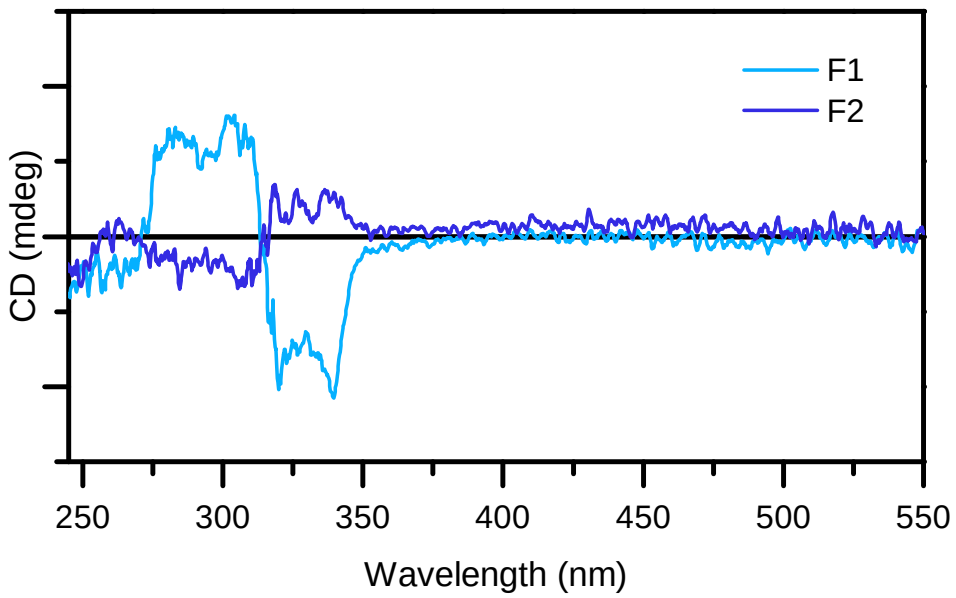

Figure 2.22: CD spectra of F1 and F2 of the helicate (**3**) resolved on cellulose with 0.2 M NaCl using a peristaltic pump.

The use of the peristaltic pump presented some challenges with cellulose columns, where the small particle size of the cellulose made it difficult to obtain a homogeneously packed column and operate at a sensible flow rate. As such attention turned to the use of positive pressure which could be operated as a normal flash column utilising a nitrogen flow to impart pressure. This technique proved as successful as the peristaltic pump, where the evolution of two bands could be seen as elution progressed. Despite efforts to improve this separation, by using of a longer column or slower flow rate, the two bands remained stubbornly overlapping. To overcome this issue, small fractions of 10 drops were collected

over the course of elution and the resulting CD spectra can be seen in Figure 2.23. The spectra obtained shows that the initial fractions contained relatively high concentrations of one enantiomer, for which the CD signal gradually decreased to nothing by the midpoint. Following this a CD signal due to the other enantiomer was observed to evolve. However, this second signal was far lower in intensity than the first, indicating a less enantiomerically pure sample.

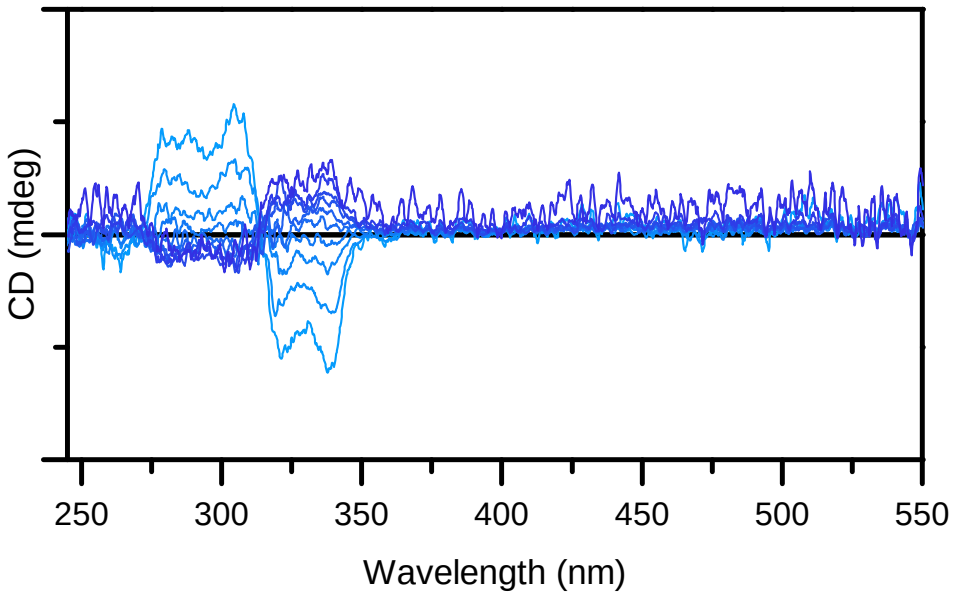

Figure 2.23: CD spectra of F1 and F2 of the helicate (**3**) resolved on cellulose with 0.2 M NaCl using positive pressure, with fractions shown as a gradient (first eluting in light blue, to last eluting in dark blue, normalised for concentration).

In order to further improve the separation, fractions containing the same enantiomer were combined and individually passed through additional cellulose columns. The front and back ends of the bands were collected for the first and second combined fractions respectively. The improvement over the course of multiple columns for fractions 1 and 2 can be seen in Figures 2.24 and 2.25. For the first eluting fraction after three columns no further significant improvement in the magnitude of the CD signals was observed, suggesting that maximum resolution by this method had been achieved. For the second eluting fraction there was a clear increase in CD signal after three columns; however, after a fourth column there was no meaningful improvement. This second fraction proved difficult the purify further, as the compound smeared significantly on the column at the tail end, leading to minute quantities of material being present in the final fraction which significantly affected the signal to noise ratio observed in the CD measurements.

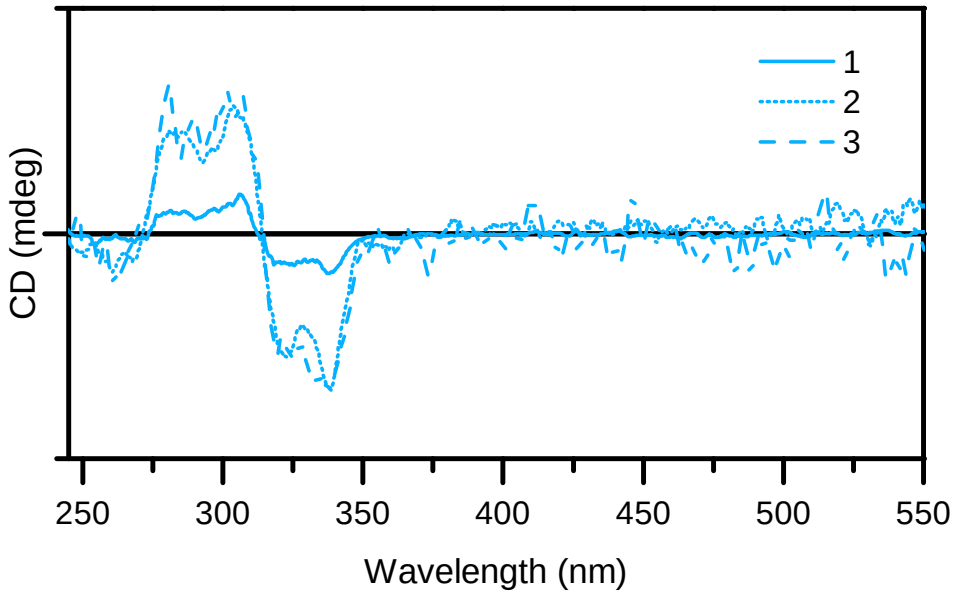

Figure 2.24: CD spectra of F1 of the helicate (**3**) resolved on cellulose with 0.2 M NaCl using positive pressure, showing improved resolution over the course of three columns (normalised for concentration).

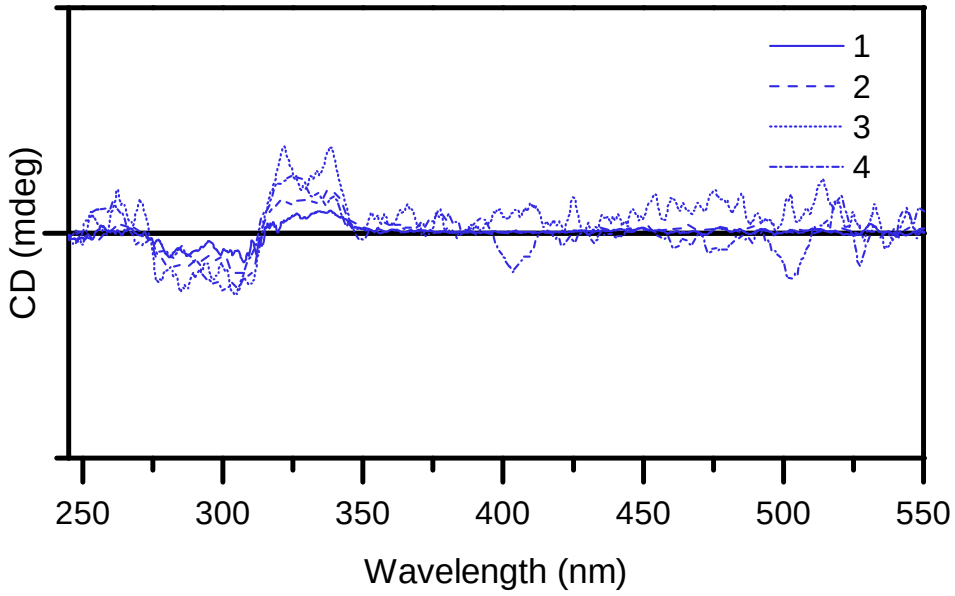

Figure 2.25: CD spectra of F2 of the helicate (**3**) resolved on cellulose with 0.2 M NaCl using positive pressure, showing improved resolution over the course of four columns (normalised for concentration).

Comparison of the most resolved samples revealed that the signal for F2 was still significantly lower than that of F1 despite numerous column cycles, as shown below in Figure 2.26. It was clear that while maximum resolution for F1 was possible by this method, F2 could not be fully resolved. In the ultraviolet (UV) region the highest magnitude of $\Delta\varepsilon$ was $\sim$ -3 $M^{-1}cm^{-1}$ at $\sim$ 330 nm while in the visible region no meaningful CD signals were

recorded. This is in contrast to the Fe(II) analogue reported by Rapenne *et al.*, where $\Delta\varepsilon$ reached $\sim$ 23 $M^{-1}cm^{-1}$ at $\sim$ 560 nm.[65] Additionally all signals observed by the authors in the UV region were over 100 times greater in magnitude than observed in this thesis for the Ru(II) compound.

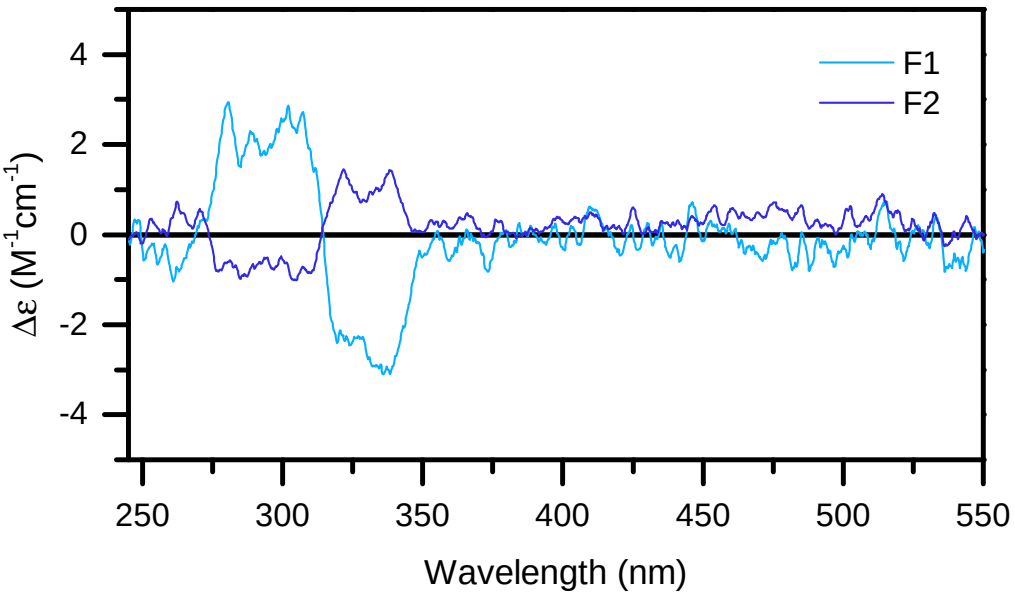

Figure 2.26: CD spectra of F1 and F2 of **3** resolved on cellulose with 0.2 M NaCl using positive pressure, showing maximum resolution achieved for both samples.

Given that complete resolution of **3** could not be achieved and F2 remaining enantiomerically impure, further experimental options were considered. Given that partial resolution had previously been observed using sodium (-)-*O,O′*-dibenzoyl-L-tartrate on a cellulose stationary phase, the two approaches were combined by taking the enantiomerically impure fraction (F2), and eluting on a cellulose column with 0.035 M sodium (-)-*O,O′*-dibenzoyl-L-tartrate. It was noted that the order of elution by the two methods was opposite and it was hoped that by taking F2 from the NaCl column any F1 remaining in this sample would precipitate and remain stuck to the column, while pure F2 would elute when treated with the chiral eluent. Unfortunately, this did not eventuate. The initial fractions collected had little to no CD signal while the later fractions and precipitated material showed the strongest CD signals, with the intensities matching the results for F2 from the NaCl columns. From this it was inferred that when using NaCl as an eluent on cellulose the cellulose interacts slightly more strongly with F2, resulting in elution of F1, closely followed by F2. Using aqueous sodium (-)-*O,O′*-dibenzoyl-L-tartrate instead approximately half to three-quarters of all compound was precipitated (depending on concentration). For the racemic mixture the eluted compound contained a slight enantiomeric excess of F2 while the precipitated band contained slightly more of F1. However, both

were still enantiomerically impure. Finally, when impure F2 (from NaCl resolution) was loaded onto cellulose and eluted with sodium (-)-*O,O′*-dibenzoyl-L-tartrate precipitation occurred but the eluted fraction still contained some F1, and the precipitate still contained some F2.

In an attempt to fine tune the resolution and improve the enantiomeric purity a range of mobile phases were screened on cellulose under positive pressure inspired by the conditions described by Kerkhoffs *et al.* for an iron(II) triple-helicate.[68] The addition of organic solvents and variation in ionic strength as well as alternative counter anions were key factors and the results are summarised in Table B.6 in Section B.7.3 (see Appendix B).

It was found that varying the strength of the NaCl eluent did not improve resolution, with increased concentration causing a single more concentrated band to elute. When ionic strength was decreased extreme smearing occurred where the loaded compound became so diffuse on the column that clear elution or separation was not be observed. Variation in the nature of the solvent showed initially promising signs, with the addition of organic solvents influencing the manner in which the compound moved down the column (causing movement in concentrated bands, rather than as a diffuse smear). However, despite this change in behaviour, little to no separation or resolution was observed and no improvement could be made to the enantiomeric purity of F2.

As a result, despite the total resolution not being attained, biological studies were undertaken primarily focussing on the resolved F1 fraction. The results of these will be discussed in **Chapter 3**.

2.5.2.1 Assignment of enantiomers

Analysis of the CD spectrum collected for the most resolved fractions (on cellulose using 0.2 M NaCl as an eluent) of the double-stranded Ru(II) helicate allowed tentative assignments of the enantiomeric excess in each fraction. Comparing the spectrum shown in Figure 2.26 above to the CD spectrum of resolved forms of the analogous Fe(II) double-stranded helicate reported by Rapenne *et al.*,[65] it was proposed that the first eluting portion using NaCl on cellulose of the Ru(II) compound (F1) contained the *M*-helicate, while the second portion (F2) contained an excess of the *P*-helicate. F1 of the Ru(II) helicate showed a negative CD response at 330 nm followed by a positive CD response at 300 nm, a trend which was similar to that seen for the Fe(II) analogue.[65]

Interestingly, this was opposite to the behaviour observed earlier for partial resolution of the Ru(II) species with sodium (-)-*O,O′*-dibenzoyl-L-tartrate on cellulose, where the

first eluting fraction shows a positive CD response as 330 nm followed by a negative CD response at 300 nm. This finding suggested that for this solid-phase/eluent combination the first eluting fraction (F1) likely contained an excess of the *P*-helicate, whilst the precipitate (subsequently eluted with aqueous sodium 4-toluenesulfonate – F2) contained an excess of the *M*-helicate.

2.6 Conclusions and future directions

In this Chapter the design and synthesis of double-stranded ruthenium helicates, since the original compound of this type described by Crane and Sauvage in 1992, has been outlined.[81] The potential for helical ruthenium(II) compounds as therapeutics has only recently begun to be investigated highlighting that the field remains underdeveloped. The synthesis of two diruthenium(II) species, a helicate (**3**), and its mesocate counterpart (**4**), have been described, both of which are novel compounds. The design of the helicate was inspired by the Fe(II) analogue reported by Rapenne *et al.* while the mesocate is only the second example in the literature of a double-stranded Ru(II) mesocate.[65] Synthesis of these compounds was complicated by the inert nature of the ruthenium metal centres and it has been noted that reaction conditions must be carefully tailored to influence the distribution of products obtained.

When the synthesis was performed in sealed tubes in a preheated oven (at 200 °C) it was found that formation of the helicate was favoured while under reflux conditions a more equal distribution of the two dinuclear products was observed. The use of alternative solvents and other ruthenium precursors under milder conditions yielded complex mixtures likely composed of high levels of polymer or other side products, with only minute amounts of dinuclear compound detectable. Using optimised reaction conditions the desired diruthenium compounds were obtained and purified chromatographically, yielding 7% and 9% for the mesocate and helicate, respectively.

The identity of the double-stranded compounds was confirmed by X-ray crystallography which showed clear structural differences between the two species. The helicate species was found to have a significantly smaller and inaccessible central cavity while in the mesocate this was far more open. Additionally 1D/2D NMR studies revealed rigidity in the mesocate structure, where the hydrogen resonances on the -(CH_2CH_2)- bridge are inequivalent for the mesocate, while appearing as a singlet for the helicate.

Calculations of the relative stability of the helicate and mesocate were conducted where the helicate was found to be the more stable isomer, both *in vacuo* and in a dielectric medium. This finding agreed with experimental observations where the helicate was the predominant product, although due to the kinetically inert nature of Ru(II) both dinuclear species were able to be isolated.

The photophysical properties of these dinuclear compounds have been investigated, showing that both isomers were non-emissive at room temperature, but at 77K in *n*-

butyronitrile they exhibited emission at $\sim$ 610 nm. However, the temporal emission characteristics were very different, with the dominant emission lifetimes of the helicate and mesocate being $\sim$ 10 µs and $\sim$ 4 ns, respectively. The large difference in emission timescale is not presently understood but could potentially be due to the mesocate having a larger radiative rate constant, causing a shorter emission decay time when compared to the helicate. It is proposed that the difference in radiative rate constant is possibly linked to the metal-ligand interactions, which depend on the differences in structure, including the metal-ligand distance and angle.

Finally, in order for the biological relevancy of these species to be probed resolution of the helicate was undertaken. Initial attempts using SP-Sephadex C-25 as a solid-phase support (which has been widely used for the resolution of other Ru(II)-containing compounds, including helicates) in conjunction with an aqueous chiral eluent were ultimately unsuccessful, with the majority of eluents causing precipitation of the helicate. When eluted with solutions containing achiral anions (such as octanoate, hexanoate, and *p*-toluenesulfonate) the helicate was found to move as a single band and no resolution was observed.

Attention turned to the use of an alternative solid-phase support, cellulose, the use of which has been pioneered by Hannon and co-workers for a variety of triple-stranded helicates. Initial screening using achiral NaCl solutions did not cause precipitation and in most cases resulted in elution of the compound as a single band. Following this eluents containing chiral anions were trialled and partial resolution was able to be achieved using a 0.0375 M sodium (-)-*O,O′*-dibenzoyl-L-tartrate eluent. The extent of this resolution was probed by use of a chiral lanthanide shift reagent ([Eu(tfc)$_3$]); however, only minimal changes in the chemical shifts of the helicate signals were observed by this method. The overall ambiguity of these results was likely due to challenges faced in identifying a suitable anion and solvent combination. Following this TRISPHAT was trialled both as a resolving agent, by chromatographic methods, and NMR shift reagent. Clear resolution was not obtained on a silica stationary phase for the TRISPHAT salt of the racemic helicate nor was the purity of the two partially resolved fractions successfully assessed by this method. As an NMR shift reagent the results were inconclusive. The two enantiomers showed differences in interaction with the chiral anion in the racemic mixture (by ^{1}H NMR methods) but the two partially resolved fractions had almost identical spectra upon addition of TRISPHAT. Together these results suggested that only partial resolution had been achieved with 0.0375 M sodium (-)-*O,O′*-dibenzoyl-L-tartrate on cellulose.

To further improve the enantiomeric separation of the helicate alternative conditions for cellulose resolution were explored. It was found that partial resolution could be achieved

when negative pressure (introduced by a peristaltic pump) was applied; however, the bands were still overlapping and the two fractions challenging to collect. Eventually, optimal resolution was achieved using a 0.2 M NaCl solution as the eluent on a cellulose stationary phase under positive pressure. After numerous column cycles consistent resolution of the first eluting fraction (F1) could be observed while the last eluting portion (F2) remained enantiomerically impure. Despite considerable efforts to improve the enantiopurity of F2 by variation of the ionic strength and addition of organic solvent to the eluent, complete resolution was unsuccessful.

With the mesocate and the two (partially resolved) enantiomers of the helicate in hand the interaction of these compounds in biological settings could be examined, where a difference in affinity and mode of binding was anticipated for the different isomers with DNA. The results of these studies are discussed in **Chapter 3**.

Overall, while the two double-stranded compounds were able to be synthesised under reflux conditions, the low yields, while on par with some other diruthenium helicates,[73,82] were still significantly lower than those synthesised under microwave conditions.[66,80] Were these compounds to find applications as therapeutics, more efficient syntheses would need to be developed. In addition, the challenges faced in the resolution of the helicate compounds were substantial and not entirely overcome. While some success was achieved on cellulose, the need for multiple column cycles and the lack of enantiomeric purity of one of the isolated fractions render this a highly inefficient process. In the future, alternative resolution conditions should be trialled, such as fractional crystallisation or chromatography using alternative eluents or solid-phase supports not explored in this Chapter. While a large number of solvent systems and anions were screened, it should be noted that the possible combinations are endless and there are few examples of resolution of ruthenium helicates in the literature to guide these selections.

The synthesis of the diruthenium(II) mesocate, only the second of its kind, demonstrates the structural variety that can be achieved when using an inert metal centre. As discussed for Fe(II), described by Rapenne *et al.*,[65] although the helicate and theoretical mesocate have similar calculated relative energies as the Ru(II) versions (as shown in this Chapter), only a helicate is seen experimentally. Interestingly, Crane and Sauvage did not detect a dinuclear compound containing face-to-face ligands (a mesocate) in the synthesis of their similar Ru(II) helicate, suggesting that additional steric bulk at the terminal ends of the ligand may influence product distribution.[81] These observations hint that with careful ligand design, the ratio of mesocate and helicate may be able to be controlled in these more inert systems and a broader range of compounds accessed than with more labile metals.

However, this sort of investigation may be more suited to a system containing ligands that can be more readily synthesised which would allow straight-forward modulation of the components, a task which would be more challenging with the di(terpyridine) ligand discussed in this Chapter.

CHAPTER 3

Biological Interactions of Double-Stranded Metallosupramolecular Assemblies

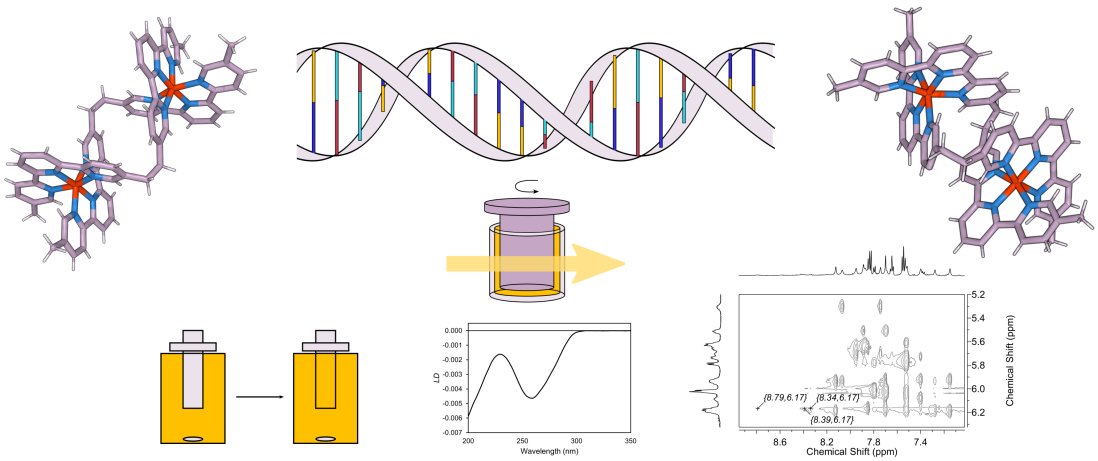

3.1 Introduction

Since the structure of DNA was first described by Watson and Crick in 1953 the role that DNA plays in cellular processes has been widely explored.[179] DNA is a critical part of all life, containing the genetic code required for the development of living organisms, and is one example of a helical motif which is common in nature.

The double helix structure of DNA consists of two intertwined strands, composed of nucleotides with repeating units containing a 2′-deoxyribose sugar bound to a negatively-charged phosphate and one of four bases - guanine (G), cytosine (C), adenine (A), or thymine (T). The repeating units are held together by phosphodiester bonds between the phosphate and hydroxyl group of the adjacent nucleotides. The double helix is formed by interaction of two strands, and the structure is stabilised by π-stacking of the adjacent bases. Hydrogen bonding between complementary bases governs the formation of base pairing, which is illustrated in Figure 3.1 below.

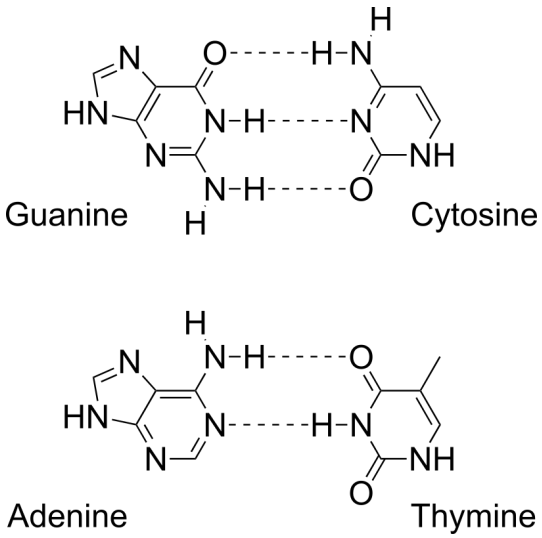

Figure 3.1: The fours bases of DNA, illustrated as their complementary base pairs (dashed bonds indicate hydrogen bonding).

The most common double-stranded structures that DNA can adopt are a right-handed helix, either A- or B-type DNA, or the left-handed helix, Z-DNA. The most common form of these to occur in natural systems is B-DNA, which composes the majority of DNA at neutral pH and physiological salt concentrations. In this form the base pairs stack in the centre of the helix, approximately perpendicular to the helical axis. Below, in Figure 3.2, an illustration of the general structure of DNA can be seen. As indicated the double helix of DNA is characterised by a major and minor groove, which are similar in depth ($\sim$ 8 Å) but differ in width. The major groove is $\sim$ 11.6 Å wide, while the minor groove is only $\sim$ 6.0 Å in width, although these measurements are sensitive to the base sequence.[180]

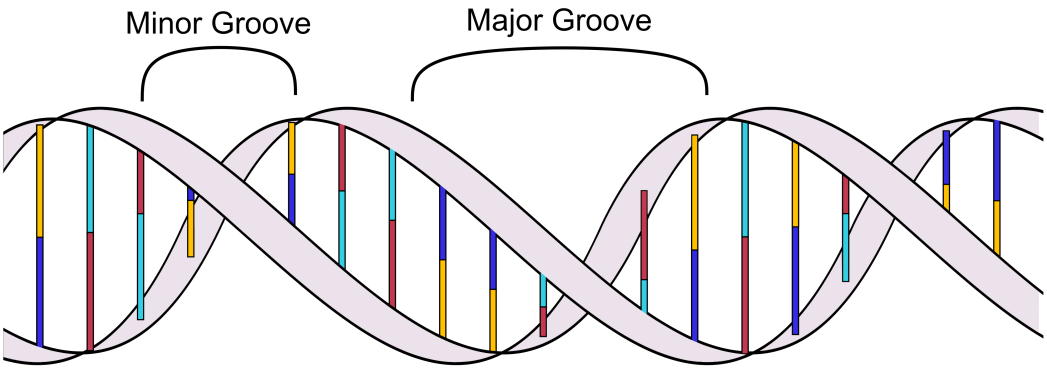

Figure 3.2: A simplified structure of B-DNA displaying the characteristic major and minor grooves.

DNA is inherently chiral and differences in the structure and topology of the major and minor groove ,due to variation in the base-pair sequence, allow for wide variety of interactions with other molecules to take place. Consequently, there has been great interest in understanding the processes by which DNA interacts with small molecules, and the way in which the physical structure, composition, and other characteristics of these molecules may impact the nature of interactions.

3.1.1 Modes of interaction with DNA

Small molecules may interact with DNA via covalent and non-covalent modes. As mentioned in **Chapter 1** *cis*-diamminedichloroplatinum (cisplatin) is a well-studied example of a molecule that forms covalent bonds with DNA. In this case the restricted geometry of cisplatin favours formation of Pt-DNA covalent bonds at the N7 position of two adjacent guanine residues.[181,182] In this way cisplatin illustrates the ability for small molecules to target specific sequences of DNA, a trait that has made them useful therapeutic tools.

Non-covalent interactions between small molecules and DNA can be classified as either electrostatic, groove binding, or intercalation. Electrostatic interactions occur between the negatively-charged phosphate ions in the backbone and cations in solution, such as magnesium or sodium.[183,184] These interactions are purely electrostatic and as a result, are non-specific in terms of the physical characteristics of the structures involved and not generally sequence-selective. More commonly small molecules, particularly metal-containing compounds, interact with DNA by groove binding or intercalation. In groove binding either the major or minor groove of DNA can be targeted, depending on the structure of the substrate. These interactions can be composed of a combination of van

der Waals, electrostatic, and hydrogen bonding forces, and the chemistry of the DNA surface plays a key role.[124] While in nature proteins readily interact non-covalently in the major groove, most small molecules of less than 1000 Da bind in the minor groove.[185] The shape and size of the major groove can vary significantly with base pair sequence, and the relatively small size of metal compounds means that they generally bind in the minor groove, or bind with less selectivity in the major groove (particularly for mononuclear compounds, which span only two - three base pairs). Finally, intercalation occurs when a substrate containing a planar polycyclic aromatic ring system inserts between two the base pairs of DNA, undergoing π-stacking.[186] Unlike electrostatic interactions, the chemical and physical characteristics of the substrate are vital in determining the strength and type of interactions that may occur in groove binding and intercalation. Additionally, molecules that interact with DNA by these mechanisms have the potential to be tailored to target a specific DNA sequence or region. A representation of groove binding and intercalation is shown in Figure 3.3.

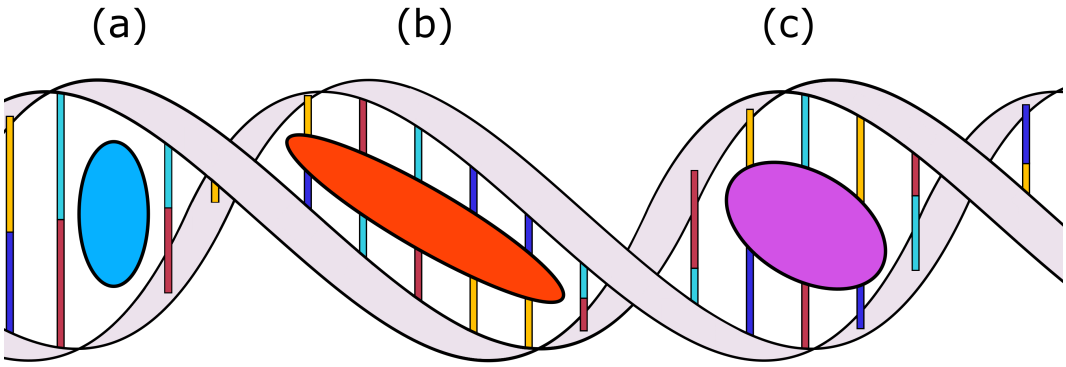

Figure 3.3: Schematic representation of possible non-covalent DNA binding modes, including (a) intercalation, (b) minor groove binding, and (c) major groove binding.

3.1.2 Interactions of metal-containing compounds with DNA

There is enormous interest in studying the interactions between DNA and small molecules for the development of new therapeutic agents.[187–189] The ability for a potential drug to bind to DNA or ribonucleic acid (RNA) at specific sites is paramount, particularly in the quest to minimise unwanted side effects caused by non-specific interactions with other cell components or nucleic acid sequences. While research initially focussed on the synthesis of small organic molecules which showed sequence selective binding, the potential of transition metal compounds was highlighted in the pioneering work of Dwyer, Lippard, Nordén, and Barton.[190–193]

Metal- and metalloid-containing compounds have been crucial in the development of drugs, dating back to the development of Salvarsan, an organoarsenic compound used for the treatment of syphilis, by Paul Ehrlich and co-workers in the 1900s, where it was the first successful application of a metalloid compound in chemotherapy.[194] Over 50 years later the development of cisplatin and its derivatives renewed interest in the study of metal-based chemotherapeutic agents.[195] Since then a wide variety of metal compounds, incorporating numerous transition metal centres and a diverse ligand library have been synthesised and their biological activity studied. Due to the range of coordination geometries available, metal species provide a high level of stereochemical variability compared to organic molecules and can introduce additional elements of chirality which may be important for recognition and interaction. Metal compounds can also be highly charged, a benefit in targeting certain biological structures, such as RNA and DNA, phospholipids, and negatively-charged protein surface regions. To date a huge range of transition metal species have been reported to bind DNA and RNA with relatively high affinity and many have shown anti-cancer activity.[196,197]

In particular, there has been growing interest in the biological properties of kinetically inert polypyridylruthenium(II) compounds. These compounds have octahedral geometry and have been shown to interact reversibly with DNA, RNA, and proteins via groove binding or intercalation. While covalent-binding ruthenium compounds have shown anti-tumour behaviour, it is thought that compounds that can reversibly bind may produce different biological activity. In addition, many polypyridylruthenium(II) species are chiral, allowing the study of enantiomeric specificity when binding to chiral biological receptors.

The biological activity of mononuclear ruthenium(II) species, utilising ligands such as 1,10-phenanthroline (phen) and derivatives, was first studied by Dwyer and co-workers and since that time there has been great interest in exploring inert ruthenium compounds of this type due to their ability to bind DNA.[198,199] As alluded to previously, chirality can play a key role in determining the strength and selectivity of interactions with DNA and RNA. In the case of $[Ru(DIP)_3]^{2+}$ where DIP refers to the 4,7-diphenyl-1,10-phenanthroline ligand (see Figure 3.4), Barton and co-workers showed that the Δ-enantiomer bound to B-DNA whereas the Λ-enantiomer bound to Z-DNA.[200]

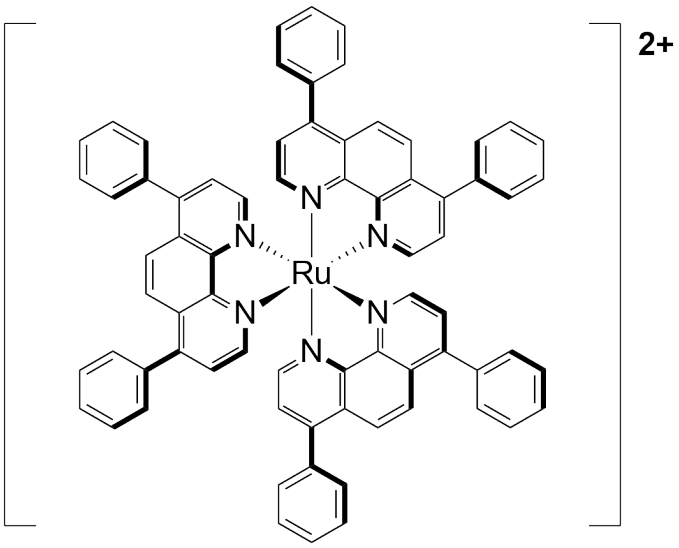

Figure 3.4: The structure of $[Ru(DIP)_3]^{2+}$, shown here as the Δ-enantiomer, which selectively bound to B-DNA.[200]

While initial studies focused on mononuclear species, this was extended to dinuclear compounds in an effort to strengthen interactions with DNA. In 1998, the dinuclear compounds $[\{Ru(bpy)_2\}_2\{\mu\text{-}bb_n\}]^{4+}$ (where bb_n = bis[4(4′-methyl-2,2′-bipyridyl)]-1,*n*-alkane, for n = 3 or 5) were reported by Kelly and co-workers.[201] For these compounds, the authors demonstrated that the dinuclear species had an increased DNA binding affinity when compared to the parent $[Ru(bpy)_3]^{2+}$ and $[Ru(bpy)_2(Me_2bpy)]^{2+}$ compounds (where bpy = 2,2′-bipyridine, and Me_2bpy = 4,4′-dimethyl-2,2′-bipyridine). In addition, Keene and co-workers have studied dinuclear ruthenium(II) compounds linked by 2,2′-bipyrimidine (bpm) and 1,4,5,8,9,12-hexaazatriphenylene (HAT), which were found to bind preferentially at DNA bulge sites.[154,202] Although these species showed promise as a probe for non-duplex type binding, the planar bridging ligand prevented binding of both ruthenium centres in the groove simultaneously. To increase the flexibility and potentially the strength of biological interactions the authors synthesised a variety of compounds based upon those described by Kelly and co-workers, of the type $[\{Ru(phen)_2\}_2\{\mu\text{-}bb_n\}]^{4+}$ (where n = 3, 5, 7, 10, 12, or 16; see Figure 3.5).[203] Subsequent separation of the isomeric forms allowed binding studies to be conducted with a range of oligonucleotide sequences. These compounds were found to bind selectively in the minor groove of DNA, with the addition of the flexible linking chain allowing the compound to follow the curvature of the DNA minor groove.

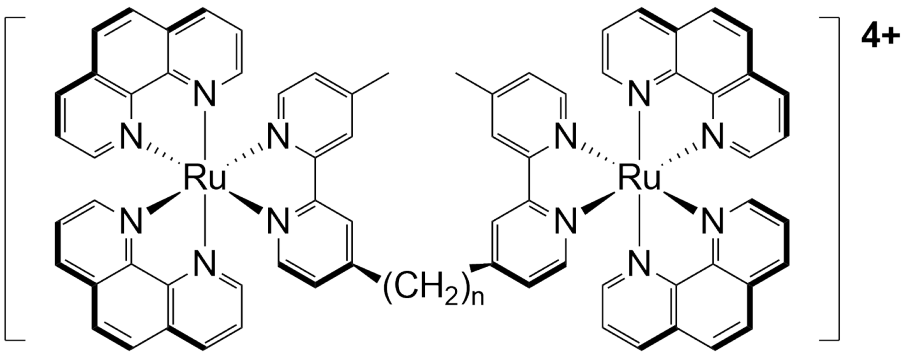

Figure 3.5: The structure of $[\{Ru(phen)_2\}_2\{\mu\text{-}bb_n\}]^{4+}$, where n = 3, 5, 7, 10, 12, or 16, which has been studied extensively by Keene and co-workers in biological settings.[203]

Of particular interest to this thesis, metallohelicates have also been explored as DNA binders.[204] Lehn and co-workers described the first example, showing a double-stranded Cu(I) helicate bound strongly to DNA using spectroscopic, DNA-melting, and electrophoretic-mobility measurements.[205] The precise mode of interaction was unable to be characterised, although the authors suggested groove-binding as the likely scenario. This work served as the inspiration for the group of Hannon, synthesising a triple-stranded Fe(II) helicate, which mimicked the dimensions of the α-helical DNA recognition unit of zinc-finger proteins.[206–209] This system has been thoroughly explored and by utilising a range of analytical techniques, the authors were able to show that the helicate bound strongly in the major groove of DNA and induced intra-molecular coiling.

The innate chirality of metallohelicates makes them ideal candidates for the chiral recognition of DNA, a useful characteristic in drug development.[210] This has been demonstrated for the system designed by Hannon (described above) where the *M*- and *P*-helicates (left- and right-handed respectively) were shown to have different interactions with DNA. While the *M*-enantiomer bound in the major groove and induced strong coiling of DNA, the binding mode of the *P*-enantiomer was more ambiguous and did not coil DNA to the same extent.[68,171,211]

This compound has also been studied with non-canonical DNA, being found to fit in the central hydrophobic cavity of a three-way DNA junction.[211,212] This particularly unusual binding mode was characterised by single crystal X-ray diffraction (SCXRD) and remains the only helicate-biomolecule interaction to be studied crystallographically.[213] Subsequently, external chiral amino acid groups have been appended to the helicate, further promoting formation of the three-way junction.[170] Yu *et al.* have also shown chiral selectivity in the binding of Fe(II) and Ni(II) helicates (containing the same ligand as the compounds studied by Hannon) with human telomeric G-quadruplex (G4) DNA, where the right-handed forms were found to stabilise antiparallel G4.[214]

In the cases discussed above, it has generally been proposed that triple-stranded helicates bind in the major groove, except for non-canonical DNA sequences. For Ru(II) helicates, although the activity in anti-bacterial,[80] anti-viral,[79] and anti-cancer[73,82] settings has been investigated, studies into the specific mode of binding with DNA have been limited. Hannon's triple-stranded Ru(II) helicate was found to distort the structure of DNA and exhibited cytotoxicity in breast-cancer cell lines.[73] Subsequently the ability to bind and cleave DNA with sequence specificity (mainly at guanine residues),[78] as well as anti-viral activity of the Ru(II) compound were described.[79] The only reports of double-stranded Ru(II) helicates and mesocates in biological studies are by Allison *et al.*, where they were tested against a human colorectal cancer cell line (HCT116).[82] The authors report that one of the helicate isomers was preferentially cytotoxic towards the null-type HCT116 $p53^{-/-}$ cancer cells, while the mesocate showed reverse selectivity, being more cytotoxic against the wild-type HCT116 $p53^{+/+}$. The helicate was found to be taken up in the nucleus of the cell and UV thermal melting profiles indicated that genomic DNA was stabilised in the presence of the compound.

Interest in studying the biological interactions of the double-stranded compounds described in **Chapter 2** of this thesis stems from the work of Glasson *et al.*, in which the binding of DNA with enantiomers of a diruthenium(II) triple-stranded helicate was studied.[66] In this case a range of oligonucleotides were immobilised on Sepharose, an affinity chromatography medium (as described by Smith *et al.*),[154] and showed close to total enantioselection of the helicate with an AT-rich dodecanucleotide, where the *P*-helicate was strongly retained while *M*-helicate eluted with the solvent front. Less efficient separations were observed for a GC-rich dodecanucleotide, a bulge tridecanucleotide, and a 6-base CT hairpin loop. In all cases substantial chiral discrimination was evident, with the *P*-helicate bound more strongly to DNA. Based on the enantioselection seen for triple-stranded helicates both by Glasson *et al.*,[66] and other authors,[171,172] it was anticipated that a chiral preference would be shown for the *M*- and *P*-enantiomers of the double-stranded Ru(II) helicate described in **Chapter 2** with oligonucleotides. Through NMR studies, which were not undertaken by Glasson *et al.*, complimented by dialysis and linear dichroism (LD) spectroscopic studies, the binding of the double-stranded diruthenium(II) mesocate (**4**) and partially resolved enantiomers of the helicate (**3**) described in **Chapter 2**, was investigated. All biological studies were undertaken in buffered aqueous solutions, using the Cl^- salts of the ruthenium(II) compounds.

3.2 Dialysis

Initially, the enantiomeric preference for DNA of a racemic mixture of the double-stranded helicate (**3**) was probed by simple dialysis experiments. This approach was used by Glasson *et al.* to show preferential binding of one enantiomer of their triple-stranded helicate to B-type DNA.[66] The concept is quite straightforward: a dialysis tube containing calf thymus DNA (ct-DNA) is immersed in a solution containing a racemic mixture of the compound of interest. This sample is stirred for 24 - 48 hours, as illustrated below (Figure 3.6), and following this, the circular dichroism (CD) spectrum of the outer solution is analysed. If an enantiomeric preference exists, this outer solution will have a signal corresponding to one hand, as the other hand is preferentially bound to the DNA in the inner tube. The molecular weight cut-off of the dialysis tubing is selected to allow the compound to permeate the membrane, while preventing the DNA from escaping.

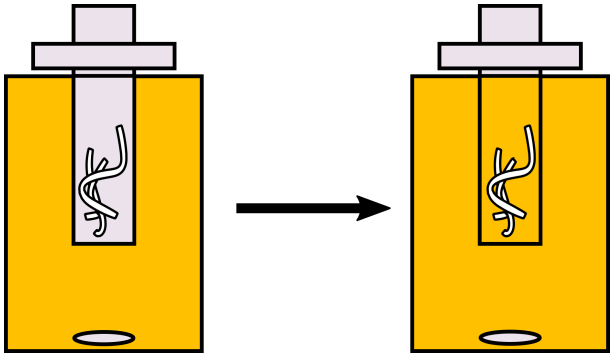

Figure 3.6: Schematic representation of the dialysis setup, showing the experiment at the start of the experiment (left), and after hours to days of dialysis (right).

To determine whether an enantiomeric preference was evident in the binding of the helicate with DNA an equilibrium dialysis experiment was performed using a racemic mixture of the helicate with ct-DNA. The solution was stirred over a period of 48 hours at room temperature and the CD spectrum of the outer solution recorded. The CD spectrum, as well as the spectra for the separated enantiomers, is shown below in Figure 3.7. It can be seen that the outer dialysis solution has no clear signals matching either enantiomer, although after 48 hours both the inner and outer solutions were observed to be orange, indicating that the helicate had permeated the dialysis tubing. From this result it can be inferred both the outer and inner (where the DNA is located) solutions must both contain the racemic mixture. This result suggests that there is no clear enantiomeric preference for the helicate in binding to generic B-DNA.

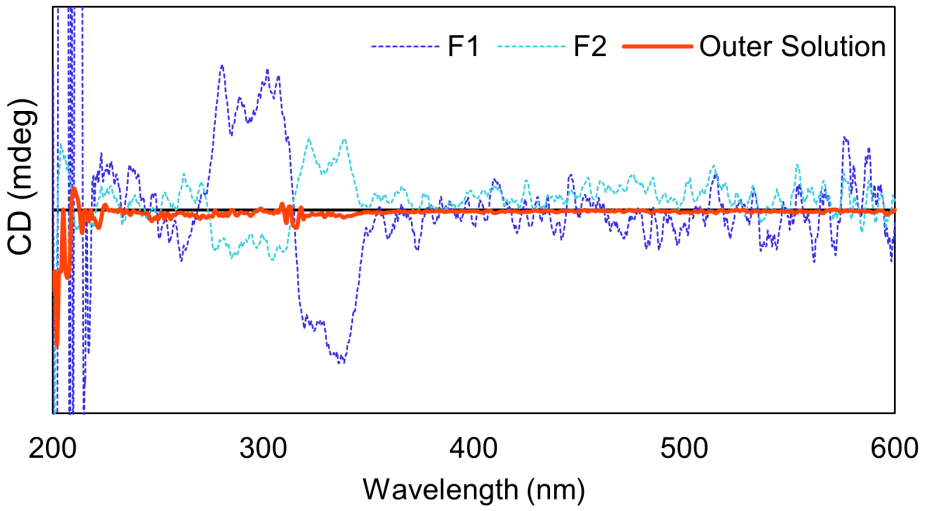

Figure 3.7: CD spectrum of the outer solution from the dialysis of $[Ru_2L_2] \cdot Cl_4$ helicate (**3**) with ct-DNA, in comparison to the partially-resolved helicate fractions (F1 and F2 for resolution on cellulose using 0.2 M NaCl), showing no enantiomeric enrichment.

Dialysis experiments were not undertaken for the mesocate (**4**) as, being an achiral molecule, no enantioselectivity would be expected.

3.3 Linear dichroism spectroscopy

To gain further insight into the interactions the diruthenium(II) compounds with DNA, linear dichroism (LD) spectroscopy was used. LD spectroscopy probes the electronic transitions of a sample that is either intrinsically oriented, or can be oriented by external forces, in this case linearly polarised electromagnetic radiation. In this way LD spectroscopy can be used to determine the orientation of a small molecule in relation to biomacromolecules, including DNA. The light is composed of parallel and perpendicular components, which can be absorbed by the molecule to different extents, producing an LD signal (according to Equation 3.1).

$$LD = A_{\parallel} - A_{\perp} \tag{3.1}$$

LD spectroscopy can be used to probe the conformation and orientation of structures, and has been widely used to understand the mode of interaction in drug-biomolecule systems.[215,216]

Orientation of the system is achieved through the used of a Coulette flow cell. The sample is placed in a chamber between an inner quartz cylinder, which is rotating at high speed, and a fixed outer quartz cylinder (see Figure 3.8). The viscous drag generated as

a result of this set-up aligns the DNA in a specific orientation. When the light passes through the cell and the sample, the difference in absorbance of light linearly polarised parallel and perpendicular to the orientation axis is measured, and thus an LD signal is collected.

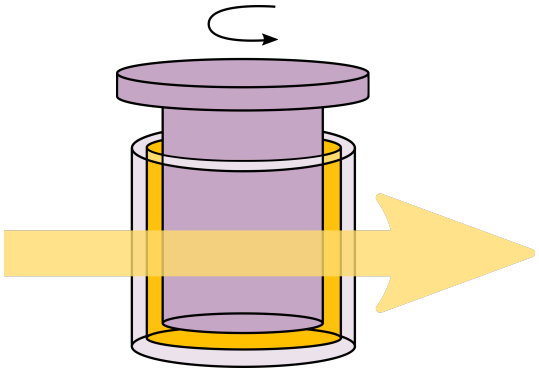

Figure 3.8: Schematic representation of the Coulette flow cell used for the linear dichroism measurements, indicating rotation of the inner quartz cylinder, and direction of light passing through the sample.

DNA has an LD spectrum which is dominated by π-π^* electronic transitions along the DNA backbone.[216] This can be seen clearly in the spectrum shown below (Figure 3.9), where a strong negative band can be observed, with a minimum at 260 nm. A second negative band can be observed at 195 nm, due to the transitions within the DNA phosphodiester backbone.

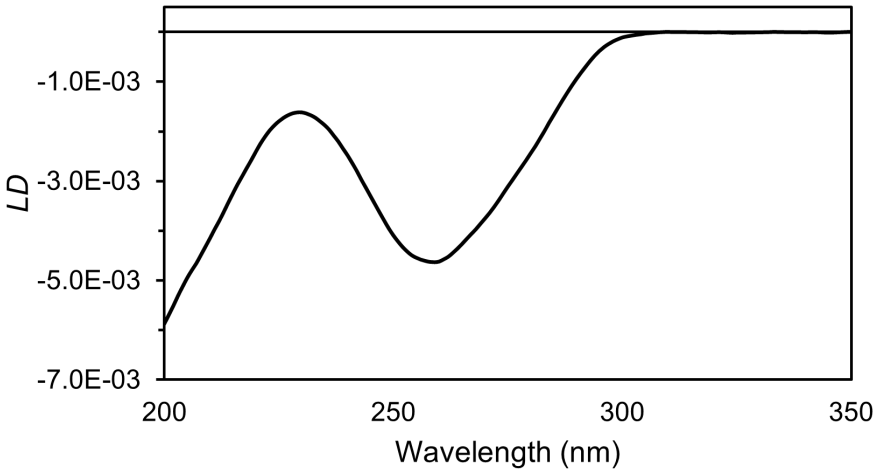

Figure 3.9: LD spectrum of free ct-DNA showing minimum at 260 nm (2×10^{-4} M; K_2HPO_4/KH_2PO_4 (10 mM), NaCl (10 mM), pH 7.3, 25 °C).

Intercalation,[217,218] groove binding,[219,220] and non-specific association of small molecules with DNA perturb the LD spectrum in different ways. Impacts on DNA conformation can also be observed, where intercalating species can stiffen the DNA (elongating the structure) whilst groove binders cause intra-molecular coiling (bending or kinking the DNA).

LD spectroscopy has been shown by Rodger and co-workers to be a useful tool in probing the interactions of metal-containing compounds with DNA.[221] This was also demonstrated by Pages *et al.* in determining the mode of binding for platinum species with ct-DNA.[222] Hannon and co-workers have applied this technique for Fe(II) helicates, showing that these compounds bind to DNA in a specific orientation, a result which in conjunction with other methods revealed major groove binding.[171,206,207] Additionally single-stranded diruthenium(II) compounds have also been studied by LD spectroscopy, showing sequence-dependent bending of DNA.[223,224]

LD experiments were performed under similar conditions to those reported by Pages *et al.*,[222] in this case adding equivalents of double-stranded diruthenium(II) compounds (described in **Chapter 2**) to ct-DNA (200 µM) in buffer {K_2HPO_4/KH_2PO_4 (10 mM, pH 7.3), NaCl (10 mM)}. The concentration of the diruthenium compound was increased over the course of 10 samples and the change in DNA signal at 260 nm monitored.

The LD titration spectrum for ct-DNA with the diruthenium(II) mesocate (**4**) is shown below in Figure 3.10. In this case there is a clear decrease in magnitude of the LD signal at 260 nm upon addition of the mesocate (**4**). This is consistent with a loss of DNA orientation, potentially from coiling or bending of the DNA by the mesocate. Reduction in magnitude of the DNA signal in this manner indicates less orientation with the Coulette flow. From this result it can be inferred that there is increased coiling or condensing of the DNA, relative to the native state. The overall change in ct-DNA response at 260 nm is presented in Figure C.1 (see Section C.3 of Appendix C)

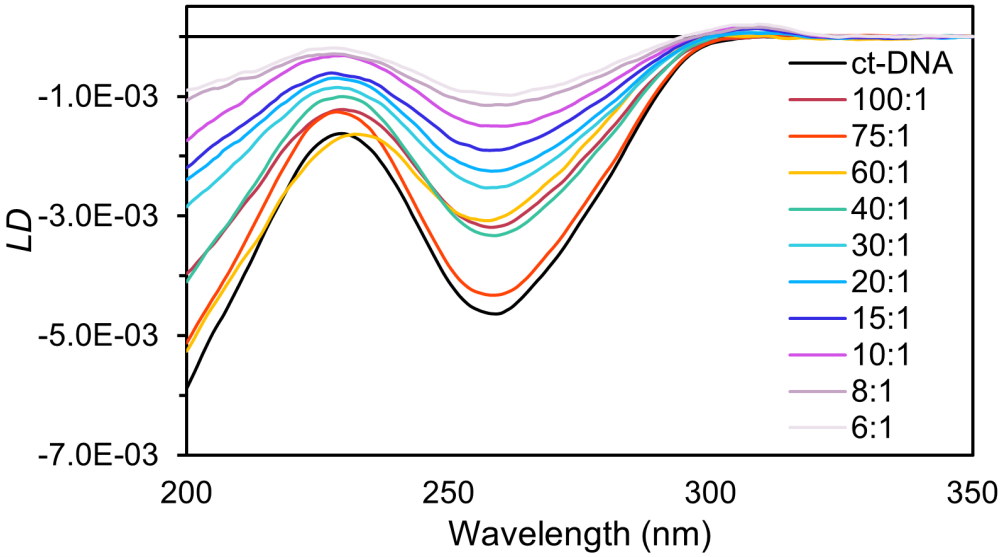

Figure 3.10: LD spectrum of free ct-DNA (2 x 10^{-4} M; K_2HPO_4/KH_2PO_4 (10 mM), NaCl (10 mM), pH 7.3, 25 °C) and in the presence of increasing concentrations of the mesocate (**4**).

The LD titration spectrum for ct-DNA with one partially-resolved enantiomer of the

helicate (in this case F2 from resolution on cellulose with 0.075 M sodium (-)-*O,O′*-dibenzoyl-L-tartrate) is shown below in Figure 3.11. LD experiments were also carried out for the other enantiomer (F1); however, precipitation was observed once the DNA/compound ratio reached 60:1 - suggesting that the diruthenium compound may perturb the orientation of DNA to such an extent that precipitation occurs. As a result no further experiments with this compound were conducted, although it was noted that upon addition of the F1 until this point, a decrease in the signal at 260 nm occurred (see Figures C.2 and C.3 in Section C.3 of Appendix C). The other partially-resolved enantiomer (F2) yielded much more promising results with no precipitation observed. Again, a clear decrease in the DNA signal at 260 nm was observed, indicating condensing of the DNA (see Figure C.4 in Section C.3 of Appendix C).

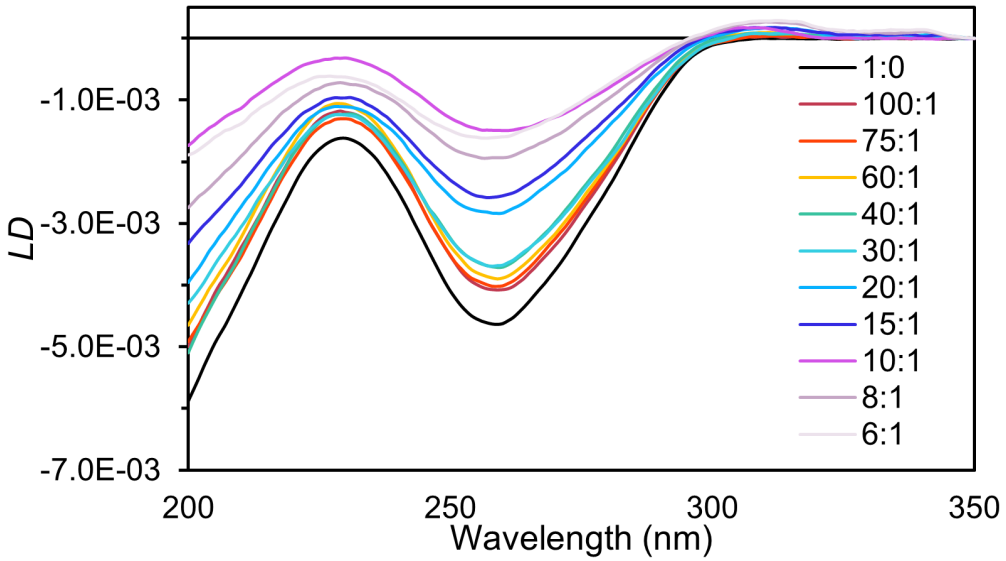

Figure 3.11: LD spectrum of free ct-DNA (2 x 10^{-4} M; K_2HPO_4/KH_2PO_4 (10 mM), NaCl (10 mM), pH 7.3, 25 °C) and in the presence of increasing concentrations of helicate (**3**; F2 from resolution on cellulose with 0.075 M sodium (-)-*O,O′*-dibenzoyl-L-tartrate).

These results suggested that the two enantiomers differed in their manner of interaction with DNA. The first fraction showed precipitation in LD experiments at a ratio of 60 : 1 (DNA/compound) whereas the second fraction remained in solution for the duration of the experiments suggesting that both enantiomers interacted with DNA but the first fraction had significantly stronger binding affinity and thus perturbed the DNA to a greater extent, causing precipitation.

While there was evidence for both the helicate and mesocate interacting with the ct-DNA binding constants were not able to be obtained through further analysis of the data. To gain insight into the nature and strength of DNA binding with both dinuclear species our attention turned to nuclear magnetic resonance (NMR) spectroscopy experiments.

3.4 Nuclear magnetic resonance spectroscopy

NMR spectroscopy is a powerful tool, first developed by Bloch,[225] and Purcell,[226] in 1946, that has been widely used for structure determination in chemistry and biochemistry. NMR spectroscopy, as well as single crystal X-ray diffraction (SCXRD), are valuable tools used in the determination of the structures of biomacromolecules, as well their interactions with small molecules. The use of SCXRD presents challenges in this area as biomacromolecules such as DNA, RNA, and proteins often do not readily crystallise. NMR spectroscopy is a useful alternative, where compounds and biomacromolecules can be studied in solution, which can be a superior representation of their native environment.

The interactions of small molecules with DNA can be studied by examining the changes in chemical shift (δ) values in a 1D NMR spectrum.[227] Upon addition of a small molecule to an oligonucleotide changes in the chemical shift and resonance broadening, which indicate the presence of such interactions, can be observed, with the changes in chemical shift possibly indicating of the mode of DNA binding[227,228] Intercalating drugs cause large upfield shifts for a number of resonances,[229,230] while smaller shifts are generally observed for groove binding drugs.[228,231,232]

2D NMR, in this case nuclear overhauser effect spectroscopy (NOESY), can give further information regarding the site of binding on an oligonucleotide. The rate of exchange between the free DNA and small molecule bound-DNA, reflected in the line width of the resonances, greatly impact the quality of data and ability for NOESY to be used to identify any specific binding site.

The DNA binding of polypyridylruthenium(II) compounds has been widely studied,[186,233,234] and bulky dinuclear ruthenium(II) species have shown to be useful probes for non-duplex DNA.[180] There are fewer examples of NMR spectroscopy being used to study the interactions of helicates and mesocates with DNA. For the triple-stranded Fe(II) helicate reported by Hannon and co-workers NMR structural studies have been carried out, investigating the interactions between the racemic helicate and a double-helical decanucleotide $\{d(GACGGCGTC)_2\}$.[206,235] These studies confirmed binding of the compound in the major groove, as evidenced by NOESY cross-peaks between the helicate and duplex resonances in this region. NMR studies have also been conducted for the *M*-enantiomer of the same compound with two oligonucleotides, $d(TATGGTACCATA)_2$ and $d(CGTACG)_2$, where a three-way junction is formed in solution.[212]

3.4.1 Selection of oligonucleotides

Previous work by Foley *et al.* showed differing binding modes for the two enantiomers of $[\{Ru(Me_2bpy)_2\}_2(\mu bpm)]^{4+}$ (bpm = 2,2′-bipyrimidine), while the *meso* diastereoisomer bound as a combination of both.[166] For all oligonucleotide sequences studied the compounds were found to bind in the minor groove. In this work the authors noted that most organic compounds and mononuclear polypyridylruthenium(II) compounds that bind DNA non-intercalatively bind in the minor groove with a strong preference for A/T-rich sequences. As a result three oligonucleotides were selected for the study in this thesis. The first was from the work of Foley *et al.*, the dodecanucleotide $d(CAATCCGGATTG)_2$ (CCGG), containing a central C/G-rich sequence. A contrasting second dodecanucleotide, $d(ACCGAATTCGGT)_2$ (AATT), containing an A/T-rich central sequence was also selected for study. Finally a bulge sequence, $d(CCGAGAATTCCGG)_2$ (bulge), used in DNA chromatography by Glasson *et al.* to study the enantio-differentiation of their Ru(II) triple-helicate was chosen.[66]

Bulges occur naturally in DNA where one strand contains nucleotides for which a complementary base is absent (a simplified representation of this is shown in Figure 3.12). DNA sequences containing bulges have greater conformational freedom compared to standard oligonucleotides and are able to causing looping-out or kinking arrangements depending on the size and nature of the bulge sequence.[180] In DNA bulges can lead to frameshift mutations (insertion or deletion of nucleotides from a DNA strand),[236–238] and while some can be beneficial,[239] others lead to disease.[240–242] Given that bulky ruthenium compounds have been shown to bind DNA only where the minor groove is adequately wide bulge structures have been proposed as a viable alternative, having a more open or flexible groove.[243]

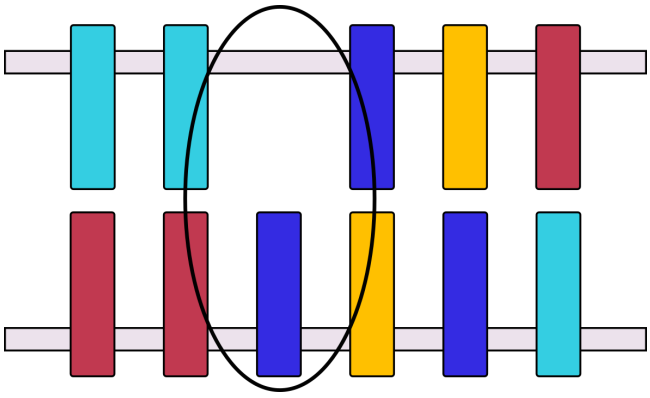

Figure 3.12: A simplified representation of a single-base bulge site, showing an unpaired base.

3.4.2 ^{1}H NMR assignments of free nucleotides

The assignment of the ^{1}H NMR resonances and solution conformation of short oligonucleotides is possible by 1D and 2D NMR spectroscopy, following established methods.[227,244,245] The different resonances of nucleotides are found in specific regions of a 1D spectrum (see Figure 3.13). Nucleotide base hydrogen resonances can be readily assigned, with aromatic non-exchangeable base hydrogens appearing between 7.0 - 8.5 ppm (H2, H6, and H8).[246,247] The H8 of adenosine is usually the most downfield signal as these hydrogens experience ring currents from neighbouring base pairs.[245] Guanosine H8 appears upfield of adenoside H8, while cytosine and thymine H6 resonate further upfield (7.1 - 6.5 ppm). Cytosine H6 resonances appear as doublets (J = 7.5 Hz) as cytosine H6 is coupled to the H5, while all other resonances in the aromatic region appear as singlets.[248] The H1′ sugar hydrogens generally give resonances between 5.5 - 6.5 ppm, H2′/H2″ and thymine methyl hydrogens appear in the range 1.4 - 3.0 ppm, H3′ hydrogens from 4.8 - 5.2 ppm, and sugar H4′/H5′/H5″ resonances between 3.8 - 4.8 ppm.[245]

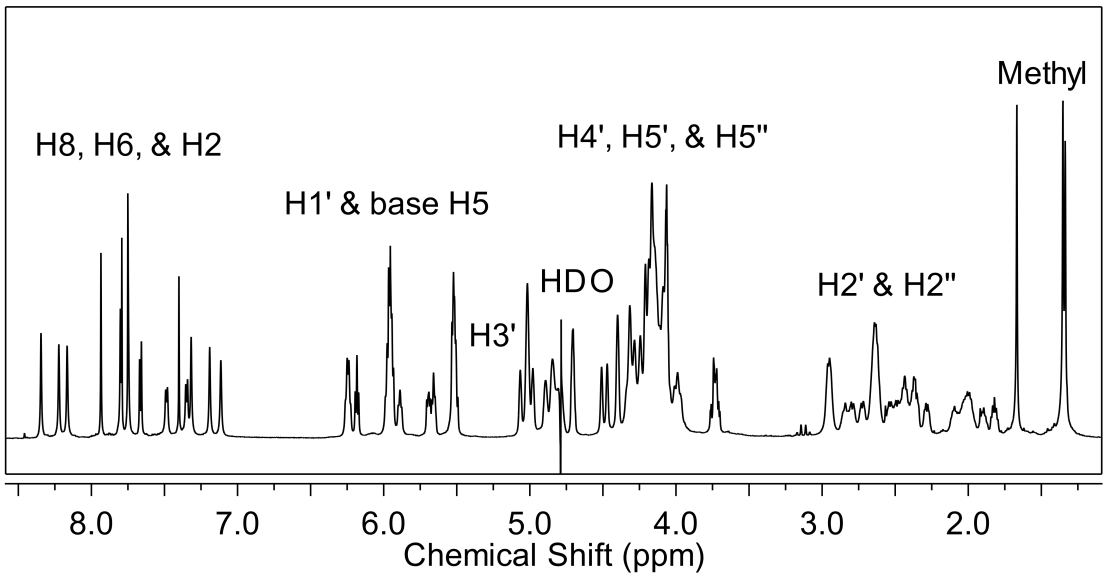

Figure 3.13: Full ^{1}H NMR spectrum of the self-complementary CCGG dodecanucleotide duplex in pH 7.0 phosphate buffer at 25 °C, giving assignments of various nucleotide hydrogens.

Using the details outlined above, the majority of oligonucleotide hydrogen resonances in the aromatic region could be assigned for all oligonucleotides selected for these studies.

For the free CCGG dodecanucleotide aromatic resonances were assigned as shown in Figure 3.14 below. The three furthest downfield resonances at 8.34, 8.22, and 8.16 ppm were assigned as AH8 base hydrogens. The doublets at 7.67, 7.49, and 7.35 ppm were identified as the CH6 base hydrogens. The furthest upfield resonances at 7.31, 7.19, and 7.11 ppm were assigned as the TH6 hydrogens of T_{11}, T_{10}, and T_4, respectively (T_{10} and

T_4 were differentiated using NOESY experiments). The GH8 resonances were assigned at 7.93, 7.80, and 7.74 ppm, with the A_9H2 and A_3H2 signals overlapping with G7 and G8 signals, respectively. The final AH2 (A_2H2) signal was identified at 7.41 ppm.

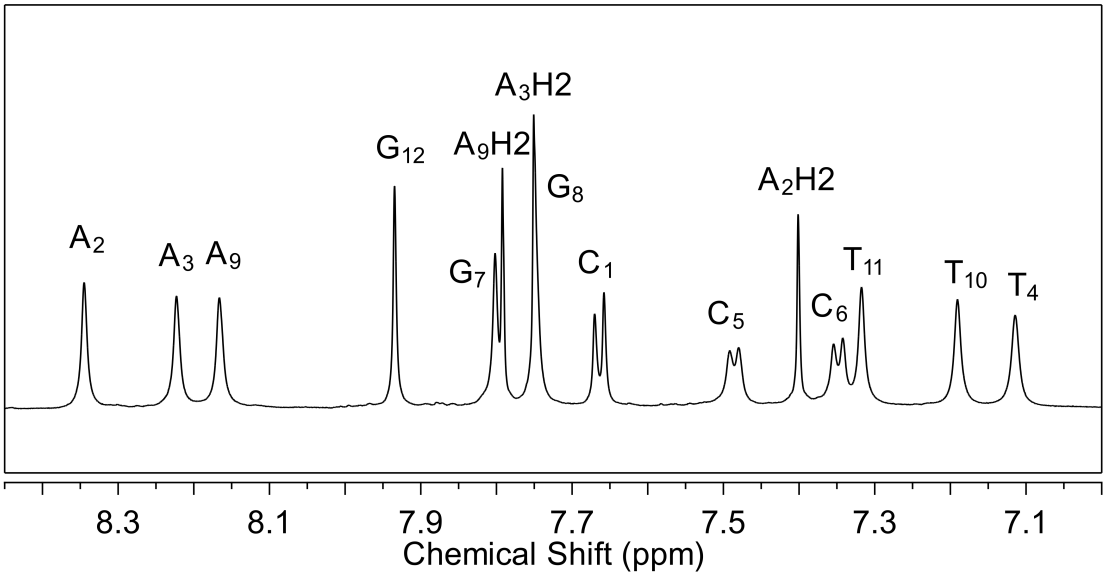

Figure 3.14: An expansion of the aromatic region of the ^{1}H NMR spectrum of the self-complementary CCGG dodecanucleotide duplex in pH 7.0 phosphate buffer at 25 °C, giving assignments of various nucleotide hydrogens.

2D NMR spectroscopy was used to assist in the identification of oligonucleotide resonances. In B-type DNA the H6 or H8 hydrogens of the bases show a nuclear overhauser effect (NOE) to the H1′, H2′, and H2″ hydrogens of the attached sugar residue, as well as the corresponding sugar hydrogens on the nucleotide in the 5′-direction, as illustrated in Figure 3.15.[229]

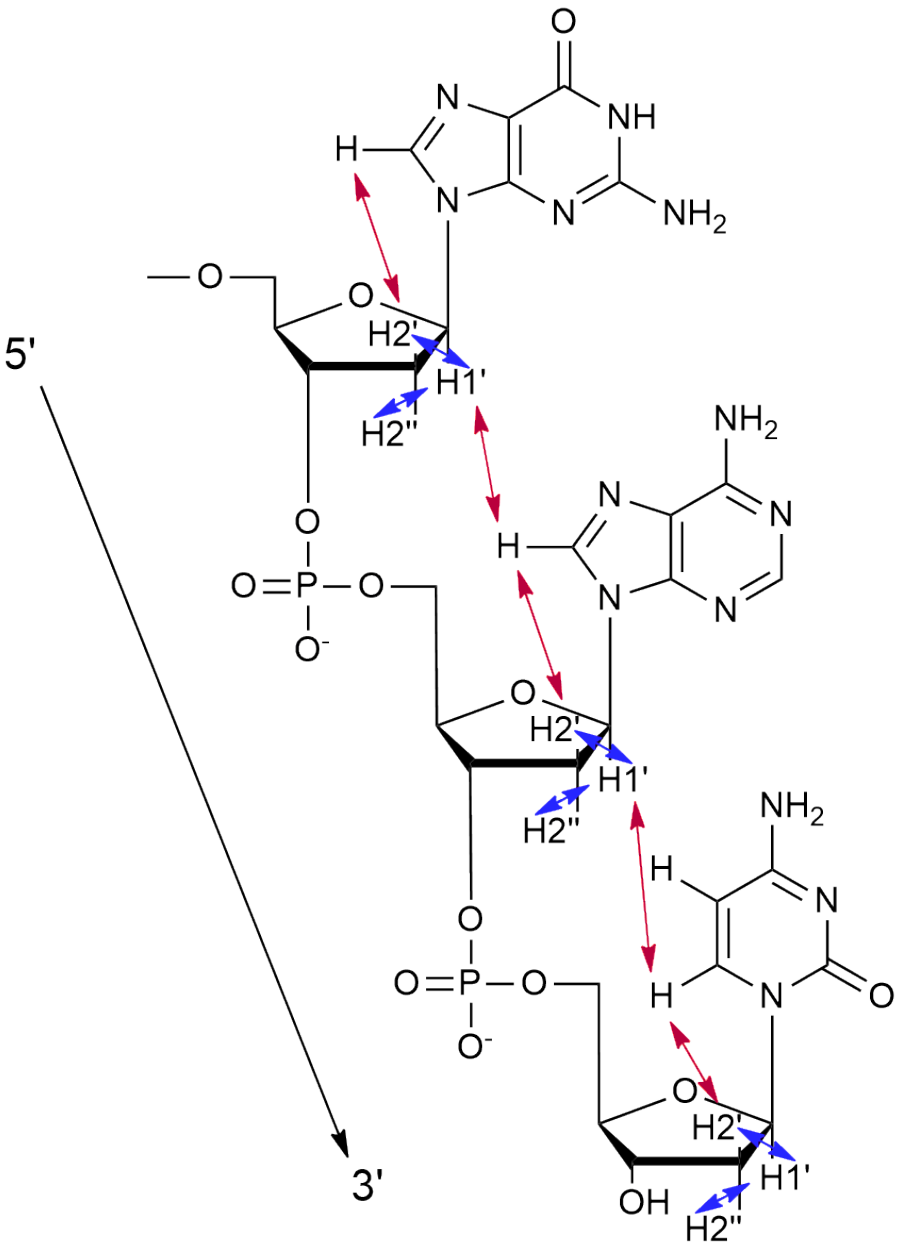

Figure 3.15: Connectivities between base hydrogens and H1′ hydrogens (shown in red) and sugar H1′ to H2′ and H2″ (shown in blue).

The NOE connectivity between base hydrogens and H1′ resonances of the sugars can be used to assign peaks in the H1′/base H5 region of the spectrum. For the CCGG dodecanucleotide the C_1H6 can be readily assigned as there is only one NOE to the H1′ hydrogens, there being no nucleotide in the 5′-direction. A cross-peak, at 5.66 - 8.34 ppm, is the NOE from the A_2H8 to the H1′ of the 5′-flanking nucleotide, C_1. The next cross-peak at 5.94 - 8.34 ppm, is the NOE from the A_2H8 hydrogen to its own H1′. Following this pattern the NOEs can be used to sequentially assign the chemical shifts of the aromatic and H1′ hydrogens for each base in the dodecanucleotide, as shown for CCGG in Figure 3.16 below.

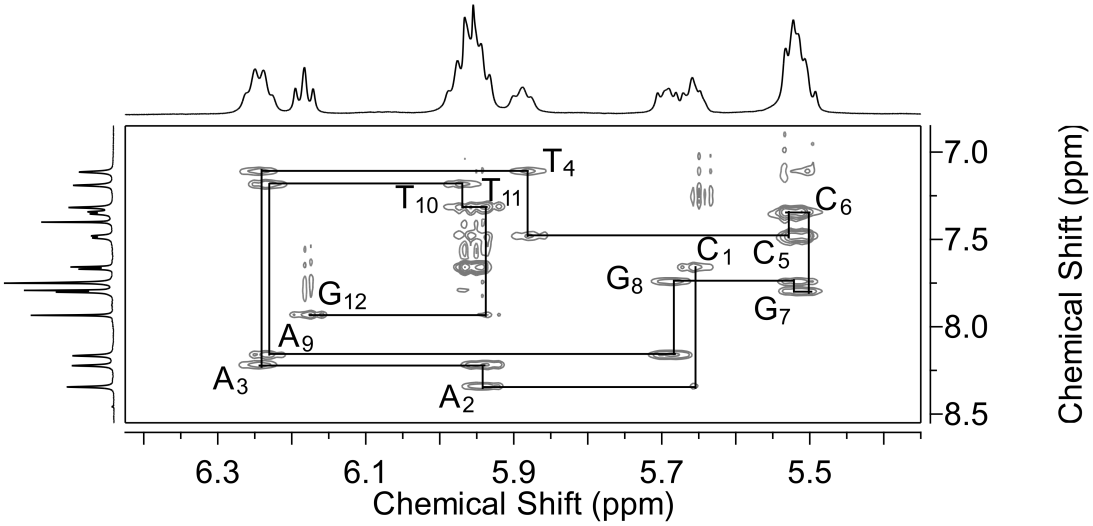

Figure 3.16: Expansion of a NOESY spectrum of the self-complementary CCGG dodecanucleotide duplex in 10 mM pH 7.0 phosphate buffer at 25 °C, showing sequential NOE connectivities between the base hydrogens and H1′ of the sugars.

By the same method the H2′ and H2″ hydrogen resonances can also be assigned. Four NOEs are anticipated for each H6 and H8 base hydrogen, two from their own sugar H2′/H2″ hydrogens, and two from the H2′/H2″ hydrogens on the corresponding sugar residue in the 5′-direction.[229] The C_1 base gives only two NOEs, to its own sugar hydrogens. The methyl hydrogens of the thymine bases were identified at 1.65, 1.34, and 1.32 ppm for T_{11}, T_{10}, and T_4, respectively (see Figure 3.17). In these cases the methyl hydrogens show NOE contacts to their H6 hydrogens and the H8 hydrogens of the nucleotide in the 5′ direction.

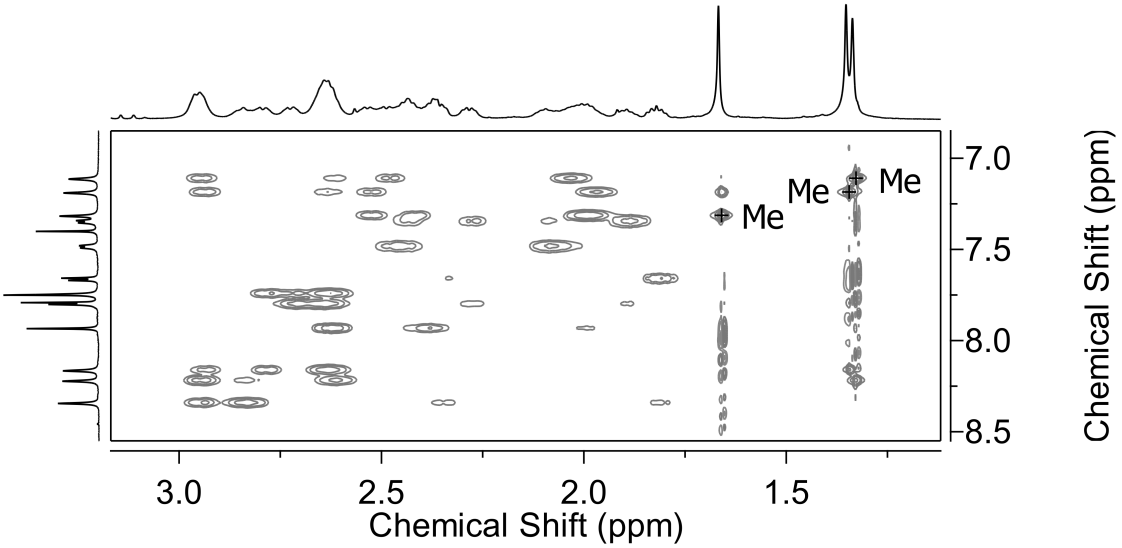

Figure 3.17: Expansion of a NOESY spectrum of the self-complementary CCGG dodecanucleotide duplex in 10 mM pH 7.0 phosphate buffer at 25°C, showing NOEs between the base hydrogens in the aromatic region and H2′, H2″ of the sugars, and methyl of the thymine bases.

The assignments of the oligonucleotide resonances were determined at 25 °C but the spectrum was also recorded as a function of temperature to allow calculation of changes in chemical shift at other temperatures upon addition of diruthenium(II) compounds (see Figure 3.18 for the CCGG dodecanucleotide, other oligonucleotides are located in Section C.4.3 of Appendix C).

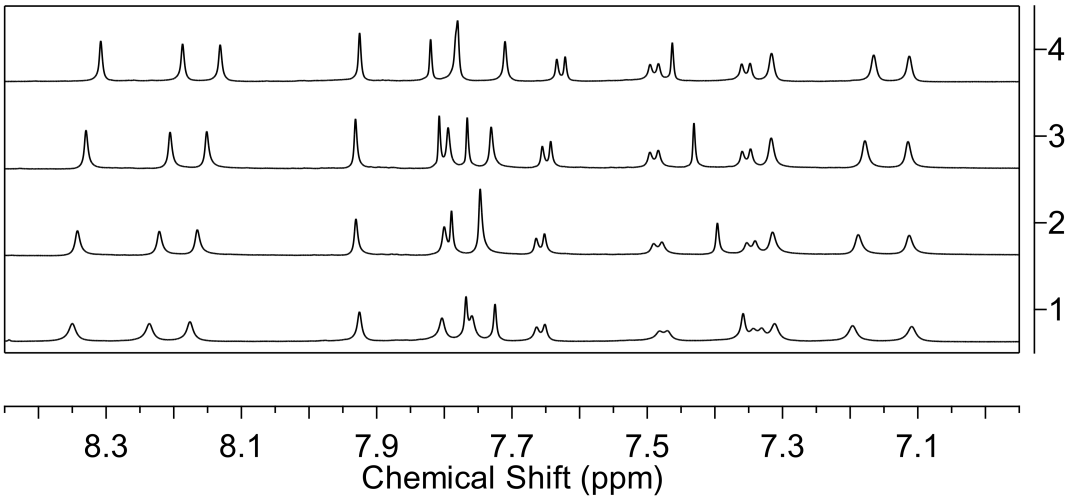

Figure 3.18: ^{1}H NMR spectrum of the aromatic hydrogens of the self-complementary CCGG dodecanucleotide duplex in pH 7.0 phosphate buffer at temperatures (1) 15 °C; (2) 25 °C; (3) 35 °C; and (4) 45 °C.

The assigned chemical shift values for the free oligonucleotides studied are shown below in Tables 3.1, 3.2, and 3.3 below, for the CCGG, and AATT dodecanucleotides, and the bulge sequence, respectively. Additional NMR spectra for assignment of the AATT and bulge oligonucleotides are included in Section C.4.3 of Appendix C.

Table 3.1: ^{1}H NMR assignment of the DNA resonances of the self-complementary CCGG dodecanucleotide duplex in D_2O and pH 7.0 phosphate buffer at 25 °C.

Base	H8/H6	AH2	H1′	H2′	H2″	Methyl
C_1	7.67		5.66	1.81	2.34	
A_2	8.34	7.41	5.94	2.83	2.94	
A_3	8.22	7.76	6.24	2.61	2.94	
T_4	7.11		5.88	2.03	2.47	1.32
C_5	7.49		5.52	2.08	2.46	
C_6	7.35		5.50	1.88	2.29	
G_7	7.80		5.52	2.64	2.71	
G_8	7.74		5.69	2.63	2.77	
A_9	8.16	7.80	6.23	2.63	2.93	
T_{10}	7.19		5.96	1.97	2.52	1.34
T_{11}	7.31		5.92	1.99	2.42	1.65
G_{12}	7.93		6.18	2.62	2.38	

Table 3.2: ^{1}H NMR assignment of the DNA resonances of the self-complementary AATT dodecanucleotide duplex in D_2O and pH 7.0 phosphate buffer at 25 °C.

Base	H8/H6	AH2	H1′	H2′	H2″	Methyl
A_1	8.26	8.08	6.27	2.70	2.82	
C_2	7.47		5.88	2.14	2.41	
C_3	7.40		5.49	1.93	2.29	
G_4	7.87		5.46	2.69	2.77	
A_5	8.13	7.26	6.01	2.71	2.94	
A_6	8.12	7.63	6.17	2.57	2.94	
T_7	7.12		5.91	1.99	2.57	1.28
T_8	7.38		6.09	2.16	2.56	1.54
C_9	7.42		5.65	1.98	2.36	
G_{10}	7.86		5.55	2.69	2.69	
G_{11}	7.81		6.10	2.62	2.73	
T_{12}	7.42		6.27	2.26	2.26	1.60

Table 3.3: ^{1}H NMR assignment of the DNA resonances of the bulge oligonucleotide duplex in D_2O and pH 7.0 phosphate buffer at 25 °C.

Base	H8/H6	AH2	H1′	H2′	H2″	Methyl
C_1	7.81		6.04	2.09	2.54	
C_2	7.53		5.63	1.96	2.27	
G_3	7.89		5.64	2.42	2.72	
A_4	7.92	7.61	5.69	2.49	2.53	
G_5	7.75		5.33	2.54	2.59	
A_6	8.05	7.32	5.96	2.67	2.89	
A_7	8.11	7.71	6.20	2.60	2.90	
T_8	7.13		5.91	2.00	2.56	1.28
T_9	7.40		6.08	2.16	2.56	1.57
C_{10}	7.52		6.19	1.96	2.18	
C_{11}	7.71		5.51	2.19	2.37	
G_{12}	7.88		5.68	2.67	2.71	
G_{13}	7.85		6.17	2.57	2.39	

3.4.3 Assignment of the free double-stranded compounds

The resonances of the free mesocate (**4**) and helicate (**3**) were assigned using standard 1D and 2D NOESY experiments. The structure of the free diruthenium species, with atom numbering, and the ^{1}H NMR spectrum of the compounds are shown in Figures 3.19 and 3.20 respectively. The assignments of the resonances are given in Table 3.4.

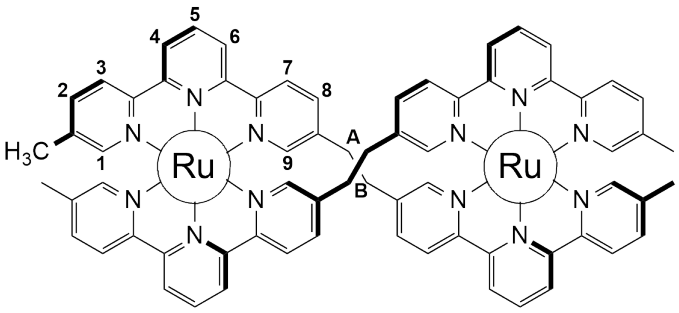

Figure 3.19: Generalised structure and numbered annotation of the Ru(II) double-stranded compounds.

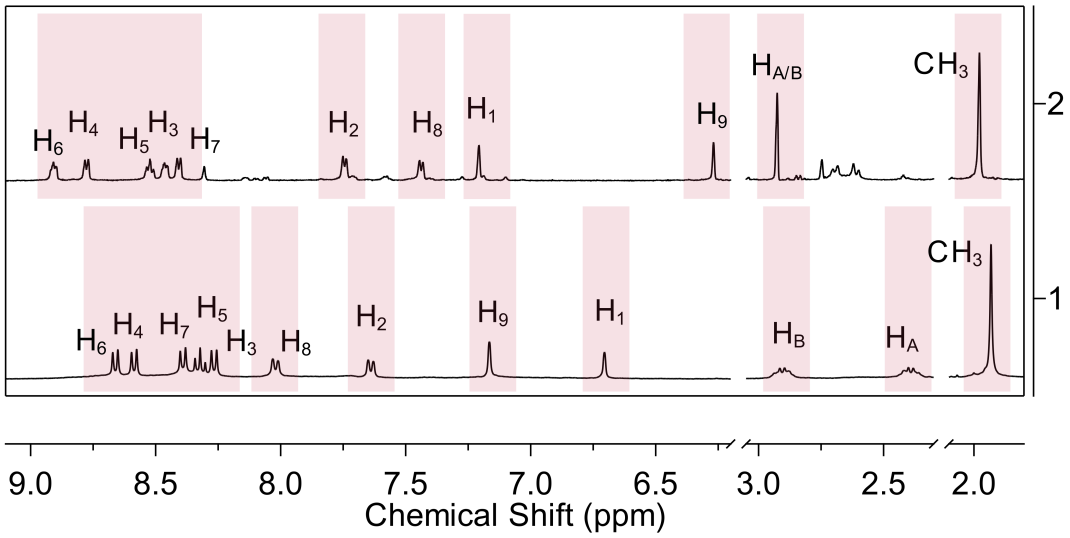

Figure 3.20: ^{1}H NMR spectrum and assignments of the free Ru(II) double-stranded compounds as Cl^- salts, showing (1) mesocate (**4**), and (2) helicate (**3**), in D_2O at 25 °C. Ru(II) compound peaks are highlighted in red.

Table 3.4: Chemical shift assignments (ppm) of the free Ru(II) double-stranded compounds as Cl^- salts in D_2O at 25 °C.

Assignment	**Mesocate** (**4**)	**Helicate** (**3**)
H_1	6.70	7.21
H_2	7.65	7.75
H_3	8.28	8.47
H_4	8.60	8.78
H_5	8.34	8.54
H_6	8.67	8.91
H_7	8.40	8.42
H_8	8.03	7.44
H_9	7.17	6.27
H_A	2.91	2.93
H_B	2.40	
CH_3	1.93	1.98

3.4.4 Mesocate (**4**) binding to the CCGG dodecanucleotide

Titration of the dodecanucleotide d(CAATCCGGATTG)$_2$ (CCGG) with the mesocate (**4**) at 25 °C revealed that upon addition of the compound an orange precipitate immediately formed resulting in very broad low intensity peaks which were barely visible above the baseline of the spectrum corresponding to the mesocate. To increase solubility the temperature was raised to 45 °C; however, even at this temperature significant precipitation was still observed. In Figure 3.21 (shown below) the ratio of added mesocate to oligonucleotide was estimated at an added ratio (R*) of approximately 0.6 equivalents, not accounting for precipitation of the compound or DNA.

Comparing the ^{1}H NMR spectrum in the aromatic region for the free CCGG to CCGG with added mesocate at 25 °C, it can be seen that there were only very small changes in the chemical shifts of the H6/H8 resonances. In this region the most noticeable shifts were for the AH2 hydrogens (highlighted in blue, see Figure 3.21). All AH2 signals showed an upfield shift of equal magnitude (0.02 ppm) compared to the free dodecanucleotide. All other dodecanucleotide hydrogens showed no change in chemical shift in the aromatic region as the mesocate ratio was increased.

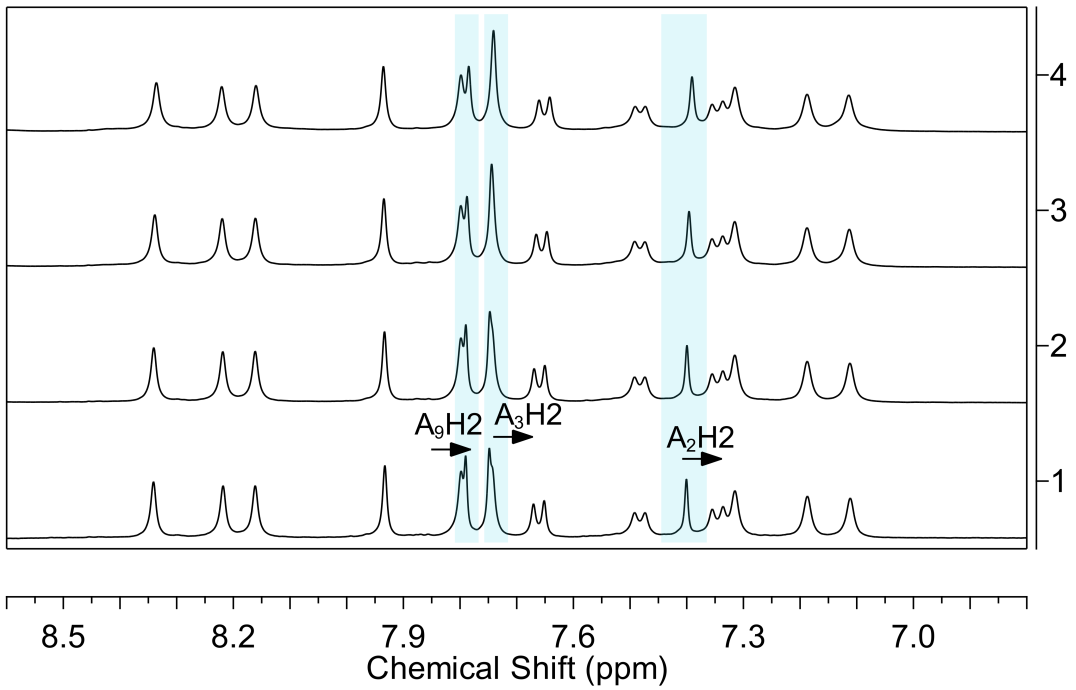

Figure 3.21: Aromatic region of the ^{1}H NMR spectrum of the titration of the CCGG dodecanucleotide with the diruthenium mesocate (**4**) in pH 7.0 phosphate buffer at 25 °C, (1) free dodecanucleotide, (2) R* = 0.1, (3) R* = 0.3, and (4) R* = 0.6. Notable changes in the chemical shift and shape of the oligonucleotide resonances are highlighted in blue.

In the H1′/base H5 region, there were very few changes in the shape and position of the

dodecanucleotide resonances upon addition of the mesocate. The most obvious variation was in the chemical shift of C_1H1' which was shifted upfield by 0.03 ppm, highlighted in blue in Figure 3.22 below.

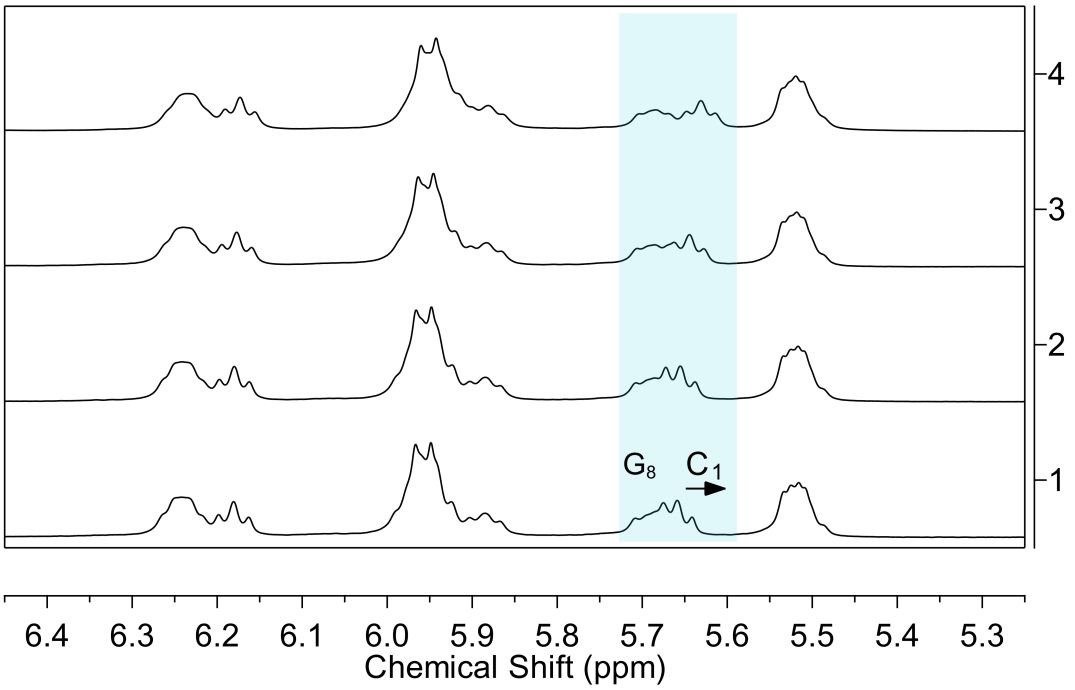

Figure 3.22: The H1′/base H5 region of the ^{1}H NMR spectrum of the titration of the CCGG dodecanucleotide with the diruthenium mesocate (**4**) in pH 7.0 phosphate buffer at 25 °C, (1) free dodecanucleotide, (2) R* = 0.1, (3) R* = 0.3, and (4) R* = 0.6. Notable changes in the chemical shift and shape of the oligonucleotide resonances are highlighted in blue.

A summary of the changes in chemical shift observed is outlined in Table 3.5 below. Outside of the H8/H6/AH2 and H1′/base H5 regions discussed above, small downfield shifts were recorded for the methyl hydrogens of the thymine residues (0.01 - 0.02 ppm in magnitude). It should be noted that while slight changes in the chemical shifts were reported for the dodecanucleotide with added mesocate across the spectrum, the magnitude of these changes (between 0.01 - 0.03 ppm) was very small compared to other dinuclear compounds studied with DNA by these methods. However, it should be noted that R* is merely the added ratio of compound, not the ratio of soluble compound to oligonucleotide. All changes in chemical shift of the DNA resonances were relative to the true compound/DNA ratio. In this case, a relative shift of 0.03 ppm may be small but is significant, given that the accuracy of chemical shift measurements is no worse that 0.01 ppm based upon the number of resonances that show change of 0.00 ppm. If the true ratio of compound/DNA could be increased to R = 1, it is anticipated that changes of greater magnitude in the chemical shift of oligonucleotide resonances would be observed. However,

the significant precipitation and broadness of mesocate signals makes it challenging to discern the true ratio. The precipitate was proposed to contain both Ru(II) compound and DNA, but perhaps in a ratio > 1.

Due to the poor solubility NOESY spectra for the CCGG dodecanucleotide with added mesocate were not collected at 25 °C, and chemical shifts for H2′ and H2″ were not recorded.

Table 3.5: ^{1}H NMR assignment of the DNA resonances of the CCGG dodecanucleotide with the diruthenium mesocate (**4**) at R* = 0.6, in D_2O and pH 7.0 phosphate buffer at 25 °C. Changes in chemical shift are given in brackets, with a negative sign indicating an upfield shift.

Base	H8/H6	AH2	H1′	Methyl
C_1	7.66 (-0.01)		5.63 (-0.03)	
A_2	8.34 (0.00)	7.39 (-0.02)	5.94 (0.00)	
A_3	8.22 (0.00)	7.74 (-0.02)	6.24 (0.00)	
T_4	7.11 (0.00)		5.88 (0.00)	1.34 (0.02)
C_5	7.50 (0.01)		5.53 (0.01)	
C_6	7.35 (0.00)		5.51 (0.01)	
G_7	7.8 (0.00)		5.52 (0.00)	
G_8	7.74 (0.00)		5.68 (-0.01)	
A_9	8.16 (0.00)	7.78 (-0.02)	6.23 (0.00)	
T_{10}	7.19 (0.00)		5.96 (-0.01)	1.35 (0.01)
T_{11}	7.31 (0.00)		5.92 (0.00)	1.67 (0.02)
G_{12}	7.94 (0.01)		6.17 (-0.01)	

Initially, it was thought that the precipitation may be due to poor solubility of the free compound in phosphate buffer. In an attempt to remedy this the sample was diluted, reducing the phosphate buffer concentration from 10 mM to 2 mM, and then 1 mM, while adding additional equivalents of the mesocate to allow peaks corresponding to the compound to be observed. Precipitation was still seen for all samples, even at the lowest phosphate buffer concentrations. In order to gain further information on the dodecanucleotide binding of the mesocate NOESY experiments were undertaken at 45 °C

to improve solubility. In these experiments the NOEs observed were of very low intensity and the only cross-peaks corresponding to the mesocate appeared to be intra-molecular mesocate-mesocate NOEs appearing downfield of the oligonucleotide signals in the aromatic region (see Figure 3.23).

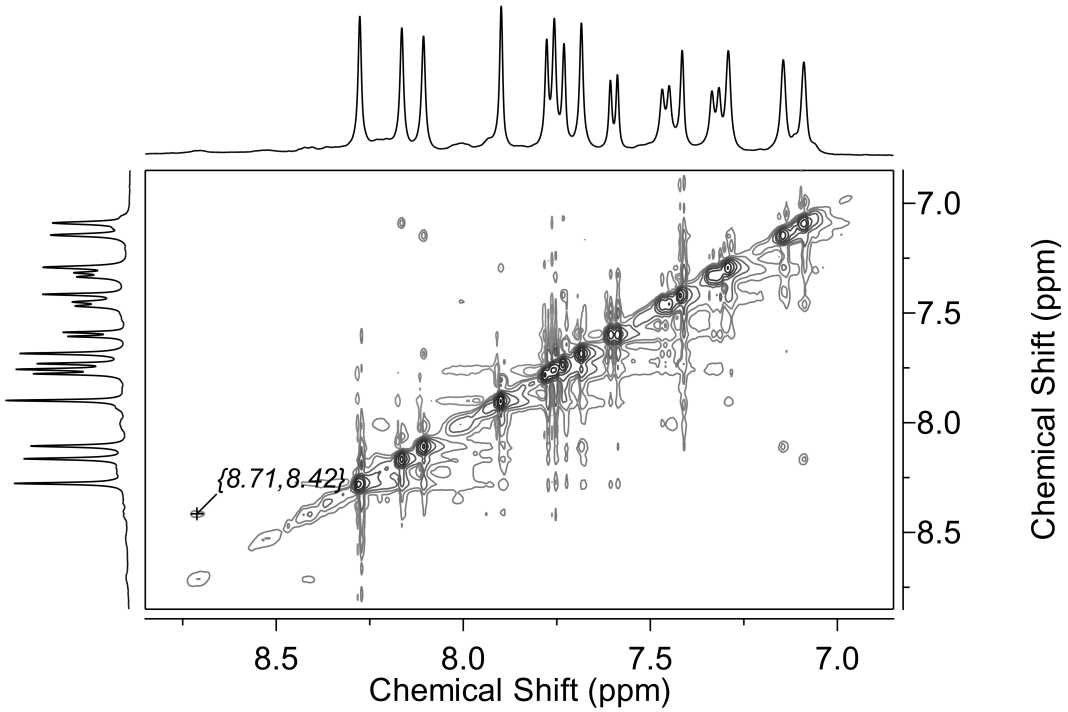

Figure 3.23: Expansion of a NOESY spectrum of the CCGG dodecanucleotide with the diruthenium mesocate (**4**) at R* = 0.6, in 1 mM pH 7.0 phosphate buffer at 25°C, showing a mesocate-mesocate intra-molecular cross-peak.

Overall, despite poor solubility preventing higher ratios of mesocate/dodecanucleotide being reached the preliminary results suggested that binding may occur in the minor groove, based on changes in the chemical shifts of AH2 oligonucleotide hydrogens upon addition of the mesocate. However, without NOEs showing contacts between the mesocate hydrogens and hydrogens located in the minor groove, it was difficult to determine the nature or strength of any inter-molecular interactions.

The solubility of the mesocate was screened in a variety of buffers to determine the cause of the precipitation. The compound was found to be soluble in all buffers tested; however, upon addition of ct-DNA immediate precipitation was observed. While some orange colour remained in solution it was clear that a large proportion of the compound was in the precipitate, as well as the DNA, which hindered efforts to characterise the nature of this interaction. Interestingly, it was noted that the racemate of the helicate, while also being soluble in buffer, did not precipitate as much when ct-DNA was added. As a result, attention turned to investigating the binding of the helicate (**3**) with oligonucleotides, and

the DNA binding of the mesocate was not further pursued by this method.

3.4.5 Helicate (**3**) binding to the CCGG dodecanucleotide

The binding of the enantiomers of the helicate (**3**) (described in **Chapter 2**) with the dodecanucleotide d(CAATCCGGATTG)$_2$ (CCGG) was investigated using the partially-resolved fractions from cellulose chromatography with 0.2 M NaCl.

3.4.5.1 F1 - Helicate (**3**) binding to CCGG

Titration of the CCGG dodecanucleotide with up to 1 equivalent of F1 of the helicate at 25 °C showed only very broad, low intensity peaks corresponding to the helicate in the aromatic region. Figure 3.24 shows the aromatic region of the ^{1}H NMR spectrum of the free CCGG, and CCGG with added F1 of the helicate. The addition of F1 induced minor changes to the chemical shift of the H6/H8 hydrogens (<0.03 ppm), with the greatest shifts (0.03 ppm) observed for the C_1H6, G_8H8, and A_9H8 resonances. Slightly larger changes were recorded for the AH2 resonances (0.02 - 0.05 ppm), with the largest an upfield shift of 0.05 ppm for A_2H2. A broad peak corresponding to the helicate appears downfield of the dodecanucleotide resonances (indicated in red below).

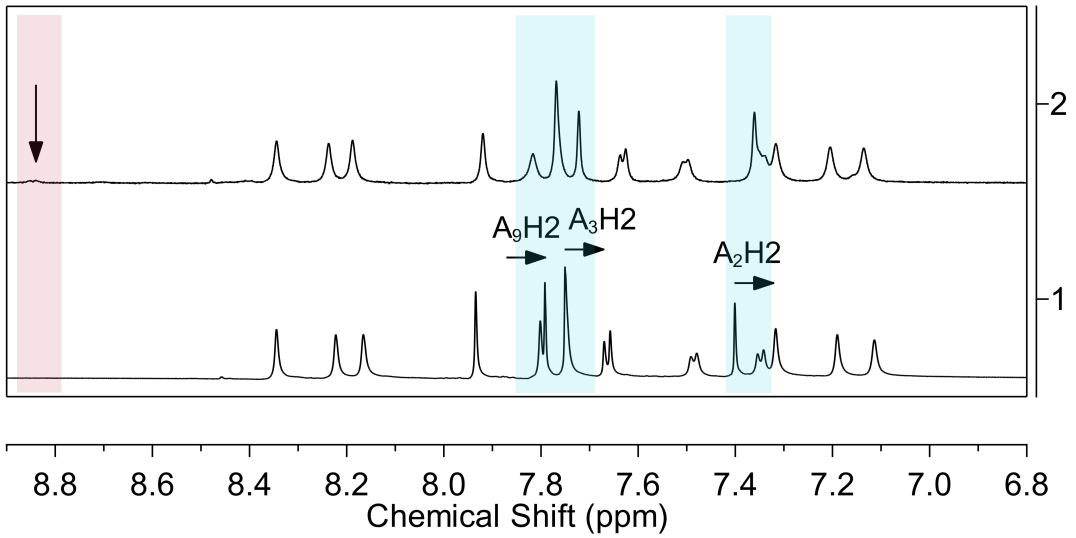

Figure 3.24: Aromatic region of the ^{1}H NMR spectrum of the titration of the CCGG dodecanucleotide with F1 of the diruthenium helicate (**3**) in pH 7.0 phosphate buffer at 25 °C. (1) free oligonucleotide, (2) R* = 1. Notable changes in the chemical shift and shape of the oligonucleotide resonances are highlighted in blue, Ru(II) compound peaks are highlighted in red.

In the H1′/base H5 region of the spectrum, more significant changes in the chemical shifts of the H1′ resonances were evident. The greatest of these was for C_1H1′, with a large

upfield shift (0.09 ppm) shown in Figure 3.25. In addition, small shifts were observed for multiple other H1′ resonances and the broadening of several signals is clearly evident in the spectrum below. Notably, upfield shifts were recorded for the G_7 and G_{12} H1′ hydrogens (0.03 ppm), while C_5, C_6, G_8, and T_{11} all exhibited downfield shifts.

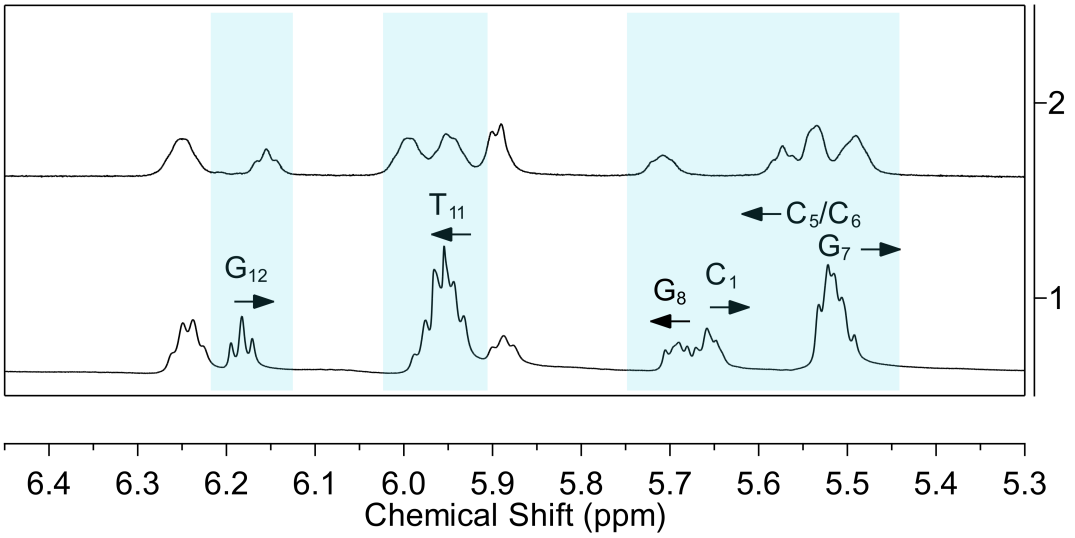

Figure 3.25: The H1′/base H5 region of the ^{1}H NMR spectrum of the titration of the CCGG dodecanucleotide with F1 of the diruthenium helicate (**3**) in pH 7.0 phosphate buffer at 25 °C. (1) free oligonucleotide, (2) R* = 1. Notable changes in the chemical shift and shape of the oligonucleotide resonances are highlighted in blue.

Further upfield, small changes in chemical shift were also seen for the H2′, H2″, and methyl hydrogens of the dodecanucleotide and a full summary of the changes in chemical shift recorded for the CCGG dodecanucleotide with F1 of the diruthenium helicate (**3**) are recorded in Table 3.6 below.

Table 3.6: ^{1}H NMR assignment of the DNA resonances of the CCGG dodecanucleotide with F1 of the diruthenium helicate (**3**) at R* = 1, in D_2O and pH 7.0 phosphate buffer at 25 °C. Changes in chemical shift are given in brackets, with a negative sign indicating an upfield shift.

Base	H8/H6	AH2	H1′	H2′	H2″	Methyl
C_1	7.64 (-0.03)		5.57 (-0.09)	1.76 (-0.05)	2.31 (-0.03)	
A_2	8.36 (0.02)	7.36 (-0.05)	5.95 (0.01)	2.85 (0.02)	2.97 (0.03)	
A_3	8.24 (0.02)	7.72 (0.02)	6.26 (0.02)	2.62 (0.03)	2.97 (0.03)	
T_4	7.13 (0.02)		5.90 (0.02)	2.07 (0.04)	2.50 (0.03)	1.35 (0.03)
C_5	7.51 (0.02)		5.54 (0.02)	2.11 (0.03)	2.48 (0.02)	
C_6	7.36 (0.01)		5.53 (0.03)	1.89 (0.01)	2.27 (-0.02)	
G_7	7.82 (0.02)		5.49 (-0.03)	2.66 (0.02)	2.71 (0.00)	
G_8	7.77 (0.03)		5.71 (0.02)	2.64 (0.01)	2.82 (0.05)	
A_9	8.19 (0.03)	7.77 (-0.03)	6.24 (0.01)	2.64 (0.01)	2.97 (0.04)	
T_{10}	7.21 (0.02)		5.99 (0.03)	2.02 (0.05)	2.56 (0.04)	1.35 (0.01)
T_{11}	7.32 (0.01)		5.95 (0.03)	2.04 (0.05)	2.43 (0.01)	1.67 (0.02)
G_{12}	7.92 (-0.01)		6.15 (-0.03)	2.64 (0.02)	2.39 (0.01)	

As shown in Figure 3.24 broad peaks corresponding to the helicate appeared downfield of the oligonucleotide resonances. The broadness and low intensity of these peaks made it challenging to confirm a 1:1 helicate - oligonucleotide ratio and upon careful observation it was found that a small amount of precipitation had occurred. The extent of the precipitation appeared to be less than that observed for the mesocate in previous experiments, but as before the ratio of soluble Ru(II) compound to oligonucleotide is denoted as R*. Endeavouring to improve the sharpness of these peaks variable temperature experiments were conducted to vary the rate of exchange. The results at 25 °C suggest that the rate of exchange between the free and oligonucleotide-bound Ru(II) compound resonances was on the intermediate timescale - thereby giving broad peaks. It was hoped that lowering the temperature could potentially shift this to slow exchange while a higher temperature could shift it to fast exchange, either of which could assist in improving the helicate signals and confirming the ratio. It was found that at lower temperatures (5 °C, 10 °C) the downfield

aromatic helicate peaks were significantly broadened, while at higher temperatures the peaks did appear to sharpen slightly; however, at no temperature did the overall intensity of the helicate peaks increase, nor did the signals become less broad. The full temperature series is shown below in Figure 3.26 with the downfield peaks corresponding to helicate highlighted in red.

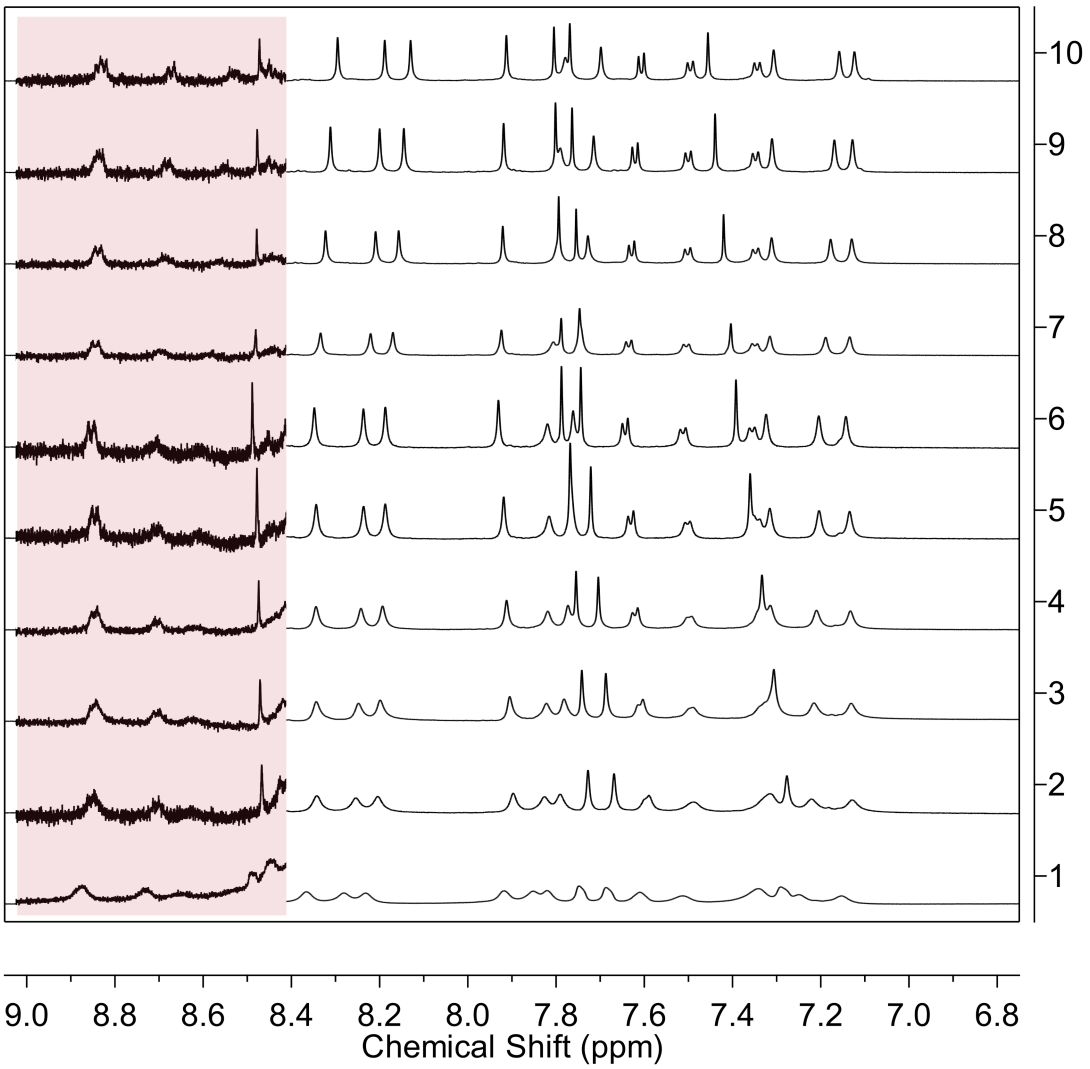

Figure 3.26: Aromatic region of the ^{1}H NMR spectrum of the titration of the CCGG dodecanucleotide with F1 of the diruthenium helicate (**3**) at R* = 1 in pH 7.0 phosphate buffer at temperatures from (1) 5 to (10) 50 °C, in 5 °C increments. The intensity of the spectrum has been increased to show downfield helicate peaks, which are highlighted in red.

To further investigate the interactions between CCGG and F1 of the helicate NOESY experiments were conducted. While some cross-peaks in the aromatic region were clearly helicate-helicate, appearing downfield of the dodecanucleotide resonances, several cross-peaks between helicate and signals further upfield were observed; however, it could not be determined whether these were intra-molecular (helicate-helicate) or inter-molecular (helicate-oligonucleotide) (see Figure 3.27). In addition, the cross-peaks were extremely

low in intensity, prompting the helicate ratio to be increased further in an attempt to improve the signal.

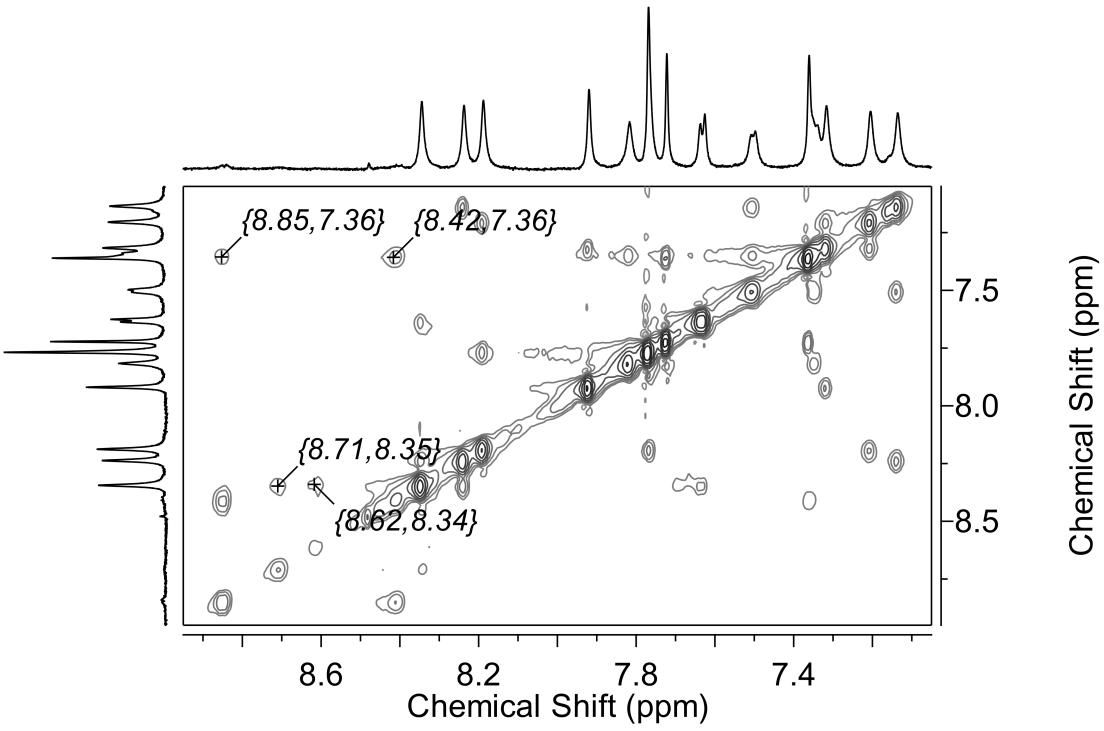

Figure 3.27: Expansion of a NOESY spectrum of the CCGG dodecanucleotide with F1 of the diruthenium helicate (**3**) at R* = 1, in pH 7.0 phosphate buffer at 25 °C, showing potential inter-molecular NOEs between the helicate and oligonucleotide H8/H6/H2 resonances.

Upon increasing the ratio of helicate to dodecanucleotide to R* = 2 additional precipitation was observed. In the 1D NMR spectrum the helicate peaks between 8.3 - 9.0 ppm increased significantly in intensity but remained extremely broad overall, as highlighted in Figure 3.28 (helicate peaks shown in red). Further variation in chemical shifts, particularly for the AH2 oligonucleotide resonances were also seen in this region, with upfield shifts increasing to 0.05 - 0.07 ppm.

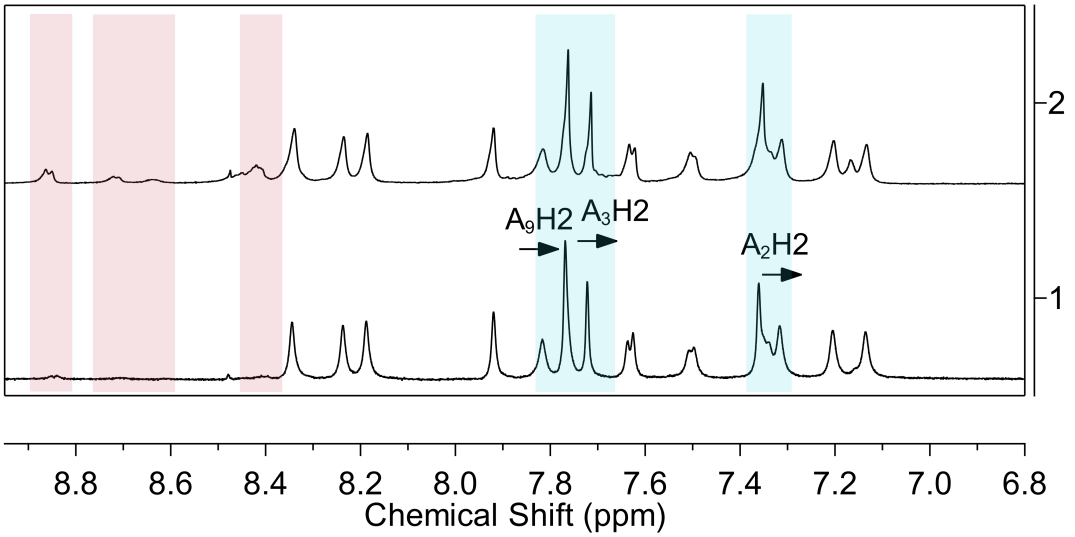

Figure 3.28: Aromatic region of the ^{1}H NMR spectrum of the titration of the CCGG dodecanucleotide with F1 of the diruthenium helicate (**3**) in pH 7.0 phosphate buffer at 25 °C. (1) R* = 1, (2) R* = 2. Notable changes in the chemical shift and shape of the oligonucleotide resonances are highlighted in blue, Ru(II) compound peaks are highlighted in red.

From the higher intensity helicate peaks, the ratio was able to be estimated by relative integration in comparison to the A_2H8, A_3H8, A_9H8 resonances at 8.34, 8.23, and 8.20 ppm, respectively (see Figure 3.29). The helicate ratio was found to be in the range R = 0.09 - 0.28. The high level of variation in this value could be influenced by the broadness of the helicate signals, as well as the ambiguity in assignment of the helicate signals, where the nuclearity, originally corresponding to two hydrogen resonances on the compound, could change depending on the nature of interaction with the dodecanucleotide. Regardless, the low integration values indicated that the true compound to DNA ratio (R) was significantly lower than the added ratio (R*).

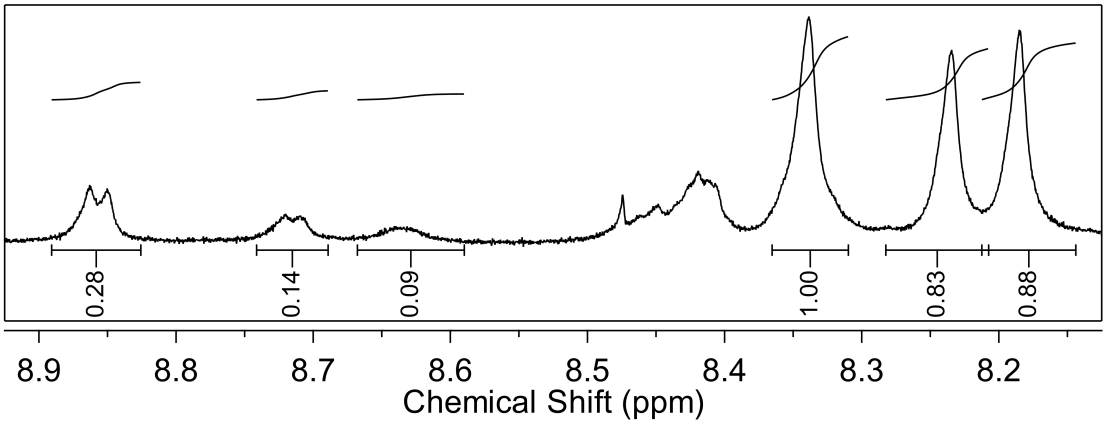

Figure 3.29: Selected region of the ^{1}H NMR spectrum of the titration of the CCGG dodecanucleotide with F1 of the diruthenium helicate (**3**) at R* = 2, in pH 7.0 phosphate buffer at 25 °C. Relative integration of broad helicate signals shown, compared to A_2H8, A_3H8, A_9H8 resonances.

Variation in chemical shift was also observed in the H1′/base H5 region of the spectrum (see Figure 3.30). While no further significant movement was observed for the C_5, C_6, G_7, G_8 or T_{11} resonances compared to R* = 1, the C_1 and G_{12} signals continued to shift upfield to give an overall change of 0.11 and 0.4 ppm, respectively.

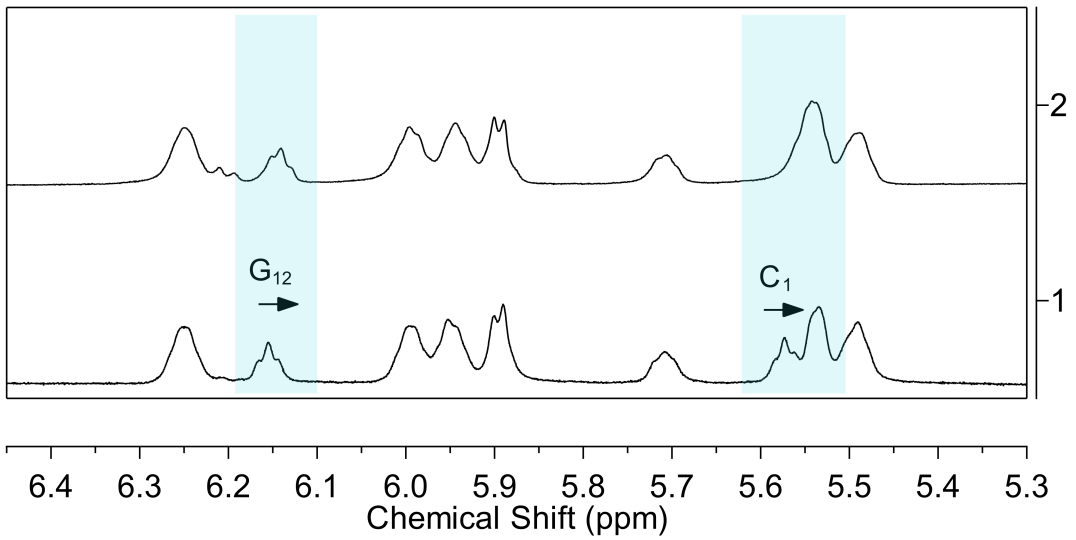

Figure 3.30: The H1′/base H5 region of the ^{1}H NMR spectrum of the titration of the CCGG dodecanucleotide with F1 of the diruthenium helicate (**3**) in pH 7.0 phosphate buffer at 25 °C. (1) R* = 1, (2) R* = 2. Notable changes in the chemical shift and shape of the oligonucleotide resonances are highlighted in blue.

Further variation in oligonucleotide chemical shift was recorded across the remainder of the spectrum, and a summary is reported in Table 3.7 below. It should be noted that the true compound-to-DNA ratio (R) estimated by relative integration is significantly lower than the added ratio (R*), and at the true R = 2 ratio it is anticipated that even greater changes in chemical shift would be observed.

Table 3.7: ^{1}H NMR assignment of the DNA resonances of the CCGG dodecanucleotide with F1 of the diruthenium helicate (**3**) at R* = 2, in D_2O and pH 7.0 phosphate buffer at 25 °C. Changes in chemical shift are given in brackets, with a negative sign indicating an upfield shift.

Base	H8/H6	AH2	H1′	H2′	H2″	Methyl
C_1	7.63 (-0.04)		5.55 (-0.11)	1.76 (-0.05)	2.30 (-0.04)	
A_2	8.34 (0.00)	7.34 (-0.07)	5.94 (0.00)	2.84 (0.01)	2.96 (0.02)	
A_3	8.23 (0.01)	7.71 (-0.05)	6.25 (0.01)	2.64 (0.03)	2.97 (0.03)	
T_4	7.13 (0.02)		5.89 (0.01)	2.07 (0.04)	2.50 (0.03)	1.35 (0.03)
C_5	7.50 (0.01)		5.54 (0.02)	2.10 (0.02)	2.47 (0.03)	
C_6	7.34 (-0.01)		5.49 (-0.01)	1.88 (0.00)	2.27 (-0.02)	
G_7	7.80 (0.00)		5.51 (-0.01)	2.65 (0.01)	2.72 (0.01)	
G_8	7.77 (0.03)		5.71 (0.02)	2.65 (0.02)	2.81 (0.04)	
A_9	8.20 (0.04)	7.75 (-0.05)	6.24 (0.01)	2.64 (0.01)	2.97 (0.04)	
T_{10}	7.21 (0.02)		5.99 (0.03)	2.01 (0.04)	2.55 (0.03)	1.37 (0.03)
T_{11}	7.32 (0.01)		5.95 (0.03)	2.03 (0.04)	2.42 (0.00)	1.66 (0.01)
G_{12}	7.92 (-0.01)		6.14 (-0.04)	2.64 (0.02)	2.38 (0.02)	

To probe any potential inter-molecular interactions, DQF-COSY and NOESY experiments were run for the sample where R* = 2 (see Figure 3.31). In the DQF-COSY spectrum several cross-peaks were noted in the aromatic region between downfield helicate peaks and peaks in the region of the base H8/H6, establishing that there were helicate peaks overlapping with the oligonucleotide in this region. This suggested that the NOE contacts observed at 1 equivalent in this region were likely helicate-helicate, rather than inter-molecular.

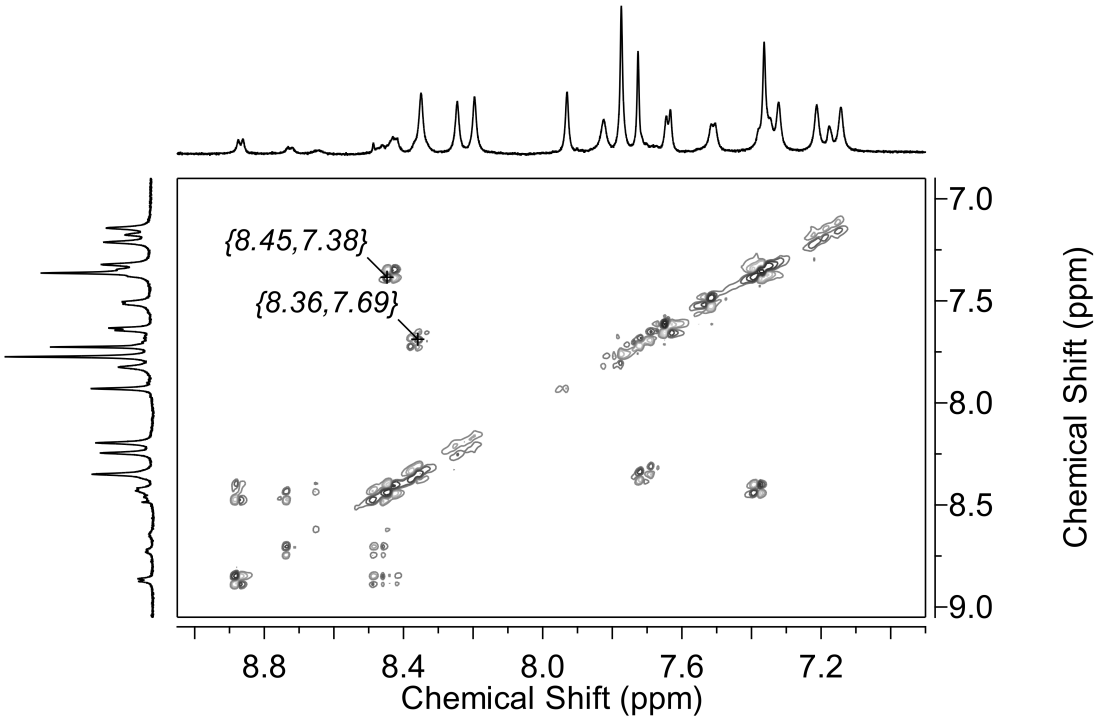

Figure 3.31: Expansion of a DQF-COSY spectrum of the CCGG dodecanucleotide with F1 of the diruthenium helicate (**3**) at R* = 2 in pH 7.0 phosphate buffer at 25 °C, indicating helicate-helicate cross-peaks at 8.45 - 7.38 ppm and 8.36 - 7.69 ppm.

The results of the NOESY experiment for the sample at R* = 2 showed stronger NOEs than observed for R* = 1. In the aromatic region cross-peaks were observed between the helicate at 7.38 ppm (which overlaps with the A_2H2/C_6 oligonucleotide peaks) and signals at 7.83 ppm, 7.73 ppm, and 7.51 ppm (see Figure 3.32). These signals could be inter-molecular contacts; however, it could not be determined with certainty whether the 7.38 ppm peak in these contacts was due to helicate or oligonucleotide. The cross-peaks could correspond to oligonucleotide-oligonucleotide contacts or helicate-helicate contacts from non-adjacent hydrogens.

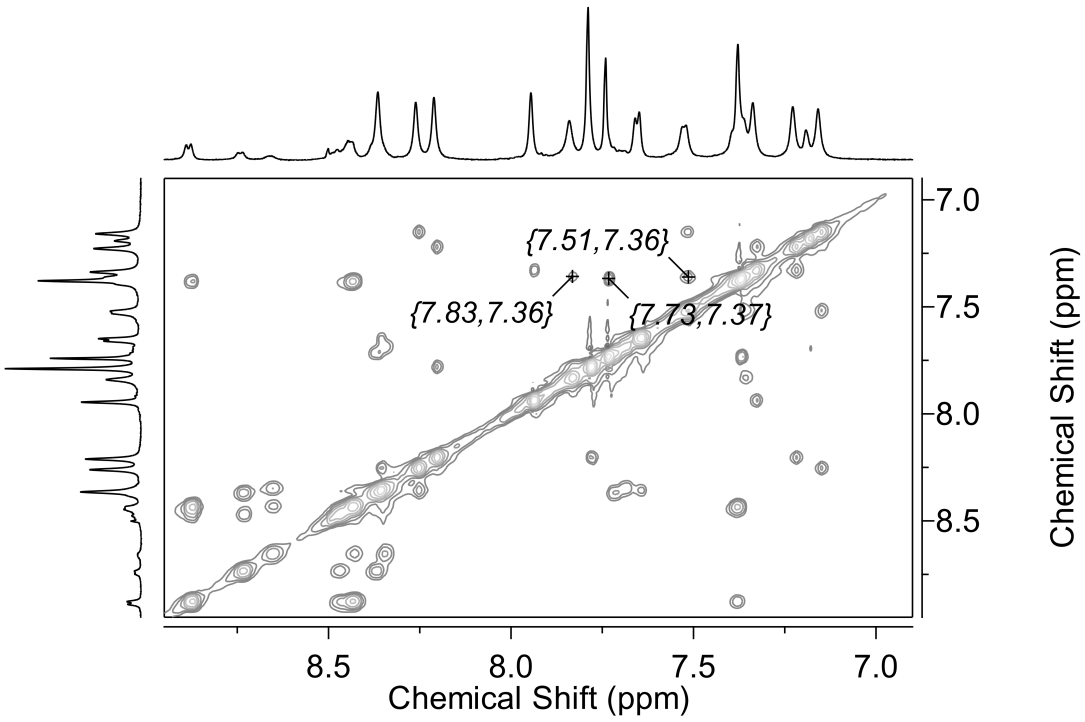

Figure 3.32: Expansion of a NOESY spectrum of the CCGG dodecanucleotide with F1 of the diruthenium helicate (**3**) at R* = 2 in pH 7.0 phosphate buffer at 25 °C, showing potential inter-molecular NOEs between the helicate and oligonucleotide H8/H6/H2 resonances.

Further upfield, a weak cross-peak was observed at 8.88 - 4.05 ppm (see Figure 3.33) which was ultimately determined to be inter-molecular. No resonances of the helicate were expected in this region, which suggested that the peak at 4.05 ppm must be oligonucleotide. While it is possible to assign the H4′ resonances by 2D NMR methods, these were not assigned in this thesis. Based on the previous assignments by Foley *et al.* in this region of the spectrum the signal at 4.05 ppm was assigned as C_1H4′.[166] The H4′ hydrogens occur nearer to the top of the minor groove compared to the H1′ hydrogens and an NOE contact in this region indicates that the helicate may be too bulky to get deep into the minor groove, hence the interaction with this resonance.

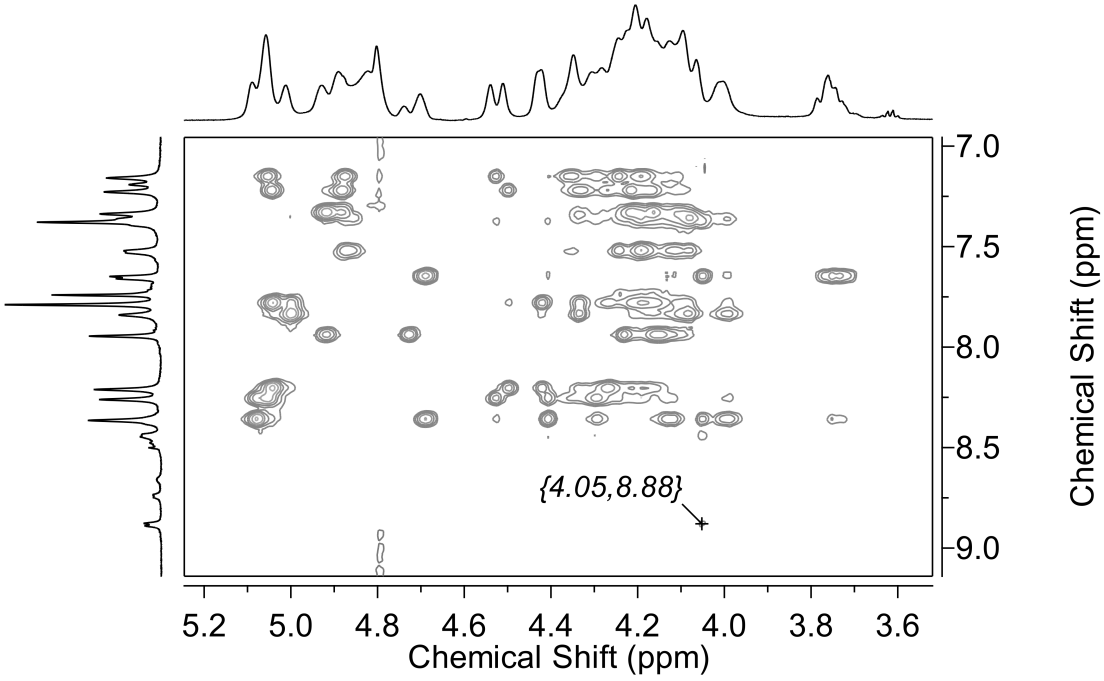

Figure 3.33: Expansion of a NOESY spectrum of the CCGG dodecanucleotide with F1 of the diruthenium helicate (**3**) at R* = 2 in pH 7.0 phosphate buffer at 25 °C, showing a potential inter-molecular NOE between the helicate and an oligonucleotide H4′ resonance.

It is possible to further assign ambiguous NOEs as either inter- or intra-molecular interactions by conducting NOESY and DQF-COSY experiments at a range of temperatures. For the purposes of this analysis these additional experiments were not undertaken as the evidence as a whole suggested that weak binding was likely to occur in the minor groove. The largest changes in chemical shift of the dodecanucleotide were seen for the AH2 and H1′ resonances, which are located in the minor groove. The presence of a possible inter-molecular NOE between a downfield helicate signal and the C_1H4′ resonance suggested that the helicate cannot fit deeply into the minor groove due to the size constraints and so interacts nearer the top of the groove, and at the end of the dodecanucleotide where there is greater flexibility.

3.4.5.2 F2-Helicate(**3**) binding to CCGG

Following these investigations the interactions of the partially-resolved F2 of the helicate with the same CCGG dodecanucleotide were explored. As observed for F1, as the concentration of F2 of the helicate increased, broad peaks emerged, most notably downfield of the oligonucleotide signals in the aromatic region, and again these were substantially broader than those of the oligonucleotide. Upon addition of 1 equivalent of F2, in the H8/H6/H2 region the largest changes in chemical shifts were observed for the A_2H2 (0.04

ppm), A_3H2 (0.03 ppm), and A_9H2 (0.02 ppm) resonances (seen Figure 3.34). In addition, as for all previous samples, an orange precipitate was observed.

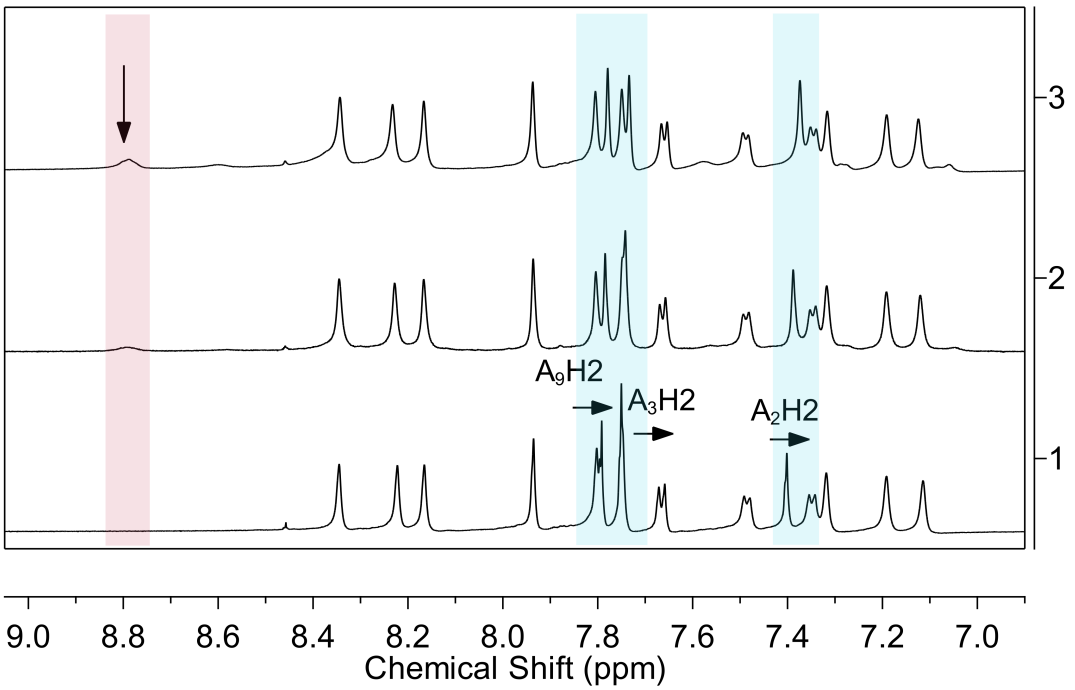

Figure 3.34: Aromatic region of the ^{1}H NMR spectrum of the titration of the CCGG dodecanucleotide with F2 of the diruthenium helicate (**3**) in pH 7.0 phosphate buffer at 25 °C. (1) free oligonucleotide, (2) R* = 0.5, (3) R* = 1. Notable changes in the chemical shift and shape of the oligonucleotide resonances are highlighted in blue, Ru(II) compound peaks are highlighted in red.

The broad downfield helicate peaks were able to be integrated, relative to the A_2H8, A_3H8, and A_9H8 residues (see Figure 3.35). As calculated for F1, the true ratio (R), containing soluble helicate and dodecanucleotide, was lower than the added ratio (R*). In this case the helicate peaks could be integrated at R = 0.45 - 0.32, relative to oligonucleotide. Interestingly, based on these integrations the true ratio of F2 of the helicate appeared to be higher than that calculated for F1 at R* = 2. This could potentially be due to a difference in DNA interaction for the two enantiomers; however, it should be noted that F2 was not enantiomerically pure and still contained some of the F1 form. In addition, the extreme broadness of the helicate signals could influence the accuracy of integration, as well as the potential presence of helicate peaks overlapping the AH8 residues.

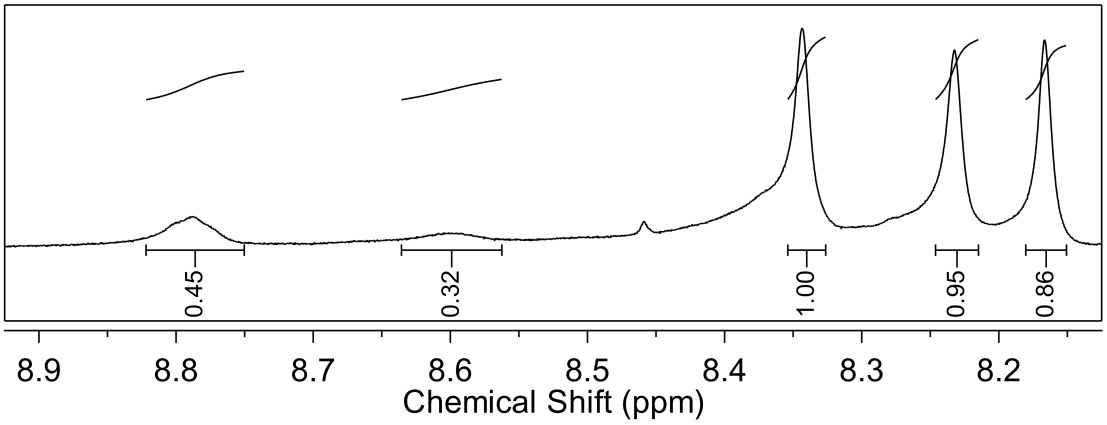

Figure 3.35: Selected region of the ^{1}H NMR spectrum of the titration of the CCGG dodecanucleotide with F2 of the diruthenium helicate (**3**) at R* = 1, in pH 7.0 phosphate buffer at 25 °C. Relative integration of broad helicate signals shown, compared to A_2H8, A_3H8, A_9H8 resonances.

In the H1′ region the most significant shift was in the position of the C_1H1′ peak, which had a substantial upfield shift (0.11 ppm). Smaller changes in the shapes of other signals in this region, notably for signals appearing at around 5.95 ppm, were also observed; however, these were often highly overlapping making it challenging to attribute the shape change to one particular resonance (see Figure 3.36).

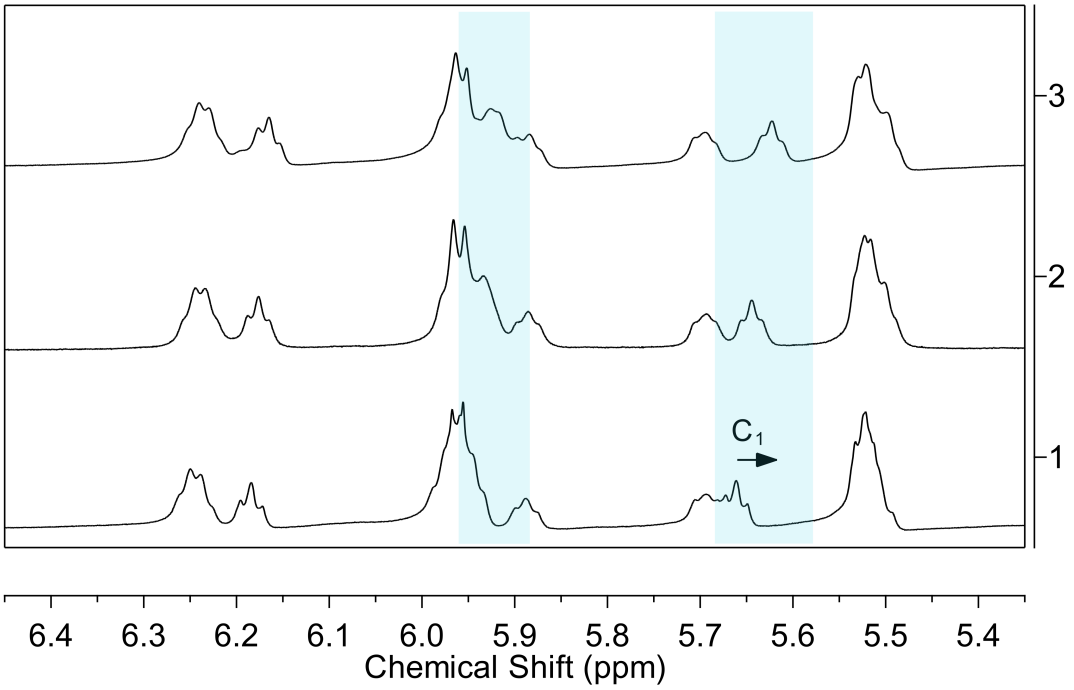

Figure 3.36: The H1′/base H5 region of the ^{1}H NMR spectrum of the titration of the CCGG dodecanucleotide with F2 of the diruthenium helicate (**3**) in pH 7.0 phosphate buffer at 25 °C. (1) free oligonucleotide, (2) R* = 0.5, (3) R* = 1. Notable changes in the chemical shift and shape of the oligonucleotide resonances are highlighted in blue.

Further upfield, little variation in the chemical shifts of the dodecanucleotide H2′, H2″, or methyl hydrogen signals was observed at this ratio, and a full summary of the changes in chemical shift is recorded in Table 3.8 below. As noted for F1, the added ratio (R*) is significantly lower than the true (R) helicate to DNA ratio. While the changes in chemical shift are small (the greatest being 0.04 ppm), were the true R = 1 ratio achieved it is anticipated that the perturbation would increase in magnitude.

Table 3.8: ^{1}H NMR assignment of the DNA resonances of the CCGG dodecanucleotide with F2 of the diruthenium helicate (**3**) at R* = 1, in D_2O and pH 7.0 phosphate buffer at 25 °C. Changes in chemical shift are given in brackets, with a negative sign indicating an upfield shift.

Base	H8/H6	AH2	H1′	H2′	H2″	Methyl
C_1	7.66 (-0.01)		5.62 (-0.04)	1.81 (0.00)	2.33 (-0.01)	
A_2	8.35 (0.01)	7.37 (-0.04)	5.93 (-0.01)	2.84 (0.01)	2.94 (0.00)	
A_3	8.23 (0.01)	7.73 (-0.03)	6.24 (0.00)	2.63 (0.02)	2.95 (0.01)	
T_4	7.13 (0.02)		5.89 (0.01)	2.05 (0.02)	2.48 (0.01)	1.34 (0.02)
C_5	7.49 (0.00)		5.53 (0.01)	2.10 (0.02)	2.46 (0.00)	
C_6	7.35 (0.00)		5.50 (0.00)	1.89 (0.01)	2.28 (-0.01)	
G_7	7.81 (0.01)		5.52 (0.00)	2.65 (0.01)	2.71 (0.00)	
G_8	7.75 (0.01)		5.70 (0.01)	2.64 (0.01)	2.79 (0.02)	
A_9	8.17 (0.01)	7.78 (-0.02)	6.23 (0.00)	2.64 (0.01)	2.94 (0.01)	
T_{10}	7.19 (0.00)		5.96 (0.00)	1.98 (0.01)	2.51 (-0.01)	1.36 (0.02)
T_{11}	7.32 (0.01)		5.92 (0.00)	2.01 (0.02)	2.41 (-0.01)	1.67 (0.02)
G_{12}	7.94 (0.01)		6.17 (-0.01)	2.63 (0.01)	2.37 (-0.01)	

For this sample, where R* = 1, a NOESY experiment was conducted. A number of cross-peaks recorded in the aromatic region appeared to be helicate-helicate as they appeared downfield of the oligonucleotide resonances. The NOE contacts at 8.85 - 7.36 ppm, and 8.42 - 7.36 ppm mirror those observed for F1 of the helicate with this oligonucleotide, and again it was unclear whether these were intra-molecular or inter-molecular. The remaining cross-peaks in this region between 8.71 - 8.35 ppm, and 8.62 - 8.34 ppm were also ambiguous in nature. While the most downfield component was clearly from the

helicate, the second coordinate could either be from the A_2H8 resonance, or a helicate peak overlapped with this signal.

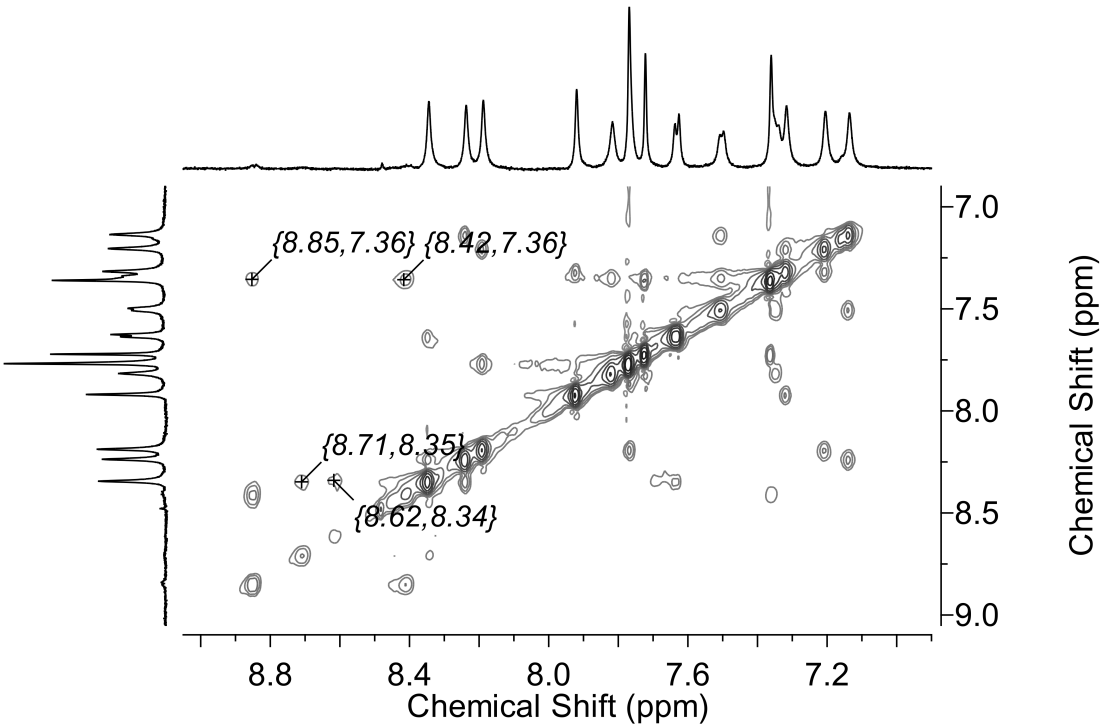

Figure 3.37: Expansion of a NOESY spectrum of the CCGG dodecanucleotide with F2 of the diruthenium helicate (**3**) at R* = 1 in pH 7.0 phosphate buffer at 25 °C, showing potential inter-molecular NOEs between the helicate and oligonucleotide H8/H6/H2 resonances.

In the remaining regions of the NOESY spectrum the majority of cross-peaks were concluded to be helicate-helicate, being similar to those observed with F1 of the helicate. For the aromatic to H3′/H4′/H5′/H5″ region weak cross-peaks were present, one of which was also observed in studies with F1 (4.05 - 8.80 ppm), suggesting a possible inter-molecular interaction between helicate and the C_1H4' resonance (see Figure 3.38). However, due to the extremely low intensity of the NOESY signals, and relatively small changes in chemical shift noted previously, this was not assigned to any specific inter-molecular interaction to avoid over-analysis of the results. The remaining cross-peaks in this region (4.38 - 8.80 ppm, and 4.13 - 8.79 ppm) may result from other helicate to H4′ inter-molecular contacts, but again due to the low intensity these were not further assigned.

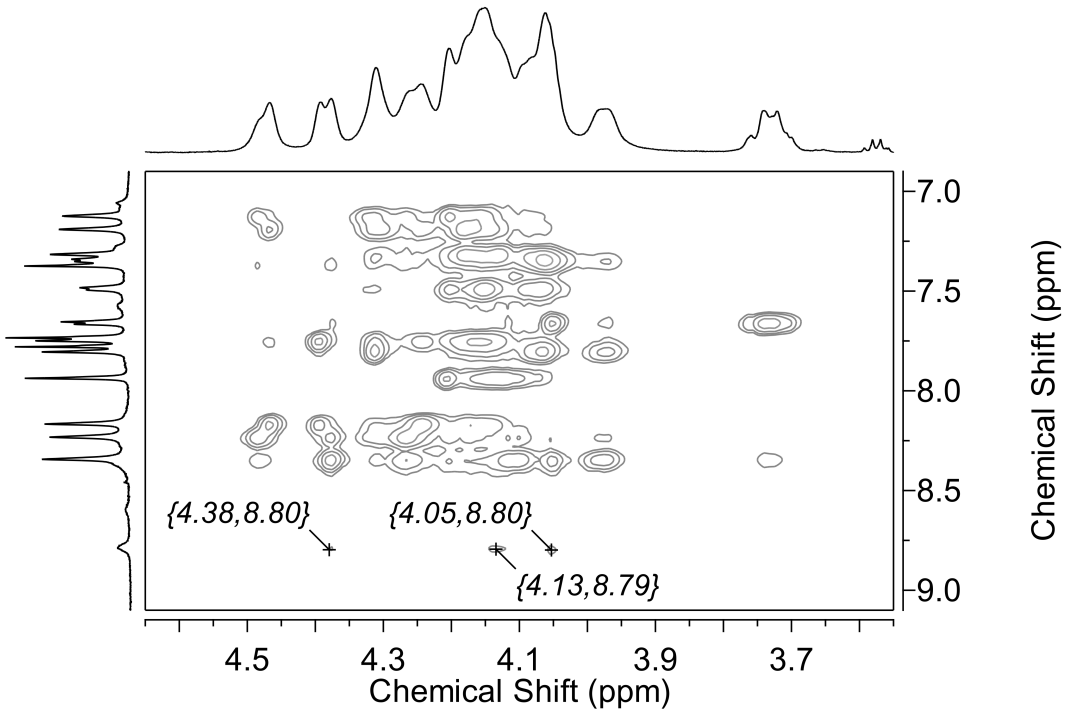

Figure 3.38: Expansion of a NOESY spectrum of the CCGG dodecanucleotide with F2 of the diruthenium helicate (**3**) at R* = 1 in pH 7.0 phosphate buffer at 25 °C, showing potential inter-molecular NOEs between the helicate and oligonucleotide H4′ resonances.

A DQF-COSY experiment was conducted for this sample to try and ascertain which NOEs were inter- or intra-molecular (see Figure 3.39). Very weak COSY cross-peaks were detected between helicate signals (downfield of the dodecanucleotide) and other peaks in the aromatic region (8.74 - 8.21 ppm, 8.73 - 8.34 ppm). NOEs had been observed in this region, although these cross-peaks were shifted slightly. However, if helicate peaks were present at 8.34 and 8.21 ppm it seemed to suggest that the NOEs in this region were likely intra-molecular in nature. Stronger COSY cross-peaks were recorded between 8.32 - 7.33 ppm and 8.31 - 7.16 ppm. Given that there are no adjacent oligonucleotide hydrogens to cause cross-peaks in this region, the presence of cross-peaks at these coordinates further supported the idea that broad low intensity helicate peaks may have been recorded at these chemical shifts. As a result it was proposed that the NOEs in this region of the spectrum could be helicate-helicate instead of inter-molecular. No further COSY cross-peaks were seen outside of this region.

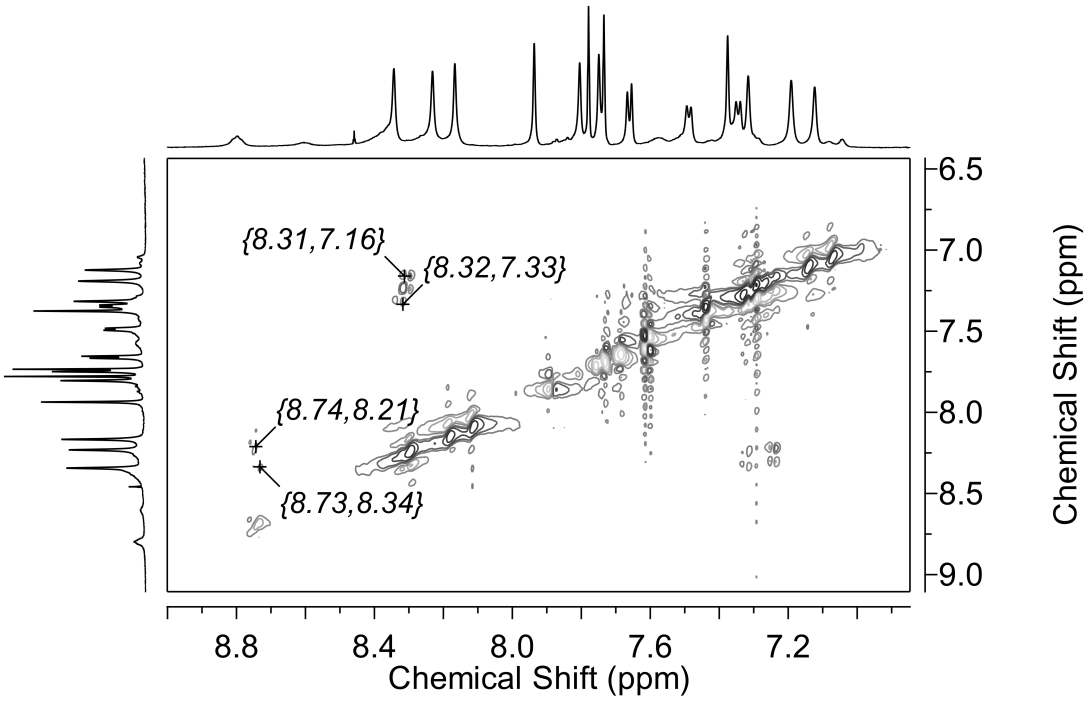

Figure 3.39: Expansion of a DQF-COSY spectrum of the CCGG dodecanucleotide with F2 of the diruthenium helicate (**3**) at R* = 1 in pH 7.0 phosphate buffer at 25 °C, showing helicate-helicate cross-peaks in the aromatic region.

From these results it was concluded that the interactions between F2 of the helicate and the CCGG dodecanucleotide were similar to those seen with F1 of the helicate; however, there were some small differences. Overall, the most downfield signals of the helicate were broader in F2 compared to F1. As noted for previous experiments with both the helicate and mesocate, a small amount of orange precipitate was observed in the bottom of the NMR tube as higher ratios of compound were reached. The increase in broadness could indicate a difference in exchange rate and potentially binding affinity, which could be further influenced by the fact that F2 was not as enantiomerically pure as F1. Despite this, the differences in results between the samples were not significant enough to warrant further investigation. The weak potential inter-molecular NOEs could be further assigned by conducting NOESY and DQF-COSY experiments at a range of temperatures; however, given the similarities with data collected using F1 of the helicate, these additional experiments were not pursued.

Overall, it appears that both F1 and F2 of the helicate may interact with the minor groove of the CCGG dodecanucleotide, which is not unexpected given the 4^+ charge of the diruthenium compound. Additionally, the helicate may be too bulky to fit within the groove itself. This conclusion is supported by the changes in the chemical shift, of which the largest in magnitude were recorded for the AH2 and H1′ resonances (which are

located in the minor groove). The presence of weak NOEs between the most downfield helicate signals and resonances in the H4′ region (located near the top of the minor groove) suggested that the helicate cannot bind deeply in the groove, potentially due to size constraints at this position.

3.4.6 Helicate (**3**) binding to the AATT dodecanucleotide

To contrast the C/G-rich oligonucleotide studied above attention turned to the second dodecanucleotide selected, one containing an A/T-rich central sequence. A/T-rich sequences are known to adopt a narrower and more flexible minor groove than C/G-rich sequences,[180] which was considered a useful property in this case as the helicate seemed to interact most strongly at this position.

3.4.6.1 F1 - Helicate (**3**) binding to AATT

To begin, the interactions of F1 of the helicate, the more enantiomerically pure sample, with the AATT dodecanucleotide (d(ACCGAATTCGGT)$_2$) were investigated. With incremental addition from 0.25 equivalents to 1 equivalent of F1 of the helicate (monitored here as R* for ratio of added compound), noticeable changes in chemical shift for oligonucleotide hydrogens in the H8/H6/H2 region were observed, as well as some slight shape changes in the H1′/base H5 region. The spectra showing these changes are shown below in Figures 3.40 and 3.41, respectively. At $\sim$ 8.1 ppm the A_5/A_6 H8 signals are almost overlapping singlets for the free dodecanucleotide at 25 °C; however, upon addition of F1 the A_6H8 signal shifts downfield to be completely overlapping. An upfield shift was observed for all AH2 signals (0.02 - 0.04 ppm), while the T_7H6 signal at 7.12 ppm exhibited a downfield shift (0.02 ppm). In the aromatic region, only very weak broad signals appeared downfield of the oligonucleotide resonances, similar to those observed for F1 with the CCGG dodecanucleotide.

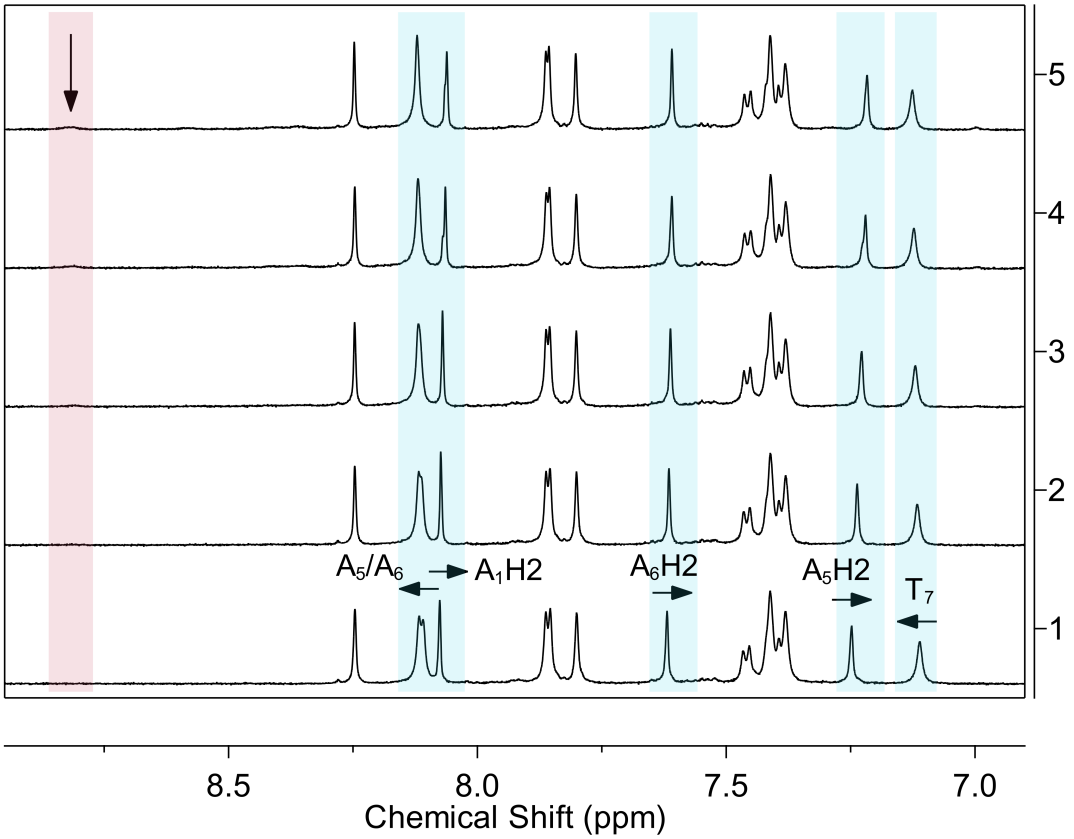

Figure 3.40: The H8/H6/AH2 region of the ^{1}H NMR spectrum of the titration of the AATT dodecanucleotide with F1 of the diruthenium helicate (**3**) in pH 7.0 phosphate buffer at 25 °C. (1) free oligonucleotide, (2) R* = 0.25 (3) R* = 0.5, (4) R* = 0.75, (5) R* = 1. Notable changes in the chemical shift and shape of the oligonucleotide resonances are highlighted in blue, Ru(II) compound peaks are highlighted in red.

From the ^{1}H NMR it was noted that in the H1′/base H5 region the main changes in resolution were for signals corresponding to A_1/T_{12} (overlapping signals at 6.25 ppm), C_9 (5.68 ppm), and G_{10} (5.57 ppm). Some of these were quite obviously upfield or downfield shifts but for others it was difficult to elucidate given the overlapping signals. This region of the spectra is shown below in Figure 3.41, with the resonances of interest highlighted.

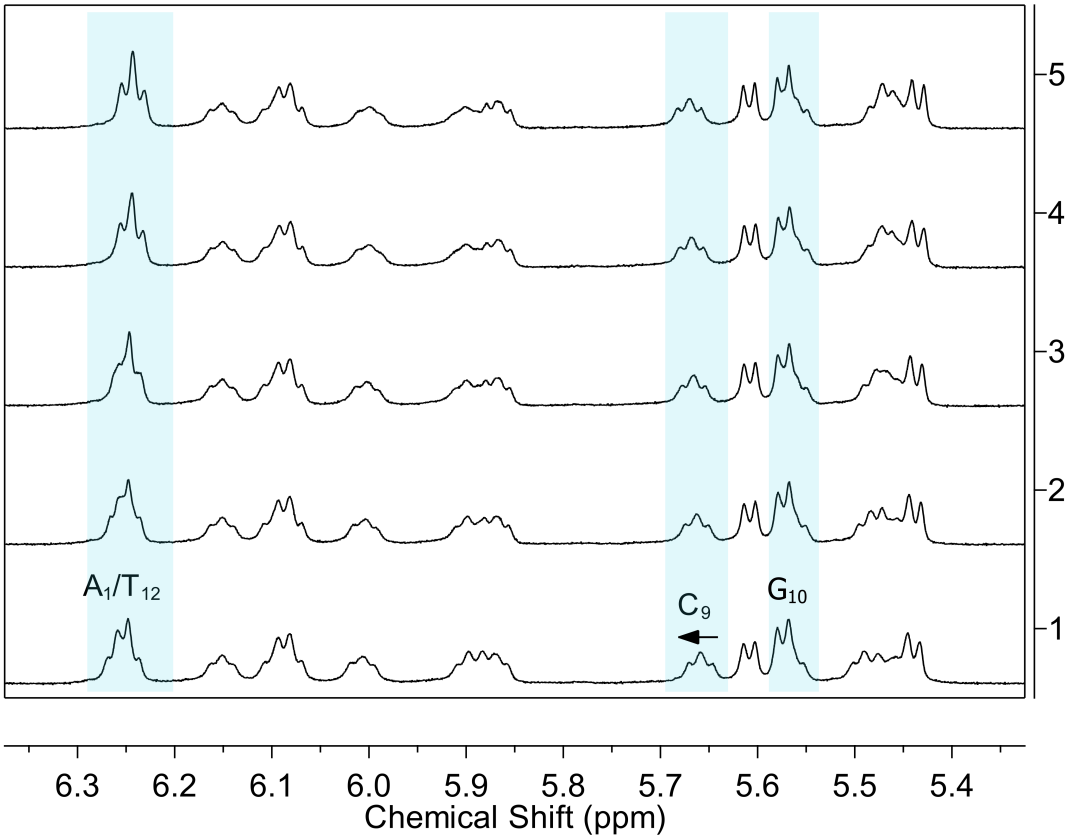

Figure 3.41: The H1′/base H5 region of the ^{1}H NMR spectrum of the titration of the AATT dodecanucleotide with F1 of the diruthenium helicate (**3**) in pH 7.0 phosphate buffer at 25 °C. (1) free oligonucleotide, (2) R* = 0.25 (3) R* = 0.5, (4) R* = 0.75, (5) R* = 1. Notable changes in the chemical shift and shape of the oligonucleotide resonances are highlighted in blue.

A NOESY experiment was also conducted at R* = 1 which showed several helicate-helicate NOEs, but no obvious NOEs from helicate to dodecanucleotide. These intramolecular contacts were seen between broad helicate peaks downfield of the oligonucleotide resonances (8.82 - 8.38 ppm, 8.60 - 8.41 ppm, 8.60 - 8.20 ppm). Additional weak cross-peaks were noted between helicate and more upfield signals; however, it was unclear whether these were due to oligonucleotide or overlapped helicate signals (8.81 - 7.43 ppm, 8.36 - 7.43 pm). The oligonucleotide peak at 7.43 ppm was identified as being the T_{12}H6 resonance, but the presence of a helicate peak at this position could not be discounted (see Figure 3.42).

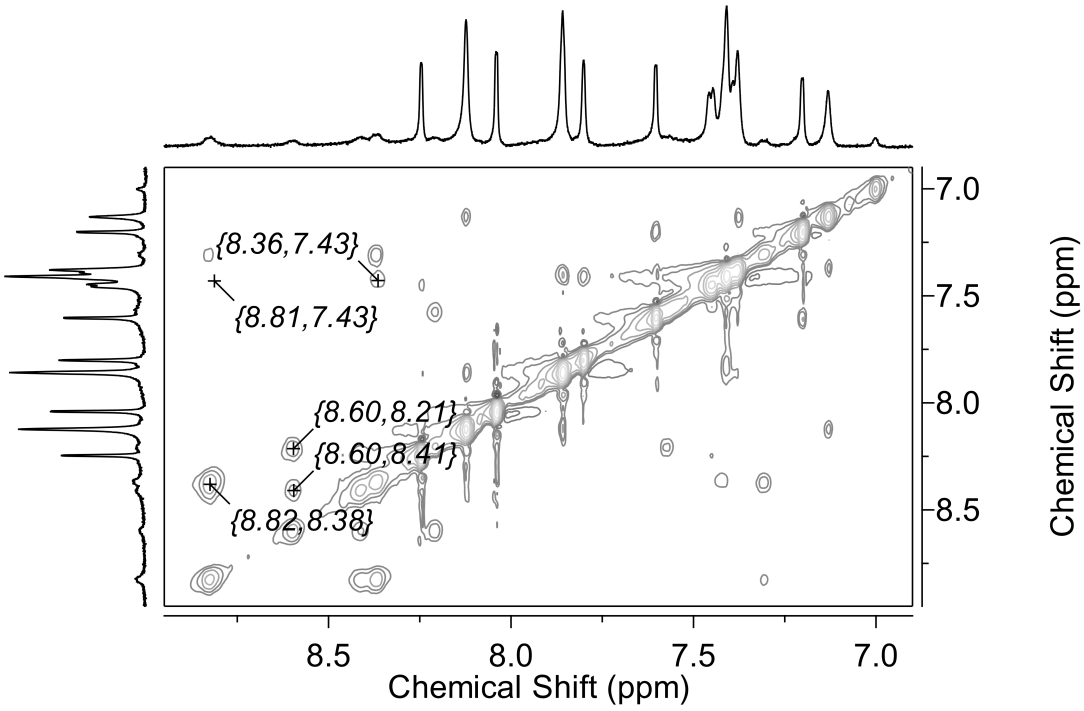

Figure 3.42: Expansion of a NOESY spectrum of the AATT dodecanucleotide with F1 of the diruthenium helicate (**3**) at R* = 1, in pH 7.0 phosphate buffer at 25°C, showing potential inter-molecular NOEs at 8.81 - 7.43 ppm, and 8.36 - 7.43 ppm between the helicate and the T_{12}H6 resonance, and additional helicate-helicate intra-molecular NOEs.

From the changes in chemical shift recorded it appeared that there may be some interaction between the oligonucleotide and F1 of the helicate, primarily with the AH2 resonances, but nothing strong enough to give clear NOEs at this ratio. Possible binding may also occur at the ends of the oligonucleotide (as observed for the CCGG dodecanucleotide), evidenced by the variation in chemical shift seen for the A_1H1′ and T_{12}H1′ resonances. Similarly to previous studies for this compound, the changes in chemical shift across the spectrum for the oligonucleotide signals were relatively small (the largest being 0.04 ppm) and the helicate exhibited only broad, low intensity peaks. Given that the greatest shifts were observed for the minor groove AH2 hydrogens it was proposed that F1 was positioned in the minor groove and at the end of the oligonucleotide where the double-helix is more flexible.

Further upfield little variation in the chemical shift of the H2′, H2″ and methyl hydrogens was recorded, which was unsurprising given that these resonances relate to positions in the major groove. The changes in chemical shift recorded for the AATT dodecanucleotide with F1 of the helicate at R* = 1 are shown in Table 3.9.

Table 3.9: ^{1}H NMR assignment of the DNA resonances of the AATT dodecanucleotide with F1 of the diruthenium helicate (**3**) at R* = 1, in D_2O and pH 7.0 phosphate buffer at 25 °C. Changes in chemical shift are given in brackets, with a negative sign indicating an upfield shift.

Base	H8/H6	AH2	H1′	H2′	H2″	Methyl
A_1	8.26 (0.00)	8.06 (-0.02)	6.25 (-0.02)	2.70 (0.00)	2.82 (0.00)	
C_2	7.46 (-0.01)		5.88 (0.00)	2.13 (-0.01)	2.40 (-0.01)	
C_3	7.40 (0.00)		5.48 (-0.01)	1.92 (-0.01)	2.26 (-0.03)	
G_4	7.87 (0.00)		5.45 (-0.01)	2.68 (-0.01)	2.76 (-0.01)	
A_5	8.13 (0.00)	7.22 (-0.04)	6.01 (0.00)	2.71 (0.00)	2.95 (0.01)	
A_6	8.12 (0.00)	7.61 (-0.02)	6.16 (-0.01)	2.57 (0.00)	2.95 (0.01)	
T_7	7.14 (0.02)		5.91 (0.00)	2.01 (0.02)	2.58 (0.01)	1.29 (0.01)
T_8	7.38 (0.00)		6.10 (0.01)	2.17 (0.01)	2.56 (0.00)	1.55 (0.01)
C_9	7.42 (0.00)		5.68 (0.03)	1.99 (0.01)	2.36 (0.00)	
G_{10}	7.87 (0.01)		5.57 (0.02)	2.68 (-0.01)	2.68 (-0.01)	
G_{11}	7.81 (0.00)		6.09 (-0.01)	2.62 (0.00)	2.73 (0.00)	
T_{12}	7.43 (0.01)		6.25 (-0.02)	2.26 (0.00)	2.26 (0.00)	1.60 (0.00)

In order to compare to the data obtained for the CCGG dodecanucleotide the ratio of F1 of the helicate to DNA was increased to R* = 2. Further changes in chemical shift for the oligonucleotide signals in the H8/H6/H2 region were observed, in the same positions as had been seen at R* = 1 (see Figure 3.43). The largest variation was again seen for the chemical shifts of the AH2 resonances, which continued to migrate upfield (shifts of 0.06 - 0.03 ppm). Aside from these resonances, little movement was observed for H8/H6 signals further supporting the idea of interactions between the helicate and dodecanucleotide occurring in the minor groove, rather than the major groove.

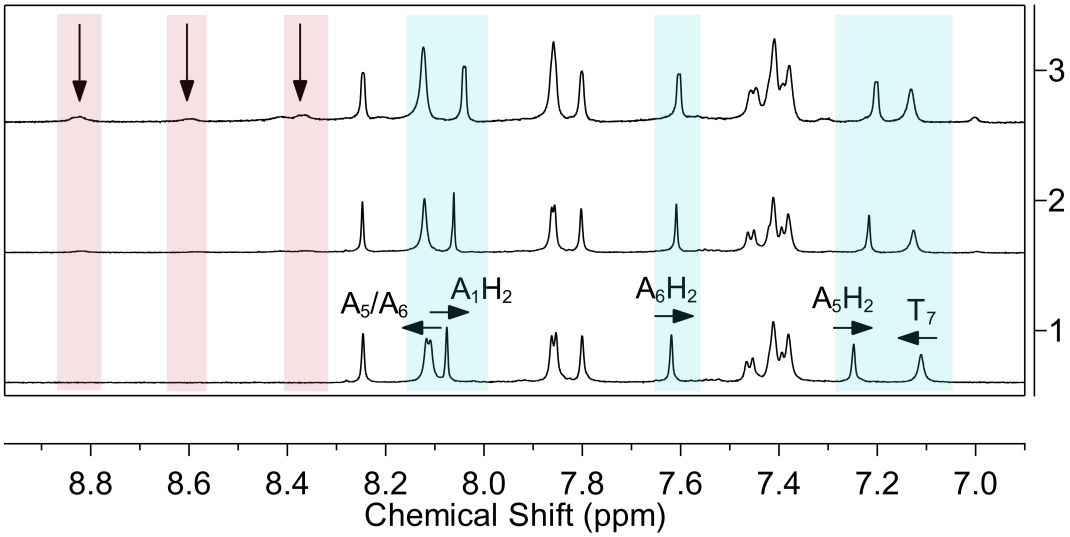

Figure 3.43: The H8/H6/H2 region of the ^{1}H NMR spectrum of the AATT dodecanucleotide with F1 of the diruthenium helicate (**3**) in pH 7.0 phosphate buffer at 25 °C. (1) free oligonucleotide, (2) R* = 1, (3) R* = 2. Notable changes in the chemical shift and shape of the oligonucleotide resonances are highlighted in blue, Ru(II) compound peaks are highlighted in red.

At R* = 2, the broad helicate peaks downfield of the oligonucleotide were at high enough intensity for an estimation of the true ratio to be made via integration, relative to the A_1H8, A_5H8/A_6H8, and A_1H2 resonances (see Figure 3.44). As calculated for the helicate with the CCGG dodecanucleotide F1, the true helicate ratio (R), containing soluble helicate and dodecanucleotide, was found to be in the range 0.15 - 0.28. Additional helicate peaks at 8.4 ppm were considered to be comprised of an unknown number of overlapping broad signals, with integration of the region indicating R = 0.77. For the most downfield helicate peaks the low integration values indicate that the true ratio of compound to DNA (R) is again significantly lower than the added ratio (R*).

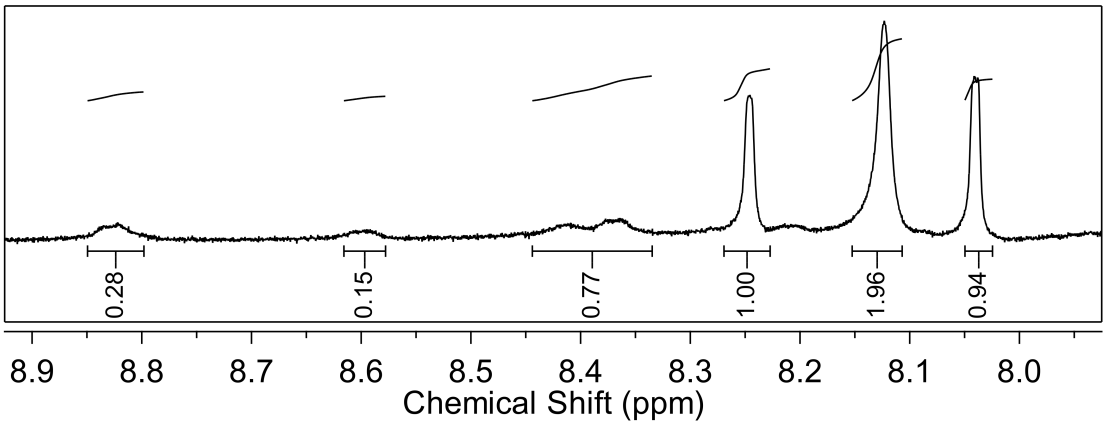

Figure 3.44: Selected region of the ^{1}H NMR spectrum of the AATT dodecanucleotide with F1 of the diruthenium helicate (**3**) at R* = 2, in pH 7.0 phosphate buffer at 25 °C. Relative integration of broad helicate signals shown, compared to A_1H8, A_5H8/A_6H8, and A_1H2 resonances.

In the H1′/base H5 region, shown in Figure 3.45 below, the largest changes recorded were upfield shifts for resonances at the terminal ends of the dodecanucleotide, A_1H1′ (0.05) and G_{12}H1′ (0.04). Movement was also observed for other H1′ resonances and although these were only relatively small in magnitude (0.02 - 0.03 ppm), they still exceeded those seen in the H8/H6 region. As for previous samples the true ratio of compound to DNA (R) was lower than the added ratio (R*) so the small perturbation in chemical shift of oligonucleotide resonances was not necessarily a true indication of significance in this case. A full summary of the chemical shift changes is recorded in Table 3.10.

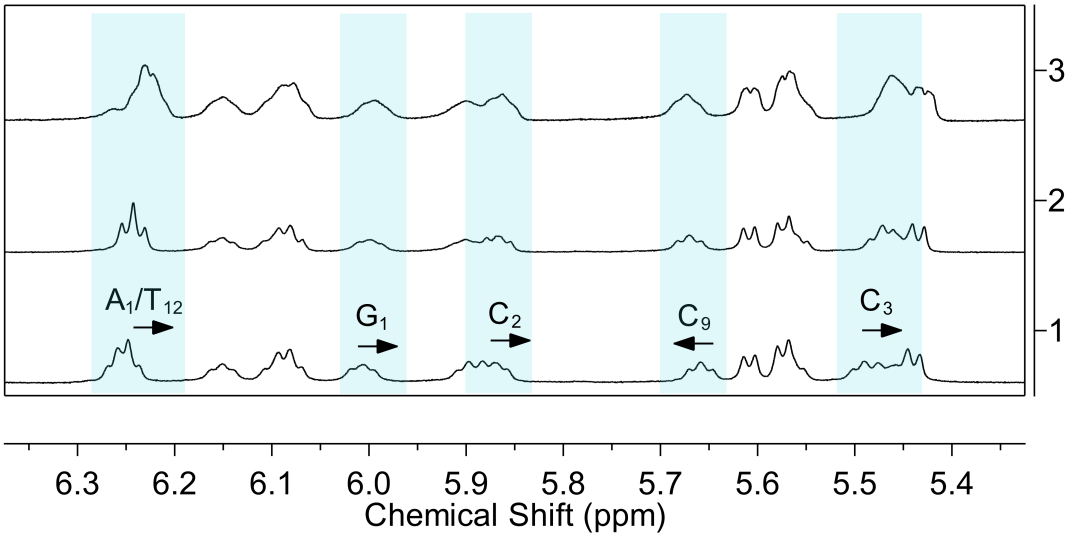

Figure 3.45: The H1′/base H5 region of the ^{1}H NMR spectrum of the AATT dodecanucleotide with F1 of the diruthenium helicate (**3**) at R* = 2 in pH 7.0 phosphate buffer at 25 °C. (1) free oligonucleotide, (2) R* = 1, (3) R* = 2. Notable changes in the chemical shift and shape of the oligonucleotide resonances are highlighted in blue.

Table 3.10: ^{1}H NMR assignment of the DNA resonances of the AATT dodecanucleotide with F1 of the diruthenium helicate (**3**) at R* = 2, in D_2O and pH 7.0 phosphate buffer at 25 °C. Changes in chemical shift are given in brackets, with a negative sign indicating an upfield shift.

Base	H8/H6	AH2	H1′	H2′	H2″	Methyl
A_1	8.25 (-0.01)	8.04 (-0.04)	6.22 (-0.05)	2.68 (-0.02)	2.80 (-0.02)	
C_2	7.45 (-0.02)		5.86 (-0.02)	2.11 (-0.03)	2.39 (-0.02)	
C_3	7.39 (-0.01)		5.46 (-0.03)	1.91 (-0.02)	2.24 (-0.05)	
G_4	7.87 (0.00)		5.45 (-0.01)	2.68 (-0.01)	2.76 (-0.01)	
A_5	7.86 (-0.01)	7.20 (-0.06)	6.00 (-0.01)	2.70 (-0.01)	2.94 (0.00)	
A_6	8.12 (0.00)	7.60 (-0.03)	6.15 (-0.02)	2.57 (0.00)	2.94 (0.00)	
T_7	7.13 (0.01)		5.90 (-0.01)	2.01 (0.02)	2.57 (0.00)	1.28 (0.00)
T_8	7.40 (0.02)		6.09 (0.00)	2.16 (0.00)	2.57 (-0.01)	1.54 (0.00)
C_9	7.41 (-0.01)		5.67 (0.02)	1.97 (0.02)	2.36 (0.00)	
G_{10}	7.86 (0.00)		5.56 (0.01)	2.68 (-0.01)	2.68 (-0.01)	
G_{11}	7.80 (-0.01)		6.08 (-0.02)	2.60 (-0.02)	2.72 (-0.01)	
T_{12}	7.43 (0.01)		6.23 (-0.04)	2.28 (0.02)	2.28 (0.00)	1.58 (-0.02)

The interactions were futher investigated by 2D NMR studies. From the NOESY spectrum potential inter-molecular interactions were identified, between 8.81 - 7.43 ppm, and 8.63 - 7.43 ppm (see Figure 3.46), appearing at higher intensity than observed at R* = 1. Further upfield, additional cross-peaks were observed between 8.36 - 6.24 ppm, and 7.00 - 6.23 ppm (see Figure 3.47). In the 1D spectrum the oligonucleotide peaks at 6.22 and 6.23 ppm were assigned as A_1H1′ and T_{12}H1′. Given that both of these resonances showed significant changes in chemical shift upon addition of F1 of the helicate, weak NOE contacts between the helicate and these H1′ signals could indicate binding of the compound in the minor groove at ends of the dodecanucleotide.

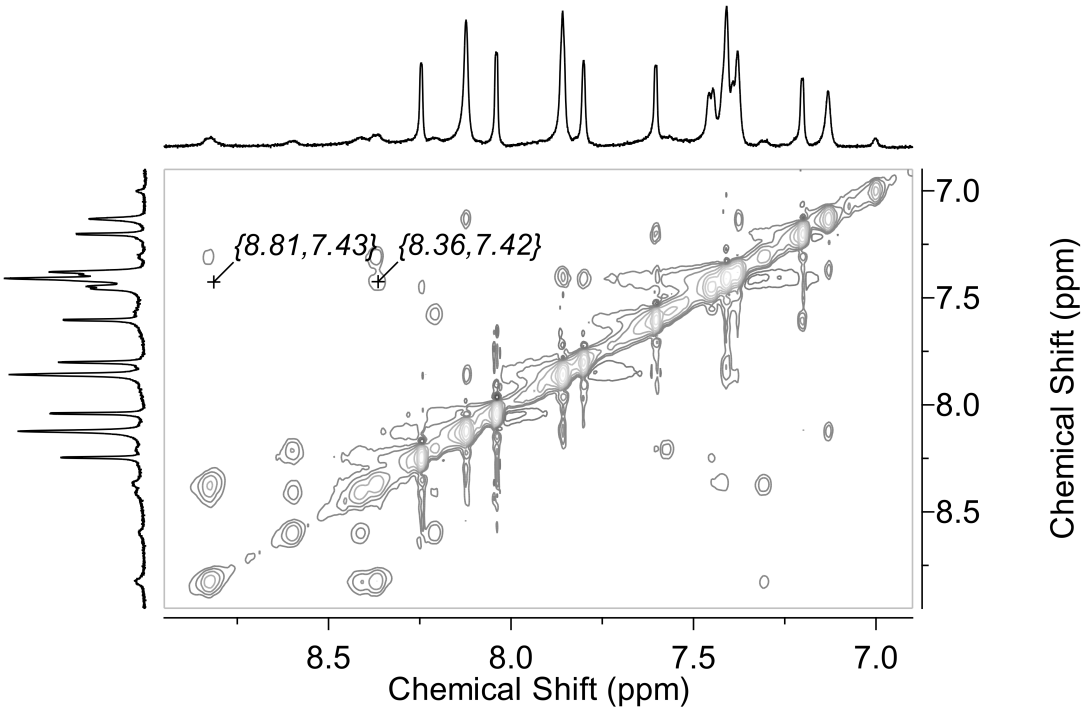

Figure 3.46: Expansion of a NOESY spectrum of the AATT dodecanucleotide with F1 of the diruthenium helicate (**3**) at R* = 2, in pH 7.0 phosphate buffer at 25 °C, showing a potential inter-molecular NOE between the helicate and the T_{12}H6 resonance.

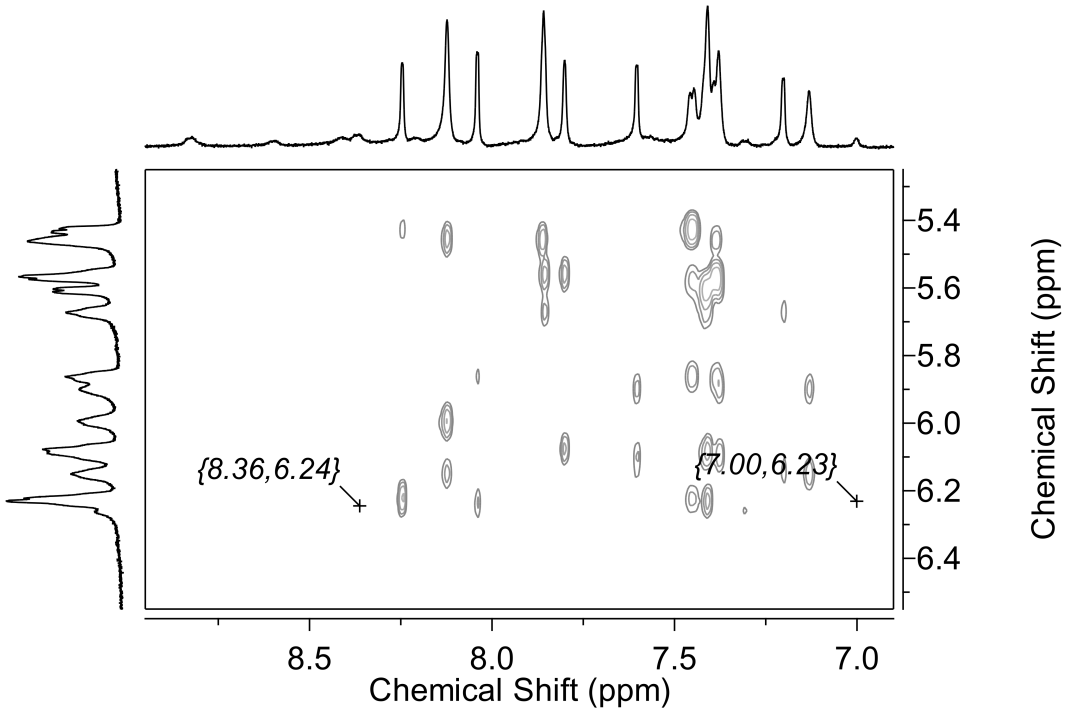

Figure 3.47: Expansion of a NOESY spectrum of the AATT dodecanucleotide with F1 of the diruthenium helicate (**3**) at R* = 2, in pH 7.0 phosphate buffer at 25 °C, showing potential inter-molecular NOEs between the helicate and H1′/base H5 resonances.

Further upfield, NOEs were also identified between 8.37 - 2.63 ppm, and 7.00 - 1.82 ppm, as shown in Figure 3.48. Given that no specific H2′, H2″ or methyl dodecanucleotide

resonances were assigned at either 2.63, or 1.82 ppm it seemed likely that these cross-peaks were intra-molecular in nature and the peaks at 2.63 and 1.82 ppm correspond to hydrogens on the -CH_2CH_2- spacer, and terminal CH_3 groups, respectively.

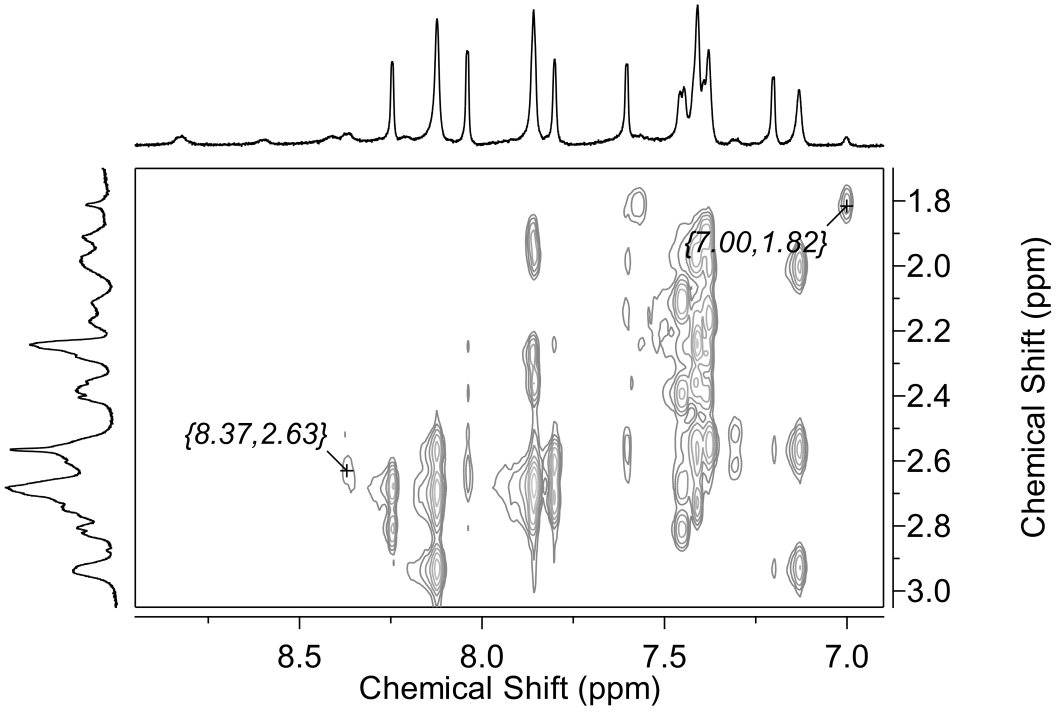

Figure 3.48: Expansion of a NOESY spectrum of the AATT dodecanucleotide with F1 of the diruthenium helicate (**3**) at R* = 2, in pH 7.0 phosphate buffer at 25 °C, showing helicate-helicate intra-molecular NOEs.

For the NOESY result at R* = 2, while some cross-peaks (particularly those most upfield and downfield) were likely helicate-helicate only, potential inter-molecular NOEs also existed. To confirm the nature of these a DQF-COSY experiment was performed and the outcome of this can be seen in Figure 3.49 below. For all potential helicate-oligonucleotide cross-peaks identified no COSY correlations were seen at these positions. As discussed above, the oligonucleotide peak at 7.43 ppm may correspond to the $T_{12}H6$ signal, although a signal from H_8 of the helicate was also expected at this position. Given there is very little change (0.01 ppm) in the chemical shift for the $T_{12}H6$ resonance with increasing equivalents of the helicate, this NOE contact could instead be a helicate-helicate interaction, with similarly low intensity recorded for the cross-peak and helicate signals overall. Alternatively, it could be a NOE contact between the downfield helicate signal and a non-adjacent hydrogen on the helicate. It would be possible to gain further information on the nature of this NOE by variable temperature NOESY/DQF-COSY or alternative 2D NMR methods but these experiments were not carried out for this thesis. Due to the broadness and low intensity of the helicate signals overall it was challenging to identify

this signal unambiguously and so the NOE could not be assigned as either inter- or intra-molecular.

For those NOE contacts in the H1′/base H5 region, no corresponding COSY signals were observed, although it should be noted that the cross-peaks at 8.36 - 6.24 ppm and 7.00 - 6.23 ppm in the NOESY were extremely weak. As a comparison, the oligonucleotide CH6 - CH5 COSY cross-peaks are noted in Figure 3.49 below and are of high intensity compared to all other cross-peaks in this spectrum. Given the strength of the CH6 - CH5 cross-peaks, it appears that the COSY cross-peaks may decrease in intensity due to the broadness of the helicate peaks because of cancellation of anti-phase components. Finally, for the NOESY cross-peaks noted further upfield (8.37 - 2.63 ppm, 7.00 - 1.82 ppm) no matching signals were present in the COSY. However, this does not rule out intra-molecular NOEs at these positions which may arise from helicate-helicate contacts from non-adjacent hydrogens. In this case, no COSY peaks would be expected as there are no hydrogens on the carbons adjacent to the -CH_2CH_2- spacer, and terminal CH_3 groups.

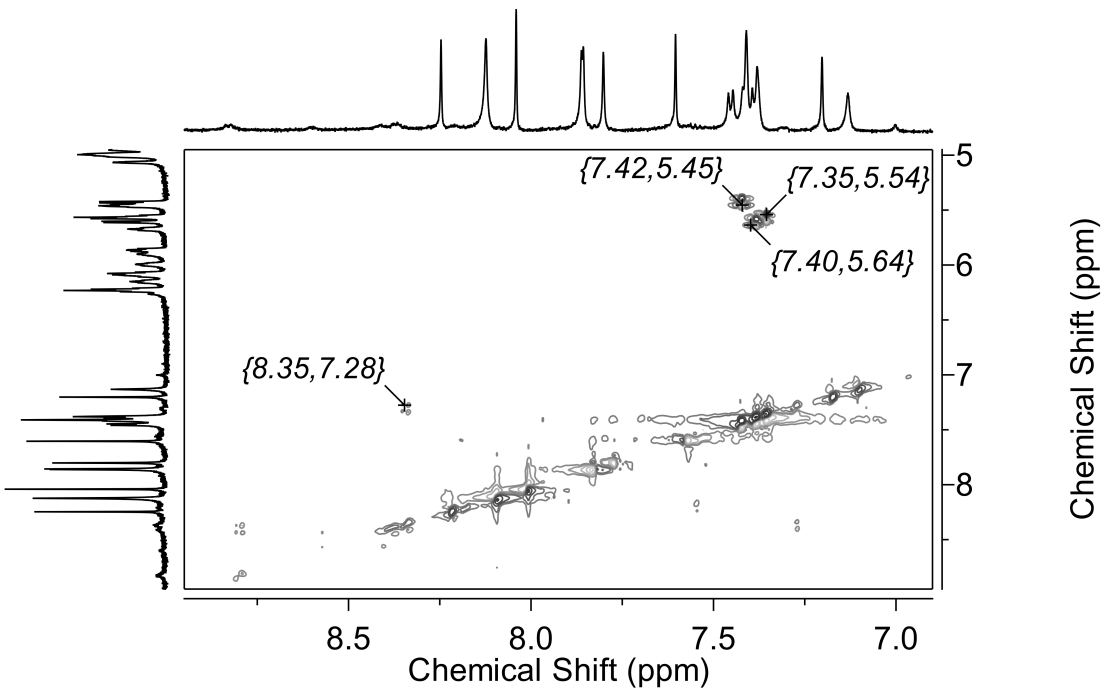

Figure 3.49: Expansion of a DQF-COSY spectrum of the AATT dodecanucleotide with F1 of the diruthenium helicate (**3**) at R* = 2, in pH 7.0 phosphate buffer at 25 °C, showing a helicate-helicate cross-peak (8.35 - 7.28 pm), and the oligonucleotide CH6 - CH5 cross-peaks (7.42 - 5.45 ppm, 7.40 - 5.64 ppm, 7.35 - 5.54 ppm).

In order to improve the broadness of the helicate signals variable temperature 1D NMR studies were performed. As shown in Figure 3.50, while some variation in the broadness of the oligonucleotide resonances was observed, little improvement could be made to the

broadness or intensity of the helicate signals in the aromatic region, despite experiments being run at a range of temperatures.

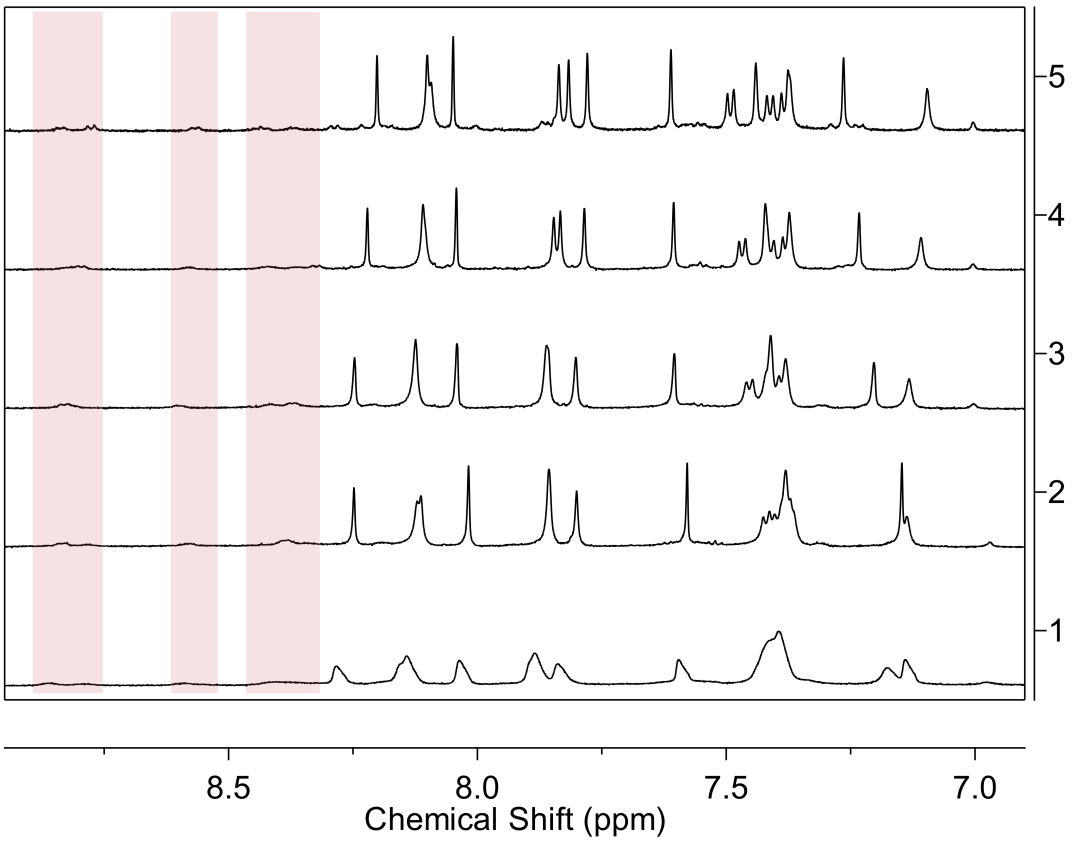

Figure 3.50: The H8/H6/H2 region of the ^{1}H NMR spectrum of the titration of the AATT dodecanucleotide with F1 of the diruthenium helicate (**3**) at R* = 2 in pH 7.0 phosphate buffer at 5°C to 45°C. (1) 5 °C, (2) 15 °C, (3) 25 °C, (4) 35 °C, (5) 45 °C. Ru(II) compound peaks are highlighted in red.

Overall, the NMR studies for F1 of the helicate with the AATT dodecanucleotide appeared to indicate that, similar to the CCGG dodecanucleotide, binding may occur in the minor groove, as evidenced by variation in chemical shifts for the AH2 resonances. This is further reinforced by potential inter-molecular NOEs between 8.36 - 6.24 ppm and 7.00 - 6.24 ppm, which could be due to interactions between the helicate and A_1H1' or $T_{12}H1'$ positions. Binding at the terminal ends of the dodecanucleotide in the minor groove was consistent with studies for the helicate with the CCGG dodecanucleotide detailed earlier in this Chapter. Some of the ambiguous assignments could be resolved by conducting NOESY and DQF-COSY experiments at a range of temperatures in the future; however, given the weak cross-peaks and broadness of the helicate signals these additional experiments were not pursued.

3.4.6.2 F2-(**3**) binding to AATT

The interactions of F2 of the helicate were next investigated with the A/T-rich dodecanucleotide. Upon addition of 1 equivalent of F2 of the helicate the major chemical shift changes in the H8/H6/H2 region were seen for the AH2 signals in an upfield direction (0.02 - 0.06 ppm). Minor variation was noted for the H8/H6 at the A_5/A_6, and T_7 positions (0.02 - 0.03 ppm), and broad peaks emerged corresponding to the helicate, most obviously downfield and upfield of the oligonucleotide resonances (see Figure 3.51).

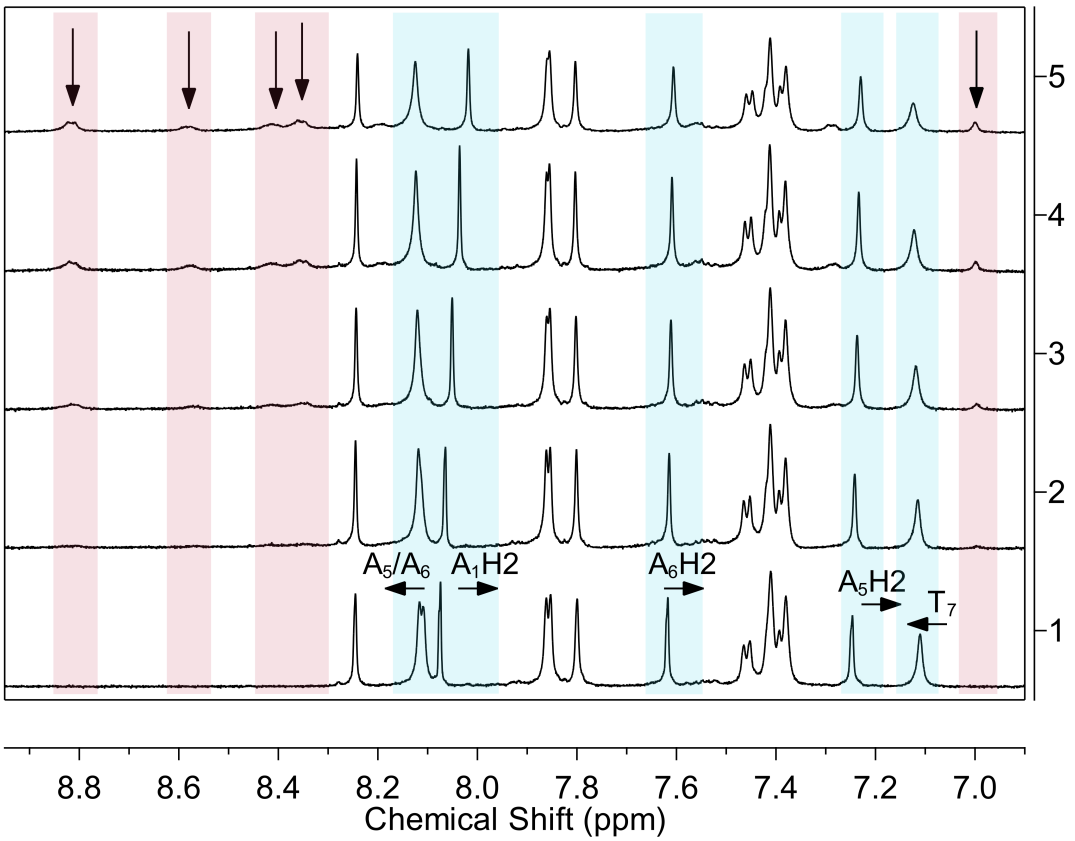

Figure 3.51: The H8/H6/H2 region of the ^{1}H NMR spectrum of the titration of the AATT dodecanucleotide with F2 of the diruthenium helicate (**3**) at R* =1 in pH 7.0 phosphate buffer at 25 °C. (1) free oligonecleotide, (2) R* = 0.25, (3) R* = 0.5, (4) R* = 0.75, (5) R* = 1. Notable changes in the chemical shift and shape of the oligonucleotide resonances are highlighted in blue, Ru(II) compound peaks are highlighted in red.

From the higher intensity helicate peaks the ratio was able to be estimated by relative integration in comparison to the A^1H8, A_5H8/A_6H8, A_1H2, and T_7H6 resonances at 8.26, 8.15, 8.02, and 7.14 ppm, respectively (see Figure 3.52). The helicate ratio was found to be in the range R = 0.22 (for the most upfield helicate peak - 7.00 ppm) - 0.54. In addition, the overlapping helicate signals at 8.4 ppm showed a relative integration of 1.31, although it was unclear how many hydrogen resonances comprised the broad peak at this position. Regardless, the comparatively low integration values indicate that the true

compound to DNA ratio (R) is significantly lower than the added ratio (R*). As seen for the helicate with the CCGG dodecanucleotide, R for F2 appeared to be slightly higher than that observed for F1.

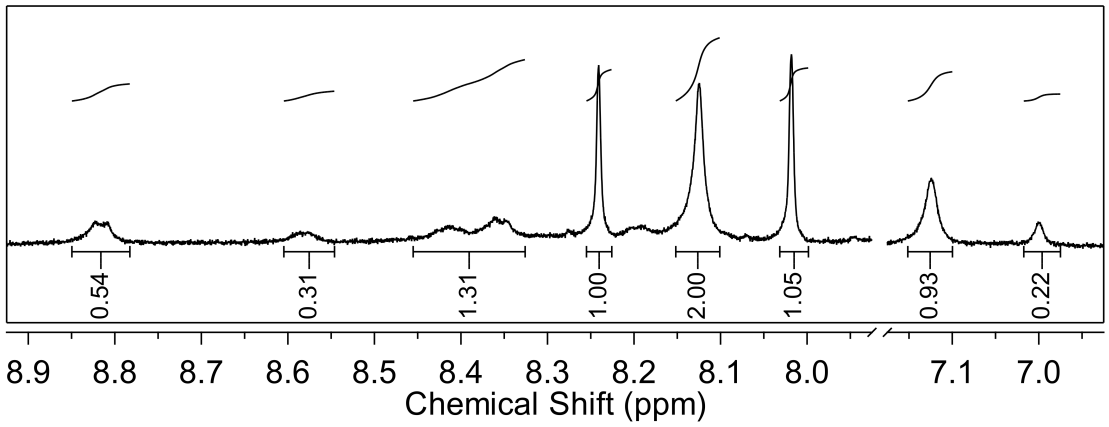

Figure 3.52: Selected region of the ^{1}H NMR spectrum of the AATT dodecanucleotide with F2 of the diruthenium helicate (**3**) at R* = 1, in pH 7.0 phosphate buffer at 25 °C. Relative integration of broad helicate signals shown, compared to A^1H8, A_5H8/A_6H8, A_1H2, and T_7H6 resonances.

In the H1′/base H5 region significant broadening of oligonucleotide signals was observed, which was not seen to the same extent for additions of F1 of the helicate (see Figure 3.53). Furthermore, upfield movement in chemical shift was recorded for the A_1H1′ (0.05 ppm), and T_{12}H1′ (0.04 ppm), matching behaviour seen with F1. Interestingly, shifts were also noted for the H1′ resonances of A_5, A_6, T_7, and C_9, which were accompanied by significant and selective broadening in some cases.

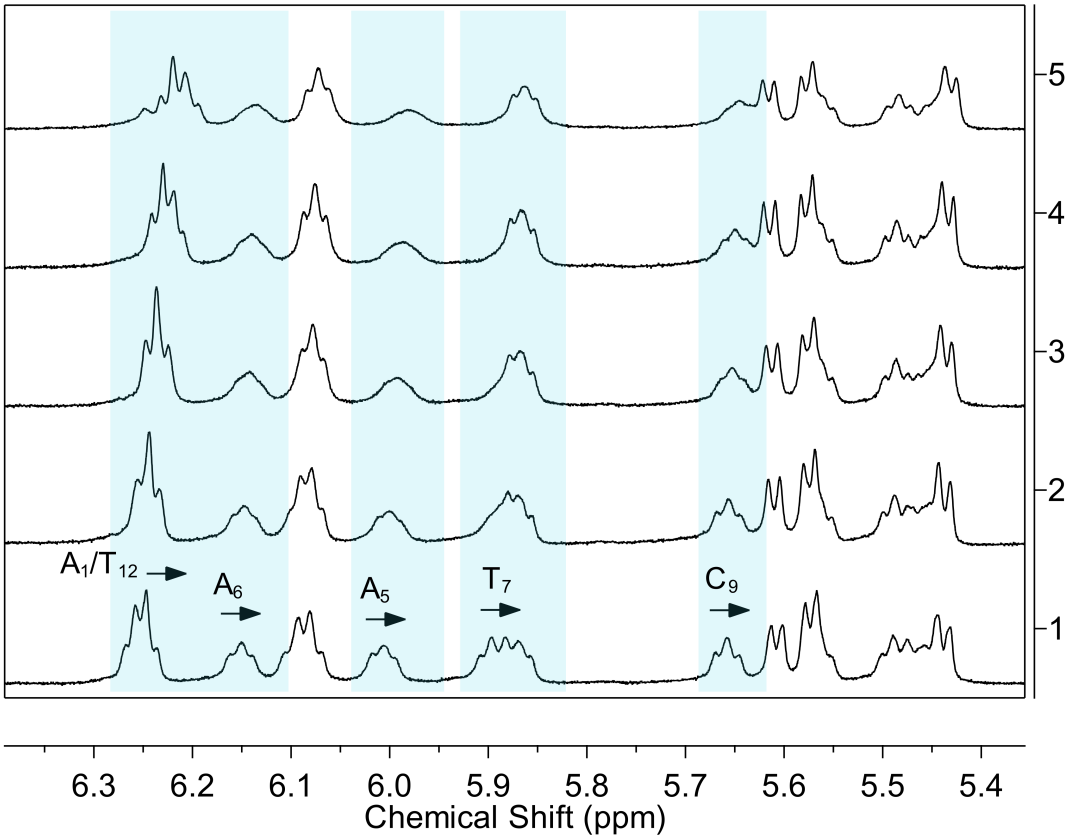

Figure 3.53: The H1′/base H5 region of the ^{1}H NMR spectrum of the titration of the AATT dodecanucleotide with F2 of the diruthenium helicate (**3**) at R* = 1 in pH 7.0 phosphate buffer at 25 °C. (1) free oligonucleotide, (2) R* = 0.25, (3) R* = 0.5, (4) R* = 0.75, (5) R* = 1. Notable changes in the chemical shift and shape of the oligonucleotide resonances are highlighted in blue.

As for previous samples there was little movement in the H2′ or H2″ signals, although a downfield shift of 0.03 ppm was recorded for the T_7 methyl hydrogens. The changes in chemical shift are summarised in Table 3.11 below. These changes, although small in magnitude compared to those reported for other Ru(II) compounds with DNA, were not insignificant particularly once the discrepancy in added compound ratio (R*) compared to the true ratio (R) was taken into account.

Table 3.11: ^{1}H NMR assignment of the DNA resonances of the AATT dodecanucleotide with F2 of the diruthenium helicate (**3**) at R =1, in D_2O and pH 7.0 phosphate buffer at 25 °C. Changes in chemical shift are given in brackets, with a negative sign indicating an upfield shift.

Base	H8/H6	AH2	H1′	H2′	H2″	Methyl
A_1	8.26 (0.00)	8.02 (-0.06)	6.22 (-0.05)	2.69 (-0.01)	2.81 (-0.01)	
C_2	7.46 (-0.01)		5.88 (0.00)	2.13 (-0.01)	2.41 (0.00)	
C_3	7.41 (0.01)		5.50 (0.01)	1.93 (0.00)	2.29 (0.00)	
G_4	7.88 (0.01)		5.46 (-0.02)	2.68 (-0.01)	2.75 (-0.02)	
A_5	8.15 (0.02)	7.23 (-0.03)	5.99 (-0.02)	2.70 (-0.01)	2.92 (-0.02)	
A_6	8.15 (0.03)	7.61 (-0.02)	6.15 (-0.02)	2.58 (-0.01)	2.92 (-0.02)	
T_7	7.14 (0.02)		5.88 (-0.03)	1.99 (0.00)	2.58 (0.01)	1.31 (0.03)
T_8	7.42 (0.04)		6.08 (-0.01)	2.17 (0.01)	2.54 (-0.02)	1.56 (0.02)
C_9	7.43 (0.01)		5.63 (-0.02)	1.98 (0.00)	2.35 (-0.01)	
G_{10}	7.87 (0.01)		5.58 (0.03)	2.68 (-0.01)	2.68 (-0.01)	
G_{11}	7.83 (0.02)		6.09 (-0.01)	2.62 (0.00)	2.73 (0.00)	
T_{12}	7.44 (0.02)		6.23 (-0.04)	2.25 (-0.01)	2.25 (-0.01)	1.61 (0.01)

For this sample analysis of the NOESY spectrum revealed similar cross-peaks as reported with the AATT dodecanucleotide and F1 of the helicate. In the aromatic region cross-peaks between 8.83 - 7.46 ppm and 8.38 - 7.46 ppm were again present (see Figure 3.54). In this case the signal at 7.46 ppm could be due to either the C_2H6 or T_{12}H6 resonance, an assignment complicated by overlapping oligonucleotide peaks at this position. Furthermore, a potential helicate peak may appear at this position at low intensity, which would be hidden underneath the DNA signals. This scenario could not be ruled out with certainty, casting doubt over this cross-peak as a true inter-molecular NOE.

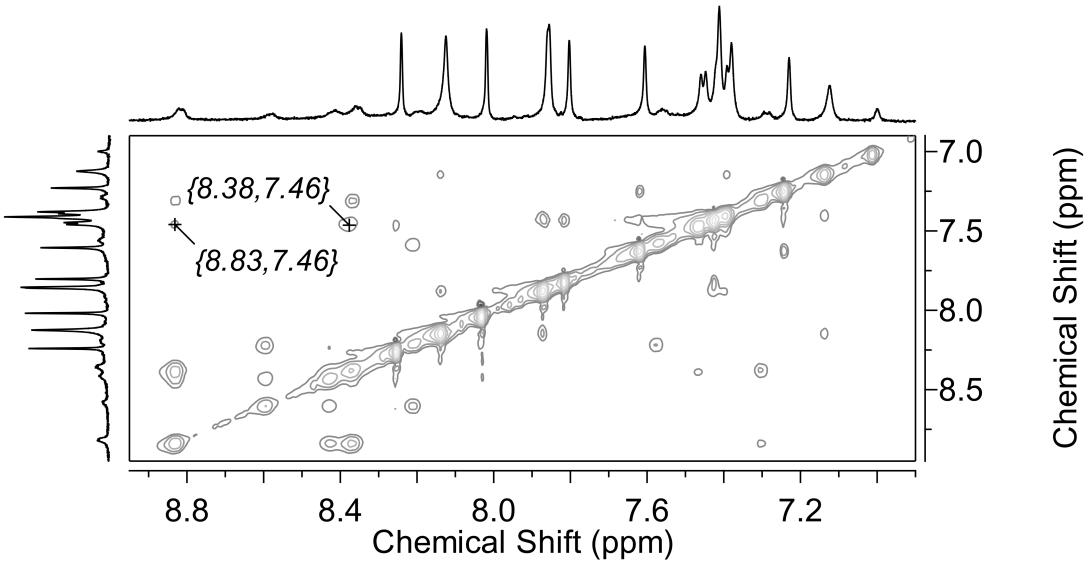

Figure 3.54: Expansion of a NOESY spectrum of the AATT dodecanucleotide with F2 of the diruthenium helicate (**3**) at R* = 1, in pH 7.0 phosphate buffer at 25 °C, showing potential inter-molecular NOEs between the helicate and oligonucleotide H6 resonances.

In the H1′/base H5 region cross-peaks to broad helicate signals in the aromatic region were seen between 8.82 - 6.25 ppm, 8.37 - 6.25 ppm, and 7.01 - 6.25 ppm (see Figure 3.55). In the ^{1}H NMR spectrum overlapping multiplets, partially due to the H1′ resonances of A_1 and T_{12}, are present in the range 6.18 - 6.26 ppm. As suggested for F1 of the helicate, this could be an inter-molecular NOE between helicate or either of these resonances; however, a hidden helicate peak is also possible at this position.

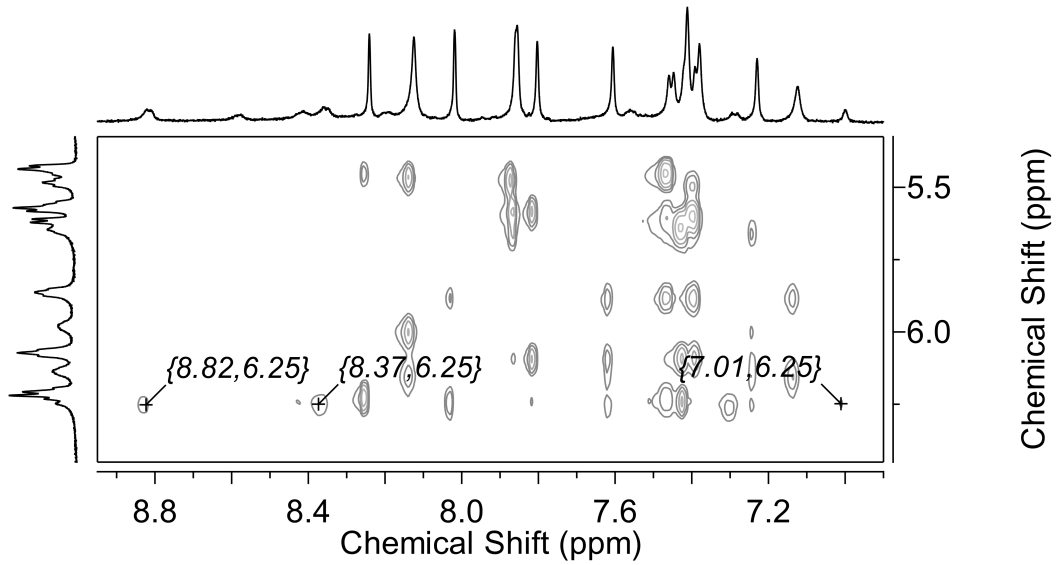

Figure 3.55: Expansion of a NOESY spectrum of the AATT dodecanucleotide with F2 of the diruthenium helicate (**3**) at R* = 1, in pH 7.0 phosphate buffer at 25 °C, showing potential inter-molecular NOEs between the helicate and oligonucleotide H1′/base H5 resonances.

Further upfield, the NOEs between 8.38 - 2.69 ppm, and 7.02 - 1.83 ppm can again

be assigned as helicate-helicate contacts, between the -CH_2CH_2- and CH_3 groups with non-adjacent aromatic hydrogens, rather than any H2′, H2″, or methyl hydrogens on the DNA (see Figure 3.56).

Again, it should be noted that across the spectrum all potential inter-molecular or helicate-helicate NOEs were very low in intensity and the presence of overlapping low intensity signals from the compound could never be discounted. Using NOESY and DQF-COSY methods across as range of temperatures is it possible to assign these overlapping signals and determine the nature of the NOEs; however, given the low intensity of signals overall, combined with the potential minor groove binding observed for F1 of the helicate with the AATT dodecanucleotide, these interactions were not further characterised.

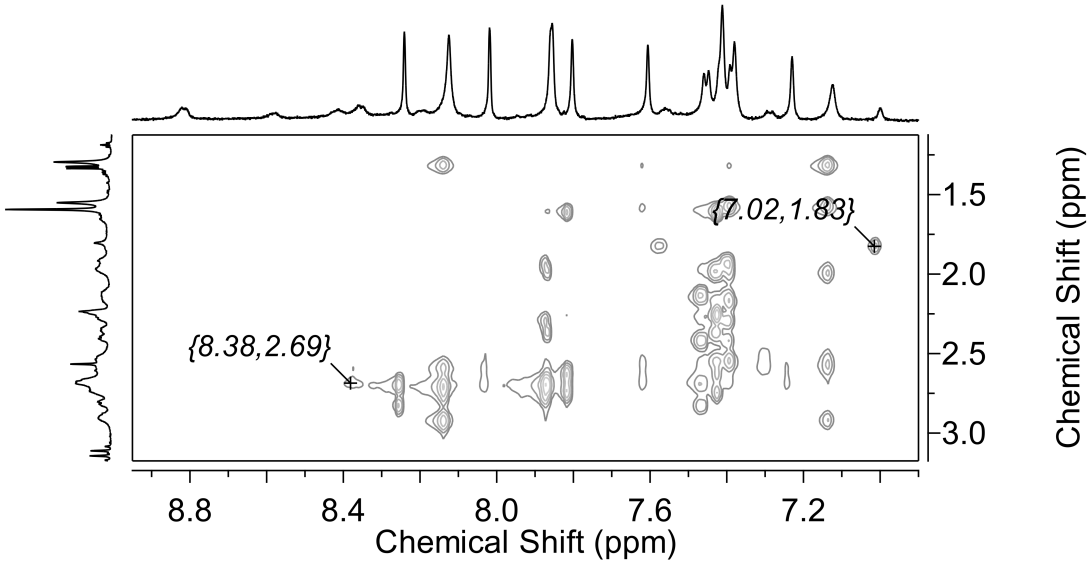

Figure 3.56: Expansion of a NOESY spectrum of the AATT dodecanucleotide with F2 of the diruthenium helicate (**3**) at R* = 1, in pH 7.0 phosphate buffer at 25 °C, showing the helicate-helicate intra-molecular NOEs.

Overall, the interactions of F2 of the helicate with the AATT dodecanucleotide were very similar to those seen with F1, despite the differences in enantiopurity of the two compounds. The greatest perturbation in chemical shift was observed for the AH2 and H1′ resonances, which was consistent with minor groove binding. While most NOEs were likely intra-molecular helicate-helicate contacts, cross-peaks between aromatic helicate peaks and the resonance at 6.25 ppm could indicate interactions with the A_1H1′ or T_{12}H1′. As noted with the CCGG dodecanucleotide, the relative integration appears to show that a greater proportion of Ru(II) compound was soluble in samples containing F2 of the helicate, although in all cases the true ratio of compound to DNA (R) was lower than R*.

3.4.7 Helicate (**3**) binding to the bulge oligonucleotide

Given that only limited NOE contacts were observed for both hands of the helicate with standard dodecanucleotides, it was hoped that by introducing additional flexibility in the oligonucleotide the strength of the binding and thus NOE contacts would be increased. The bulge sequence d(CCGAGAATTCCGG)$_2$ (bulge) was selected for further study as this sequence had previously been used in the work of Glasson *et al.* and showed preferential binding of the *P* form of a triple-stranded diruthenium(II) helicate by DNA affinity chromatography.[66] Figure 3.57 shows this sequence and the A_4 bulge.

$$C_1 - C_2 - G_3 - A_4 - G_5 - A_6 - A_7 - T_8 - T_9 - C_{10} - - - - C_{11} - G_{12} - G_{13}$$

$$G_{13} - G_{12} - C_{11} - - - - C_{10} - T_9 - T_8 - A_7 - A_6 - G_5 - A_4 - G_3 - C_2 - C_1$$

Figure 3.57: Adenine bulge tridecanucleotide d(CCGAGAATTCCGG)$_2$, containing a single bulged adenine on each strand (A_4 bulge shown in blue).

The same bulge sequence has been widely used by the Keene group to study DNA binding for a variety of dinuclear ruthenium(II) compounds.[243,249] In these studies the additional flexibility in the minor groove afforded by the adenine bulge site allowed relatively bulky compounds to bind and demonstrated the potential of non-intercalating compounds for use as diagnostic agents for DNA bulges sequences.

3.4.7.1 F1-Helicate (**3**) binding to bulge

Initially, addition of F1 of the helicate to the bulge oligonucleotide resulted in some changes to the chemical shifts of the oligonucleotide resonances, primarily around the bulge region in the ^{1}H NMR spectrum (see Figure 3.58). As for previously-studied dodecanucleotides the AH2 resonances exhibited changes in chemical shift, with a downfield shift for A_4 (0.02 ppm), while the A_6 and A_7 H2 signals shifted upfield (0.03 and 0.01, respectively). A notable variation in chemical shift for the A_4H8 peak was recorded, with a downfield shift of 0.02 ppm. Extremely low intensity signals corresponding to the helicate were barely detectable, emerging downfield of the oligonucleotide resonances in the aromatic region.

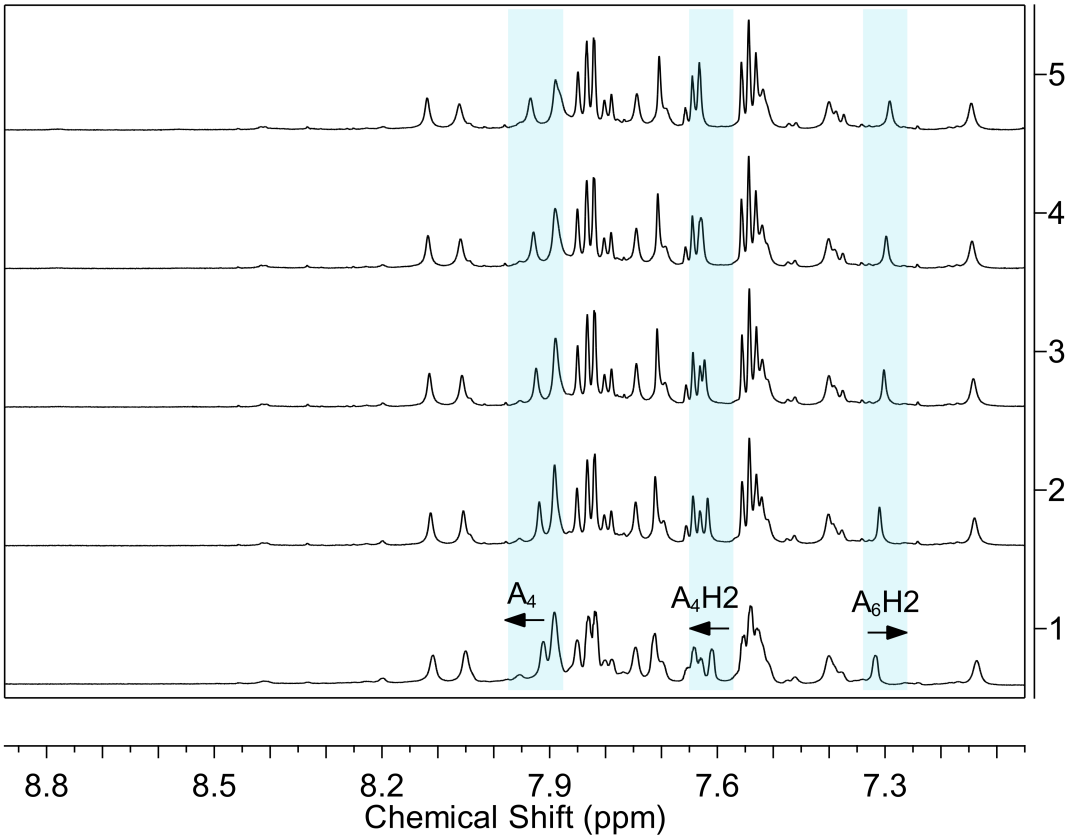

Figure 3.58: The H8/H6/H2 region of the ^{1}H NMR spectrum of the titration of the bulge oligonucleotide with F1 of the diruthenium helicate (**3**), in pH 7.0 phosphate buffer at 25 °C. (1) free oligonucleotide, (2) R* = 0.25, (3) R* = 0.5, (4) R* = 0.75, (5) R* = 1. Notable changes in the chemical shift and shape of the oligonucleotide resonances are highlighted in blue.

Slight shape changes were observed in the H1′/base H5 region, but very little variation in chemical shift was recorded (see Figure 3.59). Notably, the H1′ resonances of A_6 and T_8 converged slightly, with a small upfield and downfield shift respectively, causing shape change at this position. In addition, the G_3H1′, A_4H1′, G_{12}H1′ signals, while not showing great variation in chemical shift from the free oligonucleotide, exhibited some broadening and changes in shape of these overlapping peaks.

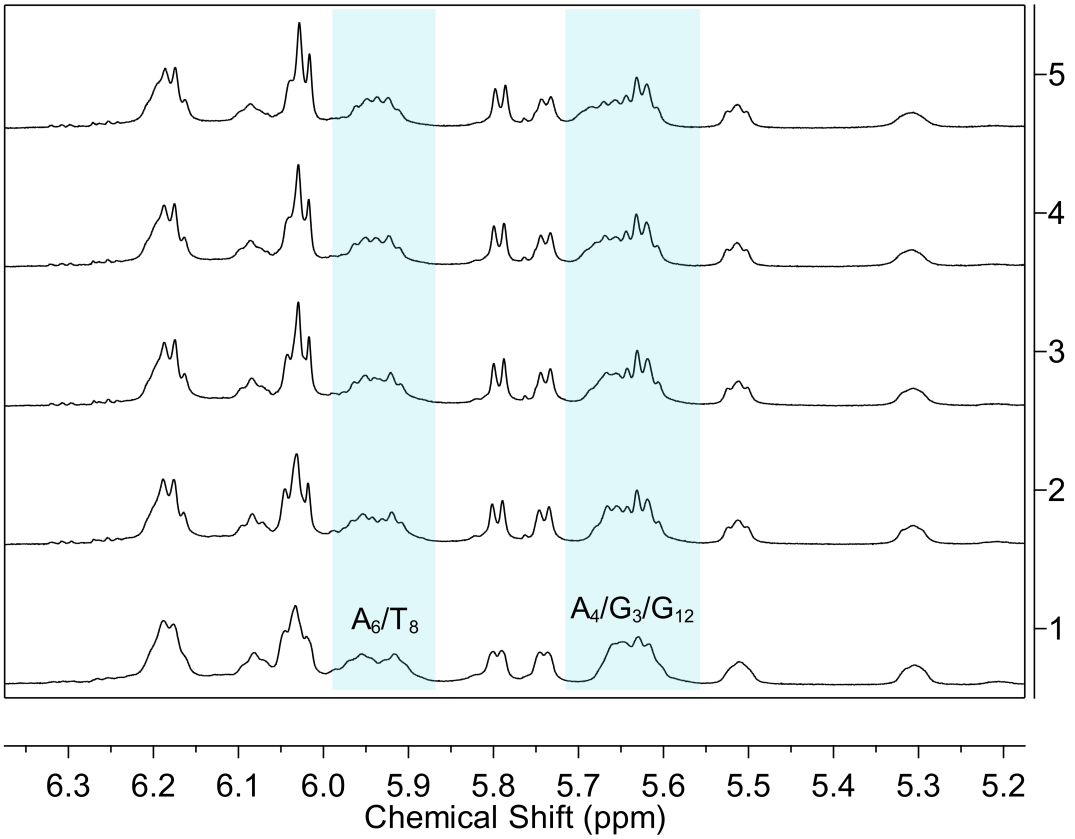

Figure 3.59: The H1′/base H5 region of the ^{1}H NMR spectrum of the titration of the bulge oligonucleotide with F1 of the diruthenium helicate (**3**), in pH 7.0 phosphate buffer at 25 °C. (1) free oligonucleotide, (2) R* = 0.25, (3) R* = 0.5, (4) R* = 0.75, (5) R* = 1. Notable changes in the chemical shift and shape of the oligonucleotide resonances are highlighted in blue.

The variation in chemical shift from the free bulge oligonucleotide upon addition of F1 of the helicate is reported in Table 3.12 below, and outside the regions noted above little change was observed in other parts of the spectrum.

Table 3.12: ^{1}H NMR assignment of the DNA resonances of the bulge oligonucleotide with F1 of the diruthenium helicate (**3**) at R* = 1, in D_2O and pH 7.0 phosphate buffer at 25 °C. Changes in chemical shift are given in brackets, with a negative sign indicating an upfield shift.

Base	H8/H6	AH2	H1′	H2′	H2″	Methyl
C_1	7.79 (-0.02)		6.02 (-0.02)	2.08 (-0.01)	2.54 (0.00)	
C_2	7.51 (-0.02)		5.62 (-0.01)	1.94 (-0.02)	2.25 (-0.02)	
G_3	7.91 (0.02)		5.64 (0.00)	2.41 (-0.01)	2.71 (-0.01)	
A_4	7.94 (0.02)	7.63 (0.02)	5.69 (0.00)	2.51 (0.02)	2.51 (-0.02)	
G_5	7.74 (-0.01)		5.31 (-0.02)	2.51 (-0.03)	2.57 (-0.02)	
A_6	8.05 (0.00)	7.29 (-0.03)	5.95 (-0.01)	2.65 (-0.02)	2.88 (-0.01)	
A_7	8.11 (0.00)	7.70 (-0.01)	6.19 (-0.01)	2.59 (-0.01)	2.90 (0.00)	
T_8	7.14 (0.01)		5.92 (0.01)	1.99 (-0.01)	2.56 (0.00)	1.27 (-0.01)
T_9	7.39 (-0.01)		6.09 (0.01)	2.16 (0.00)	2.56 (0.00)	1.56 (-0.01)
C_{10}	7.50 (-0.02)		6.19 (0.00)	1.94 (-0.02)	2.18 (0.00)	
C_{11}	7.68 (-0.03)		5.51 (0.00)	2.17 (-0.02)	2.36 (-0.01)	
G_{12}	7.88 (0.00)		5.66 (-0.02)	2.67 (0.00)	2.71 (0.00)	
G_{13}	7.85 (0.00)		6.17 (0.00)	2.56 (-0.01)	2.38 (-0.01)	

In the ^{1}H NMR spectrum there did not appear to be any clear helicate signals in the aromatic region, so the amount of the F1 of the helicate was increased to 2 equivalents. Increasing this ratio caused larger changes in chemical shift for the oligonucleotide throughout the spectrum. Slight downfield shifts were observed for the aromatic hydrogens, A_7H8, A_6H8, and A_4H8, and these signals also seemed to exhibit broadening with added helicate. A small downfield shift was observed for the T_8H6 peak, and an upfield shift for G_5H8. Variation in the chemical shifts of all of these hydrogens suggested that there may be some interaction of helicate in the bulge region of the oligonucleotide. The remaining variation in the aromatic region was seen for the A_4H2 and A_6H2 showing further downfield (0.04 ppm) and upfield (0.04 ppm) movement, respectively, again suggesting minor groove association of the helicate. Broad peaks corresponding to the helicate appeared downfield

of the oligonucleotide signals, but again these were very low intensity signals which showed significant broadening, as observed in previous studies for the helicate (see Figure 3.60).

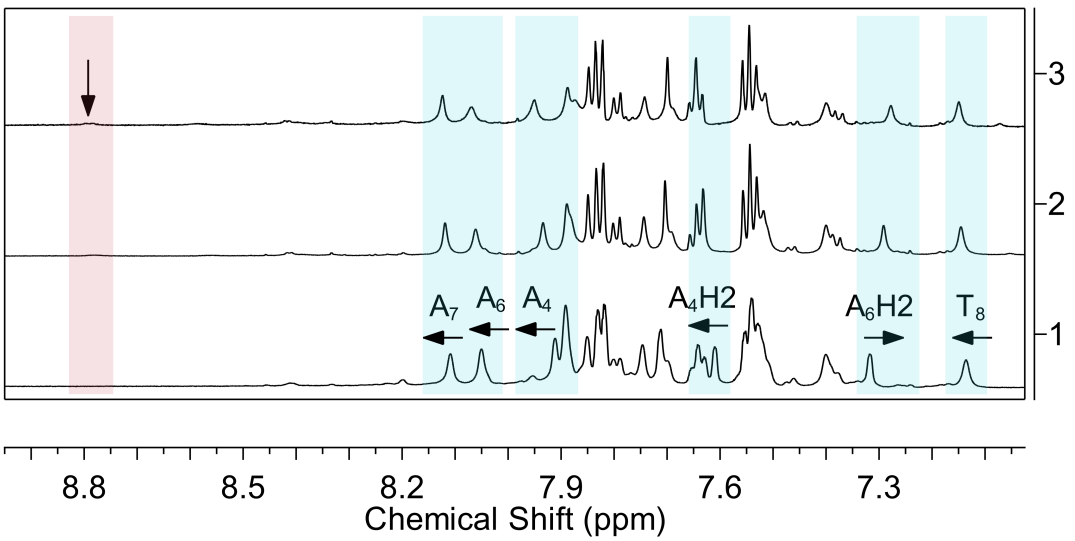

Figure 3.60: The H8/H6/H2 region of the ^{1}H NMR spectrum of the titration of the bulge oligonucleotide with F1 of the diruthenium helicate (**3**), in pH 7.0 phosphate buffer at 25 °C. (1) free oligonucleotide, (2) R* = 1, (2), R* = 2. Notable changes in the chemical shift and shape of the oligonucleotide resonances are highlighted in blue, Ru(II) compound peaks are highlighted in red.

In the H1′/base H5 region there were further changes in the shape and chemical shifts of the oligonucleotide resonances upon increasing the ratio of F1 of the helicate to 2 equivalents. Changes in the shape of the overlapping signals at $\sim$ 6.2 ppm were evident, despite no clear changes in the chemical shifts for resonances at this position (A_7H1′, C_{10}H1′, and G_{13}H1′). The A_6H1′ and T_8H1′ signals converged further to overlap, with upfield and downfield shifts respectively. The final major changes were seen for the H1′ of the A_4, G_3 and G_{12} resonances which showed downfield shifts (in the case of A_4 and G_3 - 0.02 ppm) or upfield shifts (G_{12} - 0.02 ppm) splitting the signal into broad but more separated peaks. This region of the spectrum is shown in Figure 3.61 below. Little change was seen in the oligonucleotide resonances further upfield and a full summary can be found in Table 3.13 below.

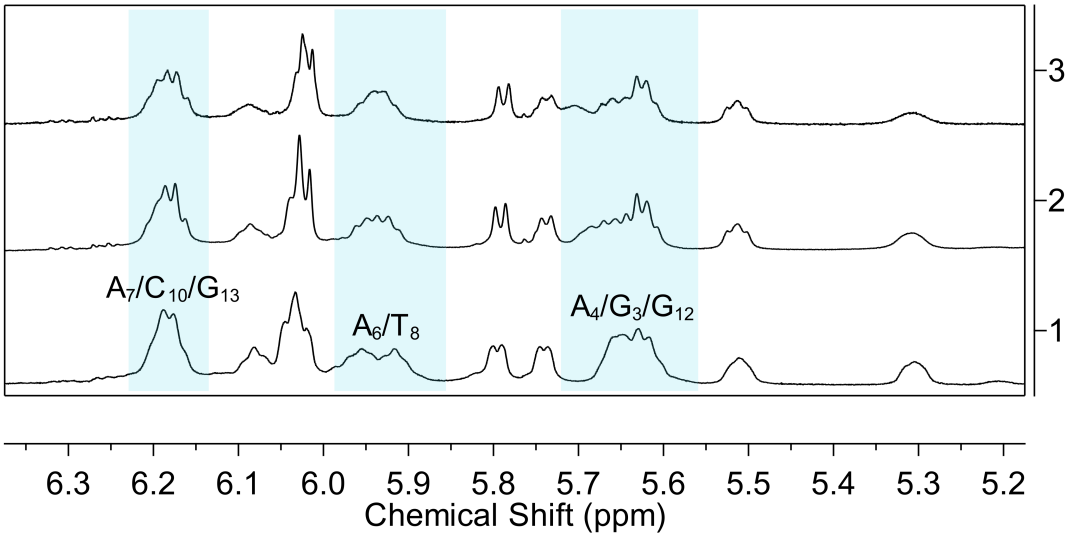

Figure 3.61: The H1′/base H5 region of the ^{1}H NMR spectrum of the titration of the bulge oligonucleotide with F1 of the diruthenium helicate (**3**), in pH 7.0 phosphate buffer at 25 °C. (1) free oligonucleotide, (2) R* = 1, (2), R* = 2. Notable changes in the chemical shift and shape of the oligonucleotide resonances are highlighted in blue.

Table 3.13: ^{1}H NMR assignment of the DNA resonances of the bulge oligonucleotide with F1 of the diruthenium helicate (**3**) at R* = 2, in D_2O and pH 7.0 phosphate buffer at 25 °C. Changes in chemical shift are given in brackets, with a negative sign indicating an upfield shift.

Base	H8/H6	AH2	H1′	H2′	H2″	Methyl
C_1	7.79 (-0.02)		6.02 (-0.02)	2.08 (-0.01)	2.55 (0.01)	
C_2	7.51 (-0.02)		5.62 (-0.01)	1.93 (-0.03)	2.26 (-0.01)	
G_3	7.87 (-0.02)		5.66 (0.02)	2.41 (-0.01)	2.71 (-0.01)	
A_4	7.94 (0.02)	7.65 (0.04)	5.71 (0.02)	2.52 (0.03)	2.52 (-0.01)	
G_5	7.74 (-0.01)		5.31 (-0.02)	2.52 (-0.02)	2.56 (-0.03)	
A_6	8.06 (0.01)	7.28 (-0.04)	5.95 (-0.01)	2.66 (-0.01)	2.88 (-0.01)	
A_7	8.12 (0.01)	7.70 (-0.01)	6.20 (0.00)	2.59 (-0.01)	2.92 (0.02)	
T_8	7.14 (0.01)		5.93 (0.02)	2.00 (0.00)	2.57 (0.01)	1.27 (-0.01)
T_9	7.39 (-0.01)		6.09 (0.01)	2.17 (0.01)	2.56 (0.00)	1.56 (-0.01)
C_{10}	7.51 (-0.01)		6.19 (0.00)	1.98 (0.02)	2.19 (0.01)	
C_{11}	7.69 (-0.02)		5.51 (0.00)	2.17 (-0.02)	2.36 (-0.01)	
G_{12}	7.88 (0.00)		5.66 (-0.02)	2.67 (0.00)	2.72 (0.01)	
G_{13}	7.85 (0.00)		6.17 (0.00)	2.56 (-0.01)	2.39 (0.00)	

To investigate these changes further a NOESY experiment was conducted and obvious helicate-helicate cross-peaks were identified downfield of the oligonucleotide resonances in the aromatic region (see Figure 3.62). Aside from these intra-molecular contacts an additional cross-peak was observed in this region between 8.35 - 7.30 ppm. At this stage it was unclear if this signal was due to intra- or inter-molecular contacts, and the presence of a helicate peak masked by oligonucleotide signals at this position could not be ruled out. If this cross-peak were inter-molecular it could potentially indicate a helicate - A_6H2 interaction, which would support the case for minor groove binding.

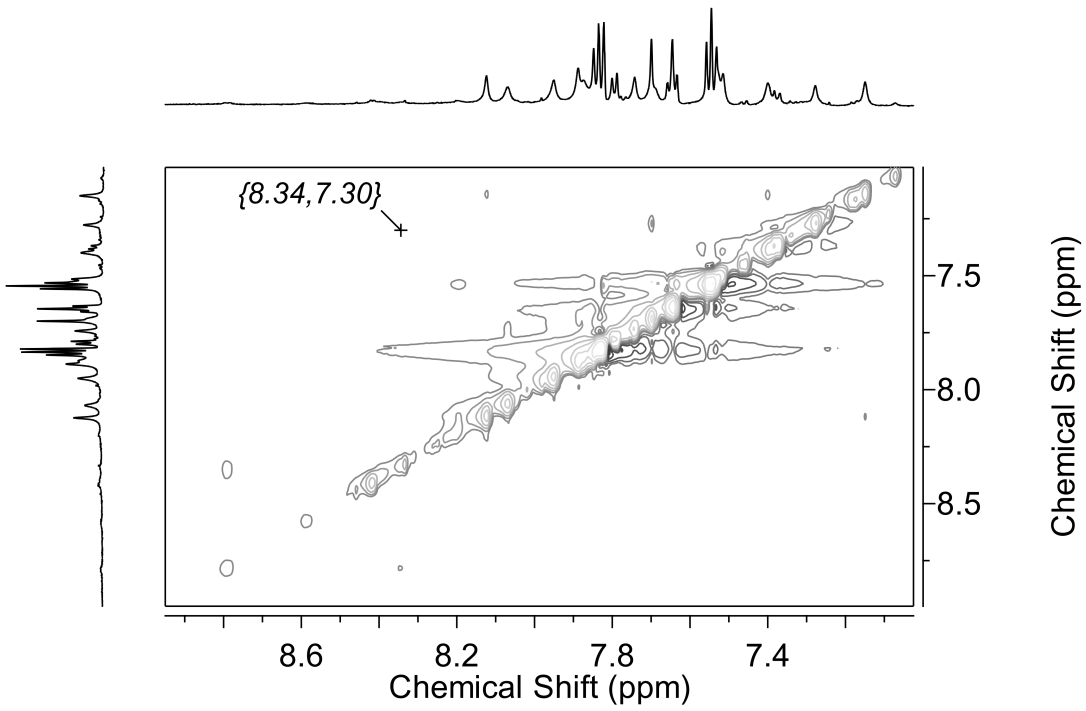

Figure 3.62: Expansion of a NOESY spectrum of the bulge oligonucleotide with F1 of the diruthenium helicate (**3**) at R* = 2, in pH 7.0 phosphate buffer at 25 °C, showing a potential inter-molecular NOE (8.34 - 7.30 ppm).

Cross-peaks in the H1′/base H5 - H8/H6/H2 regions were noted between downfield helicate signals and potential oligonucleotide resonances (see Figure 3.63). Three weak cross-peaks were seen between 8.79 - 6.17 ppm, 8.39 - 6.17 ppm, and 8.34 - 6.17 ppm. The oligonucleotide signal in the vicinity of 6.17 ppm was comprised of many overlapping resonances, including A_7H1′, C_{10}H1′, and G_{13}H1′, and a helicate peak was also observed at this position in previous samples, meaning that again an intra-molecular NOE was possible. No further potential inter-molecular NOEs were seen outside of the two regions outlined above.

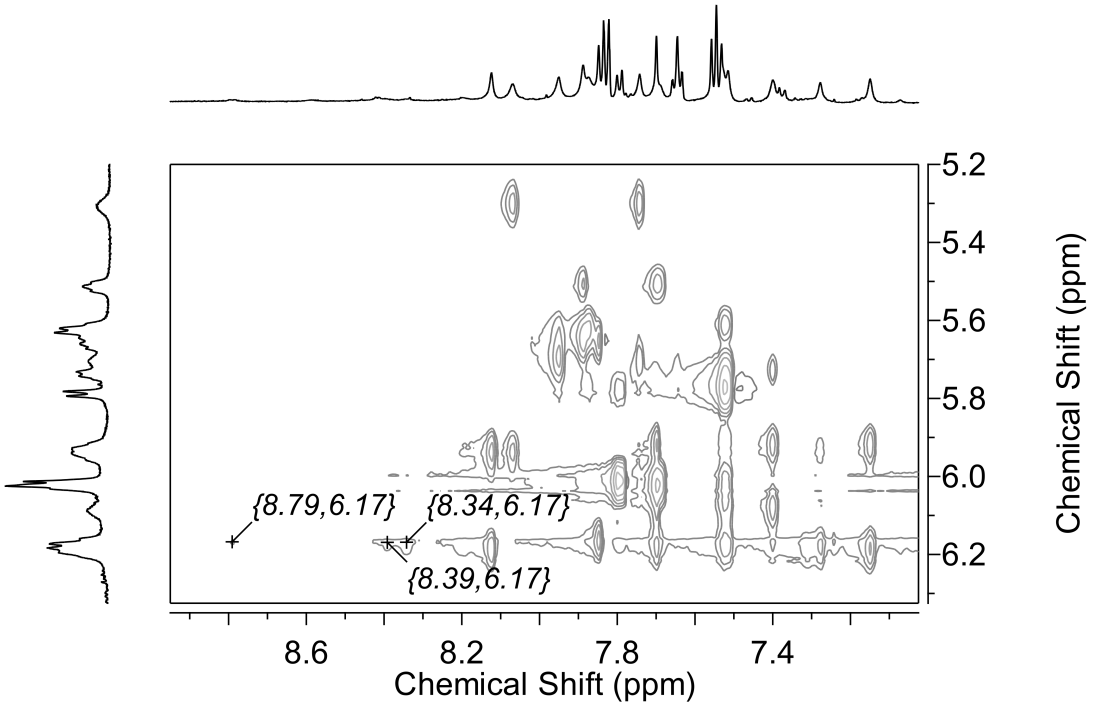

Figure 3.63: Expansion of a NOESY spectrum of the bulge oligonucleotide with F1 of the diruthenium helicate (**3**) at R* = 2, in pH 7.0 phosphate buffer at 25 °C, showing the potential inter-molecular NOEs between helicate and oligonucleotide H1′ resonances.

As the helicate peaks were significantly broadened across the spectrum it was challenging to assign clear, high intensity signals in 1D or 2D spectra. Variable temperature 1D experiments were conducted, as shown in Figure 3.64, and while the intensity of helicate signals appeared to improve slightly at 45 °C, varying the temperature did not significantly improve the broadness or solubility.

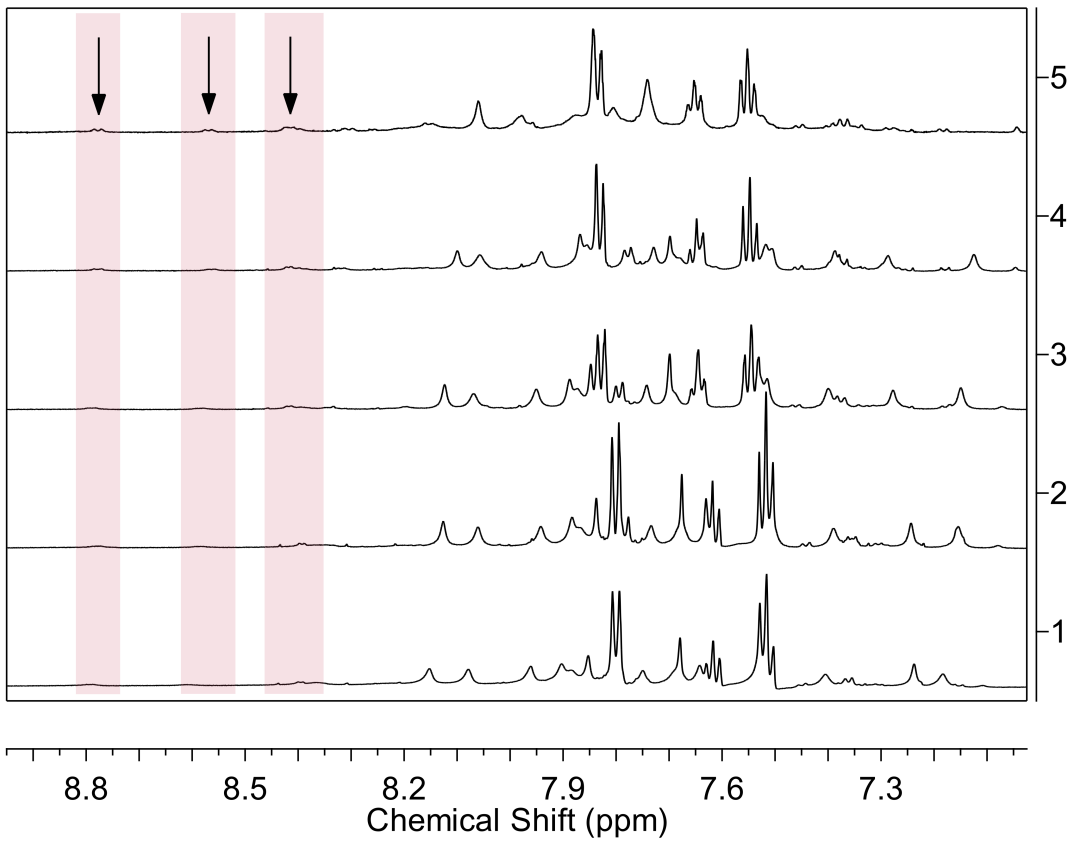

Figure 3.64: The H8/H6/H2 region of the ^{1}H NMR spectrum of the bulge oligonucleotide with F1 of the diruthenium helicate (**3**) at R* = 2, in pH 7.0 phosphate buffer at temperatures from 5°C to 25°C. (1) 5 °C, (2) 15 °C, (3) 25 °C, (4) 35 °C, (5) 45 °C. Ru(II) compound peaks are highlighted in red.

Given that variable temperature experiments did little to improve the helicate signals the ratio of compound was further increased, up to a total of 4 equivalents. Slight improvement was seen in the 1D spectrum and the aromatic regions are shown in Figure 3.65. For the most downfield helicate signals (between 8.2 - 8.9 ppm) the intensity increased but the peaks were still broad (and lower in intensity) in comparison to the oligonucleotide signals. In addition, significant precipitation was observed over the course of these experiments which may have further contributed to broadening. While the relative integrals suggest that the fraction of helicate-bound oligonucleotide is quite low, the changes in chemical shift were nonetheless recorded. While the 3:1 and 4:1 ratios are not truly correct, due to the precipitate, it is presumed that there is a greater percentage of bound oligonucleotide than in previous samples.

The changes in oligonucleotide chemical shift at R* = 4 compared to R* = 1 were seen to increase in magnitude, particularly for the AH2 resonances, with the A_4H2 resonance shifting further downfield (0.04 ppm), while upfield shifts were observed for A_6 (0.06 ppm) and A_7 (0.02 ppm). The largest variation in chemical shift for the H6 signals was in the

bulge and A/T-rich regions of the oligonucleotide. Downfield shifts were noted for A_4 (0.06 ppm), A_6 (0.03 ppm), A_7 (0.02 ppm), and T_8 (0.03 ppm). At other positions such as C_1H6 no further variation was observed compared to R* = 2. The aromatic region of the spectrum with increasing ratios of F1 of the helicate is shown in Figure 3.65.

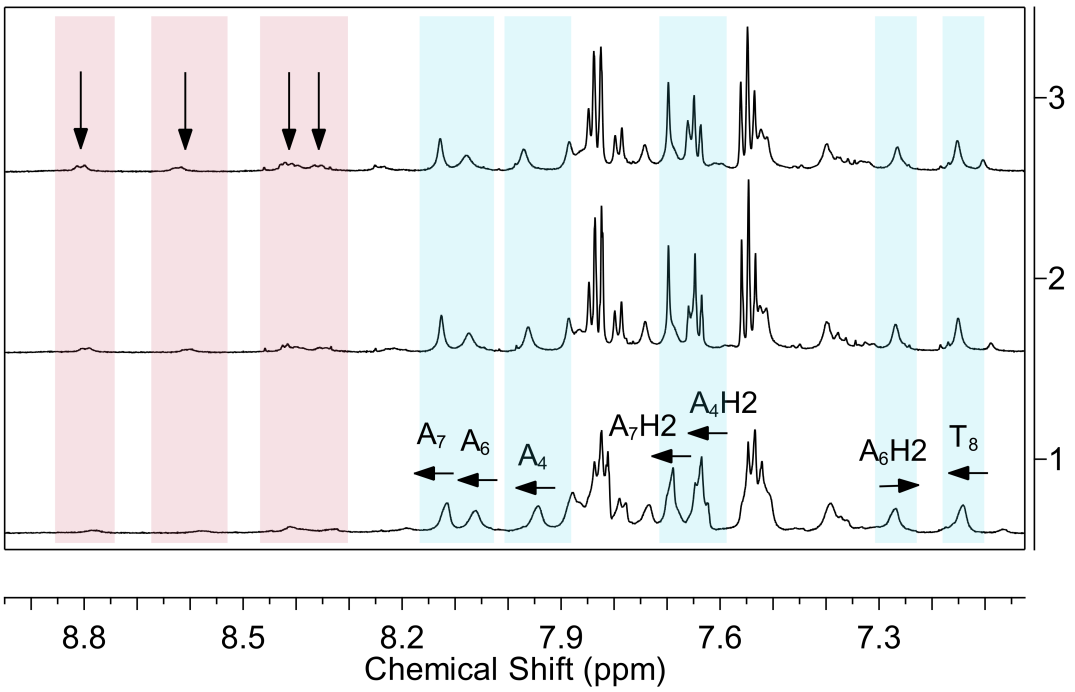

Figure 3.65: The H8/H6/H2 region of the ^{1}H NMR spectrum of the titration of the bulge oligonucleotide with F1 of the diruthenium helicate (**3**), in pH 7.0 phosphate buffer at 25 °C. (1) R* = 2, (2) R* = 3, (3) R* = 4. Notable changes in the chemical shift and shape of the oligonucleotide resonances are highlighted in blue, Ru(II) compound peaks are highlighted in red.

The increase in intensity of the broad helicate signals (indicated in Figure 3.65 in red) allowed the determination of the relative integration and estimation of the true ratio of compound to DNA present in solution. This was not carried out at lower helicate R* values as the compound signals were extremely broad.

Using the higher intensity helicate peaks the true ratio was able to be estimated by relative integration in comparison to the A_7H8, A_6H8, A_4H8, and T_8H6 resonances at 8.13, 8.08, 7.98, and 7.16 ppm, respectively (see Figure 3.66). The helicate ratio was found to be in the range R = 0.25 - 0.36. As seen for the AATT dodecanucleotide the overlapping helicate signals at 8.4 ppm showed higher relative integration (1.14) as a number of signals made up the broad peak at this position. As expected, the relative integration indicated that the proportion of soluble compound to DNA ratio (R) was significantly lower than the added ratio (R*). It was assumed that a proportion of both compound and DNA was insoluble, as evidenced by the formation of an orange precipitate.

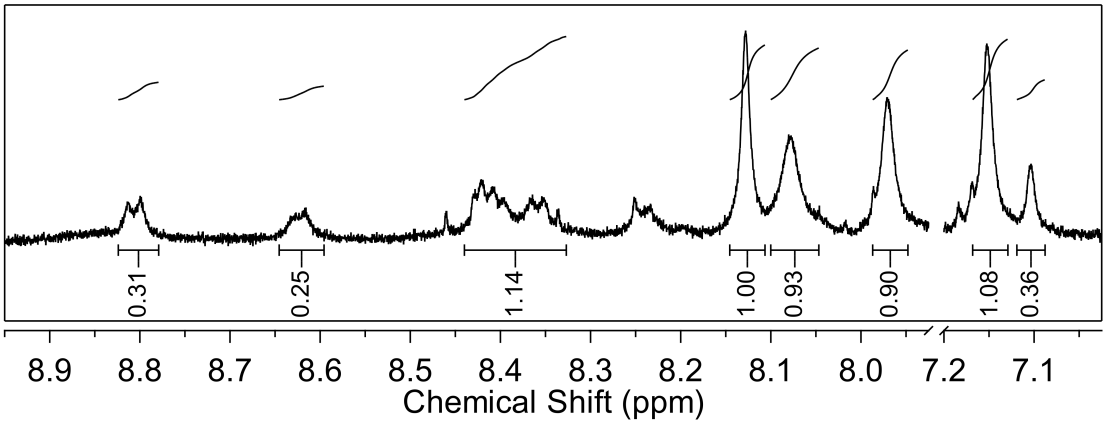

Figure 3.66: Selected region of the ^{1}H NMR spectrum of the bulge dodecanucleotide with F1 of the diruthenium helicate (**3**) at R* = 4, in pH 7.0 phosphate buffer at 25 °C. Relative integration of broad helicate signals shown, compared to the A^7H8, A_6H8, A_4H8, and T_8H6 resonances.

In the H1′/base H5 region significant selective broadening was observed for the T_9H1′ and G_5H1′ resonances. Changes in chemical shift and shape of peaks were also seen throughout this region, with the greatest change in chemical shift being recorded for the overlapping A_4H1′, G_3H1′, and G_{12}H1′ resonances (0.01 - 0.04 ppm). Despite variation in the H8/H6/H2 and H1′/base H5 regions, only very minor changes in chemical shift were recorded for the H2′, H2″, and methyl resonances (see Table 3.14).

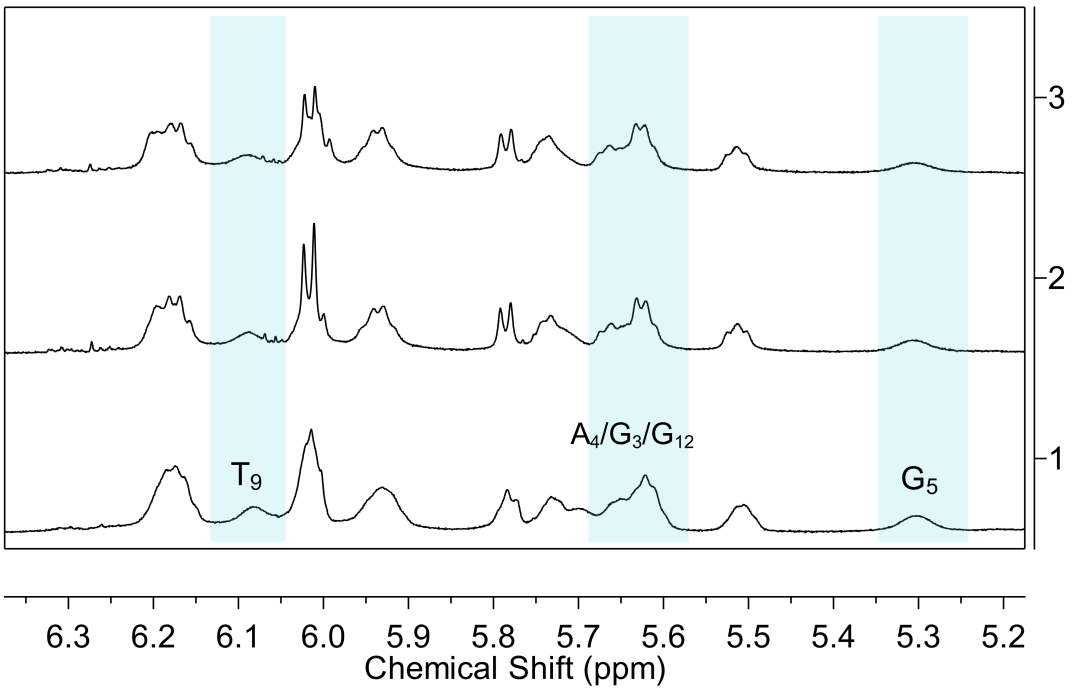

Figure 3.67: The H1′/base H5 region of the ^{1}H NMR spectrum of the titration of the bulge oligonucleotide with F1 of the diruthenium helicate (**3**), in pH 7.0 phosphate buffer at 25 °C. (1) R* = 2, (2) R* = 3, (3) R* = 4. Notable changes in the chemical shift and shape of the oligonucleotide resonances are highlighted in blue.

Table 3.14: ^{1}H NMR assignment of the DNA resonances of the bulge oligonucleotide with F1 of the diruthenium helicate (**3**) at R* = 4, in D_2O and pH 7.0 phosphate buffer at 25 °C. Changes in chemical shift are given in brackets, with a negative sign indicating an upfield shift.

Base	H8/H6	AH2	H1′	H2′	H2″	Methyl
C_1	7.79 (-0.02)		6.02 (-0.02)	2.09 (0.00)	2.54 (0.00)	
C_2	7.52 (-0.01)		5.62 (-0.01)	1.92 (-0.04)	2.24 (-0.03)	
G_3	7.87 (-0.02)		5.67 (0.03)	2.40 (-0.02)	2.72 (0.00)	
A_4	7.98 (0.06)	7.65 (0.04)	5.73 (0.04)	2.52 (0.03)	2.52 (-0.01)	
G_5	7.75 (0.00)		5.31 (-0.02)	2.53 (-0.01)	2.56 (-0.03)	
A_6	8.08 (0.03)	7.26 (-0.06)	5.94 (-0.02)	2.66 (-0.01)	2.88 (-0.01)	
A_7	8.13 (0.02)	7.69 (-0.02)	6.20 (0.00)	2.59 (-0.01)	2.92 (0.02)	
T_8	7.16 (0.03)		5.93 (0.02)	2.01 (0.01)	2.57 (0.01)	1.28 (0.00)
T_9	7.40 (0.00)		6.09 (0.01)	2.17 (0.01)	2.56 (0.00)	1.57 (0.00)
C_{10}	7.53 (0.01)		6.18 (-0.01)	1.98 (0.02)	2.17 (-0.01)	
C_{11}	7.70 (-0.01)		5.52 (0.01)	2.16 (-0.03)	2.36 (-0.01)	
G_{12}	7.89 (0.01)		5.67 (-0.01)	2.67 (0.00)	2.72 (0.01)	
G_{13}	7.85 (0.00)		6.17 (0.00)	2.56 (-0.01)	2.38 (-0.01)	

At R* = 4 a NOESY experiment was conducted and as was found at lower ratios, a number of cross-peaks looked to be helicate-helicate, appearing in the aromatic region downfield of the oligonucleotide signals (see Figure 3.68). Numerous cross-peaks were recorded between downfield helicate peaks and signals further upfield, which were overlapping with oligonucleotide peaks. Some of these, between 8.80 - 7.33 ppm, 8.41 - 7.34 ppm, and 8.37 - 7.33 ppm, did not seem to correlate to any assigned oligonucleotide resonance at 7.33/7.34 ppm, suggesting that there may be a broad, low intensity helicate peak at this position, and thus would correspond to intra-molecular contacts. This was also supposed to be the case for the cross-peak at 8.25 - 7.61 ppm, meaning that no NOEs in this region could be assigned as inter-molecular.

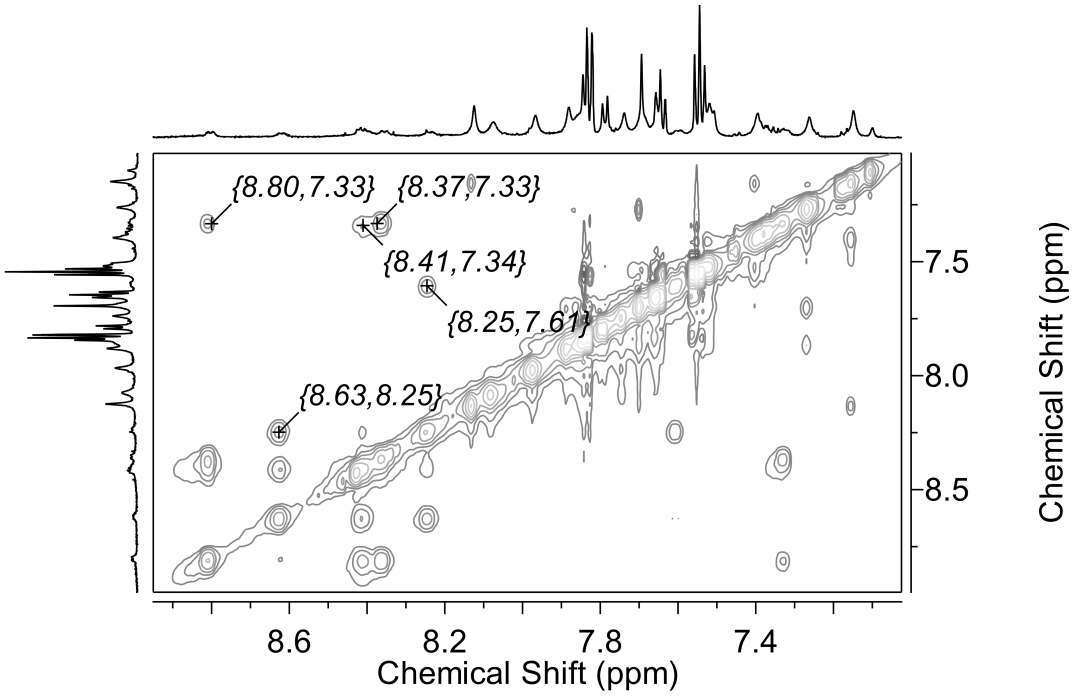

Figure 3.68: Expansion of a NOESY spectrum of the bulge oligonucleotide with F1 of the diruthenium helicate (**3**) at R* = 4, in pH 7.0 phosphate buffer at 25 °C, showing the helicate-helicate intra-molecular NOEs in the aromatic region.

Outside of the region shown in Figure 3.68, the weak cross-peaks between aromatic helicate signals and possible oligonucleotide signals in the H1′/base H5 region were again observed, between 8.81 - 6.20 ppm, 8.41 - 6.20 ppm, and 8.37 - 6.20 ppm (see Figure 3.69). Despite being slightly shifted from those identified at R* = 2 the same reasoning could be applied where it was unclear whether these represented intra- or inter-molecular NOEs.

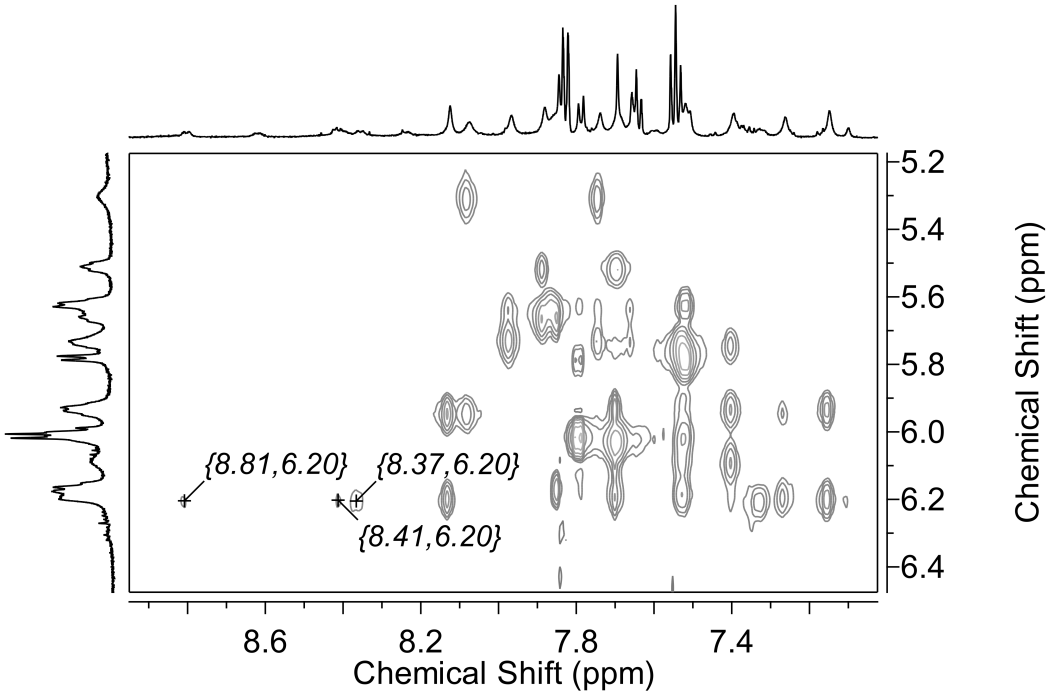

Figure 3.69: Expansion of a NOESY spectrum of the bulge oligonucleotide with F1 of the diruthenium helicate (**3**) at R* = 4, at a F1 to DNA duplex ratio of 4, in pH 7.0 phosphate buffer at 25 °C,showing potential inter-molecular NOEs between the helicate and oligonucleotide H1′/base H5 resonances.

Unlike at R* = 2, in the case of R* = 4 NOEs were seen further upfield between aromatic helicate peaks and oligonucleotide signals in the H4′/H5′/H5″ and H2′/H2″ regions of the spectra (see Figures 3.70 and 3.71, respectively). Cross-peaks were identified at 8.81 - 4.25 ppm and 8.41 - 4.14 ppm and these were the most promising candidates for inter-molecular interactions as there were unlikely to be helicate peaks in this region (the -CH_2CH_2- and CH_3 hydrogens were expected to appear further upfield). Based on the original free bulge oligonucleotide assignments in this region by Kalnik *et al.*[250] these resonances were assigned as either G_3H4′ or A_4H4′ (at 4.25 ppm), and the H4′ of $T_8/T_9/C_{10}/G_{12}/G_{13}$ (at 4.14 ppm). Given that the oligonucleotide resonances were highly overlapping in this region it was challenging to be more specific. It would be possible to assign oligonucleotide resonances in H4′ region by variable temperature 2D NMR methods; however, these experiments were not conducted for the bulge sequence in this thesis. Most importantly, without having to assign the specific residues, the fact that these NOEs appear between the helicate and peaks in the H4′ region supports the notion that helicate binding may occur near the top of the minor groove rather than deep within.[250]

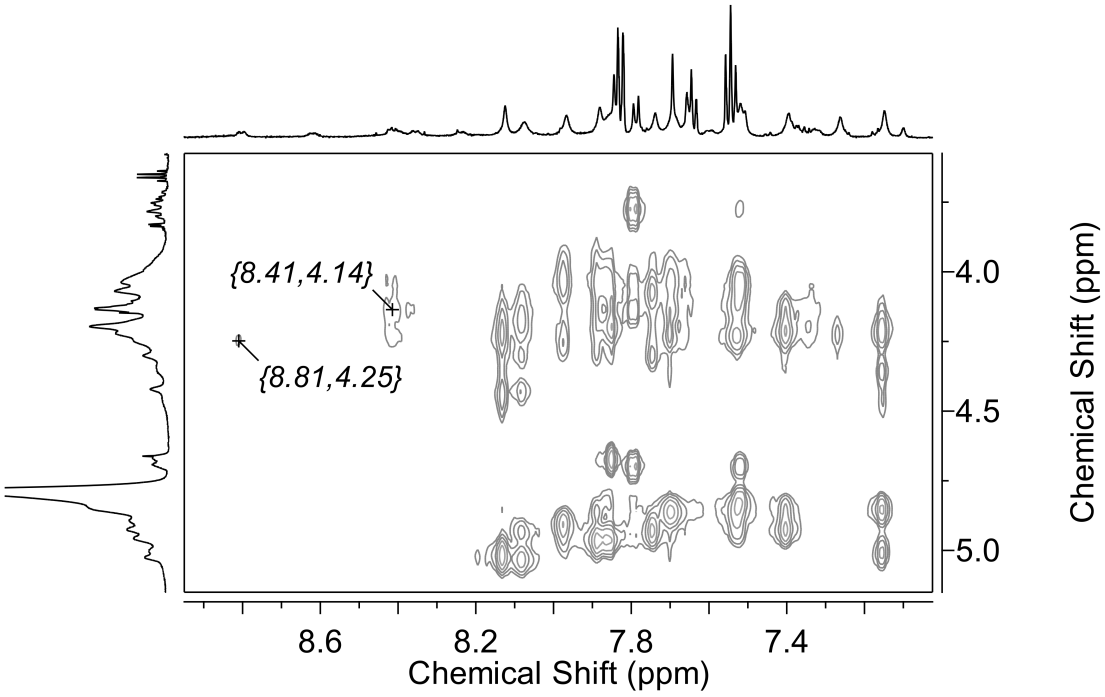

Figure 3.70: Expansion of a NOESY spectrum of the bulge oligonucleotide with F1 of the diruthenium helicate (**3**) at R* = 4, in pH 7.0 phosphate buffer at 25 °C, showing potential inter-molecular NOEs between the helicate and oligonucleotide H4′ resonances.

In the H2′/H2″ region NOEs were seen between 8.81 - 2.60 ppm, 8.41 - 2.59 ppm, and 8.36 - 2.59 ppm. Cross-peaks in this region had been encountered previously with both hands of the helicate and the AATT dodecanucleotide. Although for the bulge sequence these NOEs are shifted slightly, by comparison it seems likely that they may be from helicate aromatic hydrogens to non-adjacent hydrogens on the -CH_2CH_2- spacer. These peaks do not correlate to a specific H2′ or H2″ resonance, rather to a region of overlapping signals, and given that other evidence seems to suggest binding of the helicate in the minor groove, it is unlikely that NOEs between helicate and oligonucleotide hydrogens located in the major groove would be seen.

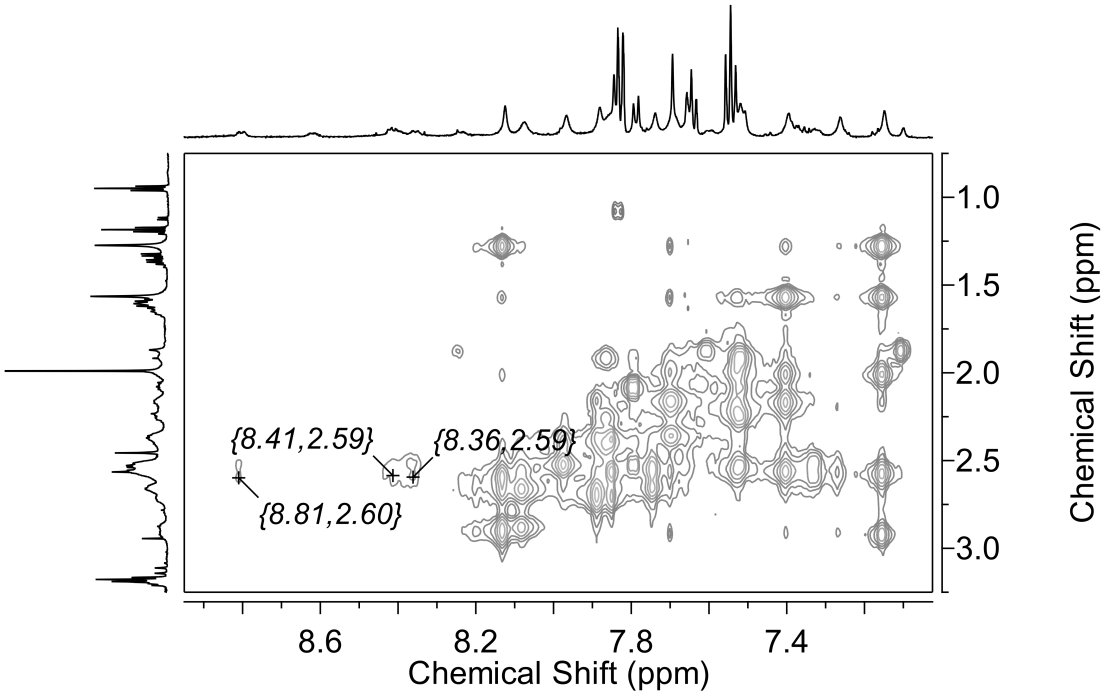

Figure 3.71: Expansion of a NOESY spectrum of the bulge oligonucleotide with F1 of the diruthenium helicate (**3**) at R* = 4, in pH 7.0 phosphate buffer at 25 °C, showing the potential helicate-helicate intra-molecular NOEs.

Based on the experiments for F1 of the helicate with the bulge oligonucleotide from R* = 1 up to R* = 4 it appears that interaction may occur in the A/T-rich region around the bulge. This is evident in the changes in chemical shift which are of the highest magnitude for the A_4, A_6, A_7, and T_8 H8 and H6 resonances. In addition, variation in the chemical shifts of all AH2 and changes in the shapes of H1′ signals suggests binding in the minor groove as the likely mode of interaction. This observation is complemented by possible inter-molecular NOEs between aromatic hydrogens on the helicate and oligonucleotide hydrogens in the H4′ region. While these resonances could be assigned more definitively as either intra- or inter-molecular by conducting NOESY and DQF-COSY experiments at a range of temperatures, it would not greatly add to the analysis which suggests an interaction of F1 of the helicate in the minor groove of the bulge oligonucleotide.

3.4.7.2 F2-Helicate (**3**) binding to bulge

To complete the study the interactions of the bulge oligonucleotide and F2 of the helicate were investigated. As seen for F1 of the helicate, with increasing additions of helicate the AH2 signals showed the clearest changes in chemical shift, as well as some small changes for H8 and H6 signals around the bulge region (see Figure 3.72). In the spectrum significant broadening can also be seen, notably for the A_6H2, A_4H8, and A_6H8 resonances.

Downfield of the oligonucleotide peaks, broad signals characteristic of the helicate were seen to emerge (highlighted in red). Due to the low intensity and broadness of these compound peaks the relative integration was not determined for this sample, preventing calculation of the true compound to DNA ratio (R). It can be assumed that a portion of compound and DNA were insoluble, evidenced by precipitation of the sample, but some compound remained in the orange-coloured solution. As such, the true ratio (R) would be lower than the added ratio of compound (R*).

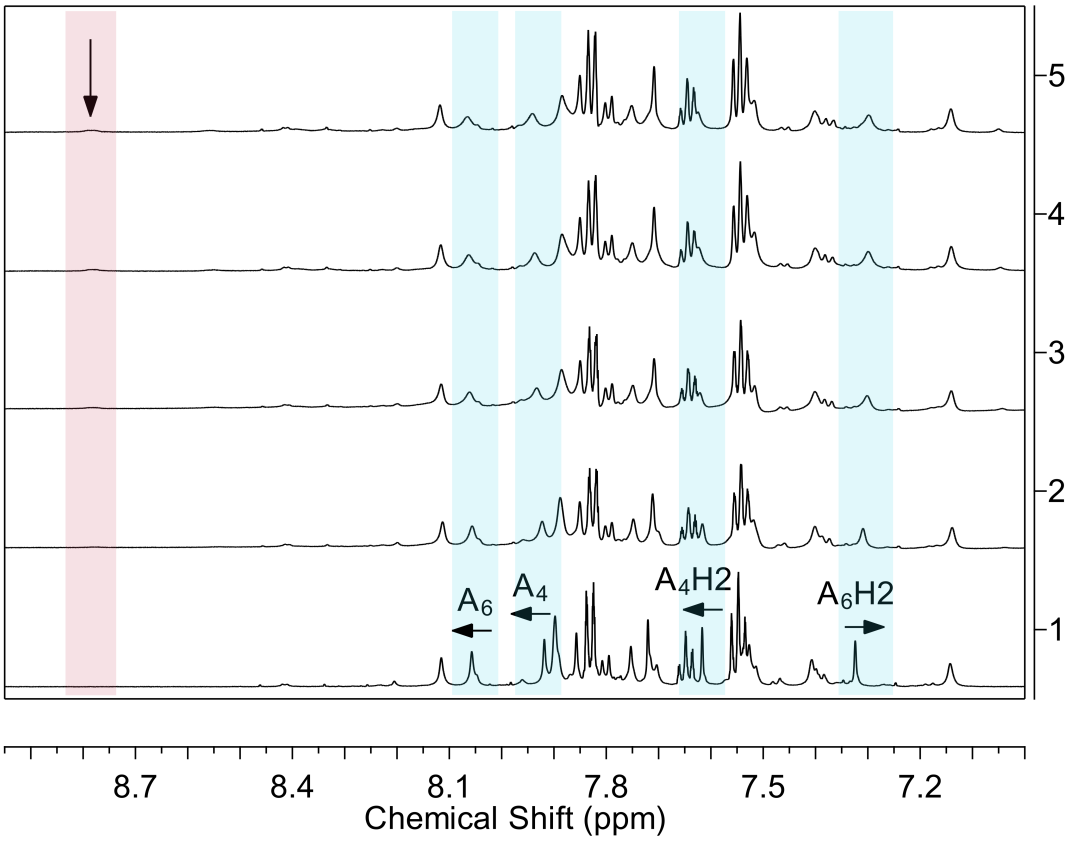

Figure 3.72: The H8/H6/H2 region of the ^{1}H NMR spectrum of the titration of the bulge oligonucleotide with F2 of the diruthenium helicate (**3**), in pH 7.0 phosphate buffer at 25 °C. (1) free oligonucleotide, (2) R* = 0.25 (3) R* = 0.5 (4) R* = 0.75 (5) R* = 1. Notable changes in the chemical shift and shape of the oligonucleotide resonances are highlighted in blue, Ru(II) compound peaks are highlighted in red.

The H1′/base H5 region upon addition of F2 of the helicate is shown in Figure 3.73 below. Minor changes in shape and chemical shift were noted for the overlapping H1′ and H5 resonances between 6.10 - 6.00 ppm (T_9H1′, C_{11}H5, C_1H1′, and C_1H5). A slight upfield shift was observed for the A_6H1′ resonance, while significant broadening was evident for C_{10}H5. Finally, a upfield shift (0.04 ppm) as well as broadening was recorded for the G_5H1′ resonance. Further upfield variation in the chemical shift of the H2′ and H2″ signals was most notable for resonances in the bulge region, ranging in magnitude

from 0.02 - 0.05 ppm. No change for the thymine methyl hydrogens was observed. A summary of changes in chemical shifts of the oligonucleotide signals are quantified in Table 3.15 below. Although many of the changes in chemical shift appear small they are still significant. The changes recorded in Table 3.15 are indicative for only the soluble portion of the helicate-DNA complex. Given that the true ratio of helicate to DNA (R) was not determined by integration the discrepancy with R* cannot be quantified. However, it can be assumed that R is lower that R*, and were the true ratio able to be increased to R = 1 the magnitude of change in chemical shift would increase further.

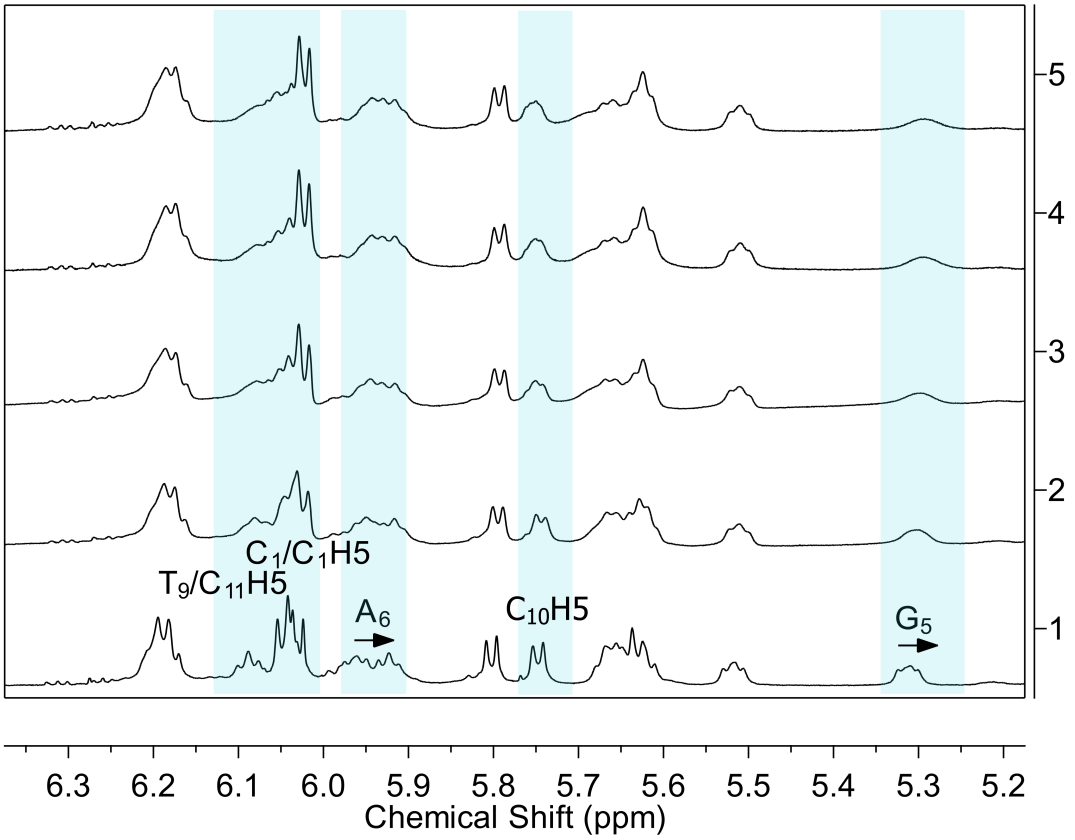

Figure 3.73: The H1′/base H5 region of the ^{1}H NMR spectrum of the titration of the bulge oligonucleotide with F2 of the diruthenium helicate (**3**), in pH 7.0 phosphate buffer at 25 °C. (1) free oligonucleotide, (2) R* = 0.25 (3) R* = 0.5 (4) R* = 0.75 (5) R* = 1. Notable changes in the chemical shift and shape of the oligonucleotide resonances are highlighted in blue.

Table 3.15: ^{1}H NMR assignment of the DNA resonances of the bulge oligonucleotide with F2 of the diruthenium helicate (**3**) at R* = 1, in D_2O and pH 7.0 phosphate buffer at 25 °C. Changes in chemical shift are given in brackets, with a negative sign indicating an upfield shift.

Base	H8/H6	AH2	H1′	H2′	H2″	Methyl
C_1	7.79 (-0.02)		6.03 (-0.01)	2.08 (-0.01)	2.53 (-0.01)	
C_2	7.52 (-0.01)		5.63 (0.00)	1.93 (-0.03)	2.25 (-0.02)	
G_3	7.88 (-0.01)		5.64 (0.00)	2.38 (-0.04)	2.71 (-0.01)	
A_4	7.94 (0.02)	7.63 (0.02)	5.69 (0.00)	2.51 (0.02)	2.51 (-0.02)	
G_5	7.75 (0.00)		5.29 (-0.04)	2.57 (0.03)	2.64 (0.05)	
A_6	8.07 (0.02)	7.30 (0.02)	5.95 (-0.01)	2.65 (-0.02)	2.86 (-0.03)	
A_7	8.12 (0.01)	7.71 (0.00)	6.20 (0.00)	2.58 (-0.02)	2.87 (-0.03)	
T_8	7.14 (0.01)		5.91 (0.00)	1.98 (-0.02)	2.54 (-0.02)	1.28 (0.00)
T_9	7.40 (0.00)		6.08 (0.00)	2.14 (-0.02)	2.54 (-0.02)	1.57 (0.00)
C_{10}	7.52 (0.00)		6.19 (0.00)	1.93 (-0.03)	2.18 (0.00)	
C_{11}	7.71 (0.00)		5.51 (0.00)	2.18 (-0.01)	2.36 (-0.01)	
G_{12}	7.89 (0.01)		5.66 (-0.02)	2.67 (0.00)	2.71 (0.00)	
G_{13}	7.85 (0.00)		6.17 (0.00)	2.55 (-0.02)	2.38 (-0.01)	

As for previous samples a NOESY spectrum for F1 of the helicate where R* = 1 was collected. In the aromatic region a weak NOE was observed, which looked to be helicate-helicate, appearing downfield of the oligonucleotide signals (between 8.78 - 8.34 ppm). Aside from this cross-peak no further NOEs were observed in the spectrum. The NOESY spectrum for the aromatic region is shown in Figure 3.74 below. Given the low intensity and broadness of the helicate peaks in the 1D spectrum, and the single low intensity intra-molecular NOE recorded, it was not surprising that further inter- or intra-molecular NOEs were not seen at this low helicate ratio.

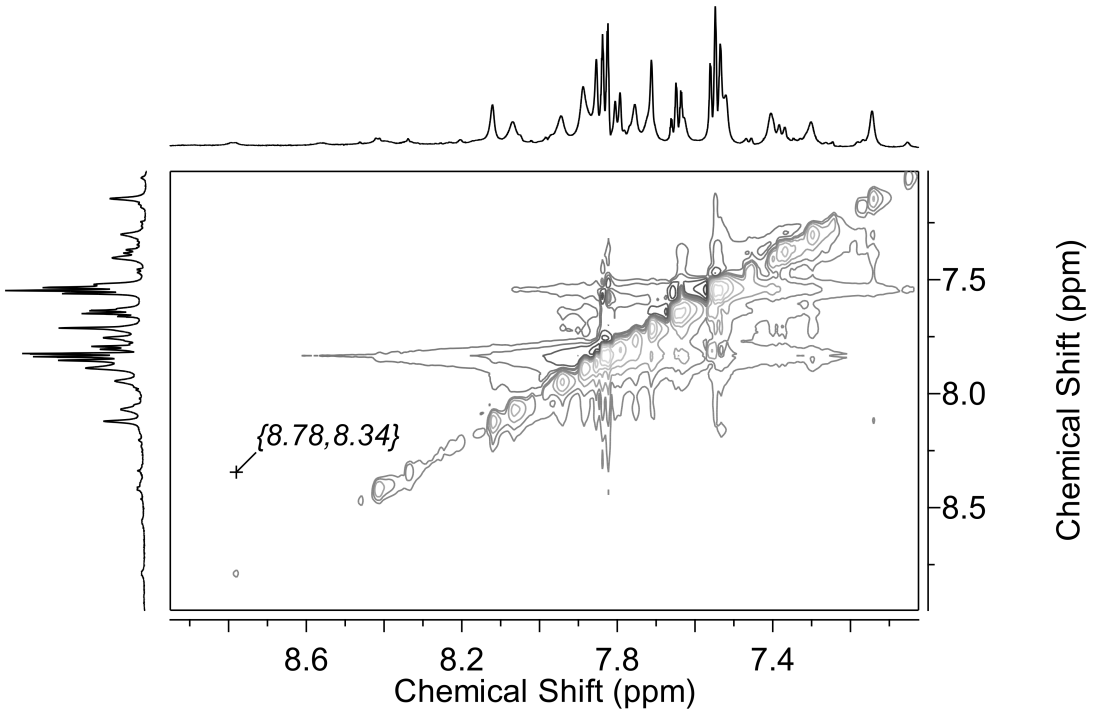

Figure 3.74: Expansion of a NOESY spectrum of the bulge oligonucleotide with F2 of the diruthenium helicate (**3**) at R* = 1, in pH 7.0 phosphate buffer at 25 °C, showing a helicate-helicate intra-molecular NOE (8.78 - 8.34 ppm).

A DQF-COSY experiment was conducted for this sample and cross-peaks were observed between downfield helicate peaks and resonances upfield, overlapping with the oligonucleotide peaks (8.40 - 7.39 ppm, 8.39 - 7.33 ppm, 8.33 - 7.34 ppm, 8.31 - 7.27 ppm). This finding indicated that there were also helicate peaks at lower intensities in this region, which were obscured by the hydrogen resonances of the DNA (see Figure 3.75).

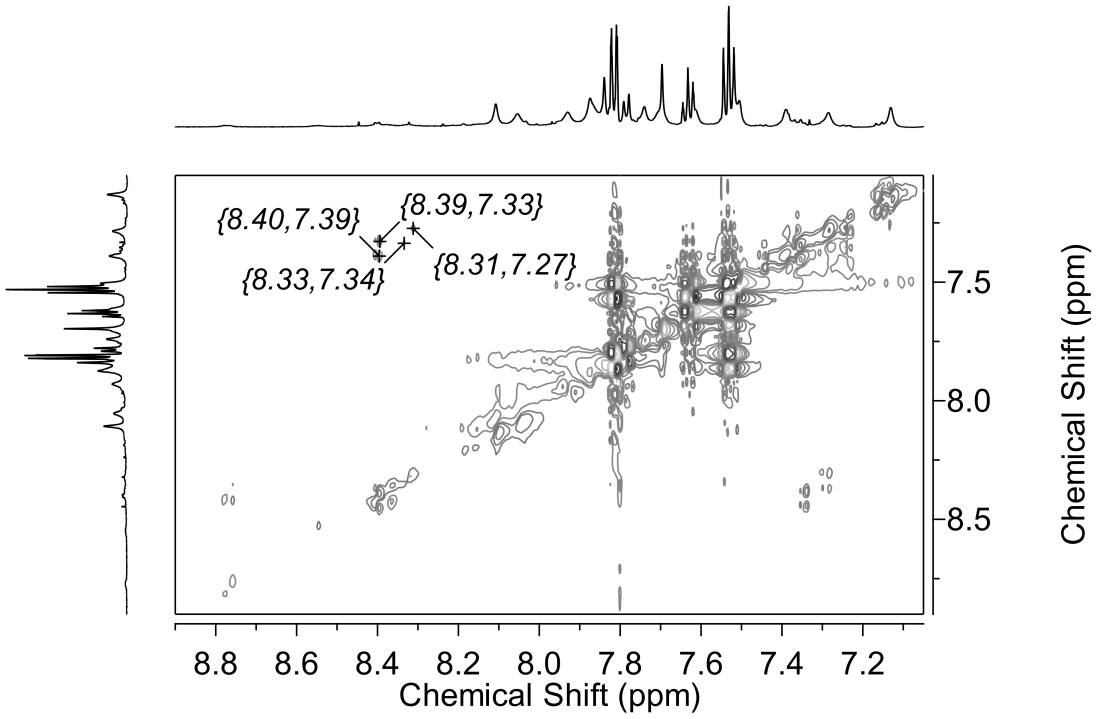

Figure 3.75: Expansion of a DQF-COSY spectrum of the bulge oligonucleotide with F2 of the diruthenium helicate (**3**) at R* = 1, in pH 7.0 phosphate buffer at 25 °C, showing the helicate-helicate cross-peaks in aromatic region.

Similarly to the interactions of F1 of the helicate with the bulge oligonucleotide, addition of F2 resulted in the greatest perturbation in chemical shift for the AH2 resonances, even at R* = 1. In the H1′/base H5 region selective broadening and variation in chemical shift was observed mainly for positions near the bulge region. This was also reflected in the H2′/H2″ signals where the greatest changes in chemical shift were observed for sugars in the bulge region. While no inter-molecular NOEs were recorded at R* = 1 the appearance of COSY cross-peaks in the aromatic region revealed the presence of broad helicate peaks overlapping with oligonucleotide resonances.

3.4.7.3 Summary of the NMR findings

For all oligonucleotides studied the strongest interactions occurred between both enantiomers of the helicate with the AH2 resonances, suggesting minor groove binding. Disappointingly, in all cases the binding was not strong enough, or in a suitable rate of exchange for clear inter-molecular NOEs to be observed. Alternatively, the absence of inter-molecular NOEs could be due to a lack of selectivity for one binding site, which leads to the compound not spending enough time (relative to mixing time) to build up an NOE with a particular hydrogen.

For the C/G rich dodecanucleotide addition of both F1 and F2 resulted in the greatest

variation in chemical shift of the AH2 and H1′ resonances, which are located in the minor groove. For both enantiomers weak NOEs were recorded between aromatic helicate signals and peaks in the H4′ region. While it could not be confirmed that these represented true inter-molecular interactions, this finding would suggest that the helicate is too bulky to fit deep within the minor groove of a standard duplex and sits closer to the top of the groove. In addition, larger perturbation in the chemical shifts of terminal resonances suggested that this bulkiness may induce binding at the end of the oligonucleotide where the duplex is less well-formed. This proposal was supported by the outcome of experiments with the AATT dodecanucleotide, where F1 and F2 of the helicate induced changes in chemical shift mainly for AH2 and H1′ resonances, particularly for the A_1H1′ and T_{12}H6. Overall, it appeared that for standard dodecanucleotides minor groove binding was favoured, despite not being of an appropriate size to fit well within the groove.

To overcome this issue, greater flexibility was introduced by probing interactions of the helicate with the bulge oligonucleotide. For both hands interactions with the AH2 resonances were evident and selective broadening of signals in the bulge region was seen, particularly at higher helicate ratios. With this oligonucleotide it appeared that there was greater interaction than in the standard dodecanucleotides. This suggested that the additional flexibility in the bulge region allowed the helicate to fit within and thus interact more strongly with the DNA sequence. With F1 of the helicate and the bulge oligonucleotide potential inter-molecular NOEs were again seen between aromatic helicate peaks and resonances in the H4′ region, at $R^* = 4$. These interactions, as well as variation in the AH2 and H1′ signals, again suggested minor groove binding, which was anticipated for the 4^+ compounds.

Across all oligonucleotides studied there did not appear to be a preference for either enantiomer, with F1 and F2 of the helicate showing very similar interactions with each sequence. This could either indicate that there was not strong enantioselectivity for these compounds with the particular oligonucleotides selected. Alternatively, given that F2 was not fully resolved (as noted in **Chapter 2**) the F1 impurity within this sample may have been sufficient to mask any enantioselective interactions with the DNA. It should be noted that for the helicate with the CCGG and AATT dodecanucleotides by relative integration the portion of soluble helicate-DNA complex appeared to be greater for samples containing F2. This could be due to a difference in solubility of the respective helicate-DNA complexes but without an enantiomerically pure sample of F2 available this observation was not further investigated.

Overall, the mesocate and the two enantiomers of the helicate were observed to

precipitate in the presence of DNA at sufficiently high concentrations resulting in significant broadening and lowering the intensity of the NMR signals of the diruthenium compounds. This broadening also presented challenges in the confident assignment of NOESY cross-peaks and determination of possible inter-molecular NOEs. Despite attempts to increase solubility or vary the rate of exchange by adjusting the experimental temperature little improvement could be made. In the case of the mesocate the precipitation was so extreme that studies, beyond those with the C/G rich dodecanucleotide, were not continued. In all cases it was found that the true helicate to DNA ratio (R) was lower than the added ratio (R*). As a result, the changes in chemical shift of oligonucleotide resonances, while small, were still significant, as a lower proportion of helicate and DNA were actually present in solution.

3.5 Conclusions and future directions

In this Chapter the interactions of the double-stranded diruthenium(II) mesocate (**4**) and partially-resolved hands of the helicate (**3**), synthesised in **Chapter 2** of this thesis, with DNA have been investigated.

Preliminary studies to probe whether an enantiomeric preference existed for the interactions of the helicate with ct-DNA were conducted using dialysis techniques. When the DNA was immersed in a solution of the racemic helicate and left to dialyse for 48 h, no enantiomeric excess was detected by CD spectroscopy. In this case, while the helicate did penetrate the dialysis membrane, there did not appear to be a preference in binding, with both the inner and outer solutions containing a racemic mixture.

The binding of these dinuclear compounds with ct-DNA was further studied by LD spectroscopy. For the mesocate (**4**), a decrease in the magnitude of the DNA LD signal at 260 nm from the native state indicated a loss of DNA orientation. This indicated that groove binding was the likely mode of interaction, as a decrease in this manner indicates less orientation of the DNA with the Coulette flow resulting from coiling or condensing of the DNA. Experiments were also conducted using two partially-resolved samples of the helicate (**3**). While precipitation was observed for one sample at a ratio of 60:1 DNA/helicate, the second sample showed a decrease in DNA LD signal at 260 nm, although not to the same extent as the mesocate. Between the two samples it appeared that the two compounds may bind with different strengths to the DNA, although binding constants could not be obtained.

Finally, NMR studies were conducted for the mesocate (**4**) and both hands of the helicate (**3**) with three different oligonucleotides. It should be noted that in the case of the helicate, F1 was fully resolved but F2 remained enantiomerically impure. Firstly, the mesocate was studied with a C/G-rich dodecanucleotide which had been shown to have different binding affinities for *meso* and chiral Ru(II) compounds by Foley *et al.*[166] Despite poor solubility of the mesocate/dodecanucleotide mixtures preventing the acquisition of clear helicate signals and inter-molecular NOEs, changes in the chemical shifts of the AH2 oligonucleotide hydrogens upon addition of the mesocate suggested that binding may occur in the minor groove. It was found that the mesocate readily precipitated in a range of buffers when either an oligonucleotide or ct-DNA was added at sufficiently high concentrations. While a coloured portion remained in solution, it seemed that both mesocate and DNA may be present in the precipitate, preventing further characterisation

of this interaction by solution-based NMR studies.

The two hands of the helicate were then studied with the same CCGG dodecanucleotide. For both F1 and F2 of the helicate the positions of the AH2 and H1′ resonances of the dodecanucleotide were found to change the most upon addition of the compound. These resonances are located in the minor groove of DNA, further suggesting that the compounds were likely to interact at this site. In addition, weak NOEs were obtained between helicate signals in the aromatic region and H4′ dodecanucleotide signals, indicating that the helicate may be to bulky to fit deeply in the minor groove, instead sitting nearer the top. This was in agreement with higher magnitude changes in chemical shift that were observed for the H1′ resonances at the terminal ends of the dodecanucleotide. Binding in this region may cause greater chemical shift perturbation as the duplex is more flexible and less well formed. Similar trends were observed for a contrasting dodecanucleotide, containing an A/T-rich sequence, for both fractions of the helicate. The largest variations in chemical shift were again seen for the AH2 and H1′ resonances, in particular for those at the ends of the DNA sequence.

Given that the helicate appeared to favour minor groove binding, despite not fitting well within the minor groove, a more flexible bulge sequence was selected for study. For F1 and F2 of the helicate changes in oligonucleotide chemical shift were seen again for the AH2 signals and for hydrogens on bases located in the bulge. Selective broadening of peaks was also observed in the aromatic and H1′/base H5 region. Potential inter-molecular NOEs were observed between aromatic helicate peaks and oligonucleotide peaks in the H4′ region. It is possible that the nature of these NOEs and identity of oligonucleotide resonances could be further elucidated by conducting NOESY and DQF-COSY experiments at a range of temperatures; however, specific assignment of the signals may not substantially impact the overall analysis. In general, the findings suggested that minor groove binding for both hands of the helicate is likely and the added flexibility of the bulge may allow stronger inter-molecular interactions.

Based on the the key findings from the NMR studies, in conjunction with results from LD spectroscopy, it appeared that minor groove binding is the most likely mode of interaction for these diruthenium(II) compounds with DNA. Comparing the NMR and dialysis experiments there does not appear to be a clear enantiomeric preference for either the *P*- or *M*-forms of the helicate with DNA, although the lack of enantiopurity of the samples in the NMR studies may have masked any preferential interactions. In the future, if fully resolved forms of the helicate can be obtained, the possibility of enantiospecific binding could be tested more thoroughly.

The largest stumbling block when studying the interactions of these compounds in any biological system appears to stem from the low solubility of the DNA-compound complexes formed. At sufficiently high ratios of DNA and compound, both the mesocate and helicate have been shown to precipitate, and this has also observed in preliminary studies with proteins by mass spectrometry. Evidently an interaction must occur between compound and biomacromolecule; however, it is not possible to characterise this further in the solution state. Furthermore, the size of the dinuclear compounds may prohibit them from binding strongly to DNA in the preferred minor groove, limiting suitability in a therapeutic context. While stronger binding was seen for the more flexible bulge oligonucleotide compared to the dodecanucleotides, the perturbation in chemical shift and strength of NOEs was small compared to other bulge probes. In order to study any DNA interactions further the basic issues of precipitation and low intensity NMR signals of the compound must be overcome. Despite observing only broad, low intensity resonances corresponding to mesocate or helicate, the true ratio of compound and DNA was able to be estimated from relative integration. It was noted that the true ratio of helicate to DNA was slightly higher for samples containing F2, compared to F1, which may hint at a difference in solubility for the helicate-DNA complexes with each enantiomer. In all cases the true ratio (R) was significantly lower than the added ratio (R*), which was reflected in the small changes recorded in chemical shift of oligonucleotide resonances. While the magnitude of these changes was small (generally smaller than 0.1 ppm), the shifts are still significant, as the accuracy of measurements is no worse than 0.01 ppm based upon the number of resonances that show 0.00 ppm shifts. It is anticipated that at the true R = 1 value the magnitude of these changes would be greatly increased and more comparable to other studies, potentially resulting in stronger NOEs.

As mentioned previously, it has been shown by Glasson *et al.*,[66] and others,[171,172] that triple-stranded helicates can exhibit enantioselective binding with DNA which initially sparked the initial interest in studying the biological interactions of the double-stranded compounds described in **Chapter 2** of this thesis. The interactions of small molecules and metal-containing compounds with oligonucleotides have been widely studied by NMR methods and it was expected that these same approaches would be applicable. The fact that none of the double-stranded compounds appeared to interact particularly strongly with DNA and the enantiomers of the helicate show did not show differences in binding is quite unexpected, given the near total enantioselectivity seen for the helicate studied by Glasson *et al.*,[66] and the numerous reports of DNA binding of polypyridylruthenium(II) compounds. While the results detailed above indicate that weak binding may occur for

the double-stranded compounds in the minor groove of DNA these interactions proved to be challenging to characterise by standard solution phase methods.

CHAPTER 4

Synthesis of Triple-Stranded Diruthenium(II) Compounds

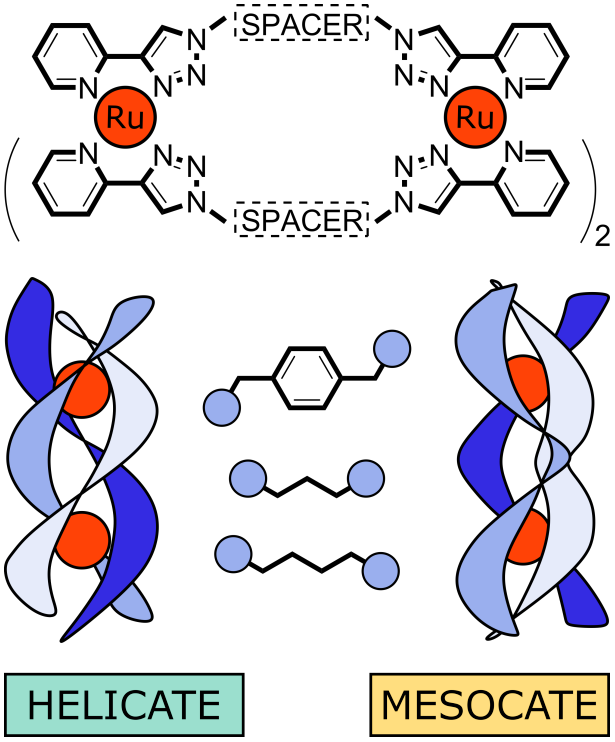

4.1 Introduction

4.1.1 Inspiration from existing triple-stranded compounds

While double-stranded species such as those discussed in **Chapter 2** of this thesis can be formed by combining di(tridentate) ligands with octahedral metal ions, replacement of the ligands with di(bidentate) analogues can yield triple-stranded compounds. The first triple-stranded helicate was proposed in 1958 by Stratton and Busch, who described a di-iron(II) helix containing three pyridinaldazine ligands.[46] Structural characterisation of triple-stranded helicates by X-ray crystallography were reported by Elliott and co-workers for triply-bridged dinuclear species based on the tris(2,2′-bipyridine)iron(II) motif,[251] and these studies were later extended to include related bipyridine-containing ligands.[252,253] As for double-stranded compounds, ligand design has been expanded beyond simple oligopyridine functionality. An early example of diversity in ligand structure was demonstrated by Williams *et al.*,[254] where three equivalents of the ligand bis(1-methyl-2-(6-methylpyridin-2-yl)-1*H*-benzo[*d*]imidazol-5-yl)methane, shown in Figure 4.1, were reacted with two equivalents of cobalt(II) perchlorate to form a dinuclear helicate.

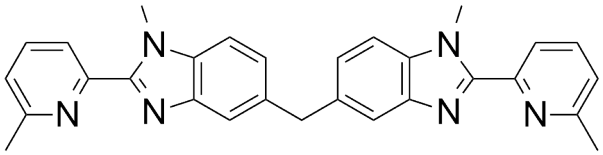

Figure 4.1: The di(benzoimidazole)pyridine ligand used by Williams *et al.*,[254] for the synthesis of a triple-stranded cobalt(II) helicate.

While many metal-containing compounds of this nature utilise nitrogen donor ligands, ligands containing oxygen donors have also been explored in helicate synthesis, including catechol and 1,3-dicarbonyl-based derivatives. One example of this was reported by Christou and co-workers,[255] in which a 3,3′-(1,3-phenylene)bis(1-phenylpropane-1,3-dione) ligand (Figure 4.2) was utilised to form a library of triple-stranded helicates containing a variety of M(III) centres.

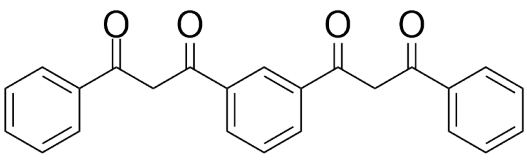

Figure 4.2: The di(β-diketone) ligand used by Christou and co-workers,[255] to synthesise Ti(III), V(III), Mn(III), and Fe(III) triple-stranded helicates.

Only a single naturally-occurring triple-stranded helicate is known, a dinuclear iron compound of the siderophone rhodotorulic acid (*N,N′*-{(3,6-dioxopiperazine-2,5-diyl)bis(butane-4,4-diyl)}bis{*N*-hydroxyacetamide}), discovered by Carrano and Raymond,[256] the ligand structure of which is shown in Figure 4.3. In this case the ligand contains oxygen donors, and the di-iron compound is produced by microorganisms to control iron uptake. Interestingly, this compound only forms as the right-handed *P*-helicate in nature.

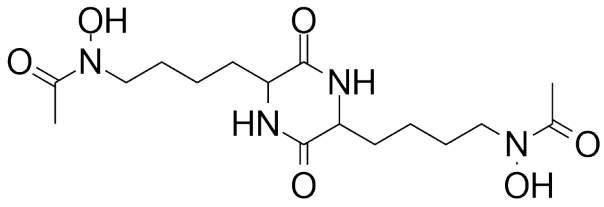

Figure 4.3: The structure of rhodotorulic acid, the ligand in the only naturally-occurring triple-stranded helicate.

The synthesis of triple-stranded helicates has been explored in the pioneering work of Hannon and co-workers, who initially studied Ni(II) compounds before extending to incorporate a wide range of transition metal centres.[67,71,73,257,258] These compounds all contain ligands which feature an imine binding domain, and thus avoid the multi-step syntheses often required in the preparation of oligopyridine ligands. A simplified version of the original ligand structure used by Hannon and co-workers is shown in Figure 4.4 below, although it should be noted that the nature of both the terminal pyridine and spacer units have since been widely modified.[71,207,259–266] These authors have studied the biological activity of a triple-stranded Fe(II) helicate with the same ligand structure and found binding to occur in the major groove of DNA.[206] Differences in the strength of interactions of the two helicate enantiomers with DNA have also been investigated, as has the binding of this compound with heteronuclear junctions.[171,212,213,235] Pertinently for this thesis, the synthesis of a Ru(II) helicate has also been developed and the ligand modified at the spacer and terminal positions to extend this series of compounds.[73,172] Interactions of the diruthenium(II) triple-stranded compounds with DNA have also been studied by linear dichroism (LD) and circular dichroism (CD) spectroscopy, showing coiling of calf thymus DNA (ct-DNA) consistent with findings for the Fe(II) analogue.[73]

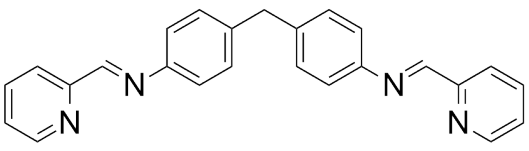

Figure 4.4: The basic structure of the di(pyridylimine) ligand designed by Hannon and co-workers,[71] and used to synthesise a range of triple-stranded helicates, including diruthenium(II) compounds.[73,172]

An alternative stepwise approach to the design of triple-stranded ruthenium-containing helicates has been demonstrated by Fletcher *et al.*[75] In that work a tethered tri(bipyridyl) ligand was used to enhance the formation of the *facial* geometrical isomer of a mono-ruthenium(II) compound. Following this, additional chelating groups were attached to facilitate formation of a heterometallic helicate (in this case Ru(II)/Fe(II), shown in Figure 4.5).

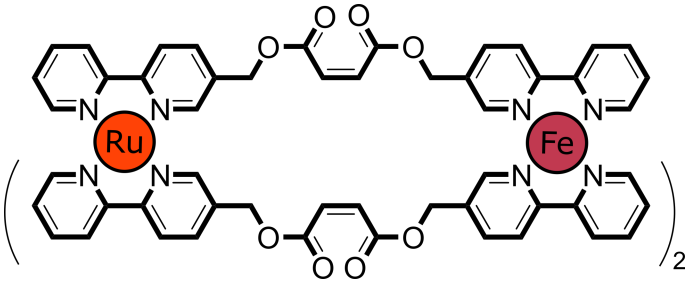

Figure 4.5: The final compound structure of the heterometallic helicate synthesised by Fletcher *et al.*,[75] using a stepwise approach.

A heterometallic compound has also been designed by Torelli *et al.*,[74] who formed a Ru(II)-*f*-block helicate the structure of which is shown in Figure 4.6. In this case mixtures of *mer* and *fac* monoruthenium(II) compounds were prepared and the geometrical isomers separated by chromatography; however, it was found that in sufficiently polar solvents isomerisation could occur. Taking advantage of this interesting behaviour, the authors found that by reacting three equivalents of ligand with one equivalent each of Ru and Lu precursors, a $[RuLu(L)_3]^{5+}$ helicate could be formed. Control of the *mer*/*fac* equilibrium was a key consideration, as only *fac*-$[RuL_3]^{2+}$ was able to coordinate the Lu(III) to form a triple-stranded helicate.

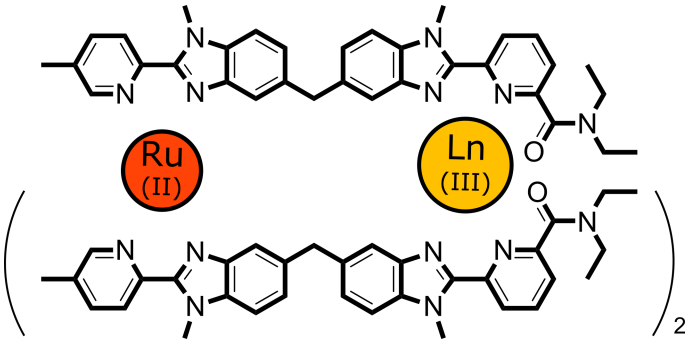

Figure 4.6: The final compound structure of the heterometallic Ru(II)-*f*-block helicate synthesised by Torelli *et al.*[74]

A final example of a heterometallic triple-stranded compound containing Ru(II) was described by Elliot and co-workers using the bipyridine-based ligands.[76] Reaction of $[Ru(DMSO)_4Cl_2]$ (DMSO = dimethyl sulfoxide) with an excess of ligand (the range of

ligands is shown in Figure 4.7 below) over three reaction cycles, followed by addition of ferrous ammonium sulfate, yielded the heterometallic Ru(II)/Fe(II) triple-stranded compound in 1% yield (by Ru). In this case the structure was not able to be determined crystallographically, although from the modelled structures included in this and later studies, it appears that the authors assigned this species as a helicate, matching the structure obtained for the di-iron(II) analogue.[267]

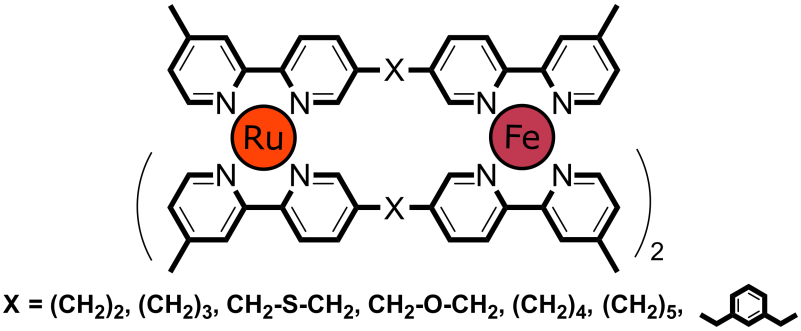

Figure 4.7: General structures of the heterometallic Ru(II)-Fe(II) compounds studied by Elliott *et al.*[76]

4.1.2 Triple-stranded Ru(II) helicates

There are far fewer examples of triple-stranded structures containing exclusively Ru(II) centres than have been reported for other transition metals. Hannon and co-workers have successfully employed imine-based ligands (see Figure 4.4) to generate diruthenium compounds, including single-, double-, and triple-stranded forms.[73,137,172] Interest in synthesising a triple-stranded Ru(II) species stemmed from the promising DNA-binding behaviour observed for compounds containing other transition metal centres. In particular, the Fe(II) helicates had been found to bind strongly and non-covalently to the major groove of DNA, inducing significant coiling,[171,206,207] and similar DNA-binding features were observed for the Ru(II) analogue.[73,78] The anti-cancer activity of the triple-stranded ruthenium helicate was also assessed and showed promising cytotoxicity against human breast cancer cells, with IC_{50} values only 2 - 5 times lower than *cis*-diamminedichloroplatinum (cisplatin). Furthermore, this compound showed anti-viral activity against the Trans Activation Response (TAR) bulge motif within the human immunodeficiency virus-1 (HIV-1), inhibiting viral transcription.[79]

Despite having such interesting behaviour in biological settings, initial reports indicated that the triple-stranded species could only be synthesised with 1% yield.[73] The yield was subsequently improved to 12 - 18% under microwave conditions,[172] although this was still significantly lower than yields reported for other dimetallic helicates utilising this ligand,

a deficit which can be ascribed to the comparatively poor lability of the Ru(II) cation.

As seen for the imine-based helicate described above the use of microwave irradiation can significantly improve yields of these types of compounds. While microwave irradiation has been widely used for the synthesis of other types of Ru(II) compounds,[268–270] it was first employed for Ru(II) helicate synthesis in 2008 by Glasson *et al.*[66] Utilising a quaterpyridine ligand (described in **Chapter 2**, with the structure shown in Figure 4.8) a triple-stranded helicate was formed with 36% yield. Initially, the authors attempted the synthesis using $RuCl_3 \cdot 3\,H_2O$ and the ligand in a 2 : 3 ratio under reflux conditions in EtOH for two weeks; however, by this method a complex mixture of products was found, including polymeric material. Instead it was found that by employing microwave irradiation in ethylene glycol at 225 °C for four and a half hours the helicate could be readily obtained. Separation of the *P*- and *M*-enantiomers was possible by chromatographic methods using an SP-Sephadex C-25 ion exchanger with 0.1 M sodium (-)-*O,O′*-dibenzoyl-L-tartrate as an eluent. DNA binding studies by dialysis (as described in **Chapter 3**), and DNA-affinity chromatography (as described by Smith *et al.*[154]) showed selective binding of the *P*-helicate in all cases.

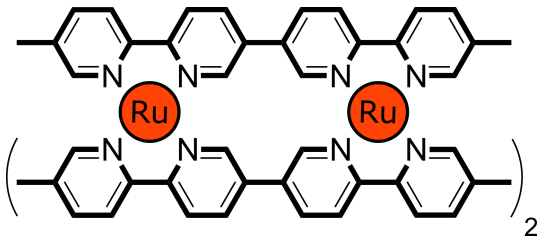

Figure 4.8: Structure of the diruthenium(II) helicate studied by Glasson *et al.*[66]

4.1.3 Exploration of 2-pyridyl-1,2,3-triazole ligands

The reaction of organic azides with terminal alkynes in a copper(I)-catalysed 1,3-cycloaddition has been widely adapted in the synthesis of ligands containing 1,4-disubstituted 1,2,3-triazole units, the general structure of which is shown in Figure 4.9.[271–276] These ligands have subsequently been used for the generation of a range of metallosupramolecular assemblies,[277–279] including macrocycles,[280–283] cages,[284,285] helicates,,[286,287] and others,[288,289] most notably by Crowley and co-workers. Initially, Vellas *et al.* showed that $[Fe_2L_3]^{4+}$ triple-stranded helicates could be formed from the assembly of Fe(II) and a extensive family of bis-2-(1-*R*-1*H*-1,2,3-triazol-4-yl) ligands.[290] This family of ligands was further explored by Wu *et al.*, by varying the shape and size of the spacer moiety, producing dinuclear compunds containing Zn(II), Ni(II), and Fe(II).[291] The authors found that while all linkers assembled to form discrete triple-stranded compounds

with octahedral metal ions, other factors affected the final dinuclear architecture – namely whether a helicate, mesocate, or mixture of both, resulted. Specifically, the orientation of the lone pairs on the noncoordinated nitrogen of the triazole unit, which point towards the interior of the assembled structure, destabilise the compounds when short ethylene spacers are present. This has been proposed to drive the formation of larger assemblies, beyond the dinuclear species expected. The length and flexibility of the spacer is also crucial in determining the product distribution, following an odd/even mesocate/helicate rule previously observed for bipyridine and catechol ligands.[292] However, in the compounds studied by Wu *et al.* once the chain length reached pentylene a mixture of isomers began to be observed.

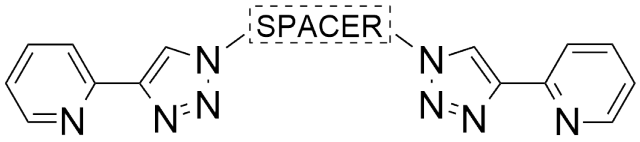

Figure 4.9: The general structure of the 1,4-disubstituted 1,2,3-triazole ligand, widely used by Crowley and co-workers,[286] and others,[291,293] in the synthesis of a wide range of metallo-supramolecular structures.

Fe(II) compounds containing ligands of this design have previously been explored in biological settings; however, the applications of these are limited by their poor stability in biological media.[290] In an attempt to improve stability Ru(II) analogues,[288] including a Ru(II) triple-stranded helicate,[80] were synthesised, again utilising microwave conditions. The triple-stranded helicate incorporated a ligand containing a 1,4-xylyl spacer and was able to be isolated in 58% yield,[80] a significant improvement on previously reported syntheses for other diruthenium helicates. Additionally, the authors were able to isolate the helicate directly from the crude reaction mixture, without requiring extensive chromatographic purification – another advantage to this method.

4.2 Synthesis of Ligands

The family of ligands described above were a promising target for the synthesis of triple-stranded compounds due to the relative ease of synthesis – via a Cu(I)-catalysed 1,3-cycloaddition of an organic azide to a terminal alkyne. These ligands contain a 1,4-functionalised 1,2,3-triazole, where the 4-position is occupied by a pyridine ring, and a spacer links the two pyridine-triazole moieties in the 1-position. As a result, two bidentate coordination sites per ligand can be generated, with N-donors located on the pyridine ring and 3-position of the triazole. As demonstrated in the extensive work of Crowley

and co-workers,[80,287,290] and others,[291,293] when combined with octahedral metal centres triple-stranded compounds of the type M_2L_3 can be formed (see Figure 4.10). The ability to readily modify the central spacer component while retaining an identical coordination environment presented an interesting avenue for the synthesis of a series of novel Ru(II) dinuclear compounds, and the opportunity to explore the factors governing product distribution of helicate and mesocate isomers. Additionally, the ease of product isolation and purification made these ligands and their corresponding compounds a desirable system for study. Finally, despite reporting excellent synthetic procedures and characterisation, Kumar *et al.* did not describe attempts to resolve the enantiomers of the diruthenium(II) helicate containing the 1,4-xylyl spacer ligand.[80] As described in **Chapter 2** of this thesis the resolution of ruthenium species can be achieved chromatographically, either by way of a chiral eluent on an SP-Sephadex C-25 cation exchanger,[65,66] or on cellulose using an achiral eluent. Using this knowledge, resolution of the existing 1,4-xylyl spacer ruthenium helicate seemed a logical next step, with the intent to probe the biological interactions of these triple-stranded compounds with DNA.

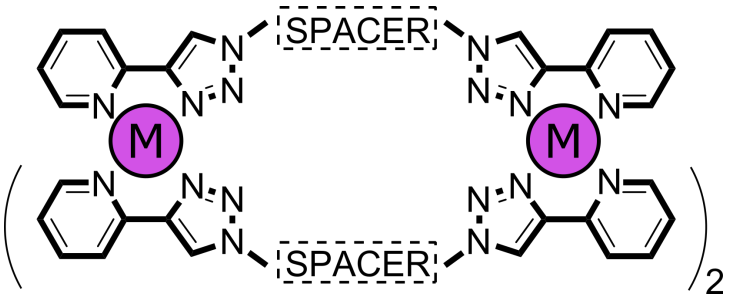

Figure 4.10: General structure of ligands incorporating a 1,4-functionalised 1,2,3-triazole, resulting in a di(bidentate) coordination environment able to form dimetallic triple-stranded compounds of the type M_2L_3 when combined with octahedral metal centres.

In this Chapter three ligands were selected for study and subjected to analogous synthetic conditions to those described by Kumar *et al.* for formation of Ru(II) compounds.[80] The first ligand chosen contained a 1,4-xylyl spacer, and was identical to the ligand used in the synthesis described by Kumar *et al.*. This spacer was then modified in length and flexibility to probe the effect of structural variation on the isomeric product distribution, consisting of either an *n*-propyl or *n*-butyl chain. The structures of these ligands can be seen in Figure 4.11 below.

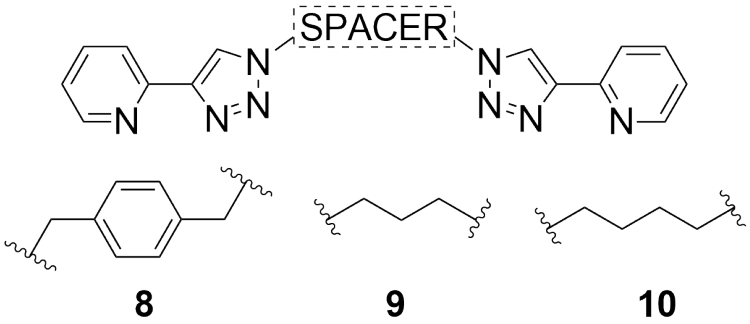

Figure 4.11: Ligands used for the synthesis of Ru(II) compounds described in this Chapter, showing the general ligand structure and specific spacer functionality.

The *precursors* – 2-{(trimethylsilyl)ethynyl}pyridine (**5**), 2-ethynylpyridine (**6**), and 1,4-bis(bromomethyl)benzene (**7**) – were synthesised following novel or modified literature procedures.[294] The *ligands* – containing a 1,4-xylyl (**8**), *n*-propyl (**9**), and *n*-butyl spacer (**10**) – were synthesised following methods outlined by Crowley and Bandeen,[286] and Wu *et al.*[291] The structures of these are illustrated in Figure 4.11.

4.3 Synthesis and Resolution of Ru(II) Compounds

4.3.1 Using a 1,4-xylyl spacer ligand (**8**)

Initially, the synthesis of the existing triple-stranded Ru(II) helicate was undertaken, following the procedures outlined by Kumar *et al.* utilising the ligand (**8**) containing the 1,4-xylyl spacer.[288] Synthesis of the $[Ru_2\mathbf{8}_2]^{4+}$ helicate (**11**) was successful and the product characterised by nuclear magnetic resonance (NMR) spectroscopy and single crystal X-ray diffraction (SCXRD). As noted by the original authors, the hydrogens on the 1,4-xylyl spacer were observed as an AB quartet by ^{1}H NMR. An ^{1}H NMR spectrum of the crude product isolated from the microwave reaction can be seen in Figure 4.12.

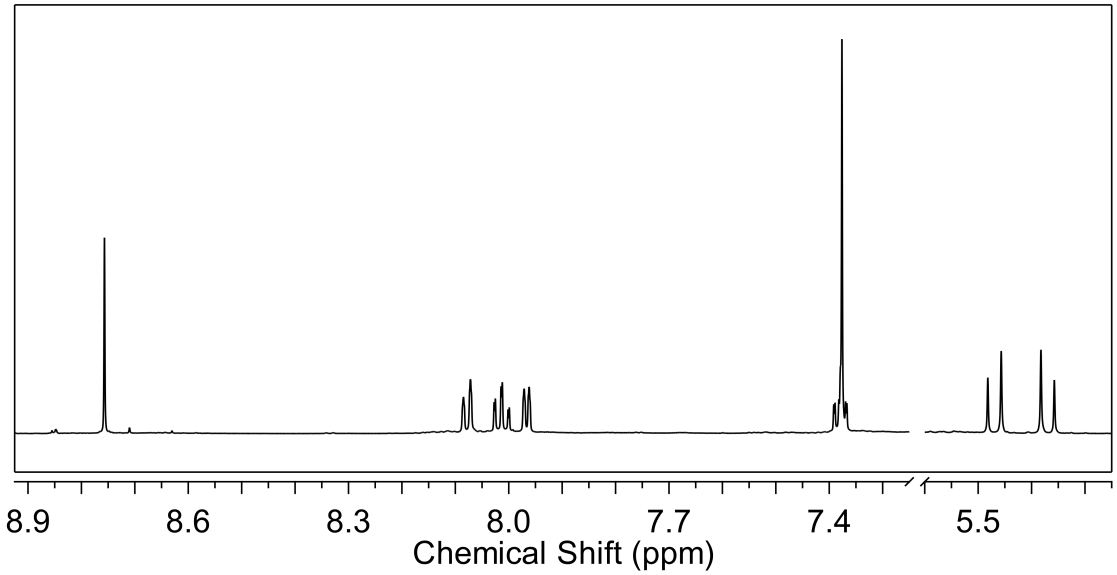

Figure 4.12: Partial ^{1}H NMR spectrum (500 MHz, CD_3CN, 298 K) showing the crude reaction mixture from the microwave reaction to form the triple-stranded diruthenium helicate (**11**), using the 1,4-xylyl spacer ligand (**8**).

The identity of the helicate, and NMR assignment was further confirmed by 1D and 2D NMR spectroscopy experiments, which are presented in Section D.2.1 of Appendix D.

4.3.1.1 Stability studies

In previous studies by Vellas *et al.*,[290] it was demonstrated that Fe(II) compounds constructed from these ligand types had poor stability as the BF_4^- salts in the presence of DMSO and the amino acid histidine.[290] This issue was alleviated by incorporation of the Ru(II) centre, reported by Kumar *et al.*, who showed after heating for three days at 50 °C as the PF_6^- salt in *d*$_6$-DMSO there was no change in the structure of the compounds (monitored by ^{1}H NMR spectroscopy and mass spectrometry).[80]

In the present study the stability of the triple-stranded Ru(II) helicate, and potential suitability in a biological setting, was probed. The compound as both the PF_6^- salt, and the Cl^- salt in CD_3CN and D_2O respectively were heated at 50 °C over 7 days and ^{1}H NMR spectra were recorded over this time period. No changes in the chemical shift or relative integration for any resonances in either sample were seen indicating high levels of stability. Interestingly, while the spectrum of the compound as the PF_6^- salt showed sharp, well-resolved signals, when analysed as the Cl^- salt all aromatic hydrogen resonances were extremely broad (with spacer hydrogen signals obscured by the solvent peak). The cause of this broadening was not further investigated, but may be due to changes in the conformation of the helicate caused by solvent or anion binding effects. The presence of helicate conformers could be probed by variable temperature NMR experiments to see

whether the resolution of the peaks by ^{1}H NMR spectroscopy can be improved; however, these studies were not undertaken in this thesis. It should be noted that all biological studies for the 1,4-xylyl spacer helicate (detailed in Section 4.5.1 of this Chapter) were carried out using the Cl^- salts of the compound, so any conformational changes that do occur may have a significant impact on DNA binding. The NMR spectra for the PF_6^- and Cl^- salts of the helicate after heating are shown in Figures D.9, and D.10, respectively, in Section D.2.1 of Appendix D.

4.3.1.2 X-ray crystallography

The structure of the triple-stranded ruthenium(II) helicate (**11**) is shown below in Figure 4.13.

Crystals suitable for X-ray diffraction were grown by vapour diffusion of diethyl ether into a dimethylformamide (DMF) solution of the compound, and the resulting structure confirmed the formation of a helicate of the type $[Ru_2\mathbf{8}_3]^{4+}$, as shown in Figure 4.13. The structure crystallises in the space group $I2/a$. Present in the asymmetric unit are half of a ruthenium(II) helicate cation, two PF_6^- anions, and one DMF molecule. The two octahedral ruthenium(II) centres are separated by 11.062 Å and bridged by three ligands such that the stereochemistry of the metal centres of each discrete unit is either $\Delta\Delta$ or $\Lambda\Lambda$ (shown as the M-helicate in Figure 4.13). Inclusion of a van der Waals surface shows almost no accessible central cavity in the structure due to the spatial orientation of the three ligands (see Figure D.37 in Section D.5.1 of Appendix D). Additionally the way in which the ligands are oriented around the metal centres provides an 'S' shaped conformation, which results in a cylindrical structure. As a result, despite being a helicate (due to the stereochemistry of the metal centres) the structure lacks the overall helical twist which was plainly observed in the double-stranded structures presented in **Chapter 2** (see Figure 4.14).

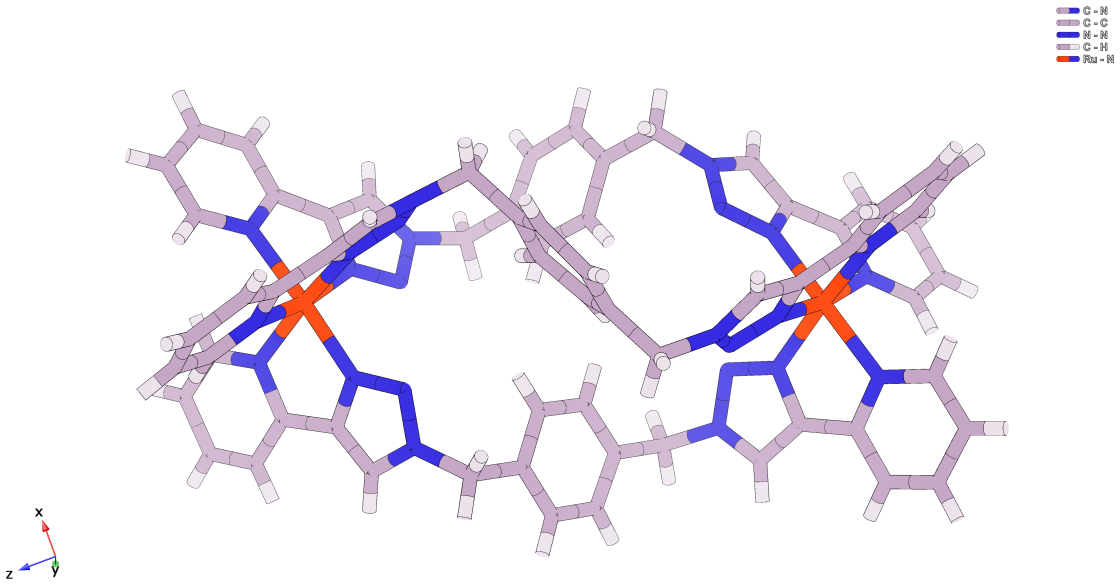

Figure 4.13: Crystallographic model showing the molecular structure of the ruthenium helicate (**11**). Solvent molecules and counter ions have been omitted for clarity.

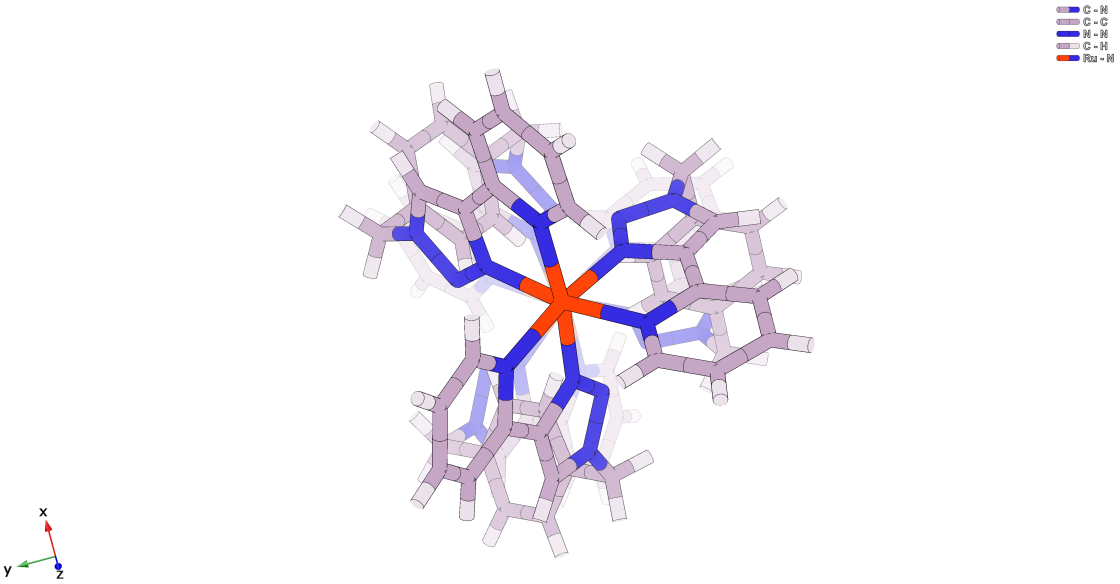

Figure 4.14: Crystallographic model showing the molecular structure of the ruthenium helicate (**11**) viewed down the two Ru(II) centres. Solvent molecules and counter ions have been omitted for clarity.

4.3.1.3 Resolution of helicate

While the synthesis of a number of related supramolecular assemblies incorporating the 1,4-xylyl spacer ligand (**8**) have been reported, there is no record of attempts to resolve any of the helicates. Given the interest in probing the enantiospecific interactions of these types of compounds with DNA (as for the double-stranded compounds described in **Chapter 3**), resolution of the triple-stranded Ru(II) helicate was pursued. Inspired by the

partial resolution achieved on a cellulose stationary phase for the double-stranded helicate described in **Chapter 2**, and complete resolution reported by Hannon and co-workers for a number of triple-stranded helicates,[67,68,172] resolution of the 1,4-xylyl spacer helicate (**11**) was initially attempted using cellulose chromatography with NaCl solutions of varying concentration. Initial attempts using 0.2 M NaCl, which had been partially successful for the compound described in **Chapter 2**, resulted in significant smearing down the length of the column, and under these conditions adequate separation was not achieved. When the concentration of NaCl was increased to 2 M a portion of yellow compound was found to elute, while the remainder was smeared down the length of the column. This second fraction could be removed by elution with 0.5 M sodium 4-toluenesulfonate, or 20% acetone/2 M NaCl.

Analysis of the two fractions (in CH_3CN once exchanged to their respective PF_6^- salts by addition of KPF_6) showed that strong CD signals were observed for both samples, which, when normalised for concentration, showed signals that were opposite in direction and equal in magnitude. From these spectra $\Delta\varepsilon$ was calculated (see Figure 4.15). In the ultraviolet (UV) region, the highest magnitude of $\Delta\varepsilon$ was ± 157 $M^{-1}cm^{-1}$ at $\sim$276 nm, while in the visible region the highest magnitude of $\Delta\varepsilon$ was ± 5 $M^{-1}cm^{-1}$ at $\sim$403 nm. It should be noted that there is a small amount of variation in the magnitude of these signals: this was attributed to a poor baseline and high background absorbance and HT voltage on the spectrophotometer, which in turn led to lower signal-to-noise ratio.

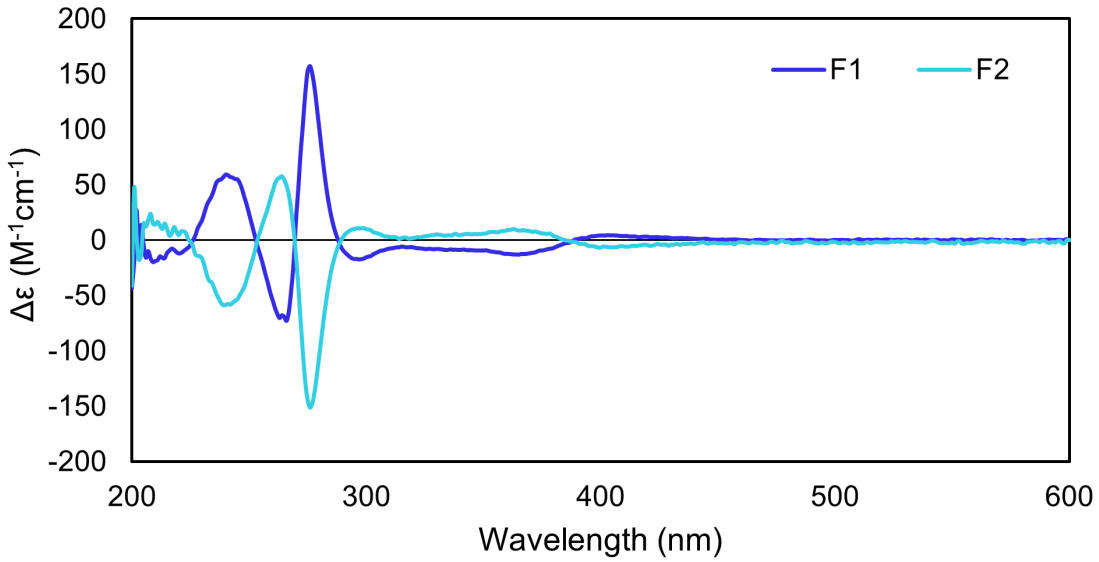

Figure 4.15: CD spectra of **11** resolved on cellulose with 2 M NaCl eluent, followed by 20% acetone/2 M NaCl. F1 refers to the first eluting fraction (aq. 2 M NaCl), F2 refers to the portion stuck to the column (eluted with 20% acetone/2 M NaCl).

The two obtained fractions were further examined using NMR and ultraviolet-visible

(UV-Vis) spectroscopy and found to have identical spectra.

From the initial screening experiments it was clear that lower concentrations of NaCl did not allow for clear separation of the helicate on cellulose. To investigate this further the ionic strength of the eluent was varied extensively.

For ionic strengths lower than 2 M NaCl (0.2 M, 1 M) the majority of the compound eluted as a single yellow band. This was collected in two fractions, separating the start (F1a) and tail end (F1b) of the eluted portion. The remaining compound was smeared down the length of the column (F2), and could be removed with 20% acetone/2 M NaCl, to give a total of 3 fractions. When analysed by CD spectroscopy it was clear that partial resolution had occurred. The first eluting fraction (F1a) contained an excess of one hand, while the third (F2) contained the other enantiomer. The intermediate (the tail end of the band; F1b) was substantially less resolved that the other fractions, with the direction of the CD trace changing with ionic strength (matching (F2) at 0.2 M NaCl; (F1a) at 1 M NaCl). The CD traces for these resolutions (normalised for concentration) are presented as Figures D.33 and D.34 in Section D.4.1 of Appendix D.

When the ionic strength was increased to 3 M NaCl a single eluting fraction was collected (F1), and a large amount of yellow compound remained smeared on the cellulose column (F2). As for previous samples this could be removed by elution with 20% acetone/2 M NaCl. For these fractions the CD response was opposite in direction, but not equal in magnitude with (F1) showing greater CD activity than (F2), the opposite trend to that observed at lower ionic strength (see Figure D.35 in Section D.4.1 of Appendix D).

From these experiments it was concluded that the dominant enantiomer present in (F2) has a greater affinity for cellulose that the enantiomer found in (F1), regardless of ionic strength. However, at low NaCl concentrations both enantiomers were able to elute, and enantiomerically pure (F2) is retained on the cellulose. At high NaCl concentrations the opposite occurs, where both enantiomers stick to the cellulose, and the eluting portion (F1) is enantiomerically pure. This pattern of behaviour suggests that there is a differences in the strength of interactions with chiral cellulose and Cl^- anions for the two helicate enantiomers. Coincidentally, 2 M NaCl appears to be an ideal ionic strength for resolution of this helicate, with similar levels of enantiomeric purity observed for (F1) from 2 M and 3M NaCl elution (see Figure D.36 in Section D.4.1 of Appendix D).

At the time of writing the resolution of this helicate, or any helicates containing similar ligands had not been reported. Furthermore, while Kumar *et al.* had reported the separation of *mer* and *fac* isomers of a related monoruthenium(II) compound, the

enantiomers of these had not been separated.[288] The two enantiomers of the 1,4-xylyl spacer helicate (**11**), previously referred to as F1 and F2 in order of elution, were tentatively assigned based on the direction of CD bands recorded in studies of other resolved Ru(II) species. Using the enantiomer assignment of $[Ru(phen)_3]^{2+}$ and $[Ru(bpy)_3]^{2+}$ by McCaffery *et al.*,[295] F1 of the triple-stranded helicate was assigned as the ΛΛ configuration (the *M*-helicate), and F2 as the ΔΔ configuration (the *P*-helicate). This assignment was in agreement with that reported by Glasson *et al.* for the resolved triple-stranded helicate containing quaterpyridine ligands, where there were similarities in the direction of the CD bands for each enantiomer.[66]

4.3.1.4 Presence of a secondary product

While in the majority of microwave syntheses a single product was present in the crude NMR spectrum, on occasion a secondary set of peaks were observed, resembling those of the helicate (see Figure 4.16). Interestingly, in the original synthesis of the helicate Kumar *et al.* made no mention of a secondary product, although this was unsurprising given the inconsistency in formation.[80]

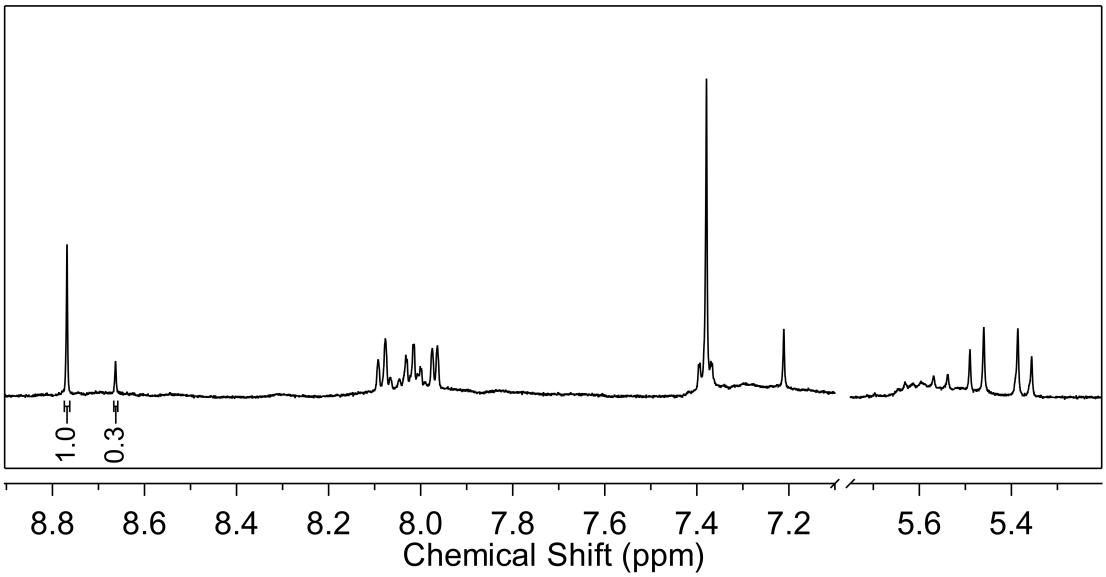

Figure 4.16: Partial ^{1}H NMR spectrum (500 MHz, CD_3CN, 298 K) showing the crude reaction mixture from the microwave reaction to form the triple-stranded diruthenium helicate (**11**), using the 1,4-xylyl spacer ligand (**8**). In this case, two products can be seen, with relative integration of 1 : 0.3.

The relationship of this unknown compound to the helicate was probed by diffusion-ordered spectroscopy (DOSY) NMR experiments, the outcome of which are shown in Figure 4.17 below. Comparison of the diffusion coefficients for the two sets of peaks revealed them to be the same size, suggesting that this second species could be another

dinuclear compound - possibly a mesocate or some other Ru_2L_3 assembly.

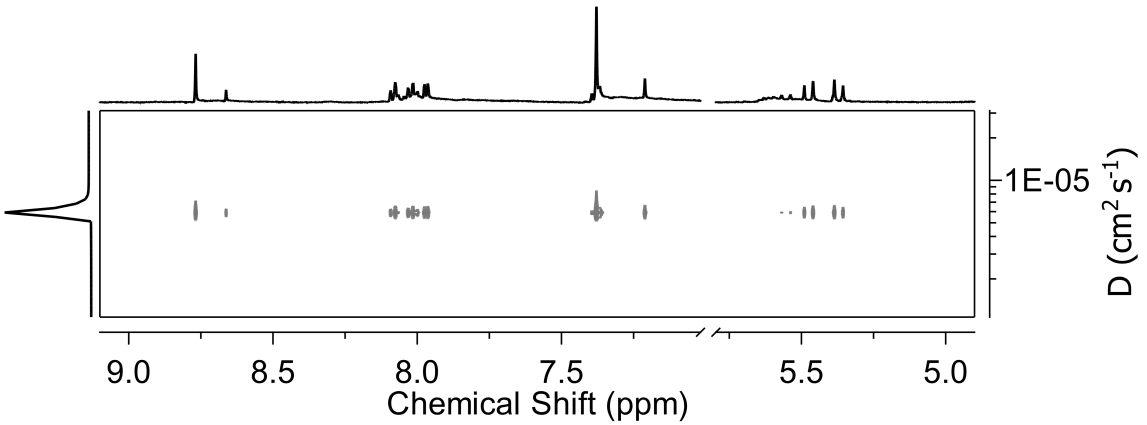

Figure 4.17: Partial ^{1}H DOSY NMR spectrum (500 MHz, CD_3CN, 298 K) of the two products from the microwave reaction using the 1,4-xylyl spacer ligand (**8**).

Initially, separation of the two species was attempted by fractional crystallisation methods, with addition of $NaBF_4$ to an aqueous solution of the Cl^- salt of the crude product. It was found that the pure helicate could be isolated from the reaction mixture, precipitating as the BF_4^- salt, while a mixture of the helicate and an unknown component remained in solution (see Figure 4.18). Despite repeated attempts to remove the remaining helicate from solution by the same method, and thus isolate the unknown compound, this was not able to be achieved, with the solution continuing to stubbornly contain a mixture of the two compounds.

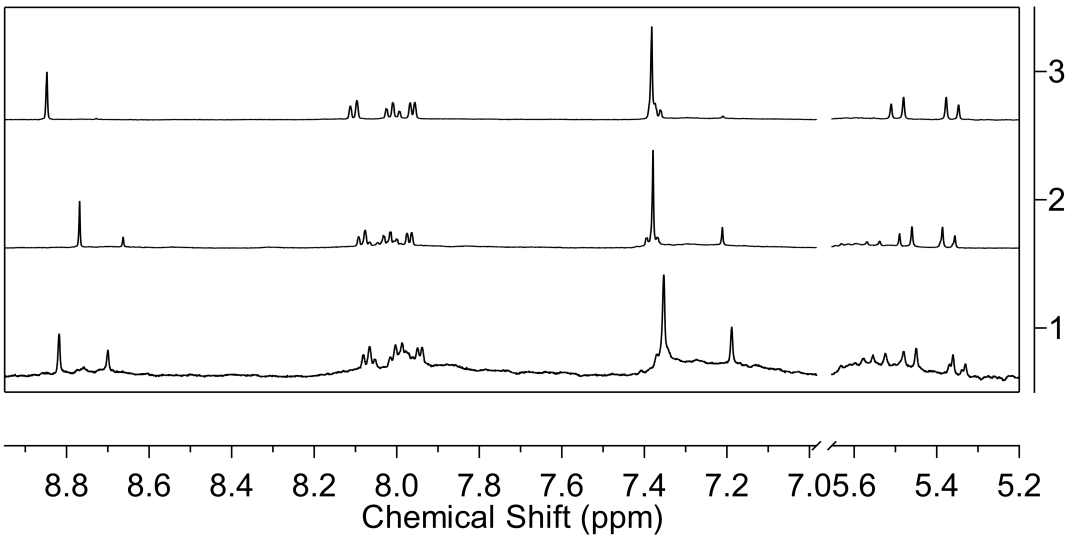

Figure 4.18: Partial ^{1}H NMR spectrum (500 MHz, CD_3CN, 298 K) showing the samples from fractional crystallisation of Ru(II) compounds containing the 1,4-xylyl spacer ligand (**8**) with BF_4^-. (1) Solution after BF_4^- addition (as PF_6^-), (2) Original mixture (as PF_6^-), (3) Initial precipitate (as BF_4^-).

Rather than attempting to remove the secondary minor product post-synthesis, attention turned to variation of the reaction conditions to try and control the initial product distribution. To probe the effect of reaction time, the duration of the reaction was doubled from five hours to ten hours. In this case it was found that the relative ratio of helicate to the secondary product decreased to 1.0 : 0.1 (see Figure 4.19), suggesting that the longer reaction time favours formation of the helicate.

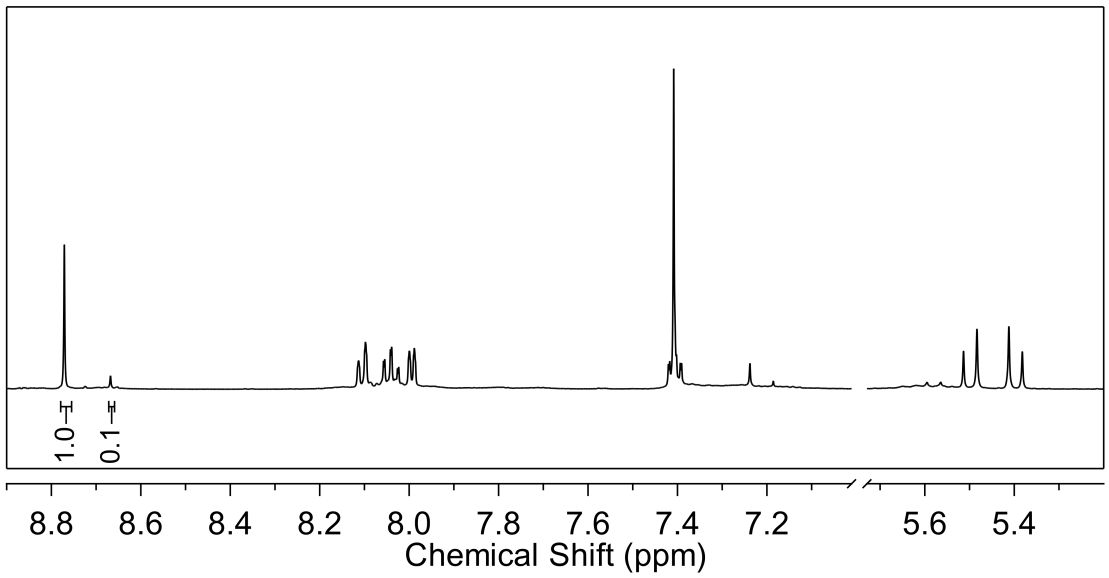

Figure 4.19: Partial ^{1}H NMR spectrum (500 MHz, CD_3CN, 298 K) of the crude reaction mixture from the 10 hour microwave reaction using the 1,4-xylyl spacer ligand (**8**), with relative integration of the triazole hydrogen resonance, showing greater distribution of the helicate in the crude product.

It was evident that by modifying the reaction conditions formation of the helicate could be favoured, and this compound could then be readily purified from the crude reaction mixture by fractional crystallisation with BF_4^-. With these approaches available the presence of the secondary unknown product did not present an insurmountable obstacle in the isolation of the desired 1,4-xylyl spacer helicate. Furthermore, the secondary species did not always appear in the crude product mixture, with some syntheses yielding only helicate (in agreement with the reports of Kumar *et al.*). Given that the helicate was the target compound in this case, and the unknown species was not able to be separated and purified from the mixture in a straightforward manner, the identity of the unknown compound was not further investigated in this thesis.

With the purified helicate, and resolved enantiomers in hand, attention turned to investigating the interactions of this compound with DNA, the results of which will be discussed later in this Chapter (see Section 4.5.1).

4.4 Modification of the spacer

Following the successful synthesis and resolution of the diruthenium triple-stranded helicate by microwave conditions described above, attention turned to extending this to generate related compounds containing the pyridine-triazole moiety by modifying the length and flexibility of the spacer. In previous work by Wu *et al.* a number of ligands of this type had already been reported, and reactions to form iron(II), nickel(II), and zinc(II) compounds undertaken.[291] In most cases a single product was obtained, and based on the structures (elucidated by X-ray crystallography) the authors asserted that distribution of the helicate and mesocate products may follow the selection rules for 2,2′-bipyridine (bpy) and catechol-base systems;[292] for ligands containing an odd-numbered spacer (for example an *n*-propyl chain) mesocate formation was favoured, whereas for even-numbered spacers (the 1,4-xylyl spacer acts as an extended $-CH_2CH_2-$ linker as the phenyl ring is rigid) helicates were favoured. The product distribution was also studied in solution (particularly in cases where crystals could not be obtained) and the authors found that the co-production of mesocate and helicate products appeared first for species containing a *n*-pentyl spacer; however the proportion of mesocate was higher, thus still somewhat supporting the odd/even rule. Further studies of Fe(II) helicates and mesocates using ligands of this type by the Crowley group supported this finding, where in most cases the product distribution did follow the odd/even rules, with the structures able to be confirmed by X-ray crystallography.[290]

In this thesis ligands containing *n*-propyl and *n*-butyl spacers were selected as potential candidates for the synthesis of diruthenium(II) compounds. While the Fe(II) analogues have previously been reported and product distribution found to follow the odd/even rules of formation,[290,291,293] this remains unexplored in a more inert system. It was proposed that by using the relatively inert Ru(II) node it may be possible to break the odd/even rules and provide access to previously unexplored helicate/mesocate pairs since alternative kinetically-preferred products may be obtained rather than the thermodynamically-preferred product.

4.4.1 Increasing flexibility: *n*-propyl spacer

The synthesis of a triple-stranded Ru(II) compound utilising the 1,3-bis{4-(pyridin-2-yl)-1*H*-1,2,3-triazol-1-yl}propane (**9**) ligand was undertaken in an analogous fashion to that containing the 1,4-xylyl spacer ligand (**11**), following the microwave conditions outlined by Kumar *et al.*[80] Synthesis of an apparently single highly-symmetrical diruthenium

compound was observed when isolated as the PF_6^- salt, and the product characterised by NMR spectroscopy and SCXRD. It was evident that some flexibility was present in the spacer region, as shown in NMR studies, where it seemed that all hydrogen signals were split into complicated multiplets - indicating a non-first order system - as was seen for the double-stranded mesocate described in **Chapter 2** of this thesis. The relevant regions of the 1D NMR spectrum are shown in Figures 4.20 and 4.21.

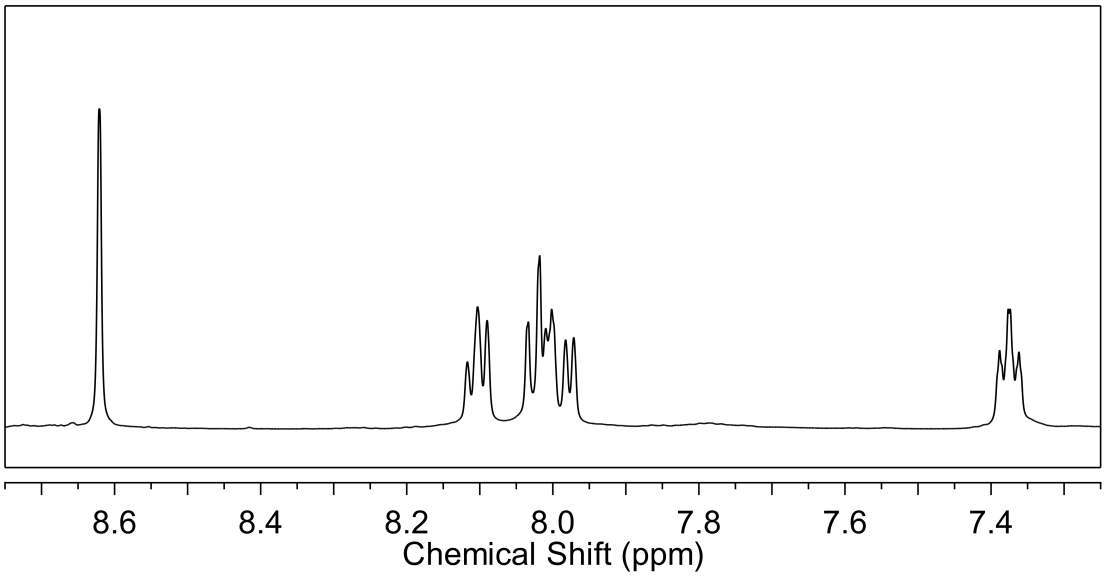

Figure 4.20: Partial ^{1}H NMR spectrum (500 MHz, CD_3CN, 298 K) showing the aromatic region of the crude reaction mixture from the microwave reaction to form the triple-stranded diruthenium compound, using the *n*-propyl spacer ligand (**9**).

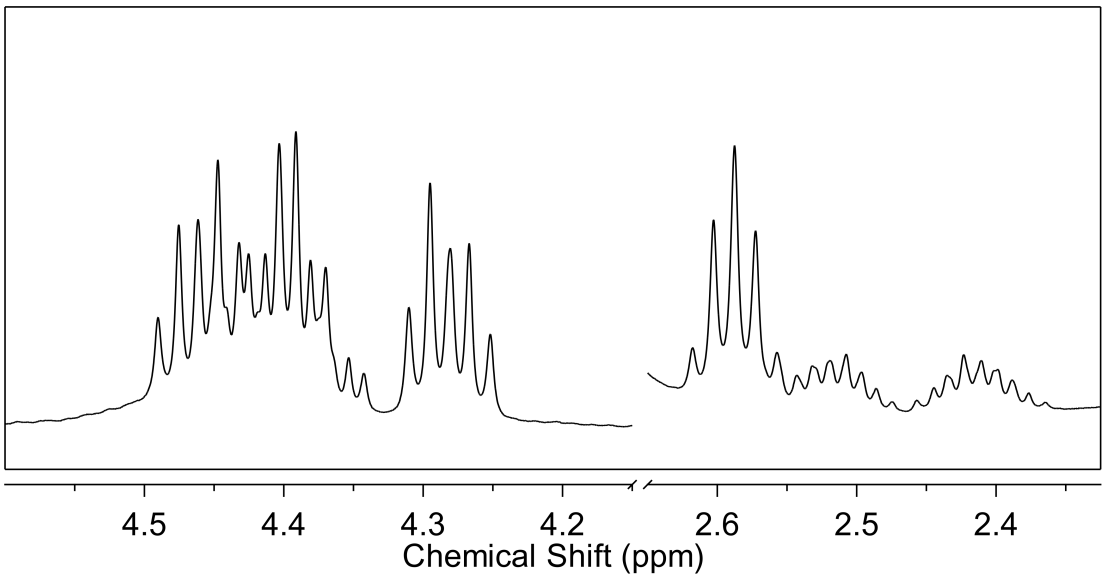

Figure 4.21: Partial ^{1}H NMR spectrum (500 MHz, CD_3CN, 298 K) showing the complicated multiplets present in the aliphatic region from the crude reaction mixture from the microwave reaction to form the triple-stranded diruthenium compound, using the *n*-propyl spacer ligand (**9**).

4.4.1.1 X-ray crystallography

The structure of the dinuclear compound was confirmed by SCXRD, revealing it to be the mesocate (**12**), which was not unexpected for a compound incorporating a ligand with an odd-numbered spacer. The structure of the mesocate (**12**) is shown below (see Figure 4.22). Crystals suitable for X-ray diffraction were grown by vapour diffusion of diisopropyl ether into an acetonitrile solution of the compound, and the resulting structure confirmed the formation of the mesocate of the type $[Ru_2\mathbf{9}_3]^{4+}$. The structure crystallises in the space group $I\ 2/m$. Present in the asymmetric unit are one and a half ruthenium(II) mesocate cations and 5.75 PF_6^- anions. The two octahedral ruthenium(II) centres are separated by 9.789 Å and bridged by three ligands such that the stereochemistry of the metal centres of each discrete unit is $\Delta\Lambda$. Inclusion of a van der Waals surface shows a small central cavity in the structure (see Figure D.38 in Section D.5.2 of Appendix D). Similarly to the 1,4-xylyl spacer helicate (**11**) discussed above, the conformation of the ligand backbone results in a cylindrical supramolecular structure, although in the case of the *n*-propyl spacer mesocate the overall ligand is bent in a 'C' shape down the length of the molecule, resulting in opposing stereochemistry at each metal centre.

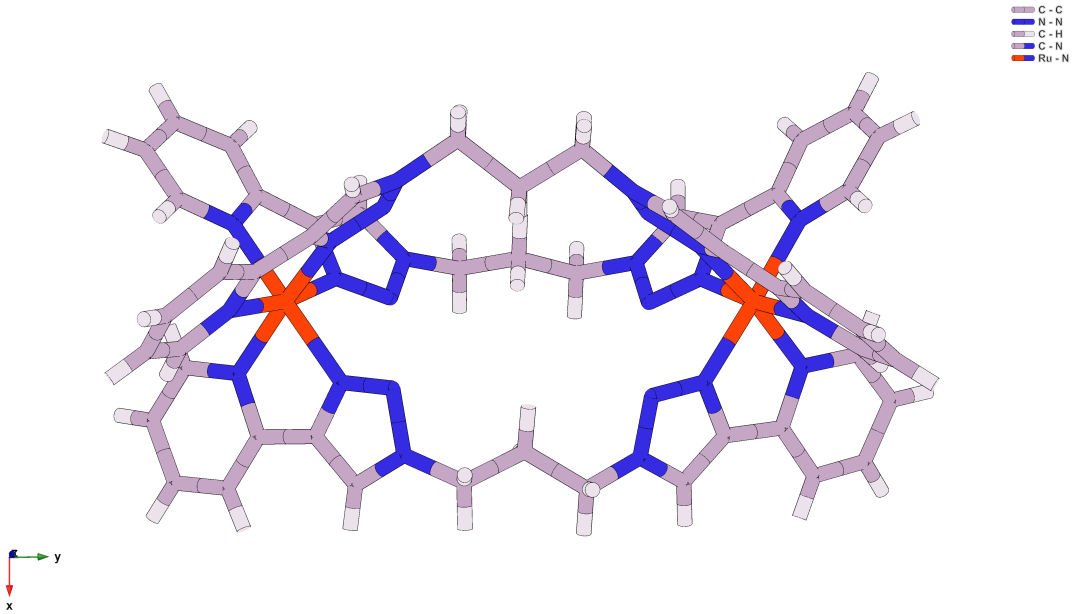

Figure 4.22: Crystallographic model showing the molecular structure of the ruthenium mesocate (**12**). Solvent molecules and counter ions have been omitted for clarity.

4.4.1.2 Probing stability and identification of the secondary product

While the ^{1}H NMR studies and crystal structure of the *n*-propyl spacer mesocate as the PF_6^- salt suggested the presence of a single product, full characterisation, including ^{13}C NMR spectroscopy, revealed anomalies. There appeared to be too many carbon signals

in the ^{13}C NMR spectrum to correspond simply to a mesocate, and 2D HSQC studies showed that the complicated multiplets, previously ascribed to the non-first-order *n*-propyl spacer hydrogens, coupled to separate carbon signals. In the ^{13}C NMR spectrum it can be seen that many of the carbon signals are highly overlapping (an example is shown in Figure 4.24) and when this was accounted for, 18 signals could be identified in total. For the single mesocate only nine unique carbon environments were expected, suggesting that there were two different compounds present in the sample. The ^{13}C NMR and HSQC spectra are shown in Figures 4.23 and 4.25, respectively.

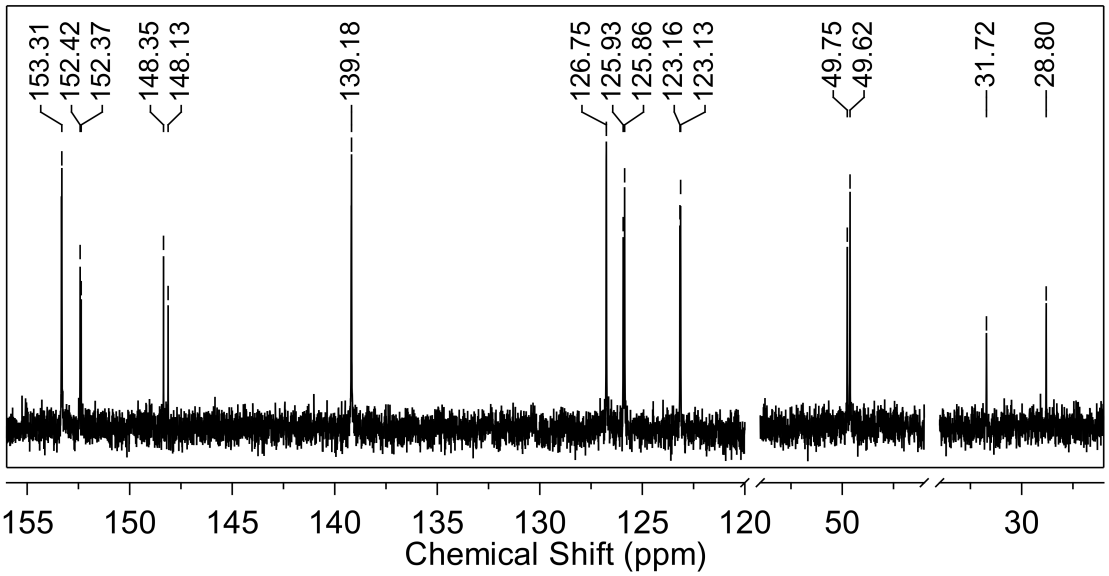

Figure 4.23: ^{13}C NMR spectrum (126 MHz, CD_3CN, 298 K) of the crude reaction mixture from the microwave reaction to form the triple-stranded diruthenium compound, using the *n*-propyl spacer ligand (**9**).

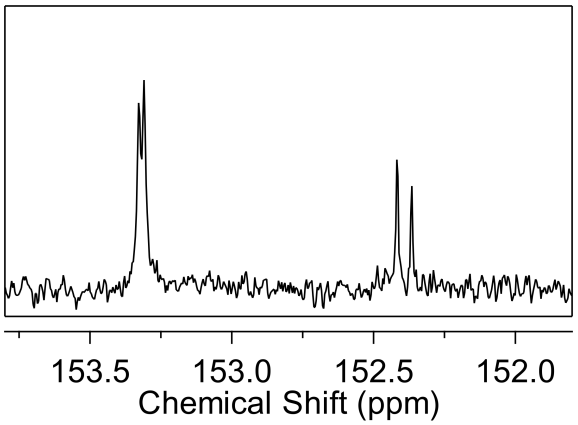

Figure 4.24: Partial ^{13}C NMR spectrum (126 MHz, CD_3CN, 298 K) of the crude reaction mixture from the microwave reaction to form the triple-stranded diruthenium compound, using the *n*-propyl spacer ligand (**9**), showing highly overlapping signals.

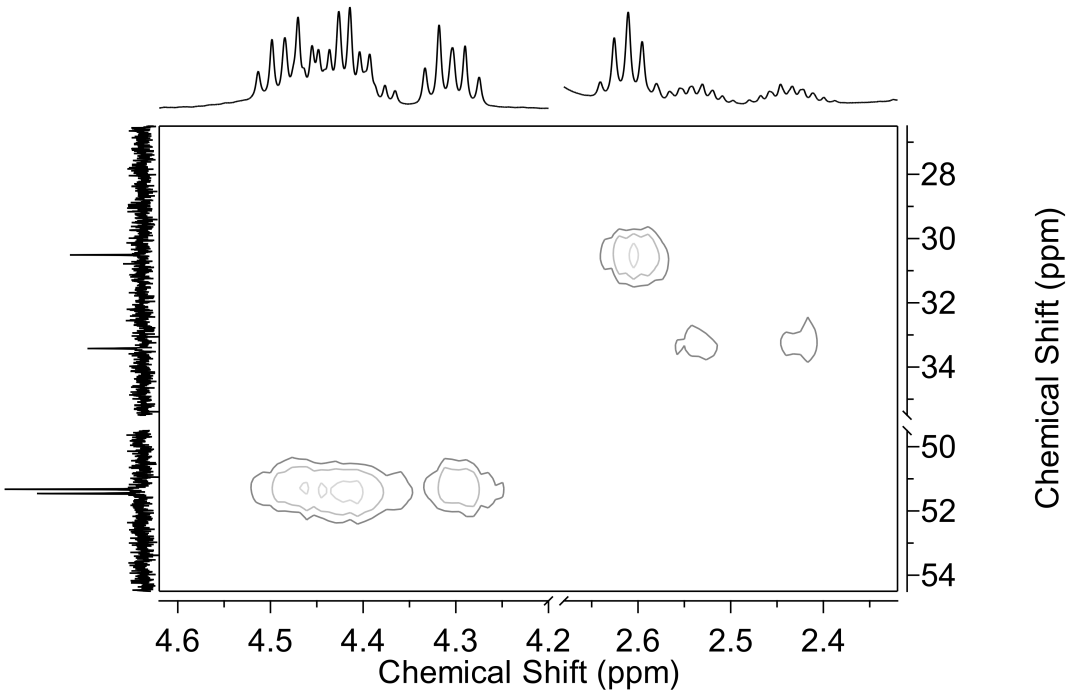

Figure 4.25: HSQC spectrum showing the cross-peaks between the *n*-propyl spacer hydrogen multiplets and separate carbon signals, for the crude reaction mixture from the microwave reaction to form the triple-stranded diruthenium compound, using the *n*-propyl spacer ligand (**9**).

This result was puzzling as the simplicity of the aromatic region of the ^{1}H NMR (Figure 4.20) suggested that a single high-symmetry species was present, however the ^{13}C and 2D NMR experiments indicated that this was not the case.

In order to rule out degradation of the diruthenium mesocate being the cause of confusion in the NMR studies, the stability of the crude product was investigated. This was done by heating the PF_6^- salt of the compound in CD_3CN at 50 °C degrees over 7 days, with NMR spectra collected periodically over this time period. In the stacked spectra it can be seen that the compound appears to be highly stable, with no changes in chemical shift or relative integration of the signals observed over this time period (the aromatic region is shown in Figure D.11 in Section D.2.2 of Appendix D).

Given that the PF_6^- salt appeared thermally stable, the stability of the crude product as the Cl^- salt was investigated in D_2O. The initial ^{1}H NMR spectrum was a revelation, clearly showing splitting of the aromatic signals into two distinct chemical species (see Figure 4.26). Analysis of the relative integration revealed that these two species were present in a 1 : 0.8 ratio. Additionally, exchange to the Cl^- salt in D_2O resulted in changes in chemical shift of the upfield multiplets corresponding to hydrogens on the *n*-propyl spacer. In these regions the multiplets were now clearly seen to be independent signals,

even for the overlapping peaks at 4.5 ppm, and separation was observed for those between 2.9 - 2.5 ppm. Overall, the ^{1}H NMR spectra of the Cl^{-} salt in these regions indicated that the crude reaction mixture undoubtedly contained two compounds.

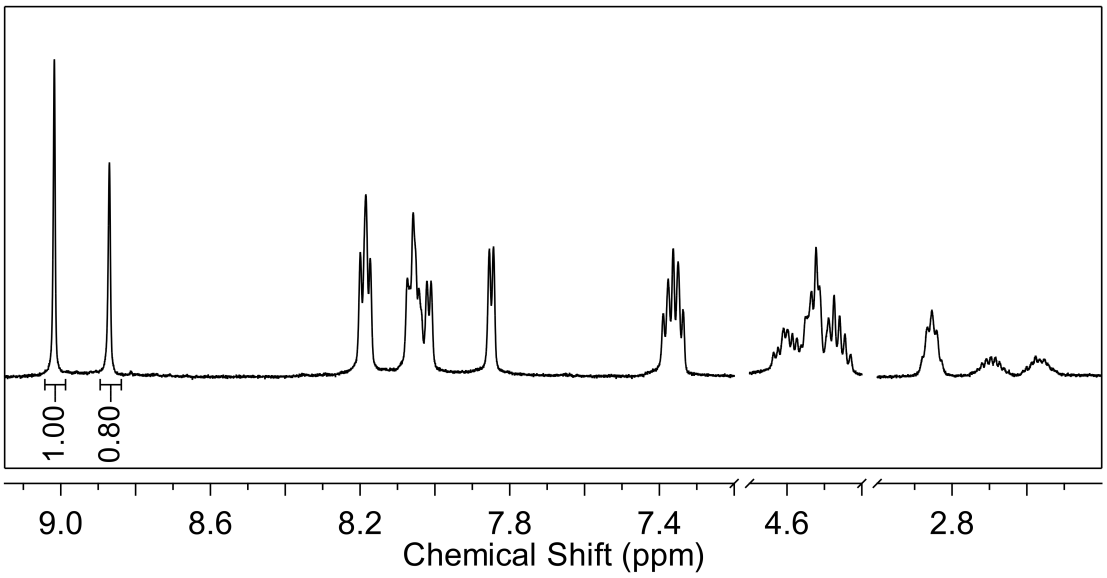

Figure 4.26: Partial ^{1}H NMR spectrum (500 MHz, D_2O, 298 K) showing the crude reaction mixture from the microwave reaction to form the triple-stranded diruthenium compound as the Cl^{-} salt, using the *n*-propyl spacer ligand (**9**).

The stability of the crude product as the Cl^{-} salt was then investigated, and the sample was heated under analogous conditions to the PF_6^{-} over a period of 7 days. Again, no change in the relative intensity or position of peaks was observed in the ^{1}H NMR, indicating that both species were stable under these conditions (the aromatic region of the spectrum is shown in Figure D.12 in Section D.2.2 of Appendix D).

The obvious presence of two species when the compound was exchanged to the Cl^{-} salt raised concerns over the composition of the initial product - which, based on the structure elucidated by X-ray crystallography, was thought to be the pure mesocate (**12**). At this stage two possible hypotheses were proposed. One option was that the product consisted of two distinct chemical species, the mesocate and either the helicate or some higher-order architecture, such as a tetrahedron or cage-type compound. In this case, the hydrogens in both compounds must exist in extremely similar environments, resulting in almost identical ^{1}H NMR signals in the aromatic region. The other option considered was that two conformers of the mesocate could exist as the Cl^{-} salt in D_2O, whereas presumably only one conformer is present as the PF_6^{-}. In this case an anion-binding equilibrium process may influence the product distribution. A Cl^{-} anion could potentially be incorporated in the central cavity of the mesocate, altering the chemical environment enough to differentiate the two species by ^{1}H NMR in D_2O, although this equilibrium

could also be solvent dependent.

The possibility of a helicate being the secondary unknown initially seemed less likely as for all examples known in the literature, as well as previous work with other diruthenium(II) compounds (described in **Chapter 2**, and later in this Chapter) mesocate and helicate products are able to be differentiated in the ^{1}H NMR spectra when isolated as the PF_6^- salts. For this reason, it seemed unlikely that the aromatic signals for compounds containing the *n*-propyl spacer ligand (**9**) in particular would be in identical (or nearly identical) chemical environments, especially when the carbon signals between the species were clearly distinguishable.

To probe the identity of the mystery product further a range of simple 1D NMR experiments were conducted in a range of solvents, with the compound as either the PF_6^- or Cl^- salt. As previously stated, for the PF_6^- salt in CD_3CN the NMR spectrum suggested the presence of a single, highly symmetrical species. When the PF_6^- salt was dissolved in *d*$_6$-DMSO splitting of the aromatic peaks began to be observed, particularly for the hydrogen on the triazole (the most downfield resonance). Overall, the spectrum was quite similar to that collected in CD_3CN, but it was clear that the other multiplets in the aromatic region were composed of two sets of overlapping signals, rather than a single set (see Figure 4.27). The *n*-propyl spacer hydrogens, appearing upfield, were highly overlapping with the solvent signals, making it difficult to differentiate the multiplets in these regions.

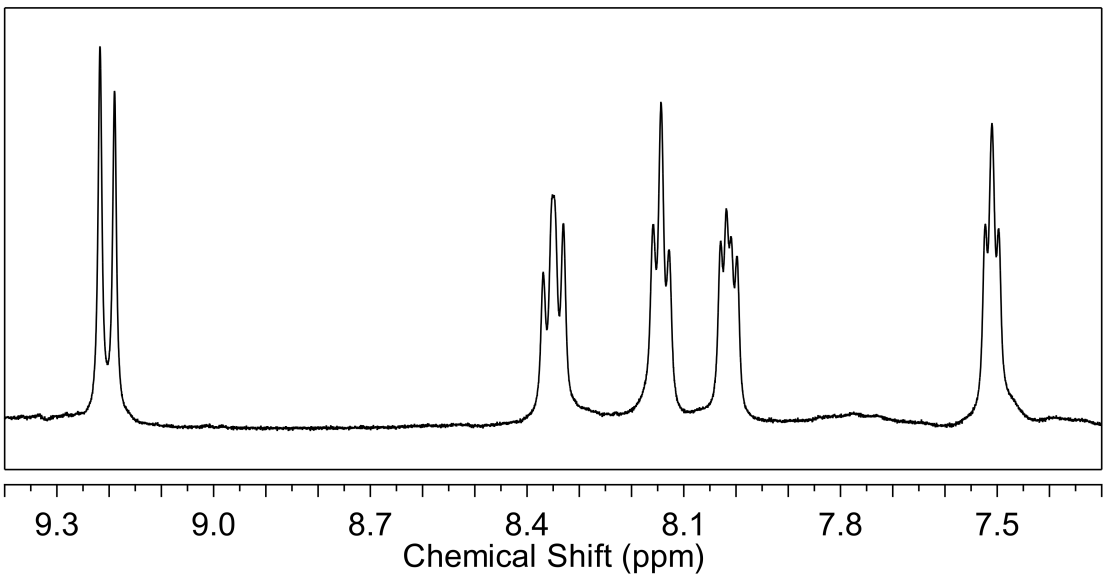

Figure 4.27: Partial ^{1}H NMR spectrum (500 MHz, *d*$_6$-DMSO, 298 K) showing the aromatic region of the crude reaction mixture from the microwave reaction to form the triple-stranded diruthenium compound in *d*$_6$-DMSO, using the *n*-propyl spacer ligand (**9**).

To compare the spectrum of the Cl^- salt in D_2O, which had clearly shown two sets of

peaks (see Figure 4.26), to the PF_6^- by means of a common solvent the Cl^- salt was also dissolved in d_6-DMSO. In this case the sample was found to be only partially soluble, with a large portion of material remaining undissolved. The spectrum for the DMSO-soluble portion was collected and is shown in Figure 4.28. This sample was found to contain mainly one set of peaks, indicating a single product, with only a small amount of a secondary product present (1.0 : 0.1 relative integration). One set of hydrogens on the *n*-propyl spacer appeared as a pair of complex multiplets at 4.50 ppm, while the other hydrogens (further upfield) were obscured by the solvent peak at 2.50 ppm.

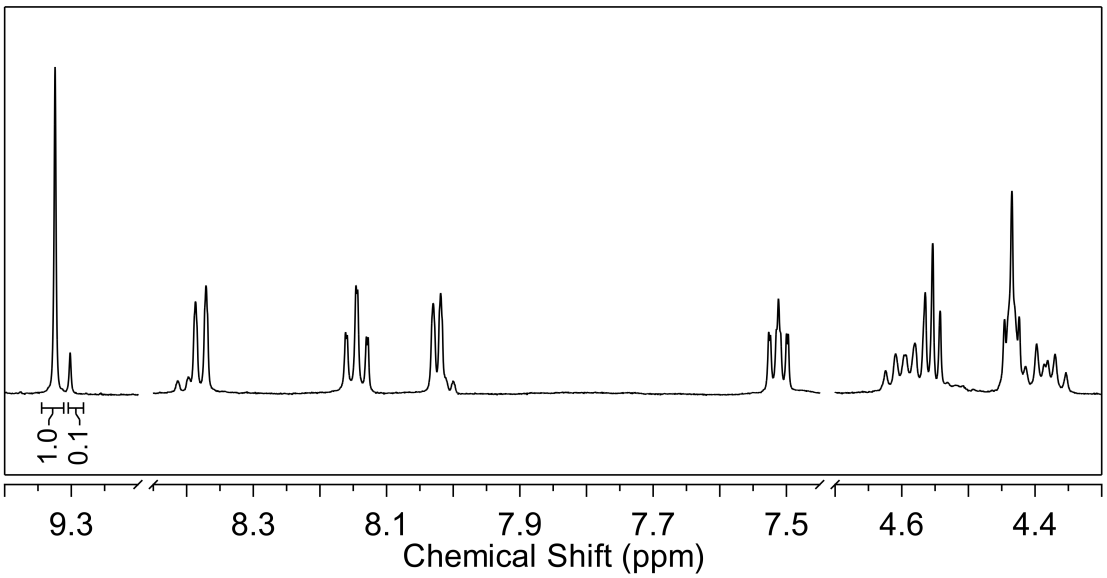

Figure 4.28: Partial ^{1}H NMR spectrum (500 MHz, d_6-DMSO, 298 K) showing the DMSO-soluble portion of the triple-stranded diruthenium compound as the Cl^- salt in d_6-DMSO, using the *n*-propyl spacer ligand (**9**).

The remaining DMSO-insoluble portion was dissolved in D_2O, and ^{1}H NMR spectrum for this sample showed a single set of peaks. Comparing this spectrum to the initial product mixture as the Cl^- salt in D_2O, the successful purification of a single compound in the DMSO-insoluble portion from the original product mixture was confirmed (see Figure 4.29).

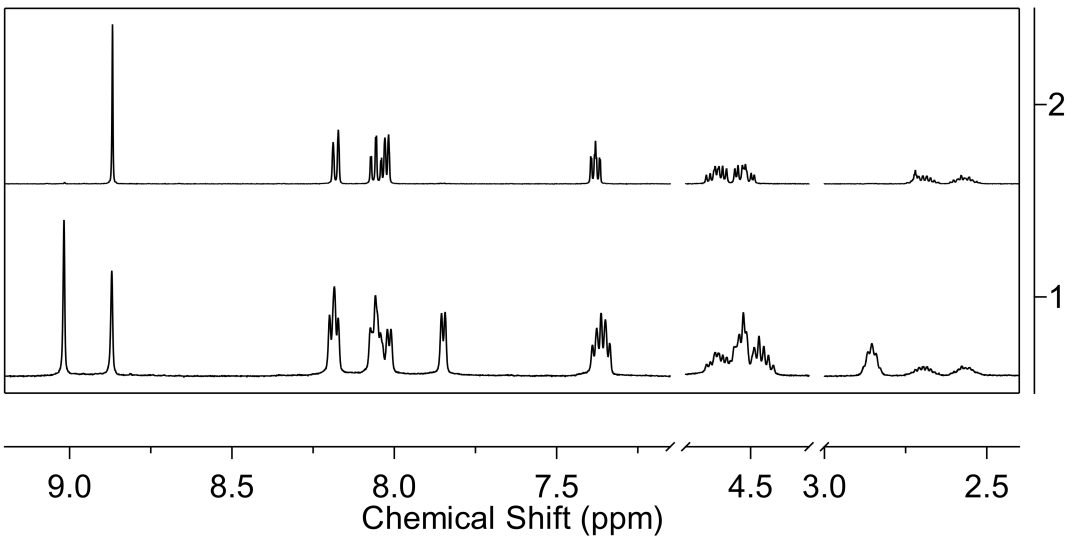

Figure 4.29: Partial ^{1}H NMR spectrum (500 MHz, D_2O, 298 K) showing the DMSO-insoluble portion of the triple-stranded diruthenium compound as the Cl^- salt in D_2O compared to the initial mixture, using the *n*-propyl spacer ligand (**9**). (1) Original Cl^- salt in D_2O, (2) Cl^- salt of DMSO-insoluble portion.

To address the possibility of one of these compounds being a larger supramolecular assembly a DOSY NMR experiment was performed for the Cl^- salt of the compound in D_2O, where it was easier to discriminate between the two chemical species. Across the spectrum all signals corresponded to compounds with a similar diffusion coefficient (see Figure D.13 in Section D.2.2 of Appendix D). From these results it seemed unlikely that the second set of peaks could arise from a larger tetrahedron or cage-type compound, and may instead be due to a dinuclear species.

To ascertain the nature of the potential dinuclear species, variable temperature NMR experiments were conducted to address whether conformers of the mesocate could be present. ^{1}H NMR spectra were run at 5 ° increments, from room temperature up to 50 °C, to monitor any changes in the ratio of the two products in the mixture as the Cl^- salt in D_2O. The results can be seen in Figure D.14 (see Section D.2.2 of Appendix D). Over this temperature gradient the aromatic signals were seen to sharpen as temperature increased, but comparison of the relative integration of the two triazole peaks showed negligible change. Despite there being no clear change in the equilibrium of the two dinuclear species under these conditions, the presence of conformers could not be entirely ruled out, as the highest temperature tested (50 °C) may not have been sufficient to allow convergence of the two forms on the NMR time-scale.

To further investigate this point the ^{1}H NMR spectra of the product as the Cl^- salt from different reactions of $RuCl_3$ and the *n*-propyl spacer ligand (**9**) were compared.

Comparing to an older sample (approximately 18 months old) the NMR spectra in D_2O revealed a different ratio of the two species by integration. While the more recent sample had a ratio of approximately 1 : 0.8, the older sample showed a 1 : 1.8 ratio (using the integration of the triazole hydrogen appearing furthest downfield; see Figure D.15 in Section D.2.2 of Appendix D). Given that a different product distribution had been observed in the two samples, the presence of two conformers in solution became more unlikely, suggesting instead that the mixture was composed of two structurally-distinct dinuclear compounds.

Furthermore, when exchanged to the Br^- salt, the ratio of species by relative integration did not change dramatically when compared to the Cl^- salt. For the mixture as the Cl^- salt the relative integration was found to be 1 : 0.8, while as the Br^- salt the ratio increased slightly to 1 : 0.9 (see Figure D.16 in Section D.2.2 of Appendix D). The change in relative integration between the Cl^- and Br^- salts is not large, which suggests that changes in the size of the counter anion does not greatly affect the distribution of products.

It was found that after two cycles of precipitation and washing with DMSO the two compounds could be isolated as pure products, with each only containing a single set of ^1H NMR signals as both the Cl^- salt in D_2O and PF_6^- in CD_3CN; the spectra of the PF_6^- salts are shown below. By examination of the stacked spectra shown in Figure 4.31, it can be seen that the majority of resonances are highly overlapping in the aromatic region in the original sample. Upfield the spectrum is far more diagnostic, as the multiplets for the hydrogens on the *n*-propyl spacer resolve into separate signals at 4.4 ppm and 2.5 ppm (see Figure 4.31). Intriguingly, the *n*-propyl spacer hydrogen signals of the DMSO-soluble compound appear as a pair of multiplets (4.4 ppm) followed by a quintet (2.5 ppm), whereas for the DMSO-insoluble compound this pattern appears to be reversed, with a multiplet at 4.4 ppm followed by a pair of multiplets at 2.5 ppm, suggesting that the major differences in chemical environment for these compounds must occur for hydrogens in the *n*-propyl spacer region.

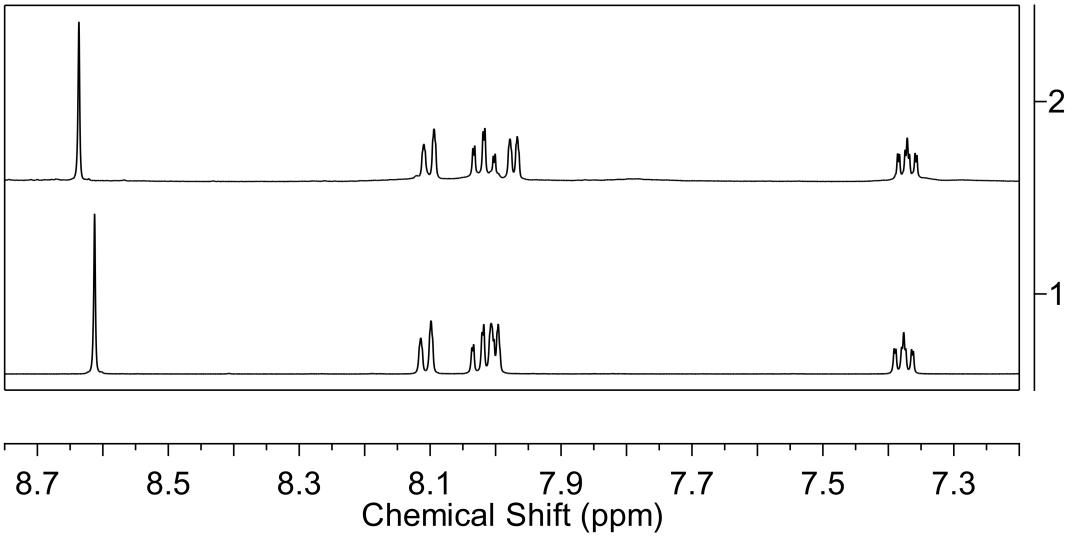

Figure 4.30: Partial ^{1}H NMR spectra (500 MHz, CD_3CN, 298 K) showing the aromatic region of the crude reaction mixture from the microwave reaction to form the triple-stranded diruthenium compound as the PF_6^- salt, using the *n*-propyl spacer ligand (**9**). (1) DMSO-insoluble, (2) DMSO-soluble.

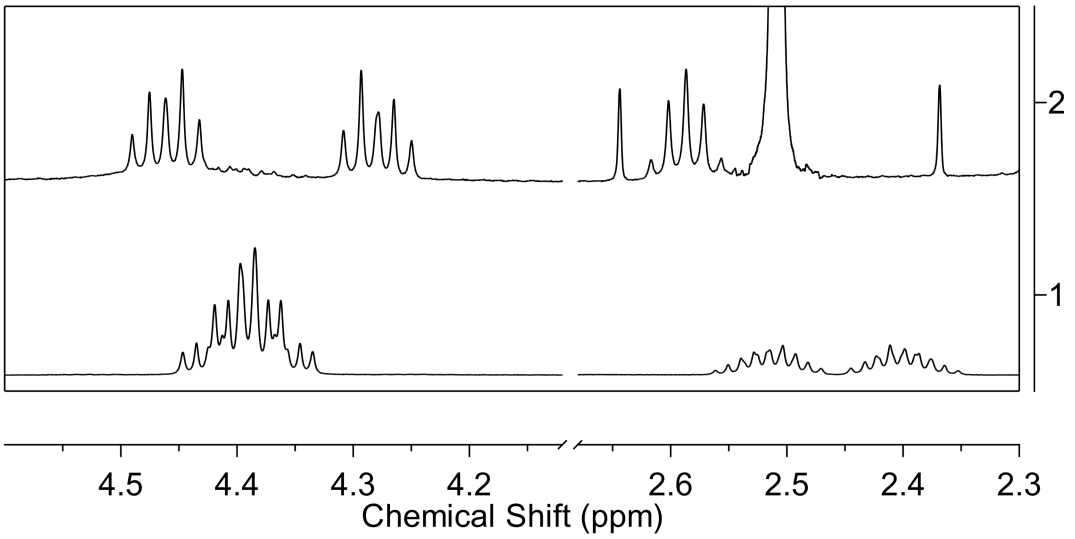

Figure 4.31: Partial ^{1}H NMR spectra (500 MHz, CD_3CN, 298 K) showing the *n*-propyl spacer region of the crude reaction mixture from the microwave reaction to form the triple-stranded diruthenium compound as the PF_6^- salt, using the *n*-propyl spacer ligand (**9**). (1) DMSO-insoluble, (2) DMSO-soluble.

Comparison of the ^{13}C NMR spectra for the two separated compounds confirmed that separation was achieved, with the DMSO-soluble and DMSO-insoluble compounds each only containing nine carbon signals, and being devoid of the overlapping peaks observed in the original PF_6^- mixture (see Figure D.17 in Section D.2.2 of Appendix D). Considering the ^{13}C - ^{1}H cross-peaks in an HSQC experiment for the two compounds it was seen that each of the *n*-propyl spacer hydrogens showed correlation to a single carbon, which

was expected given the reduction in total carbon signals and single set of peaks for the hydrogens on the *n*-propyl spacer observed for each sample (see Figures D.18 and D.19 for the DMSO-insoluble and DMSO-soluble samples respectively, in Section D.2.2 of Appendix D). For the DMSO-soluble sample it should be noted that the significant cross-peaks observed at 2.50 ppm correspond to residual DMSO remaining in the PF_6^- exchanged sample.

While extensive NMR experiments were able to show successful separation of the two compounds, the assignment of the mesocate and unknown species was still incomplete. Fortunately, crystals of both samples were able to be grown as the PF_6^- salts, and the structure of each elucidated by SCXRD.

The DMSO-insoluble fraction was dissolved in H_2O, and then exchanged to the PF_6^- salt. Crystals suitable for X-ray diffraction were grown by vapour diffusion of diisopropyl ether into a nitromethane solution of the compound, and the resulting structure confirmed the formation of the mesocate of the type $[Ru_2\mathbf{9}_3]^{4+}$ (**12**), shown in Figure 4.32. The structure crystallises in the space group $P6_3/m$. Present in the asymmetric unit are $\frac{1}{6}$ of a ruthenium(II) mesocate cation, 1 PF_6^- anion, 1 nitromethane, and $\frac{1}{3}$ of a potassium cation (remaining from conversion to the PF_6^- salt using KPF_6). The presence of potassium was confirmed by scanning electron microscopy (SEM)/energy-dispersive X-ray spectroscopy (EDX) analysis of single and crushed crystals (see Figures D.42, D.43, D.44 and Table D.5 in Section D.6 of Appendix D). The two octahedral ruthenium(II) centres are separated by 10.084 Å and bridged by three ligands such that the stereochemistry of the metal centres of each discrete unit is $\Lambda\Delta$. Inclusion of a van der Waals surface shows a central cavity in the structure, as noted previously, due to the spatial orientation of the *n*-propyl spacer (see Figure D.39 in Section D.5.3 of Appendix D).

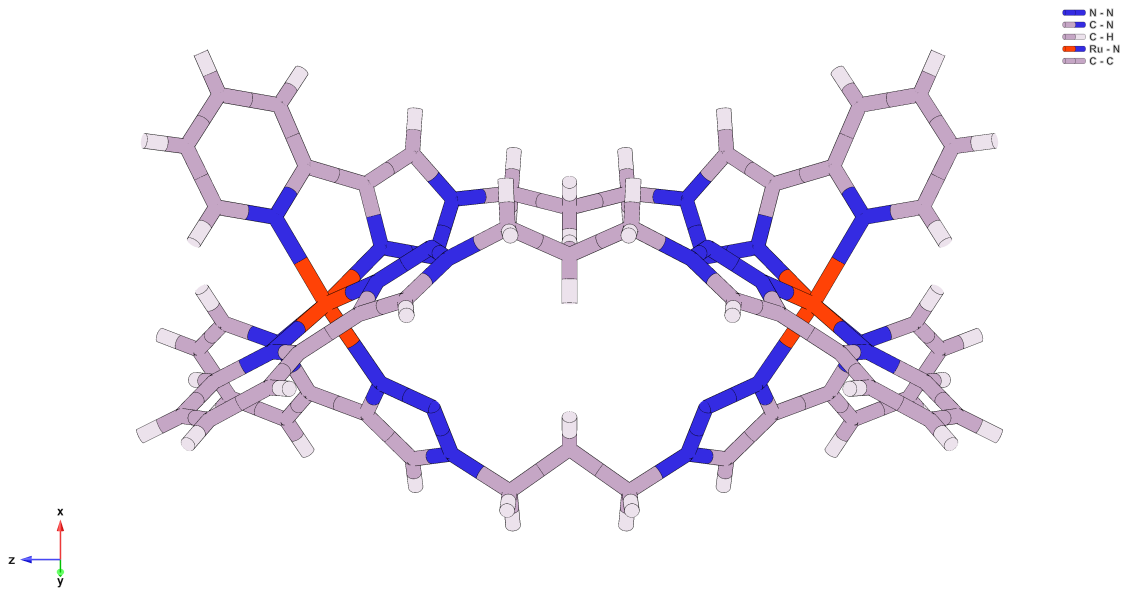

Figure 4.32: Crystallographic model showing the molecular structure of the purified ruthenium mesocate (**12**). Solvent molecules and counter ions have been omitted for clarity.

To determine the identity of the DMSO-soluble portion an excess of H_2O was added to a solution of the purified compound as the Cl^- salt in DMSO, the sample exchanged to the PF_6^- salt. Crystals suitable for X-ray diffraction were grown by vapour diffusion of diisopropyl ether into an acetonitrile solution of the compound. The resulting structure revealed the formation of a helicate of the type $[Ru_2\mathbf{9}_3]^{4+}$ (**13**), shown as the *P*-helicate in Figure 4.33. The structure crystallises in the space group *P*-31*c*. Present in the asymmetric unit are $\frac{2}{3}$ of a ruthenium(II) helicate cation and 2 $\frac{2}{3}$ PF_6^- anions. Interestingly, the structure crystallises as a mixture of enantiomers which are able to be differentiated in the extended crystal structure. Throughout the extended structure the octahedral Ru(II) centres are separated by different distances for adjacent helicate molecules, in some molecules the separation is 9.376 Å, while in others the metal centres are separated by 8.698 Å (see Figure D.40 in Section D.5.4 of Appendix D). Inclusion of a van der Waals surface shows a central cavity similar to that seen for the mesocate, due to the manner in which the ligands wrap around the metal centres (see Figure D.41 in Section D.5.4 of Appendix D).

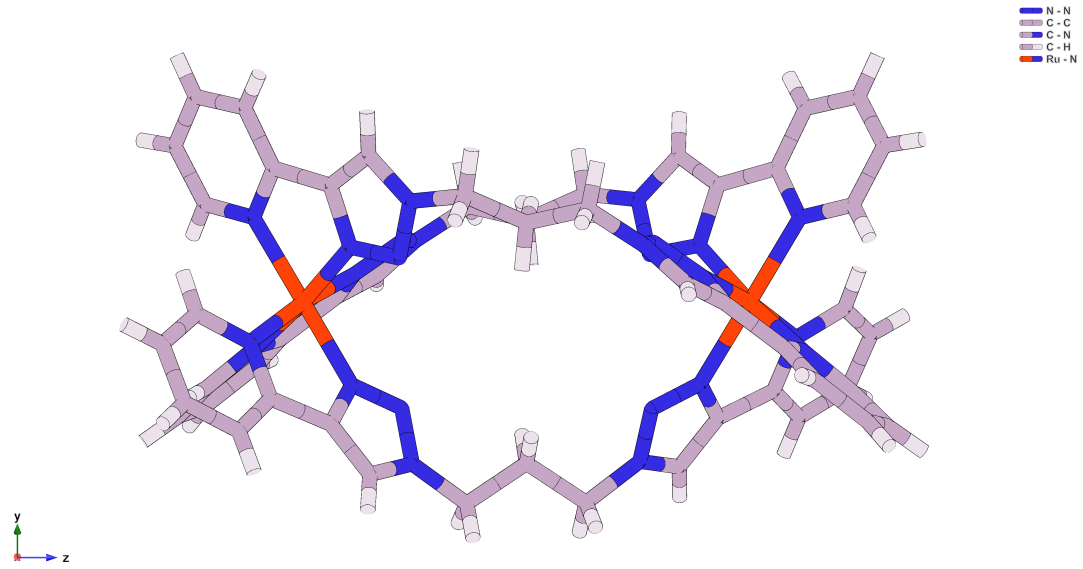

Figure 4.33: Crystallographic model showing the molecular structure of the purified ruthenium helicate (**13**). Solvent molecules and counter ions have been omitted for clarity.

The two dinuclear Ru(II) compounds containing the *n*-propyl spacer ligand (**9**) described above showed significant structural variation, aside from the obvious differences in chirality. The mesocate was a slightly longer molecule, with a Ru(II) - Ru(II) distance of 10.084 Å and a central cavity of $\sim$ 17 Å^3. Due to the elongation of the ligands down the sides of the structure, the cavity is composed of two overlapping spheres. The helicate, despite having a shorter inter-ruthenium distance, had a cavity that was larger in volume ($\sim$ 30 Å^3), and was far more cylindrical in shape than that of the mesocate due to the manner in which the ligands wrap around the two metal centres. The volume of the central cavities of both structures were calculated from the crystal structures using the program MoloVol.[296]

As had been seen for the double-stranded compounds described in **Chapter 2**, the helicate/mesocate pair synthesised from the *n*-propyl spacer ligand (**9**) showed slight differences in their UV-Vis absorbance spectra. The mesocate (**12**; DMSO-insoluble sample) had lower molar absorptivity at all wavelengths, compared to the helicate (**13**; DMSO-soluble sample). Overall, both samples showed similar molar absorptivity to the 1,4-xylyl spacer helicate. Additionally the λ_{max} for both samples were identical, except at the shortest wavelength where the peak was slightly shifted. The two spectra can be seen in Figure 4.34.

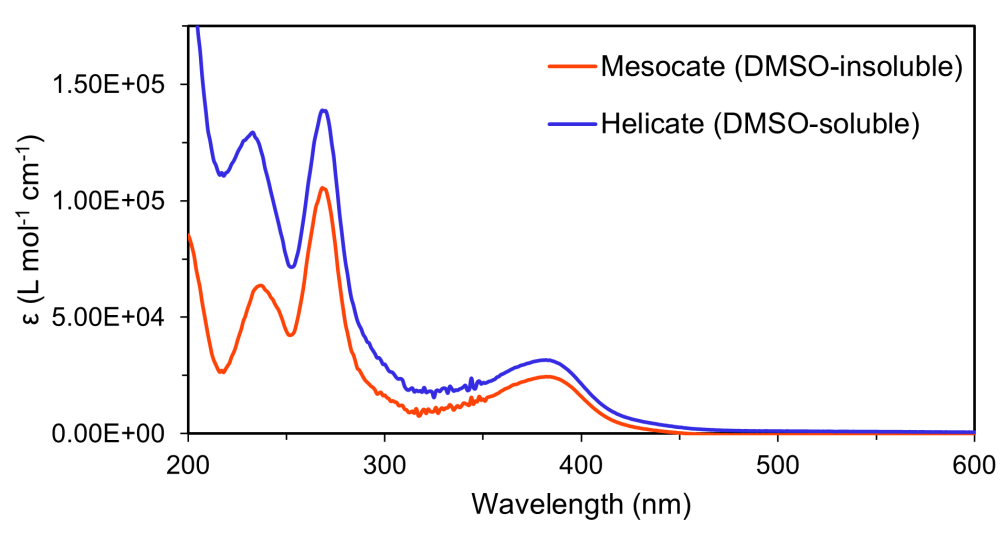

Figure 4.34: UV-Vis spectra (CH_3CN, 298 K) of the *n*-propyl spacer compounds, with the mesocate (DMSO-insoluble) shown in orange, and the helicate (DMSO-soluble) shown in blue.

As further confirmation, the high resolution electrospray ionisation mass spectrometry (HR ESI-MS) of the two dinuclear products revealed the two species to have ions of identical formula masses - *m/z* 300.2222 (corresponding to dinuclear $[Ru_2\mathbf{9}_2 - 4\,PF_6]^{4+}$). The mass spectra of the samples can be seen in Figures D.30 and D.31 in Section D.3.1 of Appendix D for the mesocate (**12**) and helicate (**13**), respectively.

4.4.1.3 Relative energy modelling

Given that both the mesocate (**12**) and helicate (**13**) were found to be present from reactions under microwave conditions, modelling of their relative energies was conducted using density functional theory (DFT) in order to better understand the product distribution. In comparison to previous compounds studied in this thesis, the *n*-propyl spacer ligand has much greater flexibility and potential for rotation within the spacer region, supporting the experimental finding that the two isomers can form in more equal amounts than seen for the double-stranded species described in **Chapter 2**. Therefore, the relative stability of the two isomers was calculated *in vacuo* and in a dielectric medium, using the dielectric constant of acetonitrile.

Table 4.1 shows the relative energy (ΔE) and relative Gibbs free energy (ΔG) *in vacuo* and in acetonitrile of the helicate with respect to the mesocate, for compounds containing the ligand **9**.

Table 4.1: Relative stability of the helicate with respect to mesocate for compounds containing the *n*-propyl spacer ligand (**9**).

	ΔE (kJ/mol)	ΔG (kJ/mol)
Vacuum	19.4	24.7
Acetonitrile	1.6	7.0

From these results it can be seen that *in vacuo* the mesocate is a more stable isomer than the helicate (where ΔE = 19.4 kJ/mol, and ΔG = 24.7 kJ/mol). This was also the case in a dielectric medium; however, the difference in stability was greatly decreased in comparison (where ΔE = 1.6 kJ/mol, and ΔG = 7.0 kJ/mol). It is noted that the double-stranded compounds discussed in **Chapter 2** had larger differences in relative energies (ΔE = -55.4 kJ/mol, and ΔG = -50.7 kJ/mol for the helicate with respect to the mesocate). In contrast, compounds containing the *n*-propyl spacer ligand (**9**) described in this Chapter showed significantly smaller differences. Full details of the methods and results of DFT calculations and modelled structures are presented in Section D.7.1 of Appendix D.

These findings are in agreement with the experimentally-observed product distribution, in which both the mesocate and helicate can be isolated in roughly equal proportions. Frustratingly, following purification of the two compounds it was often found that after hours or days mixtures were once again visible in samples when analysed by ^{1}H NMR spectroscopy. Given the small difference in relative energy of the two isomers and persistence of isomeric mixtures in the purified samples it raised the interesting question of whether the isomers could interconvert.

4.4.1.4 Interconversion of isomers

Given that different ratios of the two dinuclear products were observed between reactions (particularly comparing to the 18 month old sample) and a mixture reappeared in the sample after purification, the potential for the isomers to interconvert was investigated. Each purified sample was re-exposed to reaction conditions (200 W, 200 PSI, 225 °C; for five hours) as the Cl^- salt in ethylene glycol, and resulting product distribution analysed by NMR spectroscopy.

For the mesocate (**12**), after microwave irradiation the sample was isolated as the PF_6^- salt and then converted to the Cl^- salt to allow comparison to the original purified

sample. In this case a small amount of a secondary species was observed in the irradiated sample via ^{1}H NMR spectroscopy, with peak positions matching those observed for the helicate. The NMR spectra for this sample showing the mesocate in D_2O before and after irradiation are shown in Figure 4.35 below, with the emerging helicate resonances highlighted in yellow.

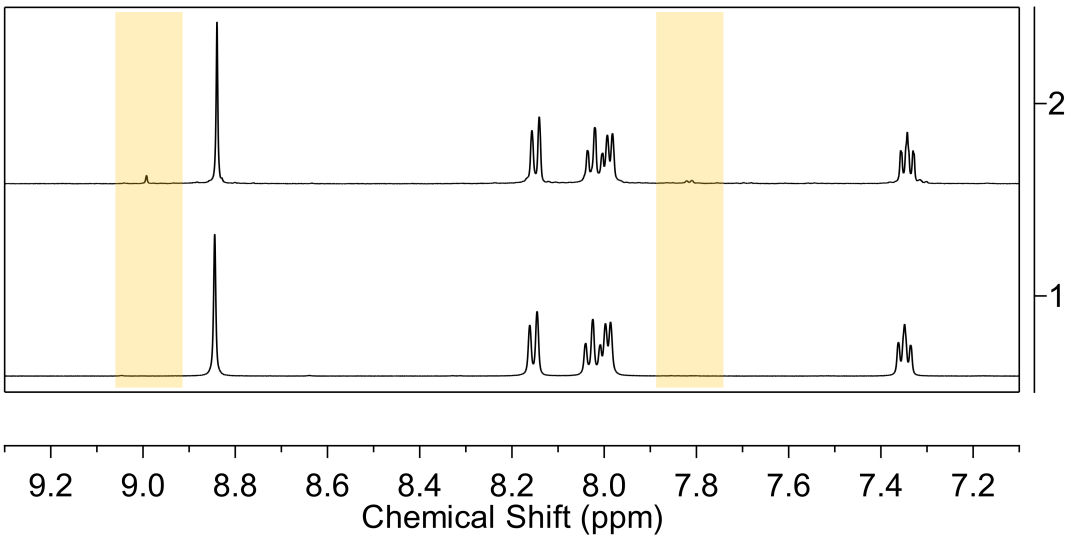

Figure 4.35: Partial ^{1}H NMR spectrum (500 MHz, D_2O, 298 K) showing the aromatic region of the mesocate (**12**) as the Cl^- salt, (1) before, and (2) after microwave irradiation. Emerging helicate resonances are highlighted in yellow.

This result indicated that under reaction conditions interconversion of the isomers was possible, although in this case it was not to the extent that had been observed for the purified samples when left for hours or days on the lab bench.

To investigate this behaviour further, a pure sample of the mesocate (**12**) as the Cl^- salt was heated in D_2O at 60 °C and 1D NMR spectra collected over the course of seven days. Under these conditions a decrease in the intensity of the triazole hydrogen resonance was observed, which was attributed to exchange with the deuterium in D_2O, while the other aromatic signals remained unchanged (see Figure 4.36). As no resonances corresponding to the helicate were seen to emerge it appeared that simply heating the sample was not enough to induce significant interconversion of the isomers.

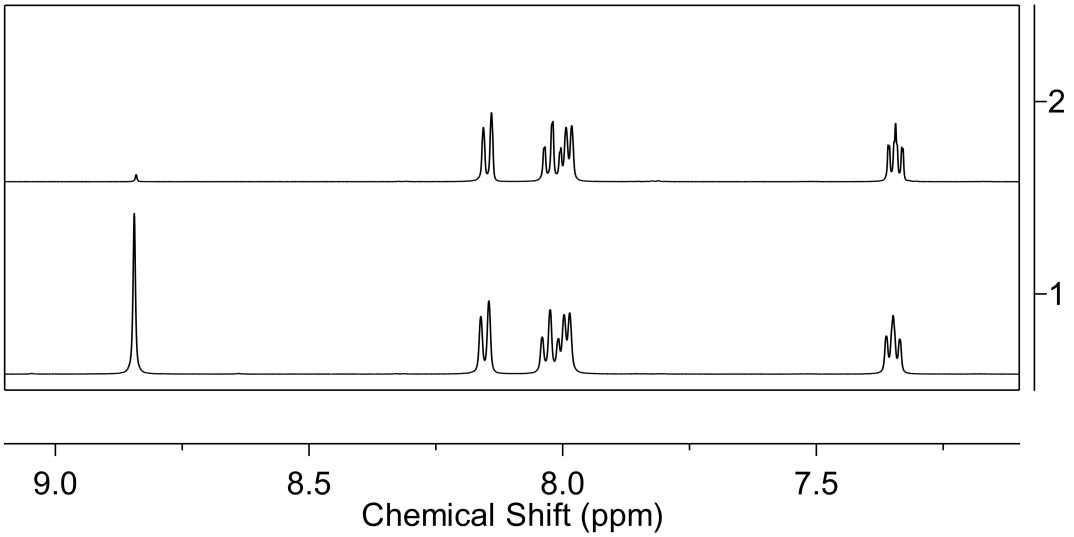

Figure 4.36: Partial ^{1}H NMR spectrum (500 MHz, D_2O, 298 K) showing the aromatic region of the mesocate (**12**) as the Cl^- salt, (1) before, and (2) after heating at 60 °C for 7 days.

For the purified helicate (**13**) heating under microwave conditions again caused a small amount of isomer interconversion. The evolution of signals corresponding to the secondary species (in this case the mesocate, highlighted in yellow) were observed (see Figure 4.37), which suggested that while only a small amount of interconversion was possible under reaction conditions, the mesocate may be the favoured product, given a slightly increased amount was formed from the helicate over the same time period.

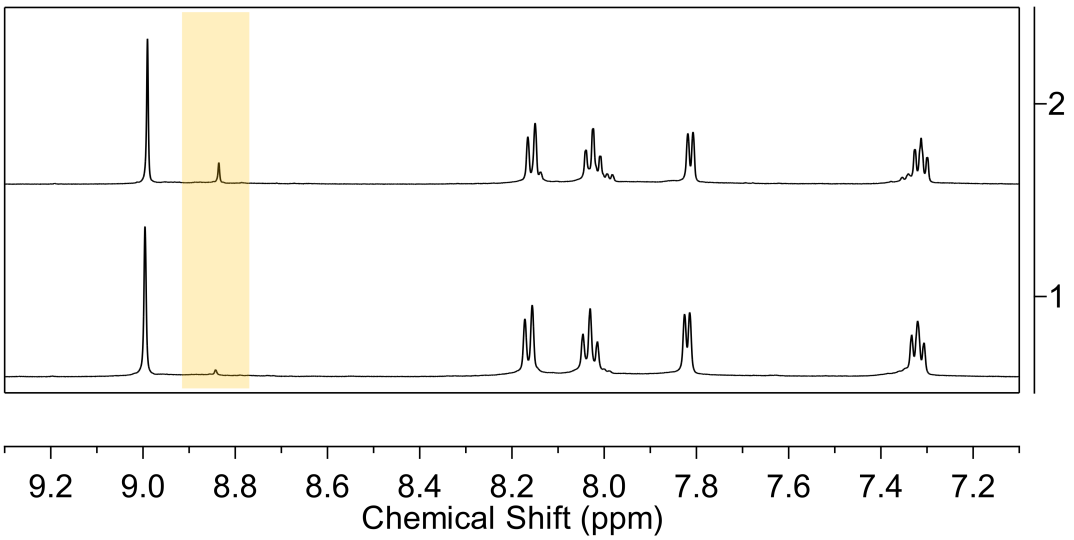

Figure 4.37: Partial ^{1}H NMR spectrum (500 MHz, D_2O, 298 K) showing the aromatic region of the helicate (**13**) as the Cl^- salt, (1) before, and (2) after microwave irradiation. It should be noted that the initial helicate sample contained a small amound of mesocate impurity. Emerging mesocate resonances are highlighted in yellow.

The helicate (**13**) was also heated as the Cl^- salt at 60 °C for 7 days, and under these

conditions very little conversion to the mesocate was observed. This outcome suggested that vigorous conditions (such as those used for the initial synthesis) were required to induce a change in isomer distribution. The NMR spectra for the helicate before and after heating are shown in Figure 4.38 below.

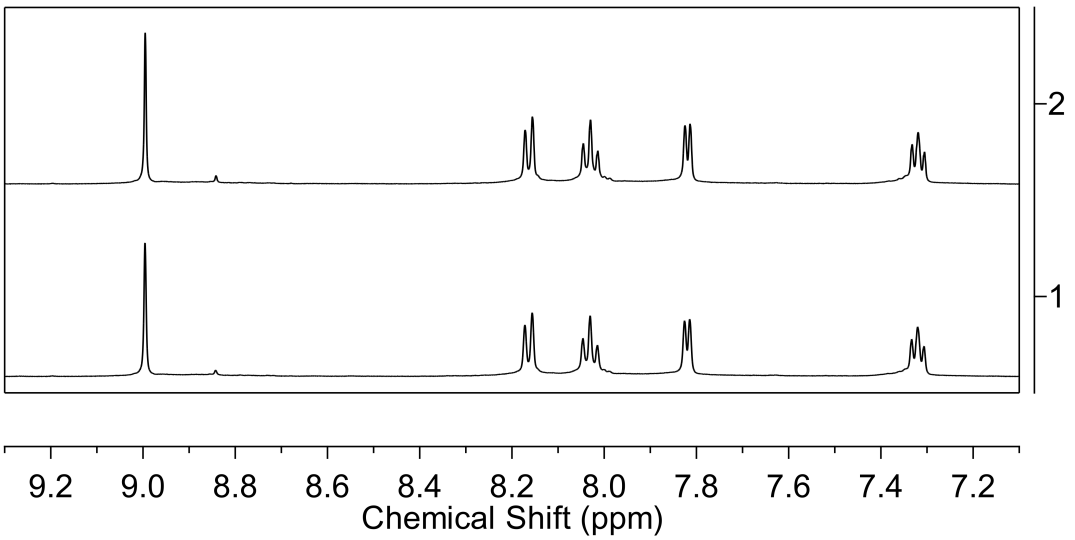

Figure 4.38: Partial ^{1}H NMR spectrum (500 MHz, D_2O, 298 K) showing the aromatic region of the helicate (**13**) as the Cl^- salt, (1) before, and (2) after heating at 60 °C for 7 days.

Given that for both samples interconversion of the isomers had not been observed to a great extent via thermal pathways, our attention turned towards using light-induced isomerisation. The samples which had previously undergone heating as the Cl^- salts in D_2O (60 °C; seven days) were left in ambient light at room temperature for 30 days, and the 1D NMR spectrum collected after this time period. For both the mesocate and helicate, significant conversion between the two isomers was observed under these conditions. The interconversion is most clearly observed in the aromatic region, where hydrogen resonances for the purified compound (either mesocate or helicate) diminished, and resonances corresponding to the other isomer emerged (see Figure 4.39, and 4.40, for the mesocate and helicate respectively). In addition the multiplets corresponding to the *n*-propyl spacer hydrogens at 4.5 ppm and 2.8 ppm greatly increased in complexity indicating the presence of both dinuclear compounds (it should be noted that the resonances at 2.8 ppm are partially obscured residual solvent peaks). The regions of the ^{1}H NMR spectra showing the greatest change after irradiation are shown in Figures 4.39 and 4.40 for samples initially containing purified mesocate and helicate, respectively. It should be noted that the intensity of the triazole hydrogen resonance in the initial mesocate sample is low which was attributed to exchange with the deuterium in D_2O after heating at 60 °C

for seven days in the previous study.

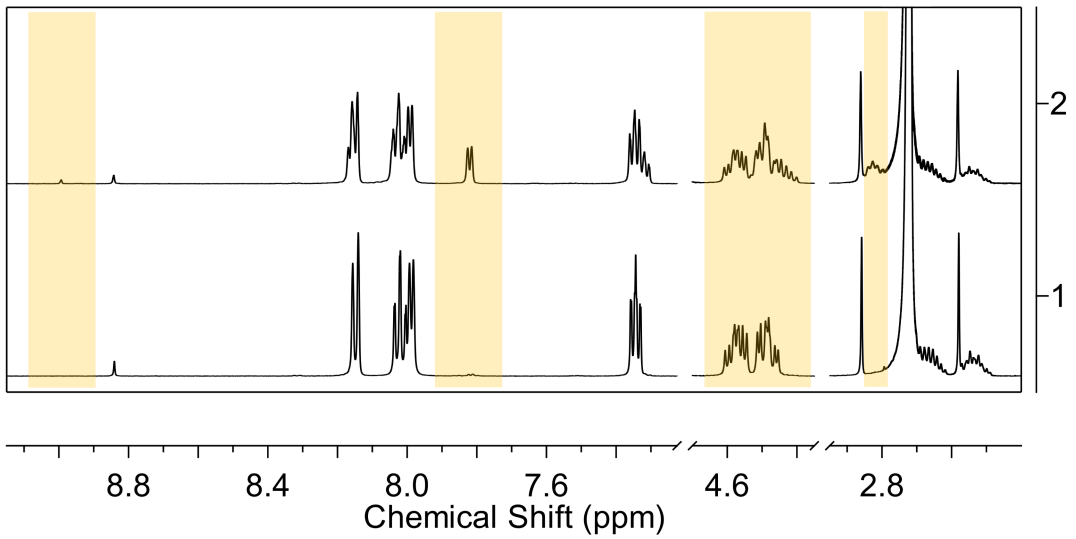

Figure 4.39: Partial ^{1}H NMR spectrum (500 MHz, D_2O, 298 K) showing selected regions of the mesocate (**12**) as the Cl^- salt, (1) before (after heating at 60 °C for 7 days), and (2) after irradiation in ambient light and heat for 30 days. Emerging helicate resonances are highlighted in yellow.

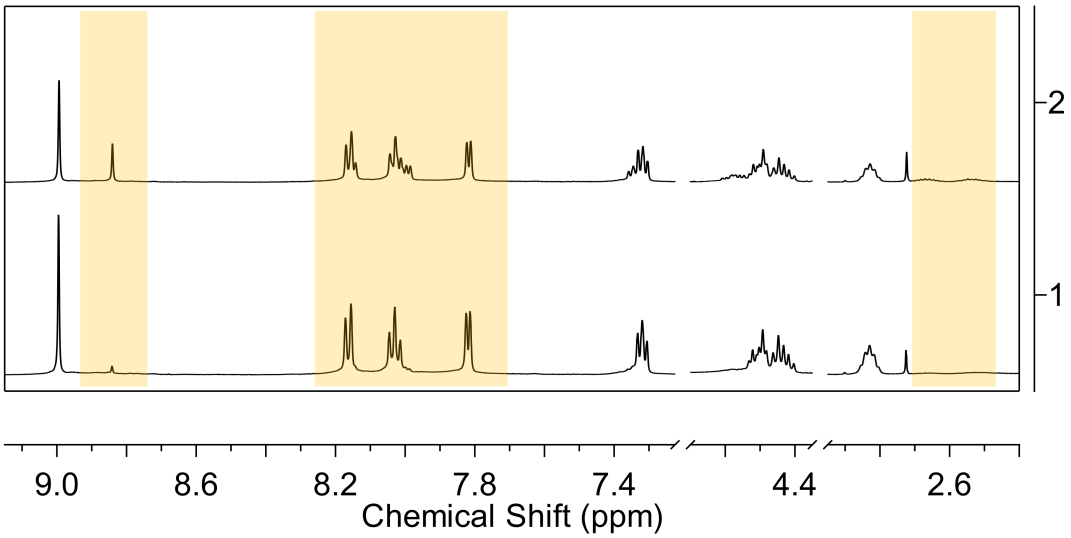

Figure 4.40: Partial ^{1}H NMR spectrum (500 MHz, D_2O, 298 K) showing selected regions of the helicate (**13**) as the Cl^- salt, (1) before (after heating at 60 °C for 7 days), and (2) after irradiation in ambient light and heat for 30 days. Emerging mesocate resonances are highlighted in yellow.

In work by Raymond and co-workers the racemisation of digallium(III) triple-stranded helicate enantiomers ($\Delta\Delta \rightleftharpoons \Lambda\Lambda$) has been proposed to proceed by a Bailar twist, where a *meso* ($\Delta\Lambda$) intermediate is formed, thus avoiding a bond-breaking mechanism.[297,298] In the case of the Bailar[299] or related Ray-Dutt twist,[300] the proposed *meso* intermediate is

considered to be of high energy, with the spacer adopting an unfavoured conformation.[301] As a result, isolation and characterisation of a *meso* intermediate has not been possible in previous studies of the racemisation process. While this process is not specifically for the interconversion of mesocates and helicates, but rather helicate-to-helicate, it represents one possible pathway to isomerisation. However, for the Ru(II) structures discussed in this Chapter containing the *n*-propyl spacer ligand, computational modelling indicated that the mesocate and helicate had similar stabilities (see Section 4.4.1.3). Due to similarities in stability both isomers are able to be isolated in this case, and conversion from $\Delta\Delta/\Lambda\Lambda \rightleftharpoons \Lambda\Delta$ can be observed. While it is possible that isomerisation may occur via a twist mechanism, there are alternative pathways to be considered.

Isomerisation may instead proceed via a bond-breaking mechanism, where at least one of the Ru - N bonds must break in order for the stereochemical rearrangement to occur. Interconversion within families of coordination cages - due to anion dependency, host-guest interactions, or post-assembly modification - has generally been seen for mesocates or helicates converting to larger architectures. These interconversions have been studied for a wide variety of metal centres,[302–309] however there are far fewer examples of simple mesocate-to-helicate isomerisation. One example can be seen in the study of spiroborate-based double-stranded compounds by Ousaka *et al.*,[310] who note that under aqueous conditions cleavage of the B - O covalent bonds (at the coordination site) can proceed, allowing isomerisation. This example is very different to the transition metal chemistry being considered in this thesis as it relates to the cleavage of covalent bonds, but nonetheless illustrates a conversion between mesocate and helicate isomers. More pertinently, Goetz and Kruger reported the formation of triple-stranded Fe(II) compounds, where both the helicate and mesocate exist in DMSO as the BF_4^- salt, but when Cl^- ions are introduced conversion to the helicate is favoured.[311] The authors propose that the preference for the helicate isomer is likely due to two Cl^- ions being bound within the cavity of the helicate, a situation which does not occur for the mesocate.

The ability to control the formation of mesocates and helicates has been a topic of great interest since the first reported mesocate structures. While some studies have supported the odd/even mesocate/helicate rule proposed by Albrecht *et al.*,[8,69] there have been exceptions to this, including the work detailed in this thesis which illustrates the challenges in controlling formation of the two dinuclear isomers. The use of ions to template the synthesis of dinuclear compounds has been explored by Kruger and co-workers (described above),[311] and Cui *et al.*,[312] by employing a range of anions in the synthesis of iron- and copper-containing compounds. In these studies it was found that in the presence of larger

tetrahedral anions mesocate formation was favoured, while smaller spherical or trigonal planar anions directed the formation of helicates.

Aside from those cases noted above, interconversion of helicates to mesocates (or vice versa) has not been reported. In the double- and triple-stranded species studied by Zhang and Dolphin, the authors particularly noted that interconversion was not possible, even upon heating to high temperatures (155 °C).[70,313] For Fe(II) species incorporating the *n*-propyl spacer ligand Wu *et al.* made no mention any instability or interconversion of the mesocate in solution, and the 1D and 2D NMR spectra appeared to indicate a single product present.[291] In terms of other Ru(II) helicate/mesocate pairs, for the double-stranded species described in **Chapter 2** the compounds appeared stable in solution as the Cl^- salts throughout the duration of all biological studies (see **Chapter 3**). In the only other example of Ru(II) helicate and mesocate mixtures, Allison *et al.* noted no changes in either the ^{1}H NMR or UV/Vis spectra for the isolated helicate and mesocate samples in 10% d_6-DMSO/D_2O (although the counter-anion was not specified) at elevated temperatures or over time.[82] As such, the isomer interconversion observed upon irradiation with visible light and at room temperature detailed in this Chapter for the *n*-propyl spacer compounds is thought to be a unique observation for this system.

Isomerisation of Ru(II) compounds by photoconversion is not unknown. The photochemical release of bpy ligands from $[Ru(bpy)_3]^{2+}$ has been reported both in dilute acid (at 95 °C)[314] and chlorinated solvents (at room temperature),[315–317] with irradiation at 436 nm. Furthermore, the photochemical release and rearrangement of ligands in mononuclear ruthenium(II) 4,4′-di-1,2,3-triazolyl compounds, which are structurally similar to the dinuclear compounds described in this Chapter, has been described for the PF_6^- salts in acetonitrile.[318,319] For the *n*-propyl spacer compounds in this thesis, meaningful interconversion of the two isomers is chiefly observed upon irradiation with visible light, rather than heating, which suggests that isomerisation may proceed through a ligand dissociation pathway, similar to that proposed for mononuclear $[Ru(bpy)_3]^{2+}$ compounds. However, a twist mechanism, as proposed in the racemisation of helicates which avoids a bond-breaking process, cannot be fully discounted, particularly in this case as the *meso* compound is a lower energy, stable product able to be isolated.

The unexpected isomerisation of the mesocate/helicate pair containing the *n*-propyl spacer ligand (**9**) was of great interest, as it suggested that the Ru(II) centres in these compounds may be more labile than previously thought. While small amounts of conversion were noted when the samples were exposed to reaction conditions or heat, more extensive isomerisation was observed upon irradiation with visible light, suggesting new pathways

to control the product distribution of dinuclear compounds. It appears that the observed interconversion of isomers is more likely to proceed via a bond-breaking mechanism, with similar behaviour noted for related monoruthenium(II) compounds; however, this unusual property was not explored further in this thesis.

4.4.2 Increasing flexibility: *n*-butyl spacer

In the results discussed above the inclusion of an *n*-propyl spacer in the ligand resulted in a mixture of dinuclear products, indicating that it was possible to break the odd/even rules of formation for compounds of this type by combining a flexible ligand with a relatively inert metal centre. Consequently, attention turned to increasing the length of the spacer further, where a mixture of isomers was again anticipated. In this case, the ligand containing an *n*-butyl spacer (**10**) was synthesised, and formation of Ru(II) compounds undertaken.

The synthesis of a triple-stranded diruthenium compound utilising the 1,4-bis{4-(pyridin-2-yl)-1*H*-1,2,3-triazol-1-yl}butane ligand (**10**) was undertaken using analogous conditions to the previously-synthesised Ru(II) compounds in this Chapter. Analysis of the crude product from a five-hour microwave reaction found it to be primarily composed of two components, with two prominent sets of aromatic signals clearly evident in the NMR spectrum. This appearance was highly suggestive of a mixture of dinuclear species (as had been seen for compounds in **Chapter 2**). However, several additional, low intensity hydrogen resonances were also present in the aromatic region of the spectrum indicating the concurrent formation of a range of other Ru(II) assemblies. As the dinuclear mesocate and helicate were the desired products attempts were made to drive formation to favour these species. Upon shortening of the reaction time (from five hours to two hours) the number of additional minor products did not appear to vary greatly, but extensive, broad underlying signals were observed in the aromatic region (shown as (1) in Figure 4.41 below). These broad signals suggested the production of polymeric material in addition to the discrete Ru(II)-containing compounds. Using the original reaction duration (five hours) two major products were observed, however upon repetition of this reaction the proportion of additional side products varied, despite identical reaction conditions and reagents being used (shown as (2), (3), and (4) in Figure 4.41). The optimal production of dinuclear compounds was found when reaction duration was increased to ten hours, where two major products were clearly observable by ^{1}H NMR spectroscopy (see (5) in Figure 4.41 below). In this case additional side products were still present; however, these were in lower abundance than seen at shorter reaction times. It should be noted that the

product distribution from the five hour reactions was seen to vary significantly (as shown below), but the ten hour reaction generated a crude product of consistent composition.

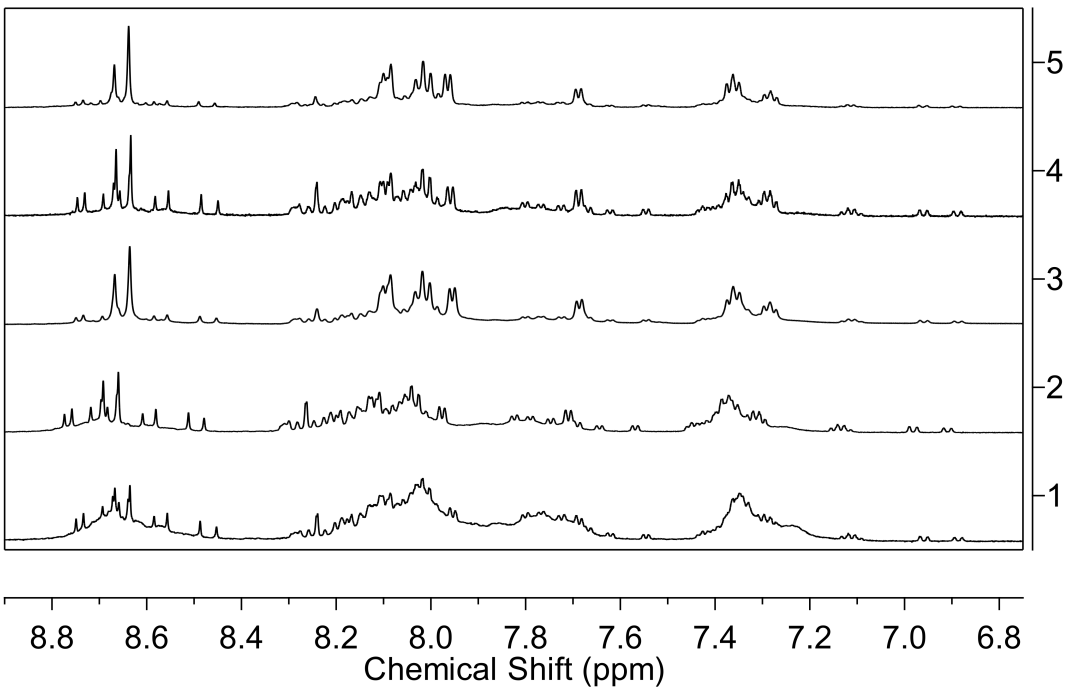

Figure 4.41: Partial ^{1}H NMR spectrum (500 MHz, CD_3CN, 298 K) showing the aromatic region from the crude reaction mixtures for varying reaction times from the microwave reaction to form ruthenium compounds using the *n*-butyl spacer ligand (**10**). (1) 2 hours, (2) - (4) 5 hours, and (5) 10 hours.

To prioritise purification of the dinuclear species isolation of the two major products from the ten hour microwave reaction was undertaken. Based on the pattern of resonances in the aromatic region it was suspected that the crude reaction mixture contained a helicate and mesocate, although given previous experience with the *n*-propyl spacer (described above) this was not entirely certain.

Separation of the two major products was attempted using the chromatographic methods which had been successful for the double-stranded compounds described in **Chapter 2**; however, it was found that the *n*-butyl spacer compounds were not readily separable in this manner. For these separations a yellow smear was observed down the length of the silica column and no separation was observed. It is proposed that retention of the compound on silica gel may be due to the free nitrogen present on the triazole which is not involved in chelation, and may interact strongly with the gel. Regardless, given that purification was not straightforward using silica gel, attention turned to the use of an alternative chromatographic stationary phase and eluent combination.

As described in **Chapter 2** of this thesis the separation of the diastereomers of Ru(II)

compounds has previously been reported chromatographically using an SP-Sephadex C-25 ion exchanger. Initial screening on this solid-phase support using aqueous solutions containing NaCl as an eluent revealed that this case all material eluted as a single yellow band at the same ionic strength (0.6 M). The co-elution of compounds supported the prospect of a mesocate/helicate pair (as both exist as 4^+ cations). Alternative eluents containing various anions were screened for the separation of the two species; however, in all cases the yellow compound either eluted as a single band, or precipitated on top of the column (generally with eluents containing chiral anions).

The relationship of the two species was probed by a DOSY NMR experiment, which revealed that both compounds had similar diffusion coefficients, indicating that they were likely of similar sizes (see Figure D.20 in Section D.2.3 of Appendix D).

Given the likely presence of a mesocate and helicate pair, attention turned to exploiting the differences in chirality to separate these compounds.

4.4.2.1 Separation via resolution

An alternative approach for the separation of the two dinuclear species, avoiding silica gel and ion exchange resin, was next explored. Rather than separating the mesocate and helicate, resolution of the helicate within the mixture of products was instead pursued. Surprisingly, it was found that the resolution of the two helicate enantiomers from this isomeric mixture was quite straightforward. Using a cellulose solid-phase support, in conjunction with an eluent containing the chiral anion (-)-*O,O'*dibenzoyl-(L)-tartrate, one portion of the yellow compound was eluted while the remainder was retained on the column. When analysed by ^{1}H NMR spectroscopy, the first fraction (shown as (1) in Figure 4.42) was found to contain both mesocate and helicate signals (and small quantities of impurities). The column was then washed with either 0.5 M sodium 4-toluenesulfonate or 20% acetone/2 M NaCl, allowing removal of the remaining yellow material. By NMR spectroscopy this fraction was found to contain essentially only a single species (see (2) in Figure 4.42).

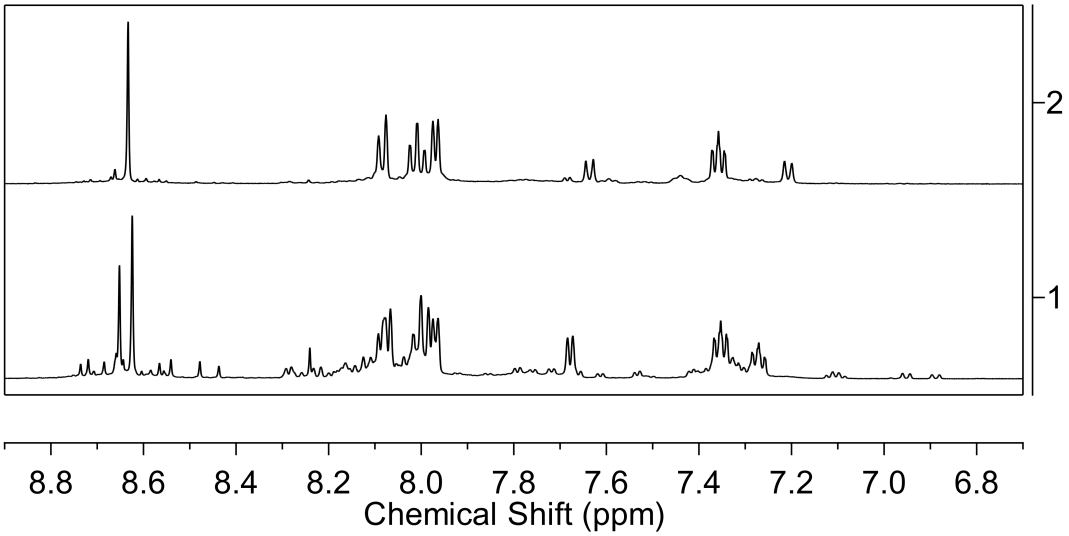

Figure 4.42: Partial ^{1}H NMR spectrum (500 MHz, CD_3CN, 298 K) showing the aromatic region from the resolution on cellulose of the ruthenium compounds using the *n*-butyl spacer ligand (**10**). (1) F1 (containing a mixture of helicate/mesocate) eluted with 0.075 M sodium (-)-*O,O'*dibenzoyl-(L)-tartrate, (2) F2 (containing one enantiomer of the helicate) eluted with 0.5 M sodium 4-toluenesulfonate.

In order to ascertain the composition of the two fractions, CD spectroscopy was performed which gave spectra of identical shape which were opposite in sign throughout the UV-Vis region (see Figure 4.43). The first-eluting fraction (F1) had lower CD activity when adjusted for concentration. This is consistent with the NMR results which show a mixture of two compounds present in (F1). For this sample higher absorbance was recorded by UV-Vis spectroscopy, but lower CD signal overall, suggesting the presence of an achiral component in the mixture, such as a mesocate. The second-eluting fraction (F2) contained a single species by NMR and had higher relative optical activity, indicating that this fraction must contain a resolved chiral compound, likely one hand of the purified helicate. By this method resolution of the two helicate enantiomers was achieved, although (F1) still contained a mixture of other products, thought to be chiefly the mesocate and one hand of the helicate.

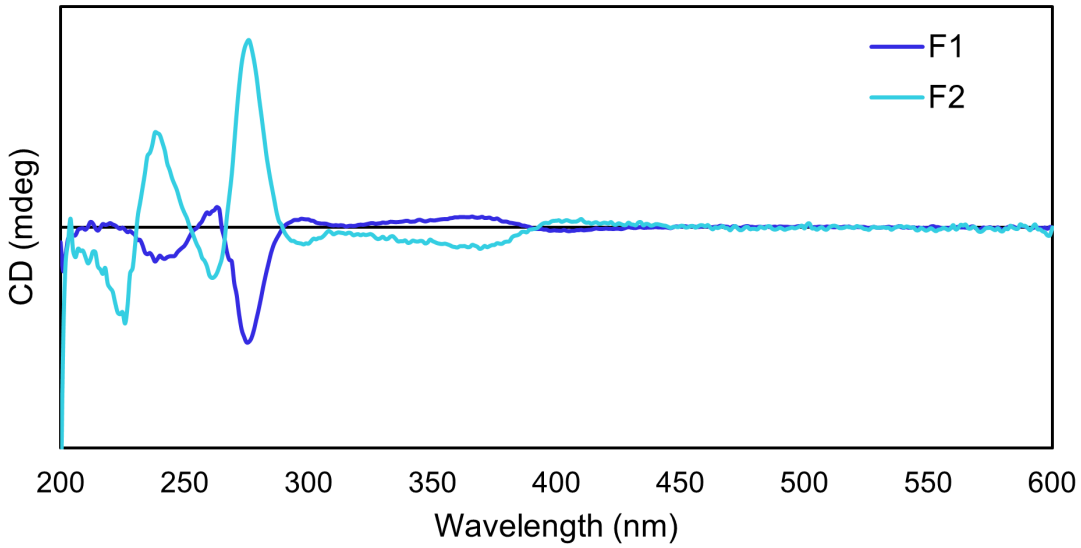

Figure 4.43: CD spectrum of the ruthenium compounds synthesised using the *n*-butyl spacer ligand (**10**), resolved on cellulose with 0.075 M sodium (-)-*O,O'*dibenzoyl-(L)-tartrate eluent, followed by 0.5 M sodium 4-toluenesulfonate. Results suggest that (F1) contains a mixture of mesocate, one hand of the helicate, and a small proportion of side products, while (F2) contains the other hand of the purified helicate.

For the second eluting fraction (F2) which contained one enantiomer of the purified helicate, further characterisation was carried out. From 1D and 2D NMR experiments the hydrogen and carbon resonances of the helicate could be assigned (the spectra are presented in Section D.2.3 of Appendix D). Following the same pattern as for the *n*-propyl spacer helicate, the hydrogens on the ligand spacer appeared as a complicated multiplet (at 4.4 ppm), and a pair of multiplets (at 1.8 ppm). The appearance of complicated multiplets for the spacer hydrogens, rather than the expected doublets, is due to the CH_2 groups becoming chemical-shift inequivalent, as well as each pair of geminal hydrogens becoming magnetically inequivalent. This has been seen for mesocates in **Chapter 2** of this thesis, and the work of Zhang and Dolphin,[70] and agrees with the results of Wu *et al.* for the synthesis of the Fe(II) analogues of these types of compounds, where broad multiplets corresponding to the spacer hydrogens were reported.[291]

The identity of the dinuclear species was further confirmed by HR ESI-MS, where the $[Ru_2\mathbf{10}_3 \cdot 2\,PF_6]^{2+}$ ion was present at *m/z* 766.1169 (see Figure D.32 in Section D.2.3 of Appendix D).

As described earlier in this Chapter for the 1,4-xylyl spacer helicate (**11**), tentative assignment of the isolated helicate enantiomers containing the *n*-butyl spacer was attempted, based on previously reported resolutions of Ru(II) compounds. Based on the direction of CD bands shown in Figure 4.43, F1 (containing a mixture of mesocate, one helicate

enantiomer, and minor side products) is proposed to contain the *P*-helicate ($\Delta\Delta$), while the purified fraction (F2) contains the *M*-helicate ($\Lambda\Lambda$).

Given that resolution had been possible using an aqueous 0.075 M sodium (-)-*O,O′*dibenzoyl-(L)-tartrate eluent it was proposed that the opposite hand of the helicate may be able to be isolated by using an eluent containing the other form of the chiral anion ((+)-*O,O′*dibenzoyl-(D)-tartrate). However, when the original mixture (containing mesocate, racemic helicate, and minor impurities) was loaded onto cellulose and eluted with this solvent the entire sample eluted as a single band. Based on this observation it was evident that the chirality of both the anion and the cellulose must play a key role in resolution of the helicate. This was shown for the 1,4-xylyl spacer helicate (described in Section 4.3.1 of this Chapter) where the importance of the chiral solid-phase support and eluent composition was clear, with variable resolution possible on cellulose using solutions containing an achiral salt (NaCl). For the *n*-butyl spacer compounds, the mesocate, minor products, and both hands of the helicate were found to co-elute from cellulose using sodium (+)-*O,O′*dibenzoyl-(D)-tartrate, and so attention turned to modifying the original reaction conditions to eliminate some of the additional minor impurities, and potentially influence the mesocate and helicate product distribution.

4.4.2.2 Alternative synthetic conditions

As shown previously, variation in reaction time in microwave conditions seemed to greatly influence the product distribution, and so the synthesis of these compounds was instead attempted under reflux conditions at 200°C for three days in ethylene glycol - which had been successful in the synthesis of double-stranded species (described in **Chapter 2**). The ^{1}H NMR spectra of the crude product from this reaction was composed of a complex mixture, as illustrated in Figure D.28 in Section D.2.3 of Appendix D. Under these conditions, while it was possible to see peaks in the aromatic region which could correspond to ruthenium-containing species, broad peaks throughout the spectrum suggested that high levels of polymeric material had also been formed. Purification was attempted using both silica and ion exchange chromatography with identical outcomes to those noted above; the isolation of any discrete supramolecular assemblies was not possible. The identity of the potential Ru(II) compounds observed in this reaction and the shorter microwave reactions was unclear, although they could possibly be larger assemblies, accessible from the 3:2 metal/ligand ratio, or other dinuclear species, as well as polymeric material. Although the desired products were unable to be separated from the reaction mixtures by the chromatographic methods noted, overall it appears that dinuclear compounds are favoured,

something which is particularly evident with increased reaction time and harsher microwave conditions.

The large number of additional peaks seen in the crude NMR spectrum and broad baseline indicative of polymeric species, suggested that reflux conditions were not sufficient to favour the formation of dinuclear products. Given the challenges experienced in attempting to purify compounds incorporating ligands of this type chromatographically a reflux synthesis approach was not further pursued in this thesis.

4.4.2.3 Separation of the helicate and mesocate

Given that separation of the helicate and mesocate species for compounds using the *n*-butyl spacer ligand (**10**) had proved to be challenging by chromatography, alternative methods were considered. The dinuclear compounds incorporating the shorter *n*-propyl spacer ligand (**9**) described in Section 4.4.1 had shown remarkably different solubilities as the Cl^- salts in DMSO, and the same approach was probed for the mixture of compounds containing the *n*-butyl spacer ligand (**10**). This sample as the Cl^- salt appeared to be completely soluble in d_6-DMSO, although when the ^{1}H NMR spectrum was collected there appeared to be predominantly a single set of resonances in the aromatic region (see Figure 4.44). It was unclear whether this indicated the presence of a single species, or if two species with highly overlapping hydrogen resonances were present.

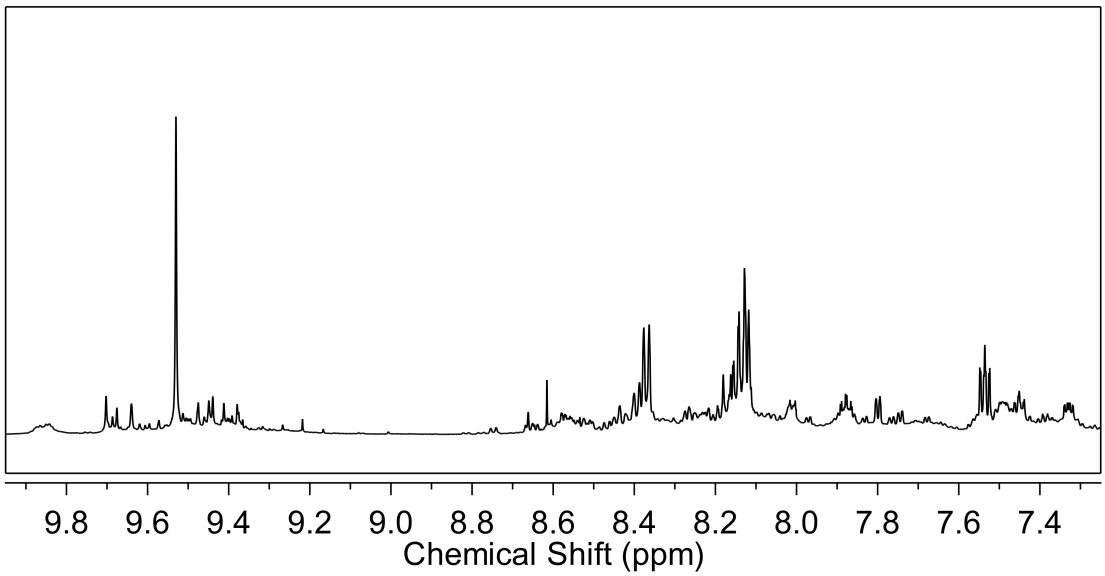

Figure 4.44: Partial ^{1}H NMR spectrum (600 MHz, d_6-DMSO, 298 K) showing the aromatic region from the crude reaction mixture for the formation of ruthenium compounds using the *n*-butyl ligand (**10**) as the Cl^- salt in DMSO.

Investigation using a rotating-frame overhauser effect spectroscopy (ROESY) experi-

ment showed only a single set of cross-peaks in the aromatic region between the major hydrogen signals (see Figure D.26 in Section D.2.3 of Appendix D). Examination in the *n*-butyl spacer region was far more informative, as the highly overlapping multiplets showed separate correlations to the triazole hydrogen resonance, as well as adjacent hydrogens on the spacer. Splitting of these signals (highlighted in yellow in Figure D.27 in Section D.2.3 of Appendix D) suggested that the DMSO-soluble compound was still comprised of two components, with highly overlapping hydrogen resonances in the aromatic region. The additional ROESY cross-peaks seen between the triazole hydrogen and upfield *n*-butyl spacer hydrogens indicated the presence of non-identical environments, as expected in a mesocate/helicate mixture.

From the experiments detailed above it appeared that the Ru(II) compounds present in the crude reaction mixture did not show the same selective solubility in DMSO as for compounds incorporating the *n*-propyl spacer ligand. Given that separation could not be readily achieved in this manner, separation of the compounds containing the *n*-butyl spacer ligand (**10**) was attempted by fractional crystallisation. The use of fractional crystallisation in the resolution of metallic compounds has been discussed in **Chapter 2** of this thesis, but it is also a useful technique in the separation of diastereomers. To find suitable conditions for separation of the Ru(II) compounds containing the *n*-butyl spacer ligand, solutions containing a range of chiral and achiral anions were screened by dropwise addition to a solution of the Cl^- salt of F1 from the resolution (the fraction containing the mesocate and one enantiomer of the helicate, predominantly).

In the first instance (-)-*O,O′*dibenzoyl-(L)-tartrate, which had proved to be a useful anion for resolution, was trialled for the separation of the helicate and mesocate. Upon addition of this anion precipitation was observed and by ^{1}H NMR spectroscopy a change helicate/mesocate ratio was evident. However, complete separation was not achieved and it was concluded that (-)-*O,O′*dibenzoyl-(L)-tartrate was not sufficiently discriminating to allow separation of the dinuclear species.

Following this PF_6^- was selected for fractional crystallisation. In this case, rapid precipitation of the compound was observed with very little yellow colour remaining in solution. ^{1}H NMR spectroscopy showed no meaningful change in the helicate-to-mesocate ratio, suggesting that the Ru(II) compounds as the PF_6^- salts were too insoluble to be separated by this methodology. SO_4^{2-} and $S_2O_6^{2-}$ were also investigated as possible alternatives; however, in both of these cases no precipitation was observed upon addition to F1 (the mesocate/helicate mixture), indicating that the SO_4^{2-} and $S_2O_6^{2-}$ salts of the Ru(II) compounds were soluble in aqueous media.

Finally, BF_4^- was trialled and the initial experiments proved promising, with a yellow precipitate observed and significant colour remaining in solution. Analysis by ^{1}H NMR spectroscopy revealed that the precipitate contained two sets of peaks (believed to correspond to the two dinuclear Ru(II) compounds) while the solution contained one major set of peaks, as well as significant proportions of minor impurities (see Figure D.29 in Section D.2.3 of Appendix D). This result indicated that it was possible to remove the minor impurities, and thus isolate a purified mixture of the dinuclear species; however, despite concerted attempts to separate the helicate and mesocate it was found that BF_4^- was not sufficiently discriminating to allow complete separation.

The highest purity samples after two rounds of fractional crystallisation were compared to the purified helicate from resolution (F2; shown as (1) below), allowing the composition of the two impure fractions to be assessed. Based on similarities in the ^{1}H NMR spectra (Figure 4.45) it appeared that in the precipitated sample (2) the helicate was the major product, although the mesocate can also be seen in this fraction (highlighted in red). In the solution (3) it is likely that both mesocate and helicate are present, in addition to a number of unidentified minor products. All key resonances relating to the dinuclear species are highlighted in yellow, with those assigned specifically to the mesocate in red, below.

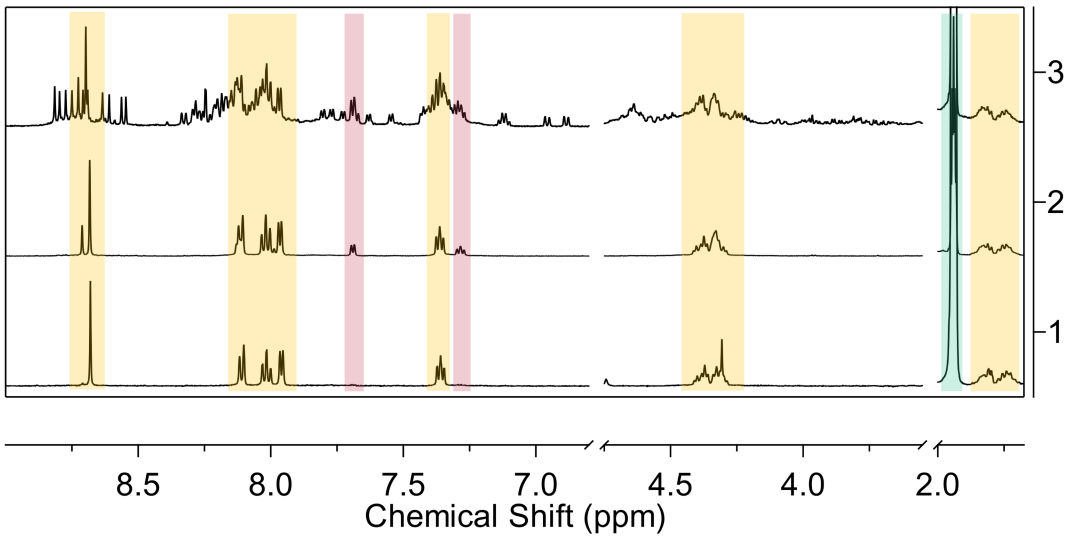

Figure 4.45: Partial ^{1}H NMR spectrum (500 MHz, CD_3CN, 298 K) comparing samples from the second round of fractional crystallisation using BF_4^- for F1, and the purified helicate enantiomer (F2 from resolution) of the Ru(II) compounds incorporating the *n*-butyl spacer ligand (**10**). (1) F2 of the helicate (shown here as the BF_4^- salt), (2) Precipitated sample (shown here as the BF_4^- salt), (3) Solution sample (shown here after exchange to the PF_6^- salt). The key resonances presumed to be due to dinuclear species are highlighed in yellow, with those assigned specifically to the mesocate in red, while peaks corresponding to the solvent are highlighted in green.

Overall, BF_4^- proved to be the most promising anion for fractional crystallisation. It was found that the dinuclear Ru(II) compounds were able to be separated from the unknown side products; however, after two cycles of fractional crystallisation neither the mesocate and helicate, or the unknowns, were completely pure. It should be noted that separation of the dinuclear species from the crude product mixture (containing all species) was also attempted using BF_4^-; however, this approach resulted in less separation. Despite not fully purifying all compounds, a 'pure' dinuclear mixture was obtained (see (2) in Figure 4.45), which may simplify diastereomer separation in future studies; however, further experiments were not pursued in this thesis.

4.4.2.4 Relative energy modelling

Despite incomplete separation of the mesocate and helicate isomers (and other species), the product distribution of the dinuclear compounds was investigated computationally by DFT. The relative stability of the helicate (**14**) and mesocate (**15**) incorporating the *n*-butyl spacer ligand (**10**) were calculated. As for the double-stranded compounds in **Chapter 2**, and *n*-propyl spacer compounds described earlier in this Chapter the calculations were performed both *in vacuo* and in a dielectric medium, using the dielectric constant of acetonitrile.

Table 4.2 shows the relative energy (ΔE) and relative Gibbs free energy (ΔG) *in vacuo* and in acetonitrile of the helicate with respect to the mesocate, for compounds containing the *n*-butyl spacer ligand (**10**).

Table 4.2: Relative stability of the *n*-butyl spacer helicate (**14**) with respect to the mesocate (**15**).

	ΔE (kJmol)	ΔG (kJ/mol)
Vacuum	3.3	-5.6
Acetonitrile	16.0	7.1

From these results it was seen that in general the mesocate was a more stable isomer than the helicate in acetonitrile, with $\Delta E = 16.0$ kJ/mol and $\Delta G = 7.1$ kJ/mol. This was not entirely reflected in the product distribution with the helicate being the primary product observed experimentally. Considering the relative stabilities of the two compounds, the calculated difference in energies was very small, particularly compared to the double-stranded compounds described in **Chapter 2**. As a result, it is unsurprising that both isomers can be detected experimentally, although, as noted for all other compounds in

this thesis, the relatively inert Ru(II) metal centre may also influence the final product distribution. The full results of the DFT calculations and the modelled structures are presented in Section D.7.2 of Appendix D.

Given the challenges faced in the separation of the dinuclear Ru(II) species containing the *n*-butyl spacer ligand, which have been discussed in detail in this Chapter, no investigations into potential isomerisation were undertaken. Dinuclear compounds containing the *n*-propyl spacer ligand showed extensive photoisomerisation, and so it is likely that those containing the *n*-butyl spacer ligand may exhibit similar behaviour. If isomerisation does occur, it may further complicate the separation of compounds which has been generally attempted by fractional crystallisation in aqueous solutions. Furthermore, the identity of multiple unknown species, which were seen in all samples regardless of reaction time or conditions, adds another layer of complexity in predicting the product distribution for supramolecular assemblies incorporating the *n*-butyl spacer ligand. The identity of these products was not further investigated in this thesis.

4.5 Biological interactions

As discussed in **Chapter 3** of this thesis, metallohelicates have elicited great interest for their potential applications in biological settings, particularly as DNA binding agents.[204] In particular, the interactions of triple-stranded compounds with DNA have been thoroughly studied by the group of Hannon, where an Fe(II) helicate was found to bind strongly in the major groove,[206–208] with the Ru(II) analogue proposed to bind in a similar fashion.[73,78,172] Of particular interest to this thesis are the enantiomer-specific interactions reported by Glasson *et al.* for a triple-stranded Ru(II) helicate with oligonucleotides,[66] which were studied by DNA-affinity chromatography,[154] and dialysis methods.

While limited biological studies have been undertaken for the existing compounds in this thesis (the anti-bacterial properties of the helicate containing the 1,4-xylyl spacer (**11**) have been screened),[80] the relatively high stability of this helicate made it a promising candidate for DNA binding. It was anticipated that the enantiomeric specificity observed for the helicate of Glasson *et al.* with DNA may also be observed in this case, and given the successful resolution of the helicate (**11**) the interactions of both enantiomers were able to be probed.

For the triple-stranded helicate containing the 1,4-xylyl spacer ligand (**11**), dialysis experiments using ct-DNA were conducted in the same manner as described in **Chapter 3**, to ascertain whether the binding of this compound to DNA showed an enantiomeric

preference. In addition, LD spectroscopy was carried out for a number of compounds, including those with modified spacers, to gain information regarding the general manner of compound-DNA interaction. Not all compounds were screened in this manner due to difficulties in separation, purification, and stability which have been outlined above.

4.5.1 1,4-Xylyl spacer helicate (**11**)

4.5.1.1 Dialysis

Dialysis of ct-DNA with a racemic mixture of the 1,4-xylyl spacer helicate (**11**), as the Cl^- salt was carried out. Over a dialysis period of 48 hours at room temperature no particular enantiomeric specificity was observed. The CD spectrum of the outer dialysis solution is shown in Figure 4.46 below, along with the two enantiomers from the resolution on cellulose detailed previously, with all samples normalised for concentration. In the CD traces it can be seen that there is no CD response in the outer dialysis solution, suggesting that there is no particular preference for one enantiomer in terms of DNA binding. The inner solution, containing the ct-DNA was observed to change colour, from colourless pre-dialysis, to yellow post-dialysis, indicating that the Ru(II) helicate was able to permeate the membrane, however the CD spectrum indicates that both solutions contain a racemic mixture.

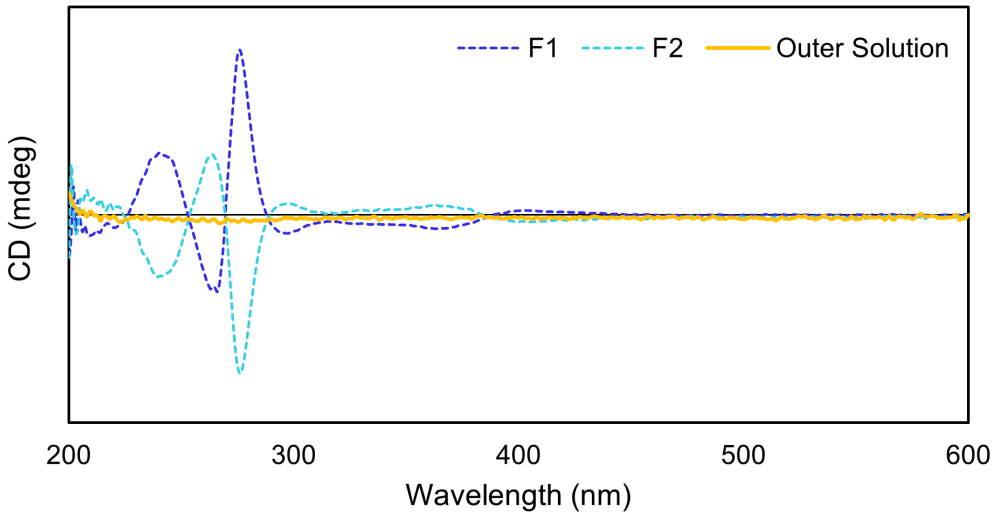

Figure 4.46: CD of the outer solution from the dialysis of the triple-stranded diruthenium(II) helicate containing the 1,4-xylyl spacer ligand (**8**; $[Ru_2L_3] \cdot Cl_4$) with ct-DNA, in comparison to the resolved helicate fractions (F1 and F2 from resolution on cellulose using 2 M NaCl), showing no enantiomeric enrichment.

Despite the lack of enantiomeric enrichment, the formation of a DNA-helicate complex could not be ruled out. In this case it may be that both hands bound to DNA by similar

mechanisms or in similar ratios, resulting in no net change in the composition of the outer solution from dialysis. However, it may also be that there are only very weak interactions between the compound and DNA, or no interactions at all, with the racemic mixture being maintained in solution as the compound equilibrates across the dialysis membrane.

4.5.1.2 LD Spectroscopy

Given that dialysis studies did not show a specific enantiomeric preference for the 1,4-xylyl spacer helicate (**11**) with DNA, further experiments were conducted to ascertain whether any DNA-helicate complex could be detected. Based on the DNA binding reported by Glasson *et al*,[66] and Hannon and co-workers,[77,172] for other triple-stranded diruthenium helicates it was anticipated that the triple-stranded compounds described in this Chapter would also interact in biological settings. In order to determine whether there was any interaction between the DNA and Ru(II) compound, LD spectroscopy studies were carried out using the two resolved fractions of the helicate. As described in **Chapter 3**, interaction of the DNA with the Ru(II) compound was expected to result in perturbation of the LD spectrum, particularly impacting the negative band at 260 nm. Species capable of intercalation can stiffen and elongate the DNA, while for groove binding species bending or kinking is expected.

Titration of F1 of the 1,4-xylyl spacer helicate (**11**) with ct-DNA showed a decrease in LD signal at 260 nm, the same trend as observed for the double-stranded compounds presented in **Chapter 3** (see Figure 4.47). A decrease in magnitude of this negative band suggests a loss of DNA orientation which may be due to coiling or bending caused by interaction with the compound, indicative of groove binding. However, in this case it was clear that the interaction did not impact the native state of the DNA to the same extent as seen for the double-stranded compounds previously. The magnitude of change at 260 nm is significantly less than for samples described in **Chapter 3**, suggesting that the compound may not bind as strongly, or in a manner that disturbs the DNA structure. The change in ct-DNA LD response at 260 nm upon addition of F1 of **11** is presented in Figure D.49 (see Section D.8.2 of Appendix D).

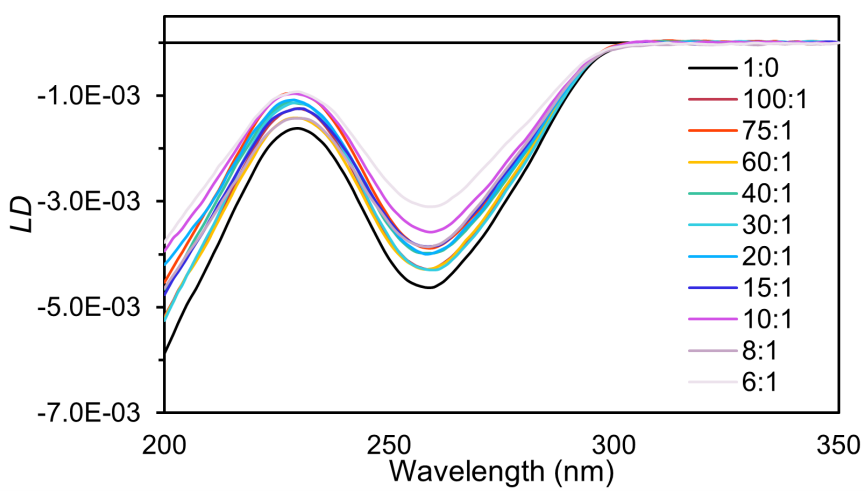

Figure 4.47: LD spectrum of ct-DNA (2×10^{-4} M; K_2HPO_4/KH_2PO_4 (10 mM), NaCl (10 mM), pH 7.3, 25 ° C) and in the presence of increasing concentrations of triple-stranded ruthenium(II) helicate (**11**) using F1 from the resolution on cellulose with 2 M NaCl.

While not suggesting particularly strong interactions between the helicate and DNA, the LD spectroscopy results nevertheless indicated that binding did occur. Given that the previous dialysis studies with this helicate had not indicated a strong enantiomeric preference for binding, further LD studies were carried out, this time using the other enantiomer from the resolution on cellulose with 2 M NaCl.

The LD titration spectrum for ct-DNA with the second enantiomer of the triple-stranded helicate (**11**) is shown below in Figure 4.48. As for F1, perturbation of the DNA LD signal at 260 nm was again observed upon addition of F2, although not in the same manner or to the same extent. The decrease at 260 nm was very small, and no clear trend was evident, with erratic variation noted for some ratios of added compound. Overall, it appeared that there may be a difference in the manner of DNA interaction for the two enantiomers, where F1 caused a noticeably larger loss of DNA orientation and F2 had less of an effect. However, the strength of binding was not able to be elucidated due to the variability in the data. The overall change in ct-DNA LD response at 260 nm upon addition of F2 of **11** is presented in Figure D.50 (see Section D.8.2 of Appendix D).

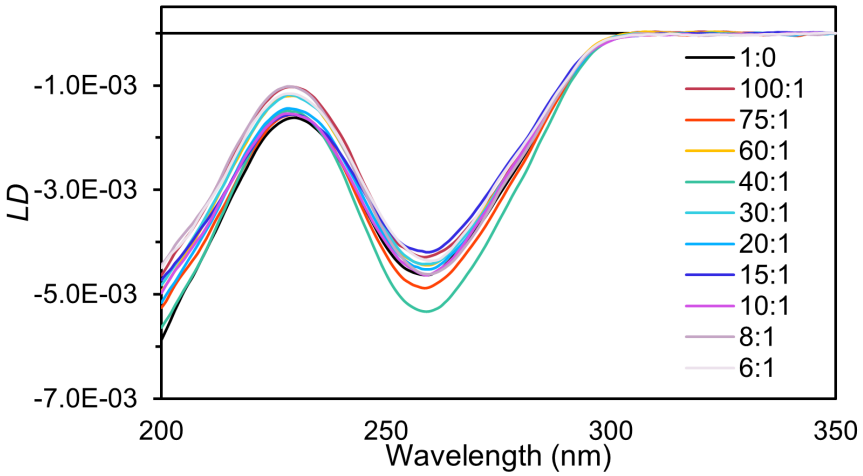

Figure 4.48: LD spectrum of ct-DNA (2×10^{-4} M; K_2HPO_4/KH_2PO_4 (10 mM), NaCl (10 mM), pH 7.3, 25 ° C) and in the presence of increasing concentrations of triple-stranded ruthenium(II) helicate (**11**) using F2 from the resolution on cellulose with 2 M NaCl.

Perturbation of the LD signals for native DNA upon addition of either enantiomer of the triple-stranded helicate (**11**) was not as pronounced as for the double-stranded compounds described in **Chapter 2** of this thesis. Furthermore, in comparison to other helicates studied by others using this method the changes in LD spectra are relatively minor. Coiling of the DNA (indicated by a decrease in DNA LD signal at 260 nm) is consistent with groove binding, although the low magnitude of this response may indicate weak or non-specific interactions between the helicate (**11**) and DNA. Given the size of the Ru(II) helicate, binding in the major groove of DNA seems more likely as the compound would be too large to fit in the minor groove. While the dialysis studies showed that there was no specific preference for DNA binding with one enantiomer over the other, when considered alongside the LD analysis, it seems that both enantiomers can interact with DNA to some degree. The LD results suggest that the manner of DNA interaction may vary between the two enantiomers, with coiling or bending observed to different extents; however, it is proposed that if the enantiomeric preference is not particularly strong and the overall interactions are quite weak, any enantiomeric enrichment present in the dialysis samples may not be detectable.

Based on these results the helicate containing the 1,4-xylyl spacer ligand does not appear to have strong interactions with DNA, or a clear enantiomeric preference. Of all the ruthenium helicates studied in this thesis this compound had the most facile synthesis and resolution, as well as high stability, which had made it a promising candidate to be studied in biological systems. One caveat is the interesting behaviour observed by NMR as the Cl^- salt in D_2O described earlier in this Chapter which suggests that changes in conformation or stability should be considered when studying this helicate in aqueous

media. Despite all redeeming synthetic qualities the compound did not show significant DNA binding, and so attention turned to other similar dinuclear compounds, containing the *n*-propyl and *n*-butyl spacer ligands, the syntheses of which have been described earlier in this Chapter.

4.5.2 *n*-Propyl spacer compounds (**12** & **13**)

At the time of the biological study, the "mystery" secondary species (later found to be the helicate) had not yet been identified in the product mixture for compounds containing the *n*-propyl spacer ligand. As a result, biological studies were carried out on what was thought to be a sample of pure mesocate, although in reality it was a mixture of dinuclear compounds. In any case, the ready interconversion of isomers which has been noted under visible light irradiation in aqueous solutions adds another layer of complexity when designing DNA binding experiments. The unique isomerisation behaviour, while being extremely interesting, potentially impacts the usefulness of these compounds in biological settings particularly as the mechanism of isomerisation has yet to be determined.

4.5.2.1 LD Spectroscopy

To ascertain whether the diruthenium compounds containing the *n*-propyl spacer ligand (**9**) were able to bind to DNA, LD experiments were conducted for the mixture of helicate (**13**) and mesocate (**12**) isomers, as at that time the presence of a secondary product had not been identified. As seen for experiments with the 1,4-xylyl spacer helicate, only a small decrease in LD signal at 260 nm was recorded (see Figure 4.49). A decrease in signal at this wavelength is consistent with condensing or coiling of the DNA, and potential groove-binding of the compound, but again this was significantly smaller than seen for previously studied double-stranded species (the change in ct-DNA LD response at 260 nm is shown in Figure D.51 in Section D.8.2 of Appendix D).

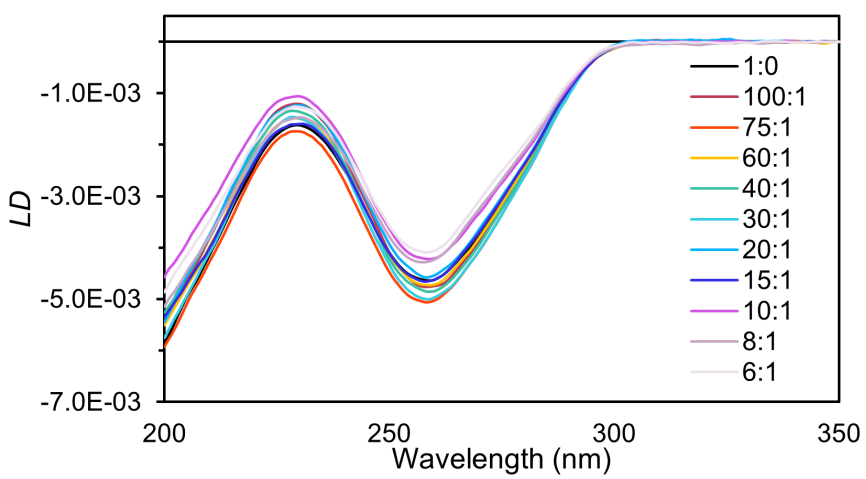

Figure 4.49: LD spectrum of free DNA (2 x 10^{-4} M; $K_2HPO_4/KHPO_4$ (10 mM), NaCl (10 mM), pH 7.3, 25 °C) and in the presence of increasing concentrations of the mesocate/helicate (**12**/**13**) mixture of the triple-stranded ruthenium(II) compounds incorporating the *n*-propyl spacer ligand (**9**).

As for the enantiomers of the 1,4-xylyl spacer helicate (**11**), the change in LD reponse was significantly lower than that observed for the double-stranded compounds (see **Chapter 3**). The recorded decrease in the DNA band at 260 nm indicated that there was some interaction between the mixture of compounds and DNA, but again the strength and specific manner of binding was not able to be determined. Once more the results suggested that the compounds may be groove binding and it is proposed that interactions likely occur in the major groove of the DNA, due to the size of the Ru(II) assemblies. In retrospect, knowing that two isomers were present in the sample (the mesocate and the helicate) it is unclear whether there is either an isomeric or enantiomeric preference in the biological interactions. Repeating these studies would be worthwhile using the purified isomers to determine whether there is a great difference in the strength or manner of DNA binding, although the potential for interconversion of the isomers should be carefully considered.

4.5.3 *n*-Butyl-spacer helicate (**14**)

The final DNA binding studies were conducted using one enantiomer of the triple-stranded helicate incorporating the *n*-butyl spacer ligand (**10**). As outlined above the separation of the mesocate and second enantiomer of the helicate (from the resolution on cellulose using 0.075 M sodium (-)-*O,O'*dibenzoyl-(L)-tartrate) has not yet been achieved, and so the interactions of this mixture of compounds with DNA was not investigated. LD spectroscopy was only conducted on the second eluting fraction from the resolution, which contained a single enantiomer of the helicate (F2 of **14**).

4.5.3.1 LD Spectroscopy

For other compounds in this Chapter only small changes were seen in the LD spectra of ct-DNA upon addition of Ru(II) helicate or mixture. In all of these cases a small decrease in magnitude at 260 nm was recorded which indicated coiling or condensing of the DNA, a trend usually associated with groove binding. Interestingly, the same behaviour was not observed upon addition of F2 of the *n*-butyl spacer helicate (**14**). For this sample a slight increase in LD signal at 260 nm was recorded (see Figure 4.50), suggesting elongation or stiffening of the DNA. This behaviour is generally seen for compounds that bind by intercalation. For F2 of this helicate the overall change in DNA signal was small (as for the other compounds described in this Chapter), but the changes were quite inconsistent between additions. Comparison of the LD response at 260 nm showed little net change in the ct-DNA signal overall (see Figure D.52 in Section D.8.2 of Appendix D) and as a result it is unclear whether there are meaningful interactions between F2 and DNA.

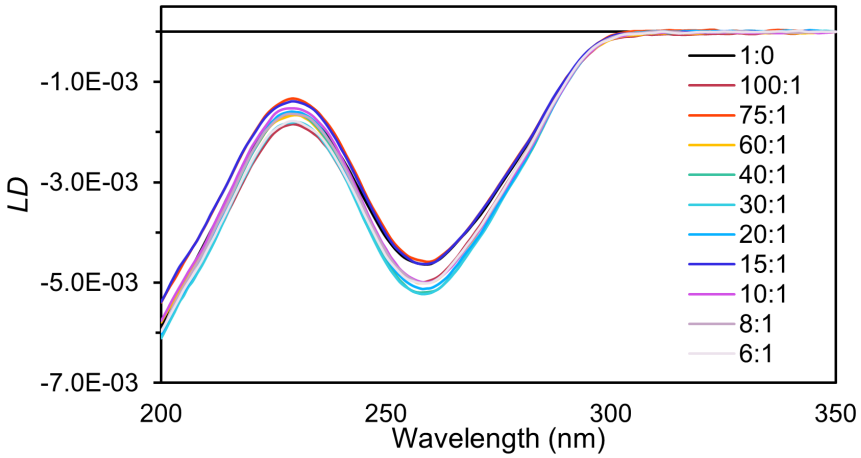

Figure 4.50: LD spectrum of free DNA (2 x 10^{-4} M; $K_2HPO_4/KHPO_4$ (10 mM), NaCl (10 mM), pH 7.3, 25 °C) and in the presence of increasing concentrations of one enantiomer (F2) of the triple-stranded ruthenium(II) helicate (**14**) incorporating the *n*-butyl spacer ligand (**10**).

Although elongation of DNA is generally associated with intercalation, it was surprising that this particular helicate would interact with DNA in such a different manner than the similar triple-stranded compounds investigated earlier in this Chapter. The variation in DNA LD signal upon further addition of the Ru(II) compound made it challenging to speculate as to the exact manner of binding, but it is proposed that the interactions are likely weak or non-specific. Repetition of these experiments using this helicate enantiomer (F2) as well as the other helicate enantiomer and mesocate isomer (contained in F1 from the resolution) would be highly informative, and provide insight into whether the compounds are weak groove binders (as proposed for the 1,4-xylyl and *n*-butyl spacer compounds) or if another mode of interaction with DNA is possible.

4.5.4 Summary of biological interactions

Based on the strong and specific DNA binding reported by others for triple-stranded Ru(II) helicates,[66,73,78,172] it was anticipated that the triple-stranded compounds described in this Chapter may be well suited to biological studies. Disappointingly, for the 1,4-xylyl spacer helicate (**11**) no enantiomeric enrichment was seen in dialysis studies with ct-DNA, suggesting that the compound did not bind in an enantiomerically specific manner. The presence of a DNA-helicate complex was established by LD spectroscopy where coiling/condensing of the DNA showed that the compound may bind in a groove, likely the major groove. Overall, the interactions appeared to be weak, particularly in comparison to those of DNA with the double-stranded compounds described in **Chapter 2** of this thesis. Furthermore, the two enantiomers of the 1,4-xylyl spacer helicate (**11**) appeared to show slight differences in the LD response upon addition to ct-DNA, although this was not compelling evidence of a clear enantiomeric preference.

LD spectroscopy studies of ct-DNA with a mixture of the mesocate (**12**) and helicate (**13**) synthesised from the *n*-propyl spacer ligand (**9**) also indicated potential groove binding, as evidenced by a small decrease in DNA LD signal at 260 nm. For these compounds the interactions were likely even weaker than those seen for the enantiomers of the 1,4-xylyl spacer helicate (**11**), although this may be exacerbated by the presence of a mixture of isomers in solution, potentially diluting the specificity of interactions.

For the final compound studied, one enantiomer (F2) of the *n*-butyl spacer helicate (**14**), the opposite behaviour was seen and stiffening/elongation of the DNA was observed by LD spectroscopy. In this case the variation in LD signal for DNA upon addition of the compound did not appear to follow a clear pattern (as had been observed for other dinuclear compounds) suggesting that the interactions were weak or non-specific. Without being able to compare to the other helicate enantiomer or mesocate isomer, which are yet to be isolated, it is not possible to reliably determine the manner of binding with DNA, and investigate whether the stereoisomers show significant differences in terms of biological interactions.

Overall, none of the compounds described in this Chapter appear to show strong DNA binding which is in contrast to biological studies of supramolecular structures containing similar ligands. For analogous Fe(II) helicates and mesocates studied by the Crowley group, molecular modelling to examine the interactions between the compounds and DNA duplex and triplex architectures has been carried out.[290] These studies revealed that all Fe(II) compounds (including those with a 1,4-xylyl spacer and *n*-propyl spacer) fit into the

major groove. This observation supports the LD spectroscopy findings described in this Chapter using the Ru(II) analogues, where groove binding was the most likely scenario.

In terms of other biological studies, for Co(III) and Ru(II) helicates synthesised by the Crowley group (where the Ru(II) helicate contained the 1,4-xylyl spacer ligand) only modest anti-bacterial activity has been shown, thought to be due to the high charge of compounds which may prevent transport through the bacterial cell membranes.[80,287] Further biological studies have recently been reported for two Co(III) compounds, a mesocate containing methylene spacer ligands and helicate containing 1,4-xylyl spacer ligands, both of which exhibited potent anti-cancer activity and good selectivity.[320] These Co(III) compounds were found to accumulate in the cell nuclei, prompting the interaction with DNA to be investigated. Both showed preference for A - T over G - C rich sequences, with LD spectroscopy studies indicating groove binding. For these Co(III) compounds a complete loss of LD signal due to DNA orientation is seen at a 10 : 1 DNA/compound ratio, which is significantly larger than the change seen for the Ru(II) compounds described in this Chapter (especially those containing the *n*-propyl and *n*-butyl spacer ligands). From comparison of these results it can be inferred that substitution of the metal centre, going from Ru(II) to Co(III), has a dramatic impact on the strength of interactions with DNA.

4.6 Conclusions and future directions

In this Chapter the design and synthesis of triple-stranded diruthenium(II) compounds has been outlined. Taking inspiration from the work of Glasson *et al.*,[66] and Kumar *et al.*,[80] the synthesis of Ru(II) compounds was undertaken utilising microwave synthesis conditions. Initially, an existing diruthenium(II) helicate (**11**), originally described by Kumar *et al.*, was successfully synthesised. This compound was able to be resolved using cellulose chromatography with eluents containing achiral anions, a technique developed by the Hannon group,[67] and ionic strength was found to be a key factor in controlling the extent of resolution. Using an aqueous 2 M NaCl eluent one enantiomer was able to be isolated, while the other was retained on the solid-phase support. Collection of the second enantiomer was possible by washing the column with either 20% acetone/2 M NaCl or 0.5 M sodium 4-toluenesulfonate. The fractions were tentatively assigned as the *M*-helicate (F1) and *P*-helicate (F2), based on reported resolutions of other mono and dinuclear Ru(II) assemblies.

While in the majority of cases the helicate was found to be the sole product, a secondary species was occasionally observable by ^{1}H NMR spectroscopy. DOSY experiments suggested that the two compounds, the helicate and unknown, had a similar diffusion coefficient, and were thus of similar size. Interestingly, in the the original work of Kumar *et al.* no secondary product was described, although it should be noted that in the work detailed in this Chapter the unknown was not consistently observed experimentally. It was found that the the helicate was able to purified by fractional crystallisation by careful addition of BF_4^- to an aqueous solution of the product mixture as the Cl^- salt. Under these conditions the helicate precipitated out as the BF_4^- salt, while a mixture of helicate and unknown remained in solution. Given that the helicate was the desired product, the identity of the unknown was not further investigated in this thesis.

The DNA-binding properties of the two enantiomers of the 1,4-xylyl spacer helicate were investigated by dialysis and LD studies. Based on the strong and selective binding of other triple-stranded ruthenium helicates with DNA seen by Glasson *et al.*,[66] and Hannon and co-workers,[77,172] it was anticipated that the 1,4-xylyl spacer helicate would exhibit enantioselective interactions. However, this was not the case with no enantiomeric enrichment observed in dialysis experiments with ct-DNA. Through LD binding studies it was established that both helicate enantiomers did interact with DNA, where coiling indicated that the compounds may bind in the major groove in a similar fashion to the Co(III) analogue studied by Crlikova *et al.*[320] While minor differences were observed in the

LD response upon addition of the two enantiomers to ct-DNA, the interactions appeared to be quite weak overall, particularly compared to those seen for the double-stranded compounds described in **Chapter 2** of this thesis, and did not show clear enantiospecificity.

The resolution of the 1,4-xylyl spacer helicate opens additional avenues for future study in biological systems, although given the DNA binding results described in this Chapter it is not necessarily anticipated that these compounds would be excellent therapeutic agents. Perhaps of more interest may be the resolution of related helicate compounds, such as those containing Fe(II) or Co(III) metal centres, which have shown more promising biological activity. Isolation of the enantiomers of these compounds would allow the study of potential enantioselective or sequence selective binding with various oligonucleotides. In addition, it was noted that for the Ru(II) helicate containing the 1,4-xylyl spacer ligand structural changes may occur upon anion exchange to the Cl^- salt and dissolution in aqueous solutions. The nature of this change (observed by NMR) is unknown at this time, and the interactions of anions or solvent with the helicate could be further studied to see whether the variation is due to conformers or some other rearrangement.

It has been proposed that the synthesis of helicates and mesocates may be governed by an odd/even rule, where ligands containing an odd-numbered spacer will favour mesocate formation, while those containing an even-numbered spacer result in helicates. This pattern has been observed for a range of labile transition metal compounds, including Fe(II) compounds utilising ligands belonging to the 2-pyridyl-1,2,3-triazole family;[290,291,293] however, it remains unexplored in a more inert system. The dinuclear product distribution was probed in this Chapter, where the 1,4-xylyl spacer ligand was modified to incorporate more flexibility. When combined with the relatively inert Ru(II) node this allowed the odd/even rules of formation to be broken, and new supramolecular assemblies accessed.

Firstly, an *n*-propyl spacer ligand was selected, and Ru(II) species prepared by identical microwave conditions to those used in the synthesis of the 1,4-xylyl spacer helicate. Initially, it appeared that only a single product was formed, which was determined by X-ray crystallography to be the expected mesocate. However, further characterisation showed that two products, with very similar NMR spectra, were present. Fortunately, the species were distinguishable by NMR as the Cl^- salts, and found to have vastly different solubilities in DMSO. As a result, separation was quite straightforward, and the two compounds were identified as the mesocate (DMSO-insoluble) and helicate (DMSO-soluble) by X-ray crystallography. Through relative energy modelling it was revealed that the mesocate was the more stable isomer; however, in comparison to the double-stranded compounds studied in **Chapter 2** the difference in stability was far lower in these triple-stranded

compounds. The similar calculated stabilities of the two isomers was in agreement with the experimentally-observed product distribution, although frustratingly it was often found that after purification isomeric mixtures were again observed in the ^{1}H NMR spectra. The potential for isomer interconversion was firstly probed by thermal methods and the purified mesocate and helicate were heated as the Cl^{-} salts in D_2O over a period of seven days, or exposed to microwave reaction conditions. Under microwave conditions a very small amount of conversion was observed; however, not to the same extent seen in the original samples by NMR spectroscopy. An alternative cause of isomerisation was investigated, and it was found that by leaving the samples in ambient light at room temperature significant conversion was observed over a period of 30 days. While the specific wavelength of light and mechanism of isomerisation was not further investigated in this thesis it was proposed that interconversion may proceed by a bond-breaking mechanism, although alternative twist mechanisms may also be possible. This is thought to be the first example of photoconversion in a mesocate/helicate pair, and certainly the only recorded isomerisation of Ru(II) mesocate and helicate species.

LD studies with DNA were undertaken using a mixture of the two isomers containing the *n*-propyl spacer ligand, as at the time of experimentation the presence of the helicate had not been discovered. For this mixture of compounds the change in LD response was even smaller than for the 1,4-xylyl spacer compounds, suggesting that while the Ru(II) species did interact with ct-DNA, likely by groove binding, the strength of interactions was substantially weaker. Given that both the mesocate and helicate species were present in this sample it is possible that any specific interactions of the isomers or enantiomers of the helicate with DNA may be masked due to the mixture of compounds present.

For the *n*-propyl spacer compounds the mechanism of photoisomerism is a point of great interest, of which the process could be further probed in future studies. Determination of the specific wavelength responsible for isomer conversion could allow the distribution of the two products to be influenced, allowing controlled formation of the mesocate or helicate. Additionally, the interactions of these compounds with anions is a key factor, where the vastly different solubilities of the Cl^{-} salts in DMSO could potentially be used to influence distribution of the isomers. Photoisomerisation of the dinuclear species, whilst being an incredibly interesting and unique observation, may present challenges in the study of these compounds in biological systems (although this could be overcome by conducting experiments in the dark). However, the extremely weak interactions seen with DNA by LD spectroscopy suggest that the Ru(II) compounds containing the *n*-propyl spacer ligands may not have exceptional biological activity, limiting their potential as therapeutics.

Further probing the validity of the odd/even rule, the length of the spacer was further increased to incorporate an *n*-butyl chain. Utilising identical microwave reaction conditions to those for other compounds in this Chapter, it was found that multiple species, more than just a pair of dinuclears, were present in the crude product mixture, adding additional complexity. Reaction time was found to be a key factor influencing the distribution of products, with shorter reaction times resulting in increased formation of polymer material, while longer reaction times drove formation of the desired dinuclear species. In this case two major products, thought to be the mesocate and helicate, were identified in the product mixture, and efforts to separate these by chromatographic means, such as those described for other Ru(II) compounds (see **Chapter 2** of this thesis, and elsewhere) proved unsuccessful. Surprisingly, it was found that resolution of the helicate enantiomers was remarkably straightforward, and using a cellulose solid-phase support in conjunction with an eluent containing a chiral anion it was found that the one enantiomer of the helicate could be isolated (F2 from the resolution). Separation of the remaining mesocate/single helicate enantiomer/minor impurities (F1 from the resolution) was pursued by fractional crystallisation. Most promisingly, it was found that partial separation could be achieved using BF_4^-. It was found that after two rounds of fractional crystallisation the unknown minor products could be successfully removed, although BF_4^- was not sufficiently discriminating to allow complete separation of the mesocate and helicate enantiomer.

The interactions of a single enantiomer of the helicate containing the *n*-butyl spacer ligand (F2 from the resolution) with DNA were probed by LD spectroscopy. In this case the DNA showed little perturbation upon addition of the compound and it was unclear whether there was any significant interaction between the helicate enantiomer and ct-DNA. While potential elongation of the DNA was noted this behaviour was in contrast to the coiling observed for the other compounds studied in this Chapter, and the limited impact on the LD response overall suggested that any interactions may be very weak or non-specific.

While the range of products obtained from reactions using the *n*-butyl spacer ligand again illustrated the ability for the odd/even rules of product formation to be broken in an inert system, full separation of all of the components could not be achieved by any methods described in this Chapter. Comprehensive identification of the proposed mesocate, and confirmation of complete resolution of the helicate are still to be undertaken. The potential for isomerisation or anion interactions, as seen for compounds containing the *n*-propyl spacer ligand, has not been investigated and the *n*-butyl spacer compounds may show similar behaviour. Furthermore, the presence of unknown side products, which may be other

dinuclear or larger assemblies, could be further characterised. By incorporating increased flexibility by way of the *n*-butyl spacer (or longer spacers) alternative metallosupramolecular architectures may be able to be accessed. As seen for the other compounds in this Chapter, the limited evidence of interactions with DNA do not seem to suggest great potential in this field; however, it would be interesting to understand why the interactions of these compounds are so modest, when for other triple-stranded diruthenium(II) helicates highly specific DNA binding has been observed. It is evident that factors beyond the number of ligand strands and choice of metal centre must be considered when designing dinuclear structures for use in biological settings, including shape, surface chemistry, and charge.

Throughout this Chapter the specific properties of a small selection of ruthenium helicates and mesocates have been presented; however, there is significant scope to extend this study further. The versatile ligand design, in which the terminal donors and spacer region can be easily modified, provides an excellent framework for building libraries of dinuclear compounds, or extending to larger supramolecular assemblies. It appears that Ru(II) compounds containing ligands of this type may show interesting anion or solvent interactions, as well as potential for photoisomerisation, properties which may be beneficial in host-guest or sensing applications. While the specific compounds described herein do not display spectacular DNA binding behaviour it is possible that with careful selection of ligands or re-design of compounds potential biological applications may be identified.

CHAPTER 5

Exploration of Larger Supramolecular Assemblies

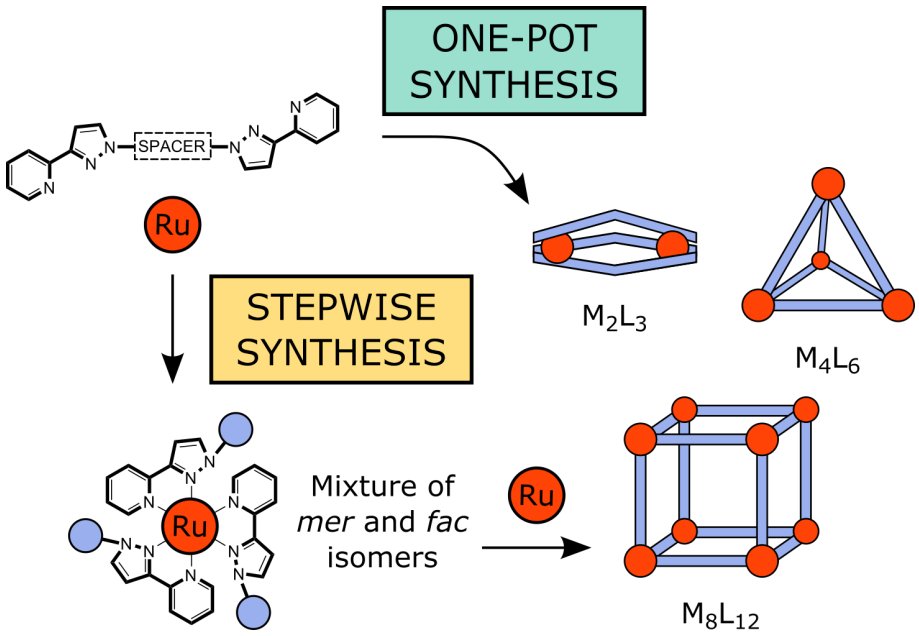

5.1 Introduction

5.1.1 Metal-organic cages

Metal-organic cages (MOCs) are formed through the self-assembly of metal ions and bridging ligands, and have been an important area of research in supramolecular chemistry over the last two decades.[94,95,321] Early work, including that by the groups of Lehn,[45] Stang,[322,323] Fujita,[324,325] Raymond,[326] Newkome,[327] Nitschke,[328,329] and others,[330–333] laid the foundation for the development of novel coordination compounds with great structural diversity. The variety of possible shapes, combined with the ability to control cavity size make these compounds useful in host-guest chemistry,[334] opening up applications in catalysis,[26,335–337] storage of reactive species,[338–340] molecular separations,[341] and drug delivery.[342–344] The potential for guest binding in MOCs gives them an advantage over other types of metallosupramolecular assemblies, such as the helicate and mesocate species discussed in **Chapters 2** and **4**, which often lack an accessible cavity.

In association with octahedral metal ions, di(bidentate) ligands can yield triple-stranded M_2L_3 structures (as seen in **Chapter 4**), or larger supramolecular assemblies with the same metal-to-ligand ratio (see Figure 5.1). While M_2L_3 gives a metallohelicate or mesocate structure, metal ions and ligands in the same stoichiometry can form tetrahedra (M_4L_6) and cubes (M_8L_{12}), or even larger cages ($M_{12}L_{18}$) .

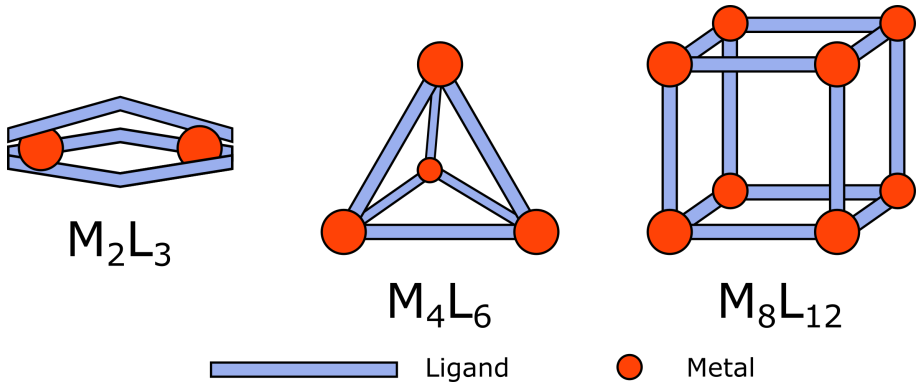

Figure 5.1: Schematic representations of possible $M_{2n}L_{3n}$ metallosupramolecular assemblies, incorporating octahedral metal ions and di(bidentate ligands).

5.1.2 Using Ruthenium(II)

Polypyridylruthenium(II) compounds have been widely explored in redox-active materials,[345] dye-sensitised solar cells,[346] water splitting,[347–349] biological labelling,[350] and as anti-cancer agents.[351–353] As a result there has been great interest in incorporating

ruthenium(II) compounds in polymers,[354–356] metal-organic frameworks (MOFs),[357–359] or MOCs.

Su and co-workers incorporated $[RuL_3]$ metalloligands with redox and photo-active applications in $[Pd_6(RuL_3)_8]^{28+}$ cages using a stepwise approach (see Figure 5.2).[360] The use of metalloligands as pre-designed building blocks contributed specific chemical functionality while combination with a more labile Pd(II) ion allowed formation of an MOC. Subsequently, the same authors showed that homochiral Δ_6 and Λ_6 cages were able to be generated using the resolved forms of the $[RuL_3]^{2+}$ metalloligands.[361] Finally, Su and co-workers used the Ru-Pd heteronuclear cage as a molecular flask for the photodimerisation of napthol derivatives.[362] The dimerisation reactions were conducted inside the cages and the product distribution was found to be impacted by confinement effects. Furthermore, when using the enantiomerically-pure cages, stereoselectivity was observed.

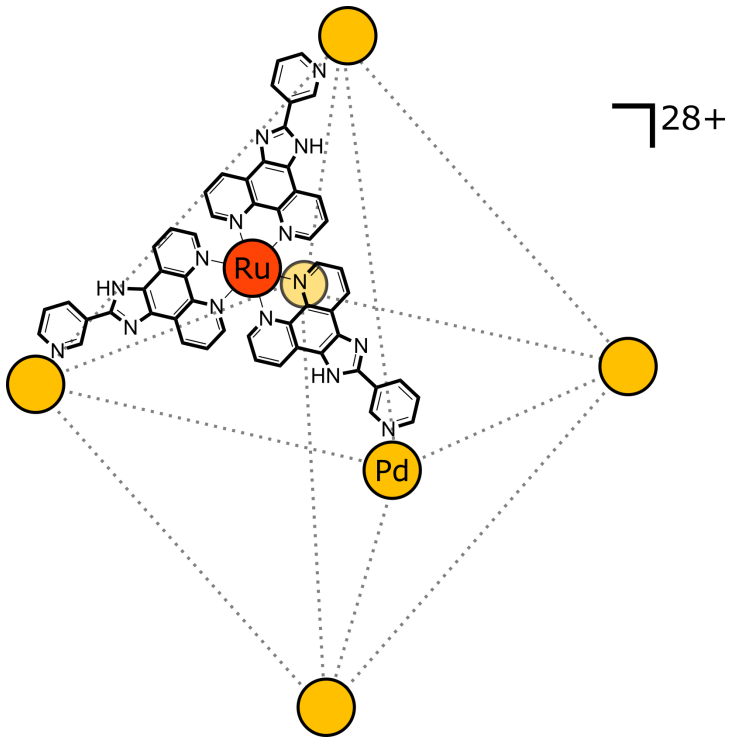

Figure 5.2: Schematic representation of the $[Pd_6(RuL_3)_8]^{28+}$ cage studied by Su and coworkers,[360–362] incorporating a $[RuL_3]^{2+}$ metalloligand on each face of the octahedral cage.

Palladium(II) has been an extremely popular partner for the linkage of ruthenium(II)-containing species in the synthesis of heterometallic cages. In work by Beves and co-workers $[Ru(tpy)_2]^{2+}$ metalloligands were employed (where tpy = 2:2′,6′:2″-terpyridine). These metalloligands were functionalised in the 4′-position with pendant pyridyl groups which allowed coordination to Pd(II) ions.[363] The authors have further expanded this original set of compounds to include modified metalloligands capable of forming diruthenium(II) species, which can be linked into a cage structure by Pd(II) ions (see Figure 5.3). By

extending the metalloligand structure a larger cavity was accessed, improving the prospect for these supramolecular assemblies in host-guest chemistry.[364]

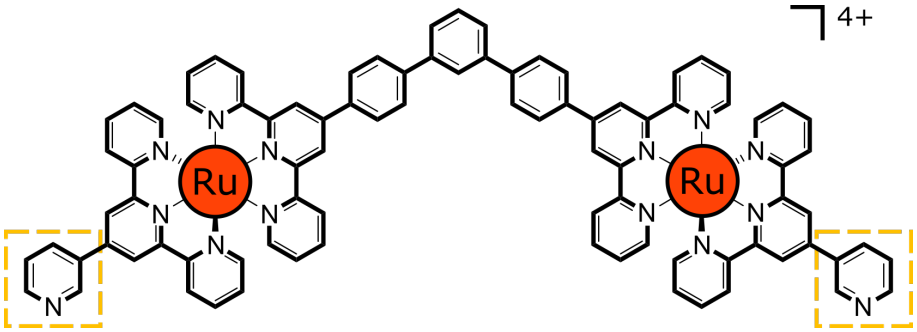

Figure 5.3: One example of a diruthenium(II) metalloligand studied by Beves and coworkers,[364] synthesised by the coupling of two $[Ru(tpy)_2]^{2+}$ metalloligands, before cage formation with Pd(II). Pd(II) ions can be coordinated at the positions outlined in yellow. The structure is shown containing 3-pyridyl pendant groups and a 3,3″-di([2,2′:6′,2″-terpyridin]-4′-yl)-1,1′:3′,1″-terphenyl core ligand; however, compounds containing 4-pyridyl pendant groups and a 4,4″-di([2,2′:6′,2″-terpyridin]-4′-yl)-1,1′:3′,1″-terphenyl core ligand, or some combination of the four components were also synthesised.

Reports of MOCs are not limited to Ru/Pd hybrids. Luis *et al.* have shown that Ru(II) metalloligands can be used in concert with Fe(II) or Zn(II) ions.[365] Ru(II) was first installed into the metalloligands before reaction with a partner metal ion, allowing formation of a tetrahedral assembly. As shown in Figure 5.4 the tetrahedron can be structured with either Fe(II)/Zn(II) at the vertices, while the photoactive polypyridylruthenium(II) species lie along the bridging ligands.

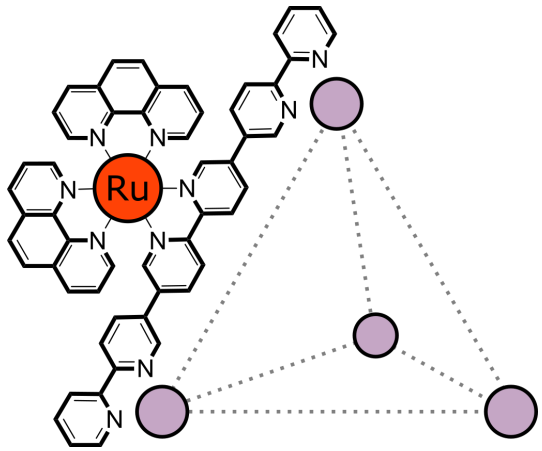

Figure 5.4: Schematic representation of the heteronuclear tetrahedra studied by Luis *et al.*,[365] where Ru(II) is coordinated to the bridging ligand, while either Fe(II) or Zn(II) occupies the vertices of the cage.

The same combination of metal ions has been explored by Chen *et al.* to synthesise Ru(II)/Zn(II), and Ru(II)/Zn(II)/Fe(II) cages.[366] In these structures a Ru(II) metalloligand containing four non-coordinated terpyridine units was formed, and the vacant

metallation sites then filled by either Zn(II) ions, or Zn(II) and Fe(II) ions to form a rare trimetallic species.

As shown above, there are several examples of heterometallic ruthenium-containing cages incorporating Ru(II) within a metalloligand. In contrast, there are few reported MOCs containing Ru(II) at the node or vertex.

One early example of a Ru-containing supramolecular cube was reported by Thomas and co-workers,[367] where eight octahedral metal corner units $\{[([9]aneS_3)Ru(DMSO)Cl_2]\}$ were combined with twelve 4,4′-bipyridine ligands, initially forming a monoruthenium compound. However, after four weeks rearrangement to a cube of $[Ru_8L_{12}]^{16+}$ stoichiometry was observed, where the ruthenium centres are bridged by 4,4′-bipyridine ligands, and capped with $[9]aneS_3$ ligands (see Figure 5.5).

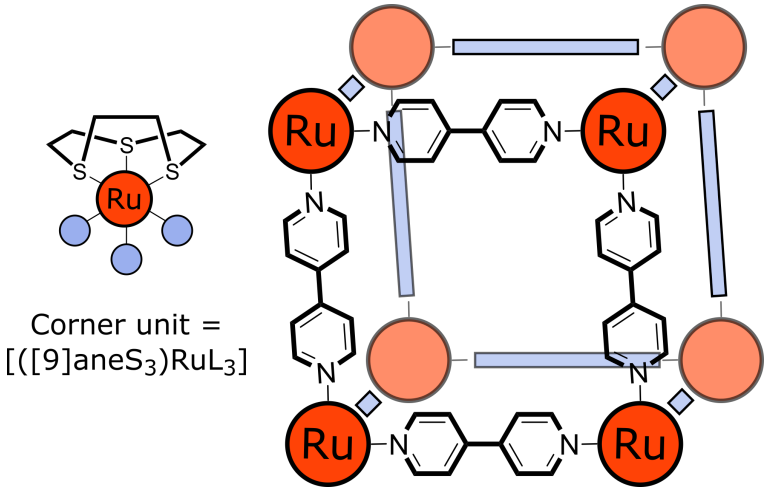

Figure 5.5: Schematic representation of the Ru(II) cube studied by Thomas and co-workers,[367] where Ru(II) is coordinated at the vertices of the cage, and capped with $[9]aneS_3$ ligands.

Two examples of Ru-containing MOCs have been reported by Cook and co-workers – a $[Ru_4L_4]^{8+}$ square metallocycle and $[Ru_4L_6]^{8+}$ truncated octahedron – in which $[Ru(bpy)_2]^{2+}$ units at the vertices were linked by 4,4′-bipyridine or 2,4,6-tris(4-pyridyl)-1,3,5-triazine ligands resulting in a metallocycle and octahedron, respectively.[368] These structures illustrate how Ru(II) can be incorporated as the sole metal ion at the node, although in this case the capping 2,2′-bipyridine (bpy) ligands aid synthesis of the cage and help to overcome the challenges faced when incorporating a relatively inert metal ion. A schematic representation of the structure of the octahedron is shown in Figure 5.6 below.

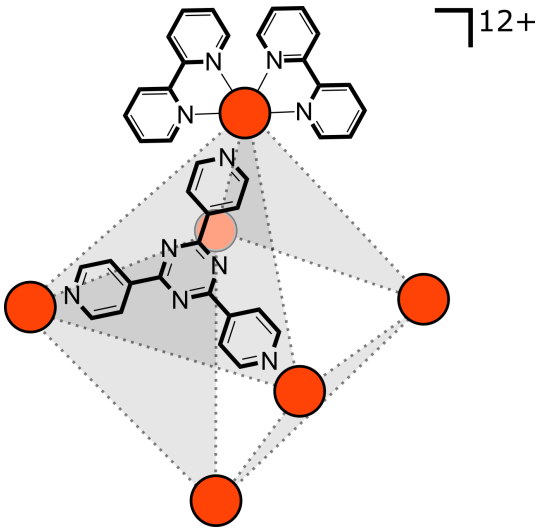

Figure 5.6: Schematic representation of the Ru(II) truncated octahedron studied by Cook and co-workers,[368] where Ru(II) is coordinated at the vertices of the cage, and capped with two bpy ligands.

Newcombe and co-workers have synthesised a highly symmetrical Ru(II) terpyridine-based spherical cage of the type $[Ru_6L_4]^{12+}$.[97] In this case the cage was synthesised via a one-pot reaction under relatively mild conditions (at reflux in $MeOH/CHCl_3$; 3 days). Each Ru(II) centre is saturatively coordinated to two terpyridinyl moieties, one arising from a tri(tridentate) ligand structure, with no additional capping or bridging ligands (see Figure 5.7).

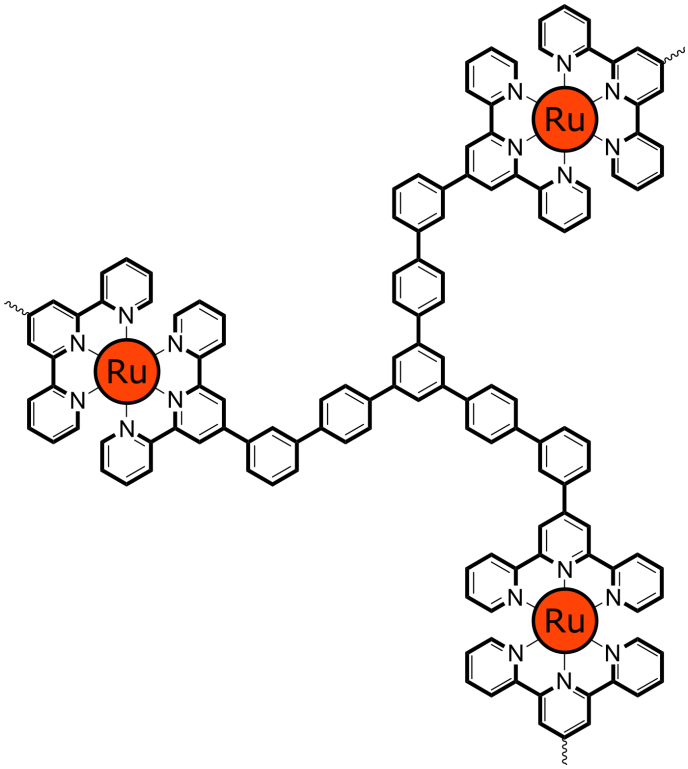

Figure 5.7: Truncated schematic representation of the Ru(II) nanosphere with the formula $[Ru_6L_4]^{12+}$, showing ligand and mode of coordination, studied by Newcombe and co-workers.[97] The full cage is composed of four ligands and six Ru(II) centres.

Finally, a variety of heterometallic cages, incorporating Ru(II) at the nodes in partnership with other transition metal ions, have been synthesised by the Ward group. The authors followed a stepwise approach to form $[RuL_3]^{2+}$ building blocks as a mixture of *mer* and *fac* isomers (see Section 5.1.3) before reaction with a more labile metal ion, such as Cd(II), Ag(I) or Co(II), led to cage assembly.[98–101] The structure of one example, a heterometallic Ru(II)/Cd(II) cube is illustrated in Figure 5.8 below.

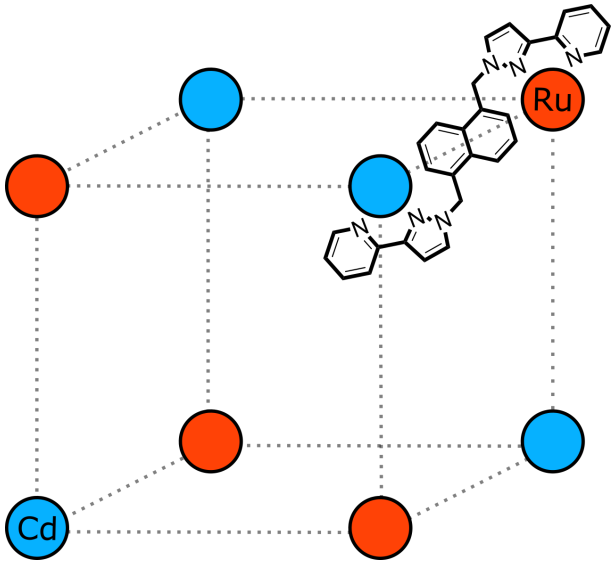

Figure 5.8: Schematic representation of the Ru(II)/Cd(II) cube, studied by Ward and co-workers.[97] The structure is composed of four $[RuL_3]^{2+}$ building blocks linked by four Cd(II) ions to form a $[M_8L_{12}]^{16+}$ cage.

While the structural variety of MOCs described above illustrates the creative ways that Ru(II) can be incorporated, at the time of writing there are very few reports of discrete cages incorporating only Ru(II) ions at the nodal positions. In this Chapter approaches to the synthesis of such supramolecular assemblies were explored, employing similar synthetic strategies to those used to form Ru(II) dinuclear complexes (described earlier in this thesis), as well as alternative stepwise approaches.

5.1.3 Ligand design strategies

The importance to the design of metallosupramolecular assemblies provided by the variation of coordination numbers and geometries exhibited by various metal centres has been described earlier in this thesis. An additional factor that must be considered is the stereoisomerism associated with the metal ligand motifs that constitute the assembly. In the present case, geometrical isomerism in octahedral centres with bidentate ligands is of particular significance. In the case where an octahedral metal centre is coordinated to three unsymmetrical bidentate ligands (A - B; where that unsymmetrical nature may

arise from substitution or non-identical coordination moieties) there are two possible geometrical isomers - meridional (*mer*) or facial (*fac*). These assignments are based on the relative positions of either end (A or B) of the ligand to the corners of the octahedron. The arrangement of each geometrical isomer is illustrated in Figure 5.9 below, using an unsymmetrically-substituted 2,2′-bipyridine ligand as an example.

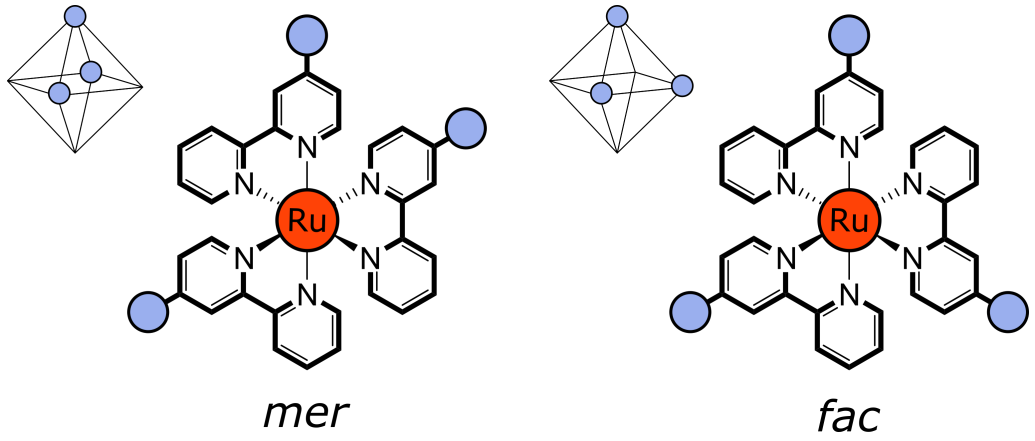

Figure 5.9: Representation of *mer* and *fac* isomers of a ruthenium compound containing unsymmetrically-substituted bpy ligands, and respective schematic representations of the meridional and facial arrangements.

Statistically, the ratio of *mer*-to-*fac* isomers for such tri(bidentate) species should be 3 : 1,[369] although certain circumstances such as the addition of bulky substituents[370–372] or use of templates,[373] have been shown to influence the expected *mer*/*fac* ratio. Isolation of the geometrical isomers can often be achieved by chromatographic separation on a range of stationary phases.[369–372,374] Furthermore, in the synthesis of the heterometallic Ru(II)/Ln(III) helicate by Torelli *et al.*, which has been described in **Chapter 4** of this thesis, the monoruthenium(II) compound was initially isolated in the expected 3 : 1 *mer*/*fac* ratio; however, subsequent conversion to the *mer*-isomer was reported was reported at room temperature.[74] This finding suggests that in some cases monoruthenium(II) species are capable of geometrical rearrangement, a property which may be a useful in the synthesis of discrete assemblies.

The impact of geometrical isomerism in the formation of MOCs containing unsymmetrical bidentate ligands has been explored by Ward and co-workers.[375] In these studies ligands contained two chelating pyrazolyl-pyridine units connected by spacers of varying steric bulk and flexibility (the generic structure is shown in Figure 5.10 below) were used to generate a great variety of assemblies, including helicates,[376–379] tetrahedra,[13,376,380–387] cubes,[93,388–391] and larger M_{12} and M_{16} cages.[18,392–395] The host-guest chemistry of these structures has been widely studied,[396–403] showing particular promise in the capture of chemical warfare agents,[404,405] and uptake and release of drug molecules.[406]

Figure 5.10: Generic structure of the di(pyrazolyl-pyridine) ligands utilised by Ward and co-workers in the synthesis of MOCs.[375] The central spacer has been extensively modulated to vary the flexiblity and functionality of the ligands.

The incorporation of Ru(II) into cages in these earlier studies was achieved by stepwise synthetic strategies. Initially, Metherell *et al.* demonstrated that mononuclear $[RuL_3]^{2+}$ species were able to be synthesised, where L is a bidentate ligand containing the pyrazolyl-pyridine motif with varying substitution on the pyrazolyl ring (see Figure 5.11).[407] These monoruthenium compounds exist as a mixture of *mer* and *fac* isomers and it was found that for the Ru(II) compound (where R = H) the separation of isomers could be achieved by reaction with a Cu(I) salt, where the *fac* isomer precipitated as a Cu(I) adduct, while the *mer* isomer remained in solution. Once the isomers had been separated (for the ligand where R = H), the substituent could be exchanged by reaction with benzoyl bromide (to R = CH_2Ph) or methyl iodide (to R = CH_3), generating a family of pure *mer* and *fac* Ru(II) compounds.

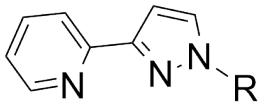

Figure 5.11: Structure of the pyrazolyl-pyridine based bidentate ligand utilised by Metherell *et al.* in the synthesis of $[RuL_3]^{2+}$ building blocks (R = H, CH_2Ph, or CH_3).[407]

This initial study served as the basis for extension to larger supramolecular assemblies, incorporating di(bidentate ligands). The first example was a Ru(II)/Cd(II) elongated cube (point group symmetry S_6), and a schematic representation of this structure is shown above in Figure 5.8.[98] The ligand selected contained a 1,5-dimethylnaphthalene spacer, which had previously been incorporated in other transition metal cages.[93,408] Firstly, the mononuclear compound $[RuL_3]^{2+}$ was synthesised, forming as a statistical mixture of *mer* and *fac* isomers in a 3 : 1 ratio. Conveniently, this ratio is ideal for heterometallic cage formation as within the cube two of the vertices (metal centres) must be *fac*, while the other six adopt a *mer* configuration. The Ru(II) compound provides four of the vertices of the cube (one *fac* and three *mer*) and the twelve ligands, so when reacted with Cd(II) a cube with alternating Ru(II)/Cd(II) arrangement is observed. Wragg *et al.* have built upon this original work, synthesising a Ru(II)/Co(II) analogue of the heterometallic cube using the same ligand.[99]

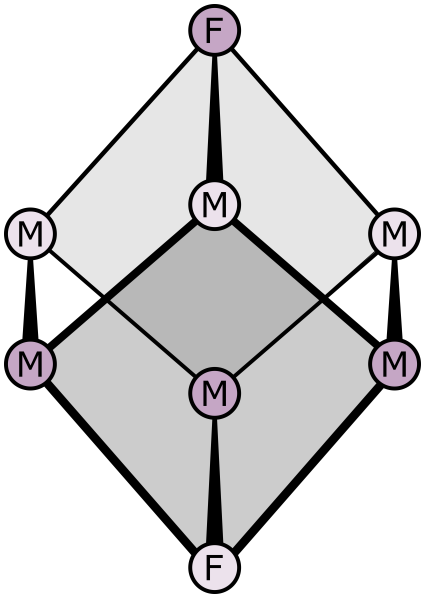

Figure 5.12: Schematic representation of the heterometallic elongated cube (point group symmetry S_6) reported by Metherell and Ward.[98] In this structure two of the metal centres are *fac*, while the remaining six adopt a *mer* configuration.

Using a similar ligand Metherell and Ward have also reported a Ru_4Ag_6 cage with adamantoid geometry.[100] In this case a di(bidentate) ligand containing a 1,4-xylyl spacer was initially employed to generate $[RuL_3]^{2+}$ compounds, with the *fac* isomer being the desired building block. The authors reported a 3 : 1 statistical mixture of *mer* and *fac* isomers (as seen in the previous study); however, these isomers were unable to be separated, and the pure *fac* isomer could not be obtained. To overcome this challenge the ligand modification strategy that had been successfully used in the synthesis of mononuclear building blocks was employed, where the monoruthenium(II) compound shown in Figure 5.11 (where R = H) was formed and geometrical isomers separated. Following this the pure *fac* isomer was alkylated with a bromomethyl compound to add the 1,4-xylyl spacer, appending the second bidentate chelation site (see Figure 5.13). Subsequent metallation with Ag(I) formed a decanuclear cage of adamantoid geometry, where each silver is four-coordinated.

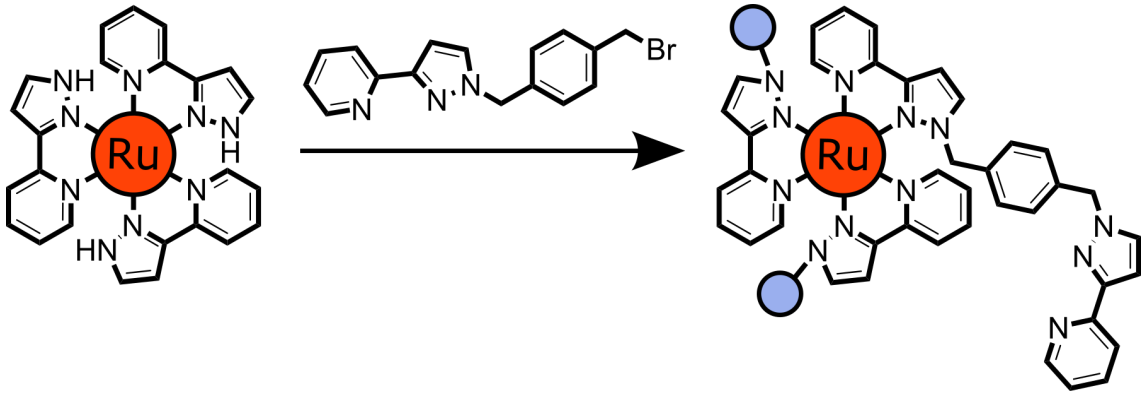

Figure 5.13: Reaction of the pyrazolyl-pyridine based monoruthenium(II) compound with 2-(1-{4-(bromomethyl)benzyl}-1*H*-pyrazol-3-yl)pyridine to form the di(bidentate) ligand, utilised by Metherell and Ward in the synthesis of an adamantoid Ru_4Ag_6 cage.[100] The blue circles represent the second bidentate chelation site, appended after synthesis of the initial monoruthenium species.

Continuing in this vein, the same process was undertaken for a ligand containing a 1,2-xylyl spacer.[101] For the initial reaction to form $[RuL_3]^{2+}$ building blocks using the full di(bidentate) ligand, a mononuclear $[RuL_2]^{2+}$ species was observed. When this monoruthenium compound was combined with Ag(I), a Ru_2Ag compound was formed where once more the Ag(I) was four-coordinate, linking two ruthenium centres. A multi-stepwise ligand modification strategy was also trialled, where the *fac* isomer of the monoruthenium compound (containing the pyrazolyl-pyridine based bidentate ligand (R = H); see Figure 5.11) was alkylated with 3-bromomethylpyridine to incorporate three pendant 3-pyridyl groups. Once reacted with Ag(I) it was found that a two-dimensional coordination network was formed.

In all of these examples a stepwise (or sometimes multi-stepwise) approach was taken in the synthesis of heterometallic cages, seeking to employ Ru(II) as an inert building block, with cage formation arising from metallation with a more labile transition metal partner. In this Chapter, two potential synthetic approaches were developed for the generation of Ru(II) cages using di(pyrazolyl-pyridine) ligands with varying spacer functionality. Firstly, "one-pot" syntheses – incorporating the knowledge gained in the synthesis of dinuclear species in **Chapters 2** and **4** of this thesis – were utilised. Based on structural similarities between the ligands studied in **Chapter 4** and those selected for study in this Chapter, it was anticipated that under analogous synthetic conditions dinuclear Ru(II) species would be formed. However, as steric bulk is introduced around the spacer region the formation of dinuclear helicates or mesocates should be disfavoured, leading to the generation of larger tetrahedral or cubic assemblies. Concurrently, utilising the stepwise tactics pioneered by Metherell and Ward, the synthesis of $[RuL_3]^{2+}$ building blocks was attempted. Once

isolated, the mononuclear compounds were reacted with further equivalents of Ru(II) precursor in an attempt to form cubic assemblies, similar to those reported by Ward and co-workers. The two synthetic pathways are illustrated in Figure 5.14 below.

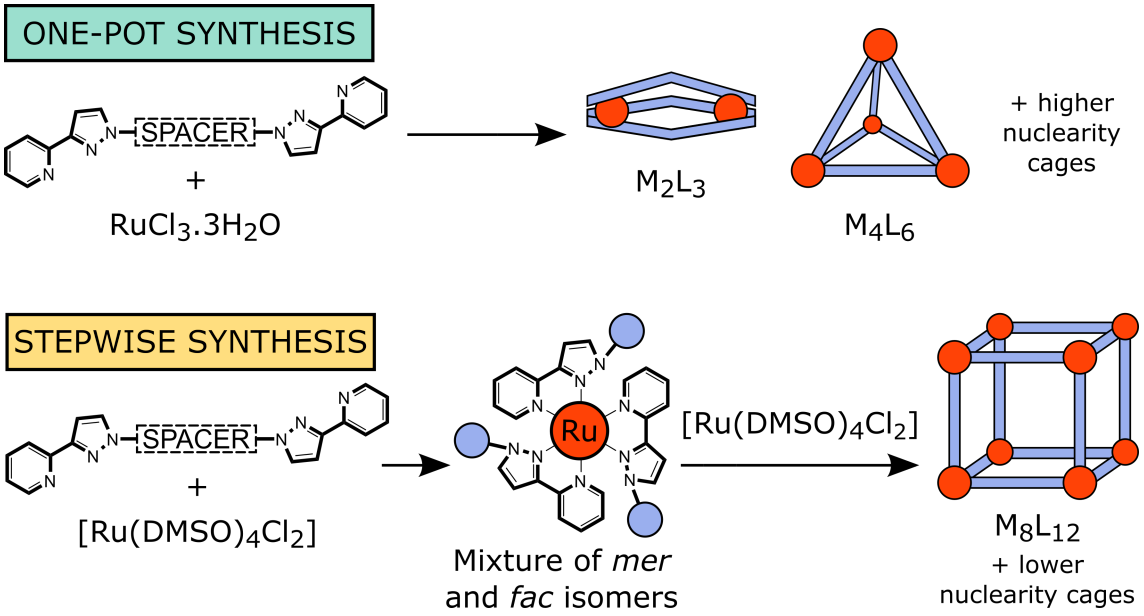

Figure 5.14: Synthetic pathways leading to the formation of Ru(II) cages pursued in this thesis.

5.2 Synthesis of Ligands

In this study three ligands were selected, inspired by those used by the Ward group, containing pyrazolyl-pyridine chelation sites with varying spacer functionality. Initially, a simple 1,4-xylyl spacer was selected, in a ligand identical to that used by Metherell and Ward (described above).[100] In addition to this simple ligand two others were selected, each with increasing steric bulk appended to the spacer unit. The first was a novel ligand, incorporating four methyl substituents (containing a 2,3,5,6-tetramethyl-1,4-xylyl spacer), while the second has been used by the Ward group in the synthesis of other metal organic cages, containing a 9,10-dimethylanthryl spacer.

The *precursors* – 3-(dimethylamino)-1-(pyridin-2-yl)prop-2-en-1-one (**16**) and 3-(2′-pyridyl)pyrazole (**17**) – were prepared according to the literature procedures,[409,410] as were the bis(bromomethyl)-substituted spacers – 1,4-bis(bromomethyl)benzene (**7**), 1,4-bis(bromomethyl)-2,3,5,6-tetramethylbenzene (**18**), and 9,10-bis(bromomethyl)anthracene (**19**).[411,412]

The *ligands* – 1,4-bis{(3-(pyridin-2-yl)-1*H*-pyrazol-1-yl)methyl}benzene (**20**) and 2,2′-(1,1′-{(2,3,5,6-tetramethyl-1,4-phenylene)bis(methylene)}bis{1*H*-pyrazole-3,1-diyl})dipyridine (**21**) – were synthesised via reaction of the appropriate

bis(bromomethyl)benzene (**7** or **18**) with 3-(2′-pyridyl)pyrazole (**17**) following conditions described by Hartshorn and Steel, and Argent *et al.*[18,413] 9,10-Bis{(3-(pyridin-2-yl)-1*H*-pyrazol-1-yl)methyl}anthracene (**22**) was synthesised via the reaction of **19** with **17** following conditions described by Tidmarsh *et al.*[93] The reaction schemes and structures of the three selected ligands are shown in Scheme 5.1, below.

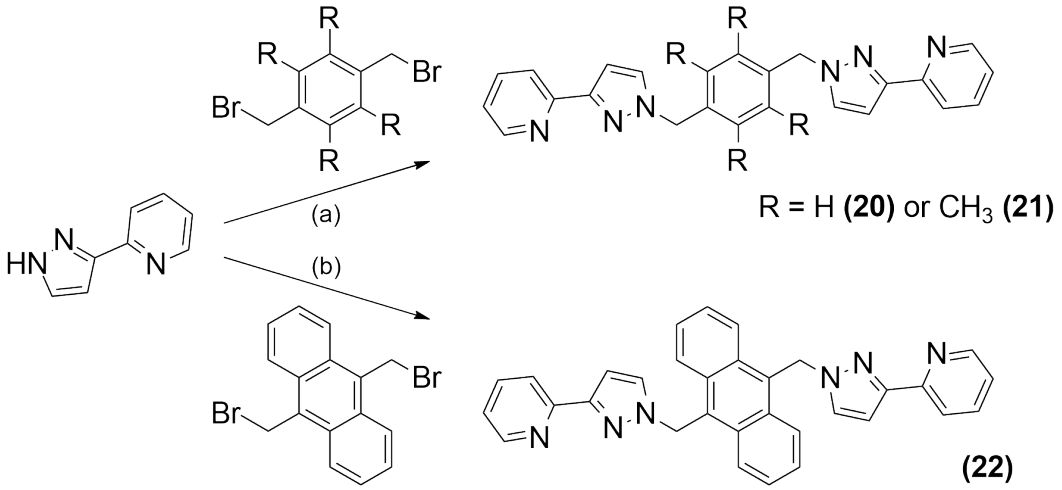

Scheme 5.1: (a) Aq. NaOH (10 M),(nBu)$_4$NOH (40%), Toluene, 60 °C, 1 h. b) Aq. NaOH (5.5 M), THF, reflux, 20 h.

5.3 Synthesis of Ruthenium Cages

5.3.1 Using a 1,4-xylyl spacer ligand

5.3.1.1 One-pot approach

Given the successful synthesis of diruthenium(II) complexes reported in **Chapter 4** of this thesis, attention firstly turned to the use of microwave irradiation, utilising conditions described by Glasson *et al.* and Kumar *et al.* for helicate formation.[66,80] Initially, the ligand containing a 1,4-xylyl spacer (**20**) was reacted with $RuCl_3 \cdot 3\,H_2O$ in a 3 : 2 metal to ligand ratio, for 5 h (200 W, 200 PSI, 225 °C). This ratio of M/L was selected to favour the formation of assemblies with $M_{2n}L_{3n}$ stoichiometry, which may include triple-stranded compounds (helicates or mesocates) similar to those studied in **Chapter 4** of this thesis. Analysis of the crude ^{1}H NMR spectrum showed some peaks in the aromatic region, although a large amount of polymeric material was thought to be present, evidenced by broad baseline signals (see Figure E.11 in Section E.2.2 of Appendix E). To remove polymeric species and purify the mixture of products column chromatography was performed (on silica gel: eluent 7 : 1 : 0.5, CH_3CN/H_2O/sat. aq. KNO_3), and three fractions collected. The first was a pale yellow, the second a dark distinct yellow band,

and the final fraction eluted as a diffuse yellow smear. Each of these was analysed by ^{1}H NMR spectroscopy and high resolution electrospray ionisation mass spectrometry (HR ESI-MS) to identify the components. The spectra of the three column fractions and the non-coordinated ligand are shown in Figure 5.15 below.

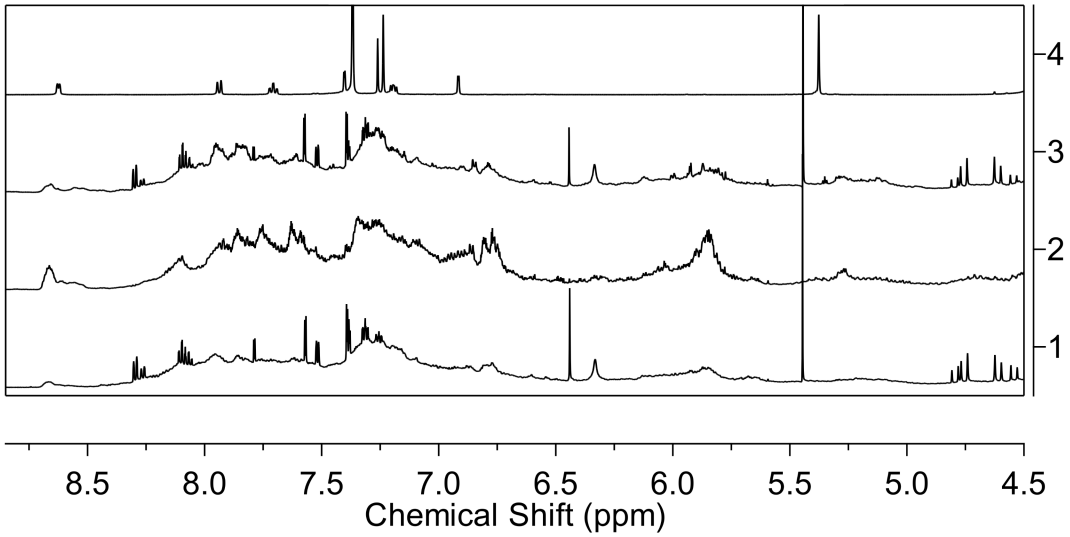

Figure 5.15: Partial ^{1}H NMR spectrum (600 MHz, CD_3CN, 298 K) showing the three fractions from purification of the crude reaction mixture of the 1,4-xylyl spacer ligand (**20**), with $RuCl_3 \cdot 3\,H_2O$ under microwave conditions (200 W, 200 PSI, 225 °C, 5 h). Fractions from chromatography are labelled in order of elution; (4) is the non-coordinated 1,4-xylyl spacer ligand (**20**; $CDCl_3$).

As illustrated above, the first (F1) and third (F3) eluting fractions were compositionally quite similar, containing a broad baseline with some sharp peaks, while fraction two (F2) was extremely broad particularly throughout the aromatic region. Overall, the presence of sharp signals was a promising sign that some discrete Ru(II) compounds had been formed, although the nature of these was not clear. For F1 and F3 no obvious mass fragments corresponding to Ru(II) species were detected at significantly high abundance by HR ESI-MS (see Figures E.19 and E.21 in Section E.3.1 of Appendix E). As a result it was unclear whether $[RuL_3]^{2+}$ building blocks or other supramolecular assemblies had been formed. For F2, while no patterns matching either $[Ru_2L_3]^{4+}$ or $[RuL_3]^{2+}$ fragmentations were detected, interestingly a 1^+ species was recorded with m/z 1030.311, matching a mononuclear $[RuL_2 \cdot PF_6]^+$ compound (see Figure E.20 in Section E.3.1 of Appendix E). While this species was unexpected, the appearance of a compound of this type is not without precedent, as Metherell and Ward reported a $[RuL_2](PF_6)_2$ species incorporating the closely-related 1,2-xylyl spacer ligand.[101] Despite efforts to further characterise this compound by X-ray crystallography, crystallisation attempts were unsuccessful; however,

it is anticipated that the structure may be similar to that reported by Metherell and Ward, with one ligand saturatively coordinated (as a tetradentate) and the other coordinated only at one end (as a bidentate; see schematic representation in Figure 5.16).

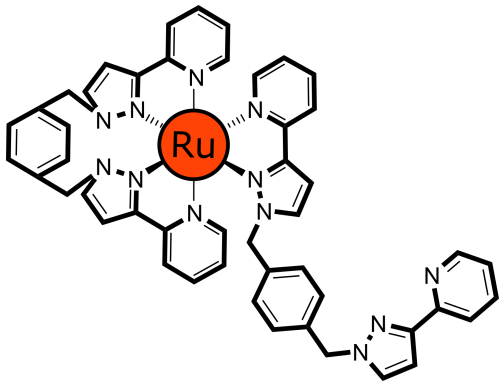

Figure 5.16: Schematic representation of the $[RuL_2]^{2+}$ species isolated from the 1,4-xylyl spacer ligand (**20**), with $RuCl_3 \cdot 3\,H_2O$ under microwave conditions (200 W, 200 PSI, 225 °C, 5 h).

Overall, it was surprising that reactions under these conditions did not yield discrete compounds, whether as helicate/mesocate species or larger supramolecular assemblies as this ligand (**20**) was structurally similar to the 1,4-xylyl spacer ligand utilised in **Chapter 4** of this thesis. The contrasting structures of the two ligands, utilising either triazole-pyridine (**8**; see **Chapter 4**) or pyrazolyl-pyridine (**20**; this Chapter) chelation sites, are shown in Figure 5.17 below. As can be seen in these structures, while the spacer and terminal N-donor type are identical (1,4-xylyl and pyridine, respectively), the second N-donor site (pyrazolyl or triazole) is substituted at different positions. As noted in **Chapter 4** reactions with the 1,4-xylyl spacer ligand (containing a triazole-pyridine coordination moiety) produced a relatively pure helicate product under analogous conditions. The 1,4-xylyl spacer ligand (**20**) utilised in this Chapter has not been extensively used for the formation of dinuclear species by others but has been shown to form larger cages with octahedral metal centres.[414] It was anticipated that by using a one-pot, microwave irradiation approach discrete saturated Ru(II) compounds may be formed, either of dinuclear or higher nuclearity. However, analysis of the isolated samples by HR ESI-MS revealed no compounds of $M_{2n}L_{3n}$ stoichiometry, highlighting that ligand design, particularly with regards to the substitution on the inner N-donor site, must play a key role in governing the formation of any supramolecular assemblies.

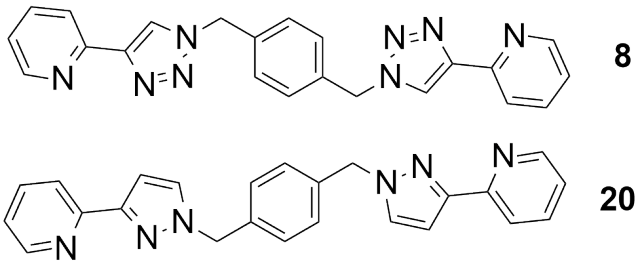

8

20

Figure 5.17: The 1,4-xylyl spacer ligand utilised in this thesis, containing either triazole-pyridine chelation sites (**8**; see **Chapter 4**) or pyrazolyl-pyridine chelation sites (**20**; this Chapter).

The M/L ratio utilised in the one-pot synthesis (2 : 3) was not expected to favour formation of monoruthenium species, and within the complex mixture of products no $[RuL_3]^{2+}$ building blocks were detected. Interestingly, the alternative mononuclear species – $[RuL_2]^{2+}$ – was seen by HR ESI-MS, which was proposed to contain one saturatively coordinated ligand (as a tetradentate) with the other ligand coordinated only as a bidentate.

Based on these findings it was concluded that the one-pot approach was not ideal for synthesising the desired $M_{2n}L_{3n}$ supramolecular assemblies incorporating the 1,4-xylyl spacer ligand (**20**). As such, an alternative synthetic approach was pursued for the formation of Ru(II) cages using this ligand, while the one-pot approach was trialled further using ligands containing a modified spacer.

5.3.1.2 Stepwise approach

As an alternative approach the synthesis of $[RuL_3]^{2+}$ building blocks was undertaken following the stepwise method described by Metherell and Ward.[98] For the work in this Chapter the aim was to generate a monoruthenium(II) compound, where the di(bidentate) ligand was coordinated in one bidentate mode, leaving a non-coordinated pyrazoyl-pyridine unit. Following isolation of the $[RuL_3]^{2+}$ compound the intent was to react this mononuclear species with an excess of ruthenium precursor to assemble a larger cage. Previous accounts in the literature using the 1,4-xylyl spacer ligand (**20**) noted that formation of a $[RuL_3]^{2+}$ species in a 3 : 1 statistical mixture of *mer* and *fac* isomers was possible.[100] However, in that record the authors required only the *fac* isomer as a precursor for their desired adamantoid cage, and abandoned the original $[RuL_3]^{2+}$ compound in favour of a stepwise mononuclear approach where the *fac* isomer could be readily purified. For the purposes of the study described in this Chapter the statistical mixture of *mer* and *fac* isomers was desirable as the intent was to assemble a Ru(II) cube, where the mononuclear Ru(II) compound comprised four of the vertices, which conveniently adopt a 1 : 3 *fac*/*mer* arrangement.

Applying the same synthetic conditions as Metherell and Ward,[98] reaction of the 1,4-xylyl spacer ligand (**20**) with $[Ru(DMSO)_4Cl_2]$ (in a 5 : 1 ratio) yielded a yellow crude product. The M/L ratio was varied from the one-pot reaction described above and a large excess of ligand used as the intent was to form an ML_3 building block, rather than directly forming species of $M_{2n}L_{3n}$ stoichiometry. Analysis of the product by ^{1}H NMR revealed far less polymeric material compared with the product of the one-pot reaction, with sharp peaks visible throughout the aromatic region (see Figure E.12 in Section E.2.2 of Appendix E).

After purification by column chromatography (on silica gel: eluent 7 : 1 : 0.5, CH_3CN/H_2O/sat. aq. KNO_3) a single yellow fraction was collected. This product was analysed by ^{1}H NMR spectroscopy and found to contain a complex mixture of products, as evidenced by the large number of overlapping peaks in the aromatic region (see Figure 5.18). Of particular interest were the most downfield resonances, assigned to the pyridyl-H6 hydrogens (see inset, below).

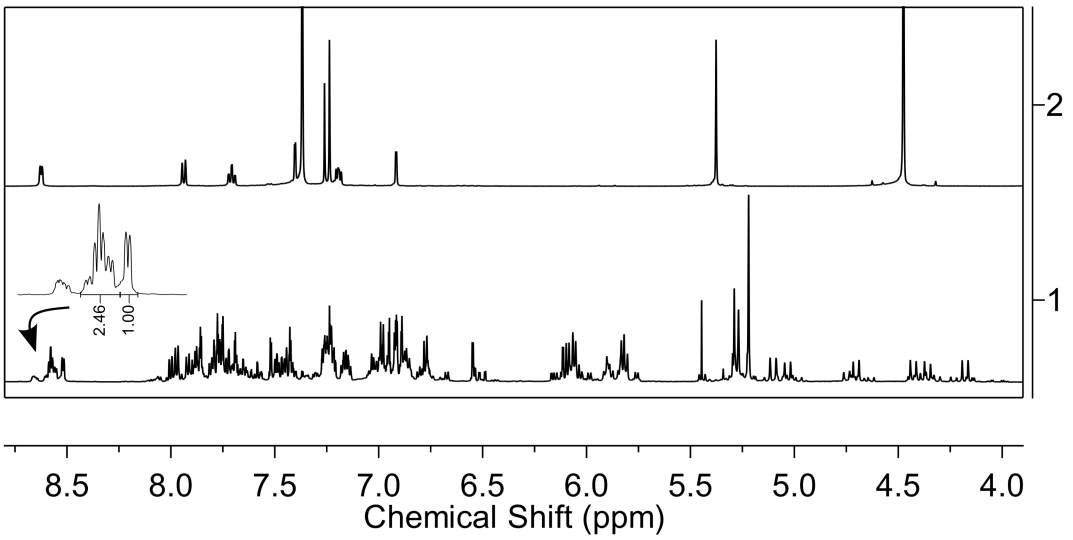

Figure 5.18: Partial ^{1}H NMR spectrum (600 MHz, CD_3CN, 298 K) showing (1) the product from the reaction of 1,4-xylyl spacer ligand (**20**) with $[Ru(DMSO)_4Cl_2]$ under reflux conditions (dropwise addition to form $[RuL_3]^{2+}$ building blocks), purified by column chromatography; (2) the non-coordinated 1,4-xylyl spacer ligand (**20**; $CDCl_3$). Inset: expansion of ^{1}H NMR spectrum showing the presence of two major signals in an approximate 2.5 : 1 ratio for one of the pyridyl-H6 hydrogens.

The complexity of the spectrum in the aromatic region was similar to that seen by Ward and Metherell,[98] where the $[RuL_3]^{2+}$ species exist as a mixture of *mer* and *fac* isomers. It was anticipated for a 3 : 1 *mer*/*fac* ratio of geometrical isomers with four independent ligand environments, four pyridyl-H6 signals would be present in a 1 : 1 : 1 : 1 ratio in the ^{1}H NMR spectrum. As indicated in Figure 5.18 above, once integrated

the pyridyl-H6 hydrogens did not match this pattern, and the two overlapping signals were present in a 2.5 : 1 ratio. Furthermore, additional signals at lower intensity were seen in this region, suggesting that Ru(II) compounds of other stoichiometries may also be present. Despite there potentially being a mixture of species, it appeared that a stepwise approach may have been somewhat successful in generating $[RuL_3]^{2+}$ building blocks. The presence of the $[RuL_3]^{2+}$ compounds was confirmed by HR ESI-MS, with *m/z* 639.2144 (corresponding to $[RuL_3 - 2PF_6]^{2+}$ species) detected. It was also noted that a mass fragment at *m/z* 1030.3112 was detected in much lower abundance, suggesting that there may be quantities of a $[RuL_2]^{2+}$ species, which had been detected in the F2 from the one-pot synthesis using this ligand. The presence of the $[RuL_2]^{2+}$ species may also account for the additional most downfield resonances in the aromatic region of the NMR spectrum above (at $\sim$ 8.7 ppm; see Figure 5.18), which match those seen in Figure 5.15 for all products of the one-pot reaction. The results of HR ESI-MS can be seen in Figure E.22 in Section E.3.1 of Appendix E.

Despite a mixture of products being obtained via a stepwise method using the $[Ru(DMSO)_4Cl_2]$ precursor, including small quantities of a $[RuL_2]^{2+}$ species, $[RuL_3]^{2+}$ was thought to be the major product present. Frustratingly the distribution of *mer* and *fac* isomers was not the statistical 3 : 1 ratio anticipated and reported by others for Ru(II) compounds containing this ligand.[100] This result suggested that other factors may have influenced formation of the mononuclear species. Given that the addition of bulky substituents has been shown to impact the expected *mer*/*fac* ratio in other tri(bidentate) species, it was proposed that the variation may be due to the presence of the non-coordinated ends of the three di(bidentate) ligands.

At this juncture alternative ruthenium precursors – $[Ru(H_2O)_6]^{2+}$ and $RuCl_3 \cdot 3\,H_2O$ – were trialled in conjunction with the 1,4-xylyl spacer ligand (**20**) under analogous conditions and ratios that had been used with $[Ru(DMSO)_4Cl_2]$ above to try and obtain the $[RuL_3]^{2+}$ compound in the desired ratio of *mer* and *fac* isomers. While these reactions initially shown promise, yielding dark yellow solutions, both were found to contain predominantly polymeric material and were not able to be readily purified by chromatographic methods.

Although the ideal ratio of geometrical isomers for cube formation was not observed in the product isolated from using the $[Ru(DMSO)_4Cl_2]$ precursor, attention turned using the $[RuL_3]^{2+}$ building blocks for the construction of a larger cage.

5.3.1.3 Building a cage

The $[RuL_3]^{2+}$ building blocks containing the 1,4-xylyl spacer ligand (**20**) described above were next combined with further equivalents of ruthenium(II). It was proposed that by reacting the monoruthenium species under similar conditions to those that had allowed formation of the building blocks – but with an excess of Ru(II) ions rather than ligand – the remaining coordination sites may be able to be metallated. To allow efficient monitoring of the reaction progress by NMR spectroscopy, cube formation was conducted in *d*$_6$-DMSO.

The initial building blocks were dissolved in *d*$_6$-DMSO as the PF_6^- salts and, after collection of the original spectrum, an excess of $[Ru(DMSO)_4Cl_2]$ (5 equivalents) was added and the sample heated at 150 ° C. While these conditions were slightly milder than those used for formation of the original building blocks, there are examples of the formation of Ru(II) compounds under even milder conditions, such as those used by Newcombe and co-workers (described in Section 5.1 of this Chapter).[97] It was proposed that the pre-formed *mer* and *fac* $[RuL_3]^{2+}$ building blocks may also direct assembly and aid formation of a larger cage.

After 24 hours of heating, significant changes were observed in the ^{1}H NMR spectrum. While the original sample can be seen to contain sharp peaks (similar to those seen in CD_3CN) for the $[RuL_3]^{2+}$ compound, addition of $[Ru(DMSO)_4Cl_2]$ and heating caused these distinct resonances to be lost, and the spectrum became extremely broad, particularly throughout the aromatic region. The reaction was continued and changes in the ^{1}H NMR monitored after three and seven days of heating (see Figure 5.19). While the initial results were promising, with the spectrum changing dramatically from that of the mononuclear $[RuL_3]^{2+}$ species, no further variation was seen. The distinctive pyridyl-H6 resonances at $\sim$ 8.5 ppm (due to the mixture of geometrical isomers for the mononuclear compound) were not present in the spectrum after reaction with $[Ru(DMSO)_4Cl_2]$, suggesting that the four unique ligand environments were lost. The overall broadness of the spectrum indicated that polymeric material may have formed, although overlapping signals in the aromatic region may also contribute to the broadening.

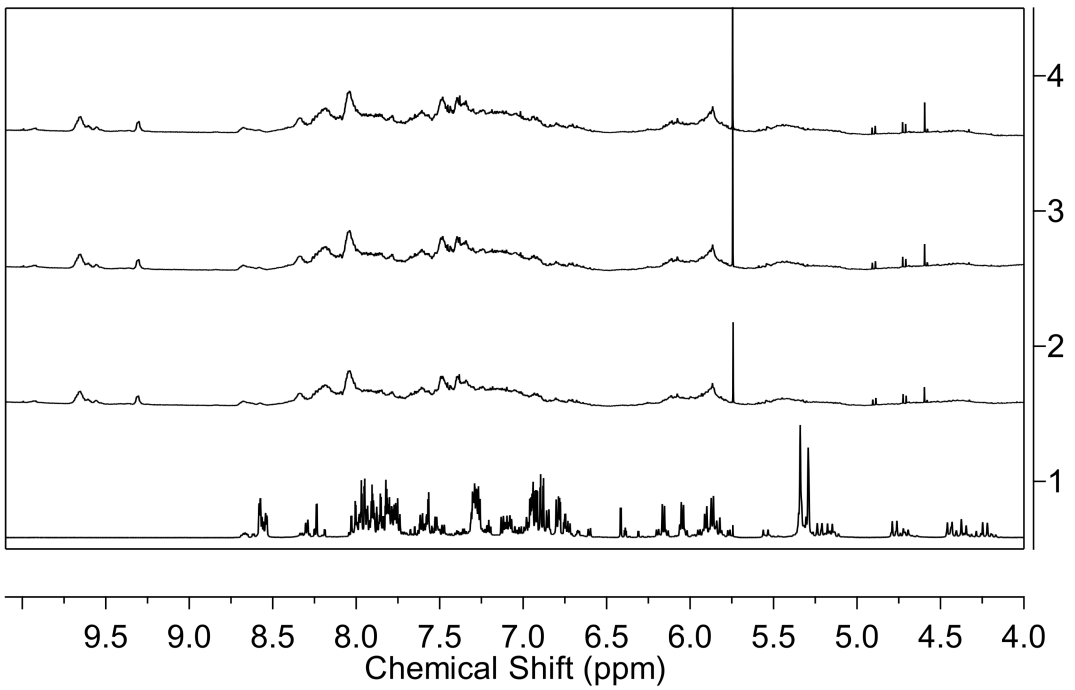

Figure 5.19: Partial ^{1}H NMR spectrum (500 MHz, d_6-DMSO, 298 K) showing the reaction of $[RuL_3]^{2+}$ building blocks containing the 1,4-xylyl spacer ligand (**20**) with $[Ru(DMSO)_4Cl_2]$ over 7 days. (1) Initial $[RuL_3]^{2+}$ compound; (2) 1 day; (2) 3 days; (3) 7 days.

While the preliminary experiment described above was not successful in forming a $[Ru_8L_{12}]^{16+}$ cube or other discrete assembly, there are many sets of synthetic conditions that may be considered in the future. In this case, the sample of mononuclear building block used lacked the ideal ratio of geometrical isomers desirable for cube formation, which may have impacted attempts to form this kind of assembly. The synthesis of the impure $[RuL_3]^{2+}$ building blocks described above provides a useful starting point for future attempts to form structures of this type. However, it should be noted that in this study the $[RuL_3]^{2+}$ compound was only able to be isolated in minute quantities after chromatographic purification. As a result this appears to be relatively inefficient approach to cage assembly overall, particularly when the final formation of the cage is reliant on coordination to a relatively inert metal centre, like Ru(II), rather than a labile metal centre.

Despite the set-backs noted above in the attempted synthesis of Ru(II) supramolecular assemblies, using the knowledge gained from the approaches discussed above attention turned to modifying the spacer of the ligand to see whether product distribution could be altered and any Ru(II) cages formed.

5.3.2 Addition of steric bulk – 2,3,5,6-tetramethyl-1,4-xylyl spacer

Given the limited success in synthesising Ru(II) cages achieved using the 1,4-xylyl spacer ligand (**20**), the ligand was redesigned to append methyl substituents to the central spacer. It was hoped that addition of steric bulk at these positions would block the production of unwanted mononuclear species (such as $[RuL_2]^{2+}$ observed previously), and drive formation of larger supramolecular assemblies, extending beyond dinuclear mesocate and helicate compounds.

A novel ligand – 2,2′-{1,1′-((2,3,5,6-tetramethyl-1,4-phenylene)bis(methylene))bis(1*H*-pyrazole-3,1-diyl}dipyridine (**21**) – was synthesised using identical procedures to those employed for the 1,4-xylyl spacer ligand (**20**), the details and characterisation of which are included in Section E.1.1 and in Section E.2.1.1 of Appendix E.

5.3.2.1 One-pot approach

With the ligand (**21**) in hand, complexation with ruthenium was firstly undertaken via a one-pot approach under microwave conditions using a 2 : 3 M/L ratio as described above. Broadening of the ligand signals in the aromatic region was observed in the NMR spectrum of the crude reaction mixture; however, this was not as substantial as seen for the 1,4-xylyl spacer compounds earlier in this Chapter (see Figure E.13 in Section E.2.3 of Appendix E). Column chromatography was undertaken (on silica gel: eluent 7 : 1 : 0.5, CH_3CN/H_2O/sat. aq. KNO_3) and two fractions were obtained, which showed promising NMR spectra (see Figure E.15 in Section E.2.3 of Appendix E). However, by HR ESI-MS analysis no mass fragments were able to be assigned to $M_{2n}L_{3n}$ stoichiometries, which were the anticipated products. It should noted for the second-eluting fraction (F2) several overlapping mass fragments corresponding to primarily +1 ions of monoruthenium(II)-containing products were identified in low abundance (based on peak splitting and intensities) but these were not able to be matched to any calculated isotope patterns.

Attempts to further purify the isolated samples were made chromatographically using an SP-Sephadex C-25 cation exchanger with an eluent containing NaCl of increasing ionic strength. In both cases the entire sample eluted as a single band at an NaCl concentration of 0.6 M, suggesting that the compounds had the same charge. Unsurprisingly, when analysed further by ^{1}H NMR spectroscopy, no meaningful change was seen for either sample when compared to the original purification on silica gel.

Overall, for one-pot reactions utilising the 2,3,5,6-tetramethyl-1,4-xylyl spacer ligand (**21**) no discrete Ru(II) cages or building blocks were able to be identified. This is in

contrast to the products of the one-pot reaction using the 1,4-xylyl spacer ligand (**20**) where a $[RuL_2]^{2+}$ compound was detected. The absence of such a species upon modification of the ligand suggested that the addition of steric bulk to the spacer ring may hinder formation of small discrete assemblies of this design. Furthermore, no assemblies of $M_{2n}L_{3n}$ stoichiometry were detectable in the product mixture. Based on structures reported by the Ward group for cages containing similar ligands it was anticipated that when complexed the spacer ring lies perpendicular to the pyrazolyl-pyridine chelation site. Given that no triple-stranded dinuclear species or tetrahedra were observed experimentally, it is proposed that the introduction of methyl substituents around the spacer ring may disfavour formation of smaller assemblies (such as M_2L_3, M_4L_6, etc.) where the methyl groups would point into the central cavity. While it was hoped that this steric hindrance may drive the formation of M_8L_{12} or larger assemblies, no compounds of this stoichiometry were detected. Again, this can be attributed to the challenges of using a relatively inert metal centre such as Ru(II), where cages of various nuclearities and polymer/oligomer may instead be formed and rearrangement to a thermodynamic product is less likely. Studies in **Chapter 4** of this thesis have demonstrated that for other Ru(II)-containing compounds the distribution of kinetic and thermodynamic products from microwave reactions can be influenced by varying reaction time. While this factor was not probed in the preliminary studies of compounds described in this Chapter utilising the 2,3,5,6-tetramethyl-1,4-xylyl spacer ligand (**21**), it is one possible avenue for future investigations.

5.3.2.2 Stepwise approach

It was evident that cages incorporating the 2,3,5,6-tetramethyl-1,4-xylyl spacer ligand (**21**) could not be readily synthesised by a one-pot approach, and so stepwise tactics were employed. Reaction of an excess of the ligand (**21**) with $[Ru(DMSO)_4Cl_2]$ (1 : 5 M/L ratio) produced a dark brown solution which, when filtered through Celite, appeared as a clear, yellow solution. The precipitate, which had been removed by filtration through Celite, was a pale brown powder containing black particles, and presumed to consist of unreacted ligand and ruthenium precursor. The compound of interest was isolated from the yellow filtrate as the PF_6^- salt and crude NMR showed a broad baseline in the aromatic region, attributed to polymeric material. Despite this, a complicated mixture of signals corresponding to coordinated ligand could also be seen, suggesting possible formation of cage compounds (see Figure E.14 in Section E.2.3 of Appendix E). Purification by column chromatography (on silica gel: eluent 7 : 1 : 0.5, CH_3CN/H_2O/sat. aq. KNO_3) was undertaken and a single fraction obtained, with a large proportion of material being

retained on the stationary phase. Once isolated as the PF_6^- salt, analysis by ^{1}H NMR revealed sharp peaks, particularly in the aromatic region, although these resonances were highly overlapping suggesting the presence of multiple different ligand environments (see Figure 5.20). The most downfield signals, two broad multiplets corresponding to the pyridyl-H6 resonances, were integrated revealing a ratio of 1.3 : 1 (see inset). It was anticipated that the pyridyl-H6 hydrogens of $[RuL_3]^{2+}$ compounds would appear at chemical shifts $\sim$ 8.5 ppm, and when integrated show the distribution of *mer*/*fac* isomers. While the signals at these positions were clearly composed of multiple overlapping resonances, it was unclear whether these indicated the presence of geometrical isomers of $[RuL_3]^{2+}$ species, or some alternative Ru(II)-containing supramolecular assembly.

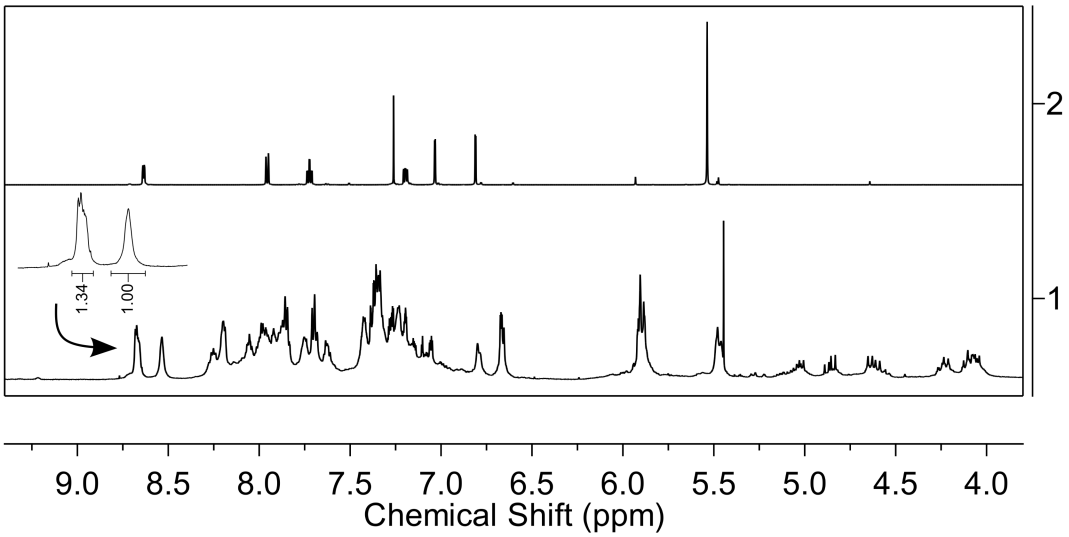

Figure 5.20: Partial ^{1}H NMR spectrum (600 MHz, CD_3CN, 298 K) showing (1) the single product from the reaction of the 2,3,5,6-tetramethyl-1,4-xylyl spacer ligand (**21**), with $Ru(DMSO)_4Cl_2$ under reflux conditions (dropwise addition to form $[RuL_3]^{2+}$ building blocks), purified by column chromatography; (2) the non-coordinated 2,3,5,6-1,4-xylyl spacer ligand (**21**; $CDCl_3$). Inset: expansion of ^{1}H NMR spectrum showing the presence of two major signals in an approximate 1.3 : 1 ratio for one of the pyridyl-H6 hydrogens.

This was further probed by HR ESI-MS, where the presence of the $[RuL_3]^{2+}$ building block was detected at *m/z* 723.3086 (corresponding to $[RuL_3 - 2PF_6]^{2+}$ species; see Figure E.25 in Section E.3.2 of Appendix E).

The detection of a $[RuL_3]^{2+}$ building block from this reaction was encouraging, indicating that addition of steric bulk in the spacer region did not preclude the formation of mononuclear compounds of this stoichiometry. Importantly, no mass fragments corresponding to a $[RuL_2]^{2+}$ species were detected (which were seen for samples containing the 1,4-xylyl spacer ligand), supporting the notion that increased steric bulk on the spacer may be sufficient to block formation of this type of mononuclear compound, where one ligand

is saturatively coordinated to the Ru(II) centre while the other has one non-coordinated chelation site. In addition, the absence of M_2L_3 species in both the one-pot and stepwise reactions using this ligand suggested that formation of smaller assemblies was also hindered. This was proposed to be due to the orientation of the spacer in the coordinated ligand, where the aromatic ring of the spacer unit is expected to lie perpendicular to the cavity of the structure and two of the CH_3 substituents would point into the cavity.

The successful preparation of Ru(II) building blocks incorporating both the 1,4-xylyl spacer and 2,3,5,6-tetramethyl-1,4-xylyl spacer ligands opens the door to building larger Ru(II)-containing cages, although improvements could be made to the yields and purity of the mononuclear compounds. Furthermore, in order to favour cube formation the mixture of geometrical isomers of the monoruthenium compounds must be better controlled. In the study outlined above further reaction of the 1,4-xylyl spacer ligand (see Section 5.3.1.3) did not lead to formation of a cube-type structure and instead generated quantities of polymer and unknown compounds. However, there are still many alternative synthetic approaches to be explored, which could include screening a variety of Ru precursors or modifying experimental conditions. Overall, the experimental design played a key role, as seen in the great differences in product formation for one-pot and stepwise reactions. No compounds of the desired $M_{2n}L_{3n}$ stoichiometry were detected in the product mixture from one-pot syntheses, in direct contrast to assemblies containing a structurally similar ligand described in **Chapter 4**. Modifying the spacer of the ligand to increase steric bulk (2,3,5,6-tetramethyl-1,4-xylyl) was found to hinder the production of small, discrete compounds with undesirable stoichiometry (such as $[RuL_2]^{2+}$) but ultimately did not drive formation of larger assemblies. This observation suggested that ligand design was a key consideration when attempting to form Ru(II) species, both with regards to the steric bulk of the spacer region and substitution on the bidentate chelation site (contrasting with the ligands in **Chapter 4** of this thesis). Throughout these studies the formation of Ru(II) supramolecular assemblies was further complicated by the relatively inert nature of the metal centre, where, unlike in more labile systems, rearrangement to a single thermodynamically-favoured product did not occur.

5.3.3 Addition of steric bulk – 9,10-dimethylanthryl spacer

Attention then turned to the final ligand selected, containing a 9,10-dimethylanthryl spacer. This ligand had previously been shown by Tidmarsh *et al.* to form cube-type cages in conjunction with Cu(II) and Zn(II) ions.[93] The synthesis of 9,10-bis{(3-(pyridin-

2-yl)-1*H*-pyrazol-1-yl)methyl}anthracene (**22**) is described in Section E.1.1 of Appendix E.

5.3.3.1 One-pot approach

Reaction of the 9,10-dimethylanthryl spacer ligand (**22**) with $RuCl_3 \cdot 3\,H_2O$ under microwave conditions yielded a dark yellow solution, with predominantly pale brown precipitate (confirmed to be unreacted ligand by ^{1}H NMR spectroscopy) containing small black particles (thought to be ruthenium precursor). The unreacted ligand could be removed by filtration through Celite, while the black material washed through. To remove the black particles, KPF_6 was added to the filtrate and the resulting yellow precipitate extracted with dichloromethane (DCM).

The ^{1}H NMR spectrum of this sample contained many signals in the aromatic region, suggesting multiple products may have been formed (see Figure E.16 in Section E.2.4 of Appendix E). Upon purification by column chromatography (on silica gel: eluent 7 : 1 : 0.5, CH_3CN/H_2O/sat. aq. KNO_3) three separate compounds were isolated. Analysis by ^{1}H NMR spectroscopy revealed that the first eluted fraction (F1) had extremely broad signals in the aromatic region (shown as (1) in Figure 5.21), and by HR ESI-MS no obvious mass fragments corresponding to Ru(II) compounds were detected. The second eluted fraction (F2) was more promising, with a large number of defined, but overlapping peaks in the ^{1}H NMR spectrum, while the third fraction (F3) had similarly sharp peaks, although these were somewhat obscured by broadening overall (see (2) and (3) respectively in Figure 5.21 below). The appearance of overlapping, sharp signals between 8.5 - 9.0 ppm in the NMR spectra of F2 and F3 were reminiscent of those assigned to the pyridyl-H6 hydrogens seen for $[RuL_3]^{2+}$ species incorporating other ligands earlier in this Chapter (see Figure 5.22). Further downfield (9.0 - 9.5 ppm) additional resonances were observed, potentially indicating the presence of other pyridyl-H6 chemical environments (see Figure 5.22). Resonances in this region were also seen in attempts to form a cube from the $[RuL_3]^{2+}$ building blocks synthesised using the 1,4-xylyl spacer ligand (see Figure 5.19 in Section 5.3.1.3), suggesting that peaks at these positions may arise from the formation of a higher order Ru(II) assembly. However, when analysed by HR ESI-MS F2 and F3 showed similar fragmentation patterns, with a dominant peak at *m/z* 738.1669, which was calculated to correspond to a $[RuL \cdot PF_6]^{1+}$ species. The HR ESI-MS for F2 is shown in Figure E.26 in Section E.3.3 of Appendix E. The stoichiometry of this compound was unexpected, and no other significant mass fragments for Ru(II)-containing compounds were observed. It was proposed that this mass fragment may arise from a partially ionised

species and may not accurately reflect the composition of F2 and F3 from the one-pot reaction. The structure of the potential $[\mathrm{RuL} \cdot \mathrm{PF_6}]^{1+}$ species was not further explored in this thesis.

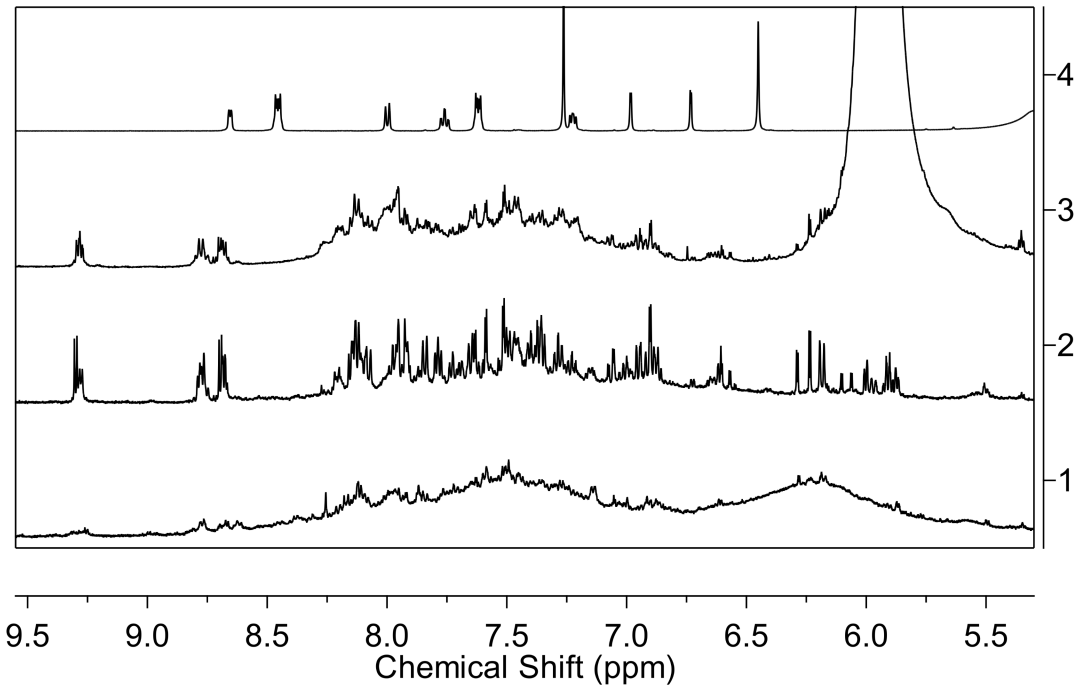

Figure 5.21: Partial ^{1}H NMR spectrum (500 MHz, CD_3CN, 298 K) showing the aromatic region from the purification of the crude reaction mixture of the 9,10-anthryl spacer ligand (**22**) with $RuCl_3 \cdot 3\,H_2O$ under microwave conditions (200 W, 200 PSI, 225 °C, 5 h). Fractions from chromatography are labelled in order of elution; (4) is the non-coordinated 9,10-anthryl spacer ligand (**22**); $CDCl_3$).

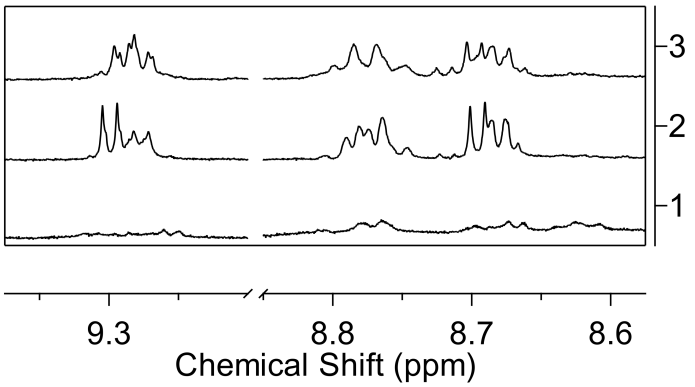

Figure 5.22: Partial ^{1}H NMR spectrum (500 MHz, CD_3CN, 298 K) showing the most downfield resonances from the purification of the crude reaction mixture of the 9,10-anthryl spacer ligand (**22**) with $RuCl_3 \cdot 3\,H_2O$ under microwave conditions (200 W, 200 PSI, 225 °C, 5 h). Fractions from chromatography are labelled in order of elution.

Based on the results described above it was clear that the addition of significant steric bulk to the spacer alone was not sufficient to drive exclusive formation of a larger Ru(II)

cage. For the products of the one-pot reaction no supramolecular assemblies of $Ru_{2n}L_{3n}$ stoichiometry were able to be detected, although downfield NMR resonances suggested that a variety of pyridyl-H6 environments were present. These were proposed to be either $[RuL_3]^{2+}$ or larger cage assemblies. As for other compounds synthesised previously in this Chapter, chromatographic purification was relatively successful at removing unwanted polymeric material; however, it was clear that a mixture of Ru(II)-containing compounds were still present in the isolated fractions. It was anticipated that the anthracene spacer would disfavour the formation of triple-stranded dinuclear species ($[Ru_2L_3]^{4+}$) and some small mononuclear compounds (such as $[RuL_2]^{2+}$), ideally leading to the generation of larger supramolecular assemblies in reactions utilising a 2 : 3 M/L ratio. Given the complex mixture of products obtained from the one-pot reaction it appeared that once again the relatively inert Ru(II) centre added an additional challenge. Where other, more labile transition metals have been shown to form cages with ligands of this type, using Ru(II) resulted in the formation of a variety of assemblies and prohibited rearrangement to a single, thermodynamically-favoured product.

5.3.3.2 Stepwise approach

Given that cages of $M_{2n}L_{3n}$ stoichiometry had not successfully been formed via one-pot methods using the 9,10-dimethylanthryl spacer ligand (**22**), a stepwise approach was pursued. After reaction of **22** with $[Ru(DMSO)_4(Cl)_2]$ (1: 5 M/L ratio) a yellow solution was observed, containing brown precipitate. This precipitate was confirmed by ^{1}H NMR spectroscopy to be unreacted ligand and was readily removed by filtration. Analysis of the ^{1}H NMR spectrum of the crude yellow product revealed a very broad baseline, although a number of peaks were discernible in the aromatic region (see Figure E.17 in Section E.2.4 of Appendix E). The presence of peaks - presumed to be coordinated ligand - was encouraging, although the pattern of signals was not as expected for a $[RuL_3]^{2+}$ species, where highly overlapping resonances were anticipated for a statistical mixture of *mer* and *fac* isomers. The addition of bulky substituents has previously been shown by others to influence the ratio of geometrical isomers in Ru(II) compounds, and it was proposed that the anthryl spacer ligand used in this study may be sufficient to favour production of the *mer* isomer. When purified by column chromatography (on silica gel: eluent 7 : 1 : 0.5, CH_3CN/H_2O/sat. aq. KNO_3) a single yellow band was observed, eluting cleanly from the column and analysis revealed a single set of dominant ligand resonances in the ^{1}H NMR spectrum (see Figure 5.23). Nine signals were detected in total, with integration and multiplicity matching those anticipated for a single, discrete compound of

high symmetry (see Figure E.17 in Section E.2.4 of Appendix E for integrated spectrum). Furthermore, the formation of a $[RuL_3]^{2+}$ species could be ruled out as additional resonances arising from *mer/fac* isomers and the different hydrogen environments of coordinated and noncoordinated ends of the ligand were not present. Despite promising ^{1}H NMR results, by HR ESI-MS analysis no meaningful Ru(II)-containing mass fragments were detected, which hindered efforts to further identify this compound.

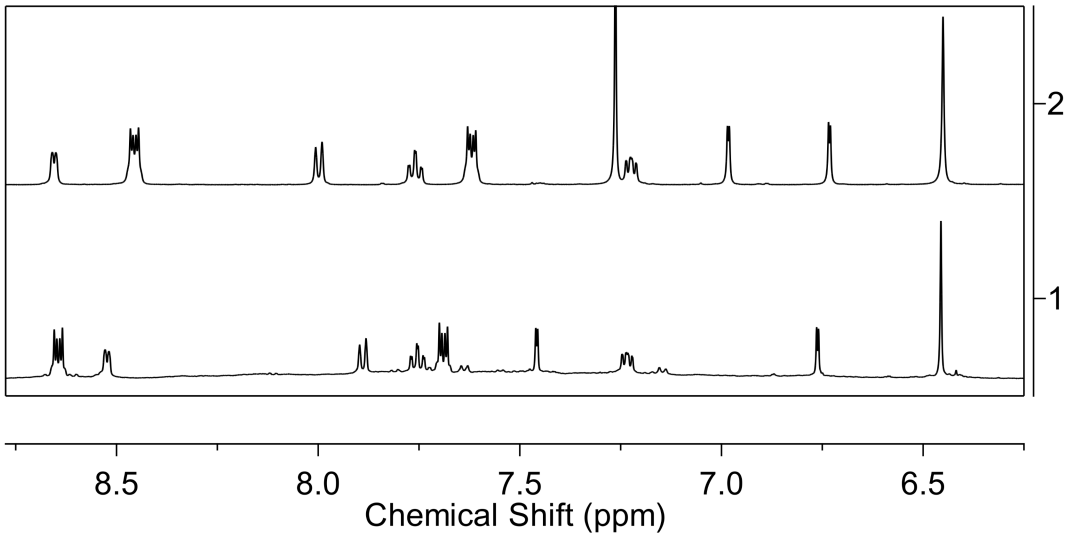

Figure 5.23: Partial ^{1}H NMR spectrum (500 MHz, CD_3CN, 298 K) showing (1) the aromatic region from the purification of the crude reaction mixture of the 9,10-dimethylanthryl spacer ligand (**22**) with $[Ru(DMSO)_4Cl_2]$ under reflux conditions (dropwise addition to form $[RuL_3]^{2+}$); (2) the non-coordinated 9,10-anthryl spacer ligand (**22**); $CDCl_3$).

Concerted efforts were made to grow crystals and elucidate the structure of the compound by X-ray crystallography; however, these were ultimately unsuccessful and the identity of the Ru(II)-containing assembly remains unknown. Given the composition of the ^{1}H NMR spectrum it was proposed that the product of the reflux reaction was a Ru(II) cage containing fully coordinated ligands. The presence of unreacted ligand in the initial product mixture may indicate formation of a compound with $M_{2n}L_{3n}$ stoichiometry, with the excess ligand remaining non-coordinated. For a compound of this type analogous hydrogens on the ligands would exist in identical chemical environments, matching the pattern of resonances seen by ^{1}H NMR spectroscopy. If a cage of high nuclearity (such as $[M_8L_{12}]^{16+}$ or larger) was formed full ionisation may not have been possible and any 1+ or 2+ ions would not have been detected in the *m/z* range used for HR ESI-MS in this study. As such, further investigation is required to ascertain the structure and nuclearity of the product from this synthesis using the 9,10-dimethylanthryl spacer ligand (**22**) ligand. While the original intent was to generate $[RuL_3]^{2+}$ building blocks, the potential isolation

of a single cage from this approach illustrates the interplay of ligand design, choice of metal centre, and reaction conditions in the formation of supramolecular assemblies. Where complex mixtures of Ru(II)-containing species were isolated from the one-pot reaction using a 2 : 3 M/L ratio, it appeared that the conditions used in the stepwise approach may favour formation of a single, discrete assembly. Specific factors, including use of a Ru(II) precursor, longer reaction time, or dropwise addition of metal salt to a solution containing excess ligand, may all play a role in directing the distribution of products and are worth investigating in future studies.

5.4 Conclusions and future directions

In this Chapter approaches to the design and synthesis of mononuclear Ru(II) building blocks and their application for larger cage compounds have been outlined. Taking inspiration from the work described in **Chapter 4** of this thesis, the synthesis of Ru(II) cages was undertaken via a one-pot approach utilising microwave conditions. Simultaneously, a stepwise path was taken, based on studies by Metherell and Ward, to form $[RuL_3]^{2+}$ building blocks for subsequent assembly into larger cages with additional ruthenium salts. A pyrazolyl-pyridine based ligand, containing a 1,4-xylyl spacer was selected for study, and the steric bulk of the spacer modulated to include additional methyl groups, or an anthracene unit.

Frustratingly, for one-pot reactions with the 1,4,-xylyl spacer ligand a complex mixture of products was observed, and when separated no compounds of $[Ru_{2n}L_{3n}]$ or $[RuL_3]$ stoichiometry were detected. This was in direct contrast to the results discussed in **Chapter 4** of this thesis, where a structurally similar ligand was employed to generate dinuclear compounds. Given that similar species were not synthesised under analogous conditions in this Chapter, it was evident that ligand design plays a key role in directing the product formation of Ru(II) assemblies. Interestingly, one of the isolated compounds was found to contain mass fragments corresponding to a $[RuL_2 \cdot PF_6]^+$ species, similar to that noted by Metherell and Ward for a compound containing 1,2-xylyl spacer ligand.[101]

Following a stepwise approach, reactions with the 1,4,-xylyl spacer ligand were found to yield $[RuL_3]^{2+}$ building blocks. The assembly of a larger cage using these pre-formed vertices was then attempted by reaction with further equivalents of a Ru precursor; however, this attempt was unsuccessful in the generation of any obvious discrete structures. Monitoring of the ^{1}H NMR spectrum over the course of a seven day reaction revealed that the Ru(II) mononuclear building blocks did react further but formation of a single discrete assembly was not observed. The appearance of significantly downfield-shifted ligand resonances in the ^{1}H NMR suggested that formation of a larger cage may have occurred; however, the concomitant formation of polymeric material and alternative products was observed. It was noted that small quantities of the $[RuL_2]^{2+}$ species were also detected in the original product mixture, and the ratio of *mer* : *fac* isomers of the $[RuL_3]^{2+}$ compound did not match the expected statistical distribution. Both of these factors added additional challenges in the formation of a larger cage, a process which is further complicated by the use of a relatively inert metal centre. The successful formation of the $[RuL_3]^{2+}$ species containing the 1,4-xylyl spacer ligand provides a useful starting point for future attempts

to form larger cages, although greater control of the product distribution, particularly with regards to the formation of geometrical isomers is paramount. Alteration of the reaction conditions screened in this Chapter for assembly of a larger cage by modifying the duration or temperature, may provide possible routes to the generation of Ru cubes or other cage-type compounds, and drive formation of a thermodynamically-favoured product.

In an attempt to direct assembly towards larger Ru cages and block formation of $[RuL_2]^{2+}$ or triple-stranded dinuclear species, the central spacer of the ligand was modulated to add steric bulk. A novel ligand containing a 2,3,5,6-tetramethyl-1,4-xylyl spacer (**21**) was synthesised, and complexation with Ru(II) attempted by one-pot and stepwise approaches. Despite ^{1}H NMR studies suggesting that discrete Ru(II) compounds had been formed by one-pot methods, no mass fragments corresponding to $M_{2n}L_{3n}$ stoichiometry were detected. Promisingly, $[RuL_3]^{2+}$ compounds were detected in the product formed by stepwise approaches, showing that inclusion of steric bulk in the spacer did not prevent formation of these monoruthenium building blocks. However, as seen for compounds containing the 1,4-xylyl spacer ligand, the distribution of geometrical isomers based on integration of the pyridyl-H6 resonances in the ^{1}H NMR spectrum was not as expected for a statistical mixture (3 : 1 *mer*/*fac*), and further assembly of a larger cage using these building blocks was not attempted.

The successful synthesis of $[RuL_3]^{2+}$ building blocks for both the 1,4-xylyl spacer (**20**) and 2,3,5,6-tetramethyl,1,4-xylyl spacer ligands by stepwise methods paves the way for the generation of larger assemblies. Following the example of Metherell and Ward, mixtures of *mer* and *fac* isomers of the mononuclear compounds described in this thesis could be reacted with more labile transition metals to form heterometallic cubes.[98] Alternatively, the separation of geometrical isomers could be attempted, before further reaction to potentially access new types of assemblies (such as the Ru/Ag adamantoid cage described elsewhere[100]). However, it is clear that the ability to control the distribution of geometrical isomers, either in the initial synthesis or subsequent separation, is crucial when considering further cage assembly following a stepwise approach. To this end, future experiments should also focus on the factors governing *mer* and *fac* isomer formation, before attempting to generate larger Ru(II) cages.

In the final section of this Chapter, the formation of Ru(II) cages containing a 9,10-dimethylanthryl spacer ligand was attempted. Products containing this ligand, which had previously been shown to form cubes with Cu(II) and Zn(II),[93] initially appeared promising when isolated from a one-pot reaction; however, the nature of any Ru(II)

compounds formed was not able to be determined by HR ESI-MS studies. While ^{1}H NMR studies indicated the potential formation of mononuclear $[RuL_3]^{2+}$ species and cages of higher nuclearity, the presence of these compounds could not be detected by HR ESI-MS. Mass fragments corresponding to a $[RuL \cdot PF_6]^+$ compound were observed in some isolated samples but these were not further characterised in this thesis. It appeared that the significant steric bulk introduced by modifying the spacer to include anthracene was sufficient to disfavour formation of small mono- or dinuclear compounds (such as $[RuL_2]^2$ and $[Ru_2L_3]^{4+}$); however, ligand design alone was not enough to direct the formation of a single larger discrete assembly. Due to the use of a relatively inert metal centre rearrangement to a thermodynamically-favoured assembly did not occur, as reflected in the products from the one-pot synthesis involving ruthenium centres where a mixture of compounds and polymer/oligomer were present.

Attention then turned to a stepwise approach, with the intent to form $[RuL_3]^{2+}$ building blocks, as described for the two ligands above. After purification a single set of resonances (totalling nine) was observed in the ^{1}H NMR spectrum for the product of this reaction, with integrations and multiplicities matching those expected for a single, discrete compound of high symmetry. When analysed by HR ESI-MS no meaningful Ru(II)-containing mass fragments were detected, hindering efforts to identity of the isolated compound. While the specific nuclearity is not known at this stage, it was proposed to be a larger cage-type assembly capable of accommodating the steric bulk of the anthracene-containing spacer, with all hydrogen resonances of the ligand in identical environments. Attempts to crystallise the compound to allow structural characterisation by X-ray crystallography are still ongoing.

The contrasting products observed from the different synthetic approaches presented in this Chapter illustrate the range of factors that influence the product distribution in supramolecular assembly. For compounds utilising ligands containing a 1,4-xylyl spacer in this Chapter compared to those in **Chapter 4**, great differences in product distribution were observed. These differences demonstrated the importance of ligand design, where by exchanging a triazole for a pyrazolyl donor, the formation of triple-stranded dinuclear species was disfavoured. In subsequent studies, when the steric bulk on the central spacer was increased the impact of reaction conditions, including choice of ruthenium precursor and stoichiometry, became more apparent. While attempts to form a Ru(II) cage or Ru(II)-containing building blocks, either by stepwise or one-pot syntheses, were met with limited success, in all cases the major challenge faced was the formation of a complex mixture of products – including assemblies of unwanted stoichiometry and polymeric

material. This was an unfortunate consequence of utilising a relatively inert metal centre such as ruthenium, and while in previous Chapters the formation of dinuclear products was favoured, this did not appear to be the case for ligands selected in this Chapter.

In **Chapter 5** of this thesis two synthetic pathways for the formation of ruthenium cages have been presented, with the approaches described herein providing a useful foundation for future investigations. The ligands selected are capable of extensive modification, particularly in the spacer region, which may allow the impact of ligand design on the product distribution to be further probed. The generation of $[RuL_3]^{2+}$ building blocks demonstrates the potential of the stepwise approach to cage design and would be highly applicable in future studies, either of Ru(II) cages or heterometallic species, providing that the *mer* and *fac* isomer distribution can be better controlled. Alternatively, the excellent procedures described by Metherell and Ward for the formation and isomer separation of ruthenium(II) compounds containing bidentate ligands,[407] would be useful in this context, where a broader range of cage structures may be accessed by tailoring the ratio of geometrical isomers employed. An additional advantage of a multi-stepwise approach such as this is the ability to generate unsymmetrical di(bidentate) ligands where a non-identical bidentate chelation site could be appended to the terminal ends of the coordinated ligands, thus further increasing the structural variety of possible assemblies. In this Chapter, the challenges faced in the synthesis of Ru(II)-containing cages have been described, with the major difficulties arising from the use of the relatively inert metal centre, both in the generation of mononuclear building blocks and larger assemblies. The implications of choosing this metal centre were evident in the complex product mixtures obtained and minute quantities of compound able to be isolated after purification, which suggested that the synthetic approaches presented in this Chapter were not the most efficient methods for Ru(II) cage formation using these ligands. There is still considerable interest in generating cages of this design, as the inert metal centre may impart useful stability, giving these assemblies an advantage over analogous structures containing other transition metals; however, further studies are required to better understand the factors controlling product distribution.

CHAPTER 6

Epilogue

6.1 Conclusions and future directions

This thesis describes approaches to the synthesis of a number of ruthenium-containing compounds ranging from dinuclear species to larger cage assemblies. The work has built upon existing protocols, and in doing so improved our understanding of how product distribution in these systems can be controlled. The chemistry of dinuclear helicates and mesocates, and larger cage structures containing labile transition metals has been widely researched; however, the incorporation of the inert metal centre Ru(II) in these assemblies is an under-explored field. This thesis firstly investigated the synthesis and purification of diruthenium double- and triple-stranded compounds. The interactions of some of these species with DNA were studied by a range of methods to establish their suitability as potential therapeutics. In addition, preliminary studies to extend beyond dinuclear species and form larger Ru(II) cage assemblies were undertaken. In summary, this study has contributed to an increased understanding of the factors governing formation of dinuclear and cage assemblies in an inert system, while also exploring the interactions of Ru(II)-containing helical mimics in biological settings.

In **Chapter 2**, methods were developed to synthesise a double-stranded helicate and mesocate pair, incorporating a di(terpyridine)-based ligand. Experimentally the helicate was the predominant product, and this finding was supported by computational modelling where the helicate was found to be the more stable isomer. The two dinuclear species were able to be separated by chromatographic methods, and despite structural similarities the pair were found to have significantly different photophysical properties. Both compounds were emissive at 77 K but the helicate and mesocate varied in terms of temporal emission characteristics, showing differing dominant emission lifetimes. Additional experiments are required to fully understand this interesting difference in emission behaviour. Finally, extensive screening was performed to determine suitable conditions for the resolution of the helicate. Cellulose, a chiral chromatographic support, proved to be the most suitable choice, and partial resolution of the helicate was achieved by elution with 0.2 M NaCl. With

the double-stranded mesocate, and partially-resolved enantiomers of the helicate in hand, investigations into the biological interactions of these compounds could be undertaken.

In the literature there are many reports of the DNA binding of Ru(II) compounds, and helicates built from other transition metals. However, there are few studies into the interactions of diruthenium helicates and mesocates with DNA. The work described in **Chapter 3** investigated the binding of the compounds described in **Chapter 2** with calf thymus DNA (ct-DNA) and three oligonucleotide sequences. Preliminary studies to probe an enantiomeric preference for the double-stranded helicate with DNA, as has been seen for other Ru(II) helicates, were undertaken using dialysis techniques. No enantiomer-specific binding was observed and attention turned to linear dichroism (LD) spectroscopy to study the interactions of the achiral mesocate and partially-resolved helicate enantiomers with DNA. All Ru(II) compounds were observed to coil/condense DNA, suggestive of groove binding, although precipitation hindered efforts to fully screen all samples. To gain greater insight into the specific type of groove binding, NMR spectroscopy studies were performed for all compounds with G/C-rich, A/T-rich, and bulge oligonucleotide sequences. In all cases weak nuclear overhauser effect (NOE) contacts between minor groove DNA resonances suggested that the double-stranded compounds interacted in the minor groove, although steric bulk prohibited binding deep within the groove. No clear differences in binding were observed for the two enantiomers or the mesocate, and the presence of extensive precipitation in all samples containing compound and DNA hindered further characterisation. The data presented in **Chapter 3** has expanded our knowledge of the interactions between double-stranded compounds of this type and DNA; however, in order to fully comprehend the nature of these interactions additional studies with the fully-resolved helicate enantiomers are needed. The size and shape of the dinuclear assemblies studied are a further limiting factor, being too large to fit within the preferred binding site – the minor groove. The synthesis of helicates with functionality that is more suited to groove binding may be required in order to develop a better understanding of how the chirality of the compounds influences the mode and strength of DNA binding.

The factors impacting helicate and mesocate formation were investigated in **Chapter 4** for a small family of triple-stranded compounds, building upon previous reports in the literature. By employing a flexible ligand and relatively inert Ru(II) centre it was found that unexplored mesocate/helicate pairs could be accessed. An important finding of this study was that a previously suggested odd/even rule of mesocate and helicate formation could be broken, and the two dinuclear species separated and helicates resolved (in most cases). Of particular interest were compounds containing an *n*-propyl spacer,

where unusual isomerisation of the dinuclear assemblies was observed upon irradiation with visible light; behaviour which has not before now been reported for a mesocate/helicate pair. Despite the relatively facile synthesis and purification of these compounds, preliminary biological studies with ct-DNA suggested that only weak binding may occur, with no clear enantiomeric preference. LD experiments indicated that groove binding was likely in most cases, in agreement with reports for other transition metal compounds containing these ligands. Based on the size and shape of the Ru(II) assemblies it is anticipated that DNA binding may occur in the major groove, in contrast to the double-stranded compounds studied in **Chapter 3** which showed interactions in the minor groove. Furthermore, the coiling of DNA, observed by LD spectroscopy for triple-stranded species was significantly smaller in magnitude than seen for the double-stranded helicate and mesocate previously, suggesting weaker levels of interaction. It is not presently understood why the triple-stranded Ru(II) compounds described in **Chapter 4** showed such modest interactions with DNA compared to the double-stranded compounds investigated in **Chapter 3** and other transition metal compounds containing similar di(triazole-pyridine) ligands. Further studies with varied oligonucleotides by LD spectroscopy or NMR methods may inform as to the manner and strength of binding. In addition, knowledge gained in the resolution of these compounds may be applied to those containing other transition metals (which have shown more promising biological activity) to allow study of any enantiospecific preference.

Chapter 5 built upon knowledge from the previous studies to extend protocols for the generation of larger metallosupramolecular assemblies. There are few examples of metal-organic cages (MOCs) containing solely Ru(II), with the majority incorporating metalloligands. Using stepwise methods reported for the formation of mixed-metal cages,[98–101] $[RuL_3]^{2+}$ building blocks were able to be synthesised using di(pyrazolyl-pyridine) ligands. Steric bulk in the spacer region of the ligands was varied and found to greatly influence product distribution. While the formation of $[RuL_3]^{2+}$ and other Ru(II) species was observed from stepwise or one-pot reactions, this study highlighted the challenges of using only a relatively inert metal centre. More specifically, for the ligands screened large amounts of polymeric material were detected in the crude product mixtures, and while purification was possible chromatographically, in most cases mixtures of Ru(II) species remained. Where $[RuL_3]^{2+}$ building blocks were isolated, further reaction with Ru(II) to generate cages did not yield the desired cube-type assemblies. Despite the preliminary nature of these studies, the stepwise method may show promise for the generation of Ru(II)-containing building blocks using a variety of ligands. In the investigation described in **Chapter 5**, the ligand design and synthetic conditions chosen greatly impacted the

product distribution. These findings pave the way for further exploration of Ru(II) cages, where the ligand range and reaction conditions can be further modulated.

The work in this thesis has explored the formation of Ru(II) supramolecular assemblies, initially investigating product distribution in dinuclear species, before extending the approach to include larger architectures. Studies were limited to a specific group of ligands, leaving a great number of potential structures unexplored and as such, there remains a significant potential for future study. Assemblies formed by different synthetic methods, or incorporating structurally-diverse ligands, may allow formation of a range of unexplored structures, which can only be isolated using a relatively inert metal centre, such as Ru(II). However, there are limitations in the use of Ru(II) centres. Harsh reaction conditions may limit ligand choices to those that are sufficiently robust, and the formation of polymeric side-products, which has been observed extensively in this thesis, may hinder the generation and isolation of discrete Ru(II) assemblies. The shape and surface chemistry of dinuclear compounds formed was also found to be of great importance, particularly in biological settings. The compounds described herein exhibited markedly different interactions with DNA, compared to double- and triple-stranded Ru(II) compounds described elsewhere. As such, when selecting ligands the resulting surface chemistry should be carefully considered to allow formation of Ru(II) assemblies that are suited for specific tasks, including binding in the major or minor groove of DNA.

Further investigation of the photophysical properties of the dinuclear compounds described in this thesis is also of considerable interest. For the double-stranded compounds described in **Chapter 2** ultrafast transient absorption measurements are currently being performed by collaborators to better understand the different excited state decay kinetics observed for the mesocate and helicate. There is also scope to explore the photoisomerism noted for the *n*-propyl spacer compounds described in **Chapter 4**. In particular, determination of the specific wavelength responsible for conversion and the extent of isomerisation possible may allow the dinuclear product distribution to be influenced. Furthermore, the scope of this study could be extended to include other Ru(II) compounds containing similar ligands, to see whether this is unique to the *n*-propyl spacer system or more broadly applicable to Ru(II) assemblies of this design.

The synthesis of larger Ru(II) cages, building on the preliminary studies of **Chapter 5**, requires additional investigation. While this thesis explored the impact of steric bulk on product distribution, it was clear that the underlying ligand scaffold greatly impacted the types of Ru(II) assemblies that could be generated. The approach to using mononuclear building blocks, of the type $[RuL_3]^{2+}$, could be extended to a multi-stepwise

pathway, where the separation of the *mer* and *fac* isomers of Ru(II) compounds containing monodentate ligands could be achieved, before functionalisation of the ligand to generate a bidentate. By using stereochemically-pure building blocks greater control may be gained over the formation of supramolecular assemblies, allowing targeted synthesis of cages with specific nuclearities. This approach has a host of possible applications, from the generation of heterometallic cages (similar to those reported elsewhere), to the generation of monoruthenium compounds containing non-symmetrical bidentate ligands. The formation of Ru(II) cubes (or other assemblies) attempted in **Chapter 5** of this thesis requires further investigation. Alternative ruthenium precursors and reaction conditions need to be trialled to identify those suitable for the assembly of the monoruthenium(II) building blocks (described in this thesis) into larger cages. Interest persists in constructing cages of this design, as the inert nature of the metal centre may impart high stability, a potentially useful property that could be exploited for host-guest chemistry. Transition metal cages incorporating similar ligands have exhibited promising results in the capture of chemical warfare agents, and uptake and release of drug molecules. It is envisaged that Ru(II) cages with analogous structures may have comparable properties, as well as enhanced stability. Furthermore, many supramolecular assemblies, including those studied in this thesis, are inherently chiral, a characteristic that may be harnessed for catalysis or sensing involving chiral molecules. Approaches to the synthesis and resolution of the ruthenium compounds described in this thesis may also be applicable to compounds containing other transition metals, and bolster further research in metallosupramolecular chemistry.

APPENDIX A

General methods

A.1 General Methods

High resolution mass spectrometry (HRMS) (ESI, positive-ion mode) experiments of samples dissolved in acetonitrile were performed using an Agilent Series 6230 TOF LC/MS. UV/Vis absorption spectra were acquired at ambient temperature on a Cary 1E UV-Visible Spectrophotometer (scan range: 600-200 nm, scan rate: 600.00 nm min^{-1}, SBW: 2.0 nm). circular dichroism (CD) spectra were acquired at ambient temperature using a Jasco J-715 spectropolarimeter (scan range: 600 - 200 nm, resolution: 1 nm, bandwidth: 2.0 nm, sensitivity: 200 mdeg, response: 1 sec, speed: 100 nm/min). Emission spectra and kinetics were acquired at 77K using an Oxford Instruments cryostat (OptistatDN), at the University of Melbourne. Steady-state emission spectra were recorded using an fluorimeter (Agilent, Eclipse) with 5 nm bandwidth on both excitation and emission monochromators. Time-resolved emission measurements were performed using a tuneable nanosecond optical parametric oscillator (Eskpla NT340) as the excitation source ($\sim$ 5 nm pulses at 10 Hz), an emission monochromator (Acton SpectraPro 300i), long-pass filter (GG550), photomultiplier tube (Hamamatsu R928), and digital oscilloscope (Teledyne/LeCroy Wavesurfer 10). Scanning Electron Microscope (SEM) images were collected on a Quanta 450 scanning electron microscope in secondary electron mode (spot size 4 and 15 KeV). Samples for SEM analysis were wet loaded onto adhesive carbon tabs and carbon coated (5 nm) prior to analysis. Electron Dispersive X-ray Analysis was collected with an Oxford Instruments Ultim Max 170 EDX attachment on the Quanta 450.

All ^{1}H NMR and ^{13}C NMR spectra were obtained using an Agilent 500 MHz NMR spectrometer operating at 500/126 MHz or a Varian Inova operating at 600/151 MHz at 25 °C, unless otherwise stated. Spectra of samples were recorded in solutions of $CDCl_3$, using TMS as an internal standard, CD_3CN, d_6-DMSO, or D_2O. The following abbreviations for hydrogen multiplicities were used: s, singlet; d, doublet; t, triplet; m, multiplet; and br, broad. ^{1}H signals were assigned with assistance of 2D NMR experiments where required.

Where possible, reactions were monitored by thin layer chromatography (TLC) on

MERCK aluminium-backed silica gel 60 F_{254} plates or MERCK aluminium-backed neutral aluminium oxide 150 F_{254} plates, and visualised under UV light at λ 254 nm. Flash column chromatography was performed using Roth (40 - 63 micron) grade silica gel or Fluka aluminium oxide (0.05 - 0.15 mm, pH 7). Vacuum liquid chromatography was performed using Sigma-Aldrich (2-25 micron) TLC silica gel. Cellulose chromatography was performed using Aldrich (20 micron) microcrystalline cellulose powder. All compounds were anion exchanged using Dowex 1X-8 (Cl) 20 - 50 mesh to form the chloride salts, or Dowex that had been anion exchanged to form the bromide salts.

Commercially-available reagents and reagent grade solvents were used without further purification unless otherwise indicated. All other solvents and reagents were purified according to the literature.[415]

APPENDIX B

Supporting Information for Chapter 2

B.1 Synthetic procedures

B.1.1 Ligand synthesis

Lithium diisopropylamide (LDA) was freshly prepared by addition of *n*-butyllithium (2.5 M in hexanes) to a solution of distilled diisopropylamine in tetrahydrofuran (THF). The *precursors* – 5-Methyl-2-(tributylstannyl)pyridine and 5,5″-dimethyl-2,2′:6′,2″-terpyridine – were prepared according to literature procedures.[132,133]

B.1.1.1 1,2-Bis{5-5′-methyl-2,2′:6′,2′-terpyridinyl)}ethane (**2**)

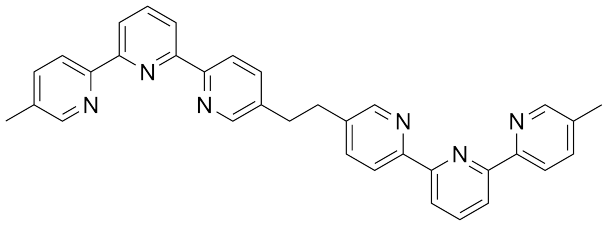

Figure B.1: 1,2-Bis{5-5′-methyl-2,2′:6′,2′-terpyridinyl)}ethane (**2**)

Using a procedure modified from that described by Rapenne *et al*,[129] a solution of 5,5″-dimethyl-2,2′:6′,2″-terpyridine (**1**) (0.50 g, 1.92 mmol; 1 equiv) in anhydrous THF (62.5 mL) was cooled to -78 °C under Ar. Freshly prepared LDA (1.93 mmol in 7.5 mL THF; 1 equiv.) was added dropwise and the reaction mixture stirred at -78 °C for 2 h. The mixture was warmed to 0 °C, and then cooled again to -78 °C. 1,2-Dibromoethane (0.74 mL, 1.61 g; 8.57 mmol; 4.5 equiv.) was added, and the reaction mixture stirred at -78 °C for 4 h, after which it was warmed to room temperature. After stirring at room temperature for a further 4 h, deionised water (50 mL) was added, and the THF removed by rotary evaporation. The aqueous solution was extracted with dichloromethane (DCM) (3 x 25 mL), washed with deionised water (2 x 25 mL), brine (1 x 25 mL), dried over $MgSO_4$, filtered, and the product purified by column chromatography (neutral Al_2O_3): initial elution with DCM removed unreacted starting material, while subsequent elution with

DCM/methanol (MeOH) (9:1 by volume) allowed isolation of crude product. The crude product was further purified by reprecipitation from DCM using diethyl ether to give **2** as a white solid (0.13 g, 26%). δ_H (500 MHz, $CDCl_3$) 8.57 - 8.46 (m, 4H), 8.39 (d, J = 7.9 Hz, 2H), 7.92 (t, J = 7.8 Hz, 1H), 7.62 (dd, J = 19.3, 7.7 Hz, 2H), 3.08 (s, 2H), 2.41 (s, 3H).

B.1.2 Dinuclear Ru(II) compounds

A solution of $RuCl_3 \cdot 3\,H_2O$ (10 mg, 0.038 mmol; 1 equiv.) and **2** (20 mg, 0.038 mmol; 1 equiv.) in ethylene glycol (10 mL) was heated to reflux under N_2 for 3 days. The reaction mixture was cooled to room temperature, deionised water added (20 mL), and filtered through Celite. NH_4PF_6 solution (4%, 5 mL) was added, the resulting precipitate isolated using centrifugation (10621 g; 5 min), washed with water, and dried under vacuum to give the crude product.

B.1.2.1 Separation of Ru(II) compounds from polymeric material

The crude pruduct was purified from polymeric material by vacuum liquid chromatography, on silica gel using 0.2 M NH_4Cl in dimethylformamide (DMF)/H_2O (4:1 by volume) as the eluent.[136] This yielded a mixture of **4** and **3** (R_f = 0.57 for a thin layer chromatography (TLC) using the same adsorbent/eluent combination).

B.1.2.2 Chromatographic separation of mesocate and helicate

The separation of **4** and **3** was achieved using a procedure modified from that outlined by Rice and co-workers for double-stranded diruthenium helicates and mesocates.[82] The mixed product obtained above was subjected to vacuum liquid chromatography, using CH_3CN/H_2O/sat. aq. KNO_3 (7 : 1 : 0.5 by volume) as the eluent.[136]

This yielded **4** as the first-eluted species (R_f = 0.36 for a TLC using the same adsorbent/eluent combination) as a red orange solid (2.4 mg, 7%). Mp > 260 °C. λ_{max} CH_3CN/nm (ε/M^{-1} cm^{-1}) 472 (5.98 x 10^3), 315 (3.43 x 10^4), 273 (2.55 x 10^4), 252 (2.45 x 10^4). δ_H (500 MHz, CD_3CN) 8.65 (d, J = 8.1 Hz, 4H), 8.58 (d, J = 8.1 Hz, 4H), 8.41 - 8.31 (m, 8H), 8.28 (d, J = 8.2 Hz, 4H), 8.00 (dd, J = 8.4 Hz, 1.5, 4H), 7.67 (dd, J = 8.2, 0.6 Hz, 4H), 7.19 (d, J = 1.5 Hz, 4H), 6.67 (d, J = 0.6 Hz, 4H), 2.97-2.84 (m, 4H), 2.56 - 2.44 (m, 4H), 2.00 (s, 12H). δ_C (126 MHz, CD_3CN) 158.28, 158.19, 157.86, 157.48, 156.78, 153.56, 141.72, 141.37, 141.32, 140.91, 138.33, 126.13, 125.57, 125.45, 125.40, 31.64, 20.09. m/z (ESI) 767.1052 ($[Ru_2\mathbf{2}_2 \cdot 2PF_6]^{2+}$).

The second product was subsequently eluted, yielding **3** ($R_f = 0.28$ for a TLC using the same adsorbent/eluent combination) as a orange solid (3.1 mg, 9%). Mp > 260 °C. λ_{max} (CH_3CN)/nm (ε/M^{-1} cm^{-1}) 476 (1.64 x 10^4), 315 (1.17 x 10^4), 276 (1.16 x 10^4), 251 (1.16 x 10^4). δ_H (500 MHz, CD_3CN) 8.83 (d, J = 8.1 Hz, 4H), 8.71 (d, J = 8.1 Hz, 4H), 8.50 (t, J = 8.1, 3.9 Hz, 4H), 8.38 (d, J = 8.3 Hz, 4H), 8.34 (d, J = 8.2 Hz, 4H) 7.74 (d, J = 7.3 Hz, 4H), 7.40 (d, J = 10.4 Hz, 4H), 7.15 (s, 4H), 6.38 (s, 4H), 2.63 (s, 8H), 2.03 (s, 12H). δ_C (126 MHz, CD_3CN) 158.47, 158.21, 157.93, 157.04, 155.22, 152.90, 141.80, 141.42, 141.16, 140.18, 138.65, 126.69, 126.21, 125.92, 125.41, 30.79, 19.88. *m/z* (ESI) 767.1061 ($[Ru_2\mathbf{2}_2 \cdot 2PF_6]^{2+}$).

B.2 Additional NMR spectra

B.2.1 Mesocate (**4**)

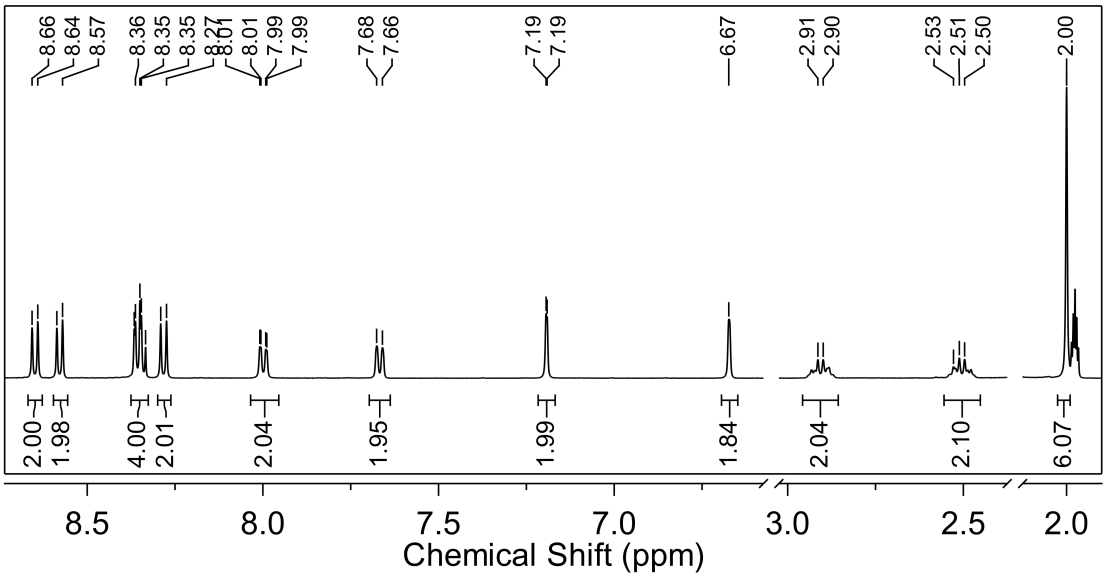

Figure B.2: ^{1}H NMR spectrum (500 MHz, CD_3CN, 298 K) showing the mesocate (**4**).

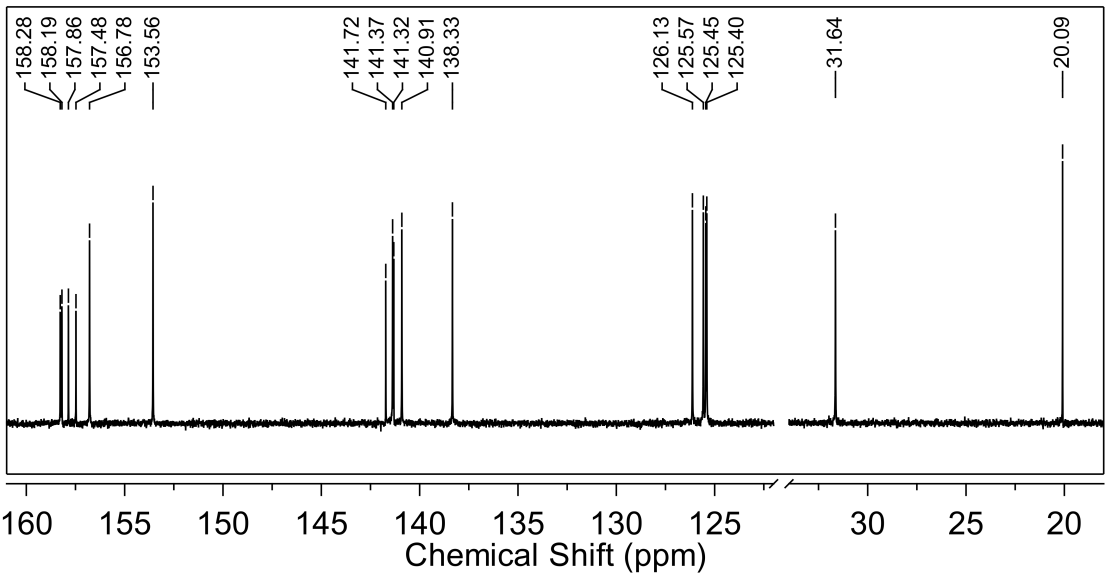

Figure B.3: ^{13}C NMR spectrum (126 MHz, CD_3CN, 298 K) showing the mesocate (**4**).

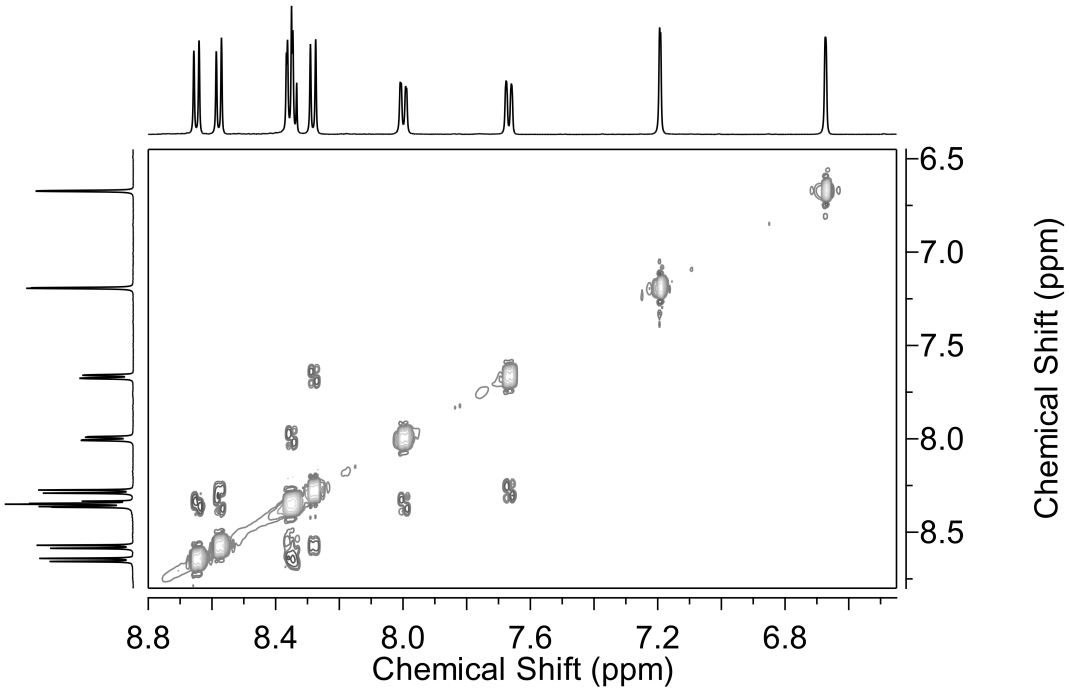

Figure B.4: Partial ^{1}H - ^{1}H ROESY NMR spectrum (500 MHz, CD_3CN, 298 K) showing the mesocate (**4**).

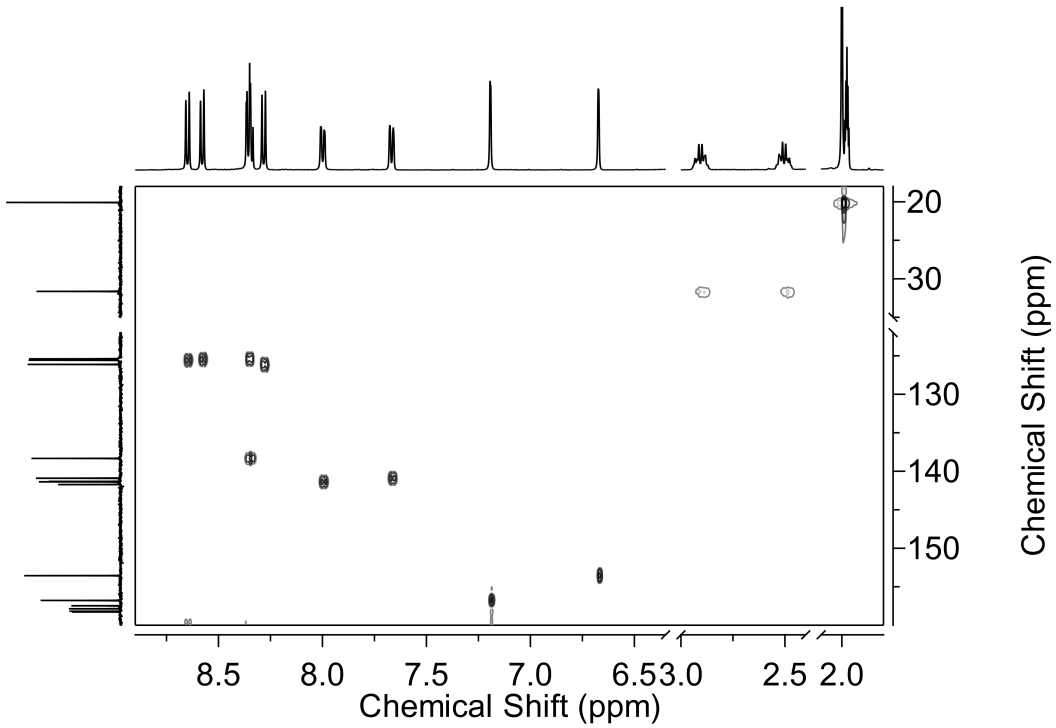

Figure B.5: Partial ^{1}H - ^{13}C HSQC NMR spectrum (CD_3CN, 298 K) showing the mesocate (**4**).

B.2.2 Helicate (**3**)

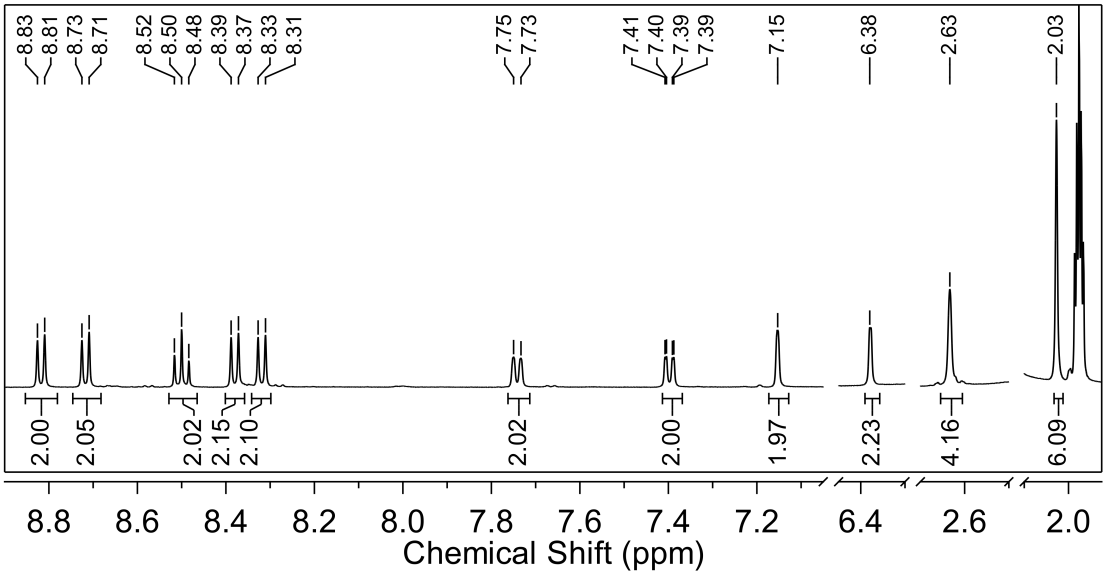

Figure B.6: ^{1}H NMR spectrum (500 MHz, CD_3CN, 298 K) showing the helicate (**3**).

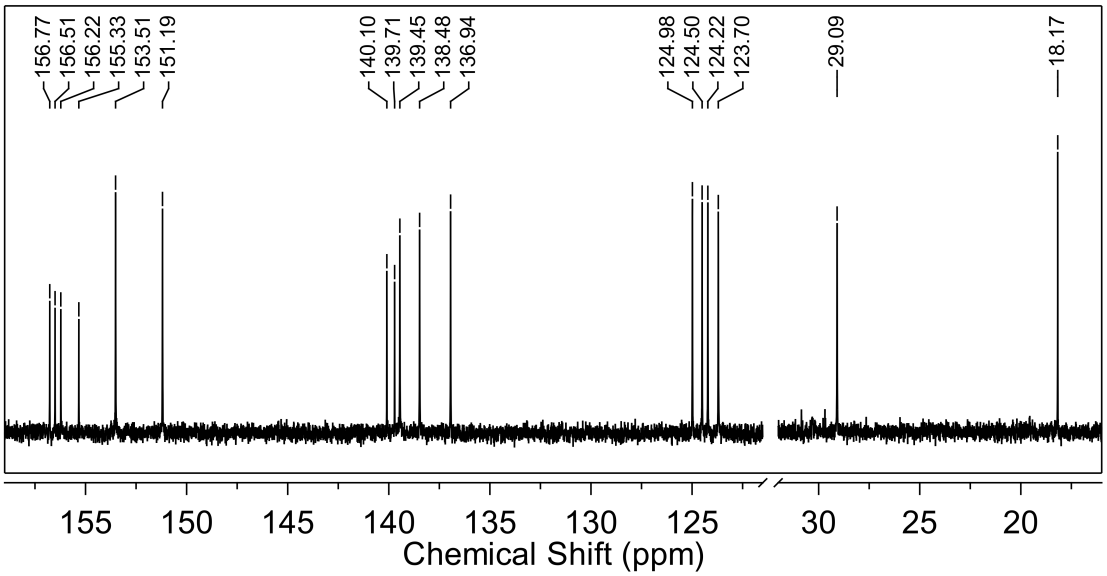

Figure B.7: ^{13}C NMR spectrum (126 MHz, CD_3CN, 298 K) showing the helicate (**3**).

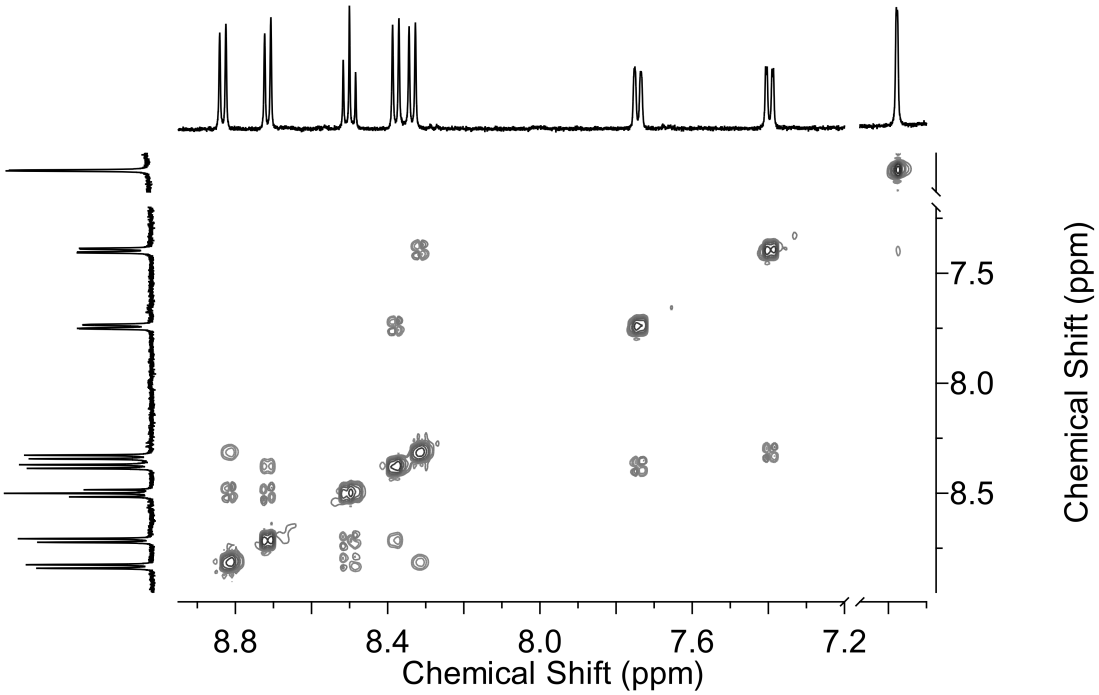

Figure B.8: Partial ^{1}H - ^{1}H ROESY NMR spectrum (500 MHz, CD_3CN, 298 K) showing the helicate (**3**).

B.3 UV-Vis spectra

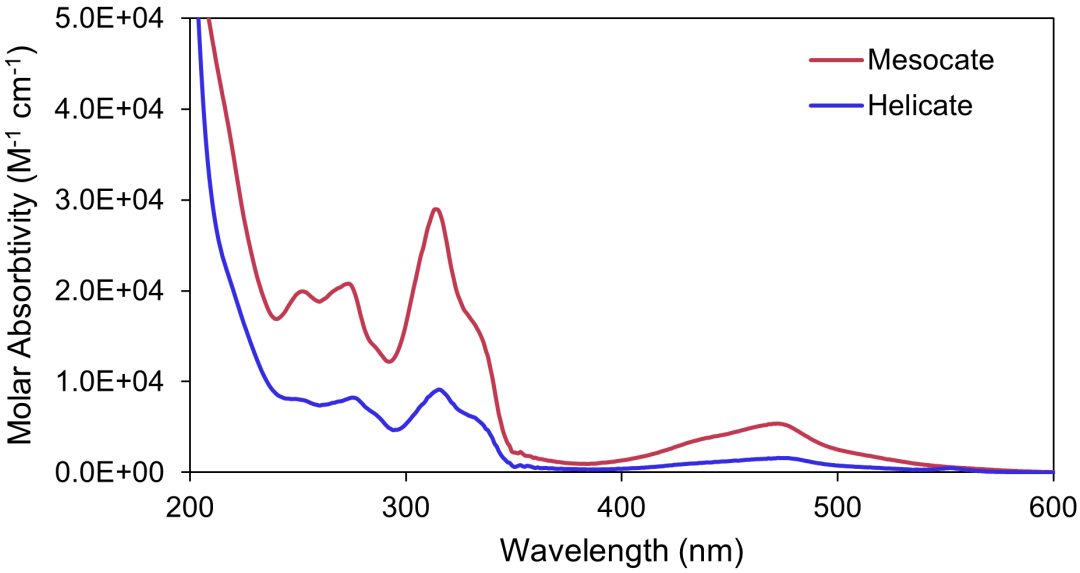

Figure B.9: UV-Vis spectra (CH_3CN, 298 K) of the ruthenium(II) mesocate (**4**) and helicate (**3**).

B.4 Mass spectrometry

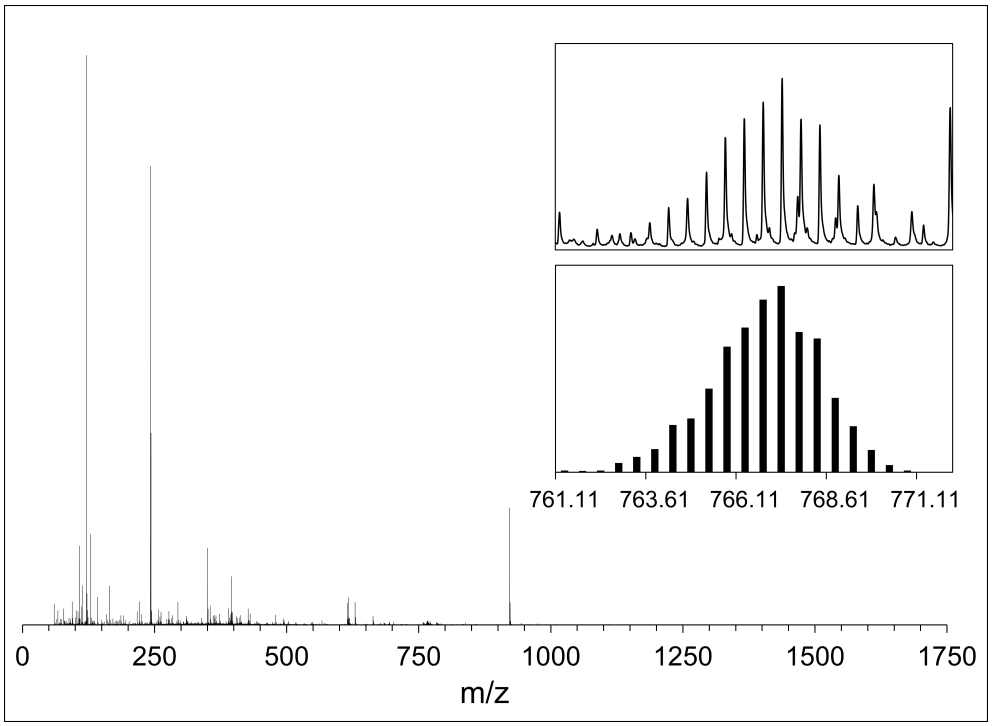

Figure B.10: Mass spectrometry of the diruthenium(II) double-stranded helicate (**3**). Full HR-ESI-MS spectrum (CH_3CN), (inset) Partial HR-ESI-MS (CH_3CN) and calculated isotopic pattern of the helicate (**3**), peak at *m/z* 767.1061 due to [**3** - $2PF_6^-$]$^{2+}$.

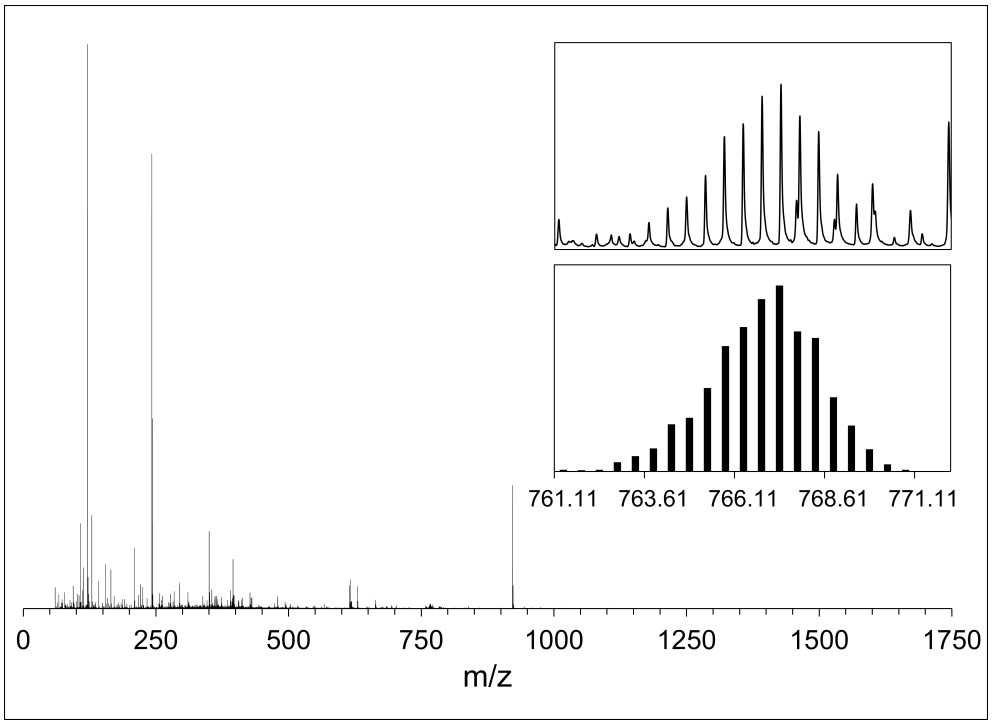

Figure B.11: Mass spectrometry of secondary product, identified as the diruthenium(II) double-stranded mesocate (**4**). Full HR-ESI-MS spectrum (CH_3CN), (inset) Partial HR-ESI-MS (CH_3CN) and calculated isotopic pattern of the mesocate (**4**), peak at *m/z* 767.1052 due to [**3** - $2PF_6^-$]$^{2+}$.

B.5 X-ray crystallography

Crystals suitable for X-ray diffraction were grown by vapour diffusion of diethyl ether into an acetonitrile solution of the compound (**3**), or diisopropyl ether into an acetonitrile solution of the compound (**4**). Single crystals were mounted in paratone-N oil on a plastic loop. X-ray diffraction data were collected at 150(2) K on an Oxford X-Calibur single crystal diffractometer (λ 0.710 73 Å) or on the MX2 beamline of the Australian Synchrotron at 100(2) K.[416] Datasets were corrected for absorption using a multi-scan method, and structures were solved by direct methods using *SHELXT*, and refined by full-matrix least-squares on F^2 by *SHELXL-2018*, interfaced through the program *X-Seed* or *OLEX*.[417–421] In general, all non-hydrogen atoms were refined anisotropically and hydrogen atoms were included as invariants at geometrically estimated positions. The crystallographic details for the structures **3** and **4** are given in Table B.1 below.

Full details of the structure determinations have been deposited with the Cambridge Crystallographic Data Centre as 1895874 (**3**) and CCDC 1895873 (**4**). Copies of this information may be obtained free of charge from The Director, CCDC, 12 Union Street, Cambridge CB2 1EZ, UK (fax: +441223-336-033, email: deposit@ccdc.cam.ac.uk).

Table B.1: Crystal data and structure refinement for **4** and **3**

Compound	Mesocate, **4**	Helicate, **3**
CCDC number	1895873	1895874
Empirical formula	$C_{68}H_{56}N_{12}Ru_2P_4F_{24}$	$C_{68}H_{56}N_{12}Ru_2P_4F_{24}$
Formula weight	1823.27	1823.26
Crystal system	Monoclinic	Monoclinic
Space group	$I2/a$	$P2_1/n$
a (Å)	28.970(4)	14.447(3)
b (Å)	9.6123(15)	26.230(5)
c (Å)	25.881(4)	25.203(5)
$\alpha(^\circ)$	90	90
$\beta(^\circ)$	100.344(16)	106.01(3)
$\gamma(^\circ)$	90	90
Volume (Å^3)	7089.9(19)	9180(3)
Z	4	4
Density (calc.) (Mg/m^3)	1.708	1.319
Absorption coefficient (mm^{-1})	0.632	0.488
F(000)	3648	3648
Crystal size (mm^3)	0.30×0.30×0.04	0.40×0.03×0.03
Θ range for data collection (°)	3.7470 to 27.2950	1.144 to 32.156
Reflections total	7271	26867
Observed reflections [R(int)]	2231 [0.2293]	15046 [0.0689]
Goodness-of-fit on F2	0.992	1.180
R_1 [I>2σ(I)]	0.1214	0.1009
wR_2 (all data)	0.2588	0.3541
Largest diff. peak and hole (e.Å^{-3})	1.115 and -0.807	1.298 and -1.416

B.5.1 Helicate packing

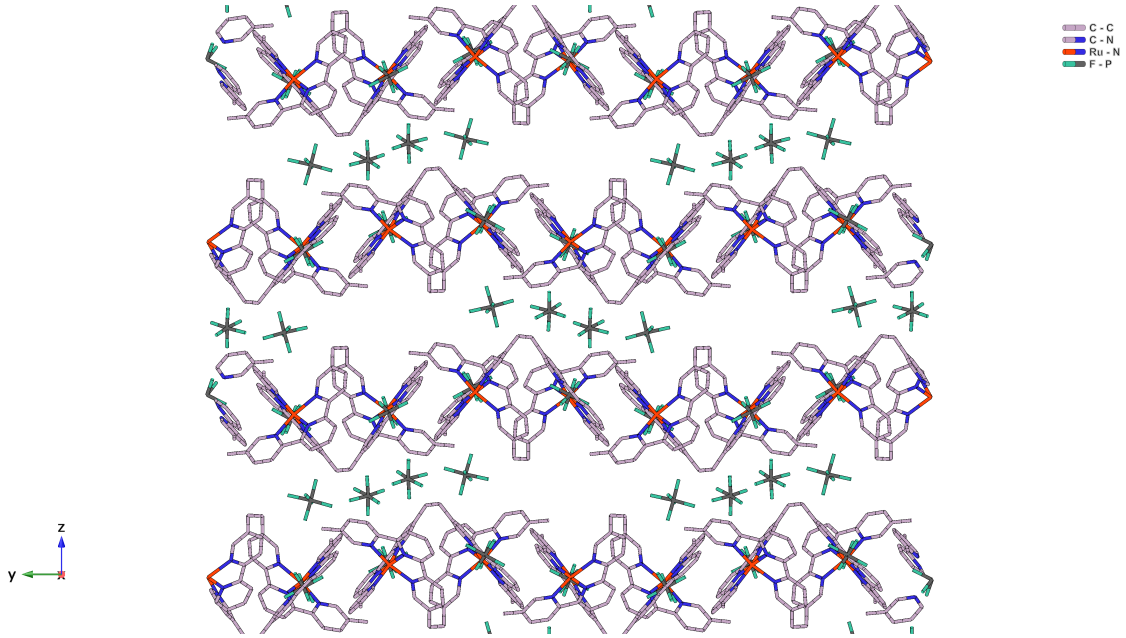

Figure B.12: Crystal structure of the diruthenium helicate (**3**) viewed down the *a*-axis, showing alternating cation/anion layers.

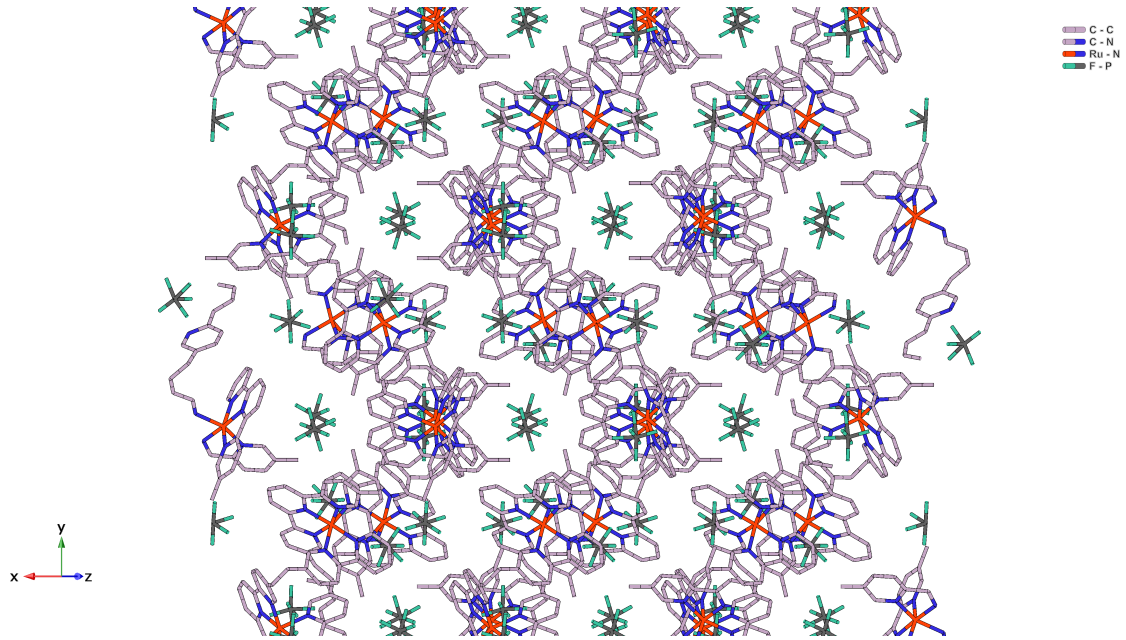

Figure B.13: Crystal structure of the diruthenium helicate (**3**) viewed in the *ab* plane, with a "loose" herringbone arrangement incorporating anions.

B.5.2 Mesocate packing

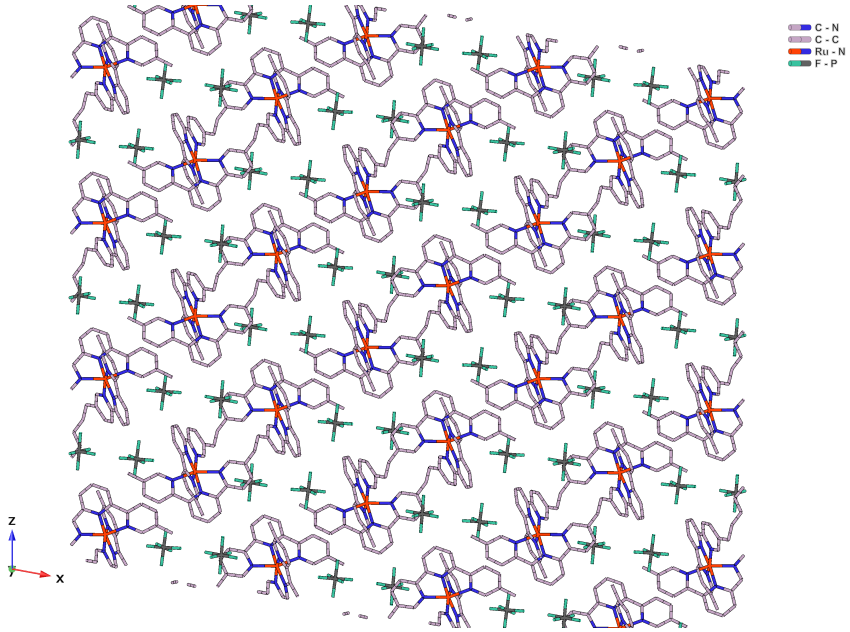

Figure B.14: Crystal structure of the diruthenium mesocate (**4**) viewed down the *b*-axis, showing integrated cation-anion entities.

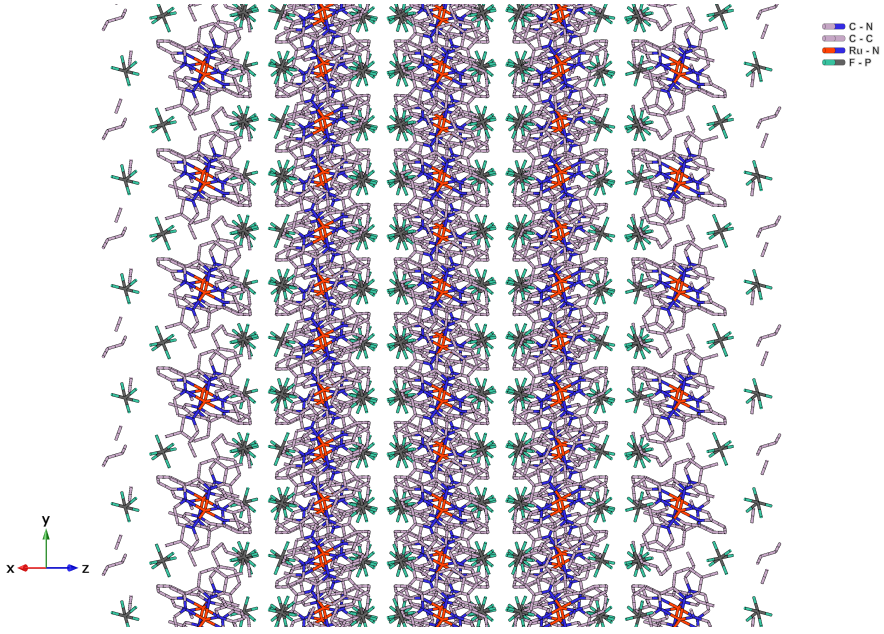

Figure B.15: Crystal structure of the diruthenium mesocate (**4**) viewed in the 1 0 1 plane, showing mesocate columns.

B.6 Computational studies

For each Ru(II) compound, density functional theory (DFT) calculations were performed with Q-Chem version 5.1,[422] on helicate or mesocate molecules extracted from the experimental X-ray crystal structure. In cases where the crystal structure was not available existing crystal structures containing other transition metal centres were modified to allow modelling of theoretical supramolecular assemblies. Single-point energy was calculated for optimised geometry in a dielectric medium using the CPCM method[423,424] and a dielectric constant for acetonitrile (35.85).[425] The Bondi radius for ruthenium of 1.482 Å was taken from Chiorescu *et al.*,[426] and multiplied by 1.2 as per the Q-Chem default, to give 1.7784 Å. The Bondi radius for iron was defined as 2.44 Å taken from Alvarez *et al.*,[427] and multiplied by 1.2 as per Q-Chem default, to give 2.928 Å. All geometries were optimised at the wB97X-D/SRSC level.[428,429] *in vacuo* Default parameters were used in all cases except for SCF convergence in geometry and frequency calculation, which was set to 10^{-7} instead of 10^{-8} due to difficulties in convergence.

B.6.1 Ru(II)-containing compounds

Table B.2: Summary of DFT results for Ru(II) compounds containing the di(terpyridine) ligand.

		Helicate (**3**)	Mesocate (**4**)	Δ (helicate - mesocate)
E (Hartree)	(*in vacuo*)	-3469.85518	-3469.85101	-0.00417191
E (kcal/mol)	(*in vacuo*)			-2.6
E (kJ/mol)	(*in vacuo*)			-11.0
E (Hartree)	(CPCM, acetonitrile)	-3470.443661	-3470.422575	-0.02108591
E (kcal/mol)	(CPCM, acetonitrile)			-13.2
E (kJ/mol)	(CPCM, acetonitrile)			-55.4
ΔH thermal (kcal/mol)	(*in vacuo*, 298.15 K)	747.3	748.2	
ΔS thermal (cal/mol.K)	(*in vacuo*, 298.15 K)	345.6	352.4	
ΔG thermal (kcal/mol)	(*in vacuo*, 298.15 K)	644.3	643.1	1.1
ΔG (kcal/mol)	(*in vacuo*, 298.15 K)			-1.5
ΔG (kJ/mol)	(*in vacuo*, 298.15 K)			-6.3
ΔG (kcal/mol)	(CPCM, acetonitrile, 298.15 K)			-12.1
ΔG (kJ/mol)	(CPCM, acetonitrile, 298.15 K)			-50.7

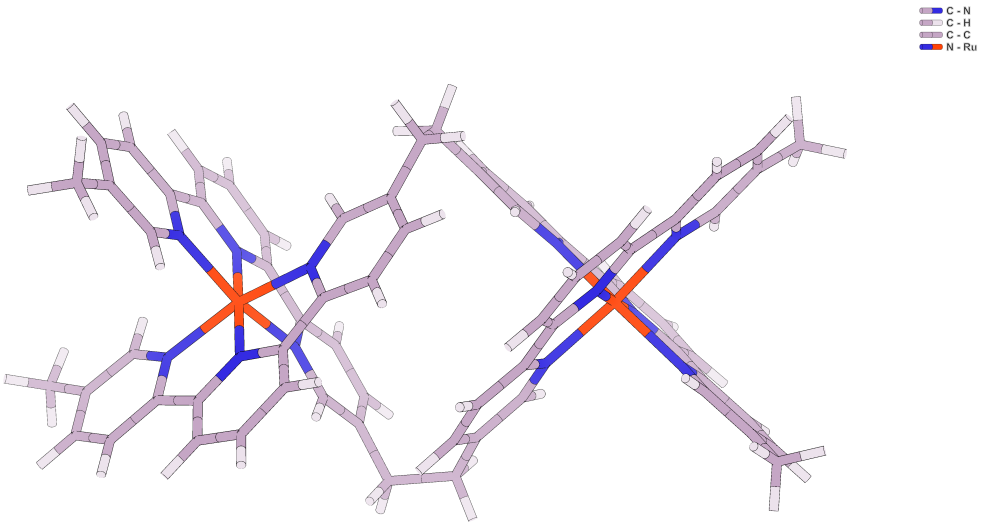

Figure B.16: DFT optimised geometry model showing the molecular structure of the ruthenium helicate (**3**), containing the di(terpyridine) ligand.

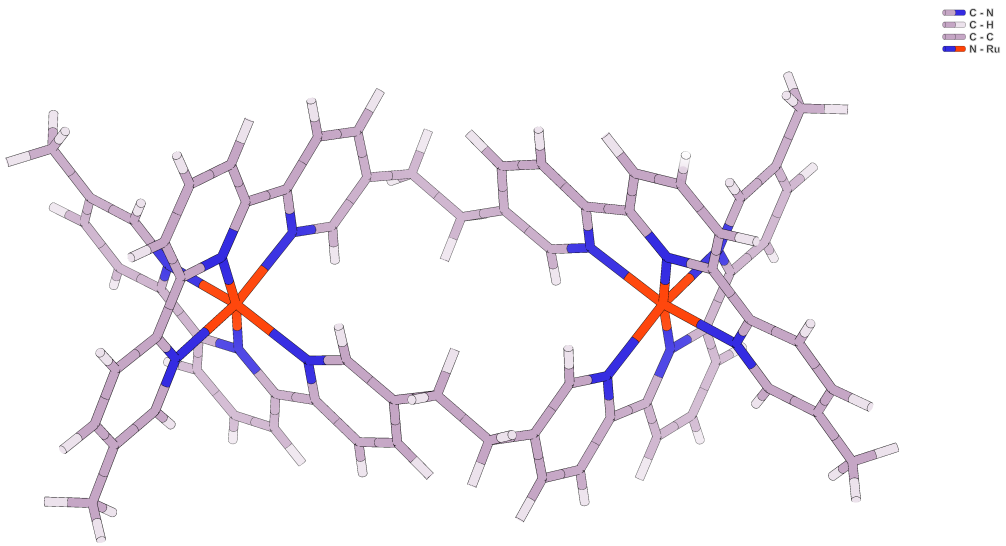

Figure B.17: DFT optimised geometry model showing the molecular structure of the ruthenium mesocate (**4**), containing the di(terpyridine) ligand.

B.6.2 Fe(II)-containing compounds

Table B.3: Summary of DFT results for Fe(II) compounds containing the di(terpyridine) ligand.

		Helicate	Theoretical Mesocate	Δ (helicate - mesocate)
E (Hartree)	(*in vacuo*)	-3527.8205	-3527.81454	-0.00595307
E (kcal/mol)	(*in vacuo*)			-3.7
E (kJ/mol)	(*in vacuo*)			-15.6
E (Hartree)	(CPCM, acetonitrile)	-3528.410511	-3528.38864	-0.021870648
E (kcal/mol)	(CPCM, acetonitrile)			-13.7
E (kJ/mol)	(CPCM, acetonitrile)			-57.4
ΔH thermal (kcal/mol)	(*in vacuo*, 298.15 K)	747.9	748.6	
ΔS thermal (cal/mol.K)	(*in vacuo*, 298.15 K)	340.9	348.2	
ΔG thermal (kcal/mol)	(*in vacuo*, 298.15 K)	646.3	624.8	1.5
ΔG (kcal/mol)	(*in vacuo*, 298.15 K)			-2.3
ΔG (kJ/mol)	(*in vacuo*, 298.15 K)			-9.4
ΔG (kcal/mol)	(CPCM, acetonitrile, 298.15 K)			-12.2
ΔG (kJ/mol)	(CPCM, acetonitrile, 298.15 K)			-51.2

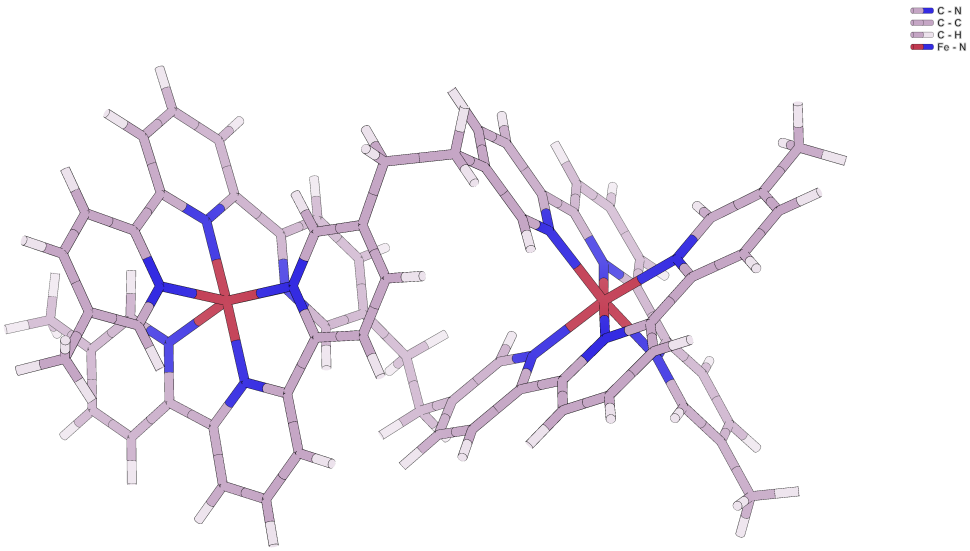

Figure B.18: DFT optimised geometry model showing the molecular structure of the iron helicate containing the di(terpyridine) ligand.

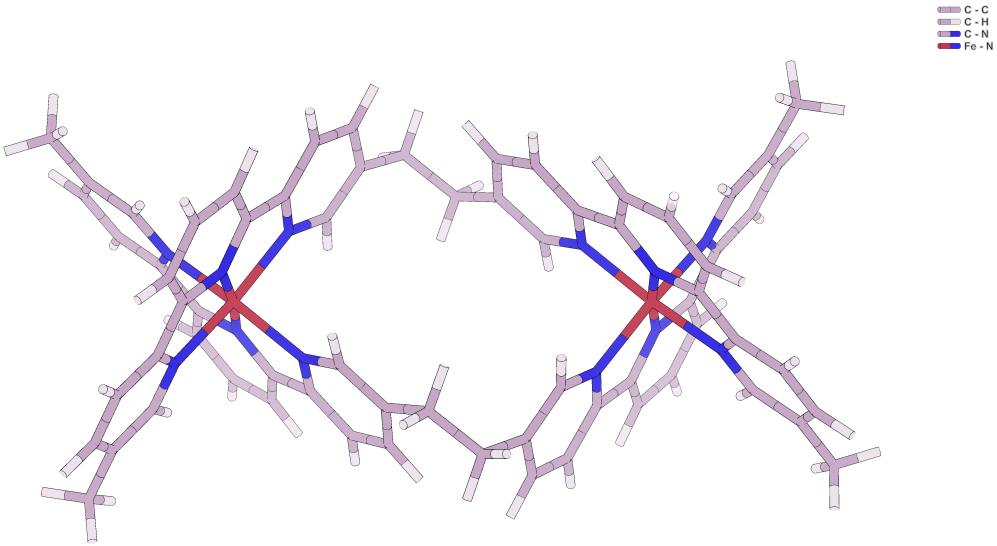

Figure B.19: DFT optimised geometry model showing the molecular structure of the theoretical iron mesocate containing the di(terpyridine) ligand.

B.7 Resolution of the helicate (**3**)

B.7.1 Using a sodium (-)-*O,O′*-dibenzoyl-L-tartrate eluent

Cellulose was mixed with H_2O to form a slurry and then packed onto a column of ∼100 mm length. A concentrated aqueous solution of *rac*-[**3**]Cl_4 was loaded and the column washed with H_2O. Subsequently the column was eluted with 0.0375 M sodium (-)-*O,O′*-dibenzoyl-L-tartrate, and the single eluting band collected. The column was then washed with 0.5 M sodium 4-toluenesufonate to collect the remaining precipitated compound. To remove the optically active anions both solutions were individually passed through a small column of silica gel and washed with copious amounts of acetone and water. Each enantiomer was removed from the silica by elution with a solution of NH_4PF_6 in acetone (4%). Water (1 mL) was added and the acetone removed by rotary evaporation. In each case the resulting solid was collected by centrifugation (10621 *g*; 5 min), washed with cold water (3 x), and dried under vacuum.

B.7.2 Using a sodium chloride eluent

Cellulose was mixed with 0.2 M NaCl to form a slurry and then packed onto a column of ∼ 30 cm length. A concentrated solution of *rac*-[**3**]Cl_4 in 0.2 M NaCl was loaded. Eluted with 0.2 M NaCl with applied pressure on top of the column afforded a broad smear, from which small fractions could be collected (10 drops). The fractions were analysed by ultraviolet-visible (UV-Vis) and circular dichroism (CD) spectroscopy to determine the enantiomeric content, and fractions of similar enantiopurity were combined and concentrated. Those fractions showing little to no resolution were combined, concentrated, and the resolution process repeated numerous times.

B.7.3 Trialled resolution conditions

Table B.4: Eluents trialled for resolution of the helicate (**3**) on an SP-Sephadex C-25 stationary phase.

Eluent	**Conc. (mol/L)**	**Outcome**
Potassium antimonyl tatrate $\mathbf{K_2Sb_2(C_4H_2O_6)_2}$	0.1	Precipitate, subsequently eluted with 2 M NaCl.
Sodium arsenyl tartrate $\mathbf{NaAsC_4H_4O_6}$	0.1	Precipitate, unable to remove.
Sodium D-camphor sulfonate $\mathbf{NaC_{10}H_{15}O_4S}$	0.1	Precipitate, subsequently eluted with 2 M NaCl.
Sodium (-)-*O,O′*-dibenzoyl-L-tartrate $\mathbf{Na_2C_{18}H_{12}O_8}$	0.2 0.075 0.0375	Precipitate. Precipitate. Precipitate.
Sodium (+)-*O,O′*-dibenzoyl-D-tartrate $\mathbf{Na_2C_{18}H_{12}O_8}$	0.0375	Eluted as a single band
Sodium chloride **NaCl**	1 0.5 0.1	Eluted as a single band. Eluted as a single broad band. No movement.
Sodium 4-toluenesufonate $\mathbf{NaCH_3C_6H_4SO_3}$	0.5 0.25 0.15	Eluted as a single band. Eluted as a single broad band. No movement.
Sodium hexanoate $\mathbf{NaCH_3(CH_2)_4COO}$	0.5 0.125	Slight smear at top, no movement. No movement.
Sodium octanoate $\mathbf{NaCH_3(CH_2)_6COO}$	0.5	Eluted as a single band.

Table B.5: Eluents trialled for resolution of **3** on a cellulose stationary phase.

Eluent	**Conc. (mol/L)**	**Outcome**
Sodium nitrate **$NaNO_3$**	0.5	One band eluted with solvent front. Second band precipitated, subsequently eluted with 0.5 M sodium 4-toluenesufonate.
MeOH/NaCl (4 : 1 v/v)	0.02	Smear down column. Very slow elution.
Sodium D-camphor sulfonate, **$NaC_{10}H_{15}O_4S$**	0.5	Eluted as a single band.
Sodium (-)-*O,O′*-dibenzoyl-L-tartrate	0.075	One band eluted close to the solvent front. Second band precipitated, subsequently eluted with 0.5 M sodium 4-toluenesufonate.
$Na_2C_{18}H_{12}O_8$	0.0375	One band eluted close to the solvent front. Second band precipitated, subsequently eluted with 0.5 M sodium 4-toluenesufonate.
	0.025	Eluted as a single band, slight smear stuck at top.
	0.018	Elute as a single band.
Sodium (+)-*O,O′*-dibenzoyl-D-tartrate	0.1	One band eluted close to the solvent front. Second band precipitated, subsequently eluted with 0.5 M sodium 4-toluenesufonate.
$Na_2C_{18}H_{12}O_8$	0.075	Eluted as a single band.
	0.0375	Eluted as a single band
Sodium chloride	2	One main band eluted close to the solvent front. Smear left on column, subsequently eluted with 0.5 M sodium 4-toluenesufonate.
NaCl	0.2	Eluted as a single band.
	0.02	One smear, slow elution. Very diffuse band.
Sodium 4-toluenesufonate	0.25	Eluted as a single band.
$NaCH_3C_6H_4SO_3$	0.15	Eluted as a single band.
Potassium antimonyl tatrate **$K_2Sb_2(C_4H_2O_6)_2$**	0.1	Eluted as one main band. Slight smear left on the column.

Table B.6: Eluents trialled for resolution of **3** on a cellulose stationary phase with positive pressure.

Eluent	**Conc. (mol/L)**	**Outcome**
Sodium chloride	0.02	Diffuse smear.
NaCl	0.1	Diffuse smear.
	0.2	Smear throughout, partial resolution at ends of band.
	2	Single band, no separation
75% EtOH/NaCl	0.2	Smear, no resolution recorded by CD.
80% MeOH/NaCl	0.2	Single band, no separation.
90% MeCN/NaCl	0.2	Single band, no separation.
MeCN		Smear, some precipitation, no resolution.
30% MeCN/KPF_6	1	No separation.

APPENDIX C

Supporting Information for Chapter 3

C.1 General methods and materials

Calf thymus DNA (ct-DNA) was obtained from Sigma Aldrich as the sodium salt and used as received. The concentrations of ct-DNA were determined spectrophotometrically using the molar extinction coefficient ε_{260} = 6600 M^{-1} cm^{-1} (all ct-DNA concentrations with respect to base pairs). The oligonucleotides $d(CAATCCGGATTG)_2$ and $d(ACCGAATTCGGT)_2$ were obtained from Sigma Aldrich. All aqueous solutions for the sample preparation and NMR studies were prepared in de-ionised milli-Q water. UV-Vis absorption spectra were acquired at ambient temperature on a Cary 1E or Cary 50 Bio UV-Visible Spectrophotometer (scan range: 600-200 nm, scan rate: 600.00 nm min^{-1}, SBW: 2.0 nm).

C.2 Dialysis

A 300 µM ct-DNA solution was made up in Tris buffer and placed on the inside of a 1 mL cellulose ester membrane Spectra/Por® Float-A-Lyzer® G2 or Sigma Aldrich Pur-A-Lyzer™ Maxi Dialysis Kit. This ct-DNA loaded dialysis tube was then submerged in a 20 µM racemic mixture of helicate (**3**) made up in Tris buffer. The dialysis was left for 24 - 48 h and the outer solution analysed using CD spectroscopy. circular dichroism (CD) spectra were acquired at ambient temperature using a Jasco J-715 spectropolarimeter (scan range: 600 - 200 nm, resolution: 1 nm, bandwidth: 2.0 nm, sensitivity: 200 mdeg, response: 1 sec, speed: 100 nm/min).

C.3 Linear dichroism

LD spectra were recorded using a Jasco 810 spectropolarimeter using a quartz capillary LD Coulette flow cell built by Crystal Precision Optics. The instrument was allowed to equilibrate for 30 minutes prior to use, and nitrogen gas flow was kept at approximately 10 L/min. A series of 10 solutions consisting of ct-DNA (167 µM), K_2HPO_4/KH_2PO_4 (10 mM, pH 7.3), NaCl (10 mM), and increasing amounts of diruthenium compound were prepared. NaCl concentration was relatively low due to the strong absorption of chloride salts at low wavelengths.[430] For each solution, spectra were obtained over the range 200 - 350 nm with a scan rate of 200 nm/min, data pitch of 1 nm, response time of 1 s, and rotation speed of 3000 rpm. 10 accumulations were collected and a baseline non-rotating spectrum was subtracted from each data set.

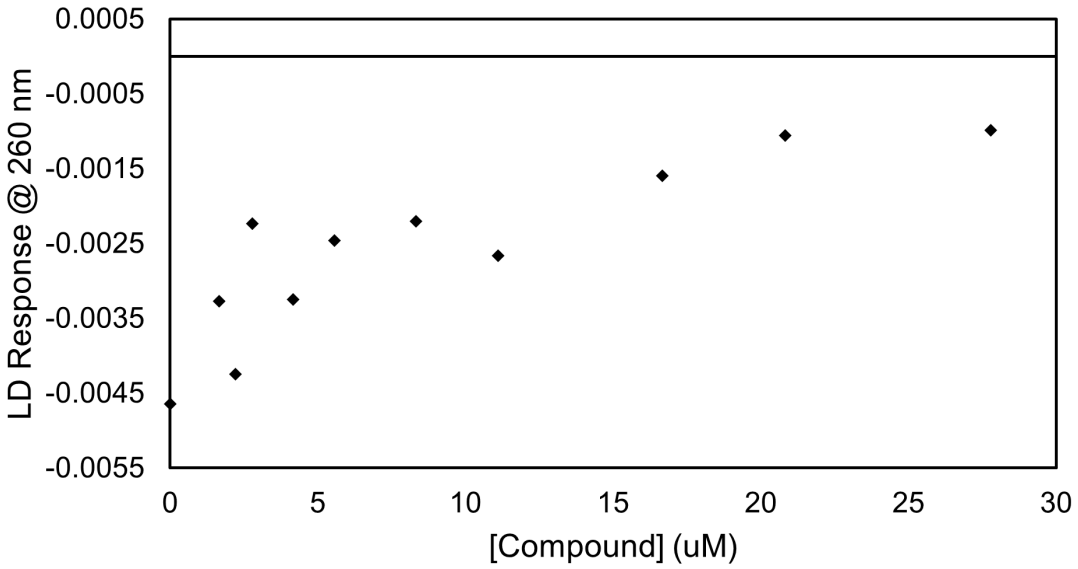

Figure C.1: linear dichroism (LD) spectrum of ct-DNA at 260 nm (2×10^{-4} M; K_2HPO_4/KH_2PO_4 (10 mM), NaCl (10 mM), pH 7.3, 25 ° C) bound with increasing concentrations of double-stranded ruthenium(II) mesocate (**4**).

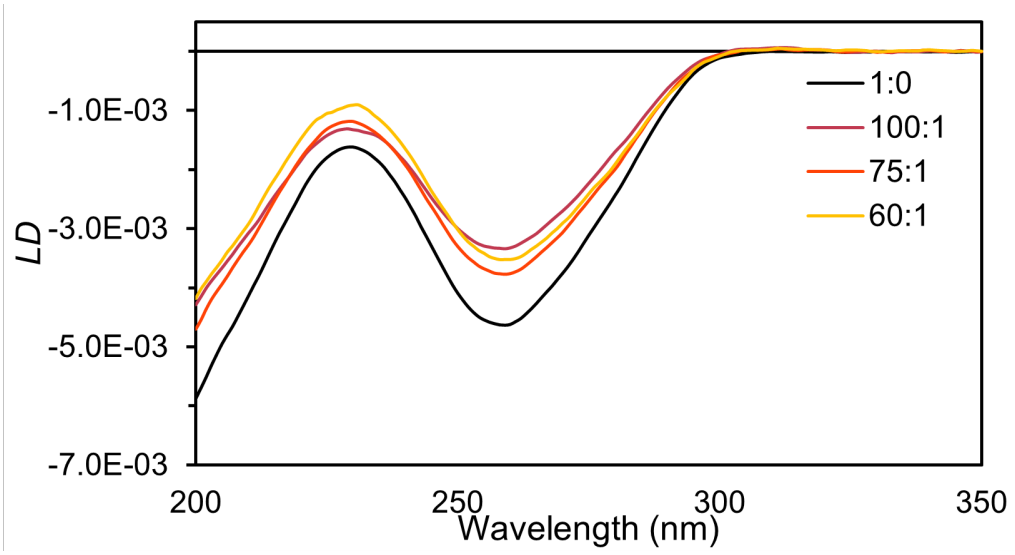

Figure C.2: LD spectrum of free ct-DNA (2 x 10^{-4} M; K_2HPO_4/KH_2PO_4 (10 mM), NaCl (10 mM), pH 7.3, 25 ° C) and in the presence of increasing concentrations of helicate (**3**; F1 from resolution on cellulose with 0.075 M sodium (-)-*O,O′*-dibenzoyl-L-tartrate). It should be noted that at a ratio of 60 : 1 precipitation was observed, preventing further experiments being conducted by this method.

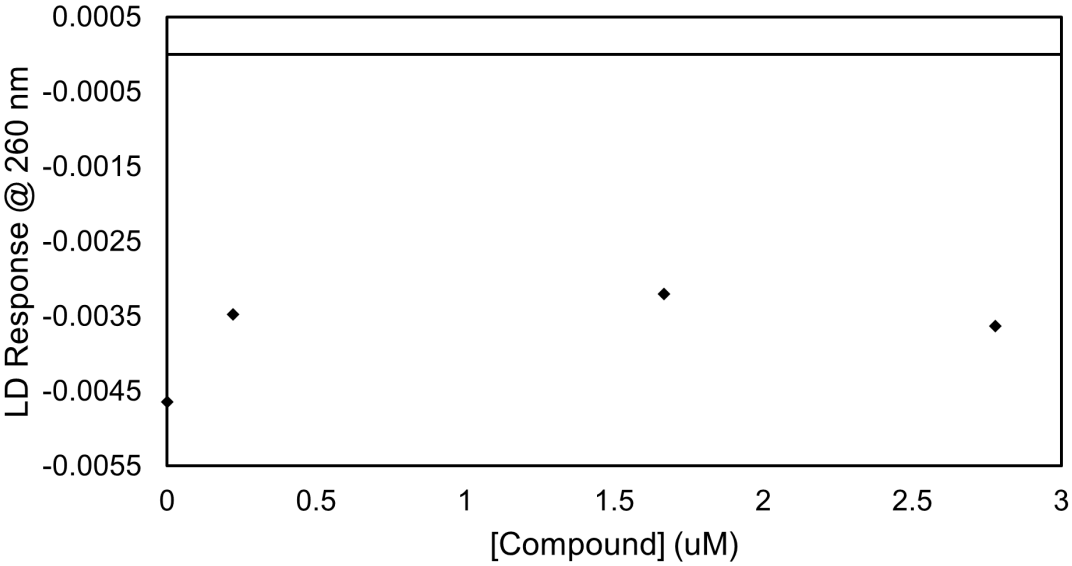

Figure C.3: LD spectrum of ct-DNA at 260 nm (2 x 10^{-4} M; K_2HPO_4/KH_2PO_4 (10 mM), NaCl (10 mM), pH 7.3, 25 ° C) bound with increasing concentrations of double-stranded ruthenium(II) helicate (**3**; F1 from resolution on cellulose with 0.075 M sodium (-)-*O,O′*-dibenzoyl-L-tartrate). It should be noted that at a ratio of 60 : 1 precipitation was observed, preventing further experiments being conducted by this method.

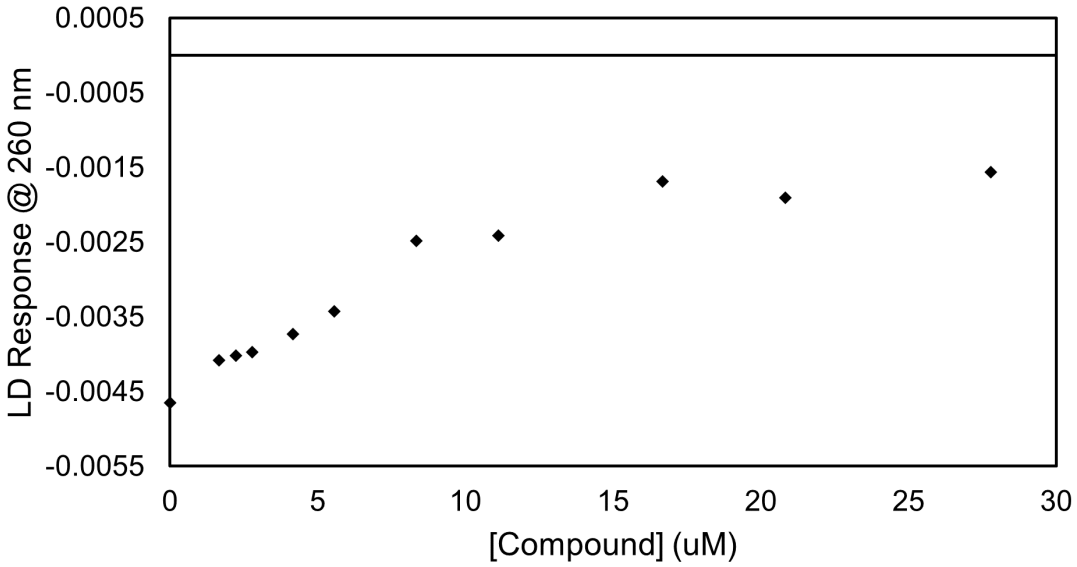

Figure C.4: LD spectrum of ct-DNA at 260 nm (2×10^{-4} M; K_2HPO_4/KH_2PO_4 (10 mM), NaCl (10 mM), pH 7.3, 25 ° C) bound with increasing concentrations of double-stranded ruthenium(II) helicate (**3**; F2 from resolution on cellulose with 0.075 M sodium (-)-*O,O′*-dibenzoyl-L-tartrate).

C.4 NMR studies

C.4.1 Sample preparation for NMR analysis

Minor impurities were removed from the oligonucleotides using a reverse-phase Waters C18 Sep-Pak cartridge. The cartridge was activated with methanol (10 mL) and washed with water (2 x 10 mL) before the aqueous oligonucleotide solution was loaded. The column cartridge was then washed with water (2 x 3 mL) and the oligonucleotide eluted with 50% v/v acetonitrile/water. Fractions of approximately 3 mL each were collected and those fractions containing the oligonucleotide (determined by UV-Vis spectroscopy) were combined and freeze-dried.

The oligonucleotides were then converted from a triethylammonium salt to a sodium salt using a CM-Sephadex column that had been equilibrated with 1 M NaCl. After elution from the CM-Sephadex column, 600 µL of phosphate buffer (10 mM, pH 7.0) containing 20 mM NaCl and 0.1 mM ethylenediaminetetraacetic acid (EDTA) was added and the solution freeze-dried. The oligonucleotide samples were dissolved in 600 µL of D_2O prior to use.

Stock solutions of the metal-containing compounds (30 mM) were prepared in D_2O and additions of the metal compound stock solutions were made directly to the oligonucleotide solution.

C.4.2 NMR spectroscopy

^{1}H NMR spectra were recorded on a Varian Unity*plus*-400 spectrometer operating at 400 MHz or a Varian Inova operating at 600 MHz at 25 °C unless otherwise stated. nuclear overhauser effect spectroscopy (NOESY) spectra were acquired with the HDO resonance suppressed using the Wet pulse sequence using a low power selective irradiation with a relaxation delay of 1.7 seconds. A spectral width of 4000 Hz was used with each free induction decay (FID) acquired over 2048 points in t_2 for 256 t_1 increments with a mixing time for NOESY spectra ranging from 100 to 300 ms. All data sets were processed with a shifted sinebell or a mild Gaussian function. Standard pulse sequences provided by the Agilent software Vnmrj 2.2C were used to record NMR spectra.

C.4.3 Additional NMR spectra

C.4.3.1 Free AATT dodecanucleotide

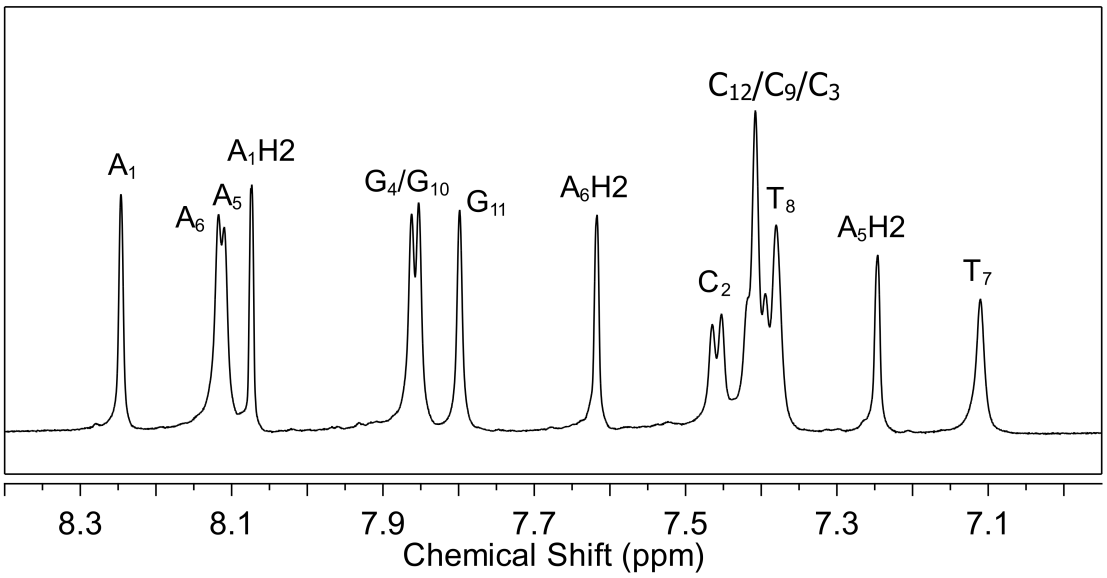

Figure C.5: An expansion of the aromatic region of the ^{1}H NMR spectrum of the self complementary AATT dodecanucleotide duplex in pH 7.0 phosphate buffer at 25 °C, giving assignments of various nucleotide hydrogens.

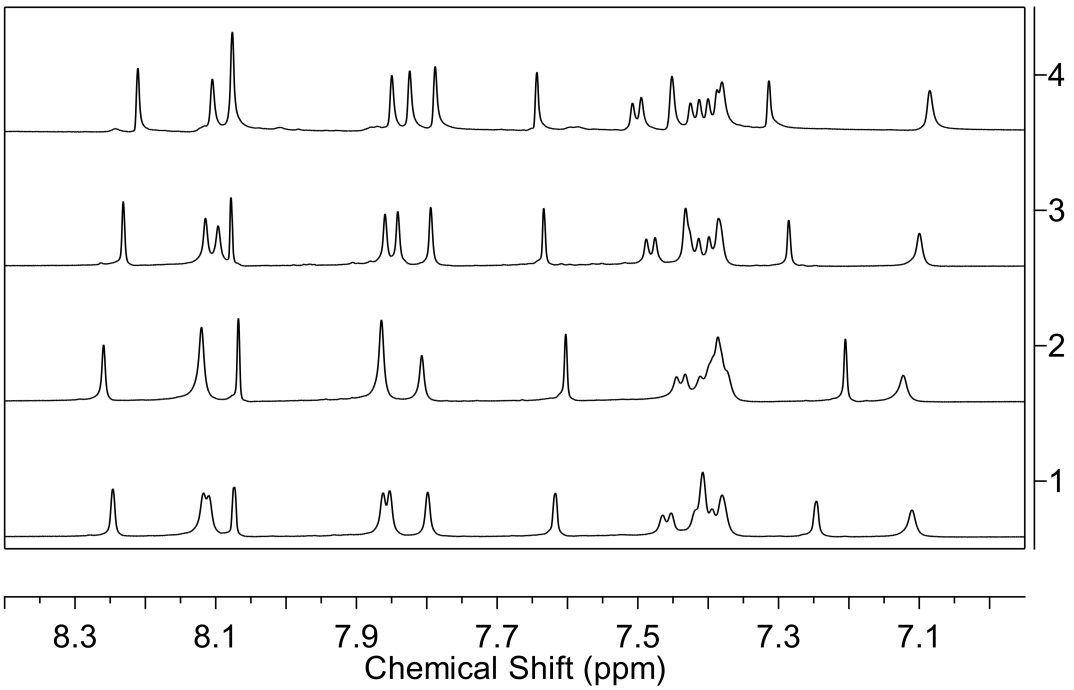

Figure C.6: An expansion of the aromatic region of the ^{1}H NMR spectrum of the self complementary AATT dodecanucleotide duplex in pH 7.0 phosphate buffer. (1) 15 °C; (2) 25 °C; (3) 35 °C; (4) 45 °C.

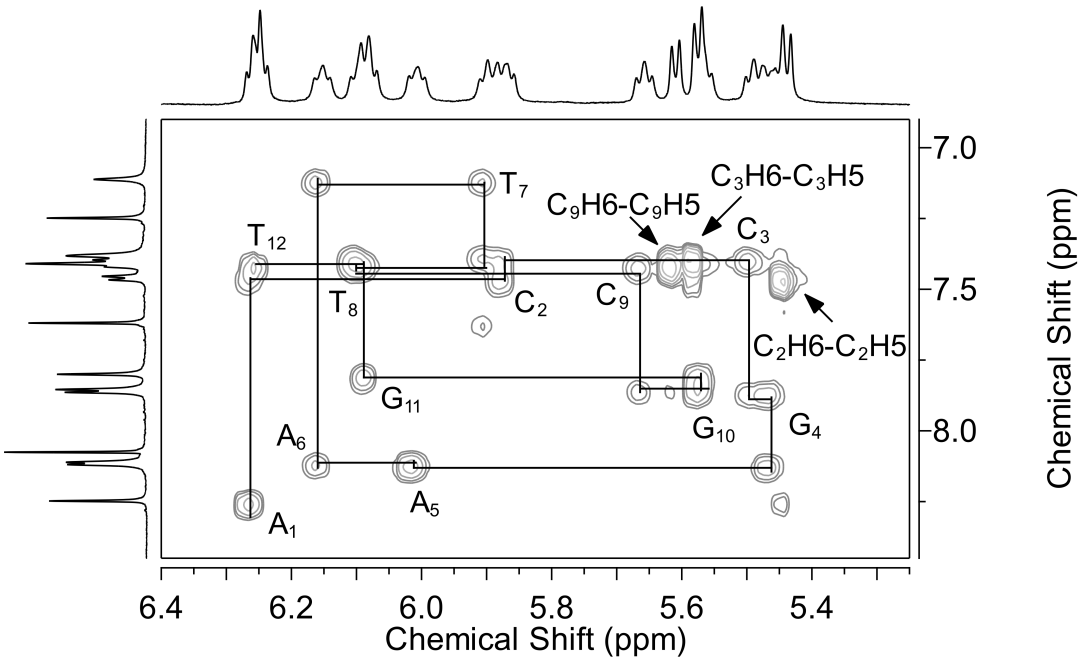

Figure C.7: Expansion of a NOESY spectrum of the self complementary AATT dodecanucleotide duplex in 10 mM pH 7.0 phosphate buffer at 25 °C, showing sequential NOE connectivities between the base hydrogens and H1′ of the sugars.

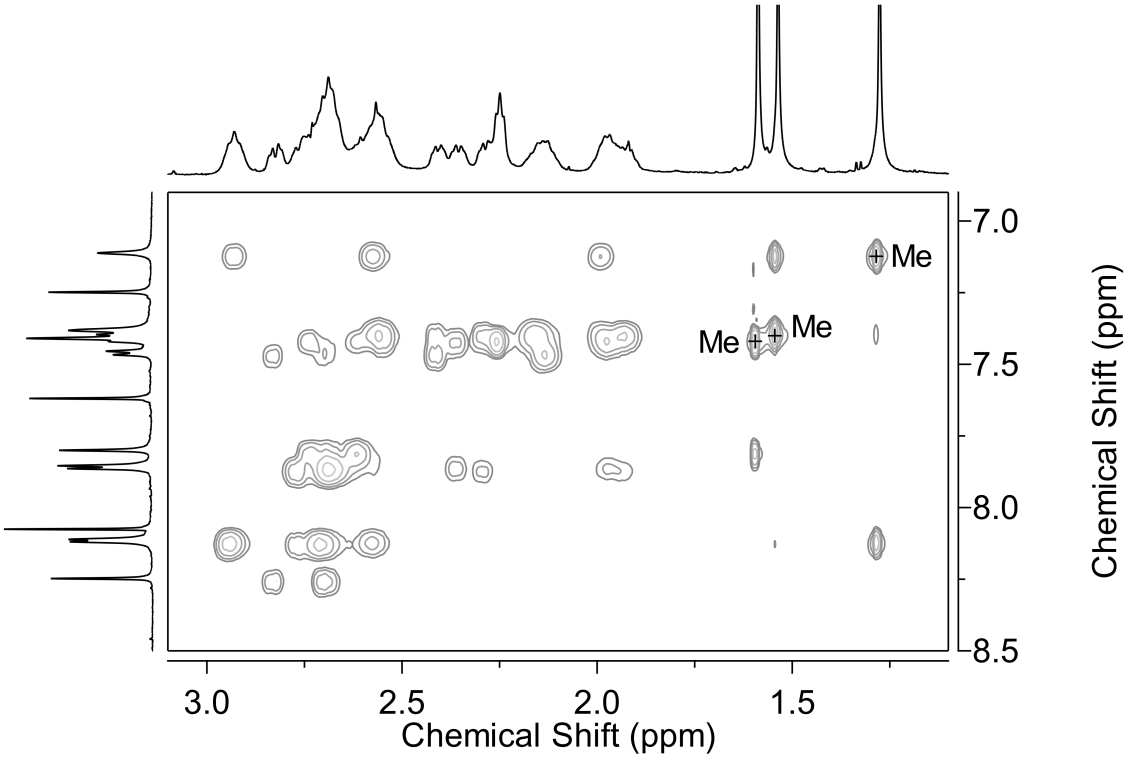

Figure C.8: Expansion of a NOESY spectrum of the self complementary AATT dodecanucleotide duplex in 10 mM pH 7.0 phosphate buffer at 25°C.

C.4.3.2 Free bulge oligonucleotide

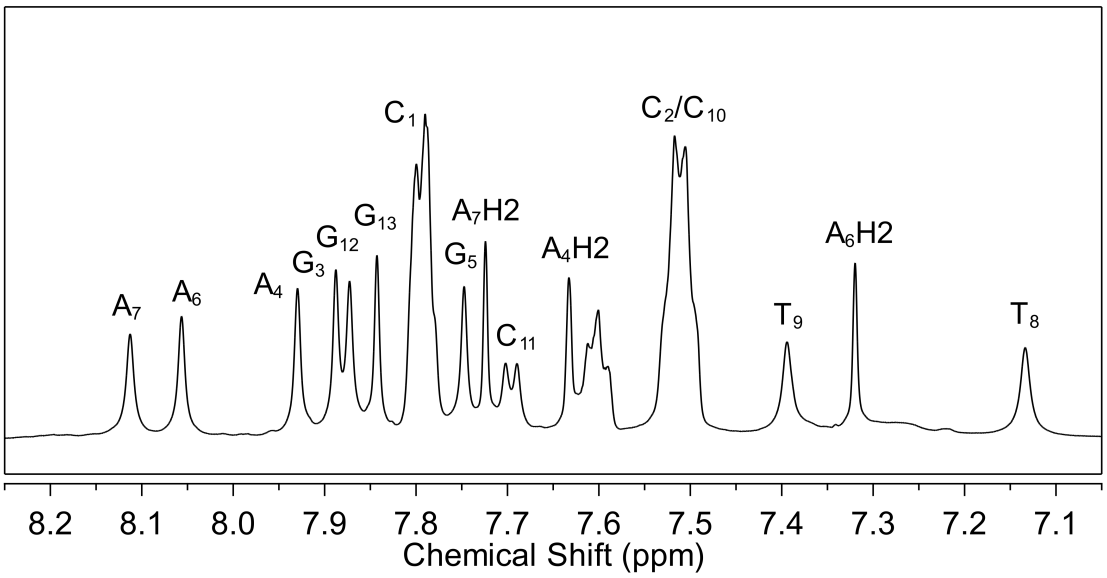

Figure C.9: An expansion of the aromatic region of the ^{1}H NMR spectrum of the bulge oligonucleotide duplex in pH 7.0 phosphate buffer at 25 °C, giving assignments of various nucleotide hydrogens.

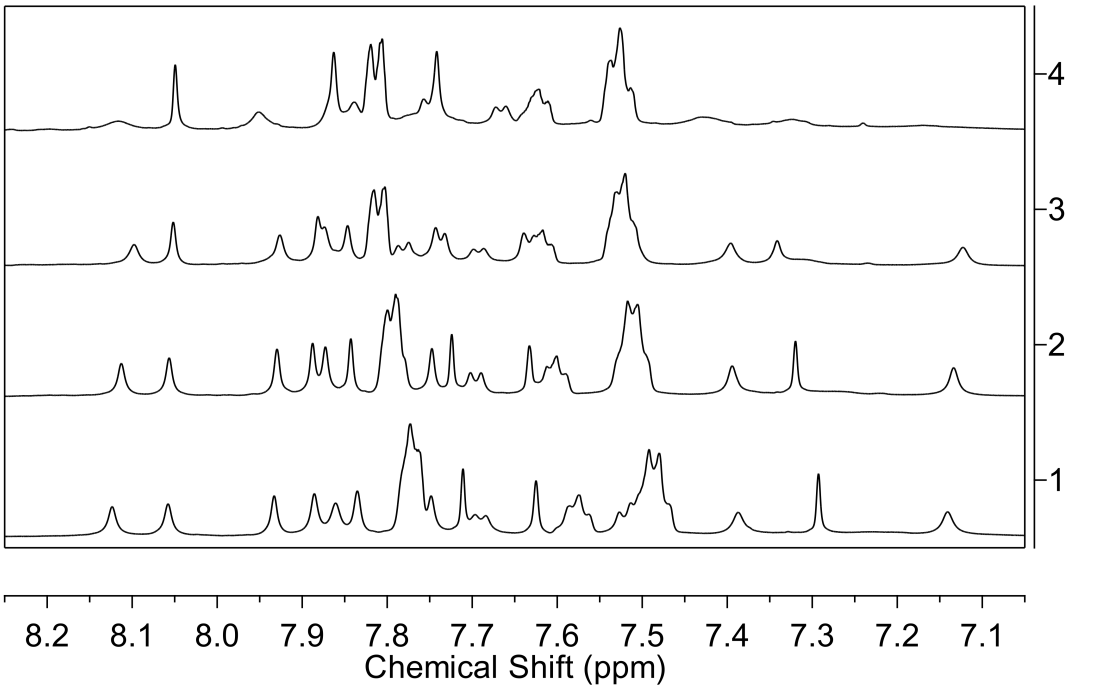

Figure C.10: An expansion of the aromatic region of the ^{1}H NMR spectrum of the bulge oligonucleotide duplex in pH 7.0 phosphate buffer. (1) 15 °C; (2) 25 °C; (3) 35 °C; (4) 45 °C.

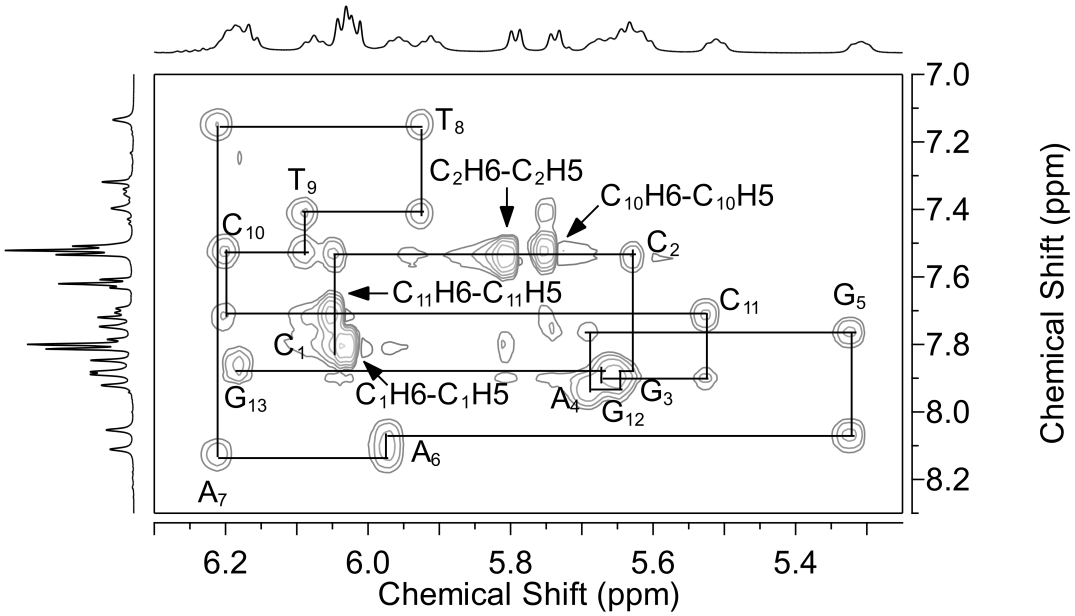

Figure C.11: Expansion of a NOESY spectrum of the bulge oligonucleotide duplex in 10 mM pH 7.0 phosphate buffer at 25 °C, showing sequential NOE connectivities between the base hydrogens and H1′ of the sugars.

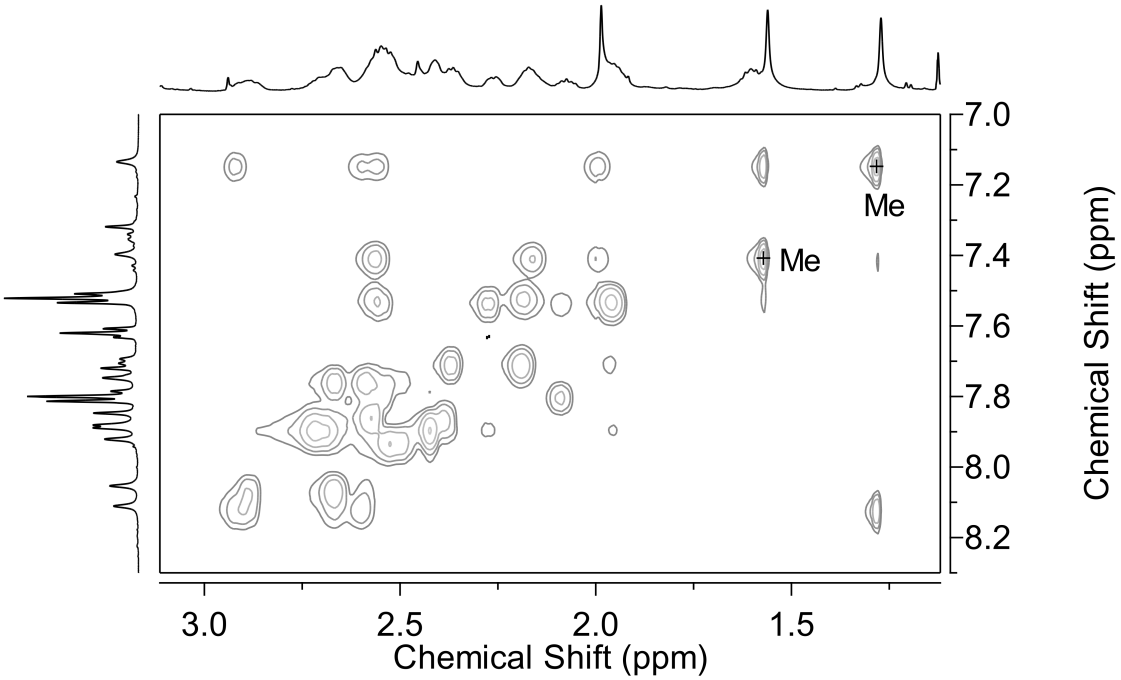

Figure C.12: Expansion of a NOESY spectrum of the bulge oligonucleotide duplex in 10 mM pH 7.0 phosphate buffer at 25°C.

APPENDIX D

Supporting Information for Chapter 4

D.1 Synthetic procedures

D.1.1 Ligand synthesis

D.1.1.1 2-{(Trimethylsilyl)ethynyl}pyridine (**5**)

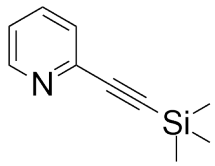

Figure D.1: 2-{(trimethylsilyl)ethynyl}pyridine (**5**)

Using a procedure modified from that described by Atobe *et al.*,[294] trimethylsilyl-acetylene (TMS-acetylene) (1.47 g, 2.1 mL, 15 mmol; 1.5 equiv.) was added to a solution of 2-chloropyridine (1.13 g, 0.93 mL, 10 mmol; 1 equiv.), CuI (0.97 g, 0.5 mmol, 0.05 equiv.), and $Pd(PPh_3)_4$ (0.23 g, 0.2 mmol; 0.02 equiv.) in distilled diisopropylamine (6.67 mL) under an Ar atmosphere. The reaction mixture was heated at reflux for 46 h. The crude product was filtered through a silica pad with DCM, and solvent removed to give **5** as a light brown oil (1.48 g, 85%). δ_H (500 MHz, $CDCl_3$) 8.57 (ddd, J = 4.8, 1.6, 0.9, 1H), 7.63 (td, J = 7.7, 1.8 Hz, 1H), 7.45 (dt, J = 7.8, 1.0 Hz, 1H), 7.22 (ddd, J = 7.6, 4.9, 1.2 Hz, 1H), 0.27 (s, 9H).

D.1.1.2 2-Ethynylpyridine (**6**)

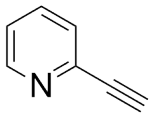

Figure D.2: 2-ethynylpyridine (**6**)

Using a procedure modified from that described by Atobe *et al.*,[294] a solution of **5** (1.28 g, 7.28 mmol; 1 equiv.), and Na_2CO_3 (0.85 g, 8.01 mmol; 1.1 equiv) in CH_3OH (22 mL)

was stirred at room temperature for 2 h. The reaction mixture was concentrated under vacuum, and the residue extracted with diethyl ether (3 x 25 mL), washed with de-ionised water (2 x 25 mL), brine (1 x 25 mL), dried over $MgSO_4$, filtered, and solvent removed to give **6** as a yellow oil (0.56 g, 75%). δ_H (500 MHz, $CDCl_3$) 8.62 - 8.57 (m, 1H), 7.66 (td, J = 7.7, 1.8 Hz, 1H), 7.48 (dt, J = 7.8, 1.0 Hz, 1H), 7.30 - 7.26 (m, 1H), 3.15 (s, 1H).

D.1.1.3 1,4-Bis(bromomethyl)benzene (**7**)

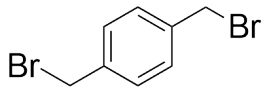

Figure D.3: 1,4-bis(bromomethyl)benzene (**7**)

A solution of 1,4-phenylenedimethanol (1.00 g, 7.24 mmol; 1 equiv.) and 48% HBr 12.6 mL, 116 mmol; 16 equiv.) in toluene (20 mL) was heated at reflux for 12 h. The reaction mixture was cooled to room temperature and saturated $NaHCO_3$ (20 mL) added. The organic layer was separated, dried over $MgSO_4$, and the product purified by column chromatography on silica gel. Elution with DCM/petroleum spirit (1:4 by volume; RF = 0.425) gave **7** as a white crystalline solid (1.55 g, 81%). δ_H (500 MHz, $CDCl_3$) 7.37 (s, 4H), 4.48 (s, 4H).

D.1.1.4 1,4-Bis{(4-(pyridin-2-yl)-1*H*-1,2,3-triazol-1-yl)methyl}benzene (**8**)

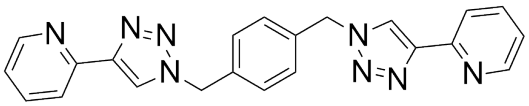

Figure D.4: 1,4-bis{(4-(pyridin-2-yl)-1*H*-1,2,3-triazol-1-yl)methyl}benzene (**8**)

Using a procedure modified from that described by Crowley and Bandeen,[286] NaN_3 (0.26 g, 3.98 mmol; 2.3 equiv.), $CuSO_4 \cdot 5\,H_2O$ (0.18 g, 0.69 mmol; 0.4 equiv.), and sodium ascorbate (0.31 g, 1.55 mmol; 0.9 equiv.) were added to a stirred solution of **7** (0.46 g, 1.72 mmol; 1 equiv.) in dimethylformamide (DMF) (5 mL) and deionised water (1 mL). **6** (380 µL, 0.39 g, 3.78 mmol; 2.05 equiv.) was added and the reaction stirred at room temperature for 48 h. 30% aq. ammonia (14 mL) and deionised water (40 mL) were added and the reaction mixture stirred at room temperature until a colour change was observed (from yellow to white precipitate, green solution). The precipitate was filtered, washed with deionised water, diethyl ether, and dried to give **8** as an off-white solid (0.55 g, 80%).

δ_H (500 MHz, $CDCl_3$) 8.53 (d, J = 4.5 Hz, 2H), 8.17 (d, J = 7.8 Hz, 2H), 8.05 (s, 2H), 7.76 (td, J = 7.7, 1.6 Hz, 2H), 7.35 (s, 4H), 5.59 (s, 4H).

D.1.1.5 1,3-Bis{4-pyridin-2-yl)-1*H*-1,2,3-triazol-1-yl}propane (**9**)

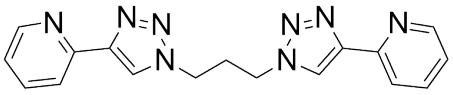

Figure D.5: 1,3-bis{4-(pyridin-2-yl)-1*H*-1,2,3-triazol-1-yl}propane (**9**)

Using a procedure modified from that described by Crowley and Bandeen,[286] a solution of 1,3-dibromopropane (0.15 mL, 0.30 g, 1.51 mmol; 1 equiv.) and NaN_3 (0.23 g, 3.47 mmol; 2.3 equiv.) in DMF (2 mL) was stirred at 80 °C for 24 h. A solution of $CuSO_4 \cdot 5\,H_2O$ (0.15 g, 0.6 mmol,; 0.4 equiv.), sodium ascorbate (0.24 g, 1.21 mmol; 0.8 equiv.), and **6** (314 µL, 0.32 g, 3.10 mmol; 2.05 equiv.) was added, and the reaction mixture stirred at room temperature for 20 h. 30% aqueous ammonia (20 mL) and deionised water (40 mL) were added and the reaction mixture stirred until a colour change was observed (from yellow to white precipitate, blue solution). The precipitate was filtered, washed with deionised water, diethyl ether, and dried to give **9** as an off-white solid (0.45 g, 90%). δ_H (500 MHz, $CDCl_3$) 8.59 (d, J = 4.6 Hz, 1H), 8.23 (s, 1H), 8.16 (d, J = 7.9 Hz, 1H), 7.78 (td, J = 7.7, 1.6 Hz, 1H), 7.26 - 7.21 (m, 1H), 4.51 (t, J = 6.5 Hz, 2H), 1.60 (s, 1H).

D.1.1.6 1,4-Bis{4-(pyridin-2-yl)-1*H*-1,2,3-triazol-1-yl}butane (**10**)

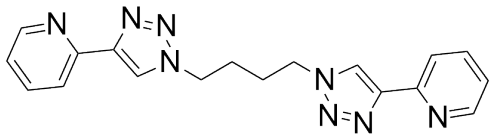

Figure D.6: 1,4-bis{4-(pyridin-2-yl)-1*H*-1,2,3-triazol-1-yl}butane (**10**)

Using a procedure modified from that described by Wu *et al.*,[291] a solution of 1,4-dibromobutane (0.36 mL, 0.65 g, 3.02 mmol; 1 equiv.) and NaN_3 (0.45 g, 6.94 mmol; 2.3 equiv.) in DMF (5 mL) was stirred at 80 °C for 24 h. A solution of $CuSO_4 \cdot 5\,H_2O$ (0.31 g, 1.20 mmol; 0.4 equiv.), sodium ascorbate (0.29 g, 2.72 mmol; 0.9 equiv.), and **6** (660 µL, 0.67 g, 6.50 mmol; 2.15 equiv.) was added, and the reaction mixture stirred at room temperature for 20 h. 30% aqueous ammonia (20 mL) and deionised water (40 mL) were added and the reaction mixture stirred until a colour change was observed (from yellow to white precipitate, blue solution). The precipitate was filtered, washed with deionised

water, diethyl ether, and dried to give **10** as an off-white solid (0.78 g, 74%). δ_H (500 MHz, $CDCl_3$) 8.56 (ddd, J = 4.8, 1.6, 0.9 Hz, 1H), 8.17 (dt, J = 7.9, 1.0 Hz, 1H), 8.15 (d, 1H), 7.78 (td, J = 7.7, 1.8 Hz, 1H), 7.23 (ddd, J = 7.5, 4.9, 1.2 Hz, 1H), 4.50 - 4.45 (m, 2H), 2.06 - 2.01 (m, 2H).

D.1.2 Ru(II) compounds

D.1.2.1 1,4-Xylyl spacer helicate (**11**)

Using a procedure modified from that described by Kumar *et al.*,[80] a solution of $RuCl_3 \cdot 3\,H_2O$ (34 mg, 0.17 mmol; 2 equiv. and **8** (100 mg, 0.25 mmol; 3 equiv.) in ethylene glycol (16 mL) was irradiated in a CEM microwave reactor at 225 °C (power 200 W, pressure 200 PSI) for 5 or 10 h. The solution was cooled to room temperature, deionised water added (20 mL), and filtered through Celite. A solution of KPF_6 (4%, 5 mL) was added, and the resulting precipitate isolated by centrifugation (10621 *g*, 5 min), washed with water, and dried under vacuum to give the helicate (**11**), as a yellow powder (0.11 g, 64%). δ_H (500 MHz, CD_3CN) 8.73 (s, 1H), 8.08 (d, J = 7.7 Hz, 1H), 8.02 (td, J = 7.7, 1.2 Hz, 1H), 7.97 (d, J = 5.5 Hz, 1H), 7.38 (m, 3H), 2.33 (ABq, J = 15.0 Hz, 2H). δ_C (126 MHz, CD_3CN) 153.20, 152.11, 149.33, 139.17, 136.81, 129.31, 126.90, 125.42, 123.40, 55.70.

D.1.2.2 *n*-Propyl spacer mesocate (**12**) and helicate (**13**)

A solution of $RuCl_3 \cdot 3\,H_2O$ (41 mg, 0.2 mmol; 2 equiv.) and **9** (100 mg, 0.3 mmol; 3 equiv.) in ethylene glycol (16 mL) was irradiated in a CEM microwave reactor at 225 °C (power 200 W, pressure 200 PSI) for 5 h. The solution was cooled to room temperature, deionised water added (20 mL), and filtered through Celite. A solution of KPF_6 (4%, 5 mL) was added, and the resulting precipitate isolated by centrifugation (10621 *g*, 5 min), washed with water, and dried under vacuum to give the crude product, as a yellow powder.

The crude product was exchanged to the Cl^- salt (Dowex 1-X8) in H_2O, the resulting yellow solution filtered, and solvent removed. Partial dissolution of the resulting solid in DMSO allowed separation of **12** and **13**, where **12** was precipitated, while **13** remained in solution.

The DMSO precipitate was collected by centrifugation (10621 *g*, 20 min), washed vigourously with DMSO (20 mL), and dissolved in H_2O. KPF_6 (4%, 5 mL) was added, and the resulting precipitate isolated by centrifigation (10621 *g*, 5 min), washed with water, and dried under vacuum to give the mesocate (**12**), as a yellow powder (0.11 g, 32%). λ_{max} CH_3CN/nm (ε/M^{-1} cm^{-1}) 382 (2.46 x 10^4), 268 (1.06 x 10^5), 237 (2.55 x 10^4). δ_H (500 MHz, CD_3CN) 8.61 (s, 1H), 8.10 (d, J = 7.5 Hz, 1H), 8.04 - 7.96 (m, 2H), 7.37 (t, J = 6.1 Hz, 1H), 4.48 - 4.33 (m, 2H), 2.61 - 2.35 (m, 1H). δ_C (126 MHz, CD_3CN) 153.36, 152.37, 148.14, 142.25, 139.22, 126.78, 125.93, 123.18, 49.77, 31.75. *m/z* (ESI) 300.0639

($[Ru_2\mathbf{9}_3]^{4+}$).

The DMSO-solution was diluted with H_2O (100 mL) and KPF_6 (4%, 5 mL) added. The resulting precipitate was isolated by centrifugation (10621 *g*, 5 min), washed with water, and dried under vacuum to give the helicate (**13**), as a yellow powder (0.14 g, 40%). λ_{max} CH_3CN/nm (ε/M^{-1} cm^{-1}) 382 (3.17 x 10^4), 268 (1.39 x 10^5), 233 (3.17 x 10^4). δ_H (500 MHz, CD_3CN) 8.63 (s, 1H), 8.10 (d, J = 7.7 Hz, 1H), 8.02 (td, J = 7.8, 1.4 Hz, 1H), 7.97 (d, J = 5.6 Hz, 1H), 7.37 (ddd, J = 7.4, 5.7, 1.4 Hz, 1H), 4.51 - 4.42 (m, 1H), 4.33 - 4.23 (m, 2H), 2.62 - 2.55 (m, 1H). δ_C (126 MHz, CD_3CN) 153.29, 152.40, 148.34, 139.16, 126.74, 125.86, 123.12, 49.59, 28.79. *m/z* (ESI) 300.0651 ($[Ru_2\mathbf{9}_3]^{4+}$).

D.1.2.3 *n*-Butyl spacer mesocate (**15**) and helicate (**14**)

A solution of $RuCl_3 \cdot 3\,H_2O$ (39 mg, 0.19 mmol; 2 equiv.) and **10** (100 mg, 0.29 mmol; 3 equiv.) in ethylene glycol (16 mL) was irradiated in a CEM microwave reactor at 225 °C (power 200 W, pressure 200 PSI) for 5 or 10 h. The solution was cooled to room temperature, deionised water added (20 mL), and filtered through Celite. A solution of KPF_6 (4%, 5 mL) was added, and the resulting precipitate isolated by centrifugation (10621 *g*, 5 min), washed with water, and dried under vacuum to give the crude product, as a yellow powder.

The crude product was exchanged to the Cl^- salt (Dowex 1-X8) in H_2O, the resulting yellow solution filtered, and concentrated. Cellulose was mixed with H_2O to form a slurry and then packed onto a column of ∼100 mm length. The concentrated aqueous solution containing the crude Ru(II) product mixture was loaded and the column eluted with 0.075 M sodium (-)-*O,O′*-dibenzoyl-L-tartrate, and the single eluting band collected. The column was then washed with 0.5 M sodium 4-toluenesulfonate/(20% acetone/2 M NaCl) to collect the remaining precipitated compound. To remove the optically active anions both solutions were individually passed through a small column of silica gel and washed with copious amounts of acetone and water. Each fraction was then removed from the silica by elution with a solution of NH_4PF_6 in acetone (4%). Water (1 mL) was added and the acetone removed by rotary evaporation. In each case the resulting solid was collected by centrifugation (10621 *g*, 5 min), washed with cold water (3x), and dried under vacuum.

The first eluting fraction, containing a mixture of mesocate and one enantiomer of the helicate, was then exchanged to the Cl^- salt (Dowex 1-X8) in H_2O and the resulting yellow solution filtered. An aqueous solution of 0.5 M $NaBF_4$ was added to the aqueous crude product Cl^- solution in a drop wise manner, until precipitation was observed. The

solution was cooled to 5 °C for 24 h, and the resulting yellow precipitate filtered.

The yellow precipitate (from two rounds of crystallisation with BF_4^-) was washed with water, and dried to give a purified mixture of mesocate and helicate as the BF_4^- salt.

The compound remaining in solution (from two rounds of crystallisation with BF_4^-) was isolated as the PF_6^- salt by addition of an aqueous solution of KPF_6 (4%, 5 mL). The resulting solid (as the PF_6^- salt) was isolated by centrifugation (10621 *g*, 5 min), washed with cold water, and dried under vacuum to give a complex mixture of dinuclear species and unknown side products, as a yellow powder.

The second eluting fraction, from the resolution on cellulose, was isolated as the PF_6^- salt and found to contain a single enantiomer of the helicate (**14**), as a yellow powder. λ_{max} CH_3CN/nm (ε/M^{-1} cm^{-1}) 382 (3.17 x 10^4), 268 (1.39 x 10^5), 233 (3.17 x 10^4). δ_H (599 MHz, CD_3CN) 8.63 (s, 1H), 8.08 (d, J = 7.9 Hz, 1H), 8.01 (td, J = 7.8, 1.4 Hz, 1H), 7.97 (d, J = 5.5 Hz, 1H), 7.35 (ddd, J = 7.3, 5.7, 1.4 Hz, 1H), 4.41 - 4.27 (m, 1H), 4.33 - 4.23 (m, 2H), 1.86 - 1.67 (m, 2H). δ_C (126 MHz, CD_3CN) 153.19, 152.27, 148.86, 139.03, 126.64, 125.60, 123.04, 52.21, 27.27. *m/z* (ESI) ($[Ru_2\mathbf{10}_3]^{4+}$).

D.2 Additional NMR spectra

D.2.1 1,4-Xylyl spacer helicate

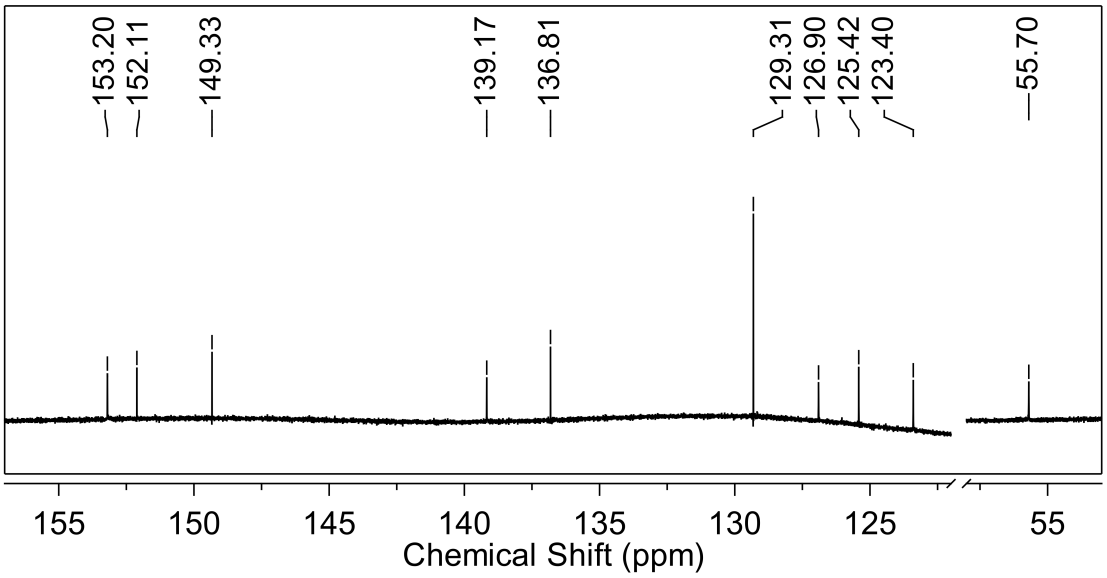

Figure D.7: Partial ^{13}C nuclear magnetic resonance (NMR) spectrum (151 MHz, CD_3CN, 298 K) showing the triple-stranded diruthenium helicate (**11**), using the 1,4-xylyl spacer ligand (**8**).

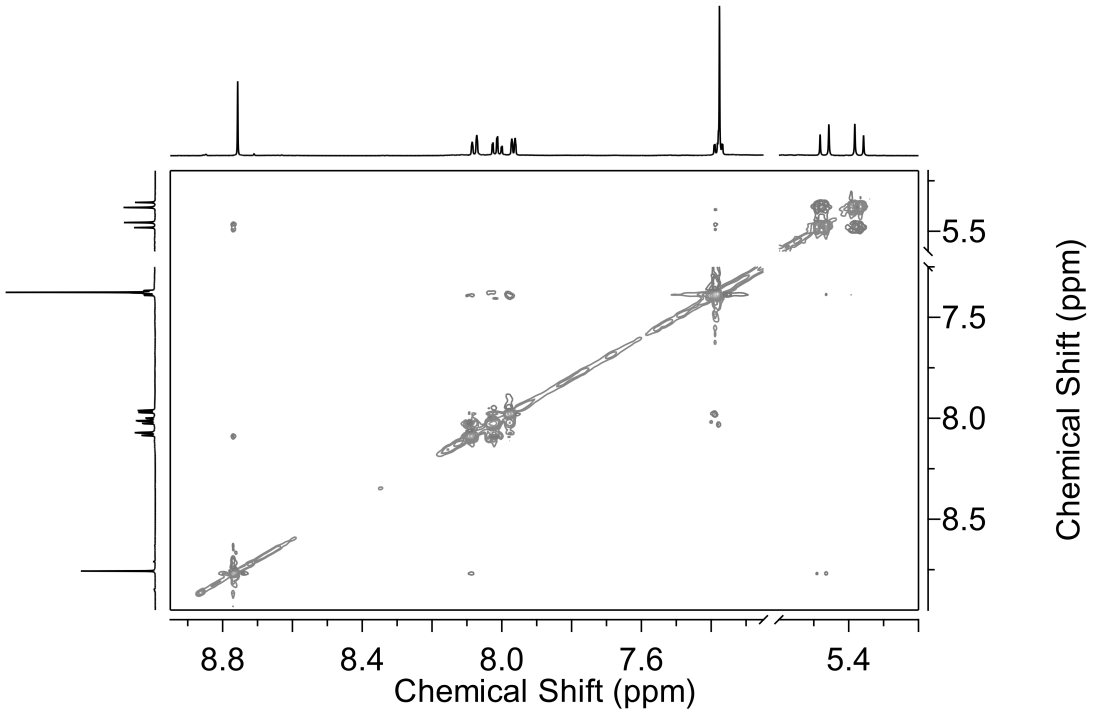

Figure D.8: ROESY NMR spectrum (600 MHz, CD_3CN, 298 K) showing the triple-stranded diruthenium helicate (**11**), using the 1,4-xylyl spacer ligand (**8**).

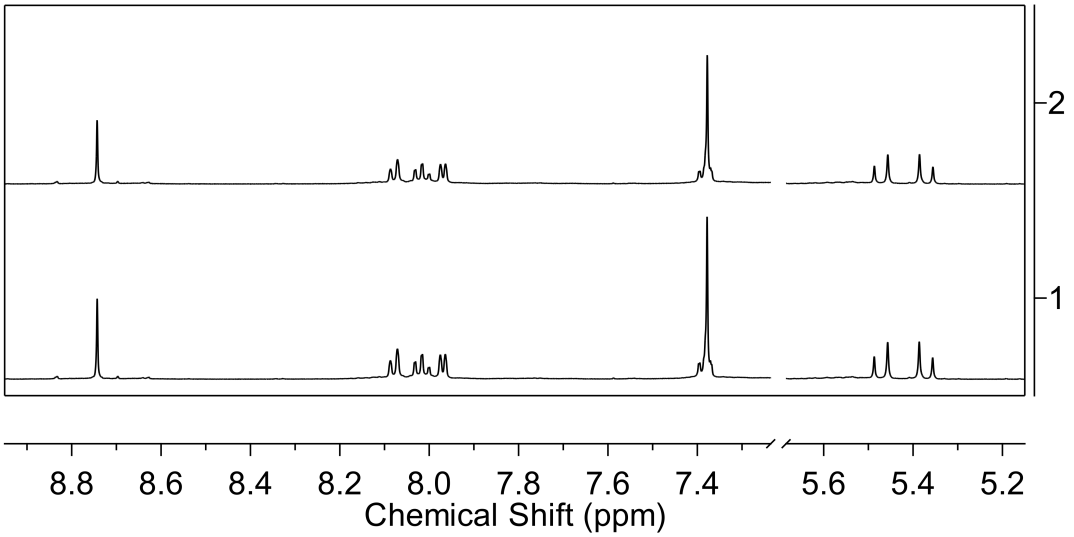

Figure D.9: Partial ^{1}H NMR spectrum (500 MHz, CD_3CN, 298 K) of the triple-stranded diruthenium helicate (**11**), as the PF_6^- salt after heating at 50 °C for 7 days.

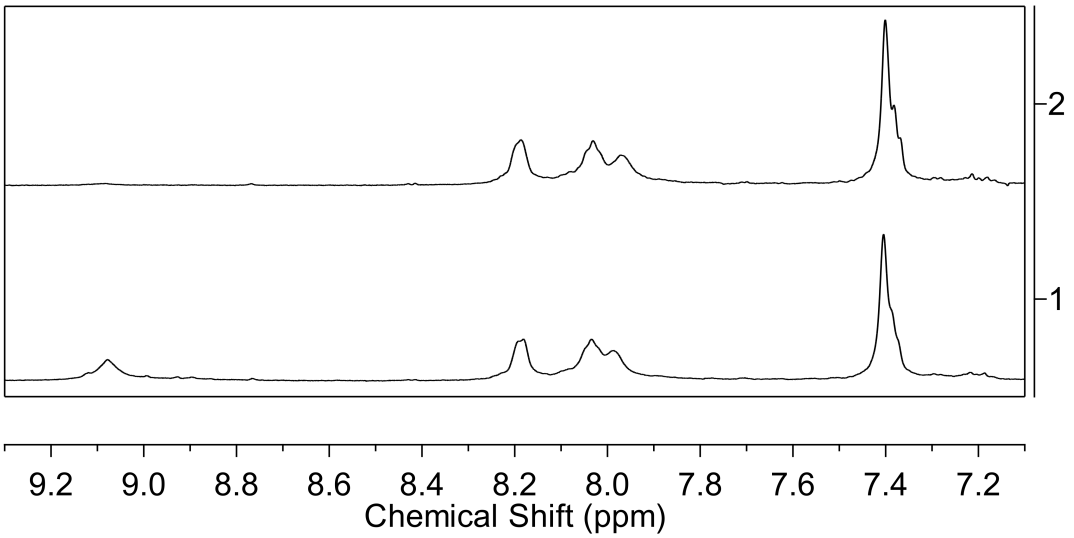

Figure D.10: Partial ^{1}H NMR spectrum (500 MHz, CD_3CN, 298 K) showing the aromatic region of the triple-stranded diruthenium helicate (**11**), as the Cl^- salt after heating at 50 °C for 7 days.

D.2.2 *n*-Propyl spacer compounds

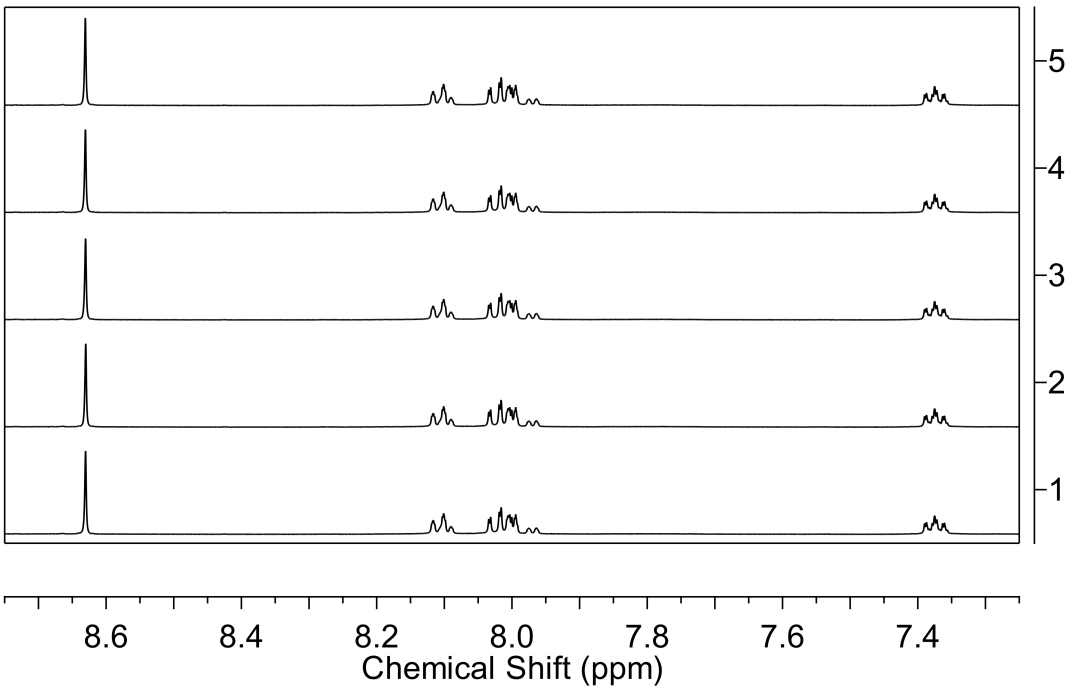

Figure D.11: Partial ^{1}H NMR spectrum (500 MHz, CD_3CN, 298 K) showing the aromatic region of the crude reaction mixture from the microwave reaction to form the triple-stranded diruthenium compound as the PF_6^- salt, using the *n*-propyl spacer ligand (**9**). (1) Initial; (2) 1 day; (3) 3 days; (4) 5 days; (5) 7 days.

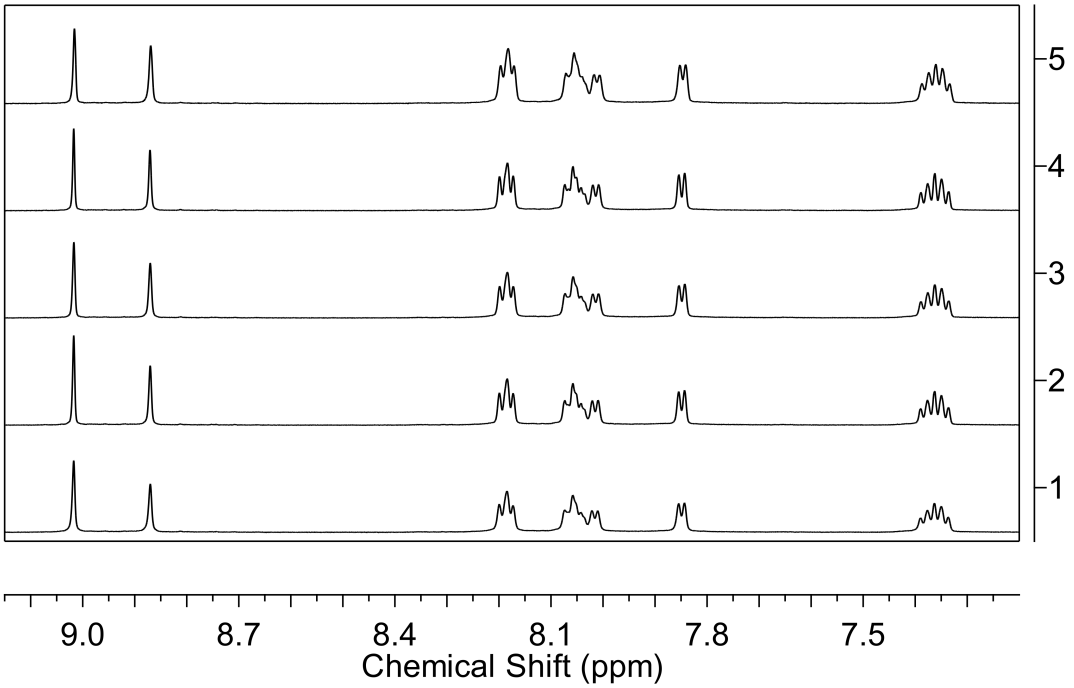

Figure D.12: Partial ^{1}H NMR spectrum (500 MHz, D_2O, 298 K) showing the aromatic region of the crude reaction mixture from the microwave reaction to form the triple-stranded diruthenium compound as the Cl salt, using the *n*-propyl spacer ligand (**9**). (1) Initial; (2) 1 day; (3) 3 days; (4) 5 days; (5) 7 days.

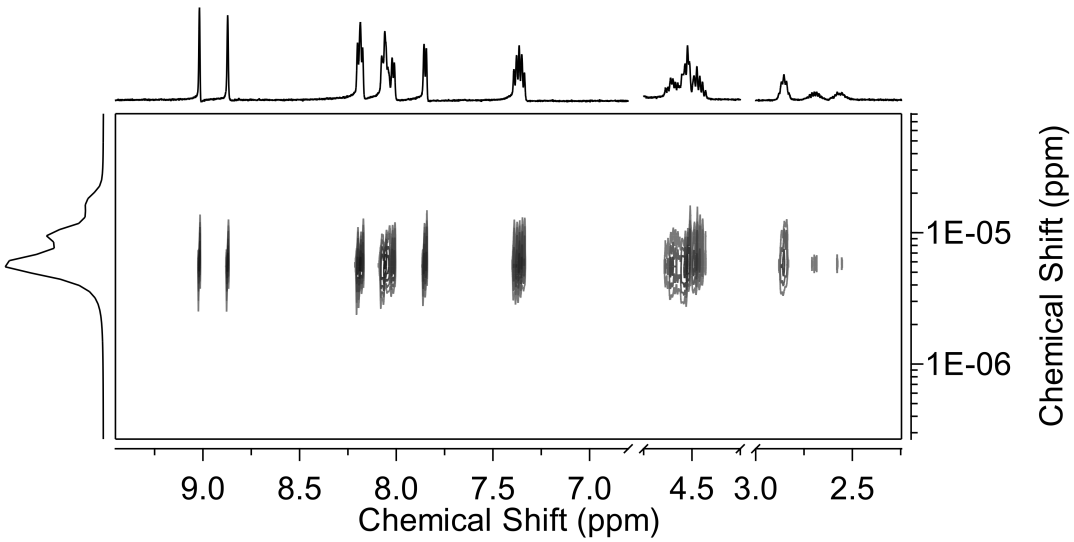

Figure D.13: ^{1}H DOSY NMR spectrum (500 MHz, D_2O, 298 K) showing the triple-stranded diruthenium compound as the Cl^- salt in D_2O, using the *n*-propyl spacer ligand (**9**).

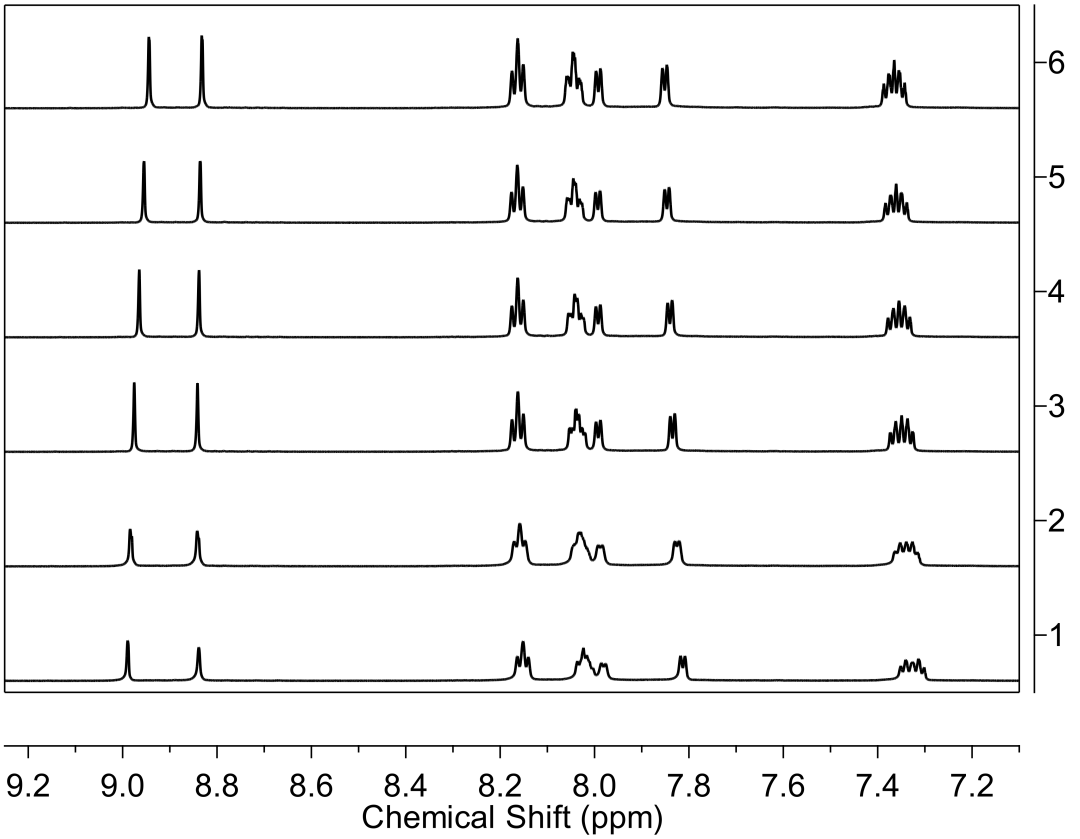

Figure D.14: Partial ^{1}H NMR spectrum (500 MHz, D_2O, 298 K) showing the aromatic region of the crude reaction mixture from the microwave reaction to form the triple-stranded diruthenium compound as the Cl^- salt, using the *n*-propyl spacer ligand (**9**). Spectra measured at (1) 25 °C; (2) 30 °C; (3) 35 °C; (4) 40 °C; (5) 45 °C; (6) 50 °C.

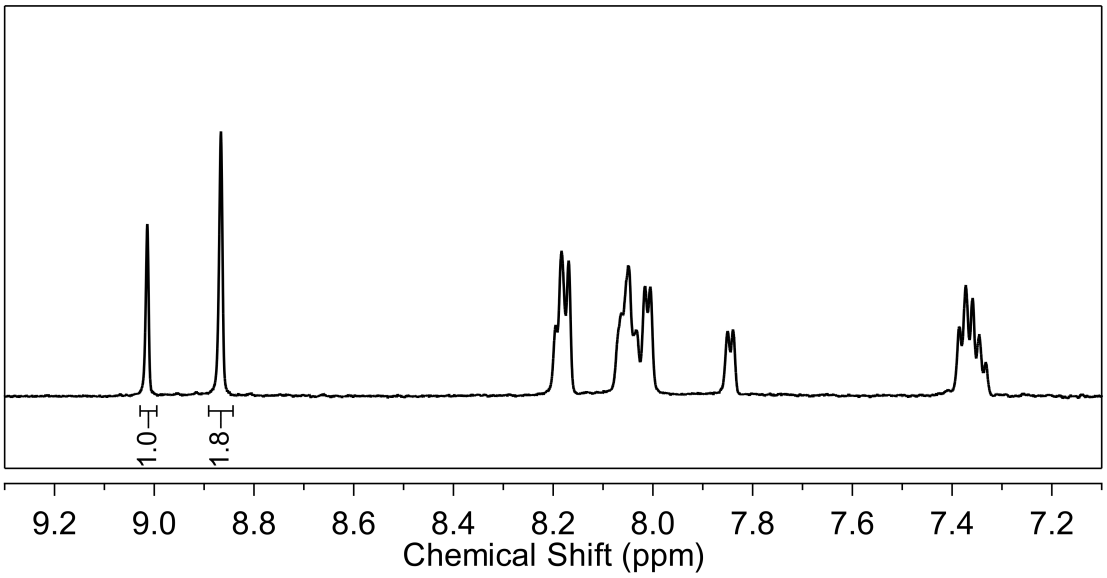

Figure D.15: Partial ^{1}H NMR spectrum (500 MHz, D_2O, 298 K) showing the aromatic region of the crude reaction mixture from the microwave reaction to form the triple-stranded diruthenium compound as the Cl^- salt, using the *n*-propyl spacer ligand (**9**). In this older sample the relative integration of the two species is 1 : 1.8.

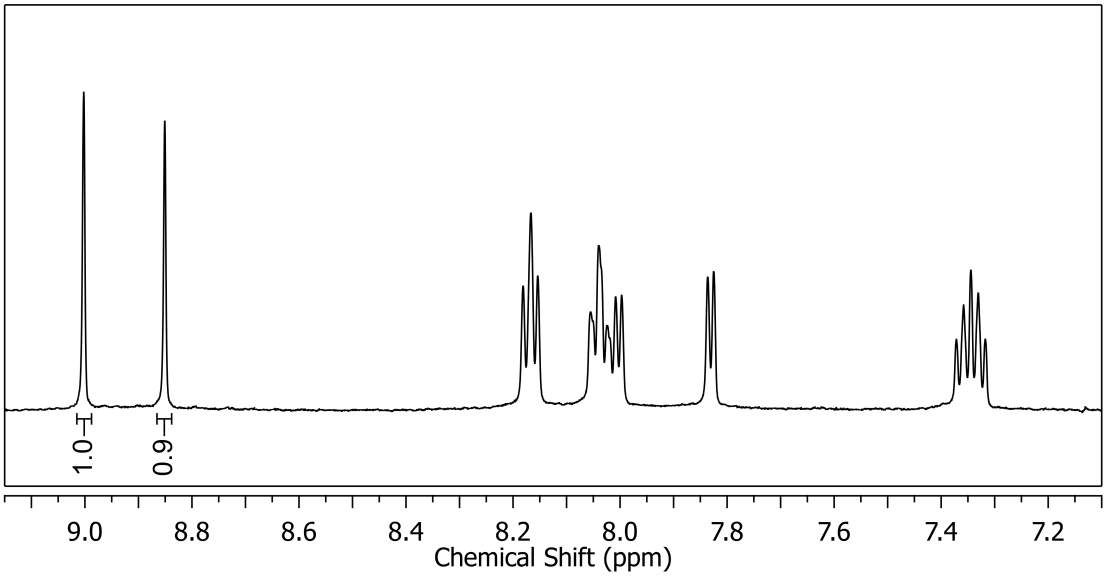

Figure D.16: Partial ^{1}H NMR spectrum (500 MHz, D_2O, 298 K) showing the aromatic region of the crude reaction mixture from the microwave reaction to form the triple-stranded diruthenium compound as the Br^- salt, using the *n*-propyl spacer ligand (**9**).

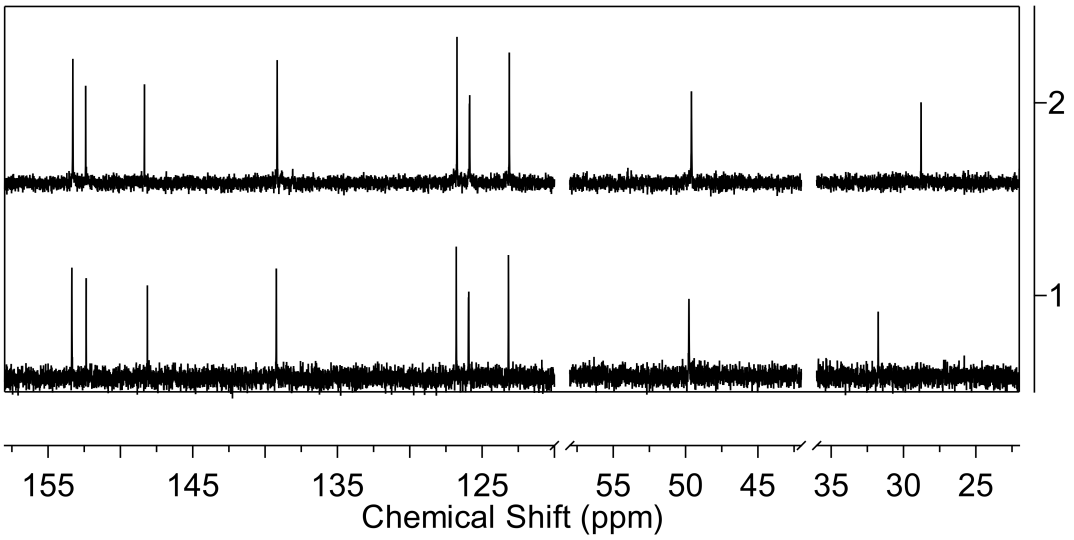

Figure D.17: Partial ^{13}C NMR spectra (126 MHz, CD_3CN, 298 K) showing the products from the microwave reaction to form the triple-stranded diruthenium compound as the PF_6^- salt, using the *n*-propyl spacer ligand (**9**). (1) DMSO-insoluble; (2) DMSO-soluble.

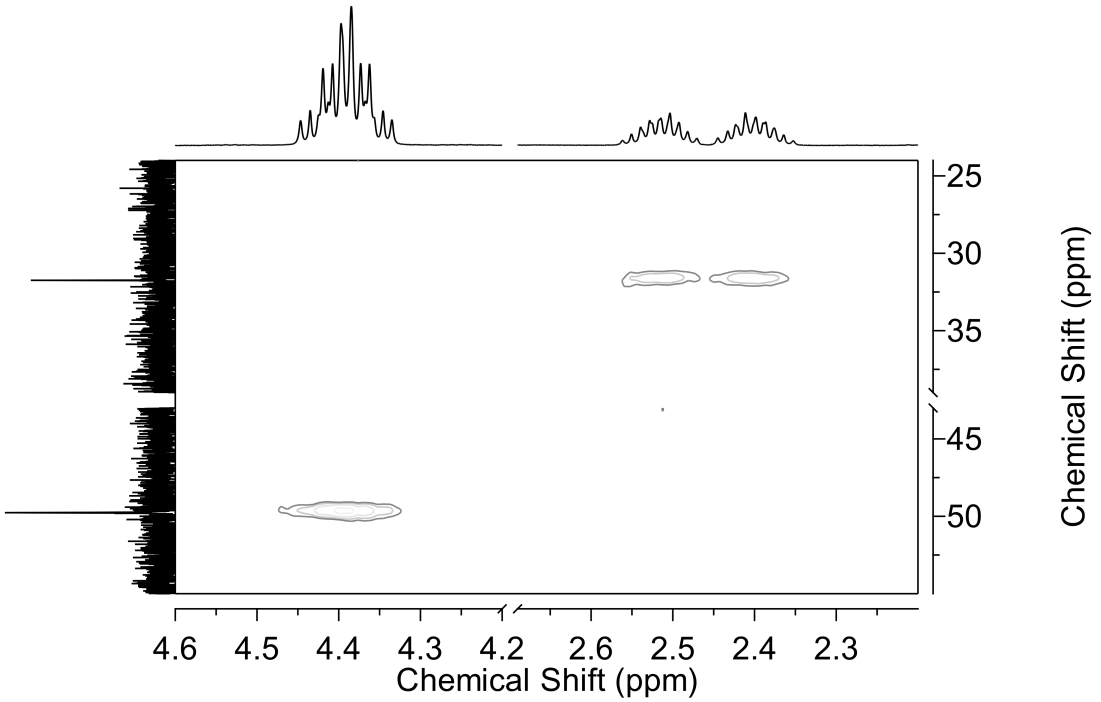

Figure D.18: HSQC spectrum showing the cross-peaks between the spacer multiplets and separate carbon signals, for the DMSO-insoluble product from the microwave reaction to form the triple-stranded diruthenium compound, using the *n*-propyl spacer ligand (**9**).

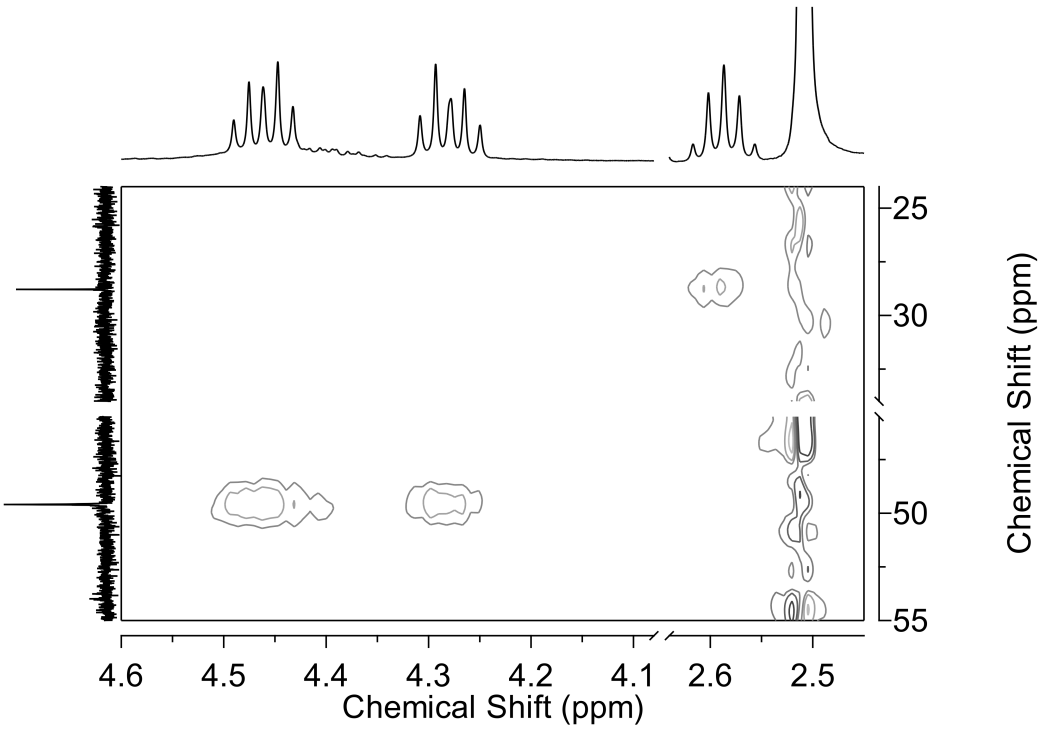

Figure D.19: HSQC NMR spectrum showing the cross-peaks between the spacer multiplets and separate carbon signals, for the DMSO-soluble product from the microwave reaction to form the triple-stranded diruthenium compound, using the *n*-propyl spacer ligand (**9**).

D.2.3 *n*-Butyl spacer compounds

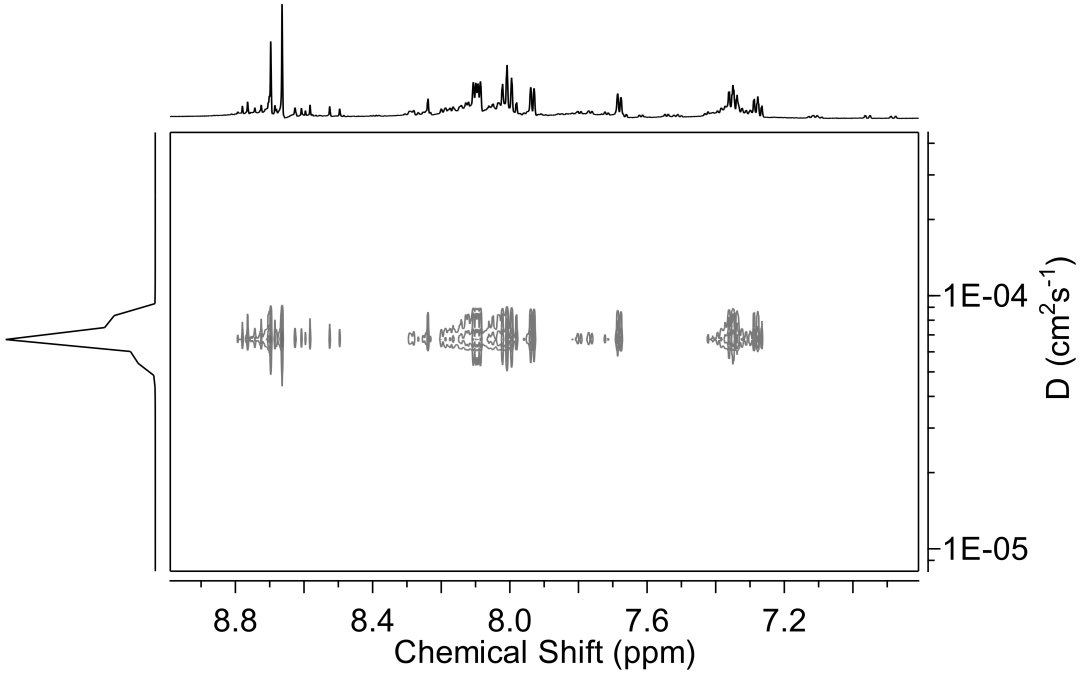

Figure D.20: ^{1}H DOSY NMR spectrum (600 MHz, CD_3CN, 298 K) showing the aromatic region of the crude product mixture as the PF_6^- salt in CD_3CN, using the *n*-butyl spacer ligand (**10**).

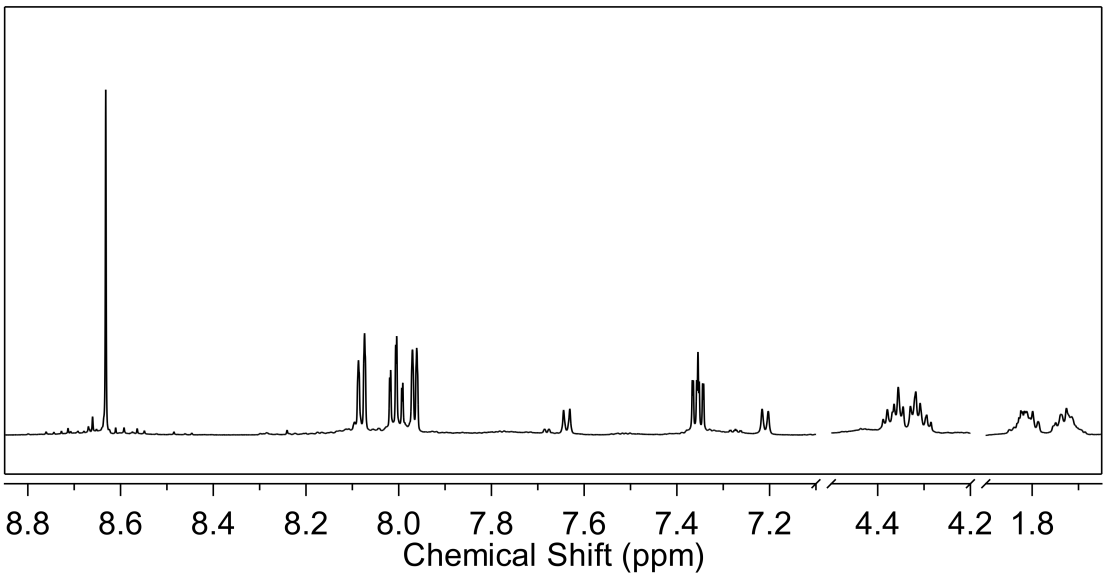

Figure D.21: Partial ^{1}H NMR spectrum (600 MHz, CD_3CN, 298 K) showing F2 from the resolution on cellulose of the *n*-butyl spacer product mixture as the PF_6^- salt in CD_3CN, using the *n*-butyl spacer ligand (**10**). F2 was eluted with 0.5 M sodium 4-toluenesulfonate, and contains one enantiomer of the triple-stranded helicate (**14**). The doublets at 7.64 and 7.22 ppm are attributed to residual 4-toluenesulfonate anions.

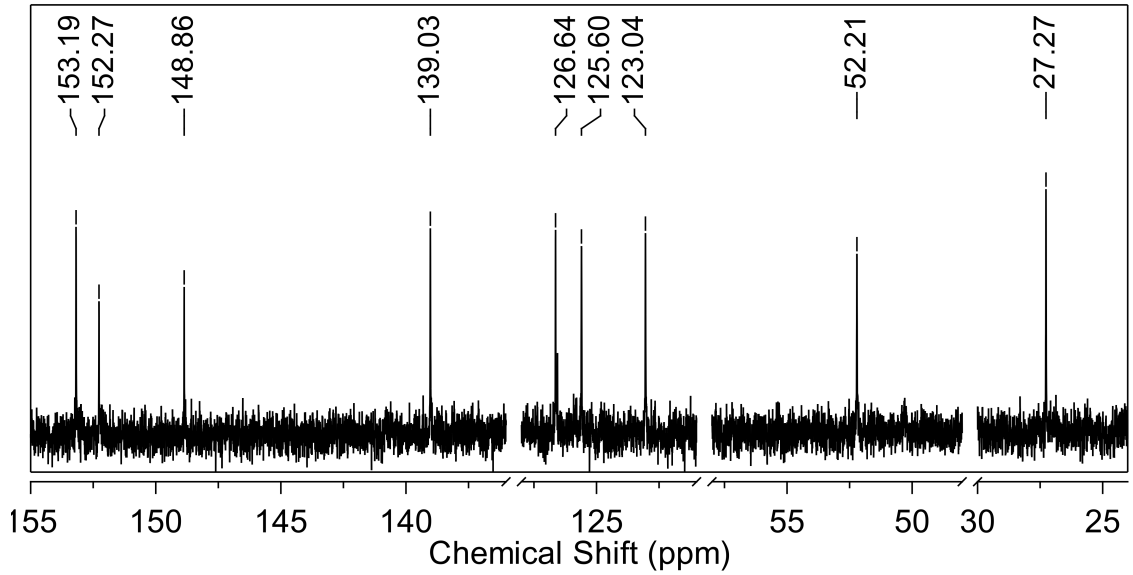

Figure D.22: Partial ^{13}C NMR spectrum (500 MHz, CD_3CN, 298 K) showing F2 from the resolution on cellulose of the *n*-butyl spacer product mixture as the PF_6^- salt in CD_3CN, using the *n*-butyl spacer ligand (**10**). F2 was eluted with 0.5 M sodium 4-toluenesulfonate, and contains one enantiomer of the triple-stranded helicate (**14**).

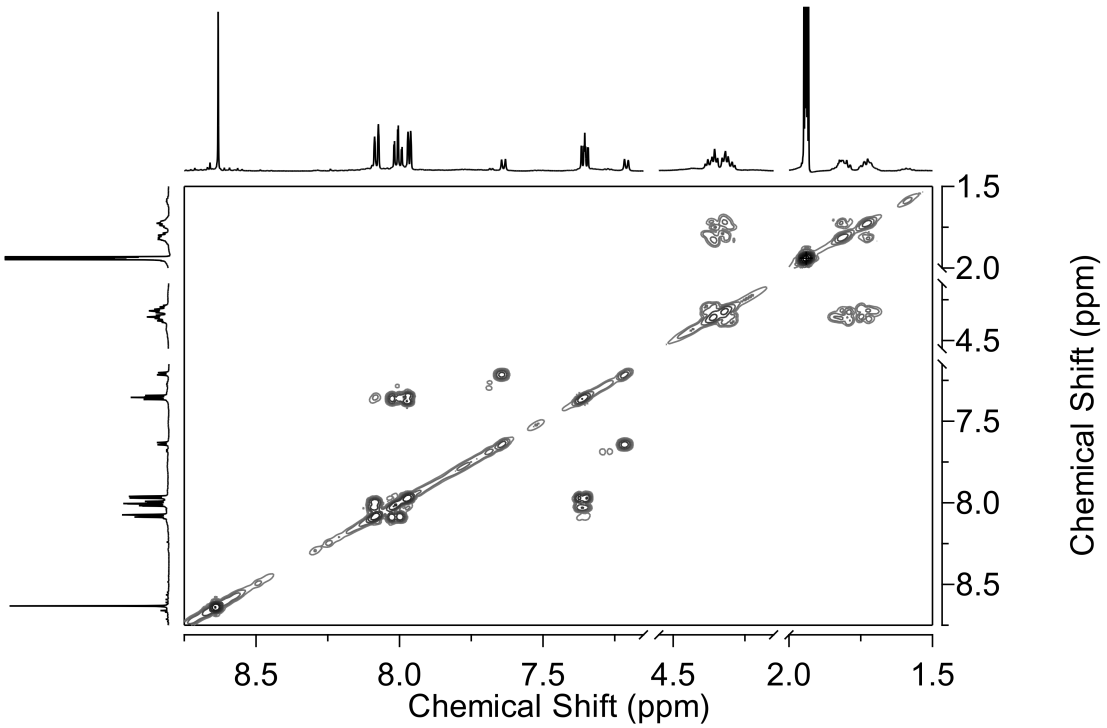

Figure D.23: COSY NMR spectrum (600 MHz, CD_3CN, 298 K) showing F2 from the resolution on cellulose of the *n*-butyl spacer product mixture as the PF_6^- salt in CD_3CN, using the *n*-butyl spacer ligand (**10**). F2 was eluted with 0.5 M sodium 4-toluenesulfonate, and contains one enantiomer of the triple-stranded helicate (**14**).

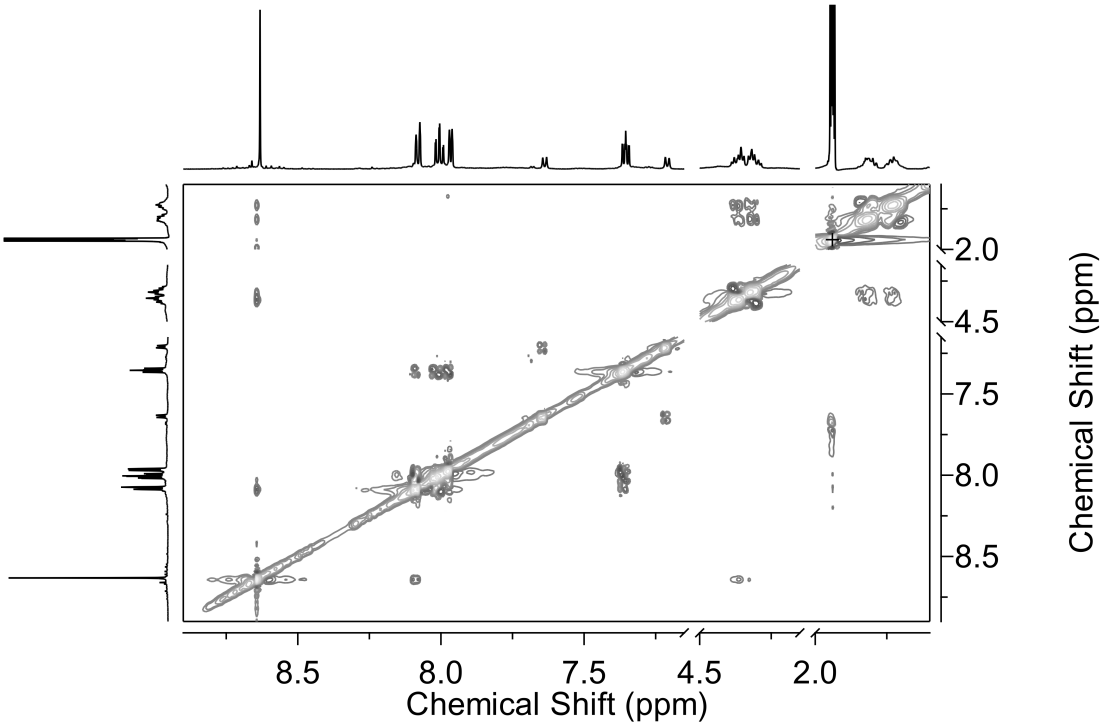

Figure D.24: ROESY NMR spectrum (600 MHz, CD_3CN, 298 K) showing F2 from the resolution on cellulose of the *n*-butyl spacer product mixture as the PF_6^- salt in CD_3CN, using the *n*-butyl spacer ligand (**10**). F2 was eluted with 0.5 M sodium 4-toluenesulfonate, and contains one enantiomer of the triple-stranded helicate (**14**).

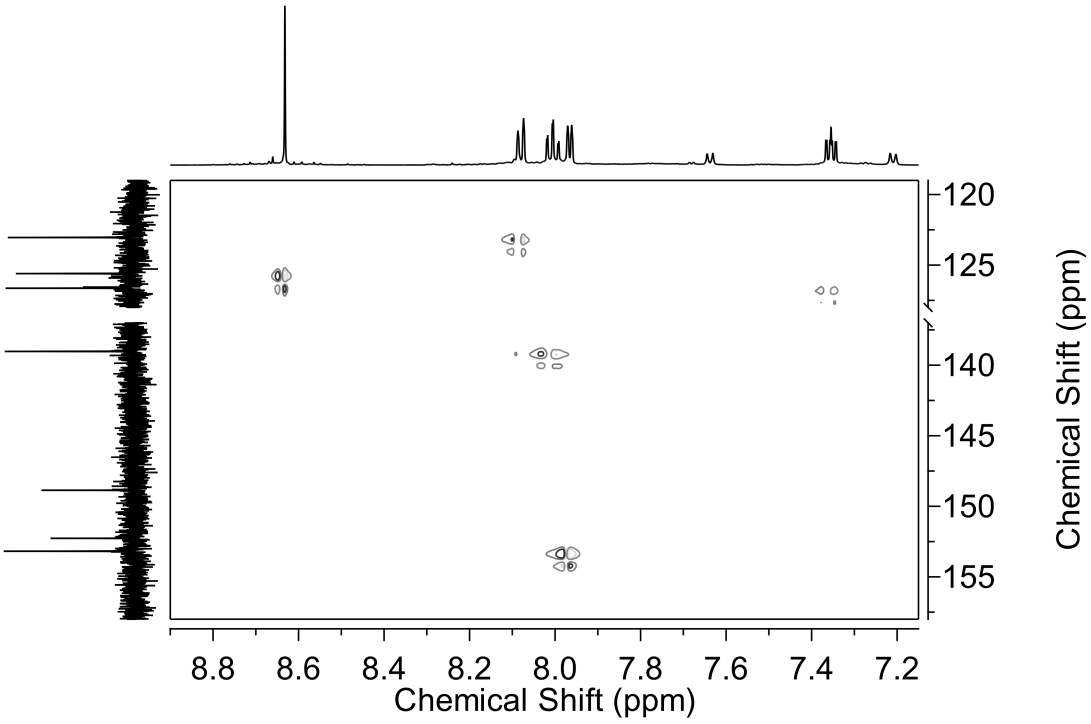

Figure D.25: HSQC NMR spectrum (600 MHz, CD_3CN, 298 K) showing the aromatic region of F2 from the resolution on cellulose of the *n*-butyl spacer product mixture as the PF_6^- salt in CD_3CN, using the *n*-butyl spacer ligand (**10**). F2 was eluted with 0.5 M sodium 4-toluenesulfonate, and contains one enantiomer of the triple-stranded helicate (**14**).

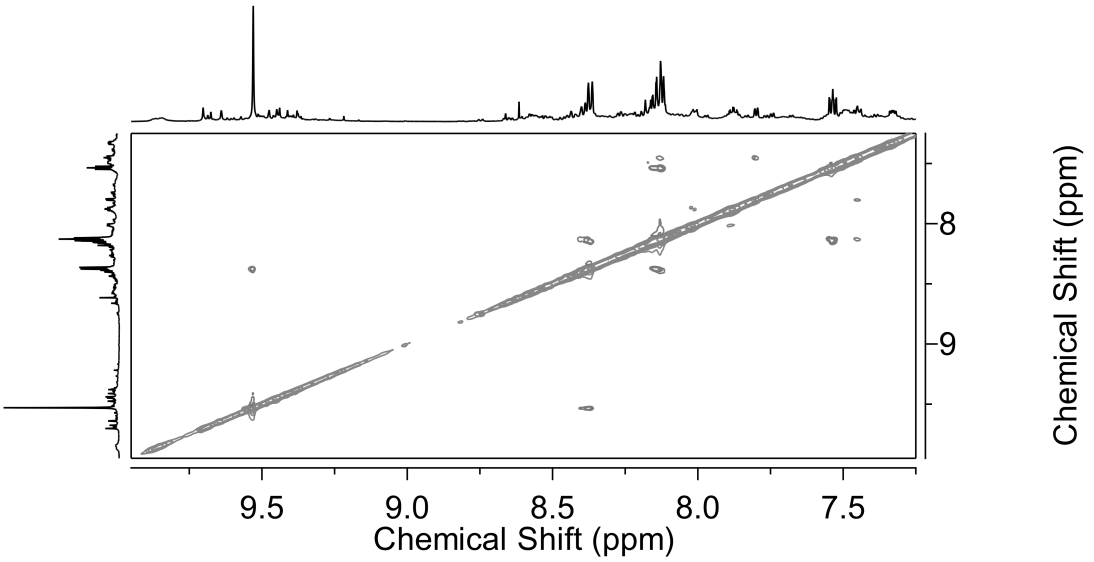

Figure D.26: rotating-frame overhauser effect spectroscopy (ROESY) NMR spectrum (600 MHz, d_6-DMSO, 298 K) showing the aromatic region from the crude reaction mixture for the formation of ruthenium compounds using the *n*-butyl spacer ligand (**10**) as the Cl^- salt in DMSO.

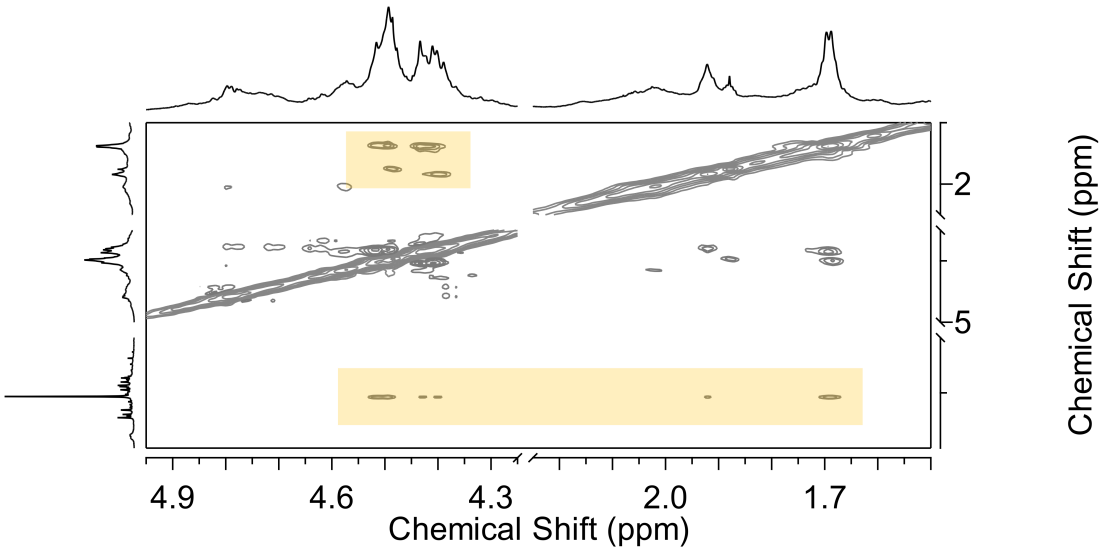

Figure D.27: ROESY NMR spectrum (600 MHz, d_6-DMSO, 298 K) showing cross-peaks between the *n*-butyl spacer hydrogens and triazole hydrogen from the crude reaction mixture for the formation of ruthenium compounds using the *n*-butyl spacer ligand (**10**) as the Cl^- salt in DMSO. Distinct correlations between hydrogen resonances are highlighted in yellow.

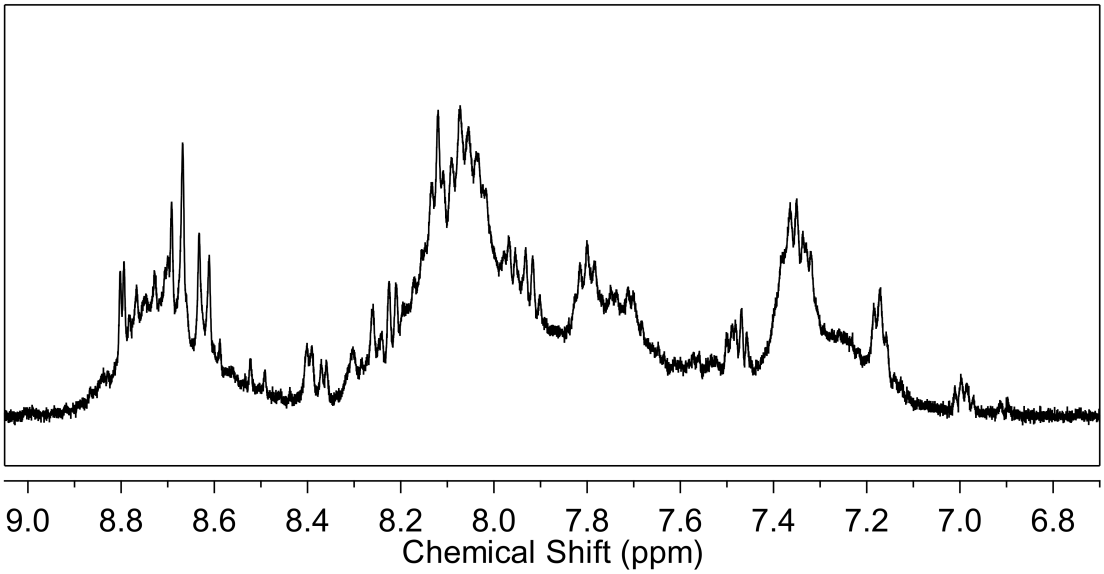

Figure D.28: Partial ^{1}H NMR spectrum (500 MHz, CD_3CN, 298 K) showing the aromatic region from the crude reaction mixture for the formation of ruthenium compounds using the *n*-butyl spacer ligand (**10**) under reflux conditions.

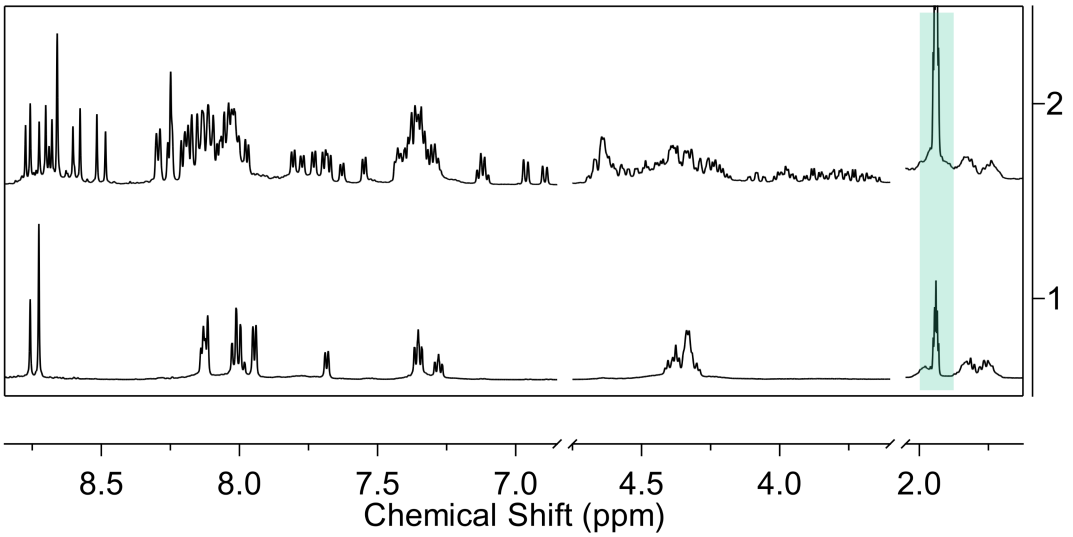

Figure D.29: Partial ^{1}H NMR spectrum (500 MHz, CD_3CN, 298 K) showing the outcomes from one round of fractional crystallisation using BF_4^- for F1 of the Ru(II) compounds incorporating the *n*-butyl spacer ligand (**10**). (1) Precipitate (shown here as the BF_4^- salt); (2) solution (shown here after exchange to the PF_6^- salt). Peaks corresponding to the solvent are highlighted in green.

D.3 Mass spectrometry

D.3.1 *n*-Propyl spacer compounds

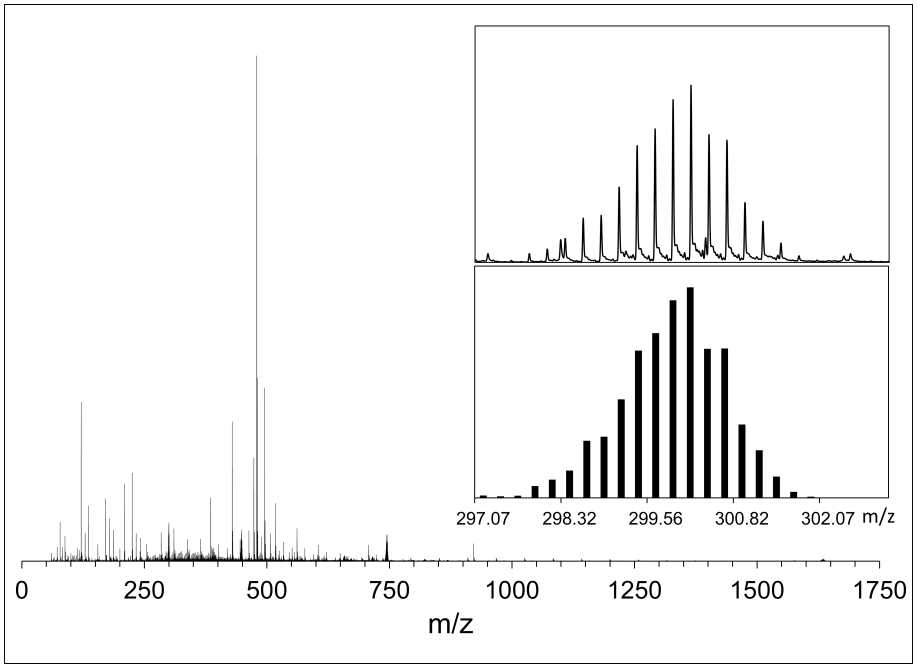

Figure D.30: Mass spectrum of the *n*-propyl spacer mesocate (**12**). Full HR-MS (CH_3CN), inset: Partial HR-MS (CH_3CN) and calculated isotopic pattern of the mesocate (**12**), peak at *m/z* 300.2222 due to [**12** - $4PF_6$]$^{4+}$.

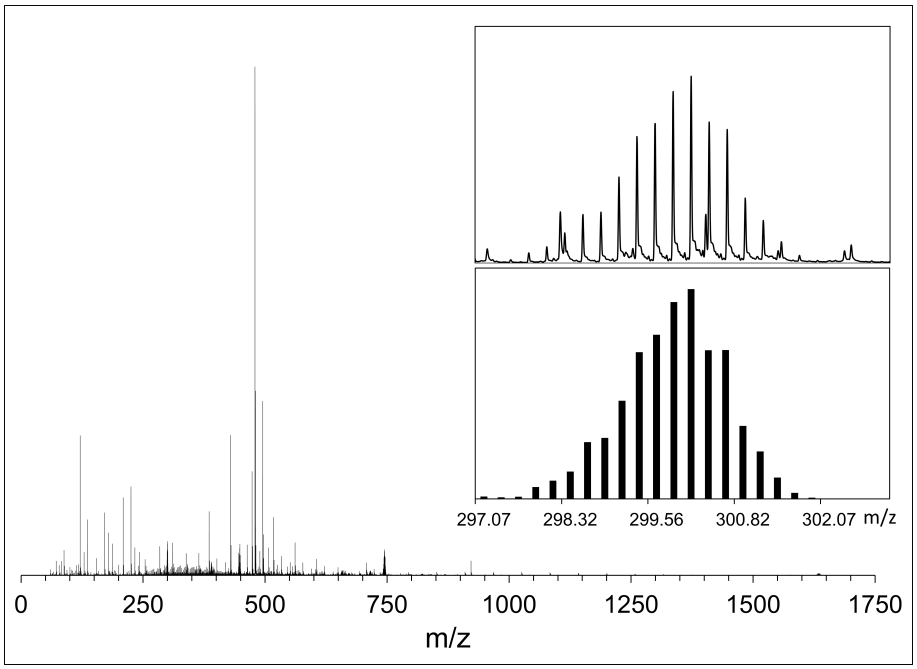

Figure D.31: Mass spectrum of the *n*-propyl spacer helicate (**13**). Full HR-MS (CH_3CN), inset: Partial HR-MS (CH_3CN) and calculated isotopic pattern of the helicate (**13**), peak at *m/z* 300.2222 due to [**13** - $4PF_6$]$_4^{+}$.

D.3.2 *n*-Butyl spacer compounds

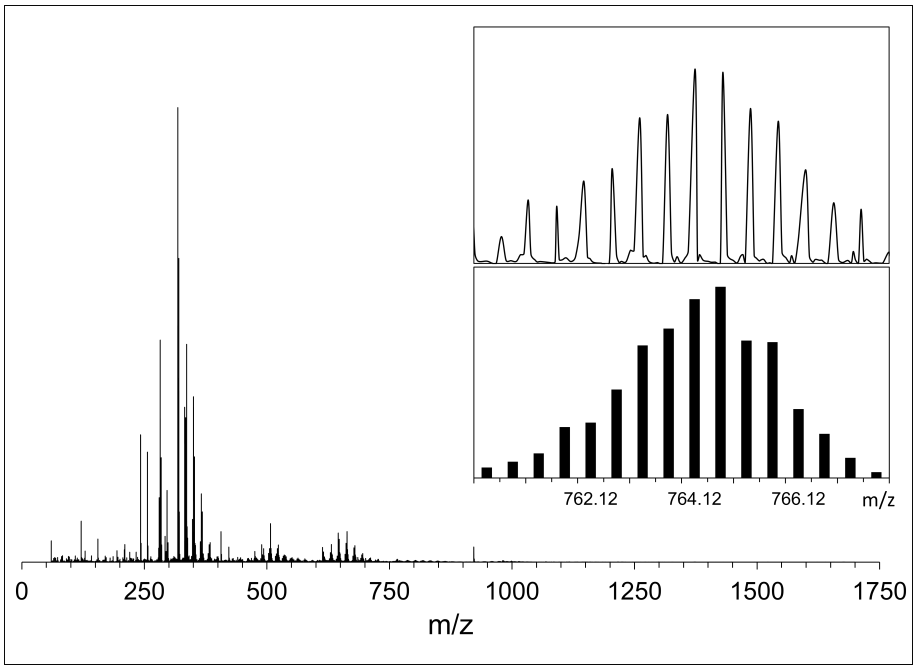

Figure D.32: Mass spectrum of one enantiomer of the *n*-butyl spacer helicate (**14**), isolated as F2 from the resolution on cellulose. Full HR-MS (CH_3CN), inset: Partial HR-MS (CH_3CN) and calculated isotopic pattern of the helicate (**14**), peak at *m/z* 766.1169 due to $[\mathbf{14} - 2PF_6]^{2+}$.

D.4 Additional circular dichroism spectroscopy

D.4.1 1,4-Xylyl spacer helicate

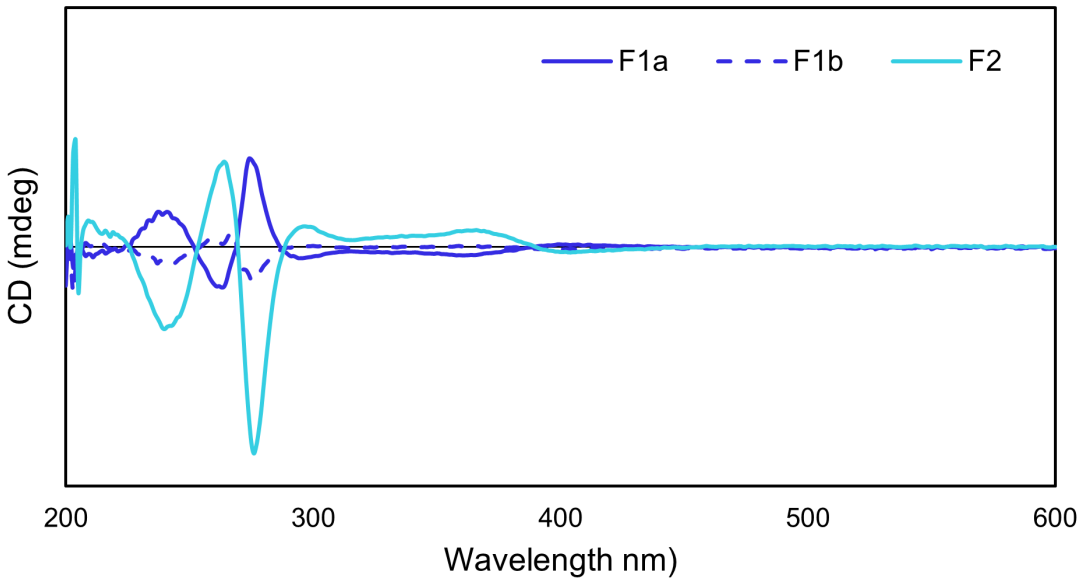

Figure D.33: CD spectra of the 1,4-xylyl spacer helicate (**11**) resolved on cellulose with 0.2 M NaCl eluent, followed by 20% acetone/2 M NaCl. F1a and F1b refer to the start and tail ends of the fraction eluted with 0.2 M NaCl, F2 refers to the compound stuck to the column which was subsequently removed with a 20% acetone/2 M NaCl wash. All traces are scaled with concentration.

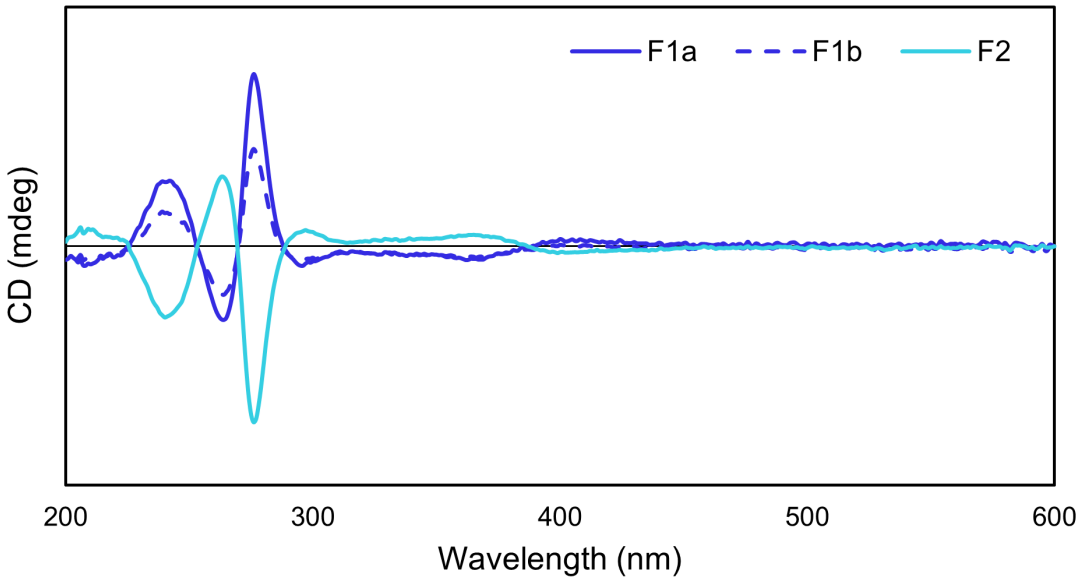

Figure D.34: CD spectra of the 1,4-xylyl spacer helicate (**11**) resolved on cellulose with 1 M NaCl eluent, followed by 20% acetone/2 M NaCl. F1a and F1b refer to the start and tail ends of the 1 M NaCl eluted fractions, F2 refers to the 20% acetone/2 M NaCl eluent. All traces are scaled with concentration.

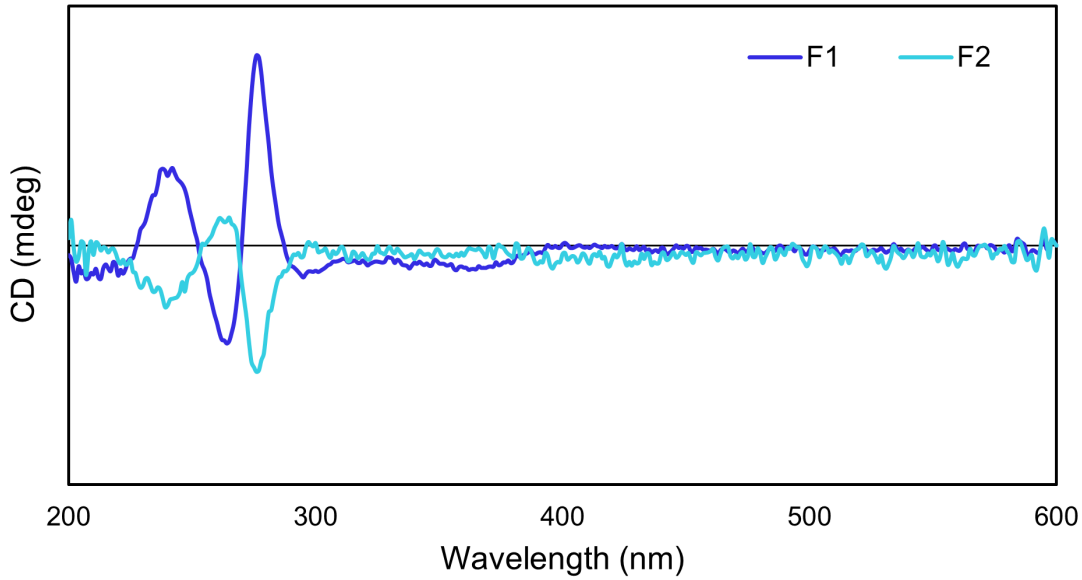

Figure D.35: CD spectra of the 1,4-xylyl spacer helicate (**11**) resolved on cellulose with 3 M NaCl eluent, followed by 20% acetone/2 M NaCl. F1 refers to the 3 M NaCl eluted fraction, F2 refers to the 20% acetone/2 M NaCl wash. All traces are scaled with concentration.

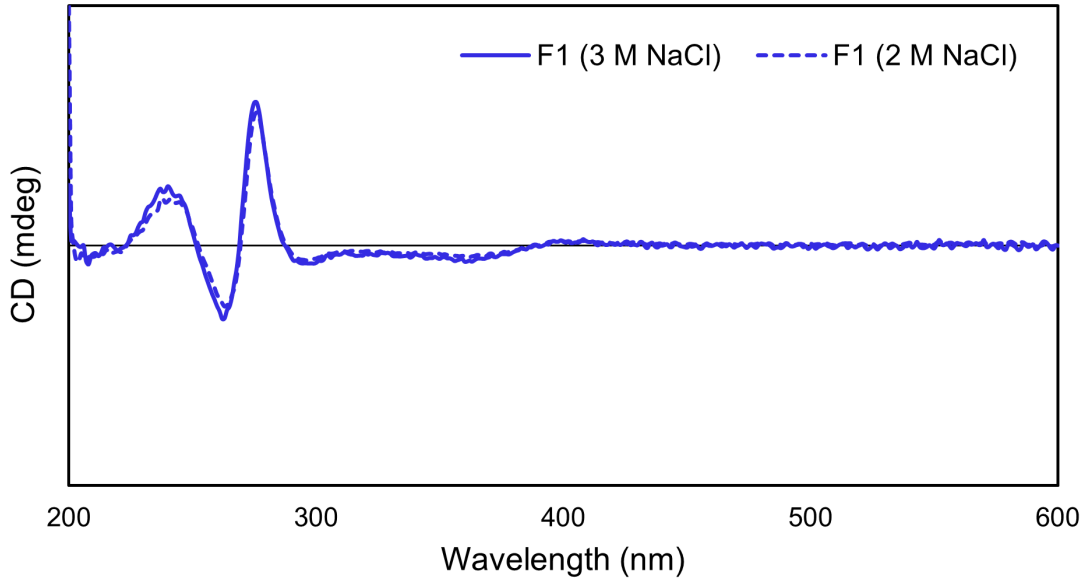

Figure D.36: CD spectra of the 1,4,-xylyl spacer helicate (**11**) resolved on cellulose comparing F1 for samples eluted with 3 M NaCl and 2 M NaCl. All traces are scaled with concentration.

D.5 X-ray crystallography

D.5.1 1,4-Xylyl spacer helicate

Crystals suitable for X-ray diffraction were grown by vapour diffusion of diethyl ether into a DMF solution of the compound (**11**). Single crystals were mounted in paratone-N oil on a plastic loop. X-ray diffraction data were collected at 150(2) K with Mo Kα radiation (λ = 0.71073 Å) using an Oxford Diffraction X-Calibur Diffractometer fitted with an Eos CCD detector. Data sets were corrected for absorption using a multi-scan method, and structures were solved by direct methods using *SHELXT*, and refined by full-matrix least-squares on F^2 by *SHELXL-2018*, interfaced through the program *X-Seed* or *OLEX*.[417–421] In general, all non-hydrogen atoms were refined anisotropically and hydrogen atoms were included as invariants at geometrically estimated positions. The crystallographic details for the 1,4-xylyl spacer helicate structure (**11**) are given in Table D.1 below.

Additional refinement details: the data for compound **11** was weak due to the small size of the crystals and the use of a home lab source to collect the data on these small crystals resulting in a low intensity dataset and a relatively high R_{int}. A series of SIMU and RIGU commands were used to achieve a satisfactory refinement of a DMF solvate and the hexafluorophosphate anions (138 restraints).

Table D.1: Crystal data and structure refinement for the 1,4-xylyl spacer helicate (**11**)

Compound	Helicate (**11**)
Empirical formula	$C_{72}H_{68}F_{24}N_{26}O_2P_4Ru_2$
Formula weight	2111.54
Temperature/K	150(2)
Crystal system	Monoclinic
Space group	$I2/a$
a /Å	26.813(3)
b /Å	14.858(2)
c /Å	24.237(3)
$\alpha/^\circ$	90
$\beta/^\circ$	91.852(12)
$\gamma/^\circ$	90
Volume /Å^3	9651(2)
Z	4
ρ_{calc}g/cm^3	1.453
μ/mm^{-1}	0.481
F(000)	4248.0
Crystal size/mm^3	0.22 × 0.06 × 0.03
Radiation	Mo Kα(λ= 0.71073)
2Θ range for data collection/$^\circ$	6.574 to 58.712
Index ranges	-36 $\leq$ h $\leq$ 36, -20 $\leq$ k $\leq$ 20, -31 $\leq$ 1 $\leq$ 33
Reflections collected	43657
Independent reflections	11802 [R_{int} = 0.1896, R_{sigma} = 0.2924]
Data/restraints/parameters	11802/138/586
Goodness-of-fit on F^2	1.121
Final R indexes [I >= 2σ(I)]	R_1 = 0.1531, wR_2 = 0.3764
Final R indexes [all data]	R_1 = 0.3331, wR_2 = 0.4748
Largest diff. peak and hole /e.Å^{-3})	1.36/-0.85

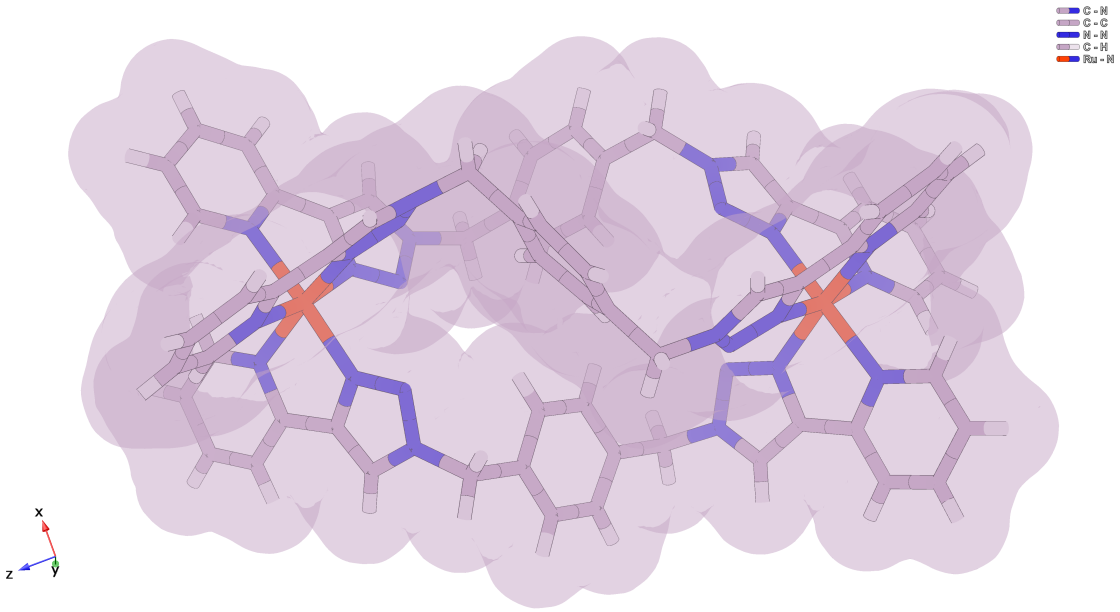

Figure D.37: Crystallographic model showing the molecular structure of the ruthenium helicate (**11**), including van der Waals surface, illustrating the inaccessible central cavity.

D.5.2 Original *n*-propyl spacer mesocate

Crystals suitable for X-ray diffraction were grown by vapour diffusion of diisopropyl ether into an acetonitrile solution of the compound (**12**). Single crystals were mounted in paratone-N oil on a plastic loop. X-ray diffraction data were collected on the MX2 beamline of the Australian Synchrotron at 100(2) K.[416] Data sets were corrected for absorption using a multi-scan method, and structures were solved by direct methods using *SHELXT*, and refined by full-matrix least-squares on F^2 by *SHELXL-2018*, interfaced through the program *X-Seed* or *OLEX*.[417–421] In general, all non-hydrogen atoms were refined anisotropically and hydrogen atoms were included as invariants at geometrically estimated positions. The crystallographic details for the original mesocate structure (**12** - original) are given in Table D.2 below.

Additional refinement details: the data for compound **12** was weak due to the very small size of the crystals and weak diffraction, despite the use of a synchrotron source. This resulted in a low intensity dataset and a relatively high R_{int}. A series of SIMU and RIGU commands were used to achieve a satisfactory refinement of the hexafluorophosphate anions, of which there are nine independent and, in some cases, partially occupied moieties. SIMU and RIGU restraints were also used for parts of the ligand backbone. The disordered nature of the hexafluorophosphate anions meant it was somewhat difficult to locate and refine the full complement of six anions required to charge balance the structure.

Table D.2: Crystal data and structure refinement for the original *n*-propyl spacer mesocate (**12**) - original

Compound	Mesocate (**12**) - original
Empirical formula	$C_{76.5}H_{72}F_{34.5}N_{36}P_{5.75}Ru_3$
Formula weight	2632.48
Temperature/K	100(2)
Crystal system	Monoclinic
Space group	*I*2/*a*
a /Å	22.469(5)
b /Å	41.080(8)
c /Å	25.590(5)
$\alpha/^\circ$	90
$\beta/^\circ$	106.08(3)
$\gamma/^\circ$	90
Volume /Å^3	22696(9)
Z	8
ρ_{calc}g/cm^3	1.541
μ/mm^{-1}	0.588
F(000)	10494.0
Crystal size/mm^3	0.10 × 0.04 × 0.04
Radiation	Synchrotron (λ= 0.71073)
2Θ range for data collection/°	1.93 to 65.246
Index ranges	$-30 \leq h \leq 30$, $-61 \leq k \leq 59$, $-34 \leq 1 \leq 34$
Reflections collected	162814
Independent reflections	32978 [$R_{int} = 0.1874$, $R_{sigma} = 0.1426$]
Data/restraints/parameters	32978/663/1429
Goodness-of-fit on F^2	0.836
Final R indexes [$I >= 2\sigma(I)$]	$R_1 = 0.1149$, $wR_2 = 0.3174$
Final R indexes [all data]	$R_1 = 0.2767$, $wR_2 = 0.4405$
Largest diff. peak and hole /e.Å^{-3})	1.04/-0.74

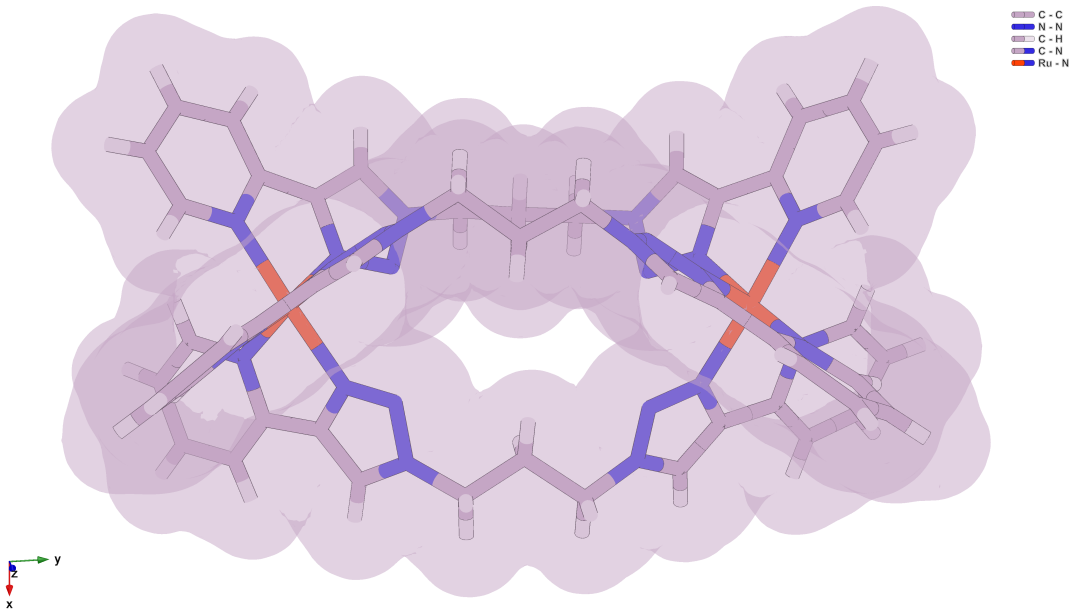

Figure D.38: Crystallographic model showing the molecular structure of the ruthenium mesocate (**12**), including van der Waals surface, illustrating the accessible central cavity.

D.5.3 Purified *n*-propyl spacer mesocate

Crystals suitable for X-ray diffraction were grown by vapour diffusion from diisopropyl ether/nitromethane (**12** - purified). Single crystals were mounted in paratone-N oil on a plastic loop. X-ray diffraction data were collected on the MX2 beamline of the Australian Synchrotron at 100(2) K.[416] Data sets were corrected for absorption using a multi-scan method, and structures were solved by direct methods using *SHELXT*, and refined by full-matrix least-squares on F^2 by *SHELXL-2018*, interfaced through the program *X-Seed* or *OLEX*.[417–421] In general, all non-hydrogen atoms were refined anisotropically and hydrogen atoms were included as invariants at geometrically estimated positions. The crystallographic details for the structure of the purified mesocate (**12** - purified) are given in Table D.3 below.

Additional refinement details: the structure was charge balanced by a potassium cation that was identified in the structure and then confirmed by EDX measurements on samples of the crystals. The potassium cation forms an intriguing anionic potassium hexafluorophosphate cluster with the potassium lying on the 6_3 screw axis and K - F contacts in the range 2.7 - 2.8 Å. A series of SIMU and RIGU commands were used to achieve a satisfactory refinement of the hexafluorophosphate anions, with one of these being disordered. A disordered nitromethane solvate molecule was also located in the structure. Finally, DFIX restraints were used to build a chemically sensible model of the nitromethane solvate molecule and the hexafluorophosphate anions.

Table D.3: Crystal data and structure refinement for the purified *n*-propyl spacer mesocate (**12** - purified)

Compound	Mesocate (**12**) - purified
Empirical formula	$C_{57}H_{66}N_{30}F_{30}P_5Ru_2KO_{12}$
Formula weight	2329.48
Temperature/K	100(2)
Crystal system	Hexagonal
Space group	$P6_3/m$
a /Å	13.6801(19)
b /Å	13.6801(19)
c /Å	28.911(6)
$\alpha/^\circ$	90
$\beta/^\circ$	90
$\gamma/^\circ$	120
Volume /Å^3	4685.7(16)
Z	2
ρ_{calc}g/cm^3	1.651
μ/mm^{-1}	0.580
F(000)	2332.0
Crystal size/mm^3	0.20 × 0.05 × 0.05
Radiation	Synchrotron (λ= 0.71073)
2Θ range for data collection/°	3.438 to 57.07
Index ranges	-15 ≤ h ≤ 15, -16 ≤ k ≤ 16, -31 ≤ 1 ≤ 30
Reflections collected	58862
Independent reflections	3256 [R_{int} = 0.0497, R_{sigma} = 0.0162]
Data/restraints/parameters	3256/226/261
Goodness-of-fit on F^2	1.062
Final R indexes [I >= 2σ(I)]	R_1 = 0.0447, wR_2 = 0.1162
Final R indexes [all data]	R_1 = 0.0456, wR_2 = 0.1171
Largest diff. peak and hole /e.Å^{-3})	1.57/-0.77

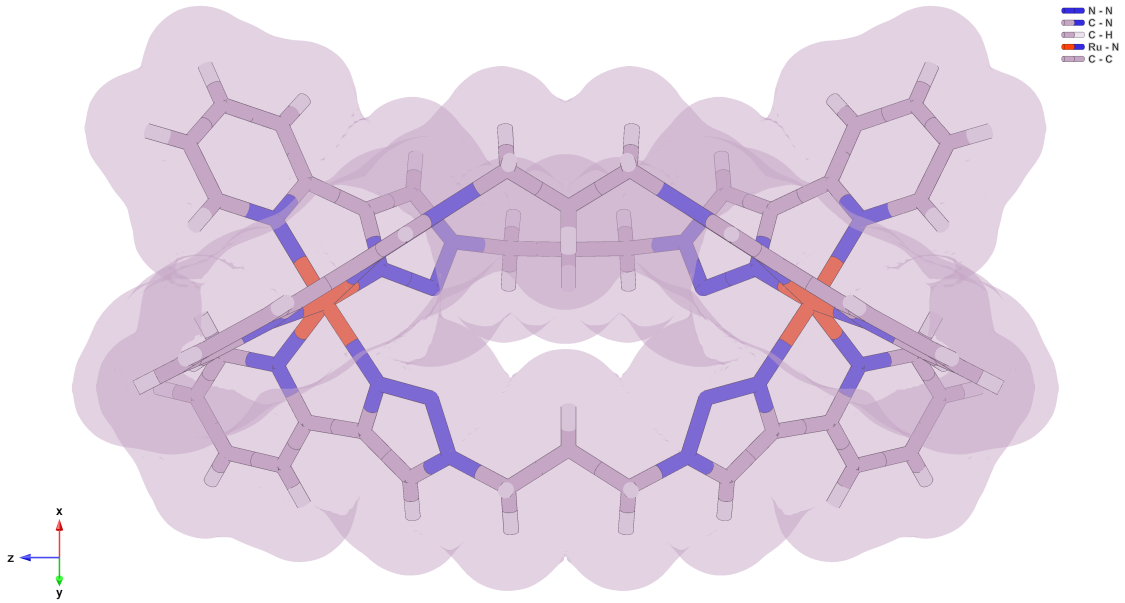

Figure D.39: Crystallographic model showing the molecular structure of the purified ruthenium mesocate (**12**), including van der Waals surface, illustrating the accessible central cavity.

D.5.4 Purified *n*-propyl spacer helicate

Crystals suitable for X-ray diffraction were grown by vapour diffusion of diisopropyl ether into an acetonitrile solution of the compound (**13** - purified). Single crystals were mounted in paratone-N oil on a plastic loop. X-ray diffraction data were collected on the MX2 beamline of the Australian Synchrotron at 100(2) K.[416] Data sets were corrected for absorption using a multi-scan method, and structures were solved by direct methods using *SHELXT*, and refined by full-matrix least-squares on F^2 by *SHELXL-2018*, interfaced through the program *X-Seed* or *OLEX*.[417–421] In general, all non-hydrogen atoms were refined anisotropically and hydrogen atoms were included as invariants at geometrically estimated positions. The crystallographic details for the structure of the purified mesocate (**12** - purified) are given in Table D.4 below.

Additional refinement details: the structure crystallises with two independent helicate molecules in the asymmetric unit, one constituting half the molecule and the second one sixth of the helicate. A large number of SIMU, RIGU and ISOR restraints were needed to achieve a satisfactory refinement of the hexafluorophosphate anions and the ligands in the structure. DFIX restraints were used to build a chemically sensible model of the hexafluorophosphate anions

Table D.4: Crystal data and structure refinement for the purified *n*-propyl spacer helicate (**13** - purified)

Compound	Helicate (**13**) - purified
Empirical formula	$C_{35}H_{33.5}N_{16.5}F_{16}P_{2.67}Ru_{1.33}$
Formula weight	1206.63
Temperature/K	100(2)
Crystal system	Trigonal
Space group	*P*-31*c*
a /Å	30.364(4)
b /Å	30.364(4)
c /Å	17.632(4)
$\alpha/^\circ$	90
$\beta/^\circ$	90
$\gamma/^\circ$	120
Volume /Å^3	14079(5)
Z	12
ρ_{calc}g/cm^3	1.708
μ/mm^{-1}	0.641
F(000)	7220.0
Crystal size/mm^3	0.40 x 0.30 x 0.10
Radiation	Synchrotron (λ= 0.71073)
2Θ range for data collection/$^\circ$	1.548 to 57.242
Index ranges	-35 $\leq$ h $\leq$ 34, -36 $\leq$ k $\leq$ 36, -21 $\leq$ 1 $\leq$ 21
Reflections collected	170137
Independent reflections	10449 [R_{int} = 0.1223, R_{sigma} = 0.0538]
Data/restraints/parameters	10449/913/602
Goodness-of-fit on F^2	1.225
Final R indexes [I >= 2σ(I)]	R_1 = 0.1655, wR_2 = 0.3891
Final R indexes [all data]	R_1 = 0.2867, wR_2 = 0.4760
Largest diff. peak and hole /e.Å^{-3})	3.00/-0.92

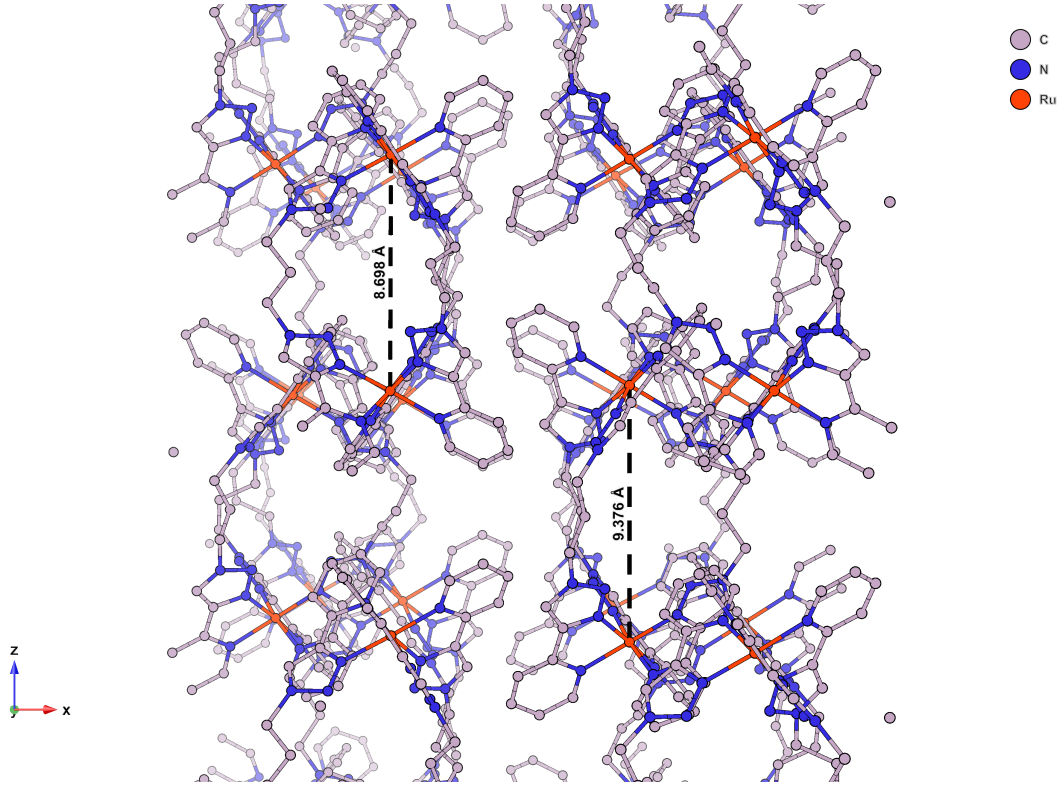

Figure D.40: Crystallographic model showing the molecular structure of the purified ruthenium helicate (**13**), indicating the differences in Ru - Ru distance recorded for adjacent helicate molecules (hydrogens and anions have been omitted for clarity).

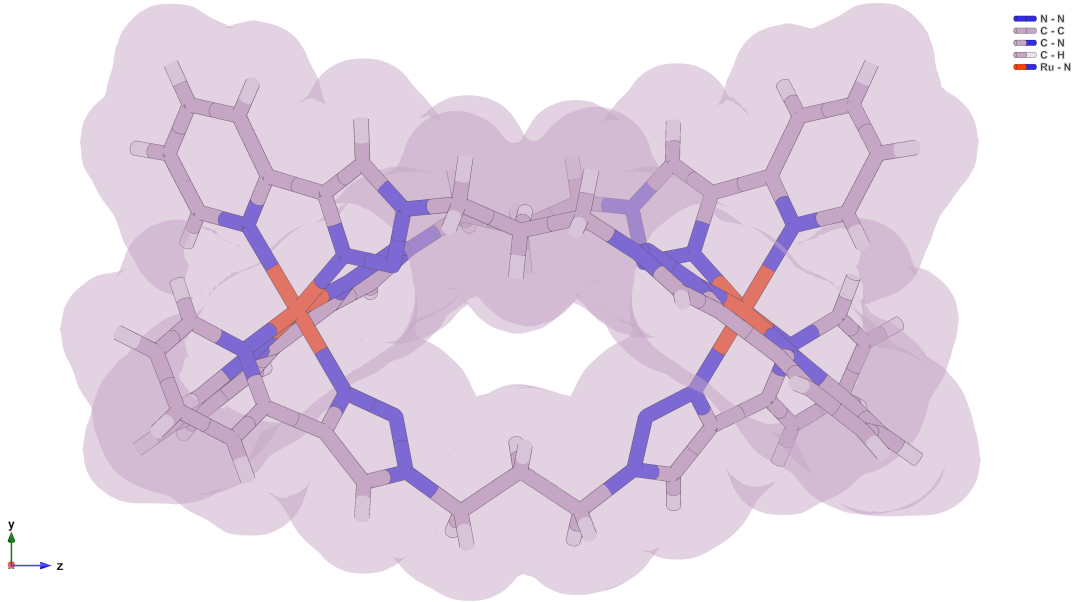

Figure D.41: Crystallographic model showing the molecular structure of the purified ruthenium helicate (**13**), including van der Waals surface, illustrating the accessible central cavity.

D.6 SEM/EDX

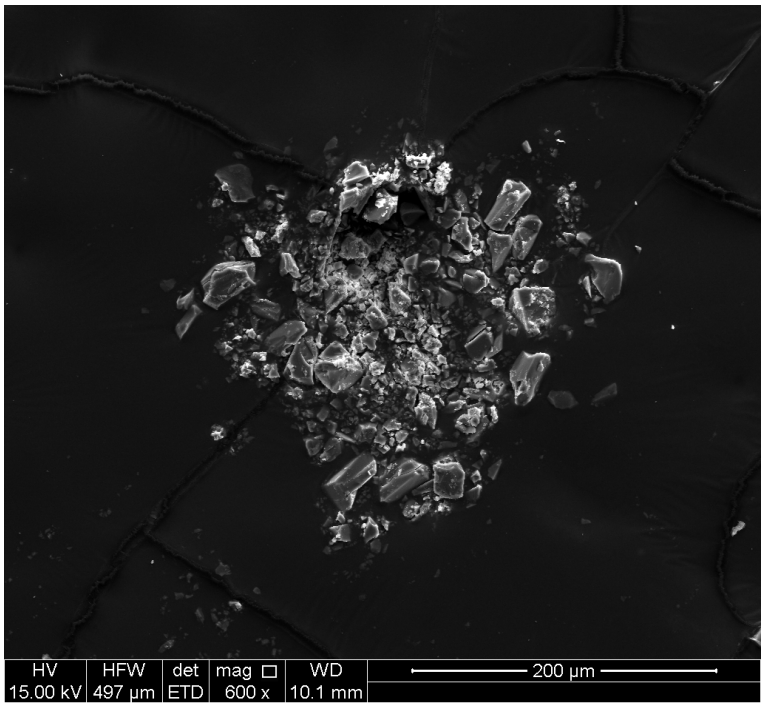

Figure D.42: SEM image of crushed crystals of the purified ruthenium mesocate (**12**).

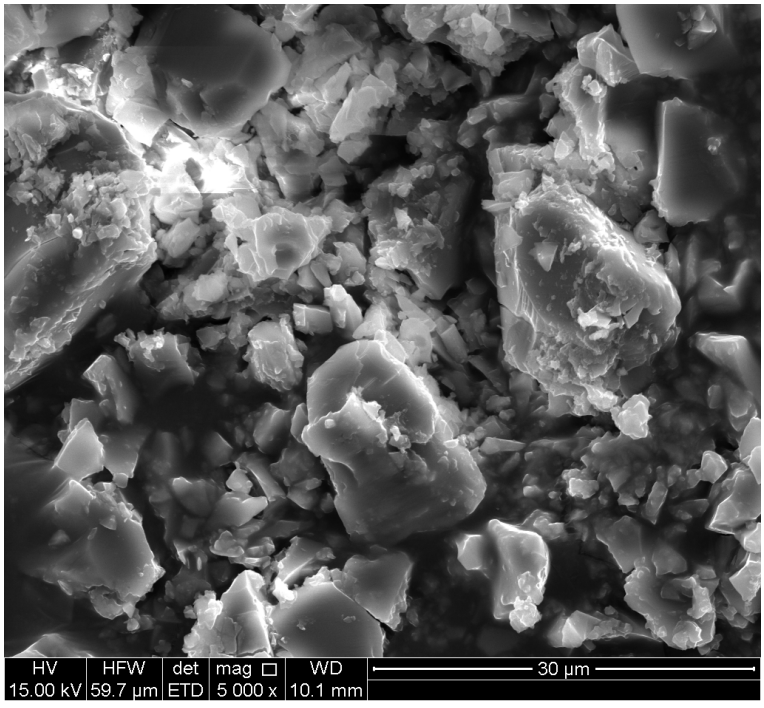

Figure D.43: SEM image of crushed crystals of the purified ruthenium mesocate (**12**).

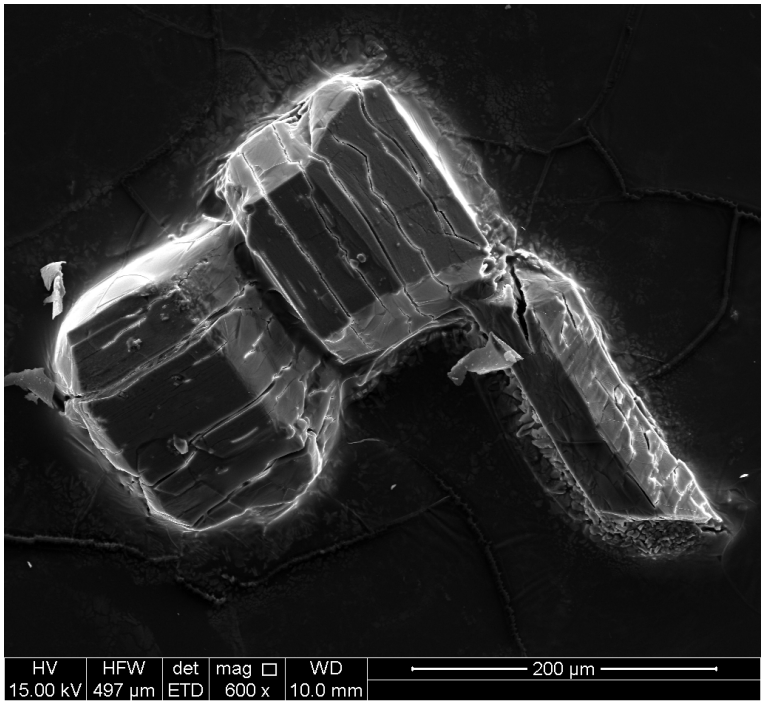

Figure D.44: SEM image of single crystals of the purified ruthenium mesocate (**12**).

Table D.5: Summary of Ru and K content in crystalline samples of the purified *n*-propyl spacer mesocate (**12**)

	Crushed Crystals	Single Crystals
K : Ru (SEM/EDX, %)	33 : 66 $\pm$ 1	27 : 73 $\pm$ 8

D.7 Computational studies

For each Ru(II) compound density functional theory (DFT) calculations were performed with Q-Chem version 5.1,[422] on helicate or mesocate molecules extracted from the experimental X-ray crystal structure. In cases where the crystal structure was not available existing crystal structures containing other transition metal centres, or ligands, were modified to allow modelling of theoretical supramolecular assemblies. Single-point energy was calculated for optimised geometry in dielectric medium using CPCM method[423,424] and a dielectric constant for acetonitrile (35.85).[425] The Bondi radius for ruthenium of 2.05 Å taken from Alvarez *et al.*,[427] and multiplied by 1.2 as per Q-Chem default, to give 2.46 Å. All geometries were optimised at the wB97X-D/SRSC level,[428,429] *in vacuo*. Default parameters were used in all cases except for SCF convergence in geometry and frequency calculation, which was set to 10^{-7} instead of 10^{-8} due to difficulties in convergence.

D.7.1 *n*-Propyl spacer compounds

Table D.6: Summary of DFT results for *n*-propyl spacer compounds

		Helicate (**13**)	Mesocate (**12**)	Δ (helicate - mesocate)
E (Hartree)	(*in vacuo*)	-3473.873752	-3473.881127	0.007374745
E (kcal/mol)	(*in vacuo*)			4.6
E (kJ/mol)	(*in vacuo*)			19.4
E (Hartree)	(CPCM, acetonitrile)	-3474.479852	-3474.479238	0.000613577
E (kcal/mol)	(CPCM, acetonitrile)			0.4
E (kJ/mol)	(CPCM, acetonitrile)			1.6
ΔH thermal (kcal/mol)	(*in vacuo*, 298.15 K)	668.5	668.2	
ΔS thermal (cal/mol.K)	(*in vacuo*, 298.15 K)	323.5	327.0	
ΔG thermal (kcal/mol)	(*in vacuo*, 298.15 K)	572.0	570.7	1.3
ΔG (kcal/mol)	(*in vacuo*, 298.15 K)			5.9
ΔG (kJ/mol)	(*in vacuo*, 298.15 K)			24.7
ΔG (kcal/mol)	(CPCM, acetonitrile, 298.15 K)			1.7
ΔG (kJ/mol)	(CPCM, acetonitrile, 298.15 K)			7.0

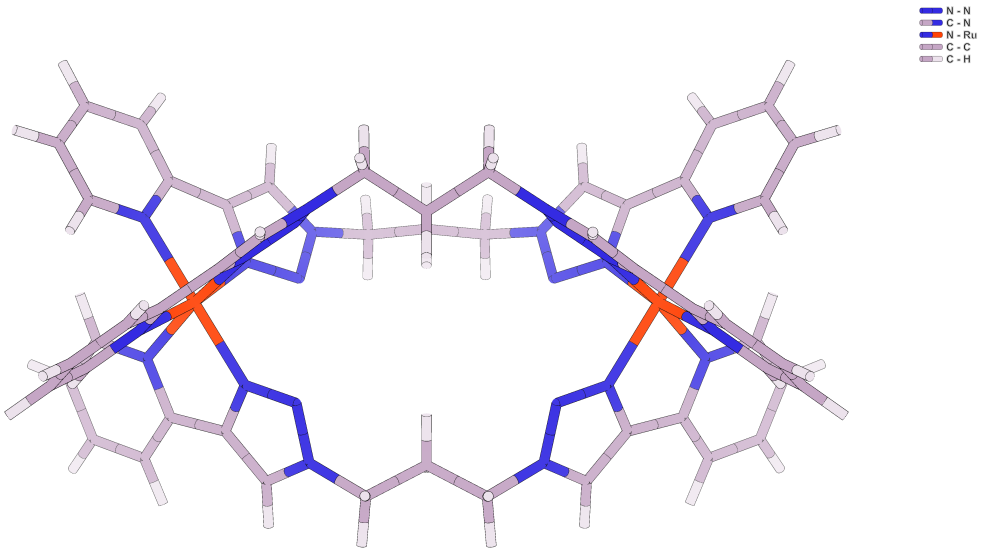

Figure D.45: Geometry optimised model showing the molecular structure of the ruthenium mesocate (**12**), containing the *n*-propyl spacer ligand (**9**).

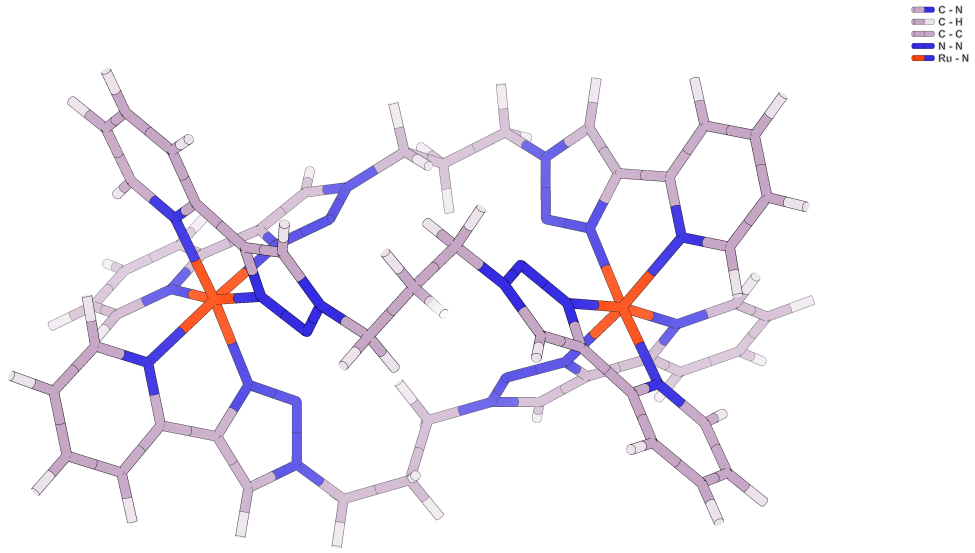

Figure D.46: Geometry optimised model showing the molecular structure of the ruthenium helicate (**13**), containing the *n*-propyl spacer ligand (**9**).

D.7.2 *n*-Butyl spacer compounds

Table D.7: Summary of DFT results for *n*-butyl spacer compounds

		Helicate (**14**)	Mesocate (**15**)	Δ (helicate - mesocate)
E (Hartree)	(*in vacuo*)	-3591.795153	-3591.796411	0.001258183
E (kcal/mol)	(*in vacuo*)			0.8
E (kJ/mol)	(*in vacuo*)			3.3
E (Hartree)	(CPCM, acetonitrile)	-3592.376807	-3592.382894	0.006086851
E (kcal/mol)	(CPCM, acetonitrile)			3.8
E (kJ/mol)	(CPCM, acetonitrile)			16.0
ΔH thermal (kcal/mol)	(*in vacuo*, 298.15 K)	725.1	724.7	
ΔS thermal (cal/mol.K)	(*in vacuo*, 298.15 K)	348.7	340.2	
ΔG thermal (kcal/mol)	(*in vacuo*, 298.15 K)	621.1	623.2	-2.1
ΔG (kcal/mol)	(*in vacuo*, 298.15 K)			-1.3
ΔG (kJ/mol)	(*in vacuo*, 298.15 K)			-5.6
ΔG (kcal/mol)	(CPCM, acetonitrile, 298.15 K)			1.7
ΔG (kJ/mol)	(CPCM, acetonitrile, 298.15 K)			7.1

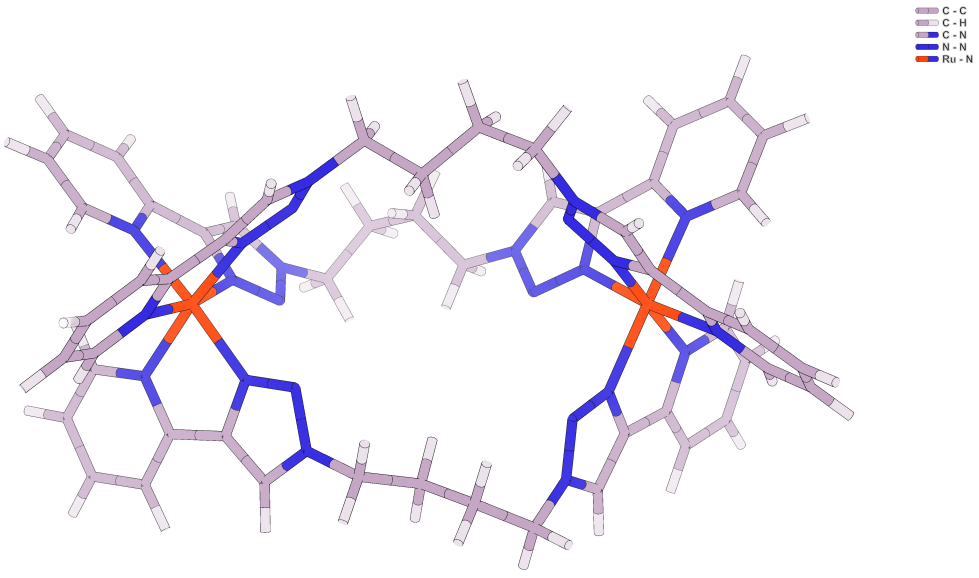

Figure D.47: Geometry optimised model showing the molecular structure of the ruthenium mesocate (**15**), containing the *n*-butyl spacer ligand (**10**).

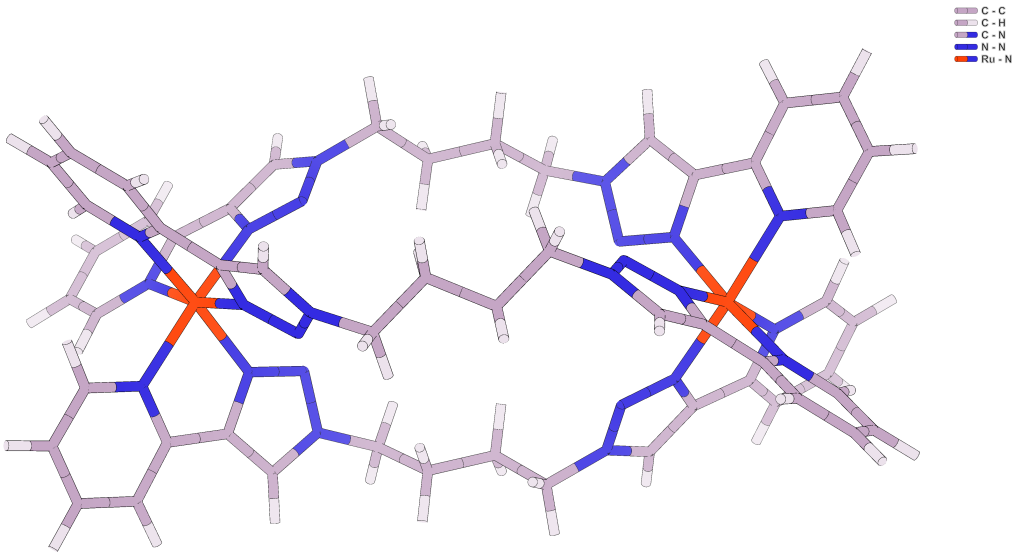

Figure D.48: Geometry optimised model showing the molecular structure of the ruthenium helicate (**14**), containing the *n*-butyl spacer ligand (**10**).

D.8 Biological studies

D.8.1 Dialysis

A 300 µM calf thymus DNA (ct-DNA) solution was made up in Tris buffer and placed on the inside of a 1 mL cellulose ester membrane Spectra/Por® Float-A-Lyzer® G2 or Sigma Aldrich Pur-A-Lyzer™ Maxi Dialysis Kit. This ct-DNA loaded dialysis tube was then submerged in a 20 µM racemic mixture of 1,4-xylyl spacer helicate (**11**) made up in Tris buffer. The dialysis was left for 24 - 48 h and the outer solution analysed using CD spectroscopy. circular dichroism (CD) spectra were acquired at ambient temperature using a Jasco J-715 spectropolarimeter (scan range: 600 - 200 nm, resolution: 1 nm, bandwidth: 2.0 nm, sensitivity: 200 mdeg, response: 1 sec, speed: 100 nm/min).

D.8.2 Linear dichroism

LD spectra were recorded using a Jasco 810 spectropolarimeter using a quartz capillary LD Coulette flow cell built by Crystal Precision Optics. The instrument was allowed to equilibrate for 30 minutes prior to use, and nitrogen gas flow was kept at approximately 10 L/min. A series of 10 solutions consisting of ct-DNA (167 µM), K_2HPO_4/KH_2PO_4 (10 mM, pH 7.3), NaCl (10 mM), and increasing amounts of diruthenium compound were prepared. NaCl concentration was relatively low due to the strong absorption of chloride salts at low wavelengths.[430] For each solution, spectra were obtained over the range 200 - 350 nm with a scan rate of 200 nm/min, data pitch of 1 nm, response time of 1 s, and rotation speed of 3000 rpm. 10 accumulations were collected and a baseline non-rotating spectrum was subtracted from each data set.

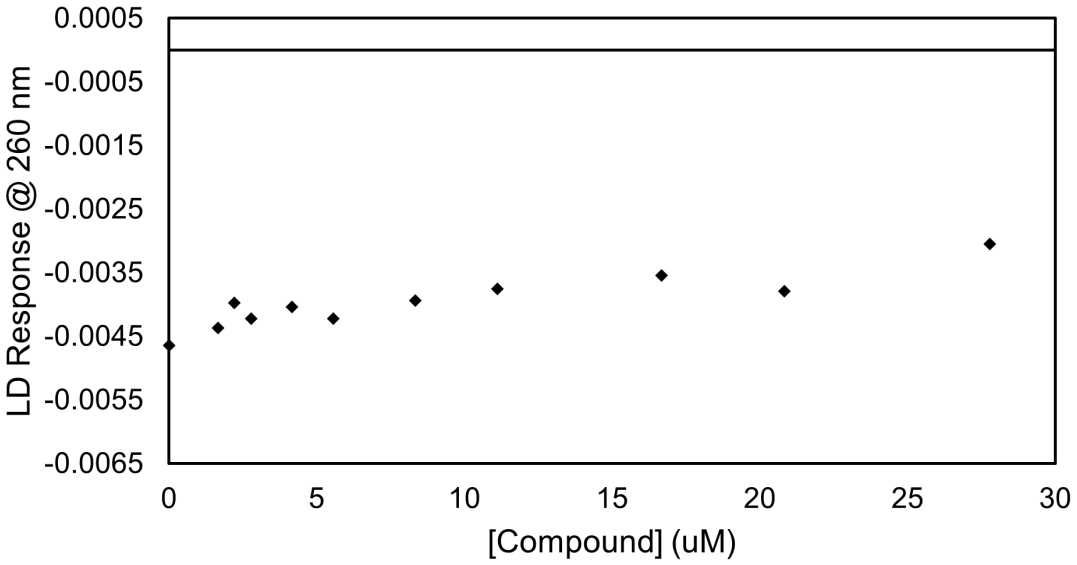

Figure D.49: linear dichroism (LD) spectrum of ct-DNA at 260 nm (2 x 10^{-4} M; $K_2HPO_{4/}KH_2PO_4$ (10 mM), NaCl (10 mM), pH 7.3, 25 ° C) bound with increasing concentrations of triple-stranded ruthenium(II) helicate (**11**) incorporating the 1,4-xylyl spacer ligand (**8**) using F1 from the resolution on cellulose with 2 M NaCl.

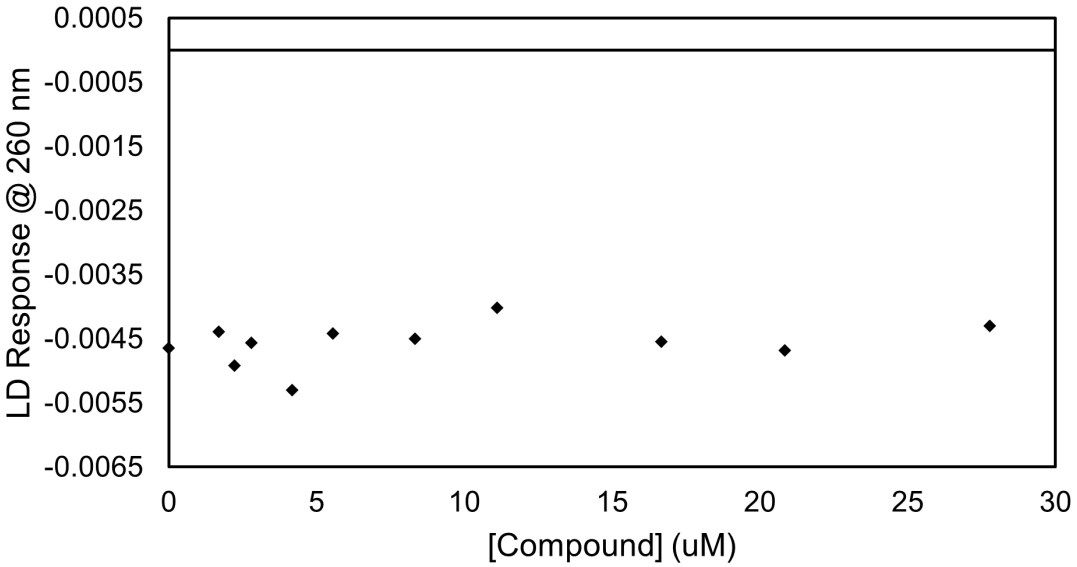

Figure D.50: LD spectrum of ct-DNA at 260 nm (2 x 10^{-4} M; $K_2HPO_{4/}KH_2PO_4$ (10 mM), NaCl (10 mM), pH 7.3, 25 ° C) bound with increasing concentrations of triple-stranded ruthenium(II) helicate (**11**) incorporating the 1,4-xylyl spacer ligand (**8**) using F2 from the resolution on cellulose with 2 M NaCl.

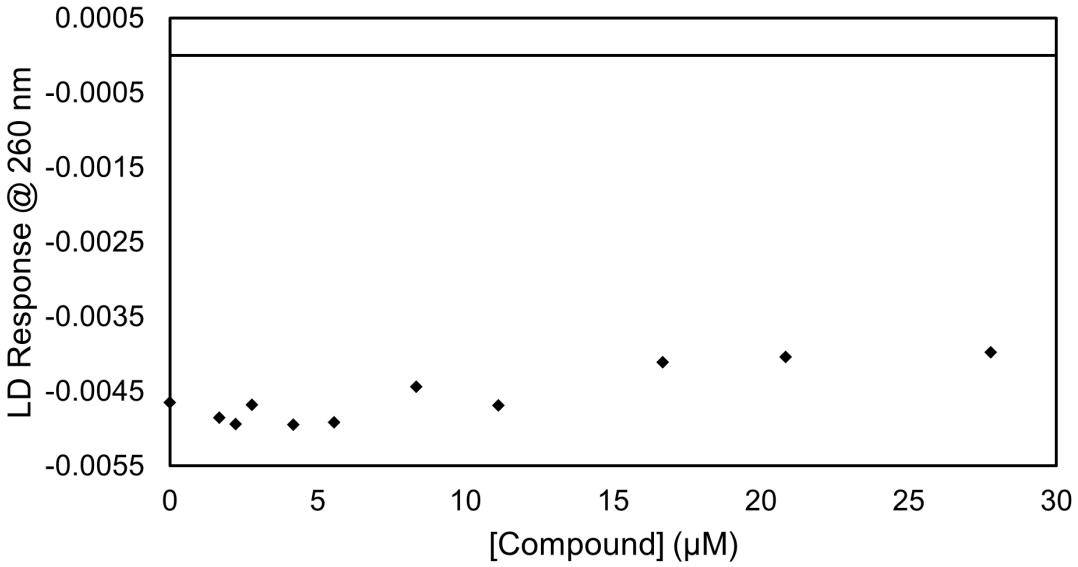

Figure D.51: LD response of ct-DNA at 260 nm (2 x 10^{-4} M; K_2HPO_4/$KHPO_4$ (10 mM), NaCl (10 mM), pH 7.3, 25 °C) bound with increasing concentrations of the mesocate/helicate (**12**/**13**) mixture of the triple-stranded ruthenium(II) compounds incorporating the *n*-propyl spacer ligand (**9**).

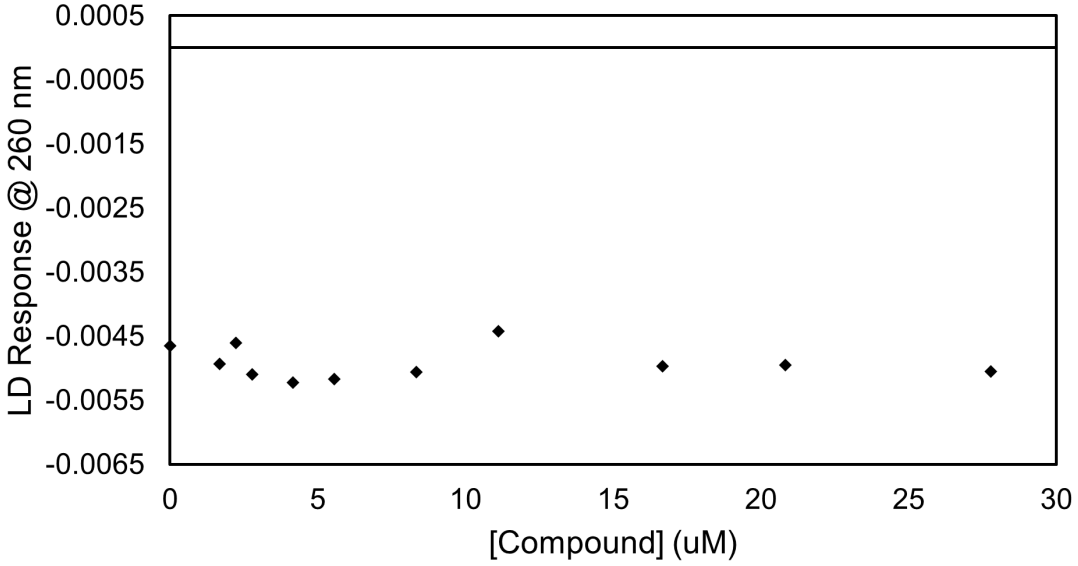

Figure D.52: LD response of ct-DNA at 260 nm (2 x 10^{-4} M; K_2HPO_4/$KHPO_4$ (10 mM), NaCl (10 mM), pH 7.3, 25 °C) bound with increasing concentrations of one enantiomer of the helicate (**14**) incorporating the *n*-butyl spacer ligand (**10**) (F2 from the resolution on cellulose).

APPENDIX E

Supporting Information for Chapter 5

E.1 Synthetic procedures

E.1.1 Ligand synthesis

1,4-Bis(bromomethyl)benzene (**7**) was prepared as described in **Chapter 4**.

E.1.1.1 3-(Dimethylamino)-1-(pyridin-2-yl)prop-2-en-1-one (**16**)

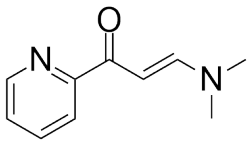

Figure E.1: 3-(Dimethylamino)-1-(pyridin-2-yl)prop-2-en-1-one (**16**)

Using a procedure modified from that described by Yu *et al.*,[409] a solution of 2-acetylpyridine (5.40 g, 5.00 mL, 45.0 mmol; 1 equiv.) in *N,N*-dimethylformamide dimethyl acetal (10 mL, 75 mmol; 1.7 equiv.) was heated to 110 °C for 1.5 h. The reaction mixture was cooled to ∼5 °C for 12 h, and the resulting precipitate collected by vacuum filtration, washed with cold petroleum spirit, and dried to give **16** as a red-orange solid (6.79 g, 86%). δ_H (500 MHz, $CDCl_3$) 8.59 (m, 1H), 8.10 (m 1H), 7.86 (dd, J = 12.7, 5.2 Hz, 1H), 7.74 (m, 1H), 7.30 (m, 1H), 6.41 (br d, J = 11.7 Hz, 1H), 3.11 (s, 3H), 2.93 (s, 3H).

E.1.1.2 3-(2′-Pyridyl)pyrazole (**17**)

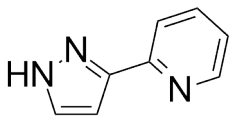

Figure E.2: 3-(2′-Pyridyl)pyrazole (**17**)

Using a procedure modified from that described by Salinis Uber *et al.*,[410] a solution of **16** (7.29 g, 41.4 mmol; 1 equiv.) and ∼ 50 - 60% hydrazine hydrate (29.0 mL, 137 mmol;

3.3 equiv.) in EtOH (100 mL) was heated to 60 °C for 30 mins. The reaction mixture was cooled to room temperature, and deionised water (30 mL) added. The organic solvent was removed by rotary evaporation, and the resulting precipitate filtered, washed with water (2 x 20 mL), diethyl ether (2 x 20 mL), and dried to give **17** as a cream solid (5.51 g , 92%). δ_H (500 MHz, $CDCl_3$) 12.32 (br s, 1H), 8.69 (m, 1H), 7.77 (m, 2H), 7.67 (d, J = 2.0 Hz, 1H), 7.24 (m, 1H), 6.81 (d, J = 2.0 Hz, 1H).

E.1.1.3 1,4-Bis(bromomethyl)-2,3,5,6-tetramethylbenzene (**18**)

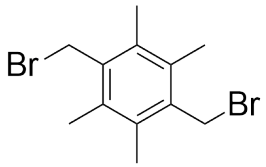

Figure E.3: 1,4-Bis(bromomethyl)-2,3,5,6-tetramethylbenzene (**18**)

Using a procedure modified from that described by Van der Made and Van der Made,[411] 33% HBr/acetic acid (5.36 mL) was added dropwise to a solution of 1,2,4,5-tetramethylbenzene (2.00 g, 14.8 mmol; 1 equiv.) and paraformaldehyde (0.94 g, 31.2 mmol; 0.83 equiv.) in acetic acid (12 mL) over 30 mins at room temperature and the solution then heated to 80 °C for 12 h. The reaction mixture was cooled to room temperature and the resulting precipitate collected by vacuum filtration. The precipitate was dissolved in dichloromethane (DCM), dried over $MgSO_4$, filtered, and the organic solvent removed by rotary evaporation. The crude product was recrystallised from ethyl acetate (EtOAc) to give **18** as a fluffy white solid (3.67 g, 77%). δ_H (500 MHz, $CDCl_3$) 4.60 (s, 4H), 2.33 (s, 12H).

E.1.1.4 9,10-Bis(bromomethyl)anthracene (**19**)

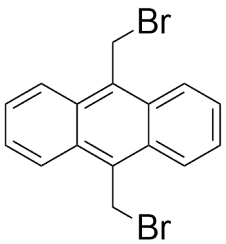

Figure E.4: 9,10-Bis(bromomethyl)anthracene (**19**)

Using a procedure modified from that described by Zhou and Sun,[412] a solution of anthracene (2.00 g, 11.3 mmol; 1 equiv.), paraformaldehyde (0.34 g, 11.2 mmol; 1 equiv.),

and cetyltrimethylammonium bromide (0.045 g, 0.12 mmol; 0.01 equiv.) in glacial acetic acid (2.8 mL) was stirred at room temperature. 48% HBr was added dropwise over 1 h, and the reaction mixture then heated to 80 °C for 5 h. The reaction was cooled to room temperature, and the resulting precipitate filtered, washed with water, and dried to give **19** as a yellow solid (2.58 g, 63%). δ_H (500 MHz, $CDCl_3$) 8.39 (m, 4H), 7.69 (m, 4H), 5.52 (s, 4H).

E.1.1.5 1,4-Bis{(3-(pyridin-2-yl)-1*H*-pyrazol-1-yl)methyl}benzene (**20**)

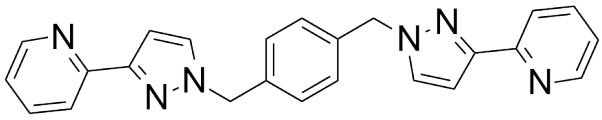

Figure E.5: 1,4-Bis{(3-(pyridin-2-yl)-1*H*-pyrazol-1-yl)methyl}benzene (**20**)

Using a procedure modified from that described by Argent *et al.*,[18] a solution of **7** (0.18 g, 0.67 mmol; 1 equiv.), **17** (0.21 g, 1.48 mmol; 2.2 equiv.), 10 M NaOH (1.8 mL), and 40% Bu_4NOH (13 µL) in toluene (4.5 mL) was heated to 60 °C for 1 h. The reaction mixture was cooled to room temperature, deionised water (50 mL) added, the organic layer separated, dried over $MgSO_4$, and solvent removed under reduced pressure to give **20** as a white solid (0.18 g, 68%). δ_H (500 MHz, $CDCl_3$) 8.62 (d, J = 4.8 Hz, 2H), 7.94 (d, J = 7.9 Hz, 2H), 7.71 (m, 2H), 7.40 (d, J = 2.3 Hz, 2H), 7.24 (s, 4H), 7.18 (m, 2H), 6.92 (d, J = 2.2 Hz, 2H), 5.38 (s, 4H).

E.1.1.6 2,2′-(1,1′-{(2,3,5,6-Tetramethyl-1,4-phenylene)bis(methylene)}bis{1*H*-pyrazole-3,1-diyl})dipyridine (**21**)

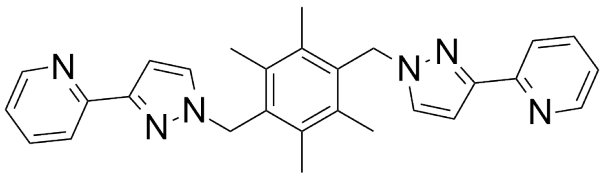

Figure E.6: 2,2′-(1,1′-{(2,3,5,6-Tetramethyl-1,4-phenylene)bis(methylene)}bis{1*H*-pyrazole-3,1-diyl})dipyridine (**21**)

21 was synthesised using a identical procedure described for **20** above. A solution of **18** (0.50 g, 1.56 mmol; 1 equiv.), **17** (0.50 g, 3.43 mmol; 2.2 equiv.), 10 M NaOH (5 mL), and 40% Bu_4NOH (37.5 µL) in toluene (12.5 mL) was heated to 60 °C for 1 h. The reaction mixture was cooled to room temperature, deionised water (50 mL) added, the organic

layer separated, dried over $MgSO_4$, and solvent removed under reduced pressure to give **21** as a white solid (0.26 g, 38%). δ_H (600 MHz, $CDCl_3$) 8.62 (m, 2H), 7.96 (d, J = 7.9 Hz, 2H), 7.72 (td, J = 7.7, 1.8 Hz, 2H), 7.21 (m, 2H), 7.03 (d, J = 2.3 Hz, 2H), 6.81 (d, J = 2.3 Hz, 2H), 5.54 (s, 4H), 2.31 (s, 12H). δ_C (151 MHz, $CDCl_3$) 152.39, 151.77, 149.49, 136.52, 135.19, 131.96, 129.53, 122.30, 120.05, 104.03, 51.47, 16.58. m/z (ESI) 449.2448 (MH^+).

E.1.1.7 9,10-Bis{(3-(pyridin-2-yl)-1*H*-pyrazol-1-yl)methyl}anthracene (**22**)

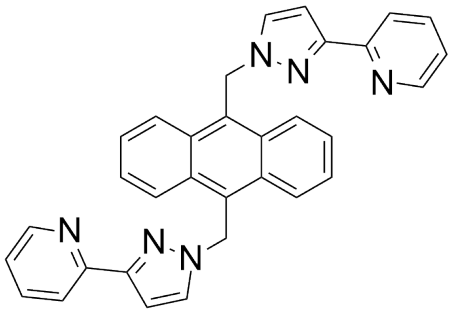

Figure E.7: 9,10-Bis{(3-(pyridin-2-yl)-1*H*-pyrazol-1-yl)methyl}anthracene (**22**)

Using a procedure modified from that described by Tidmarsh *et al.*,[93] aqueous NaOH (5.5 M, 2.50 mL) was added to a solution of **19** (0.25 g, 0.69 mmol; 1 equiv.) and **17** (0.2 g, 1.35 mmol; 2 equiv.) in THF (30 mL) and the reaction mixture heated at reflux for 24 h. The reaction was cooled to room temperature, and the resulting precipitate collected by filtration to give **22** as a pale yellow solid (0.27 g, 81%). δ_H (500 MHz, $CDCl_3$) 8.65 (d, J = 4.3 Hz, 1H), 8.46 (dd, J = 6.9. 3.2 Hz, 2H), 8.00 (d, J = 7.9 Hz, 1H), 7.77 (dd, J = 7.7, 1.6 Hz, 1H), 7.62 (dd, J = 6.9, 3.1 Hz, 2H), 7.22 (m, 1H), 6.98 (d, J = 2.3 Hz, 1H), 6.73 (d, J = 2.3 Hz, 1H), 6.45 (s, 2H).

E.1.2 Ru(II) compounds

E.1.2.1 One-pot approach

Following a modified procedure from that described by Kumar *et al.*,[80] a solution of $RuCl_3 \cdot 3\,H_2O$ (67 mmol; 2 equiv.) and ligand (100 mmol: 3 equiv.) in ethylene glycol (8 mL) was irradiated in a CEM microwave reactor at 225 °C (200 W, 200 PSI) for 5 h. The solution was cooled to room temperature, deionised water (20 mL) added, and filtered through Celite. A solution of KPF_6 (5 mL; 4%) was added to the filtrate, and the resulting precipitate collected by centrifugation (10621 *g*, 5 min), washed with water, and dried under vacuum to give the crude Ru(II)-containing product.

E.1.2.2 Stepwise approach

Following a modified procedure from that described by Metherell and Ward,[98] a solution of ligand (121 mmol; 5 equiv.) in ethylene glycol (12 mL) was heated at reflux until dissolved. A solution of $[Ru(DMSO)_4Cl_2]$ (24 mmol; 1 equiv.) in H_2O/ethylene glycol (18 mL/1.5 mL; 12 : 1) was added dropwise over 30 mins, and the resulting mixture heated at reflux for 24 h. The solution was cooled to room temperature, deionised water (30 mL) added, and filtered through Celite. A solution of KPF_6 (5 mL; 4%) was added to the filtrate, and the resulting precipitate collected by centrifugation (10621 *g*, 5 min), washed with water, and dried under vacuum to give the crude Ru(II)-containing product.

E.1.2.3 Separation of products

For all compounds, unless otherwise indicated, the mixture of products was purified chromatographically, on silica gel using CH_3CN/H_2O/sat. aq. KNO_3 (7:1:0.5 by volume) as the eluent.

E.2 Additional NMR spectra

E.2.1 Novel Ligand

E.2.1.1 2,2′-(1,1′-{(2,3,5,6-Tetramethyl-1,4-phenylene)bis(methylene)}bis{1*H*-pyrazole-3,1-diyl})dipyridine (**21**)

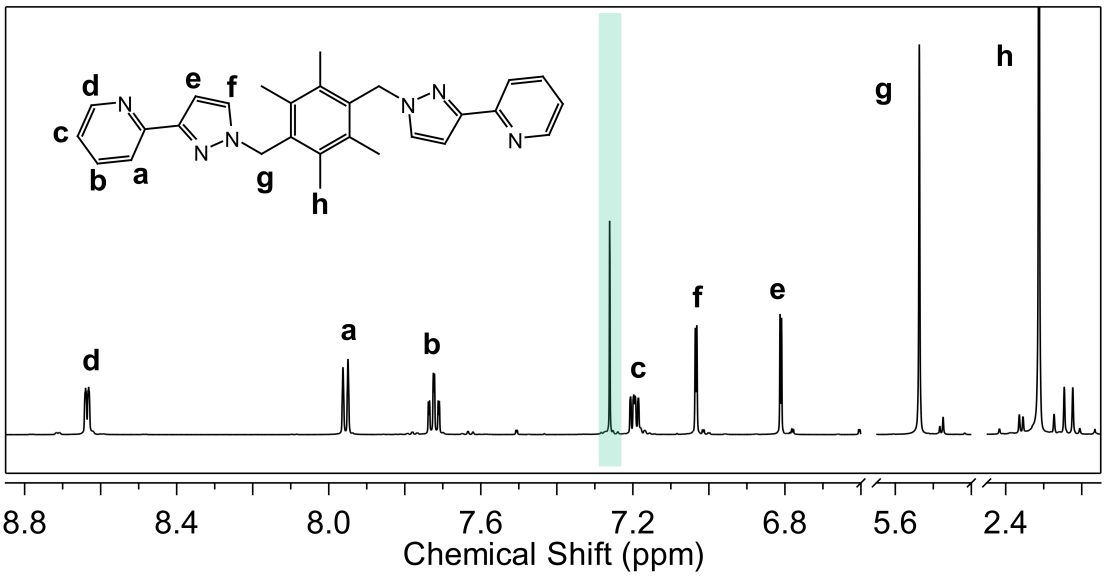

Figure E.8: Partial ^{1}H NMR spectrum (600 MHz, $CDCl_3$, 298 K) of 2,2′-(1,1′-{(2,3,5,6-Tetramethyl-1,4-phenylene)bis(methylene)}bis{1*H*-pyrazole-3,1-diyl})dipyridine (**21**). Residual solvent is highlighted in green.

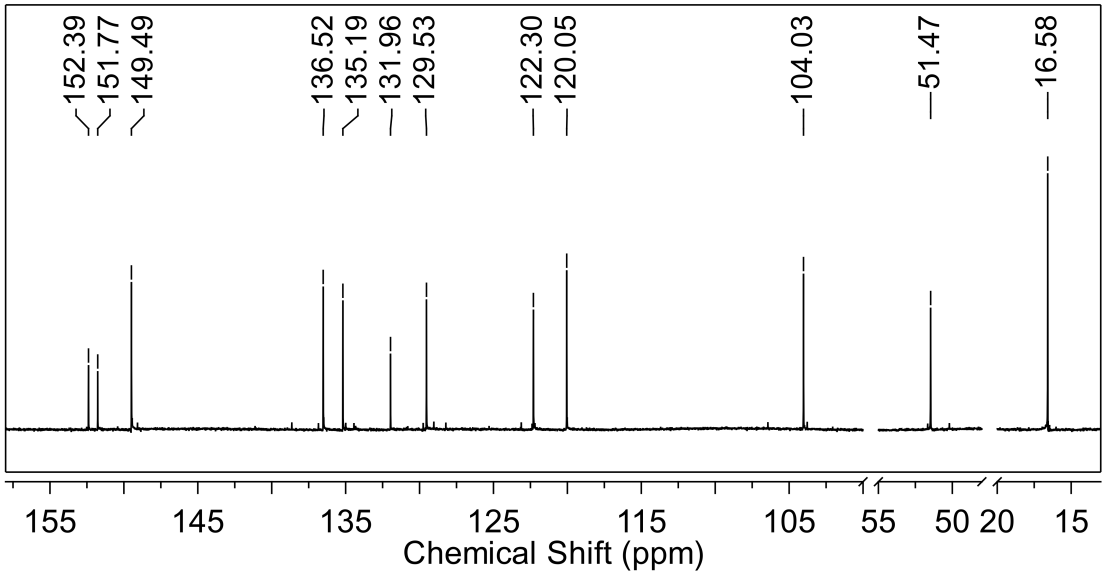

Figure E.9: Partial ^{13}C NMR spectrum (151 MHz, $CDCl_3$, 298 K) of 2,2′-(1,1′-{(2,3,5,6-Tetramethyl-1,4-phenylene)bis(methylene)}bis{1*H*-pyrazole-3,1-diyl})dipyridine (**21**).

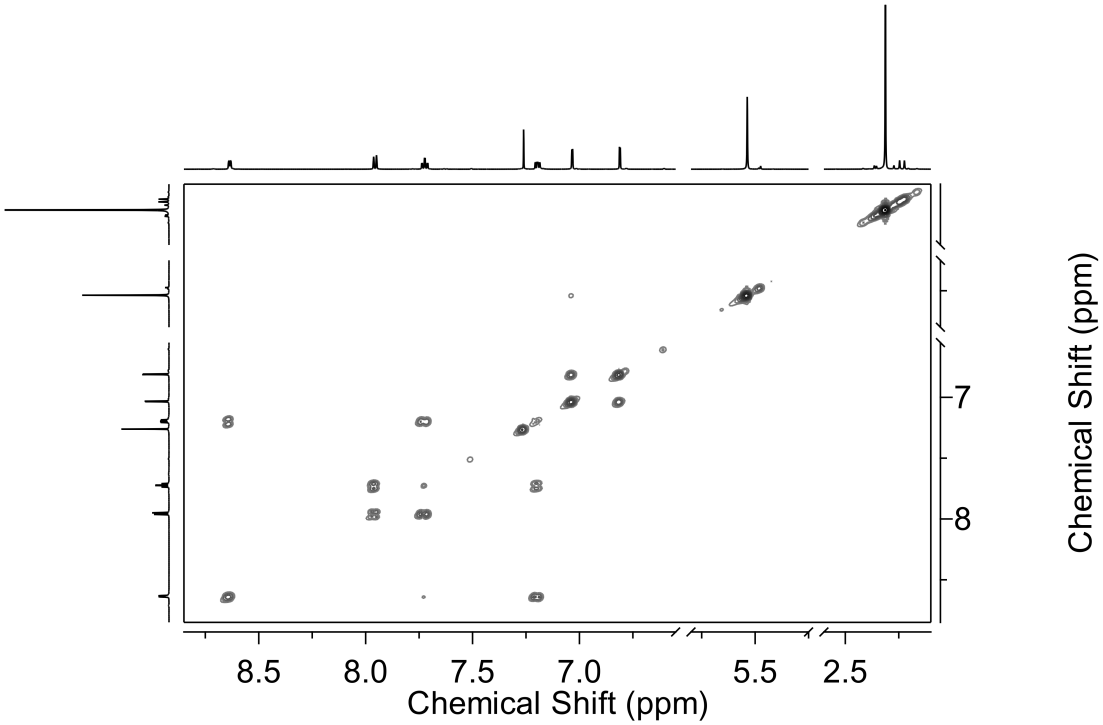

Figure E.10: Partial COSY NMR spectrum ($CDCl_3$, 298 K) of 2,2′-(1,1′-{(2,3,5,6-Tetramethyl-1,4-phenylene)bis(methylene)}bis{1*H*-pyrazole-3,1-diyl})dipyridine (**21**).

E.2.2 1,4-Xylyl spacer compounds

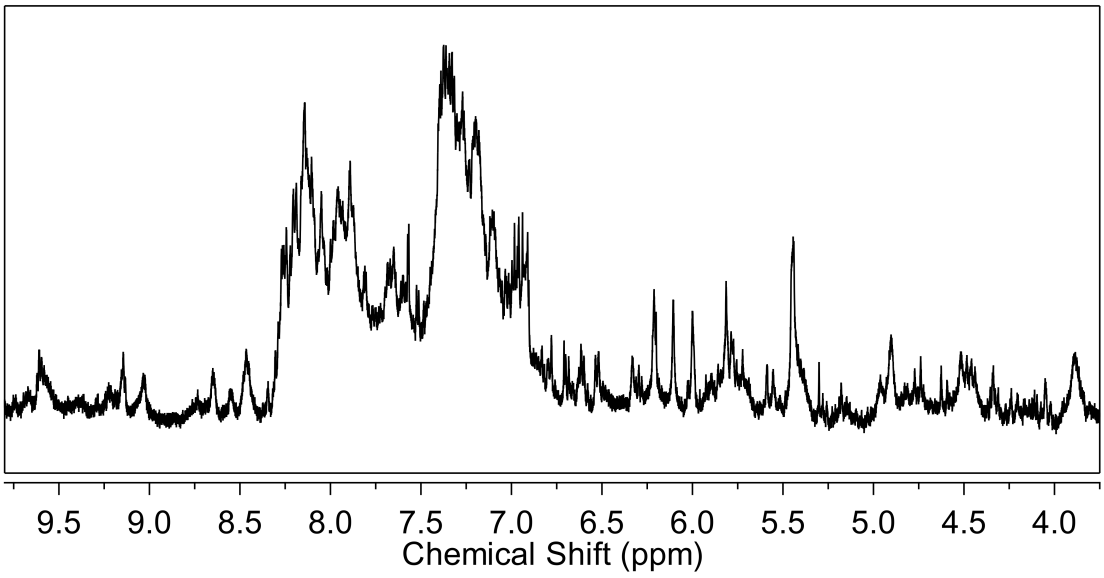

Figure E.11: Partial ^{1}H NMR spectrum (500 MHz, CD_3CN, 298 K) showing the crude product from the reaction of the 1,4-xylyl spacer ligand (**20**), with $RuCl_3 \cdot 3\,H_2O$ under microwave conditions (200 W, 200 PSI, 225 °C; 5 h).

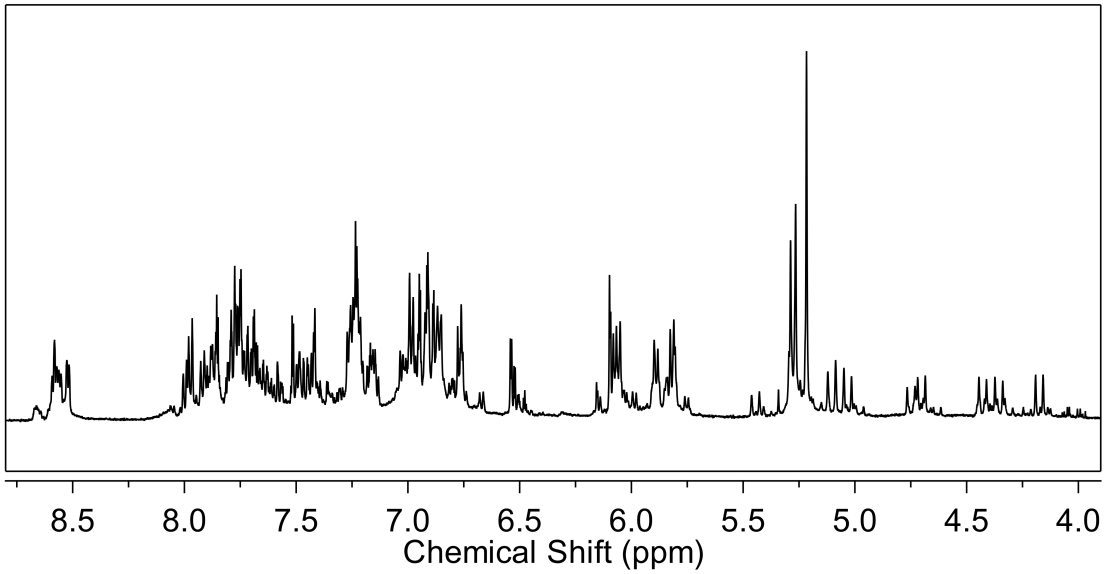

Figure E.12: Partial ^{1}H NMR spectrum (500 MHz, CD_3CN, 298 K) showing the aromatic region of the crude product from the reaction of 1,4-xylyl spacer ligand (**20**) with $[Ru(DMSO)_4Cl_2]$ under reflux conditions (dropwise addition to form $[RuL_3]^{2+}$ building blocks).

E.2.3 2,3,5,6-Tetramethyl-1,4-xylyl spacer compounds

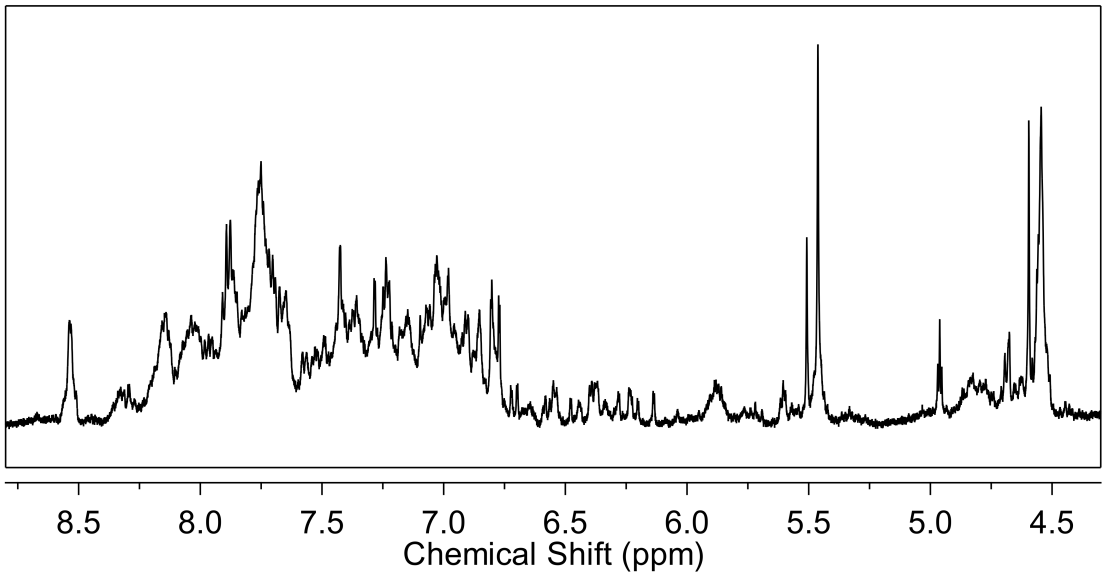

Figure E.13: Partial ^{1}H NMR spectrum (500 MHz, CD_3CN, 298 K) showing the crude product from the reaction of 2,3,5,6-tetramethyl-1,4-xylyl spacer ligand (**21**), with $RuCl_3 \cdot 3\,H_2O$ under microwave conditions (200 W, 200 PSI, 225 °C; 5 h).

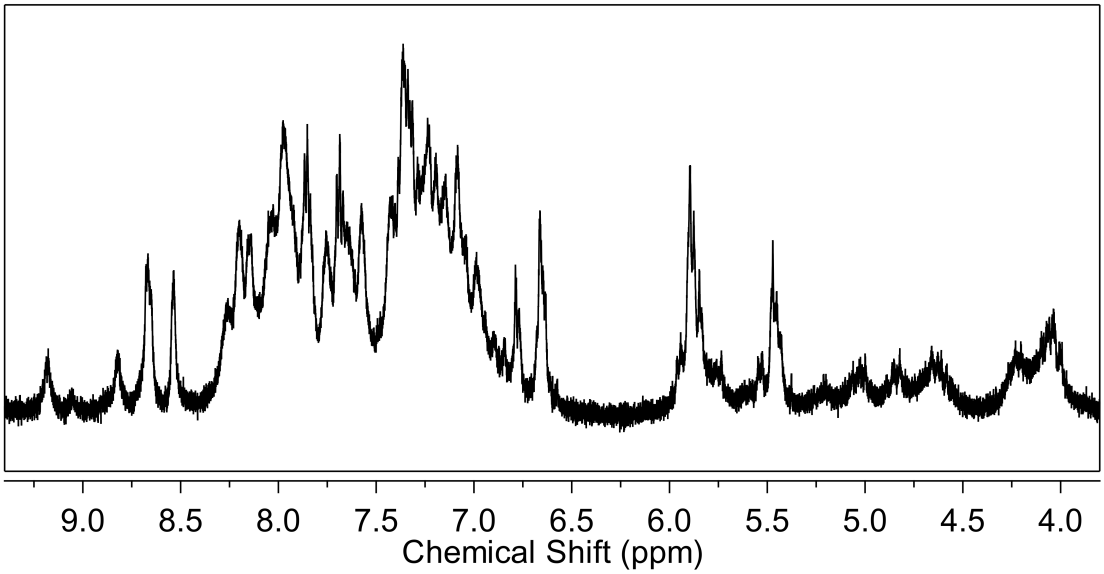

Figure E.14: Partial ^{1}H NMR spectrum (500 MHz, CD_3CN, 298 K) showing the crude product from the reaction of the 2,3,5,6-tetramethyl-1,4-xylyl spacer ligand (**21**), with $Ru(DMSO)_4Cl_2$ under reflux conditions (dropwise addition to form $[RuL_3]^{2+}$ building blocks).

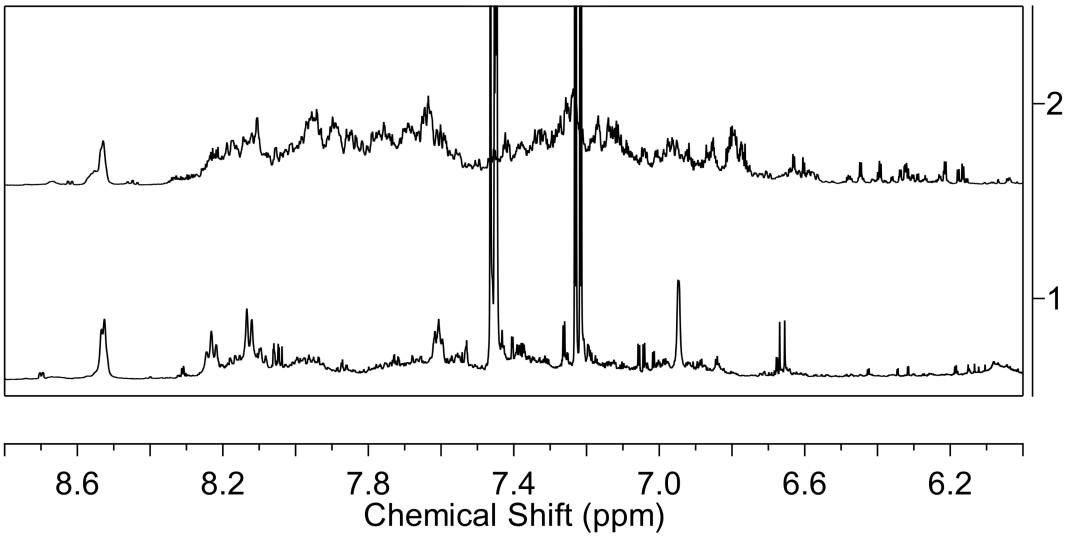

Figure E.15: Partial ^{1}H NMR spectrum (600 MHz, CD_3CN, 298 K) showing the two fractions from purification of the crude reaction mixture of the 2,3,5,6-1,4-xylyl spacer ligand (**21**) with $RuCl_3 \cdot 3\,H_2O$ under microwave conditions (200 W, 200 PSI, 225 °C; 5 h). Fractions from chromatography are labelled in order of elution.

E.2.4 9,10-Dimethylanthryl spacer compounds

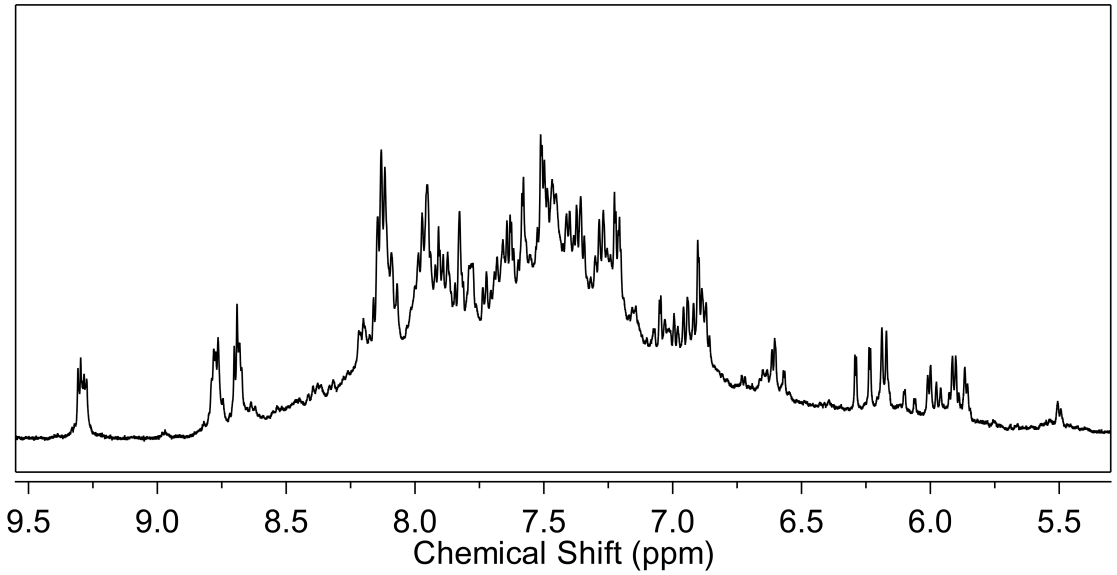

Figure E.16: Partial ^{1}H NMR spectrum (500 MHz, CD_3CN, 298 K) showing the aromatic region of the crude product from the reaction of anthryl spacer ligand (**22**), with $RuCl_3 \cdot 3\,H_2O$ under microwave conditions (200 W, 200 PSI, 225 °C; 5 h).

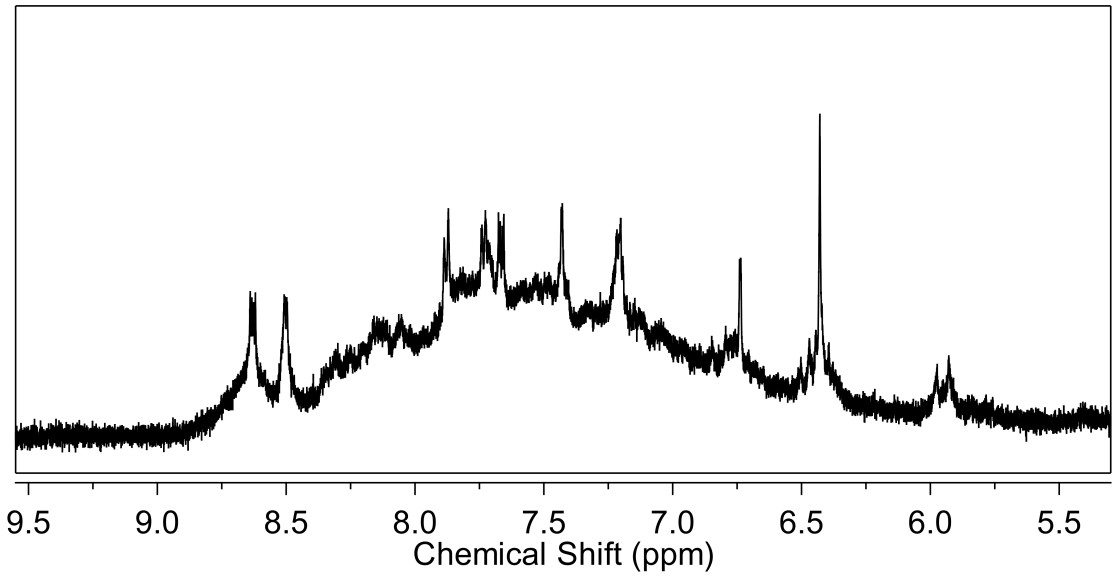

Figure E.17: Partial ^{1}H NMR spectrum (500 MHz, CD_3CN, 298 K) showing the aromatic region of the crude product from the reaction of anthryl spacer ligand, **22**, with $Ru(DMSO)_4Cl_2$ under reflux conditions (dropwise addition to form $[RuL_3]^{2+}$).

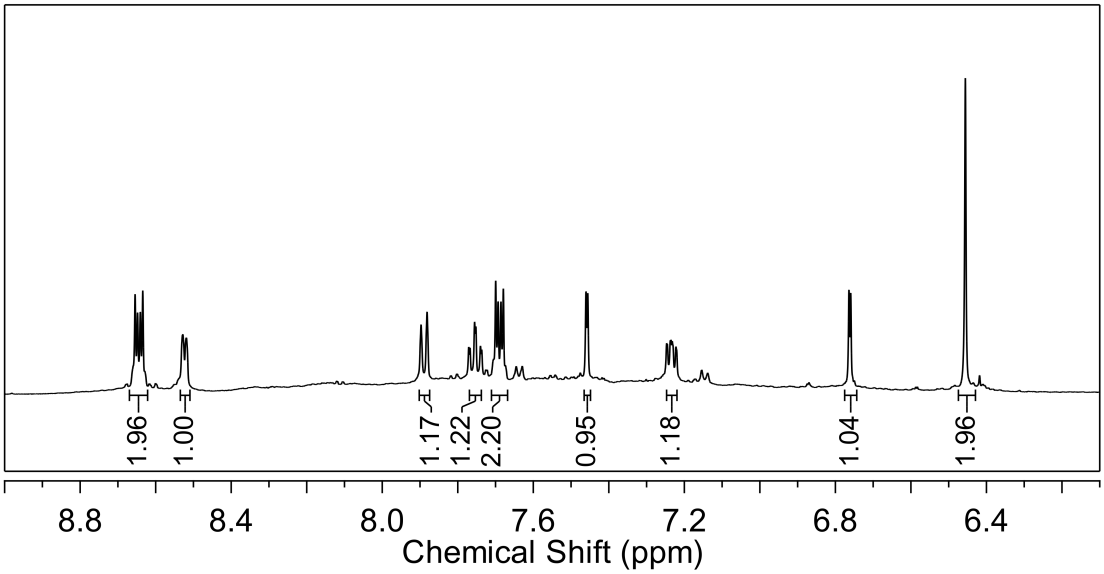

Figure E.18: Partial ^{1}H NMR spectrum (500 MHz, CD_3CN, 298 K) showing (1) the aromatic region from the purification of the crude reaction mixture of the 9,10-dimethylanthryl spacer ligand (**22**) with $[Ru(DMSO)_4Cl_2]$ under reflux conditions (dropwise addition to form $[RuL_3]^{2+}$) including integration of resonances.

E.3 Mass spectrometry

E.3.1 1,4-Xylyl spacer compounds

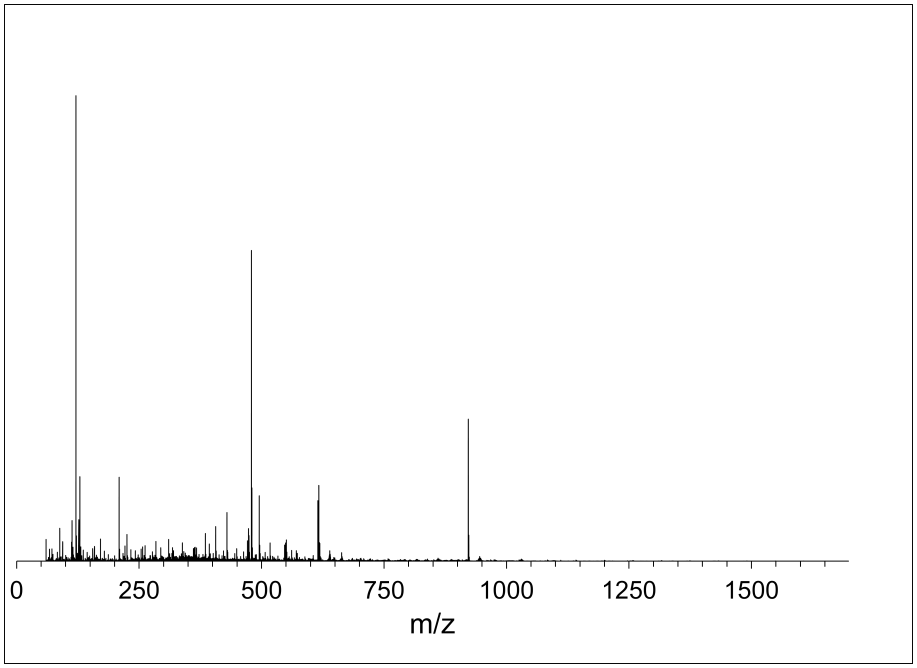

Figure E.19: Full mass spectrum (CH_3CN) of the first eluting fraction (F1) from the one-pot synthesis of Ru(II) cages by microwave methods, using the 1,4-xylyl spacer ligand (**20**).

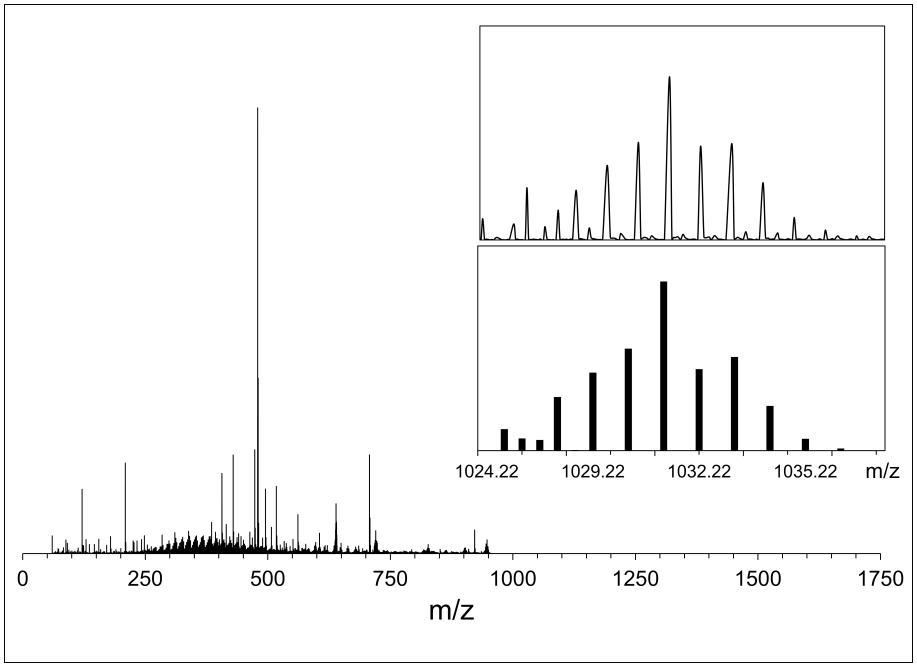

Figure E.20: Mass spectrum of the second eluting fraction (F2) from the one-pot synthesis of Ru(II) cages by microwave methods, using the 1,4-xylyl spacer ligand (**20**). Full HR-MS (CH_3CN), inset: Partial HR-MS (CH_3CN) and calculated isotopic pattern of the monoruthenium species $[RuL_2]^{2+}$, peak at *m/z* 1030.31 due to $[RuL_2 - 1PF_6]^{1+}$.

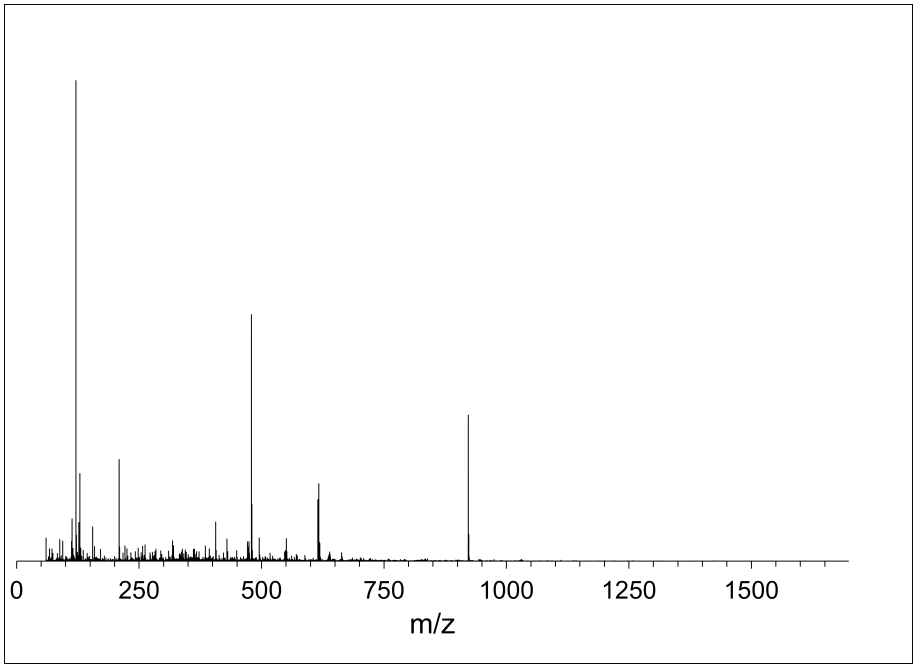

Figure E.21: Full mass spectrum (CH_3CN) of the third eluting fraction (F3) from the one-pot synthesis of Ru(II) cages by microwave methods, using the 1,4-xylyl spacer ligand (**20**).

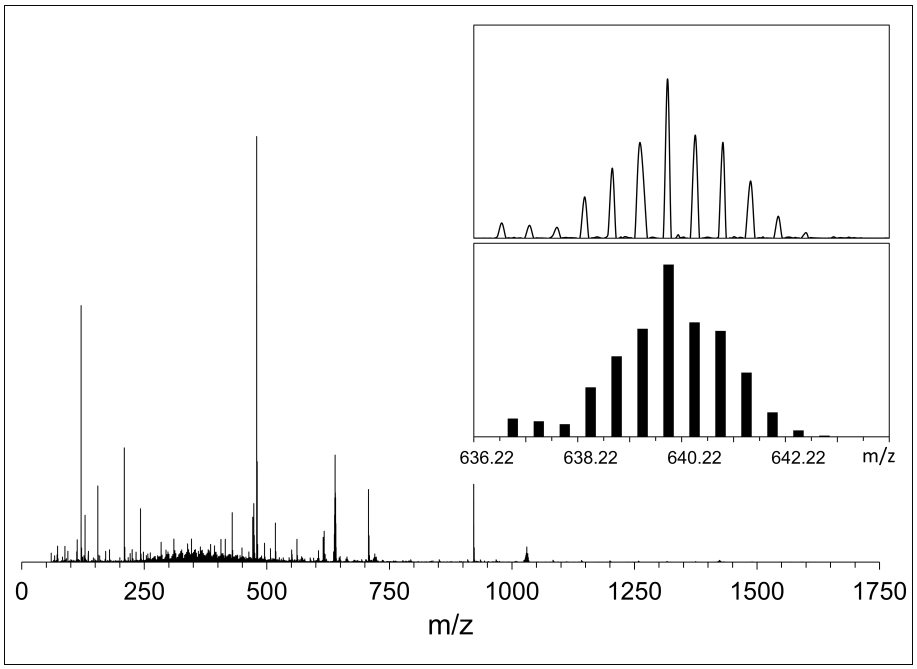

Figure E.22: Mass spectrum of the first eluting fraction (F1) from the stepwise synthesis of Ru(II) cages, using the 1,4-xylyl spacer ligand (**20**). Full HR-MS (CH_3CN), inset: Partial HR-MS (CH_3CN) and calculated isotopic pattern of the monoruthenium species $[RuL_3]^{2+}$, peak at m/z 639.3146 due to $[RuL_3 - 2PF_6]^{2+}$.

E.3.2 2,3,5,6-Tetramethyl-1,4-xylyl spacer compounds

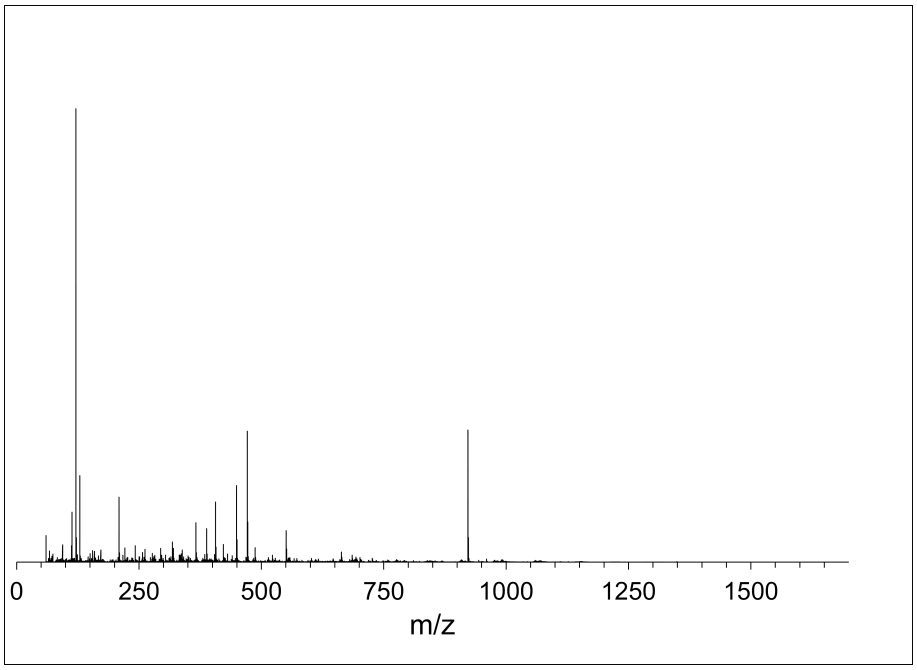

Figure E.23: Full mass spectrum (CH_3CN) of the first eluting fraction (F1) from the one-pot synthesis of Ru(II) cages by microwave methods, using the 2,3,5,6-tetramethyl-1,4-xylyl spacer ligand (**21**).

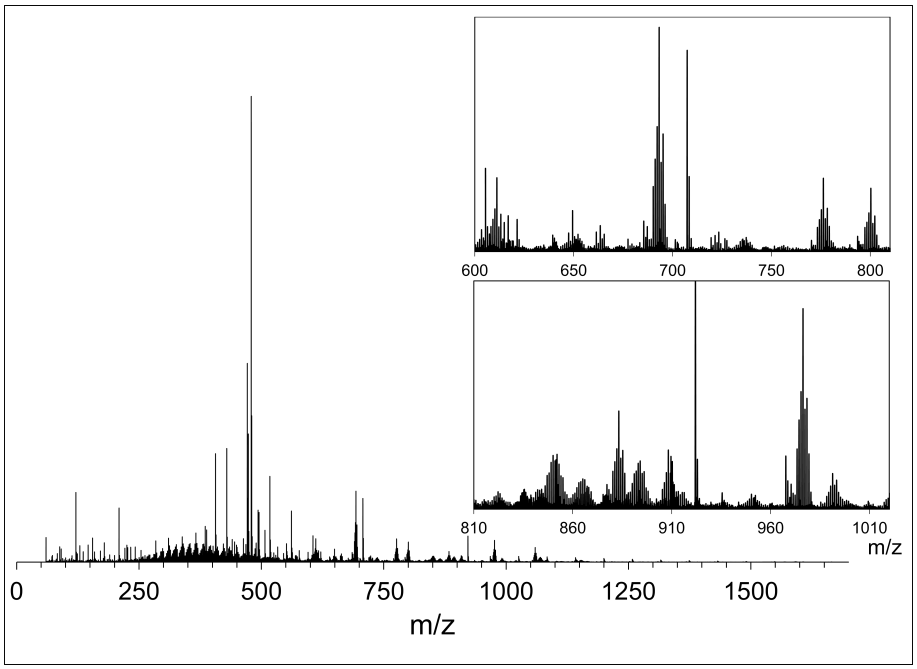

Figure E.24: Mass spectrum of the second eluting fraction (F2) from the one-pot synthesis of Ru(II) cages by microwave methods, using the 2,3,5,6-tetramethyl-1,4-xylyl spacer ligand (**21**). Full HR-MS (CH_3CN), inset: selected regions of interest showing highly overlapping Ru(II)-containing mass fragments.

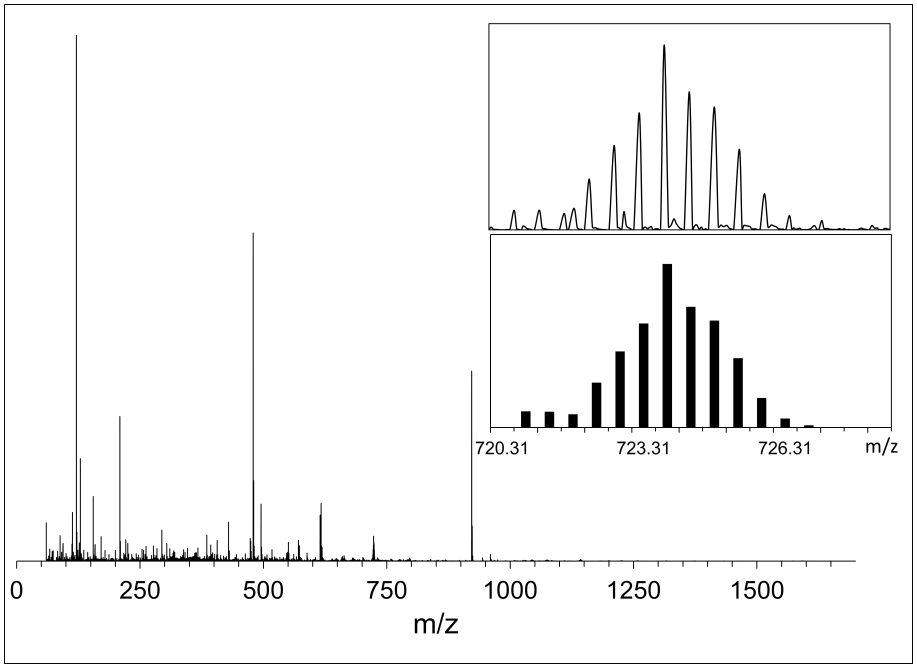

Figure E.25: Mass spectrum of the first eluting fraction (F1) from the stepwise synthesis of Ru(II) cages, using the 2,3,5,6-tetramethyl-1,4-xylyl spacer ligand (**21**). Full HR-MS (CH_3CN), inset: Partial HR-MS (CH_3CN) and calculated isotopic pattern of the monoruthenium species $[RuL_3]^{2+}$, peak at *m/z* 723.3086 due to $[RuL_3 - 2PF_6]^{2+}$.

E.3.3 9,10-Dimethylanthryl spacer compounds

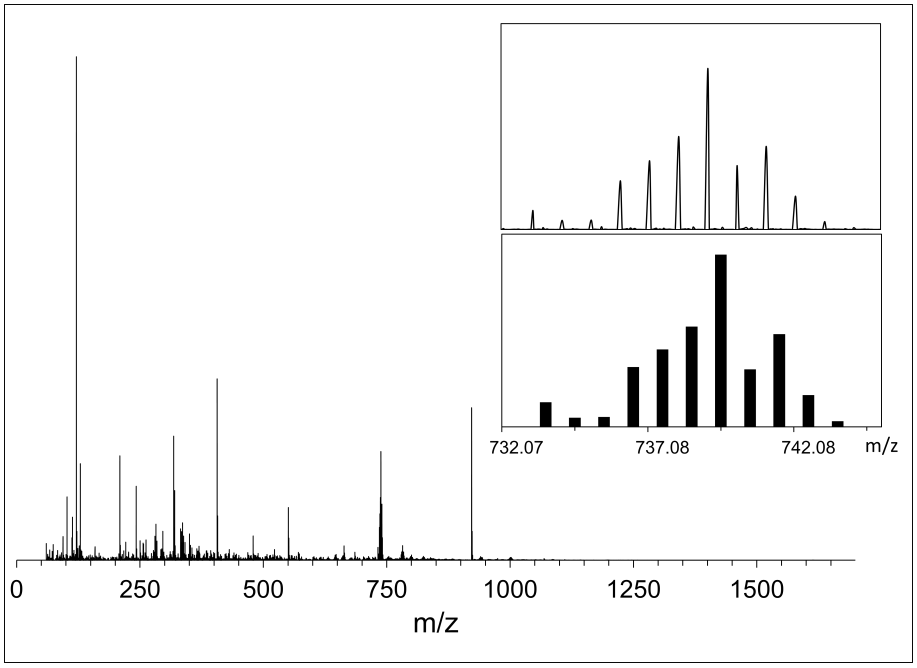

Figure E.26: Mass spectrum of the second fraction (F2) from the one-pot synthesis of Ru(II) cages by microwave methods, using the 9,10-dimethylanthryl spacer ligand (**22**). Full HR-MS (CH_3CN), inset: Partial HR-MS (CH_3CN) and calculated isotopic pattern of the monoruthenium species $[RuL_1]^{2+}$, peak at *m/z* 738.1669 due to $[RuL_1 - 1PF_6]^{1+}$.

APPENDIX F

Addendum: Responses to Examiners Reports

F.1 Examiner 1

F.1.1 Chapter 3

Page 97. The examiner proposed that molecular modelling could be used to show/see whether the helicate is too bulky to fit within the minor groove.

Molecular modelling or docking studies could definitely be carried out to ascertain whether the steric bulk of the compounds could hinder minor groove binding; however, these methods were not utilised in this thesis.

F.1.2 Chapter 4

Page 159. The examiner proposed that X-ray crystallography could be used to confirm the assignment of the resolved triple-stranded helicate.

X-ray crystallography would be an excellent means of confirming the proposed enantiomer assignment in this case. However, despite repeated efforts crystals of either resolve fraction have not been obtained.

Page 160. The examiner noted that ESI-MS could be used to further investigate the identity of the unknown product.

For the Ru(II) compounds in this thesis HR ESI-MS was only used for the characterisation of purified samples, rather than mixtures of products. Furthermore, if the unknown product was of $[Ru_2L_3]^{4+}$ stoichiometry, as has been proposed in the text, it would have an identical mass spectrum to the helicate.

Page 161 and 170. The examiner noted that ESI-MS could be used to further investigate the identity of the unknown product.

As noted above, in this thesis HR ESI-MS was not carried out for any products containing mixtures of Ru(II) compounds.

Page 161. The examiner suggested that the unknown product was likely the mesocate.

Comments speculating as to the nature of the unknown product, including reference to a possible mesocate, have been made on page 159.

Page 164. The examiner queried the number of PF_6^- anions present in the asymmetric unit (5.75).

The structure is charged balanced but not enough PF_6^- positions could be identified with sufficient occupancy to provide a charge balanced formula.

Page 164. The examiner queried whether the original crystal structure of the n-propyl mesocate was similar to the Fe^{2+} or Ni^{2+} analogues.

For the triple-stranded Ru(II) compounds described in this thesis no direct comparisons of the crystal structures have been made. It is likely that some discrepancies in inter-metallic distance (as seen for the double-stranded compounds in **Chapter 2**) and overall conformation would be noted, although these may not solely be due to substitution of the metal centre, and may be influenced by crystal packing effects due to the choice of different solvents and anions.

Page 174. The examiner queried whether the crystal structure of the purified n-propyl mesocate was similar to the original structure (shown on Page 164).

In this thesis no direct comparison of the two crystal structures was made, although it is anticipated that some differences would be present likely due to the choice of crystallisation solvent, which varied between the two samples.

Page 182. The examiner queried the inclusion of an example of meso-cate/helicate isomerisation utilising covalent bond cleavage.

As noted in this section this example is included purely for completeness, as it illustrates isomerisation of double-stranded compounds.

Page 203. The examiner suggested that the difference in DNA binding strength seen for Ru(II) and Co(III) compounds is likely due to the higher charge.

This point has been mentioned earlier in the section in relation to anti-bacterial studies; however, it is equally applicable in the context of DNA interactions.

Page 205. The examiner suggested that the compounds did not have to bind DNA to be active (in a therapeutic context).

While in this thesis biological studies were centred around the ability for the Ru(II) compounds to bind to DNA, for which the results showed weak interactions, this outcome does not preclude other biological activity. The compounds may have stronger interactions with different cellular features/regions, or in alternative biological settings; however, these were not explored in this work.

F.2 Examiner 2

F.2.1 Chapter 2

Page 25. Ideally any components of a crystal structure that are accounted for by SQUEEZE should be approximately identified (elemental analysis, TGA, TGA-IR) and included in the formula, then density differences do not occur. This is not always possible though.

The difference in density observed between the helicate and mesocate samples is likely attributed to solvent composition. Due to limited material no compositional analysis was available to provide definitive identification of the solvent.

Page 31. What is the reason for the difference in length of the complexes when changing from Ru to Fe?

The difference in inter-metallic distance in the double-stranded helicates when Ru(II) is substituted for Fe(II) may not solely by due to the choice of metal centre and is likely influenced by the crystallisation conditions utilised for each compound. These crystal packing effects may impact the conformation of the helicate molecules, thus altering the overall compound length.

Page 34. Although the high quantum yields of Ru species is noted as being of interest, no values are given for the compounds in this chapter.

The quantum yields of the Ru species were not addressed in this discussion, and the data is not currently available.

F.2.2 Chapter 3

Very small changes in the ppm values of signals are reported. It is noted that these are small compared to other compounds, but by how much (order of magnitude, more/less)? How indicative is this of binding strength? There are other instances where strength is mentioned (e.g., 3.4.7.3) but it is not clear if this is directly correlated to ppm shifts (typically "strength" implies kJ/mol or some knowledge of the binding constant).

The changes in chemical shift reported upon addition of the Ru(II) compounds to oligonucleotide have been noted to be very small. As a comparison, in another study Patterson *et al.* reported perturbation of >0.2 ppm for some resonances of the identical bulge oligonucleotide upon addition of a dinuclear Ru(II) compound at R= 1 (it should be noted that in this case R is the true ratio of soluble oligonucleotide/Ru compound, rather than the added ratio R* discussed above).[243] In this thesis for the same oligonucleotide the largest change in chemical shift recorded was 0.06 ppm (for F1 of the helicate at R* = 4). Changes in chemical shift can be used to determine the association constant for the binding of the metal compound to an oligonucleotide using the following equation:

$$K_{\text{ass}} = \frac{[M - DNA]}{[M][DNA]} \tag{F.1}$$

where [M-DNA] is the concentration of the metal compound-bound oligonucleotide and [DNA] and [M] are the concentrations of the free oligonucleotide and metal compound, respectively. [M-DNA], [M], and [DNA] in the above equation can be estimated from the following equation and the initial concentrations of the metal complex and dodecanucleotide.

$$\delta_{\text{obs}} = \chi_{\text{f}}\delta_{\text{f}} + \chi_{\text{b}}\delta_{\text{b}} \tag{F.2}$$

where δ_{obs} is the observed chemical shift of the metal complex resonances, χ_{f} and χ_{b} are the mole fractions of free and bound metal complex and δ_{f} and δ_{b} are the chemical shifts of the resonances of the free and bound metal complex.

In this particular case, as has been noted in the main text, while many of the changes in chemical shift for these compounds with DNA appear small they are still significant. Those recorded are indicative only for the soluble portion of the compound-DNA complex, and it was assumed that the true ratio of compound to DNA (R) was significantly lower that R* (the added ratio). It is anticipated that were the true ratio able to be increased to R = 1 the magnitude of change in chemical shift would also increase; however, due to

issues with solubility and resonance broadening this was not possible in the current study.

F.2.3 Chapter 4

Page 161. The case of an unknown product is always fun, especially when it only turns up on occasion. Is there any speculation about its nature?

Comments speculating as to the nature of the unknown product have been made on page 159.

References

[1] Pedersen, C. J. The discovery of crown ethers (Nobel Lecture). *Angewandte Chemie International Edition* **1988**, *27*, 1021–1027.

[2] Lehn, J.-M. Supramolecular chemistry - scope and perspectives molecules, supermolecules, and molecular devices (Nobel Lecture). *Angewandte Chemie International Edition* **1988**, *27*, 89–112.

[3] Cram, D. J. The design of molecular hosts, guests, and their complexes (Nobel Lecture). *Angewandte Chemie International Edition* **1988**, *27*, 1009–1020.

[4] Lee, S. J.; Lin, W. Chiral metallocycles: rational synthesis and novel applications. *Accounts of Chemical Research* **2008**, *41*, 521–537.

[5] Fujita, M. Metal-directed self-assembly of two- and three-dimensional synthetic receptors. *Chemical Society Reviews* **1998**, *27*, 417–425.

[6] Leininger, S.; Olenyuk, B.; Stang, P. J. Self-assembly of discrete cyclic nanostructures mediated by transition metals. *Chemical Reviews* **2000**, *100*, 853–908.

[7] Zhao, L.; Northrop, B. H.; Zheng, Y.-R.; Yang, H.-B.; Lee, H. J.; Lee, Y. M.; Park, J. Y.; Chi, K.-W.; Stang, P. J. Self-selection in the self-assembly of isomeric supramolecular squares from unsymmetrical bis(4-pyridyl)acetylene ligands. *Journal of Organic Chemistry* **2008**, *73*, 6580–6586.

[8] Albrecht, M. "Let's twist again" - Double-stranded, triple-stranded, and circular helicates. *Chemical Reviews* **2001**, *101*, 3457–3497.

[9] Hannon, M. J.; Childs, L. J. Helices and helicates: beautiful supramolecular motifs with emerging applications. *Supramolecular Chemistry* **2004**, *16*, 7–22.

[10] Rohs, R.; West, S. M.; Sosinsky, A.; Liu, P.; Mann, R. S.; Honig, B. The role of DNA shape in protein-DNA recognition. *Nature* **2009**, *461*, 1248–53.

[11] Marquis, A.; Smith, V.; Harrowfield, J.; Lehn, J.-M.; Herschbach, H.; Sanvito, R.; Leize-Wagner, E.; Van Dorsselaer, A. Messages in molecules: ligand/cation coding and self-recognition in a constitutionally dynamic system of heterometallic double helicates. *Chemistry – A European Journal* **2006**, *12*, 5632–5641.

[12] Albrecht, M.; Janser, I.; Fröhlich, R. Catechol imine ligands: from helicates to supramolecular tetrahedra. *Chemical Communications* **2005**, 157–165.

[13] Argent, S. P.; Riis-Johannessen, T.; Jeffery, J. C.; Harding, L. P.; Ward, M. D. Diastereoselective formation and optical activity of an M_4L_6 cage complex. *Chemical Communications* **2005**, 4647–4649.

[14] Biros, S.; Yeh, R.; Raymond, K. Design and formation of a large tetrahedral cluster using 1,1′-binaphthyl ligands. *Angewandte Chemie International Edition* **2008**, *47*, 6062–6064.

[15] Clegg, J. K.; Lindoy, L. F.; Moubaraki, B.; Murray, K. S.; McMurtrie, J. C. Triangles and tetrahedra: metal directed self-assembly of metallo-supramolecular structures incorporating bis-β-diketonato ligands. *Dalton Transactions* **2004**, 2417–2423.

[16] Saalfrank, R. W.; Demleitner, B.; Glaser, H.; Maid, H.; Bathelt, D.; Hampel, F.; Bauer, W.; Teichert, M. Enantiomerisation of tetrahedral homochiral $[M_4L_6]$ clusters: synchronized four bailar twists and six atropenantiomerisation processes monitored by temperature-dependent dynamic ^{1}H NMR spectroscopy. *Chemistry – A European Journal* **2002**, *8*, 2679–2683.

[17] Yamashita, K.; Kawano, M.; Fujita, M. Ru(II)-cornered coordination cage that senses guest inclusion by colour change. *Chemical Communications* **2007**, 4102–4103.

[18] Argent, S. P.; Adams, H.; Riis-Johannessen, T.; Jeffery, J. C.; Harding, L. P.; Ward, M. D. High-nuclearity homoleptic and heteroleptic coordination cages based on tetra-capped truncated tetrahedral and cuboctahedral metal frameworks. *Journal of the American Chemical Society* **2006**, *128*, 72–73.

[19] Argent, S. P.; Adams, H.; Riis-Johannessen, T.; Jeffery, J. C.; Harding, L. P.; Clegg, W.; Harrington, R. W.; Ward, M. D. Complexes of Ag(I), Hg(I) and Hg(II) with multidentate pyrazolyl-pyridine ligands: from mononuclear complexes to coordination polymers *via* helicates, a mesocate, a cage and a catenate. *Dalton Transactions* **2006**, 4996–5013.

[20] Abourahma, H.; Coleman, A. W.; Moulton, B.; Rather, B.; Shahgaldian, P.; Zaworotko, M. J. Hydroxylated nanoballs: synthesis, crystal structure, solubility and crystallization on surfaces. *Chemical Communications* **2001**, 2380–2381.

[21] Baxter, P. N. W.; Lehn, J.-M.; Kneisel, B. O.; Baum, G.; Fenske, D. The designed self-assembly of multicomponent and multicompartmental cylindrical nanoarchitectures. *Chemistry – A European Journal* **1999**, *5*, 113–120.

[22] Eddaoudi, M.; Kim, J.; Wachter, J. B.; Chae, H. K.; O'Keeffe, M.; Yaghi, O. M. Porous metal-organic polyhedra: 25 Å cuboctahedron constructed from 12 $Cu_2(CO_2)_4$ paddle-wheel building blocks. *Journal of the American Chemical Society* **2001**, *123*, 4368–4369.

[23] Han, M.; Engelhard, D. M.; Clever, G. H. Self-assembled coordination cages based on banana-shaped ligands. *Chemical Society Reviews* **2014**, *43*, 1848–1860.

[24] Schmidt, A.; Casini, A.; Kühn, F. E. Self-assembled M_2L_4 coordination cages: synthesis and potential applications. *Coordination Chemistry Reviews* **2014**, *275*, 19–36.

[25] Jaya Prakash, M.; Oh, M.; Liu, X.; Han, K. N.; Seong, G. H.; Lah, M. S. Edge-directed $[(M_2)_2L_4]$ tetragonal metal-organic polyhedra decorated using a square paddle-wheel secondary building unit. *Chemical Communications* **2010**, *46*, 2049–2051.

[26] Brown, C. J.; Toste, F. D.; Bergman, R. G.; Raymond, K. N. Supramolecular catalysis in metal-ligand cluster hosts. *Chemical Reviews* **2015**, *115*, 3012–3035.

[27] Otte, M. Size-selective molecular flasks. *ACS Catalysis* **2016**, *6*, 6491–6510.

[28] Ueda, Y.; Ito, H.; Fujita, D.; Fujita, M. Permeable self-assembled molecular containers for catalyst isolation enabling two-step cascade reactions. *Journal of the American Chemical Society* **2017**, *139*, 6090–6093.

[29] Zava, O.; Mattsson, J.; Therrien, B.; Dyson, P. Evidence for drug release from a metalla-cage delivery vector following cellular internalisation. *Chemistry – A European Journal* **2010**, *16*, 1428–1431.

[30] Samanta, S. K.; Moncelet, D.; Briken, V.; Isaacs, L. Metal-organic polyhedron capped with cucurbit[8]uril delivers doxorubicin to cancer cells. *Journal of the American Chemical Society* **2016**, *138*, 14488–14496.

[31] Schmitt, F.; Freudenreich, J.; Barry, N. P. E.; Juillerat-Jeanneret, L.; Süss-Fink, G.; Therrien, B. Organometallic cages as vehicles for intracellular release of photosensitizers. *Journal of the American Chemical Society* **2012**, *134*, 754–757.

[32] Meng, W.; Breiner, B.; Rissanen, K.; Thoburn, J. D.; Clegg, J. K.; Nitschke, J. R. A self-assembled M_8L_6 cubic cage that selectively encapsulates large aromatic guests. *Angewandte Chemie International Edition* **2011**, *50*, 3479–3483.

[33] García-Simón, C.; Garcia-Borrás, M.; Gómez, L.; Parella, T.; Osuna, S.; Juanhuix, J.; Imaz, I.; Maspoch, D.; Costas, M.; Ribas, X. Sponge-like molecular cage for purification of fullerenes. *Nature Communications* **2014**, *5*, 5557.

[34] Zhang, W.-Y.; Lin, Y.-J.; Han, Y.-F.; Jin, G.-X. Facile separation of regioisomeric compounds by a heteronuclear organometallic capsule. *Journal of the American Chemical Society* **2016**, *138*, 10700–10707.

[35] Yan, X.; Cook, T. R.; Wang, P.; Huang, F.; Stang, P. J. Highly emissive platinum(II) metallacages. *Nature Chemistry* **2015**, *7*, 342–348.

[36] Neelakandan, P. P.; Jiménez, A.; Nitschke, J. R. Fluorophore incorporation allows nanomolar guest sensing and white-light emission in M_4L_6 cage complexes. *Chemical Science* **2014**, *5*, 908–915.

[37] Roy, B.; Ghosh, A. K.; Srivastava, S.; D'Silva, P.; Mukherjee, P. S. A Pd_8 tetrafacial molecular barrel as carrier for water insoluble fluorophore. *Journal of the American Chemical Society* **2015**, *137*, 11916–11919.

[38] Chambron, J.-C.; Collin, J.-P.; Heitz, V.; Jouvenot, D.; Kern, J.-M.; Mobian, P.; Pomeranc, D.; Sauvage, J.-P. Rotaxanes and catenanes built around octahedral transition metals. *European Journal of Organic Chemistry* **2004**, *2004*, 1627–1638.

[39] Sauvage, J.-P. Transition metal-complexed catenanes and rotaxanes as molecular machine prototypes. *Chemical Communications* **2005**, 1507–1510.

[40] Champin, B.; Mobian, P.; Sauvage, J.-P. Transition metal complexes as molecular machine prototypes. *Chemical Society Reviews* **2007**, *36*, 358–366.

[41] Meyer, C. D.; Joiner, C. S.; Stoddart, J. F. Template-directed synthesis employing reversible imine bond formation. *Chemical Society Reviews* **2007**, *36*, 1705–1723.

[42] Lee, J.; Farha, O. K.; Roberts, J.; Scheidt, K. A.; Nguyen, S. T.; Hupp, J. T. Metal-organic framework materials as catalysts. *Chemical Society Reviews* **2009**, *38*, 1450–1459.

[43] Li, J.-R.; Kuppler, R. J.; Zhou, H.-C. Selective gas adsorption and separation in metal-organic frameworks. *Chemical Society Reviews* **2009**, *38*, 1477–1504.

[44] Li, J.-R.; Sculley, J.; Zhou, H.-C. Metal-organic frameworks for separations. *Chemical Reviews* **2012**, *112*, 869–932.

[45] Lehn, J.-M.; Rigault, A.; Siegel, J.; Harrowfield, J.; Chevrier, B.; Moras, D. Spontaneous assembly of double-stranded helicates from oligobipyridine ligands and copper(I) cations: structure of an inorganic double helix. *Proceedings of the National Academy of Sciences of the United States of America* **1987**, *84*, 2565–2569.

[46] Stratton, W. J.; Busch, D. H. The complexes of pyridinaldazine with iron(II) and nickel(II). *Journal of the American Chemical Society* **1958**, *80*, 1286–1289.

[47] Greenwald, M.; Wessely, D.; Goldberg, I.; Cohen, Y. Bis(bipyridine)-phenanthroline double-stranded helicates of the d^{10} metals: zinc(II), silver(I) and copper(I) helicates. *New Journal of Chemistry* **1999**, *23*, 337–344.

[48] Glasson, C. R. K.; Meehan, G. V.; Motti, C. A.; Clegg, J. K.; Turner, P.; Jensen, P.; Lindoy, L. F. New nickel(II) and iron(II) helicates and tetrahedra derived from expanded quaterpyridines. *Dalton Transactions* **2011**, *40*, 10481–10490.

[49] Zhang, T.; Zhang, G.-L.; Zhou, L.-P.; Guo, X.-Q.; Sun, Q.-F. Stereocontrolled self-assembly of luminescent lanthanide helicates and their enantiodifferentiation using Δ-TRISPHAT as the NMR resolving agent. *Tetrahedron: Asymmetry* **2017**, *28*, 550–554.

[50] Speed, S.; Pointillart, F.; Mulatier, J.-C.; Guy, L.; Golhen, S.; Cador, O.; Le Guennic, B.; Riobé, F.; Maury, O.; Ouahab, L. Photophysical and magnetic properties in complexes containing 3d/4f elements and chiral phenanthroline-based helicate-like ligands. *European Journal of Inorganic Chemistry* **2017**, *2017*, 2100–2111.

[51] Lützen, A.; Hapke, M.; Griep-Raming, J.; Haase, D.; Saak, W. Synthesis and stereoselective self-assembly of double- and triple-stranded helicates. *Angewandte Chemie International Edition* **2002**, *41*, 2086–2089.

[52] Golla, U.; Adhikary, A.; Mondal, A. K.; Tomar, R. S.; Konar, S. Synthesis, structure, magnetic and biological activity studies of bis-hydrazone derived Cu(II) and Co(II) coordination compounds. *Dalton Transactions* **2016**, *45*, 11849–63.

[53] Hagiwara, H.; Tanaka, T.; Hora, S. Synthesis, structure, and spin crossover above room temperature of a mononuclear and related dinuclear double helicate iron(II) complexes. *Dalton Transactions* **2016**, *45*, 17132–17140.

[54] Bullock, S. J.; Felton, C. E.; Fennessy, R. V.; Harding, L. P.; Andrews, M.; Pope, S. J.; Rice, C. R.; Riis-Johannessen, T. Coumarin-based luminescent ligand that forms helicates with dicationic metal ions. *Dalton Transactions* **2009**, 10570–3.

[55] Chen, W.; Tang, X.; Dou, W.; Wang, B.; Guo, L.; Ju, Z.; Liu, W. The construction of homochiral lanthanide quadruple-stranded helicates with multiresponsive sensing properties toward fluoride anions. *Chemistry – A European Journal* **2017**,

[56] Furusho, Y.; Goto, H.; Itomi, K.; Katagiri, H.; Miyagawa, T.; Yashima, E. Synthesis and optical resolution of a Cu(I) double-stranded helicate with ketimine-bridged tris(bipyridine) ligands. *Chemical Communications* **2011**, *47*, 9795–7.

[57] Hasenknopf, B.; Lehn, J.-M.; Kneisel, B. O.; Baum, G.; Fenske, D. Self-assembly of a circular double helicate. *Angewandte Chemie International Edition* **1996**, *35*, 1838–1840.

[58] Provent, C.; Rivara-Minten, E.; Hewage, S.; Brunner, G.; Williams, A. F. Solution equilibria of enantiopure helicates: the role of concentration, solvent and stacking interactions in self-assembly. *Chemistry – A European Journal* **1999**, *5*, 3487–3494.

[59] Mamula, O.; Monlien, F. J.; Porquet, A.; Hopfgartner, G.; Merbach, A. E.; von Zelewsky, A. Self-assembly of multinuclear coordination species with chiral bipyridine ligands: silver complexes of 5,6-CHIRAGEN(*o*,*m*,*p*-xylidene) ligands and equilibrium behaviour in solution. *Chemistry – A European Journal* **2001**, *7*, 533–539.

[60] Hasenknopf, B.; Lehn, J.-M.; Baum, G.; Fenske, D. Self-assembly of a heteroduplex helicate from two different ligand strands and Cu(II) cations. *Proceedings of the National Academy of Sciences of the United States of America* **1996**, *93*, 1397–1400.

[61] Howson, S. E.; Bolhuis, A.; Brabec, V.; Clarkson, G. J.; Malina, J.; Rodger, A.; Scott, P. Optically pure, water-stable metallo-helical 'flexicate' assemblies with antibiotic activity. *Nature Chemistry* **2012**, *4*, 31–36.

[62] Constable, E. C.; Kulke, T.; Baum, G.; Fenske, D. Diastereoselective formation of chiral helicates. *Inorganic Chemistry Communications* **1998**, *1*, 80–82.

[63] von Zelewsky, A. *Stereochemistry of coordination compounds*; John Wiley & Sons: Chichester, England, 1996.

[64] Keene, F. R. Isolation and characterisation of stereoisomers in di- and tri-nuclear complexes. *Chemical Society Reviews* **1998**, *27*, 185–194.

[65] Rapenne, G.; Patterson, B. T.; Sauvage, J.-P.; Keene, F. R. Resolution, X-ray structure and absolute configuration of a double-stranded helical diiron(II) bis(terpyridine) complex. *Chemical Communications* **1999**, 1853–1854.

[66] Glasson, C. R. K.; Meehan, G. V.; Clegg, J. K.; Lindoy, L. F.; Smith, J. A.; Keene, F. R.; Motti, C. Microwave synthesis of a rare $[Ru_2L_3]^{4+}$ triple helicate and its interaction with DNA. *Chemistry – A European Journal* **2008**, *14*, 10535–10538.

[67] Hannon, M. J.; Meistermann, I.; Isaac, C. J.; Blomme, C.; Aldrich-Wright, J. R.; Rodger, A. Paper: a cheap yet effective chiral stationary phase for chromatographic resolution of metallo-supramolecular helicates. *Chemical Communications* **2001**, 1078–1079.

[68] Kerckhoffs, J.; Peberdy, J. C.; Meistermann, I.; Childs, L. J.; Isaac, C. J.; Pearmund, C. R.; Reudegger, V.; Khalid, S.; Alcock, N. W.; Hannon, M. J.; Rodger, A. Enantiomeric resolution of supramolecular helicates with different surface topographies. *Dalton Transactions* **2007**, 734–742.

[69] Albrecht, M.; Kotila, S. Formation of a "*meso*-helicate" by self-assembly of three bis(catecholate) ligands and two titanium(IV) ions. *Angewandte Chemie International Edition* **1995**, *34*, 2134–2137.

[70] Zhang, Z.; Dolphin, D. A triple-stranded helicate and mesocate from the same metal and ligand. *Chemical Communications* **2009**, 6931–6933.

[71] Hannon, M. J.; Painting, C. L.; Jackson, A.; Hamblin, J.; Errington, W. An inexpensive approach to supramolecular

architecture. *Chemical Communications* **1997**, 1807–1808.

[72] Rodger, A.; Sanders, K. J.; Hannon, M. J.; Meistermann, I.; Parkinson, A.; Vidler, D. S.; Haworth, I. S. DNA structure control by polycationic species: polyamine, cobalt ammines, and di-metallo transition metal chelates. *Chirality* **2000**, *12*, 221–236.

[73] Pascu, G. I.; Hotze, A. C. G.; Sanchez-Cano, C.; Kariuki, B. M.; Hannon, M. J. Dinuclear ruthenium(II) triple-stranded helicates: luminescent supramolecular cylinders that bind and coil DNA and exhibit activity against cancer cell lines. *Angewandte Chemie International Edition* **2007**, *46*, 4374–4378.

[74] Torelli, S.; Delahaye, S.; Hauser, A.; Bernardinelli, G.; Piguet, C. Ruthenium(II) as a novel labile partner in thermodynamic self-assembly of heterobimetallic d-f triple-stranded helicates. *Chemistry – A European Journal* **2004**, *10*, 3503–3516.

[75] Fletcher, N. C.; Brown, R. T.; Doherty, A. P. New stepwise approach to inert heterometallic triple-stranded helicates. *Inorganic Chemistry* **2006**, *45*, 6132–6134.

[76] Elliott, C. M.; Derr, D. L.; Matyushov, D. V.; Newton, M. D. Direct experimental comparison of the theories of thermal and optical electron-transfer: studies of a mixed-valence dinuclear iron polypyridyl complex. *Journal of the American Chemical Society* **1998**, *120*, 11714–11726.

[77] Ducani, C.; Leczkowska, A.; Hodges, N. J.; Hannon, M. J. Noncovalent DNA-binding metallo-supramolecular cylinders prevent DNA transactions in vitro. *Angewandte Chemie International Edition* **2010**, *49*, 8942–5.

[78] Malina, J.; Hannon, M.; Brabec, V. Interaction of dinuclear ruthenium(II) supramolecular cylinders with DNA: sequence-specific binding, unwinding, and photocleavage. *Chemistry – A European Journal* **2008**, *14*, 10408–10414.

[79] Cardo, L.; Nawroth, I.; Cail, P. J.; McKeating, J. A.; Hannon, M. J. Metallo supramolecular cylinders inhibit HIV-1 TAR-TAT complex formation and viral replication *in cellulo*. *Scientific Reports* **2018**, *8*, 13342.

[80] Kumar, S. V.; Lo, W. K. C.; Brooks, H. J. L.; Crowley, J. D. Synthesis, structure, stability and antimicrobial activity of a ruthenium(II) helicate derived from a bis-bidentate "click" pyridyl-1,2,3-triazole ligand. *Inorganica Chimica Acta* **2015**, *425*, 1–6.

[81] Crane, J. D.; Sauvage, J.-P. A dinuclear double-stranded helical complex containing two ruthenium(II) bis-terpyridine units. *New Journal of Chemistry* **1992**, *16*, 649–650.

[82] Allison, S. J.; Cooke, D.; Davidson, F. S.; Elliott, P. I. P.; Faulkner, R. A.; Griffiths, H. B. S.; Harper, O. J.; Hussain, O.; Owen-Lynch, P. J.; Phillips, R. M.; Rice, C. R.; Shepherd, S. L.; Wheelhouse, R. T. Ruthenium-containing linear helicates and mesocates with tuneable p53-selective cytotoxicity in colorectal cancer cells. *Angewandte Chemie International Edition* **2018**, *57*, 9799–9804.

[83] Ho, P. K. K.; Cheung, K. K.; Che, C. M. Double-helical ruthenium complexes of 2,2′:6′,2″,2‴: 6‴,2⁗-quinquepyridine (qpy) for multi-electron oxidation reactions. *Chemical Communications* **1996**, 1197–1198.

[84] Baxter, P. N. W.; Lehn, J.-M.; Rissanen, K. Generation of an equilibrating collection of circular inorganic copper(I) architectures and solid-state stabilisation of the dicopper helicate component. *Chemical Communications* **1997**, 1323–1324.

[85] Hasenknopf, B.; Lehn, J.-M.; Boumediene, N.; Leize, E.; Van Dorsselaer, A. Kinetic and thermodynamic control in self-assembly: sequential formation of linear and circular helicates. *Angewandte Chemie International Edition* **1998**, *37*, 3265–3268.

[86] Zangrando, E.; Casanova, M.; Alessio, E. Trinuclear metallacycles: metallatriangles and much more. *Chemical Reviews* **2008**, *108*, 4979–5013.

[87] Lippert, B.; Sanz Miguel, P. J. Metallatriangles and metallasquares: the diversity behind structurally characterized examples and the crucial role of ligand symmetry. *Chemical Society Reviews* **2011**, *40*, 4475–4487.

[88] Caulder, D. L.; Raymond, K. N. The rational design of high symmetry coordination clusters. *Journal of the Chemical Society, Dalton Transactions* **1999**, 1185–1200.

[89] Custelcean, R.; Bonnesen, P. V.; Duncan, N. C.; Zhang, X.; Watson, L. A.; Van Berkel, G.; Parson, W. B.; Hay, B. P. Urea-functionalized M_4L_6 cage receptors: anion-templated self-assembly and selective guest exchange in aqueous solutions. *Journal of the American Chemical Society* **2012**, *134*, 8525–8534.

[90] Meng, W.; Ronson, T. K.; Nitschke, J. R. Symmetry breaking in self-assembled M_4L_6 cage complexes. *Proceedings of the National Academy of Sciences of the United States of America* **2013**, *110*, 10531.

[91] Hristova, Y. R.; Smulders, M. M. J.; Clegg, J. K.; Breiner, B.; Nitschke, J. R. Selective anion binding by a "Chameleon" capsule with a dynamically reconfigurable exterior. *Chemical Science* **2011**, *2*, 638–641.

[92] Yang, J.; Chang, X.-Y.; Sham, K.-C.; Yiu, S.-M.; Kwong, H.-L.; Che, C.-M. M_8L_{12} cubic cages with all facial Δ or facial Λ configuration: effects of surface anions on the occupancy of the cage and anion exchange. *Chemical Communications* **2016**, *52*, 5981–5984.

[93] Tidmarsh, I. S.; Faust, T. B.; Adams, H.; Harding, L. P.; Russo, L.; Clegg, W.; Ward, M. D. Octanuclear cubic

coordination cages. *Journal of the American Chemical Society* **2008**, *130*, 15167–15175.

[94] Cook, T. R.; Stang, P. J. Recent developments in the preparation and chemistry of metallacycles and metallacages via coordination. *Chemical Reviews* **2015**, *115*, 7001–45.

[95] Pilgrim, B. S.; Champness, N. R. Metal-organic frameworks and metal-organic cages - a perspective. *ChemPlusChem* **2020**, *85*, 1842–1856.

[96] Martín Díaz, A. E.; Lewis, J. E. M. Structural flexibility in metal-organic cages. *Frontiers in Chemistry* **2021**, *9*.

[97] Xie, T.-Z.; Liao, S.-Y.; Guo, K.; Lu, X.; Dong, X.; Huang, M.; Moorefield, C. N.; Cheng, S. Z. D.; Liu, X.; Wesdemiotis, C.; Newkome, G. R. Construction of a highly symmetric nanosphere via a one-pot reaction of a tristerpyridine ligand with Ru(II). *Journal of the American Chemical Society* **2014**, *136*, 8165–8168.

[98] Metherell, A. J.; Ward, M. D. Stepwise synthesis of a Ru_4Cd_4 coordination cage using inert and labile subcomponents: introduction of redox activity at specific sites. *Chemical Communications* **2014**, *50*, 6330–6332.

[99] Wragg, A. B.; Metherell, A. J.; Cullen, W.; Ward, M. D. Stepwise assembly of mixed-metal coordination cages containing both kinetically inert and kinetically labile metal ions: introduction of metal-centred redox and photophysical activity at specific sites. *Dalton Transactions* **2015**, *44*, 17939–17949.

[100] Metherell, A. J.; Ward, M. D. Stepwise assembly of an adamantoid Ru_4Ag_6 cage by control of metal coordination geometry at specific sites. *Chemical Communications* **2014**, *50*, 10979–10982.

[101] Metherell, A. J.; Ward, M. D. Ru(II)/Ag(I) mixed-metal complexes based on kinetically inert Ru(II) complexes with pendant binding sites as subcomponents. *Polyhedron* **2015**, *89*, 260–270.

[102] Pan, M.; Wu, K.; Zhang, J.-H.; Su, C.-Y. Chiral metal-organic cages/containers (MOCs): From structural and stereochemical design to applications. *Coordination Chemistry Reviews* **2019**, *378*, 333–349.

[103] Campbell, F.; Plante, J. P.; Edwards, T. A.; Warriner, S. L.; Wilson, A. J. *N*-alkylated oligoamide α-helical proteomimetics. *Organic & Biomolecular Chemistry* **2010**, *8*, 2344–51.

[104] Rosenberg, B.; Van Camp, L.; Krigas, T. Inhibition of cell division in *Escherichia coli* by electrolysis products from a platinum electrode. *Nature* **1965**, *205*, 698–699.

[105] Rosenberg, B.; Van Camp, L.; Grimley, E. B.; Thomson, A. J. The inhibition of growth or cell division in *Escherichia coli* by different ionic species of platinum(IV) complexes. *Journal of Biological Chemistry* **1967**, *242*, 1347–1352.

[106] Rosenberg, B.; Van Camp, L.; Trosko, J. E.; Mansour, V. H. Platinum compounds: a new class of potent antitumour agents. *Nature* **1969**, *222*, 385–386.

[107] Wang, D.; Lippard, S. J. Cellular processing of platinum anticancer drugs. *Nature Reviews Drug Discovery* **2005**, *4*, 307–320.

[108] Hannon, M. J. Metal-based anticancer drugs: from a past anchored in platinum chemistry to a post-genomic future of diverse chemistry and biology. *Pure and Applied Chemistry* **2007**, *79*, 2243–2261.

[109] Jamieson, E. R.; Lippard, S. J. Structure, recognition, and processing of cisplatin-DNA adducts. *Chemical Reviews* **1999**, *99*, 2467–2498.

[110] Frederick, C. A.; Lippard, S. J.; Rosenzweig, A. C.; Takahara, P. M. Crystal structure of double-stranded DNA containing the major adduct of the anticancer drug cisplatin. *Nature* **1995**, *377*, 649–652.

[111] Hoffmann, J. S.; Locker, D.; Villani, G.; Leng, M. HMG_1 protein inhibits the translesion synthesis of the major DNA cisplatin adduct by cell extracts. *Journal of Molecular Biology* **1997**, *270*, 539–543.

[112] Dasari, S.; Tchounwou, P. B. Cisplatin in cancer therapy: molecular mechanisms of action. *European Journal of Pharmacology* **2014**, *740*, 364–78.

[113] Heffeter, P.; Jungwirth, U.; Jakupec, M.; Hartinger, C.; Galanski, M.; Elbling, L.; Micksche, M.; Keppler, B.; Berger, W. Resistance against novel anticancer metal compounds: differences and similarities. *Drug resistance updates* **2008**, *11*, 1–16.

[114] Stewart, D. J. Tumor and host factors that may limit efficacy of chemotherapy in non-small cell and small cell lung cancer. *Critical reviews in oncology/hematology* **2009**, *75*, 173–234.

[115] Ott, I.; Gust, R. Non platinum metal complexes as anti-cancer drugs. *Archiv der Pharmazie (Weinheim)* **2007**, *340*, 117–126.

[116] Gianferrara, T.; Bratsos, I.; Alessio, E. A categorization of metal anticancer compounds based on their mode of action. *Dalton Transactions* **2009**, 7588–7598.

[117] Levina, A.; Mitra, A.; Lay, P. A. Recent developments in ruthenium anticancer drugs. *Metallomics* **2009**, *1*, 458–470.

[118] Clarke, M. J. Ruthenium metallopharmaceuticals. *Coordination Chemistry Reviews* **2002**, *232*, 69–93.

[119] Ang, W. H.; Dyson, P. J. Classical and non-classical ruthenium-based anticancer drugs: towards targeted chemotherapy. *European Journal of Inorganic Chemistry* **2006**, *2006*, 3993–3993.

[120] Flint, K. L.; Collins, J. G.; Bradley, S. J.; Smith, T. A.; Sumby, C. J.; Keene, F. R. Synthesis and characterisation of helicate and mesocate forms of a double-stranded diruthenium(II) complex of a di(terpyridine) ligand. *Australian Journal of Chemistry* **2019**, *72*, 762–768.

[121] Constable, E. C.; Ward, M. D.; Tocher, D. A. Spontaneous assembly of a double-helical binuclear complex of 2,2′:6′,2″:6″,2‴:6‴,2⁗:6⁗,2⁗′:6⁗′,2⁗′′-sexipyridine. *Journal of the American Chemical Society* **1990**, *112*, 1256–1258.

[122] Vos, J. G.; Kelly, J. M. Ruthenium polypyridyl chemistry; from basic research to applications and back again. *Dalton Transactions* **2006**, 4869–4883.

[123] Paris, J. P.; Brandt, W. W. Charge transfer luminescence of a ruthenium(II) chelate. *Journal of the American Chemical Society* **1959**, *81*, 5001–5002.

[124] Gill, M. R.; Thomas, J. A. Ruthenium(II) polypyridyl complexes and DNA - from structural probes to cellular imaging and therapeutics. *Chemical Society Reviews* **2012**, *41*, 3179–3192.

[125] Cook, T. R.; Vajpayee, V.; Lee, M. H.; Stang, P. J.; Chi, K.-W. Biomedical and biochemical applications of self-assembled metallacycles and metallacages. *Accounts of Chemical Research* **2013**, *46*, 2464–2474.

[126] Kaner, R. A.; Scott, P. Metallohelices: potential mimetics of α-helical peptides in cancer treatment? *Future Medicinal Chemistry* **2015**, *7*, 1–4.

[127] Bruijnincx, P. C. A.; Sadler, P. J. New trends for metal complexes with anticancer activity. *Current Opinion in Chemical Biology* **2008**, *12*, 197–206.

[128] Baum, G.; Constable, E. C.; Fenske, D.; Housecroft, C. E.; Kulke, T.; Neuburger, M.; Zehnder, M. Regio- and diastereo-selective formation of dicopper(I) and disilver(I) double helicates with chiral 6-substituted 2,2′:6′,2″-terpyridines. *Journal of the Chemical Society, Dalton Transactions* **2000**, 945–959.

[129] Rapenne, G.; Dietrich-Buchecker, C.; Sauvage, J.-P. Copper(I)- or iron(II)-templated synthesis of molecular knots containing two tetrahedral or octahedral coordination sites. *Journal of the American Chemical Society* **1999**, *121*, 994–1001.

[130] Dietrich-Buchecker, C. O.; Sauvage, J.-P.; Kintzinger, J. P.; Maltese, P.; Pascard, C.; Guilhem, J. A dicopper(I) trefoil knot and its parent ring compounds - synthesis, solution studies and X-ray structures. *New Journal of Chemistry* **1992**, *16*, 931–942.

[131] Dietrich-Buchecker, C. O.; Nierengarten, J.-F.; Sauvage, J.-P.; Armaroli, N.; Balzani, V.; De Cola, L. Dicopper(I) trefoil knots and related unknotted molecular systems: influence of ring size and structural factors on their synthesis and electrochemical and excited-state properties. *Journal of the American Chemical Society* **1993**, *115*, 11237–11244.

[132] Schubert, U. S.; Eschbaumer, C.; Heller, M. Stille-type cross-coupling - an efficient way to various symmetrically and unsymmetrically substituted methyl-bipyridines: toward new ATRP catalysts. *Organic Letters* **2000**, *2*, 3373–3376.

[133] Seckin, T.; Özdemir, I.; Köytepe, S.; Gürbüz, N. Preparation and catalytic properties of a Ru(II) coordinated polyimide supported by a ligand containing terpyridine units. *Journal of Inorganic and Organometallic Polymers* **2009**, *19*, 143–151.

[134] Evans, I. P.; Spencer, A.; Wilkinson, G. Dichlorotetrakis(dimethyl sulphoxide)ruthenium(III) and its use as a source material for some new ruthenium(III) complexes. *Journal of the Chemical Society, Dalton Transactions* **1973**, 204–209.

[135] Bernhard, P.; Bürgi, H.-B.; Hauser, J.; Lehmann, H.; Ludi, A. Syntheses and crystal and molecular structures of hexaaquaruthenium(II) *p*-toluenesulfonate and hexaaquaruthenium(III) *p*-toluenesulfonate, $[Ru(H_2O)_6](C_7H_7SO_3)_2$ and $[Ru(H_2O)_6](C_7H_7SO_3)_3{\cdot}3H_2O$. *Inorganic Chemistry* **1982**, *21*, 3936–3941.

[136] Coll, J. C.; Bowden, B. F. The application of vacuum liquid chromatography to the separation of terpene mixtures. *Journal of Natural Products* **1986**, *49*, 934–936.

[137] Hotze, A. C. G.; Kariuki, B. M.; Hannon, M. J. Dinuclear double-stranded metallosupramolecular ruthenium complexes: potential anticancer drugs. *Angewandte Chemie International Edition* **2006**, *45*, 4839–4842.

[138] Sun, B.; Southam, H. M.; Butler, J. A.; Poole, R. K.; Burgun, A.; Tarzia, A.; Keene, F. R.; Collins, J. G. Synthesis, isomerisation and biological properties of mononuclear ruthenium complexes containing the bis[4(4′-methyl-2,2′-bipyridyl)]-1,7-heptane ligand. *Dalton Transactions* **2018**, *47*, 2422–2434.

[139] Spek, A. *PLATON* SQUEEZE: a tool for the calculation of the disordered solvent contribution to the calculated structure factors. *Acta Crystallographica Section C: Crystal Structure Communications* **2015**, *71*, 9–18.

[140] Juris, A.; Balzani, V.; Barigelletti, F.; Campagna, S.; Belser, P.; von Zelewsky, A. Ru(II) polypyridine complexes: photophysics, photochemistry, eletrochemistry, and chemiluminescence. *Coordination Chemistry Reviews* **1988**, *84*, 85–277.

[141] Amini, A.; Harriman, A.; Mayeux, A. The triplet excited state of ruthenium(II) bis(2,2′:6′,2″-terpyridine): comparison between experiment and theory. *Physical Chemistry Chemical Physics* **2004**, *6*, 1157–1164.

[142] Lakshmanan, R.; Shivaprakash, N. C.; Sindhu, S. Orange fluorescent Ru(III) complexes based on 4′-aryl substituted 2,2′:6′,2″-terpyridine for OLEDs application. *Journal of Fluorescence* **2018**, *28*, 173–182.

[143] Hua, X.; von Zelewsky, A. Enantiomerically pure chiral $Ru^{II}(L\text{-}L)_2$ building blocks for coordination compounds. *Inorganic Chemistry* **1995**, *34*, 5791–5797.

[144] Hua, X.; von Zelewsky, A. First stereospecific preparation of a polynuclear coordination compound. Use of Λ-Ru^{II}(*o*-phen)$_2$ as a chiral building block. *Inorganic Chemistry* **1991**, *30*, 3796–3798.

[145] Hiort, C.; Lincoln, P.; Norden, B. DNA binding of Δ- and Λ-$[Ru(phen)_2DPPZ]^{2+}$. *Journal of the American Chemical Society* **1993**, *115*, 3448–3454.

[146] Bosnich, B.; Dwyer, F. P. Bis-1,10-phenanthroline complexes of divalent ruthenium. *Australian Journal of Chemistry* **1966**, *19*, 2229–2233.

[147] Burstall, F. H. Optical activity dependent on co-ordinated bivalent ruthenium. *Journal of the Chemical Society* **1936**, 173–175.

[148] Burstall, F. H.; Dwyer, F. P.; Gyarfas, E. C. 194. Optical activity dependent on a six-covalent bivalent osmium complex. *Journal of the Chemical Society* **1950**, 953–955.

[149] Dwyer, F. P.; Gyarfas, E. C. The chemistry of ruthenium. Part VI. The existence of the tris-o-phenanthroline ruthenium II and the tris-o-phenanthroline ruthenium III ions in entantiomorphous forms. *Journal and Proceedings of the Royal Society of New South Wales* **1949**, *83*, 170–173.

[150] Aldrich-Wright, J. R.; Greguric, I.; Vagg, R. S.; Vickery, K.; Williams, P. A. Development of DNA-immobilised chromatographic stationary phases for optical resolution and DNA-affinity comparison of metal complexes. *Journal of Chromatography A* **1995**, *718*, 436–443.

[151] Holder, E.; Schoetz, G.; Schurig, V.; Lindner, E. Synthesis and enantiomer separation of a modified tris(2,2′-bipyridine)ruthenium(II) complex. *Tetrahedron: Asymmetry* **2001**, *12*, 2289–2293.

[152] Shelton, C. M.; Seaver, K. E.; Wheeler, J. F.; Kane-Maguire, N. A. P. Application of capillary electrophoresis for the assessment of enantiomeric purity of α-diimine transition metal complexes. *Inorganic Chemistry* **1997**, *36*, 1532–1533.

[153] Lacour, J.; Torche-Haldimann, S.; Jodry, J. J.; Ginglinger, C. F. F. Ion pair chromatographic resolution of tris(diimine)ruthenium(II) complexes using TRISPHAT anions as resolving agents. *Chemical Communications* **1998**, 1733–1734.

[154] Smith, J. A.; Keene, F. R. Separation of stereoisomers of dinuclear metal complexes by binding affinity chromatography using non-duplex DNA. *Chemical Communications* **2006**, 2583–2585.

[155] Yoshikawa, Y.; Yamasaki, K. Chromatographic resolution of metal complexes on sephadex ion exchangers. *Coordination Chemistry Reviews* **1979**, *28*, 205–229.

[156] Searle, G. H. The role of ion-association in the chromatographic separation of isomeric cationic cobalt(III)-amine complexes on cation-exchange resins, particularly SP-Sephadex. *Australian Journal of Chemistry* **1977**, *30*, 2625–2637.

[157] Kojima, M.; Yoshikawa, Y.; Yamasaki, K. Isomerism of the metal complexes containing multidentate ligands. III. Geometric and optical isomers of the tris(2-methyl-1,2-propanediamine)cobalt(III) ion. *Bulletin of the Chemical Society of Japan* **1973**, *46*, 1687–1689.

[158] Rutherford, T. J.; Pellegrini, P. A.; Aldrich-Wright, J.; Junk, P. C.; Keene, F. R. Isolation of enantiomers of a range of tris(bidentate)ruthenium(II) species using chromatographic resolution and stereoretentive synthetic methods. *European Journal of Inorganic Chemistry* **1998**, *1998*, 1677–1688.

[159] Dupureur, C. M.; Barton, J. K. Structural studies of Λ- and Δ-$[Ru(phen)_2dppz]^{2+}$ bound to $d(GTCGAC)_2$: characterization of enantioselective intercalation. *Inorganic Chemistry* **1997**, *36*, 33–43.

[160] Fletcher, N. C.; Keene, F. R. New synthetic route to monocarbonyl polypyridyl complexes of ruthenium: their stereochemistry and reactivity. *Journal of the Chemical Society, Dalton Transactions* **1998**, 2293–2302.

[161] Rutherford, T. J.; Quagliotto, M. G.; Keene, F. R. Chiral $[Ru(pp)_2(CO)_2]^{2+}$ species (pp = bidentate polypyridyl ligand) and their use in the stereoselective synthesis of ligand-bridge dinuclear complexes. *Inorganic Chemistry* **1995**, *34*, 3857–3858.

[162] Kelso, L. S.; Reitsma, D. A.; Keene, F. R. Spectral and electrochemical properties of the diastereoisomeric forms of azobis(2-pyridine)-bridged diruthenium species. *Inorganic Chemistry* **1996**, *35*, 5144–5153.

[163] Reitsma, D. A.; Keene, F. R. Diastereoisomeric forms of ligand-bridged dimetallic diruthenium(II) and ruthenium(II)-osmium(II) species containing bidentate polypyridyl ligands. *Journal of the Chemical Society, Dalton Transactions* **1993**, 2859–2860.

[164] Rutherford, T. J.; Keene, F. R. Stereoisomers in heterometallic (Ru_2Os) and heteroleptic homometallic (RuRu′Ru″) trinuclear complexes incorporating the bridging ligand HAT (1,4,5,8,9,12-hexaazatriphenylene). *Journal of the Chemical Society, Dalton Transactions* **1998**, 1155–1162.

[165] Rutherford, T. J.; Keene, F. R. Isolation of the stereoisomers of $[\{Ru(bpy)_2\}_2\{Os(bpy)_2\}(\mu\text{-HAT})]^{6+}$ (HAT = 1,4,5,8,9,12-hexaazatriphenylene; bpy = 2,2′-bipyridine). *Inorganic Chemistry* **1997**, *36*, 3580–3581.

[166] Foley, F. M.; Keene, F. R.; Collins, J. G. The DNA binding of the ΔΔ-, ΔΛ- and ΛΛ-stereoisomers of

[{Ru(Me_2bpy)$_2$}$_2$(μ-bpm)]$^{4+}$. *Journal of the Chemical Society, Dalton Transactions* **2001**, 2968–2974.

[167] Yeomans, B.; Kelso, L.; Tregloan, P.; Keene, F. R. Redox characteristics and anion association behaviour of stereoisomeric forms of mono- and oligonuclear metal complexes using high pressure electrochemistry. *European Journal of Inorganic Chemistry* **2001**, *2001*, 239–246.

[168] Fletcher, N. C.; Junk, P. C.; Reitsma, D. A.; Keene, F. R. Chromatographic separation of stereoisomers of ligand-bridged diruthenium polypyridyl species. *Journal of the Chemical Society, Dalton Transactions* **1998**, 133–138.

[169] Fletcher, N. C.; Keene, F. R. Anion interactions with (polypyridyl)ruthenium complexes, and their importance in the cation-exchange chromatographic separation of stereoisomers of dinuclear species. *Journal of the Chemical Society, Dalton Transactions* **1999**, 683–690.

[170] Cardo, L.; Sadovnikova, V.; Phongtongpasuk, S.; Hodges, N. J.; Hannon, M. J. Arginine conjugates of metallosupramolecular cylinders prescribe helicity and enhance DNA junction binding and cellular activity. *Chemical Communications* **2011**, *47*, 6575–6577.

[171] Meistermann, I.; Moreno, V.; Prieto, M. J.; Moldrheim, E.; Sletten, E.; Khalid, S.; Rodger, P. M.; Peberdy, J. C.; Isaac, C. J.; Rodger, A.; Hannon, M. J. Intramolecular DNA coiling mediated by metallosupramolecular cylinders: differential binding of P and M helical enantiomers. *Proceedings of the National Academy of Sciences of the United States of America* **2002**, *99*, 5069–5074.

[172] Łęczkowska, A. Non-covalent DNA-binding ruthenium anticancer drugs. Thesis, 2011.

[173] Lacour, J.; Jodry, J. J.; Ginglinger, C.; Torche-Haldimann, S. Diastereoselective ion pairing of TRISPHAT anions and tris(4,4′-dimethyl-2,2′-bipyridine)iron(II). *Angewandte Chemie International Edition* **1998**, *37*, 2379–2380.

[174] Ratni, H.; Jodry, J. J.; Lacour, J.; Kündig, E. P. [*n*-Bu_4N][Δ-TRISPHAT] salt, an efficient NMR chiral shift reagent for neutral planar chiral tricarbonylchromium complexes. *Organometallics* **2000**, *19*, 3997–3999.

[175] Lacour, J.; Jodry, J. J.; Monchaud, D. Configurational ordering of a cationic dinuclear triple helicate by chiral TRISPHAT anions. *Chemical Communications* **2001**, 2302–2303.

[176] Lacour, J.; Ginglinger, C.; Favarger, F.; Torche-Haldimann, S. Application of TRISPHAT anion as NMR chiral shift reagent. *Chemical Communications* **1997**, 2285–2286.

[177] Barton, J. K.; Nowick, J. S. Application of chiral lanthanide-induced shift reagents to optically active cations: the use of tris[3-(trifluoromethylhydroxymethylene)-(+)-camphorato]europium(III) to determine the enantiomeric purity of tris(phenanthroline)ruthenium(II) dichloride. *Journal of the Chemical Society, Chemical Communications* **1984**, 1650–1652.

[178] Jodry, J.; Lacour, J. Efficient resolution of a dinuclear triple helicate by asymmetric extraction/precipitation with TRISPHAT anions as resolving agents. *Chemistry – A European Journal* **2000**, *6*, 4297–4304.

[179] Watson, J. D.; Crick, F. H. C. Molecular structure of nucleic acids - a structure for deoxyribose nucleic acid. *Nature* **1953**, *171*, 737–738.

[180] Keene, F. R.; Smith, J. A.; Collins, J. G. Metal complexes as structure-selective binding agents for nucleic acids. *Coordination Chemistry Reviews* **2009**, *253*, 2021–2035.

[181] Bancroft, D. P.; Lepre, C. A.; Lippard, S. J. ^{195}Pt NMR kinetic and mechanistic studies of *cis*- and *trans*-diamminedichloroplatinum(II) binding to DNA. *Journal of the American Chemical Society* **1990**, *112*, 6860–6871.

[182] Sherman, S. E.; Lippard, S. J. Structural aspects of platinum anticancer drug interactions with DNA. *Chemical Reviews* **1987**, *87*, 1153–1181.

[183] Eichhorn, G. L.; Shin, Y. A. Interaction of metal ions with polynucleotides and related compounds. XII. The relative effect of various metal ions on DNA helicity. *Journal of the American Chemical Society* **1968**, *90*, 7323–7328.

[184] Sigel, H. Interactions of metal ions with nucleotides and nucleic acids and their constituents. *Chemical Society Reviews* **1993**, *22*, 255–267.

[185] Brabec, V.; Kasparkova, J. Ruthenium coordination compounds of biological and biomedical significance. DNA binding agents. *Coordination Chemistry Reviews* **2018**, *376*, 75–94.

[186] Zeglis, B. M.; Pierre, V. C.; Barton, J. K. Metallo-intercalators and metallo-insertors. *Chemical Communications* **2007**, 4565–4579.

[187] Gurova, K. New hopes from old drugs: revisiting DNA-binding small molecules as anticancer agents. *Future Oncology* **2009**, *5*, 1685–704.

[188] Pindur, U.; Jansen, M.; Lemster, T. Advances in DNA-ligands with groove binding, intercalating and/or alkylating activity: chemistry, DNA-binding and biology. *Curr Med Chem* **2005**, *12*, 2805–47.

[189] Boer, D. R.; Canals, A.; Coll, M. DNA-binding drugs caught in action: the latest 3D pictures of drug-DNA complexes. *Dalton Transactions* **2009**, 399–414.

[190] Shulman, A.; Dwyer, F. P. In *Chelating agents and metal chelates*; Dwyer, F. P., Mellor, D. P., Eds.; Academic Press:

New York, 1964; Chapter 9, pp 383–441.

[191] Jennette, K. W.; Lippard, S. J.; Vassiliades, G. A.; Bauer, W. R. Metallointercalation reagents. 2-Hydroxyethanethiolato(2,2′,2′′-terpyridine)-platinum(II) monocation binds strongly to DNA by intercalation. *Proceedings of the National Academy of Sciences of the United States of America* **1974**, *71*, 3839–3843.

[192] Nordén, B.; Lincoln, P.; Akerman, B.; Tuite, E. DNA interactions with substitution-inert transition metal ion complexes. *Metal Ions in Biological Systems* **1996**, *33*, 177–252.

[193] Pyle, A. M.; Barton, J. K. In *Progress in Inorganic Chemistry*; Lippard, S. J., Ed.; Wiley Interscience: New York, 1990; Vol. 38; pp 413–475.

[194] Aminov, R. I. A brief history of the antibiotic era: lessons learned and challenges for the future. *Frontiers in Microbiology* **2010**, *1*, 134–134.

[195] Wong, E.; Giandomenico, C. M. Current status of platinum-based antitumor drugs. *Chemical Reviews* **1999**, *99*, 2451–2466.

[196] Komor, A. C.; Barton, J. K. The path for metal complexes to a DNA target. *Chemical Communications* **2013**, *49*, 3617–3630.

[197] Garbutcheon-Singh, K. B.; Grant, M. P.; Harper, B. W.; Krause-Heuer, A. M.; Manohar, M.; Orkey, N.; Aldrich-Wright, J. R. Transition metal based anticancer drugs. *Current Topics in Medicinal Chemistry* **2011**, *11*, 521–542.

[198] Dwyer, F. P.; Reid, I. K.; Shulman, A.; Laycock, G. M.; Dixson, S. The biological interactions of 1,10-phenanthroline and 2,2′-bipyridine hydrochlorides, quaternary salts and metal chelates and related compounds. *Australian Journal of Experimental Biology and Medical Science* **1969**, *47*, 203–218.

[199] Li, F.; Collins, J. G.; Keene, F. R. Ruthenium complexes as antimicrobial agents. *Chemical Society Reviews* **2015**, *44*, 2529–2542.

[200] Friedman, A. E.; Kumar, C. V.; Turro, N. J.; Barton, J. K. Luminescence of ruthenium(II) polypyridyls: evidence for intercalative binding to Z-DNA. *Nucleic Acids Research* **1991**, *19*, 2595–2602.

[201] O'Reilly, F.; Kelly, J.; Kirsch-De Mesmaeker, A. Interaction of a series of bimetallic ruthenium(II) bipyridyl complexes with DNA. *Chemical Communications* **1996**, 1013–1014.

[202] Buck, D. P.; Spillane, C. B.; Collins, J. G.; Keene, F. R. Binding of a dinuclear ruthenium(II) complex to the TAR region of the HIV-AIDS viral RNA. *Molecular BioSystems* **2008**, *4*, 851–854.

[203] Morgan, J. L.; Spillane, C. B.; Smith, J. A.; Buck, D. P.; Collins, J. G.; Keene, F. R. Dinuclear ruthenium(II) complexes with flexible bridges as non-duplex DNA binding agents. *Dalton Transactions* **2007**, 4333–4342.

[204] Li, X.; Shi, Z.; Wu, J.; Wu, J.; He, C.; Hao, X.; Duan, C. Lighting up metallohelices: from DNA binders to chemotherapy and photodynamic therapy. *Chemical Communications* **2020**, *56*, 7537–7548.

[205] Schoentjes, B.; Lehn, J.-M. Interaction of double-helical polynuclear copper(I) complexes with double-stranded DNA. *Helvetica Chimica Acta* **1995**, *78*, 1–12.

[206] Hannon, M. J.; Moreno, V.; Prieto, M. J.; Moldrheim, E.; Sletten, E.; Meistermann, I.; Isaac, C. J.; Sanders, K. J.; Rodger, A. Intramolecular DNA coiling mediated by a metallo-supramolecular cylinder. *Angewandte Chemie International Edition* **2001**, *40*, 880–884.

[207] Uerpmann, C.; Malina, J.; Pascu, M.; Clarkson, G. J.; Moreno, V.; Rodger, A.; Grandas, A.; Hannon, M. J. Design and DNA binding of an extended triple-stranded metallo-supramolecular cylinder. *Chemistry – A European Journal* **2005**, *11*, 1750–1756.

[208] Khalid, S.; Hannon, M. J.; Rodger, A.; Rodger, P. M. Simulations of DNA coiling around a synthetic supramolecular cylinder that binds in the DNA major groove. *Chemistry – A European Journal* **2006**, *12*, 3493–3506.

[209] Parajó, Y.; Malina, J.; Meistermann, I.; Clarkson, G. J.; Pascu, M.; Rodger, A.; Hannon, M. J.; Lincoln, P. Effect of bridging ligand structure on the thermal stability and DNA binding properties of iron(II) triple helicates. *Dalton Transactions* **2009**, 4868–4874.

[210] Qu, X.; Trent, J. O.; Fokt, I.; Priebe, W.; Chaires, J. B. Allosteric, chiral-selective drug binding to DNA. *Proceedings of the National Academy of Sciences of the United States of America* **2000**, *97*, 12032.

[211] Malina, J.; Hannon, M.; Brabec, V. Recognition of DNA three-way junctions by metallosupramolecular cylinders: gel electrophoresis studies. *Chemistry – A European Journal* **2007**, *13*, 3871–3877.

[212] Cerasino, L.; Hannon, M. J.; Sletten, E. DNA three-way junction with a dinuclear iron(II) supramolecular helicate at the center: a NMR structural study. *Inorganic Chemistry* **2007**, *46*, 6245–6251.

[213] Oleksi, A.; Blanco, A. G.; Boer, R.; Usón, I.; Aymamí, J.; Rodger, A.; Hannon, M. J.; Coll, M. Molecular recognition of a three-way DNA junction by a metallosupramolecular helicate. *Angewandte Chemie International Edition* **2006**, *45*, 1227–1231.

[214] Yu, H.; Wang, X.; Fu, M.; Ren, J.; Qu, X. Chiral metallo-supramolecular complexes selectively recognize human

telomeric G-quadruplex DNA. *Nucleic Acids Research* **2008**, *36*, 5695–5703.

[215] Nordén, B.; Kubista, M.; Kurucsev, T. Linear dichroism spectroscopy of nucleic acids. *Quarterly Reviews of Biophysics* **1992**, *25*, 51–170.

[216] Dafforn, T. R.; Rodger, A. Linear dichroism of biomolecules: which way is up? *Current Opinion in Structural Biology* **2004**, *14*, 541–546.

[217] Dalla Via, L.; Gia, O.; Marciani Magno, S.; Da Settimo, A.; Primofiore, G.; Da Settimo, F.; Simorini, F.; Marini, A. M. Dialkylaminoalkylindolonaphthyridines as potential antitumour agents: synthesis, cytotoxicity and DNA binding properties. *European Journal of Medicinal Chemistry* **2002**, *37*, 475–486.

[218] Patel, K. K.; Plummer, E. A.; Darwish, M.; Rodger, A.; Hannon, M. J. Aryl substituted ruthenium bis-terpyridine complexes: intercalation and groove binding with DNA. *Journal of Inorganic Biochemistry* **2002**, *91*, 220–229.

[219] Nguyen, B.; Hamelberg, D.; Bailly, C.; Colson, P.; Stanek, J.; Brun, R.; Neidle, S.; David Wilson, W. Characterization of a novel DNA minor-groove complex. *Biophysical Journal* **2004**, *86*, 1028–1041.

[220] Lee, S.; Lee, Y.-A.; Lee, H. M.; Lee, J. Y.; Kim, D. H.; Kim, S. K. Rotation of periphery methylpyridine of *meso*-tetrakis(*n*-*N*-methylpyridiniumyl)porphyrin (n = 2, 3, 4) and its selective binding to native and synthetic DNAs. *Biophysical Journal* **2002**, *83*, 371–381.

[221] Rodger, A.; Dorrington, G.; Ang, D. L. Linear dichroism as a probe of molecular structure and interactions. *Analyst* **2016**, *141*, 6490–6498.

[222] Pages, B. J.; Sakoff, J.; Gilbert, J.; Rodger, A.; Chmel, N. P.; Jones, N. C.; Kelly, S. M.; Ang, D. L.; Aldrich-Wright, J. R. Multifaceted studies of the DNA interactions and in vitro cytotoxicity of anticancer polyaromatic platinum(II) complexes. *Chemistry – A European Journal* **2016**, *22*, 8943–8954.

[223] McDonnell, U.; Hicks, M. R.; Hannon, M. J.; Rodger, A. DNA binding and bending by dinuclear complexes comprising ruthenium polypyridyl centres linked by a bis(pyridylimine) ligand. *Journal of Inorganic Biochemistry* **2008**, *102*, 2052–2059.

[224] McDonnell, U.; Kerchoffs, J. M.; Castineiras, R. P.; Hicks, M. R.; Hotze, A. C.; Hannon, M. J.; Rodger, A. Synthesis and cytotoxicity of dinuclear complexes containing ruthenium(II) bipyridyl units linked by a bis(pyridylimine) ligand. *Dalton Transactions* **2008**, 667–75.

[225] Bloch, F. The principle of nuclear induction. *Science* **1953**, *118*, 425.

[226] Purcell, E. M. Research in nuclear magnetism. *Science* **1953**, *118*, 431.

[227] Feigon, J.; Denny, W. A.; Leupin, W.; Kearns, D. R. Interactions of antitumor drugs with natural DNA: proton NMR study of binding mode and kinetics. *Journal of Medicinal Chemistry* **1984**, *27*, 450–465.

[228] Chen, S. M.; Leupin, W.; Rance, M.; Chazin, W. J. Two-dimensional NMR studies of d(GGTTAATGCGGT)·d(ACCGCATTAACC) complexed with the minor groove binding drug SN-6999. *Biochemistry* **1992**, *31*, 4406–4413.

[229] Buck, D. P.; Collins, J. G. In *Metallointercalators: Synthesis and Techniques to Probe Their Interactions with Biomolecules*; Aldrich-Wright, J., Ed.; Springer Vienna: Vienna, 2011; pp 143–157.

[230] Brodie, C. R.; Collins, J. G.; Aldrich-Wright, J. R. DNA binding and biological activity of some platinum(II) intercalating compounds containing methyl-substituted 1,10-phenanthrolines. *Dalton Transactions* **2004**, 1145–1152.

[231] Collins, J. G.; Sleeman, A. D.; Aldrich-Wright, J. R.; Greguric, I.; Hambley, T. W. A ^{1}H NMR study of the DNA binding of ruthenium(II) polypyridyl complexes. *Inorganic Chemistry* **1998**, *37*, 3133–3141.

[232] Hu, S.; Weisz, K.; James, T. L.; Shafer, R. H. ^{1}H-NMR studies on d(GCTTAAGC)$_2$ and its complex with berenil. *European Journal of Biochemistry* **1992**, *204*, 31–38.

[233] Erkkila, K. E.; Odom, D. T.; Barton, J. K. Recognition and reaction of metallointercalators with DNA. *Chemical Reviews* **1999**, *99*, 2777–2796.

[234] Metcalfe, C.; Thomas, J. A. Kinetically inert transition metal complexes that reversibly bind to DNA. *Chemical Society Reviews* **2003**, *32*, 215–224.

[235] Moldrheim, E.; Hannon, M. J.; Meistermann, I.; Rodger, A.; Sletten, E. Interaction between a DNA oligonucleotide and a dinuclear iron(II) supramolecular cylinder; an NMR and molecular dynamics study. *Journal of Biological Inorganic Chemistry* **2002**, *7*, 770–780.

[236] Streisinger, G.; Owen, J. Mechanisms of spontaneous and induced frameshift mutation in bacteriophage T4. *Genetics* **1985**, *109*, 633–659.

[237] Hoffmann, G. R.; Fuchs, R. P. Mechanisms of frameshift mutations: insight from aromatic amines. *Chemical Research in Toxicology* **1997**, *10*, 347–59.

[238] Strauss, B. S. Frameshift mutation, microsatellites and mismatch repair. *Mutation Research* **1999**, *437*, 195–203.

[239] Samson, M.; Libert, F.; Doranz, B. J.; Rucker, J.; Liesnard, C.; Farber, C. M.; Saragosti, S.; Lapoumeroulie, C.;

Cognaux, J.; Forceille, C.; Muyldermans, G.; Verhofstede, C.; Burtonboy, G.; Georges, M.; Imai, T.; Rana, S.; Yi, Y.; Smyth, R. J.; Collman, R. G.; Doms, R. W.; Vassart, G.; Parmentier, M. Resistance to HIV-1 infection in caucasian individuals bearing mutant alleles of the CCR-5 chemokine receptor gene. *Nature* **1996**, *382*, 722–5.

[240] Scholes, A. G. M.; Field, J. K. In *Oral pathology: actual diagnostic and prognostic aspects*; Seifert, G., Ed.; Springer Berlin Heidelberg: Berlin, Heidelberg, 1996; pp 201–222.

[241] Li, J.; Yen, C.; Liaw, D.; Podsypanina, K.; Bose, S.; Wang, S. I.; Puc, J.; Miliaresis, C.; Rodgers, L.; McCombie, R.; Bigner, S. H.; Giovanella, B. C.; Ittmann, M.; Tycko, B.; Hibshoosh, H.; Wigler, M. H.; Parsons, R. PTEN, a putative protein tyrosine phosphatase gene mutated in human brain, breast, and prostate cancer. *Science* **1997**, *275*, 1943–7.

[242] Austin, M. A.; Hutter, C. M.; Zimmern, R. L.; Humphries, S. E. Genetic causes of monogenic heterozygous familial hypercholesterolemia: a HuGE prevalence review. *American Journal of Epidemiology* **2004**, *160*, 407–20.

[243] Patterson, B. T.; Collins, J. G.; Foley, F. M.; Keene, F. R. Dinuclear ruthenium(II) complexes as probes for DNA bulge sites. *Journal of the Chemical Society, Dalton Transactions* **2002**, 4343–4350.

[244] Patel, D. J.; Shapiro, L.; Hare, D. Sequence-dependent conformation of DNA duplexes. The AATT segment of the d(G-G-A-A-T-T-C-C) duplex in aqueous solution. *Journal of Biological Chemistry* **1986**, *261*, 1223–1229.

[245] Scheek, R. M.; Boelens, R.; Russo, N.; Van Boom, J. H.; Kaptein, R. Sequential resonance assignments in proton NMR spectra of oligonucleotides by two-dimensional NMR spectroscopy. *Biochemistry* **1984**, *23*, 1371–1376.

[246] Feigon, J.; Leupin, W.; Denny, W. A.; Kearns, D. R. Two-dimensional proton nuclear magnetic resonance investigation of the synthetic deoxyribonucleic acid decamer d(ATATCGATAT). *Biochemistry* **1983**, *22*, 5943–5951.

[247] Patel, D. J.; Pardi, A.; Itakura, K. DNA conformation, dynamics, and interactions in solution. *Science* **1982**, *216*, 581.

[248] Feigon, J.; Wright, J. M.; Leupin, W.; Denny, W. A.; Kearns, D. R. Use of two-dimensional NMR in the study of a double-stranded DNA decamer. *Journal of the American Chemical Society* **1982**, *104*, 5540–5541.

[249] Smith, J. A.; Collins, J. G.; Patterson, B. T.; Keene, F. R. Total enantioselectivity in the DNA binding of the dinuclear ruthenium(II) complex $[\{Ru(Me_2bpy)_2\}_2(\mu\text{-bpm})]^{4+}$ bpm = 2,2′-bipyrimidine; Me_2bpy = 4,4′-dimethyl-2,2′-bipyridine. *Dalton Transactions* **2004**, 1277–1283.

[250] Kalnik, M. W.; Norman, D. G.; Swann, P. F.; Patel, D. J. Conformation of adenosine bulge-containing deoxytridecanucleotide duplexes in solution: extra adenosine stacks into duplex independent of flanking sequence and temperature. *Journal of Biological Chemistry* **1989**, *264*, 3702–3712.

[251] Serr, B. R.; Andersen, K. A.; Elliott, C. M.; Anderson, O. P. A triply-bridged dinuclear tris(bipyridine)iron(II) complex: synthesis and electrochemical and structural studies. *Inorganic Chemistry* **1988**, *27*, 4499–4504.

[252] Elliott, C. M.; Derr, D. L.; Ferrere, S.; Newton, M. D.; Liu, Y. P. Donor/acceptor coupling in mixed-valent dinuclear iron polypyridyl complexes: experimental and theoretical considerations. *Journal of the American Chemical Society* **1996**, *118*, 5221–5228.

[253] Ferrere, S.; Elliott, C. M. Electrochemical studies of structurally related triply-bridged dinuclear tris(bipyridine)iron(II) complexes: an electrostatic model for site-site interaction. *Inorganic Chemistry* **1995**, *34*, 5818–5824.

[254] Williams, A. F.; Piguet, C.; Bernardinelli, G. A self-assembling triple-helical Co^{II}_2 complex: synthesis and structure. *Angewandte Chemie International Edition* **1991**, *30*, 1490–1492.

[255] Grillo, V. A.; Seddon, E. J.; Grant, C. M.; Aromí, G.; Bollinger, J. C.; Folting, K.; Christou, G. Bis(β-diketonate) ligands for the synthesis of bimetallic complexes of Ti^{III}, V^{III}, Mn^{III} and Fe^{III} with a triple-helix structure. *Chemical Communications* **1997**, 1561–1562.

[256] Carrano, C. J.; Raymond, K. N. Coordination chemistry of microbial iron transport compounds. 10. Characterization of the complexes of rhodotorulic acid, a dihydroxamate siderophore. *Journal of the American Chemical Society* **1978**, *100*, 5371–5374.

[257] Hannon, M. J.; Painting, C. L.; Alcock, N. W. A metallo-supramolecular double-helix containing a major and a minor groove. *Chemical Communications* **1999**, 2023–2024.

[258] Childs, L. J.; Alcock, N. W.; Hannon, M. J. Assembly of nano-scale circular supramolecular arrays through π-π aggregation of arc-shaped helicate units. *Angewandte Chemie International Edition* **2001**, *40*, 1079–1081.

[259] Lavalette, A.; Hamblin, J.; Marsh, A.; Haddleton, D. M.; Hannon, M. J. Interfacing supramolecular and macromolecular chemistry: metallo-supramolecular triple-helicates incorporated into polymer networks. *Chemical Communications* **2002**, 3040–3041.

[260] Hamblin, J.; Jackson, A.; Alcock, N. W.; Hannon, M. J. Triple helicates and planar dimers arising from silver(I) coordination to directly linked bis-pyridylimine ligands. *Journal of the Chemical Society, Dalton Transactions* **2002**, 1635–1641.

[261] Hamblin, J.; Childs, L. J.; Alcock, N. W.; Hannon, M. J. Directed one-pot syntheses of enantiopure dinuclear silver(I) and copper(I) metallo-supramolecular double helicates. *Journal of the Chemical Society, Dalton Transactions* **2002**, 164–169.

[262] Tuna, F.; Hamblin, J.; Clarkson, G.; Errington, W.; Alcock, N. W.; Hannon, M. J. Helical (isotactic) and syndiotactic silver(I) metallo-supramolecular coordination polymers assembled from a readily prepared bis-pyridylimine ligand containing a 1,5-naphthalene spacer. *Chemistry – A European Journal* **2002**, *8*, 4957–4964.

[263] Childs, L. J.; Alcock, N. W.; Hannon, M. J. Assembly of a nanoscale chiral ball through supramolecular aggregation of bowl-shaped triangular helicates. *Angewandte Chemie International Edition* **2002**, *41*, 4244–4247.

[264] Lavalette, A.; Tuna, F.; Clarkson, G.; Alcock, N. W.; Hannon, M. J. Aggregation of metallo-supramolecular architectures by metallo-assembled hydrogen bonding sites. *Chemical Communications* **2003**, 2666–2667.

[265] Tuna, F.; Lees, M. R.; Clarkson, G. J.; Hannon, M. J. Readily prepared metallo-supramolecular triple helicates designed to exhibit spin-crossover behaviour. *Chemistry – A European Journal* **2004**, *10*, 5737–5750.

[266] Iqbal, P.; Mayanditheuar, M.; Childs, L. J.; Hannon, M. J.; Spencer, N.; Ashton, P. R.; Preece, J. A. Preparation of novel banana-shaped triple helical liquid crystals by metal coordination. *Materials* **2009**, *2*, 146–168.

[267] Larson, S. L.; Hendrickson, S. M.; Ferrere, S.; Derr, D. L.; Elliott, C. M. Energy transfer in rigidly-linked heterodinuclear Ru(II)/Fe(II) polypyridyl complexes: distance and linkage dependence. *Journal of the American Chemical Society* **1995**, *117*, 9381–9381.

[268] Greene, D. L.; Mingos, D. M. P. Application of microwave dielectric loss heating effects for the rapid and convenient synthesis of ruthenium(II) polypyridine complexes. *Transition Metal Chemistry* **1991**, *16*, 71–72.

[269] Matsumura-Inoue, T.; Tanabe, M.; Minami, T.; Ohashi, T. A remarkably rapid synthesis of ruthenium(II) polypyridine complexes by microwave irradiation. *Chemistry Letters* **1994**, *23*, 2443–2446.

[270] Jandrasics, E.; Kolp, B.; Wolny, J. A.; von Zelewsky, A. The stereochemistry of the oxidation of diamines and of the reduction of diimines in the coordination sphere of ruthenium(II). *Inorganica Chimica Acta* **1998**, *272*, 153–161.

[271] Rostovtsev, V. V.; Green, L. G.; Fokin, V. V.; Sharpless, K. B. A stepwise huisgen cycloaddition process: copper(I)-catalyzed regioselective "ligation" of azides and terminal alkynes. *Angewandte Chemie International Edition* **2002**, *41*, 2596–2599.

[272] Tornøe, C. W.; Christensen, C.; Meldal, M. Peptidotriazoles on solid phase: [1,2,3]-triazoles by regiospecific copper(I)-catalyzed 1,2-dipolar cycloadditions of terminal alkynes to azides. *Journal of Organic Chemistry* **2002**, *67*, 3057–3064.

[273] Wu, P.; Fokin, V. V. Catalytic azide-alkyne cycloaddition: reactivity and applications. *Aldrichimica Acta* **2007**, *40*, 7–17.

[274] Meldal, M.; Tornøe, C. W. Cu-catalyzed azide-alkyne cycloaddition. *Chemical Reviews* **2008**, *108*, 2952–3015.

[275] Liang, L.; Astruc, D. The copper(I)-catalyzed alkyne-azide cycloaddition (CuAAC) "click" reaction and its applications. An overview. *Coordination Chemistry Reviews* **2011**, *255*, 2933–2945.

[276] Zhu, L.; Brassard, C. J.; Zhang, X.; Guha, P. M.; Clark, R. J. On the mechanism of copper(I)-catalyzed azide–alkyne cycloaddition. *The Chemical Record* **2016**, *16*, 1501–1517.

[277] Crowley, J. D.; Goldup, S. M.; Lee, A.-L.; Leigh, D. A.; McBurney, R. T. Active metal template synthesis of rotaxanes, catenanes and molecular shuttles. *Chemical Society Reviews* **2009**, *38*, 1530–1541.

[278] Crowley, J. D.; McMorran, D. A. In *Click Triazoles*; Košmrlj, J., Ed.; Springer Berlin Heidelberg: Berlin, Heidelberg, 2012; pp 31–83.

[279] van Hilst, Q. V. C.; Lagesse, N. R.; Preston, D.; Crowley, J. D. Functional metal complexes from CuAAC "click" bidentate and tridentate pyridyl-1,2,3-triazole ligands. *Dalton Transactions* **2018**, *47*, 997–1002.

[280] Gower, M. L.; Crowley, J. D. Self-assembly of silver(I) metallomacrocycles using unsupported 1,4-substituted-1,2,3-triazole "click" ligands. *Dalton Transactions* **2010**, *39*, 2371–2378.

[281] Crowley, J. D.; Lee, A.-L.; Kilpin, K. J. 1,3,4-Trisubstituted-1,2,3-triazol-5-ylidene 'click' carbene ligands: synthesis, catalysis and self-assembly. *Australian Journal of Chemistry* **2011**, *64*, 1118–1132.

[282] Kilpin, K. J.; Paul, U. S. D.; Lee, A.-L.; Crowley, J. D. Gold(I) "click" 1,2,3-triazolylidenes: synthesis, self-assembly and catalysis. *Chemical Communications* **2011**, *47*, 328–330.

[283] Preston, D.; Tucker, R. A.; Garden, A. L.; Crowley, J. D. Heterometallic $[M_nPt_n(L)_{2n}]^{x+}$ macrocycles from dichloromethane-derived bis-2-pyridyl-1,2,3-triazole ligands. *Inorganic Chemistry* **2016**, *55*, 8928–34.

[284] Crowley, J. D.; Gavey, E. L. Use of di-1,4-substituted-1,2,3-triazole "click" ligands to self-assemble dipalladium(II) coordinatively saturated, quadruply stranded helicate cages. *Dalton Transactions* **2010**, *39*, 4035–4037.

[285] Scott, S. Ø.; Gavey, E. L.; Lind, S. J.; Gordon, K. C.; Crowley, J. D. Self-assembled palladium(II) "click" cages: synthesis, structural modification and stability. *Dalton Transactions* **2011**, *40*, 12117–12124.

[286] Crowley, J. D.; Bandeen, P. H. A multicomponent CuAAC "click" approach to a library of hybrid polydentate 2-pyridyl-1,2,3-triazole ligands: new building blocks for the generation of metallosupramolecular architectures. *Dalton Transactions* **2010**, *39*, 612–623.

[287] Vasdev, R. A.; Preston, D.; Scottwell, S. Ø.; Brooks, H. J.; Crowley, J. D.; Schramm, M. P. Oxidatively locked

$[Co_2L_3]^{6+}$ cylinders derived from bis(bidentate) 2-pyridyl-1,2,3-triazole "click" ligands: synthesis, stability, and antimicrobial studies. *Molecules* **2016**, *21*.

[288] Kumar, S. V.; Scottwell, S. Ø.; Waugh, E.; McAdam, C. J.; Hanton, L. R.; Brooks, H. J.; Crowley, J. D. Antimicrobial properties of tris(homoleptic) ruthenium(II) 2-pyridyl-1,2,3-triazole "click" complexes against pathogenic bacteria, including methicillin-resistant *Staphylococcus aureus* (MRSA). *Inorganic Chemistry* **2016**, *55*, 9767–9777.

[289] Ross, D. A.; Preston, D.; Crowley, J. D. Self-assembly with 2,6-bis(1-(pyridin-4-ylmethyl)-1*H*-1,2,3-triazol-4-yl)pyridine: silver(I) and iron(II) complexes. *Molecules* **2017**, *22*.

[290] Vellas, S. K.; Lewis, J. E. M.; Shankar, M.; Sagatova, A.; Tyndall, J. D. A.; Monk, B. C.; Fitchett, C. M.; Hanton, L. R.; Crowley, J. D. $[Fe_2L_3]^{4+}$ cylinders derived from bis(bidentate) 2-pyridyl-1,2,3-triazole "click" ligands: synthesis, structures and exploration of biological activity. *Molecules* **2013**, *18*, 6383–6407.

[291] Wu, N.; Melan, C. F. C.; Stevenson, K. A.; Fleischel, O.; Guo, H.; Habib, F.; Holmberg, R. J.; Murugesu, M.; Mosey, N. J.; Nierengarten, H.; Petitjean, A. Systematic study of the synthesis and coordination of 2-(1,2,3-triazol-4-yl)-pyridine to Fe(II), Ni(II) and Zn(II); ion-induced folding into helicates, mesocates and larger architectures, and application to magnetism and self-selection. *Dalton Transactions* **2015**, *44*, 14991–15005.

[292] Albrecht, M. How do they know? Influencing the relative stereochemistry of the complex units of dinuclear triple-stranded helicate-type complexes. *Chemistry – A European Journal* **2000**, *6*, 3485–3489.

[293] Stevenson, K. A.; Melan, C. F. C.; Fleischel, O.; Wang, R. Y.; Petitjean, A. Solid-state self-assembly of triazolylpyridine-based helicates and mesocate: control of the metal-metal distances. *Crystal Growth & Design* **2012**, *12*, 5169–5173.

[294] Atobe, S.; Sonoda, M.; Suzuki, Y.; Yamamoto, T.; Masuno, H.; Shinohara, H.; Ogawa, A. Palladium-catalyzed oxidative homocoupling reaction of terminal acetylenes using *trans*-bidentatable 1-(2-pyridylethynyl)-2-(2-thienylethynyl)benzene. *Research on Chemical Intermediates* **2013**, *39*, 359–370.

[295] McCaffery, A. J.; Mason, S. F.; Norman, B. J. Optical rotatory power of co-ordination compounds. Part XII. Spectroscopic and configurational assignments for the tris-bipyridyl and -phenanthroline complexes of the di- and tri-valent iron-group metal ions. *Journal of the Chemical Society A: Inorganic, Physical, Theoretical* **1969**, 1428–1441.

[296] Maglic, R., J. B. Lavendomme MoloVol: an easy-to-use program to calculate various volumes and surface areas of chemical structures and identify cavities. *ChemRxiv* **2021**, *Preprint*.

[297] Kersting, B.; Meyer, M.; Powers, R. E.; Raymond, K. N. Dinuclear catecholate helicates: their inversion mechanism. *Journal of the American Chemical Society* **1996**, *118*, 7221–7222.

[298] Meyer, M.; Kersting, B.; Powers, R. E.; Raymond, K. N. Rearrangement reactions in dinuclear triple helicates. *Inorganic Chemistry* **1997**, *36*, 5179–5191.

[299] Bailar, J. C. Some problems in the stereochemistry of coordination compounds: Introductory lecture. *Journal of Inorganic and Nuclear Chemistry* **1958**, *8*, 165–175.

[300] Ray, P.; Dutt, N. Kinetics and mechanism of racemization of optically active cobaltic trisbiguanide complex. *Journal of the Indian Chemical Society* **1943**, *20*, 81–92.

[301] Albrecht, M.; Janser, I.; Houjou, H.; Fröhlich, R. Long-range stereocontrol in the self-assembly of two-nanometer-dimensioned triple-stranded dinuclear helicates. *Chemistry – A European Journal* **2004**, *10*, 2839–2850.

[302] Riddell, I. A.; Hristova, Y. R.; Clegg, J. K.; Wood, C. S.; Breiner, B.; Nitschke, J. R. Five discrete multinuclear metal-organic assemblies from one ligand: deciphering the effects of different templates. *Journal of the American Chemical Society* **2013**, *135*, 2723–2733.

[303] Scherer, M.; Caulder, D. L.; Johnson, D. W.; Raymond, K. N. Triple helicate-tetrahedral cluster interconversion controlled by host-guest interactions. *Angewandte Chemie International Edition* **1999**, *38*, 1587–1592.

[304] Baxter, P. N. W.; Lehn, J.-M.; Baum, G.; Fenske, D. Self-assembly and structure of interconverting multinuclear inorganic arrays: a [4x5]-AgI_{20} grid and an AgI_{10} quadruple helicate. *Chemistry – A European Journal* **2000**, *6*, 4510–4517.

[305] Li, B.; Zhang, W.; Lu, S.; Zheng, B.; Zhang, D.; Li, A.; Li, X.; Yang, X.-J.; Wu, B. Multiple transformations among anion-based $A_{2n}L_{3n}$ assemblies: bicapped trigonal antiprism A_8L_{12},tetrahedron A_4L_6, and triple helicate A_2L_3 (A = anion). *Journal of the American Chemical Society* **2020**, *142*, 21160–21168.

[306] Roberts, D. A.; Pilgrim, B. S.; Sirvinskaite, G.; Ronson, T. K.; Nitschke, J. R. Covalent post-assembly modification triggers multiple structural transformations of a tetrazine-edged Fe_4L_6 tetrahedron. *Journal of the American Chemical Society* **2018**, *140*, 9616–9623.

[307] Burke, M. J.; Nichol, G. S.; Lusby, P. J. Orthogonal selection and fixing of coordination self-assembly pathways for robust metallo-organic ensemble construction. *Journal of the American Chemical Society* **2016**, *138*, 9308–9315.

[308] Siddique, R. G.; Arachchige, K. S. A.; Al-Fayaad, H. A.; Brock, A. J.; Micallef, A. S.; Luis, E. T.; Thoburn, J. D.; McMurtrie, J. C.; Clegg, J. K. The kinetics and mechanism of interconversion within a system of $[Fe_2L_3]^{4+}$ helicates and $[Fe_4L_6]^{8+}$ cages. *Chemical Communications* **2021**, *57*, 4918–4921.

[309] Bai, X.; Jia, C.; Zhao, Y.; Yang, D.; Wang, S.-C.; Li, A.; Chan, Y.-T.; Wang, Y.-Y.; Yang, X.-J.; Wu, B. Peripheral templation-modulated interconversion between an A_4L_6 tetrahedral anion cage and A_2L_3 triple helicate with guest capture/release. *Angewandte Chemie International Edition* **2018**, *57*, 1851–1855.

[310] Ousaka, N.; Shimizu, K.; Suzuki, Y.; Iwata, T.; Itakura, M.; Taura, D.; Iida, H.; Furusho, Y.; Mori, T.; Yashima, E. Spiroborate-based double-stranded helicates: *meso*-to-*racemo* isomerization and ion-triggered springlike motion of the *racemo*-helicate. *Journal of the American Chemical Society* **2018**, *140*, 17027–17039.

[311] Goetz, S.; Kruger, P. E. A new twist in anion binding: metallo-helicate hosts for anionic guests. *Dalton Transactions* **2006**, 1277–1284.

[312] Cui, F. J.; Li, S. G.; Jia, C. D.; Mathieson, J. S.; Cronin, L.; Yang, X. J.; Wu, B. Anion-dependent formation of helicates versus mesocates of triple-stranded M_2L_3 (M = Fe^{2+}, Cu^{2+}) complexes. *Inorganic Chemistry* **2012**, *51*, 179–187.

[313] Zhang, Z.; Dolphin, D. Synthesis of triple-stranded complexes using bis(dipyrromethene) ligands. *Inorganic Chemistry* **2010**, *49*, 11550–11555.

[314] Van Houten, J.; Watts, R. J. Photochemistry of tris(2,2′-bipyridyl)ruthenium(II) in aqueous solutions. *Inorganic Chemistry* **1978**, *17*, 3381–3385.

[315] Gleria, M.; Minto, F.; Beggiato, G.; Bortolus, P. Photochemistry of tris(2,2′-bipyridine)ruthenium(II) in chlorinated solvents. *Journal of the Chemical Society, Chemical Communications* **1978**, 285a–285a.

[316] Durham, B.; Caspar, J. V.; Nagle, J. K.; Meyer, T. J. Photochemistry of $Ru(bpy)_3^{2+}$. *Journal of the American Chemical Society* **1982**, *104*, 4803–4810.

[317] Yamagishi, A.; Naing, K.; Goto, Y.; Taniguchi, M.; Takahashi, M. Formation of optically active $[Ru(bipy)_2Cl_2]$ (bipy = 2,2′-bipyridyl) by photodissociation of $[Ru(bipy)_3]Cl_2$ in dichloromethane. *Journal of the Chemical Society, Dalton Transactions* **1994**, 2085–2089.

[318] Scattergood, P. A.; Khushnood, U.; Tariq, A.; Cooke, D. J.; Rice, C. R.; Elliott, P. I. P. Photochemistry of $[Ru(pytz)(btz)_2]^{2+}$ and characterization of a κ1-btz ligand-loss intermediate. *Inorganic Chemistry* **2016**, *55*, 7787–7796.

[319] Dixon, I. M.; Heully, J.-L.; Alary, F.; Elliott, P. I. P. Theoretical illumination of highly original photoreactive ^{3}MC states and the mechanism of the photochemistry of Ru(II) tris(bidentate) complexes. *Physical Chemistry Chemical Physics* **2017**, *19*, 27765–27778.

[320] Crlikova, H.; Malina, J.; Novohradsky, V.; Kostrhunova, H.; Vasdev, R. A. S.; Crowley, J. D.; Kasparkova, J.; Brabec, V. Antiproliferative activity and associated DNA interactions of $[Co_2L_3]^{6+}$ cylinders derived from bis(bidentate) 2-pyridyl-1,2,3-triazole ligands. *Organometallics* **2020**, *39*, 1448–1455.

[321] Debata, N. B.; Tripathy, D.; Sahoo, H. S. Development of coordination driven self-assembled discrete spherical ensembles. *Coordination Chemistry Reviews* **2019**, *387*, 273–298.

[322] Stang, P. J.; Olenyuk, B. Self-assembly, symmetry, and molecular architecture: coordination as the motif in the rational design of supramolecular metallacyclic polygons and polyhedra. *Accounts of Chemical Research* **1997**, *30*, 502–518.

[323] Seidel, S. R.; Stang, P. J. High-symmetry coordination cages via self-assembly. *Accounts of Chemical Research* **2002**, *35*, 972–983.

[324] Harris, K.; Fujita, D.; Fujita, M. Giant hollow M_nL_{2n} spherical complexes: structure, functionalisation and applications. *Chemical Communications* **2013**, *49*, 6703–6712.

[325] Fujita, M.; Tominaga, M.; Hori, A.; Therrien, B. Coordination assemblies from a Pd(II)-cornered square complex. *Accounts of Chemical Research* **2005**, *38*, 369–378.

[326] Caulder, D. L.; Raymond, K. N. Supermolecules by design. *Accounts of Chemical Research* **1999**, *32*, 975–982.

[327] Eryazici, I.; Moorefield, C. N.; Newkome, G. R. Square-planar Pd(II), Pt(II), and Au(III) terpyridine complexes: their syntheses, physical properties, supramolecular constructs, and biomedical activities. *Chemical Reviews* **2008**, *108*, 1834–1895.

[328] Nitschke, J. R. Construction, substitution, and sorting of metallo-organic structures via subcomponent self-assembly. *Accounts of Chemical Research* **2007**, *40*, 103–112.

[329] Smulders, M. M. J.; Riddell, I. A.; Browne, C.; Nitschke, J. R. Building on architectural principles for three-dimensional metallosupramolecular construction. *Chemical Society Reviews* **2013**, *42*, 1728–1754.

[330] Gianneschi, N. C.; Masar, M. S.; Mirkin, C. A. Development of a coordination chemistry-based approach for functional supramolecular structures. *Accounts of Chemical Research* **2005**, *38*, 825–837.

[331] You, C.-C.; Würthner, F. Self-assembly of ferrocene-functionalized perylene bisimide bridging ligands with Pt(II) corner to electrochemically active molecular squares. *Journal of the American Chemical Society* **2003**, *125*, 9716–9725.

[332] Ward, M. D.; McCleverty, J. A.; Jeffery, J. C. Coordination and supramolecular chemistry of multinucleating ligands

containing two or more pyrazolyl-pyridine 'arms'. *Coordination Chemistry Reviews* **2001**, *222*, 251–272.

[333] McMorran, D. A.; Steel, P. J. The first coordinatively saturated, quadruply stranded helicate and its encapsulation of a hexafluorophosphate anion. *Angewandte Chemie International Edition* **1998**, *37*, 3295–3297.

[334] Rizzuto, F. J.; von Krbek, L. K. S.; Nitschke, J. R. Strategies for binding multiple guests in metal-organic cages. *Nature Reviews Chemistry* **2019**, *3*, 204–222.

[335] Yoshizawa, M.; Klosterman, J. K.; Fujita, M. Functional molecular flasks: new properties and reactions within discrete, self-assembled hosts. *Angewandte Chemie International Edition* **2009**, *48*, 3418–38.

[336] Wang, Q.-Q.; Gonell, S.; Leenders, S. H. A. M.; Dürr, M.; Ivanović-BurmazoviĆ, I.; Reek, J. N. H. Self-assembled nanospheres with multiple endohedral binding sites pre-organize catalysts and substrates for highly efficient reactions. *Nature Chemistry* **2016**, *8*, 225–230.

[337] Sinha, I.; Mukherjee, P. S. Chemical transformations in confined space of coordination architectures. *Inorg Chem* **2018**, *57*, 4205–4221.

[338] Fiedler, D.; Bergman, R. G.; Raymond, K. N. Stabilization of reactive organometallic intermediates inside a self-assembled nanoscale host. *Angewandte Chemie International Edition* **2006**, *45*, 745–748.

[339] Vardhan, H.; Verpoort, F. Metal-organic polyhedra: catalysis and reactive intermediates. *Advanced Synthesis & Catalysis* **2015**, *357*, 1351–1368.

[340] Galan, A.; Ballester, P. Stabilization of reactive species by supramolecular encapsulation. *Chemical Society Reviews* **2016**, *45*, 1720–1737.

[341] Zhang, D.; Ronson, T. K.; Zou, Y.-Q.; Nitschke, J. R. Metal-organic cages for molecular separations. *Nature Reviews Chemistry* **2021**, *5*, 168–182.

[342] Zhao, D.; Tan, S.; Yuan, D.; Lu, W.; Rezenom, Y. H.; Jiang, H.; Wang, L.-Q.; Zhou, H.-C. Surface functionalization of porous coordination nanocages via click chemistry and their application in drug delivery. *Advanced Materials* **2011**, *23*, 90–93.

[343] Casini, A.; Woods, B.; Wenzel, M. The promise of self-assembled 3D supramolecular coordination complexes for biomedical applications. *Inorg Chem* **2017**, *56*, 14715–14729.

[344] Schmidt, A.; Molano, V.; Hollering, M.; Pöthig, A.; Casini, A.; Kühn, F. E. Evaluation of new palladium cages as potential delivery systems for the anticancer drug cisplatin. *Chemistry – A European Journal* **2016**, *22*, 2253–2256.

[345] Prier, C. K.; Rankic, D. A.; MacMillan, D. W. C. Visible light photoredox catalysis with transition metal complexes: applications in organic synthesis. *Chemical Reviews* **2013**, *113*, 5322–5363.

[346] Grätzel, M. Dye-sensitized solar cells. *Journal of Photochemistry and Photobiology C: Photochemistry Reviews* **2003**, *4*, 145–153.

[347] Blakemore, J. D.; Crabtree, R. H.; Brudvig, G. W. Molecular catalysts for water oxidation. *Chemical Reviews* **2015**, *115*, 12974–13005.

[348] Ozawa, H.; Sakai, K. Photo-hydrogen-evolving molecular devices driving visible-light-induced water reduction into molecular hydrogen: structure-activity relationship and reaction mechanism. *Chemical Communications* **2011**, *47*, 2227–2242.

[349] Parent, A. R.; Sakai, K. Progress in base-metal water oxidation catalysis. *ChemSusChem* **2014**, *7*, 2070–2080.

[350] Zeng, L.; Gupta, P.; Chen, Y.; Wang, E.; Ji, L.; Chao, H.; Chen, Z.-S. The development of anticancer ruthenium(II) complexes: from single molecule compounds to nanomaterials. *Chemical Society Reviews* **2017**, *46*, 5771–5804.

[351] Mari, C.; Pierroz, V.; Ferrari, S.; Gasser, G. Combination of Ru(II) complexes and light: new frontiers in cancer therapy. *Chemical Science* **2015**, *6*, 2660–2686.

[352] Yang, M.; Bierbach, U. Metal-containing pharmacophores in molecularly targeted anticancer therapies and diagnostics. *European Journal of Inorganic Chemistry* **2017**, *2017*, 1561–1572.

[353] Barry, N. P. E.; Sadler, P. J. Exploration of the medical periodic table: towards new targets. *Chemical Communications* **2013**, *49*, 5106–5131.

[354] Sun, W.; Li, S.; Hüpler, B.; Liu, J.; Jin, S.; Steffen, W.; Schubert, U. S.; Butt, H.-J.; Liang, X.-J.; Wu, S. An amphiphilic ruthenium polymetallodrug for combined photodynamic therapy and photochemotherapy in vivo. *Advanced Materials* **2017**, *29*, 1603702.

[355] Sun, Y.; Chen, Z.; Puodziukynaite, E.; Jenkins, D. M.; Reynolds, J. R.; Schanze, K. S. Light harvesting arrays of polypyridine ruthenium(II) chromophores prepared by reversible addition-fragmentation chain transfer polymerization. *Macromolecules* **2012**, *45*, 2632–2642.

[356] Friebe, C.; Görls, H.; Jäger, M.; Schubert, U. S. Linear metallopolymers from ruthenium(II)-2,6-di(quinolin-8-yl)pyridine complexes by electropolymerization - formation of redox-stable and emissive films. *European Journal of Inorganic Chemistry* **2013**, *2013*, 4191–4202.

[357] Zhang, W.; Li, B.; Ma, H.; Zhang, L.; Guan, Y.; Zhang, Y.; Zhang, X.; Jing, P.; Yue, S. Combining ruthenium(II) complexes with metal-organic frameworks to realize effective two-photon absorption for singlet oxygen generation. *ACS Applied Materials & Interfaces* **2016**, *8*, 21465–71.

[358] Chen, R.; Zhang, J.; Chelora, J.; Xiong, Y.; Kershaw, S. V.; Li, K. F.; Lo, P.-K.; Cheah, K. W.; Rogach, A. L.; Zapien, J. A.; Lee, C.-S. Ruthenium(II) complex incorporated UiO-67 metal-organic framework nanoparticles for enhanced two-photon fluorescence imaging and photodynamic cancer therapy. *ACS Applied Materials & Interfaces* **2017**, *9*, 5699–5708.

[359] Zhang, S.; Li, L.; Zhao, S.; Sun, Z.; Luo, J. Construction of interpenetrated ruthenium metal-organic frameworks as stable photocatalysts for CO_2 reduction. *Inorganic Chemistry* **2015**, *54*, 8375–8379.

[360] Li, K.; Zhang, L.-Y.; Yan, C.; Wei, S.-C.; Pan, M.; Zhang, L.; Su, C.-Y. Stepwise assembly of $Pd_6(RuL_3)_8$ nanoscale rhombododecahedral metal-organic cages via metalloligand strategy for guest trapping and protection. *Journal of the American Chemical Society* **2014**, *136*, 4456–4459.

[361] Wu, K.; Li, K.; Hou, Y.-J.; Pan, M.; Zhang, L.-Y.; Chen, L.; Su, C.-Y. Homochiral D_4-symmetric metal-organic cages from stereogenic Ru(II) metalloligands for effective enantioseparation of atropisomeric molecules. *Nature Communications* **2016**, *7*, 10487.

[362] Guo, J.; Xu, Y.-W.; Li, K.; Xiao, L.-M.; Chen, S.; Wu, K.; Chen, X.-D.; Fan, Y.-Z.; Liu, J.-M.; Su, C.-Y. Regio- and enantioselective photodimerization within the confined space of a homochiral ruthenium/palladium heterometallic coordination cage. *Angewandte Chemie International Edition* **2017**, *56*, 3852–3856.

[363] Yang, J.; Bhadbhade, M.; Donald, W. A.; Iranmanesh, H.; Moore, E. G.; Yan, H.; Beves, J. E. Self-assembled supramolecular cages containing ruthenium(II) polypyridyl complexes. *Chemical Communications* **2015**, *51*, 4465–4468.

[364] Shen, C.; Kennedy, A. D. W.; Donald, W. A.; Torres, A. M.; Price, W. S.; Beves, J. E. Self-assembled supramolecular cages containing dinuclear ruthenium(II) polypyridyl complexes. *Inorganica Chimica Acta* **2017**, *458*, 122–128.

[365] Luis, E. T.; Iranmanesh, H.; Arachchige, K. S. A.; Donald, W. A.; Quach, G.; Moore, E. G.; Beves, J. E. Luminescent tetrahedral molecular cages containing ruthenium(II) chromophores. *Inorganic Chemistry* **2018**, *57*, 8476–8486.

[366] Chen, M.; Wang, J.; Chakraborty, S.; Liu, D.; Jiang, Z.; Liu, Q.; Yan, J.; Zhong, H.; Newkome, G. R.; Wang, P. Metallosupramolecular 3D assembly of dimetallic $Zn_4[RuL_2]_2$ and trimetallic $Fe_2Zn_2[RuL_2]_2$. *Chemical Communications* **2017**, *53*, 11087–11090.

[367] Roche, S.; Haslam, C.; Heath, S. L.; Thomas, J. A. Self-assembly of a supramolecular cube. *Chemical Communications* **1998**, 1681–1682.

[368] Hauke, C. E.; Oldacre, A. N.; Fulong, C. R. P.; Friedman, A. E.; Cook, T. R. Coordination-driven self-assembly of ruthenium polypyridyl nodes resulting in emergent photophysical and electrochemical properties. *Inorganic Chemistry* **2018**, *57*, 3587–3595.

[369] Brown, R. T.; Fletcher, N. C.; Nieuwenhuyzen, M.; Keyes, T. E. The isolation and secondary functionalisation of the *mer*- and *fac*-isomers of tris(5-hydroxymethyl-2,2′-bipyridine) complexes of ruthenium (II). *Inorganica Chimica Acta* **2005**, *358*, 1079–1088.

[370] Predieri, G.; Vignali, C.; Denti, G.; Serroni, S. Characterization of *mer* and *fac* isomers of $[Ru(2,3{-}dpp)_3][PF_6]_2$ (2,3-dpp=2,3-bis(2-pyridyl)pyrazine) by ^1H and ^{99}Ru NMR spectroscopy. Proton assignment by 2D techniques. *Inorganica Chimica Acta* **1993**, *205*, 145–148.

[371] Fletcher, N. C.; Nieuwenhuyzen, M.; Rainey, S. The isolation and purification of tris-2,2′-bipyridine complexes of ruthenium(II) containing unsymmetrical ligands. *Journal of the Chemical Society, Dalton Transactions* **2001**, 2641–2648.

[372] Armstrong, E. A. P.; Brown, R. T.; Sekwale, M. S.; Fletcher, N. C.; Gong, X. Q.; Hu, P. The unexpected preference for the *fac*-isomer with the tris(5-ester-substituted-2,2′-bipyridine) complexes of ruthenium(II). *Inorganic Chemistry* **2004**, *43*, 1714–1722.

[373] Weizman, H.; Libman, J.; Shanzer, A. A novel template method for preparing unidirectional kinetically inert metal complexes. *Journal of the American Chemical Society* **1998**, *120*, 2188–2189.

[374] Rutherford, T. J.; Reitsma, D. A.; Keene, F. R. Stereochemistry in tris(bidentate ligand)ruthenium(II) complexes containing unsymmetrical polypyridyl ligands. *Journal of the Chemical Society, Dalton Transactions* **1994**, 3659–3666.

[375] Ward, M. D. Polynuclear coordination cages. *Chemical Communications* **2009**, 4487–4499.

[376] Fleming, J. S.; Mann, K. L. V.; Couchman, S. M.; Jeffery, J. C.; McCleverty, J. A.; Ward, M. D. Double-helical dinuclear copper(I) and mononuclear copper(II) complexes of a compartmental tetradentate bridging ligand: crystal structures and spectroscopic properties. *Journal of the Chemical Society, Dalton Transactions* **1998**, 2047–2052.

[377] Stephenson, A.; Ward, M. D. A triple helix of double helicates: three hierarchical levels of self-assembly in a single structure. *Chemical Communications* **2012**, *48*, 3605–3607.

[378] Stephenson, A.; Ward, M. D. Coordination chemistry of Ag(I) with bridging ligands based on pyrazolyl-pyridine

termini: polymers, helicates and a bow-tie. *RSC Advances* **2012**, *2*, 10844–10853.

[379] Cullen, W.; Hunter, C. A.; Ward, M. D. An interconverting family of coordination cages and a *meso*-helicate; effects of temperature, concentration, and solvent on the product distribution of a self-assembly process. *Inorganic Chemistry* **2015**, *54*, 2626–2637.

[380] Fleming, J. S.; Mann, K. L. V.; Carraz, C.-A.; Psillakis, E.; Jeffery, J. C.; McCleverty, J. A.; Ward, M. D. Anion-templated assembly of a supramolecular cage complex. *Angewandte Chemie International Edition* **1998**, *37*, 1279–1281.

[381] Paul, R. L.; Bell, Z. R.; Jeffery, J. C.; McCleverty, J. A.; Ward, M. D. Anion-templated self-assembly of tetrahedral cage complexes of cobalt(II) with bridging ligands containing two bidentate pyrazolyl-pyridine binding sites. *Proceedings of the National Academy of Sciences of the United States of America* **2002**, *99*, 4883.

[382] Tidmarsh, I. S.; Taylor, B. F.; Hardie, M. J.; Russo, L.; Clegg, W.; Ward, M. D. Further investigations into tetrahedral M_4L_6 cage complexes containing guest anions: new structures and NMR spectroscopic studies. *New Journal of Chemistry* **2009**, *33*, 366–375.

[383] Al-Rasbi, N. K.; Sabatini, C.; Barigelletti, F.; Ward, M. D. Red-shifted luminescence from naphthalene-containing ligands due to π-stacking in self-assembled coordination cages. *Dalton Transactions* **2006**, 4769–4772.

[384] Paul, R. L.; Couchman, S. M.; Jeffery, J. C.; McCleverty, J. A.; Reeves, Z. R.; Ward, M. D. Effects of metal co-ordination geometry on self-assembly: a dinuclear double helicate complex and a tetranuclear cage complex of a new bis-bidentate bridging ligand. *Journal of the Chemical Society, Dalton Transactions* **2000**, 845–851.

[385] Paul, R. L.; Argent, S. P.; Jeffery, J. C.; Harding, L. P.; Lynam, J. M.; Ward, M. D. Structures and anion-binding properties of M_4L_6 tetrahedral cage complexes with large central cavities. *Dalton Transactions* **2004**, 3453–3458.

[386] Hall, B. R.; Manck, L. E.; Tidmarsh, I. S.; Stephenson, A.; Taylor, B. F.; Blaikie, E. J.; Griend, D. A. V.; Ward, M. D. Structures, host-guest chemistry and mechanism of stepwise self-assembly of M_4L_6 tetrahedral cage complexes. *Dalton Transactions* **2011**, *40*, 12132–12145.

[387] Hall, B. R.; Adams, H.; Ward, M. D. A family of tetrahedral coordination cages with different symmetries by assembly of bis-bidentate bridging ligands with first-row transition metal dications. *Supramolecular Chemistry* **2012**, *24*, 499–507.

[388] Bell, Z. R.; Harding, L. P.; Ward, M. D. Self-assembly of a molecular M_8L_{12} cube having S_6 symmetry. *Chemical Communications* **2003**, 2432–2433.

[389] Argent, S. P.; Adams, H.; Harding, L. P.; Ward, M. D. A closed molecular cube and an open book: two different products from assembly of the same metal salt and bridging ligand. *Dalton Transactions* **2006**, 542–544.

[390] Stephenson, A.; Ward, M. D. An octanuclear coordination cage with a 'cuneane' core - a topological isomer of a cubic cage. *Dalton Transactions* **2011**, *40*, 7824–7826.

[391] Stephenson, A.; Ward, M. D. Molecular squares, cubes and chains from self-assembly of bis-bidentate bridging ligands with transition metal dications. *Dalton Transactions* **2011**, *40*, 10360–10369.

[392] Bell, Z. R.; Jeffery, J. C.; McCleverty, J. A.; Ward, M. D. Assembly of a truncated-tetrahedral chiral $[M_{12}(\mu\text{-})L_8]^{24+}$ cage. *Angewandte Chemie International Edition* **2002**, *41*, 2515–2518.

[393] Argent, S. P.; Adams, H.; Riis-Johannessen, T.; Jeffery, J. C.; Harding, L. P.; Mamula, O.; Ward, M. D. Coordination chemistry of tetradentate N-donor ligands containing two pyrazolyl-pyridine units separated by a 1,8-naphthyl spacer: dodecanuclear and tetranuclear coordination cages and cyclic helicates. *Inorganic Chemistry* **2006**, *45*, 3905–3919.

[394] Al-Rasbi, N. K.; Tidmarsh, I. S.; Argent, S. P.; Adams, H.; Harding, L. P.; Ward, M. D. Mixed-ligand molecular paneling: dodecanuclear cuboctahedral coordination cages based on a combination of edge-bridging and face-capping ligands. *Journal of the American Chemical Society* **2008**, *130*, 11641–11649.

[395] Stephenson, A.; Sykes, D.; Ward, M. D. Cu_{12} and Cd_{16} coordination cages and their Cu_3 and Cd_3 subcomponents, and the role of inter-ligand π-stacking in stabilising cage complexes. *Dalton Transactions* **2013**, *42*, 6756–6767.

[396] Piper, J. R.; Cletheroe, L.; Taylor, C. G. P.; Metherell, A. J.; Weinstein, J. A.; Sazanovich, I. V.; Ward, M. D. Photoinduced energy- and electron-transfer from a photoactive coordination cage to bound guests. *Chemical Communications* **2017**, *53*, 408–411.

[397] Argent, S. P.; Jackson, F. C.; Chan, H. M.; Meyrick, S.; Taylor, C. G. P.; Ronson, T. K.; Rourke, J. P.; Ward, M. D. A family of diastereomeric dodecanuclear coordination cages based on inversion of chirality of individual triangular cyclic helicate faces. *Chemical Science* **2020**, *11*, 10167–10174.

[398] Whitehead, M.; Turega, S.; Stephenson, A.; Hunter, C. A.; Ward, M. D. Quantification of solvent effects on molecular recognition in polyhedral coordination cage hosts. *Chemical Science* **2013**, *4*, 2744–2751.

[399] Cullen, W.; Thomas, K. A.; Hunter, C. A.; Ward, M. D. pH-Controlled selection between one of three guests from a mixture using a coordination cage host. *Chemical Science* **2015**, *6*, 4025–4028.

[400] Turega, S.; Whitehead, M.; Hall, B. R.; Haddow, M. F.; Hunter, C. A.; Ward, M. D. Selective guest recognition by a self-assembled paramagnetic cage complex. *Chemical Communications* **2012**, *48*, 2752–2754.

[401] Turega, S.; Cullen, W.; Whitehead, M.; Hunter, C. A.; Ward, M. D. Mapping the internal recognition surface of an octanuclear coordination cage using guest libraries. *Journal of the American Chemical Society* **2014**, *136*, 8475–8483.

[402] Turega, S.; Whitehead, M.; Hall, B. R.; Meijer, A. J. H. M.; Hunter, C. A.; Ward, M. D. Shape-, size-, and functional group-selective binding of small organic guests in a paramagnetic coordination cage. *Inorganic Chemistry* **2013**, *52*, 1122–1132.

[403] Cullen, W.; Metherell, A. J.; Wragg, A. B.; Taylor, C. G. P.; Williams, N. H.; Ward, M. D. Catalysis in a cationic coordination cage using a cavity-bound guest and surface-bound anions: inhibition, activation, and autocatalysis. *Journal of the American Chemical Society* **2018**, *140*, 2821–2828.

[404] Taylor, C. G. P.; Piper, J. R.; Ward, M. D. Binding of chemical warfare agent simulants as guests in a coordination cage: contributions to binding and a fluorescence-based response. *Chemical Communications* **2016**, *52*, 6225–6228.

[405] Taylor, C. G. P.; Metherell, A. J.; Argent, S. P.; Ashour, F. M.; Williams, N. H.; Ward, M. D. Coordination-cage-catalysed hydrolysis of organophosphates: cavity- or surface-based? *Chemistry – A European Journal* **2020**, *26*, 3065–3073.

[406] Cullen, W.; Turega, S.; Hunter, C. A.; Ward, M. D. pH-dependent binding of guests in the cavity of a polyhedral coordination cage: reversible uptake and release of drug molecules. *Chemical Science* **2015**, *6*, 625–631.

[407] Metherell, A. J.; Cullen, W.; Stephenson, A.; Hunter, C. A.; Ward, M. D. *Fac* and *mer* isomers of Ru(II) tris(pyrazolylpyridine) complexes as models for the vertices of coordination cages: structural characterisation and hydrogen-bonding characteristics. *Dalton Transactions* **2014**, *43*, 71–84.

[408] Li, F.; Sciortino, N. F.; Clegg, J. K.; Neville, S. M.; Kepert, C. J. Self-assembly of an octanuclear high-spin Fe^{II} molecular cage. *Australian Journal of Chemistry* **2014**, *67*, 1625–1628.

[409] Yu, X. Y.; Deng, L.; Zheng, B.; Zeng, B. R.; Yi, P.; Xu, X. A spectroscopic study on the coordination and solution structures of the interaction systems between biperoxidovanadate complexes and the pyrazolylpyridine-like ligands. *Dalton Transactions* **2014**, *43*, 1524–33.

[410] Salinas Uber, J.; Vogels, Y.; van den Helder, D.; Mutikainen, I.; Turpeinen, U.; Fu, W. T.; Roubeau, O.; Gamez, P.; Reedijk, J. Pyrazole-based ligands for the [copper–TEMPO]-mediated oxidation of benzyl alcohol to benzaldehyde and structures of the Cu coordination compounds. *European Journal of Inorganic Chemistry* **2007**, *2007*, 4197–4206.

[411] Van der Made, A. W.; Van der Made, R. H. A convenient procedure for bromomethylation of aromatic compounds. Selective mono-, bis-, or trisbromomethylation. *Journal of Organic Chemistry* **1993**, *58*, 1262–1263.

[412] Zhou, L.-P.; Sun, Q.-F. A self-assembled Pd_2L_4 cage that selectively encapsulates nitrate. *Chemical Communications* **2015**, *51*, 16767–16770.

[413] Hartshorn, C. M.; Steel, P. J. Bis(3-(2-pyridyl)pyrazol-1-ylmethyl)benzenes: doubly-chelating binucleating ligands and encapsulation of a linear trisilver(I) moiety. *Inorganic Chemistry Communications* **2000**, *3*, 476–481.

[414] Stephenson, A.; Argent, S. P.; Riis-Johannessen, T.; Tidmarsh, I. S.; Ward, M. D. Structures and dynamic behavior of large polyhedral coordination cages: an unusual cage-to-cage interconversion. *Journal of the American Chemical Society* **2011**, *133*, 858–870.

[415] Armarego, W. L. F.; Chai, C. In *Purification of Laboratory Chemicals (Seventh Edition)*; Armarego, W. L. F., Chai, C., Eds.; Butterworth-Heinemann: Boston, 2013; Chapter 4, pp 103–554.

[416] Aragão, D.; Aishima, J.; Cherukuvada, H.; Clarken, R.; Clift, M.; Cowieson, N. P.; Ericsson, D. J.; Gee, C. L.; Macedo, S.; Mudie, N.; Panjikar, S.; Price, J. R.; Riboldi-Tunnicliffe, A.; Rostan, R.; Williamson, R.; Caradoc-Davies, T. T. MX2: a high-flux undulator microfocus beamline serving both the chemical and macromolecular crystallography communities at the Australian Synchrotron. *Journal of Synchrotron Radiation* **2018**, *25*, 885–891.

[417] Sheldrick, G. Phase annealing in *SHELX*-90: direct methods for larger structures. *Acta Crystallographica Section A: Foundations of Crystallography* **1990**, *46*, 467–473.

[418] Sheldrick, G. *SHELXT* - integrated space-group and crystal-structure determination. *Acta Crystallographica Section A: Foundations of Crystallography* **2015**, *71*, 3–8.

[419] Sheldrick, G. Crystal structure refinement with *SHELXL*. *Acta Crystallographica Section C: Crystal Structure Communications* **2015**, *71*, 3–8.

[420] Barbour, L. J. X-Seed - a software tool for supramolecular crystallography. *Journal of Supramolecular Chemistry* **2001**, *1*, 189–191.

[421] Dolomanov, O. V.; Blake, A. J.; Champness, N. R.; Schroder, M. OLEX: new software for visualization and analysis of extended crystal structures. *Journal of Applied Crystallography* **2003**, *36*, 1283–1284.

[422] Shao, Y.; Gan, Z.; Epifanovsky, E.; Gilbert, A. T. B.; Wormit, M.; Kussmann, J.; Lange, A. W.; Behn, A.; Deng, J.; Feng, X.; Ghosh, D.; Goldey, M.; Horn, P. R.; Jacobson, L. D.; Kaliman, I.; Khaliullin, R. Z.; Kuš, T.; Landau, A.; Liu, J.; Proynov, E. I.; Rhee, Y. M.; Richard, R. M.; Rohrdanz, M. A.; Steele, R. P.; Sundstrom, E. J.; Woodcock, H. L.; Zimmerman, P. M.; Zuev, D.; Albrecht, B.; Alguire, E.; Austin, B.; Beran, G. J. O.; Bernard, Y. A.; Berquist, E.; Brandhorst, K.; Bravaya, K. B.; Brown, S. T.; Casanova, D.; Chang, C. M.; Chen, Y.; Chien, S. H.; Closser, K. D.;

Crittenden, D. L.; Diedenhofen, M.; Distasio, R. A.; Do, H.; Dutoi, A. D.; Edgar, R. G.; Fatehi, S.; Fusti-Molnar, L.; Ghysels, A.; Golubeva-Zadorozhnaya, A.; Gomes, J.; Hanson-Heine, M. W. D.; Harbach, P. H. P.; Hauser, A. W.; Hohenstein, E. G.; Holden, Z. C.; Jagau, T. C.; Ji, H.; Kaduk, B.; Khistyaev, K.; Kim, J.; King, R. A.; Klunzinger, P.; Kosenkov, D.; Kowalczyk, T.; Krauter, C. M.; Lao, K. U.; Laurent, A. D.; Lawler, K. V.; Levchenko, S. V.; Lin, C. Y.; Liu, F.; Livshits, E.; Lochan, R. C.; Luenser, A.; Manohar, P.; Manzer, S. F.; Mao, S. P.; Mardirossian, N.; Marenich, A. V.; Maurer, S. A.; Mayhall, N. J.; Neuscamman, E.; Oana, C. M.; Olivares-Amaya, R.; Oneill, D. P.; Parkhill, J. A.; Perrine, T. M.; Peverati, R.; Prociuk, A.; Rehn, D. R.; Rosta, E.; Russ, N. J.; Sharada, S. M.; Sharma, S.; Small, D. W.; Sodt, A. Advances in molecular quantum chemistry contained in the Q-Chem 4 program package. **2015**,

[423] Cossi, M.; Rega, N.; Scalmani, G.; Barone, V. Energies, structures, and electronic properties of molecules in solution with the C-PCM solvation model. *Journal of Computational Chemistry* **2003**, *24*, 669–681.

[424] Tomasi, J.; Mennucci, B.; Cammi, R. Quantum mechanical continuum solvation models. *Chemical Reviews* **2005**, *105*, 2999–3094.

[425] Côté, J.-F.; Brouillette, D.; Desnoyers, J. E.; Rouleau, J.-F.; St-Arnaud, J.-M.; Perron, G. Dielectric constants of acetonitrile, γ-butyrolactone, propylene carbonate, and 1,2-dimethoxyethane as a function of pressure and temperature. *Journal of Solution Chemistry* **1996**, *25*, 1163–1173.

[426] Chiorescu, I.; Deubel, D. V.; Arion, V. B.; Keppler, B. K. Computational electrochemistry of ruthenium anticancer agents. unprecedented benchmarking of implicit solvation methods. *Journal of Chemical Theory and Computation* **2008**, *4*, 499–506.

[427] Alvarez, S. A cartography of the van der Waals territories. *Dalton Transactions* **2013**, *42*, 8617–8636.

[428] Chai, J.-D.; Head-Gordon, M. Systematic optimization of long-range corrected hybrid density functionals. *The Journal of Chemical Physics* **2008**, *128*, 084106.

[429] Chai, J.-D.; Head-Gordon, M. Long-range corrected hybrid density functionals with damped atom–atom dispersion corrections. *Physical Chemistry Chemical Physics* **2008**, *10*, 6615–6620.

[430] Kelly, S. M.; Price, N. C. The use of circular dichroism in the investigation of protein structure and function. *Current Protein & Peptide Science* **2000**, *1*, 349–384.